

NASA Contractor Report 182230

Thermal Barrier Coating Life Prediction Model Development

Phase I - Final Report

J.T. DeMasi, K.D. Sheffler and M. Ortiz
UNITED TECHNOLOGIES CORPORATION
Pratt & Whitney
Commercial Engine Business

December 1989

Prepared for
National Aeronautics and Space Administration

NASA Lewis Research Center
21000 Brookpark Road
Cleveland, Ohio 44135

Under Contract NAS3-23944



National Aeronautics and
Space Administration

(NASA-CR-182230) THERMAL BARRIER COATING
LIFE PREDICTION MODEL DEVELOPMENT, PHASE I
Final Report (PMA) 338 P CSCL 21F

63/07

UNCLAS
0252161

N90-13398

FOREWORD

The Final Report contained in this document covers the activities performed during Phase I of the NASA HOST Program, "Thermal Barrier Coating Life Prediction Model Development", under Contract NAS3-23944. The objective of this effort was to develop and verify Thermal Barrier Coating life prediction technology for gas turbine hot section components. The NASA program manager is Dr. Robert A. Miller. The program was conducted in the Pratt & Whitney Materials Engineering and Research Laboratory under the direction of Mr. H. A. Hauser. The Pratt & Whitney Project Manager was Dr. Keith D. Sheffler and the principal investigator was Jeanine DeMasi. Mr. Thomas Hajek served as the Analytical Manager and Mr. Milton Ortiz served as the analytical investigator and was responsible for analytical modeling efforts. A note of thanks to Mr. Frederick Kopper and Leon Matysuk for the analytical efforts made early in this program. A substantial portion of the modeling efforts and ceramic testing were conducted under subcontract at the Southwest Research Institute, San Antonio, Texas, under the direction of Dr. Thomas A. Cruse. Substantial program contributions in the areas of structural interpretation and test instrumentation were made by Mr. Neal P. Andersson, Mr. Merritt Wight, and Mr. Russell Shenstone. Special thanks to Mr. Raymond Skurzeuski, Mr. Claude Clavette, Mr. Donald Broadhurst, Mr. Frederick Wiese and Mr. Arnold LaPete for their efforts in specimen preparation and testing.

TABLE OF CONTENTS

<u>Section</u>	<u>Page</u>
1.0 SUMMARY	1
2.0 INTRODUCTION	3
3.0 PHASE I - FAILURE MODES ANALYSES AND MODEL DEVELOPMENT	5
3.1 Task I - Failure Mechanism Determination	6
3.1.1 Task IA Experimental Design	6
3.1.2 Task IB.1 Conduct Critical Experiments	13
3.1.2.1 Furnace Exposure Tests	13
3.1.2.1.1 Furnace Test Results and Microstructural Evaluation	17
3.1.2.2 Cyclic Thermal Exposure Tests	45
3.1.2.2.1 Cyclic Thermal Exposure Test Results	48
3.1.2.2.2 Microstructural Evaluation for Cyclic Thermal Exposure Tests	53
3.1.2.2.3 Fractional Exposure Burner Rig Test Results	77
3.1.2.3 Cyclic Hot Corrosion Tests	82
3.1.2.3.1 High Corrodent Level Test Results	87
3.1.2.3.2 Low Corrodent Level Test Results	96
3.1.2.3.3 Fractional Exposure Hot Corrosion Test Results	97
3.1.3 Task IB.2 Determine Physical/Mechanical Properties	107
3.1.3.1 Physical Property Tests	108
3.1.3.2 Preliminary Mechanical Testing	110
3.1.3.3 Southwest Research Institute Mechanical Test Program	112
3.1.3.3.1 Southwest Research Institute Test Results	117
3.1.3.3.1.1 Uniaxial Tension and Compression Test Results	117
3.1.3.3.1.2 Creep Behavior	124
3.1.3.3.1.3 Fatigue Behavior	126
3.1.3.3.1.4 Fracture Toughness	127
3.1.4 Task IC - Predominant Mode Determinations	128
3.1.4.1 Task IC.1 Develop Preliminary Life Prediction System	128
3.1.4.2 Task IC.2 Verification Tests	132
3.2 Task II - Major Mode Life Prediction Model	140
3.2.1 Task IIA - Experimental Design	140
3.2.2 Task IIB - Experiments/Analysis and Model Development	144
3.2.2.1 Cyclic Thermal Exposure Test Results and Microstructural Analysis	145
3.2.2.2 Advanced Life Prediction Model Development	167
3.3 Task III - Model Verification	181
3.3.1 Task IIIA Experimental Design	181
3.3.2 Task IIIB Verification Test/Analysis/Recommendations	182
3.3.2.1 Task IIIB Microstructural Evaluation	184

TABLE OF CONTENTS (Continued)

<u>Section</u>	<u>Page</u>
4.0 CONCLUSIONS	191
REFERENCES	193
APPENDICES	
A SUMMARY OF WEIGHT GAIN DATA FOR FURNACE EXPOSED SPECIMENS	196
B CYCLIC BURNER RIG TEST DETAILS	199
C CORROSION BURNER RIG TEST DETAILS	201
D EXPERIMENTAL PROCEDURES USED TO MEASURE PHYSICAL PROPERTIES	203
E STRESS - STRAIN AND CREEP CURVES FOR ALL MECHANICAL PROPERTY TESTS CONDUCTED AT SOUTHWEST RESEARCH INSTITUTE	204
F USER'S AND PROGRAMMER'S GUIDE TO TBCLIF	240
G TBCLIF LISTING AND EXAMPLE PROBLEM	258

LIST OF ILLUSTRATIONS

<u>Figure</u>	<u>Title</u>	<u>Page</u>
1	Thermal Barrier Coating System Microstructure	5
2	Typical Thermal Barrier Coating Engine Failure Mode	7
3	Task I Test Plan to Evaluate Thermal Barrier Coating Failure Life	14
4	Burner Rig Coating Evaluation Specimen	15
5	Task I Furnace Exposure Test Plan to Evaluate Thermal Barrier Coating Static Failure Life	16
6	Test Data Showing Thermal Exposure Atmosphere Effects on Coating Durability	19
7	Photomicrograph of Typical Furnace Tested Failed Coating	19
8	X-Ray Diffraction Results of Furnace Exposed Test Specimens	21
9	Light Photomicrograph of Post-Test Microstructure. Failed After Furnace Exposure in Air at 1149°C (2100°F) with 80 Hour Inspection Intervals (240 hrs/3 cycles)	23
10	Light Photomicrograph of Post-Test Microstructure. Furnace Exposure in Argon of 1149°C (2100°F) with 80 Hour Inspection Intervals (1040 hrs/13 Cycles)	23
11	Light Photomicrograph of Post-Test Microstructure. Failed After Furnace Exposure in Air at 1149°C (2100°F) with 10 Hour Inspection Intervals (160 hrs/16 cycles)	24
12	Light Photomicrograph of Post-Test Microstructure. Failed After Furnace Exposure in Air at 1204°C (2200°F) with 10 Hour Inspection Intervals (60 hrs/6 cycles)	24
13	Light Photomicrograph of Post-Test Microstructure After Furnace Exposure in Air (90 hrs/1149°C (2100°F)/1 cycle 60%)	25
14	Light Photomicrograph of Post-Test Microstructure After Fractional Furnace Exposure in Air (135 hrs/1149°C (2100°F)/1 cycle 90%)	25
15	Light Photomicrograph of Post-Test Microstructure After 150 Hr Fractional Exposure at 1149°C (2100°F) in Air	26
16a	Back Scatter Image of Post-Test Microstructure. Furnace Exposure in Argon at 1149°C (2100°F) for 1040 Hours (80 hour cycles - 13 cycles)	28

LIST OF ILLUSTRATIONS (Continued)

<u>Figure</u>	<u>Title</u>	<u>Page</u>
16 (b-c)	Back Scatter Images of Post-Test Microstructure. Furnace Exposure in Argon at 1149°C (2100°F) for 1040 Hours (80 hour cycles - 13 cycles)	29
16 (d-h)	Energy Dispersion Spectrographs for Elements Present at Various Locations Corresponding to Figure 16b. Argon Exposed 1149°C (2100°F) for 1040 Hours (80 hour cycles - 13 cycles)	30
17 (a-j)	Post-Test Microstructure. Furnace Exposure in Argon at 1149°C (2100°F) for 1040 Hours (80 hour cycles - 13 cycles)	31
18a	Back Scatter Image of Post-Test Microstructure. Furnace Exposure in Air at 1149°C (2100°F) for 240 Hours (80 hour cycles - 3 cycles)	36
18 (b-c)	Back Scatter Image of Post-Test Microstructure. Furnace Exposure in Air at 1149°C (2100°F) for 240 Hours (80 hour cycles - 3 cycles)	37
18 (d-g)	Energy Dispersion Spectrographs for Elements Present at Various Locations Corresponding to Figure 18b. Air Exposed 1149°C (2100°F) for 240 Hours (80 hour cycles - 3 cycles)	38
18 (h-k)	Energy Dispersion Spectrographs for Elements Present at Various Locations Corresponding to Figure 18b. Air Exposed 1149°C (2100°F) for 240 Hours (80 hour cycles - 3 cycles)	39
19 (a-j)	Back Scatter Image of Post-Test Microstructure. Furnace Exposure in Air at 1149°C (2100°F) for 240 Hours (80 hour cycles - 3 cycles)	40
20	Task I Clean Fuel Cyclic Burner Rig Test Program	45
21	Typical Burner Rig Cycle Thermocouple Data	46
22	Photomicrograph of Typical Burner Rig Failed Specimen	47
23	Test Data Showing Coating Life Dependent on Temperature, "Cyclic Content"	50
24	Test Data Showing Air Pre-Exposure Degrades Cyclic Life	51
25	Test Data Showing "INERT" Pre-Exposure Does Not Effect Coating Performance	52
26	Test Data Showing Ceramic Thickness Effects	52
27a	Light Photomicrograph of Baseline Pre-Test Microstructure (DI Test)	54

LIST OF ILLUSTRATIONS (Continued)

<u>Figure</u>	<u>Title</u>	<u>Page</u>
27b	Light Photomicrograph of Baseline Post-Test Microstructure (D1 Test) After 175 hrs at 1149°C (2100°F)/Short Cycle/Fast Heat-Up	54
28a	Light Photomicrograph of Baseline Pre-Test Microstructure (D2 Test)	55
28b	Light Photomicrograph of Baseline Post-Test Microstructure (D2 Test) After 435 hrs at 1094°C (2000°F)/Short Cycle/Fast Heat-Up Rate	55
29a	Light Photomicrograph of Baseline Pre-Test Condition (E Test)	56
29b	Light Photomicrograph of Baseline Post-Test Microstruture (E Test) After 142 hrs at 1149°C (2100°F)/Short Cycle Slow Heat-Up Rate	56
30a	Light Photomicrograph of Baseline Pre-Test Microstructure (F Test)	57
30b	Light Photomicrograph of Baseline Post-Test Microstruture (F Test) After 70 hrs at 1149°C (2100°F)/Long Cycle Fast Heat-Up Rate	57
31a	Light Photomicrograph of Pre-Burner Rig Microstructure (D1 Test) for Air Pre-Exposed Specimen 1149°C (2100°F)/40hrs)	58
31b	Light Photomicrograph of Post-Burner Rig Microstructure (D1 Test) for Air Pre-Exposed Specimen 1149°C (2100°F)/40 hrs) After 50 hrs at 2100°F/Short Cycle/Fast Heat-Up Rate	58
32a	Light Photomicrograph of Pre-Burner Rig Microstructure 56 (D2 Test) for Air Pre-Exposed Specimen 1149°C (2000°F)/100hrs)	59
32b	Light Photomicrograph of Post-Burner Rig Microstructure (D2 Test) for Air Pre-Exposed Specimen (1149°C (2100°F)/100 hrs) After 215 hrs at 1094°C (2000°F)/Short Cycle/Fast Heat-Up Rate	59
33a	Light Photomicrograph of Pre-Burner Rig Microstructure (E2 Test) for Air Pre-Exposed Specimen (1149°C (2100°F)/40 hrs)	60
33b	Light Photomicrograph of Post-Burner Rig Microstructure (E2 Test) for Air Pre-Exposed Specimen (1149°C (2100°F)/40 hrs) After 39 hrs at 1094°C (2000°F)/Short Cycle/Slow Heat-Up Rate	60

LIST OF ILLUSTRATIONS (Continued)

<u>Figure</u>	<u>Title</u>	<u>Page</u>
34a	Light Photomicrograph of Pre-Burner Rig Microstructure (F1 Test) for Air Pre-Exposed Specimen (1149°C (2100°F)/40 hrs)	61
34b	Light Photomicrograph of Post-Burner Rig Microstructure (F1 Test) for Air Pre-Exposed Specimen (1149°C (2100°F)/40 hrs) After 16 hrs at 2100°F/Long Cycle/Fast Heat-Up Rate	61
35a	Light Photomicrograph of Pre-Burner Rig Microstructure (D1 Test) for Argon Pre-Exposed Specimen (1149°C (2100°F)/40 hrs)	62
35b	Light Photomicrograph of Post-Burner Rig Microstructure (D1 Test) for Argon Pre-Exposed Specimens After 67 hrs at 1149°C (2100°F)/Short Cycle/Fast Heat-Up Rate	62
36a	Light Photomicrograph for Pre-Burner Rig Microstructure (D2 Test) for Argon Pre-Exposed Specimen (1094°C (2000°F)/100 hrs)	63
36b	Light Photomicrograph of Post Burner Rig Microstructure (D2 Test) for Argon Pre-Exposed Specimen (1094°C (2000°F)/100 hrs) After 708 hrs at 1094°C (2000°F)/Short Cycle/Fast Heat-Up Rate	63
37a	Light Photomicrograph for Pre-Burner Rig Microstructure (E Test) for Argon Pre-Exposed Specimen (1194°C (2100°F)/40 hrs)	64
37b	Light Photomicrograph of Post Burner Rig Microstructure (E Test) for Argon Pre-Exposed Specimen (1194°C (2100°F)/40 hrs) After Short Cycle/Slow Heat-Up Rate	64
38a	Light Photomicrograph for Pre-Burner Rig Microstructure (F Test) for Argon Pre-Exposed Specimen (1194°C (2100°F)/40 hrs)	65
38b	Light Photomicrograph of Post Burner Rig Microstructure (F Test) for Argon Pre-Exposed Specimen (1194°C (2100°F)/40 hrs) After Long Cycle/Fast Heat-Up Rate	65
39a	Light Photomicrograph of Pre-Test Microstructure (D1 Test) for a Thin Ceramic Specimen	67
39b	Light Photomicrograph of Post-Test Microstructure (D1 Test) for Thin Ceramic Specimen After 243 hrs at 1194°C (2100°F)/Short Cycle/Fast Heat-Up Rate	67
40a	Light Photomicrograph of Pre-Test Microstructure (D2 Test) for a Thin Ceramic Specimen	68

LIST OF ILLUSTRATIONS (Continued)

<u>Figure</u>	<u>Title</u>	<u>Page</u>
40b	Light Photomicrograph of Post-Test Microstructure (D2 Test) for a Thin Ceramic Specimen After 492 hrs at 1094°C (2000°F)/Short Cycle/Fast Heat-Up Rate	68
41a	Light Photomicrograph of Pre-Test Microstructure (E Test) for a Thin Ceramic Specimen	69
41b	Light Photomicrograph of Post Burner Rig Test Microstructure (E Test) for Thin Ceramic Specimen After 162 hrs at 1149°C (2100°F)/Short Cycle/Slow Heat-Up Rate	69
42a	Light Photomicrograph of Pre-Test Microstructure (F Test) for a Thin Ceramic Specimen	70
42b	Light Photomicrograph of Post Burner Rig Test Microstructure (F Test) for Thin Ceramic Specimen After 116 hrs at 1149°C (2100°F)/Long Cycle/Fast Heat-Up Rate	70
43a	Light Photomicrograph of Post Burner Rig Test Microstructure (D1 Test) for a Thick Ceramic Specimen	71
43b	Light Photomicrograph of Post Burner Rig Test Microstructure (D1 Test) for a Thick Ceramic Specimen After 160 Hrs at 1149°C (2100°F) Short Cycle/Fast Heat-Up Rate	71
44a	Light Photomicrograph of Pre-Test Microstructure (D2 Test) for a Thick Ceramic Specimen	72
44b	Light Photomicrograph of Post Burner Rig Test Microstructure (D2 Test) for Thick Ceramic Specimen After 454 hrs at 1149°C (2100°F)/Short Cycle/Fast Heat-Up Rate	72
45a	Light Photomicrograph of Pre-Test Microstructure (E Test) for a Thick Ceramic Specimen	73
45b	Light Photomicrograph of Post Burner Rig Test Microstructure (E Test) for a Thick Ceramic Specimen After 121 hrs at 1149°C (2100°F)/Short Cycle/Slow Heat-Up Rate	73
46a	Light Photomicrograph of Pre-Test Microstructure (F Test) for a Thick Ceramic Specimen	74
46b	Light Photomicrograph of Post Burner Rig Test Microstructure (F Test) for Thick Ceramic Specimen After 54 hrs at 1149°C (2100°F)/Long Cycle/Fast Heat-Up Rate	74

LIST OF ILLUSTRATIONS (Continued)

<u>Figure</u>	<u>Title</u>	<u>Page</u>
47	Thermal Barrier Coating Damage Progression	79
48	Back Scatter Image of Thermal Barrier Coating After 90 Hours of Burner Rig Test Time 1149°C (2100°F)/Short Cycle/Fast Heat-Up Rate	83
49	Back Scatter Image of Thermal Barrier Coating After 105 Hours of Burner Rig Test Time at 1149°C (2100°F)/Short Cycle/Fast Heat-Up Rate	84
50	Back Scatter Image of Thermal Barrier Coating After 105 Hours of Burner Rig Test Time at 1149°C (2100°F)/Short Cycle/Fast Heat-Up Rate	85
51	Back Scatter Image of Thermal Barrier Coating After 135 Hours of Burner Rig Test Time at 1149°C (2100°F)/Short Cycle/Fast Heat-Up Rate	86
52	Task I Hot Corrosion Test Program	87
53	Cyclic Hot Corrosion Test Specimen Showing Multi-level Flaking of the Ceramic	88
54a	Pre-Test Hot Corrosion Test Specimen; 35 ppm Artificial Sea Salt/ 899°C (1650°F)/1 Hour Cycle	89
54b	Post-Test Hot Corrosion Test Specimen Showing In-Plane Ceramic Cracking in Central and Upper Portion of Ceramic Layer After 693 hrs at 35 ppm Artificial Sea Salt/899°C (1650°F)/1 Hour Cycle	89
55a	Pre-Test Hot Corrosion Test Specimen; 35 ppm Artificial Sea Salt/899°C (1650°F)/1 Hour Cycle	90
55b	Post-Test Hot Corrosion Test Specimen After 1000 hrs at 35 ppm Artificial Sea Salt/899°C (1650°F)/1 Hour Cycle	90
56	Cyclic Hot Corrosion Test Specimen Surface (HST-086) After 450 Hrs/899°C/(1650°F) - High Corrodent Level Test	91
57	Cyclic Hot Corrosion Test Specimen After 450 Hrs at 899°C/(1650°F). High 35 ppm Corrodent Level in Area Near Failure.	92
58	Cyclic Hot Corrosion Post-Test Specimen After 1000 hrs at 899°C/(1650°F)/Long Cycle/35 ppm Artificial Sea Salt/1.3% SO ₃	94

LIST OF ILLUSTRATIONS (Continued)

<u>Figure</u>	<u>Title</u>	<u>Page</u>
59	Light Photomicrograph of Test Specimen After 1000 hrs at 899°C/(1650°F)/ Long Cycle/10 ppm Synthetic Sea Salt/1.3% SO ₃ - Condition J	97
60	Post Test Specimen Microstruture After 1000 hrs with Artificial Sea Salt 10ppm and 899°C/(1650°F) Host Test "J"	98
61	Post Test Specimen Microstruture After 1000 hrs with Artificial Sea Salt 10ppm and 899°C/(1650°F) Host Test "J"	99
62a	Post-Test Fractional (10% Life) Hot Corrosion Specimen Microstructure, 65 hrs/899°C/(1650°F)/35 ppm Na ₂ SO ₄	101
62b	Post-Test Fractional (20% Life) Hot Corrosion Specimen Microstructure, 130 hrs/899°C/(1650°F)/35 ppm Na ₂ SO ₄	101
62c	Post-Test Fractional (30% Life) Hot Corrosion Specimen Microstructure, 185 hrs/899°C/(1650°F)/35 ppm Na ₂ SO ₄	102
62d	Post-Test Fractional (40% Life) Hot Corrosion Specimen Microstructure, 250 hrs/899°C/(1650°F)/35 ppm Na ₂ SO ₄	102
62e	Post-Test Fractional (50% Life) Hot Corrosion Specimen Microstructure, 315 hrs/899°C/(1650°F)/35 ppm Na ₂ SO ₄	103
62f	Post-Test Fractional (60% Life) Hot Corrosion Specimen Microstructure, 380 hrs/899°C/(1650°F)/35 ppm Na ₂ SO ₄	103
62g	Post-Test Fractional (70% Life) Hot Corrosion Specimen Microstructure, 445 hrs/899°C/(1650°F)/35 ppm Na ₂ SO ₄	104
62h	Post-Test Fractional (80% Life) Hot Corrosion Specimen Microstructure, 510 hrs/899°C/(1650°F)/35 ppm Na ₂ SO ₄	104
62i	Post-Test Fractional (90% Life) Hot Corrosion Specimen Microstructure, 575 hrs/899°C/(1650°F)/35 ppm Na ₂ SO ₄	105
63	Bulk Ceramic Microstructure Used for Physical/Mechanical Property Tests	107
64	Bulk Four Point Bend Specimen Geometry	111
65a	Room Temperature Four Point Bend Test Results for Bulk Plasma Sprayed 7 w/o Y ₂ O ₃ - ZrO ₂	111
65b	Fracture Surface of Four Point Bend Test Specimen	112
66	Mechanical Property Test Plan for Bulk Ceramic	113

LIST OF ILLUSTRATIONS (Continued)

<u>Figure</u>	<u>Title</u>	<u>Page</u>
67	Compression Specimen	113
68	Compression Test Apparatus	114
69	Test Rig	114
70	Tensile Specimen Geometry	115
71	Tensile Test Apparatus	116
72	Wafer Specimen	116
73	Fatigue Stress Cycle	117
74	Representative Strain Tolerant Ceramic Tensile Stress Strain Curves at Various Temperatures. Room temperature strain data measured by strain gauge; temperature curves obtained from corrected cross head displacement.	121
75	In-plane Temperature Elevated Tensile Properties of Strain Tolerant Ceramic	122
76	Representative Strain Tolerant Ceramic Compressive Stress-Strain Curves at Various Temperatures. Compressive strains calculated from corrected crosshead displacement.	123
77	Typical Compressive Failure Mode	123
78	In-plane Elevated Temperature Compressive Properties of Strain Tolerant Ceramic	124
79	Stress Versus Creep Rate	125
80	Creep Rate Versus Temperature	126
81	S-N Curve for 7YSZ (538°C (1000°F) and 871°C (1600°F) data plotted together)	127
82	Axisymmetric Finite Element Model Breakup of Substrate, Bond Coat, and Thermal Barrier Coating	129
83	Ideally Inelastic Behavioral Model Used to Represent Ceramic Stress-Strain Behavior	130
84	Conceptual Model of Thermally Driven Ceramic Stress-Strain Cycle Under Initial Elastic/Perfect Plastic Model	131
85	Preliminary Life Model Correlation	132

LIST OF ILLUSTRATIONS (Continued)

<u>Figure</u>	<u>Title</u>	<u>Page</u>
86	Single Rotating, Internally-Cooled Tube Test Specimen Geometry	133
87	Predicted Cycles Versus Observed Cycles for the Task IC Verification Tests	134
88	Damage Versus Number of Cycles Showing All Three Verification Tests	135
89	Critical Oxide Thickness Ratio Versus Number of Cycles for the Three Verification Tests	135
90	(a) Post-Test Specimen After 105.87 Test Hours/524 Cycles, 12 Minute Burner Rig Cycle, Cooled I.D. (b) Post-Test Microstructure Near Spalled Area	137
91	(a) Post-Test Specimen After 88.37 Test Hours/884 Cycles, 6 Minute Burner Rig Cycle, Cooled I.D. (b) Post-Test Microstructure Near Spalled Area	138
92	(a) Post-Test Specimen After 138 Test Hours/686 Cycles, 12 Minute Burner Rig Cycle, Uncooled I.D. (b) Post-Test Microstructure Near Spalled Area	139
93	Task II Predictions: Oxide Thickness Ratio at Failure Versus Strain Ratio	141
94	2.5 cm (one-inch) Diameter Instrumented Specimen Design	142
95	Transient External Metal Temperature of the TBC Coated Specimen	143
96	Transient Metal Temperature Response During Initial Heat-Up	143
97	Transient TBC Temperature Response During Initial Heat-Up	144
98	Oxide Emphasis Test #1 Post-Test Specimen Microstructure	147
99	Oxide Emphasis Test #2 Post-Test Specimen Microstructure	148
100	Oxide Emphasis Test #3 Post-Test Specimen Microstructure	149
101	Oxide Emphasis Test #4 Post-Test Specimen Microstructure	150
102	Oxide Emphasis Test #5 Post-Test Specimen Microstructure	151
103	Oxide Emphasis Test #6 Post-Test Specimen Microstructure	152

LIST OF ILLUSTRATIONS (Continued)

<u>Figure</u>	<u>Title</u>	<u>Page</u>
104	Oxide Emphasis Test #7 Post-Test Specimen Microstructure	153
105	Oxide Emphasis Test #8 Post-Test Specimen Microstructure	154
106	Oxide Emphasis Test #9 Post-Test Specimen Microstructure	155
107	Oxide Emphasis Test #10 Post-Test Specimen Microstructure	156
108	Oxide Emphasis Test #11 Post-Test Specimen Microstructure	157
109	Oxide Emphasis Test #12 Post-Test Specimen Microstructure	158
110	Mixed Mode Oxide Emphasis Test #13 Post-Test Specimen Microstructure	159
111	Mixed Mode Oxide Emphasis Test #14 Post-Test Specimen Microstructure	160
112	Mixed Mode Oxide Emphasis Test #15 Post-Test Specimen Microstructure	161
113	Mixed Mode Oxide Emphasis Test #16 Post-Test Specimen Microstructure	162
114	Mixed Mode Oxide Emphasis Test #17 Post-Test Specimen Microstructure	163
115	Mixed Mode Oxide Emphasis Test #18 Post-Test Specimen Microstructure	164
116	Small Radius Test #19 Post-Test Specimen Microstructure	165
117	Small Radius Test #20 Post-Test Specimen Microstructure	166
117A	Drag Stress (k) in Thermal Barrier Coating Walker Model	168
118	Comparison of Uniaxial Tensile Data (Room Temperature) and Modified Walker Model Predictions	169
119	Comparison of Uniaxial Tensile Data 1094°C (2000°F) and Modified Walker Model Predictions	170
120	Comparison of Uniaxial Tensile Data and Compressive Data 538°C (1000°F) and Modified Walker Model Predictions	170
121	Comparison of Uniaxial Tensile Data and Compressive Data 1094°C (2000°F) and Modified Walker Model Predictions	171

LIST OF ILLUSTRATIONS (Continued)

<u>Figure</u>	<u>Title</u>	<u>Page</u>
122	Comparison of Uniaxial Tensile - Creep Data 982°C (1800°F) and and Modified Walker Model Predictions	171
123	Comparison of Uniaxial Tensile-Creep Data 982°C (1800°F) and Modified Walker Model Prediction	172
124	One-Dimensional Walker Model Prediction of Stress-Strain Cycle for Burner Rig Experiment at Cracking Location Just Above Interface in Ceramic	173
125	Predicted Stress-Strain Hysteresis Loop for Oxide Emphasis Loop for Oxide Emphasis Test #1	174
126	Predicted Stress-Strain Hysteresis Loop for Strain Emphasis Test #12	174
127	Predicted Stress-Strain Hysteresis Loop for Mixed Mode Test #16	175
128	Calculated vs Measured Oxidation Thickness for Burner Rig Specimens	176
129	Oxide Thickness Ratio Used in Life Correlation	177
129A	Predicted Stress Strain Hysteresis Loop Using Walker Model	178
130	Life Prediction Model Correlation Using Optimized Oxide Growth Rate Model: Calculated vs Experimental Cycle Life	179
131	Calculated vs Experimental Cycle Life Using Measured Oxide Thickness	180
132	Cyclic Life vs Inelastic Strain Range for Task II Tests	180
133	Time at Maximum Cycle Temperature vs Maximum Cycle Temperature for Task II Tests	181
134	Task II Verification Test Results Predicted Using the Advanced Model Correlation	183
135	Temperature vs Cycles to Failure for Task III Mixed Strain Emphasis Tests	185
136	HT-46 Strain Emphasis Burner Rig Verification Test #1	186

LIST OF ILLUSTRATIONS (Continued)

<u>Figure</u>	<u>Title</u>	<u>Page</u>
137	HT-66 Oxide Emphasis Burner Rig Verification Test #2	187
138	HT-49 Mixed Strain Emphasis Burner Rig Verification Test #3	188
139	HT-54 Mixed Strain Emphasis Burner Rig Verification Test #4	189
140	6-124-2 Strain Emphasis Quartz Lamp Heater Verification Test #5	190

LIST OF TABLES

<u>Table</u>	<u>Title</u>	<u>Page</u>
I	Nominal Composition of Program Materials	6
II	Evaluation of Engine Exposed PWA 264 Coated Components	11
III	Metallic and Ceramic Powder Analyses	15
IV	Low Pressure Plasma Spray Conditions	16
V	Air Plasma Spray Conditions	16
VI	Inspection Interval for Task 1B Furnace Tests	17
VII	Summary of Air and Argon Furnace Exposure Test Results	18
VIII	Metallographic Evaluation of Selected Furnace Exposure Specimens After Exposure	22
IX	Comparative Summary of Task 1B Burner Rig Test Results	48
X	Burner Rig Test Results	49
XI	X-Ray Diffraction Analysis of Some Representative Post-Test Specimens	75
XII	Fractional Exposure Test (Condition G) Results	78
XIII	Cyclic Hot Corrosion Test Results (Condition H) High Corrodent Level	88
XIV	Artificial Sea Salt Composition	96
XV	X-Ray Diffraction Analyses of Some Representative Cyclic Hot Corrosion Post-Test Specimens (High Corrodent Level)	96
XVI	X-Ray Diffraction Analyses of Some Representative Post-Test Specimens, Cyclic Hot Corrosion Test (Low Corrodent Level)	100
XVII	X-Ray Diffraction Analyses of Fractional Exposure, Cyclic Hot Corrosion Test Specimens	106
XVIII	Coating Property Tests	108
XIX	Thermal Conductivity of 7w/o $Y_2O_3-ZrO_2$	108
XX	Specific Heat of 7w/o $Y_2O_3-ZrO_2$	108
XXI	Thermal Expansion of 7w/o $Y_2O_3-ZrO_2$	109

LIST OF TABLES (Continued)

<u>Table</u>	<u>Title</u>	<u>Page</u>
XXII	The Thermal Conductivity of NiCoCrAlY	109
XXIII	The Specific Heat of NiCoCrAlY	109
XXIV	Thermal Expansion of NiCoCrAlY	110
XXV	Uniaxial Compression Property Test Data	118
XXVI	Uniaxial Tension Property Test Data	118
XXVII	Compression-Creep Property Test Data	119
XXVIII	Tension-Creep Property Test Data	119
XXIX	Fatigue Property Test Data	120
XXX	Fracture Mechanics Property Test Data	120
XXXI	Verification Test Results	134
XXXII	Task II Planned Test Matrix	141
XXXIII	Task II Experimental Results and New Model Predictions	146
XXXIV	Planned Conditions for Task III Experiments Model Verification Tests	182
XXXV	Task III Model Verification - Experimental and Projected Results	183

1.0 SUMMARY

The goals of this program were to identify and understand TBC failure modes, generate quantitative TBC life data, and develop and verify a TBC life prediction model.

The coating studied in this program is a two layer thermal barrier system incorporating a nominal 0.25mm (0.010 in) outer layer of seven weight percent yttria partially stabilized zirconia plasma deposited over an inner layer of highly oxidation resistant low pressure plasma sprayed NiCoCrAlY bond coating. This coating, designated PWA264, currently is in flight service on a number of stationary turbine components in Pratt & Whitney Commercial engines.

An initial review of experimental and flight service components indicated that the predominant mode of TBC failure involves thermomechanical spallation of the ceramic coating layer. This ceramic spallation involves the formation of a dominant crack in the ceramic coating parallel to and closely adjacent to the metal-ceramic interface.

Results from a laboratory test program designed to study the influence of various "driving forces" such as temperature, thermal cycle frequency, environment, coating thickness, etc. on ceramic coating spalling life suggest that bond coat oxidation damage at the metal-ceramic interface contributes significantly to thermomechanical cracking in the ceramic layer. Low cycle rate furnace testing in air and in argon clearly shows a dramatic increase in spalling life in a non-oxidizing environment. Elevated temperature pre-exposure of TBC specimens in air causes a proportionate reduction of cyclic thermal spalling life, whereas pre-exposure in argon does not.

Interrupted cyclic thermal exposure (burner rig) testing shows that thermomechanical ceramic spallation is a progressive damage mode. Subcritical microcrack link-up is proposed as the mode of failure. Initial metallographic observations shows major subcritical cracking initiating above the metal-ceramic interface and not at the bond-coat asperities which are inherent in the TBC system being studied. Since early experimental results showed that bond coat oxidation is a significant factor in the cyclic spalling life of the ceramic coating, it is assumed that this environmental driver magnifies the mechanical driving force due to thermal loading in the burner rig.

Mechanical property tests show that the bulk as-plasma sprayed 7w/o Y_2O_3 - ZrO_2 exhibits a highly non-linear stress-strain response in uniaxial tension and compression. Also, it was shown that this material exhibits a significant creep response. Low cycle fatigue characteristics observed over a narrow stress range indicate that stress levels above a critical stress threshold will result in rapid damage accumulation.

The life prediction model focuses on the two major damage modes identified in the laboratory testing described above. The first of these modes involves a mechanical driving force, resulting from cyclic strains and stresses caused by thermally induced and externally imposed loads. The second damage mode, based on the experimental results, is an environmental driving force which appears to be related to "oxidation damage" due to the in-service growth of a NiCoCrAlY oxide scale at the metal-ceramic interface.

Based on the apparently "mechanical" mode of ceramic failure, (near interfacial cracking), and on the difficulty in finding metallographic evidence of a direct physical link between the growing oxide scale and incipient cracking in specimens exposed to a relatively small fraction of expected life, it was elected to employ an existing phenomenological fatigue model (Manson - Coffin) as the basis for the TBC life model. In traditional form, this model relates cyclic inelastic strain range to number of cycles to fatigue failure. The model incorporates the environmental effect by modifying the mechanical driver in such a way as to reduce the apparent fatigue strength of the ceramic layer. The use of inelastic strain range as a damage driver for the ceramic coating layer is considered justified in view of the previously mentioned nonlinearity observed in constitutive tests conducted on strain tolerant ceramic material, including the observation of an open hysteresis loop in preliminary tests with reversed loading.

The mathematical form of the model shown below expresses a relationship between the number of cycles to spallation failure (N_f), cyclic inelastic strain range ($\Delta\epsilon_i$), and bond coat oxide accumulation.

$$(\Delta\epsilon_i / \Delta\epsilon_f)^b = N_f$$

where $\Delta\epsilon_i$ = Total cyclic inelastic strain range

$\Delta\epsilon_f$ = failure strain

N_f = Number of cycles to failure

b = Constant

$$\Delta\epsilon_f = \Delta\epsilon_{f0} (1 - \delta/\delta_c)^c + \Delta\epsilon_i (\delta/\delta_c)^d$$

where δ_c is the critical oxide thickness which will cause ceramic failure in a single thermal cycle. The static failure strain, $\Delta\epsilon_{f0}$, is the strain required to fail the ceramic in the absence of bond coat oxidation.

The failure strain, $\Delta\epsilon_f$, is a function of the inelastic strain and is reduced by the strain due to the oxide thickness ratio, δ/δ_c , where δ_c is the critical oxide thickness which will cause ceramic failure in a single thermal cycle. The static failure strain, $\Delta\epsilon_{f0}$, is the strain required to fail the ceramic in the absence of bond coat oxidation.

For a mission comprised of N cycles, the damage accumulated by cyclic inelastic strain and oxide growth will equal $1/N$. The Miner's Rule assumption is used in that failure of the TBC occurs when $\sum 1/N \geq 1.0$.

Using this model, results of twenty calibration tests conducted over a wide range of oxidative and strain range intensities were correlated to establish values of the constants b , c , d , $\Delta\epsilon_{f0}$, and δ_c . With one exception, the optimized constants correlated all of these results within a factor of ± 3 on calculated vs observed life. Results of six additional verification tests conducted at conditions which were substantially different from the twenty calibration tests also were predicted within a factor of ± 3 on life by the optimized equation.

2.0 INTRODUCTION

Ceramic coatings have been utilized in aircraft gas turbine engines for over twenty years, primarily as an add-on technique to increase the durability of already reliable coatings. More recently, thermal barrier coating has been used to protect selected high pressure turbine components as well as combustors and augmentors. For these early turbine applications, no specific design methodology was needed and coating lives (ceramic spalling resistance) were determined to be adequate based on experimental engine testing. Future applications for thermal barrier coatings, which emphasize performance improvement (as opposed to durability extension), will require more sophisticated design tools and lifetime prediction methods.

The objective of this program is to establish a methodology to predict thermal barrier coating life in an environment simulative of that experienced by gas turbine airfoils. Initial work was conducted to determine failure modes of thermal barrier coatings in the aircraft engine environment. Analytical studies then were coupled with appropriate physical and mechanical property determinations to derive a coating life prediction model for the dominant failure mode.

The program to accomplish these objectives is divided into two phases. Phase I (36 months) was directed towards identification and modeling of the predominant failure mode, including verification. This report includes all results from Phase I. Phase II (24 months) will adapt this model to a recently developed Electron Beam-Physical Vapor Deposited (EB-PVD) coating which has substantially improved performance compared with the plasma deposited coating investigated in Phase I. Specific technical tasks conducted to accomplish the Phase I program objectives are described below:

- o Task I - The objective of this task was to identify the relative importance of various TBC degradation and failure modes and to develop a preliminary life prediction model for further development in Phase II. Specific modes addressed included degradation resulting from static and cyclic thermal exposure and hot corrosion.
- o Task II - The objective of this task was to design, conduct and analyze experiments to obtain data for major mode life prediction model development. Design of the experiments was based on results of Task I. Test parameters were varied to cover the range of parameters anticipated in engine service of thermal barrier coated turbine components.
- o Task III - The validity of the model developed in Task II was assessed through a series of six approved benchmark engine mission simulation tests.

Phase II will include the following four technical tasks:

- o Task V - The objective of this task is to design and conduct experiments to determine physical and mechanical properties required for subsequent analytical and life modeling. Ceramic property test specimens will be fabricated by EB-PVD using the same parameters used to make the thermal barrier coating layer. For physical property test samples, EB-PVD ceramic thick specimens having a microstructure which most closely represents the thin ceramic microstructure that will be manufactured. Mechanical property tests will be conducted on the composite metal-ceramic system.

- o Task VI - The objective of this task is to evaluate the effects of bond coat oxidation and develop an empirical oxidation model based on quantification and characterization of the MCrAlY oxide scale developed during thermal exposure. Burner rig, cyclic furnace and static furnace tests will provide information concerning the effects and rate of oxidation of the metallic bond coat on ceramic spallation life. These tests will address the effects of thermal pre-exposure in oxidizing and non-oxidizing environments, critical oxide thickness and growth rate as a function of temperature, and provide information on progressive damage. Oxide growth rates and thicknesses will be determined through metallographic examination and quantitative analyses will be conducted to further characterize the oxide.
- o Task VII - The objective of this task is to develop a life prediction model for the EB-PVD ceramic coatings by adapting the life prediction system developed for plasma sprayed coatings in Phase I of this program. The approach involves generation and correlation of design data, incorporation of a constitutive bond coat model and employment of a more accurate bond coat oxide growth model. Property test data will be used to enhance the analytical understanding of the thermal barrier coating behavior.
- o Task VIII - The objective of this task is to fully challenge the life prediction model developed for EB-PVD ceramic coatings. Experiments designed to test the model's validity will expose specimens to a maximum of 1000 hours at simulated engine conditions. The experiments will emphasize strain, oxide and mixed modes so that the model will account for singular and synergistic degradation modes. Life prediction analyses will be conducted to evaluate the results of the experiments and the validity of the model will be judged according to how closely the model predicts TBC life for each engine simulation test. Recommendations for further research or refinement required to arrive at a satisfactory engine life prediction methodology for EB-PVD ceramic coatings shall be made, if necessary.

ORIGINAL PAGE
BLACK AND WHITE PHOTOGRAPH
3.0 PHASE I - FAILURE MODES ANALYSES AND MODEL DEVELOPMENT

The objectives of this phase were to identify thermal barrier coating degradation modes which lead to coating failure, determine the relative importance of these degradation modes in aircraft engine applications, and develop and verify a life prediction model for the predominant mode of engine failure of thermal barrier coatings.

These objectives were accomplished in three tasks. The objective of the first task was to identify and determine the relative importance of TBC failure modes, including development and verification of a preliminary correlative life prediction model for the predominant mode of failure. The objective of the second task was to refine the model developed in Task I, including generation of a substantial body of experimental failure data for model calibration. Additional data was generated in the third task to verify the optimized model developed in Task II.

The thermal barrier coating evaluated in Phase I is designated PWA 264. It consists of an air plasma sprayed 7 w/o Y_2O_3 - partially stabilized ZrO_2 outer layer and a low pressure chamber sprayed metallic inner layer. The ceramic layer is nominally $0.25 \pm 0.05mm$ (0.010 ± 0.002 inches) thick, and is approximately 80% dense. The NiCoCrAlY layer is nominally fully dense and is $0.13 \pm 0.03mm$ (0.005 ± 0.001 inches) thick with surface roughness: 158-178 AA. The TBC coating system is shown in Figure 1. The substrate alloy used in Phase I is equiaxed B1900+Hf, designated PWA 1455. Its composition as well as the NiCoCrAlY bond coat composition are shown in Table I.

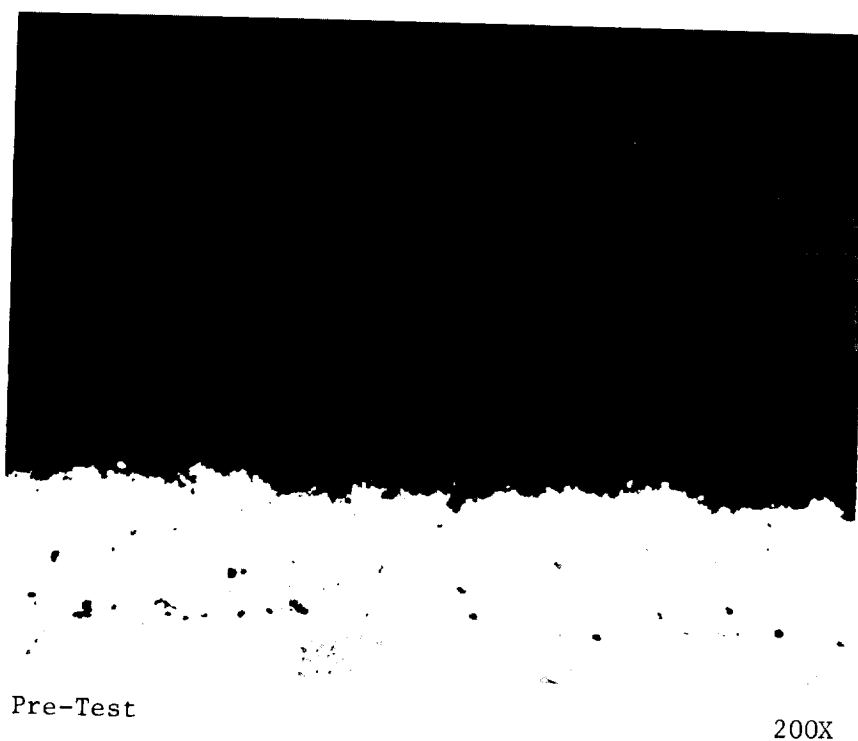


Figure 1 Thermal Barrier Coating System Microstructure

TABLE I
NOMINAL COMPOSITION OF PROGRAM MATERIALS
(Weight Percent)

	Ni	Co	Cr	Al	Mo	Ta	Hf	Ti	B	C	Y
PWA 1455	Remainder	10.0	8.0	6.0	6.0	4.25	1.15	1.0	0.015	0.1	-
PWA 1376	Remainder	22	18	12	-	-	-	-	-	-	0.4

3.1 Task I - Failure Mechanism Determination

The objectives of this task were to identify thermal barrier coating degradation modes which lead to coating failure, determine the relative importance of these modes in aircraft engine applications, and develop and verify a preliminary correlative life prediction model for the predominant failure mode.

The approach to accomplish these objectives included an initial review of the thermal barrier coating literature and of Pratt & Whitney engine experience with thermal barrier coated turbine components to identify potential modes of thermal barrier coating degradation and to determine which of these modes appear to predominate in engine service (Task IA). Results were used to establish a laboratory simulative engine test program (Task IB). Results of this test program were used to critically assess the relative importance of various degradation modes as they relate to coating service life. Also included in Task IB was a subtask to measure physical and mechanical properties of coating system materials which were required for analytical modeling and preliminary correlative life prediction system development which was conducted in the first part of Task IC. This effort was followed by additional laboratory testing to verify the preliminary model and to provide a basis for model refinement in Task II.

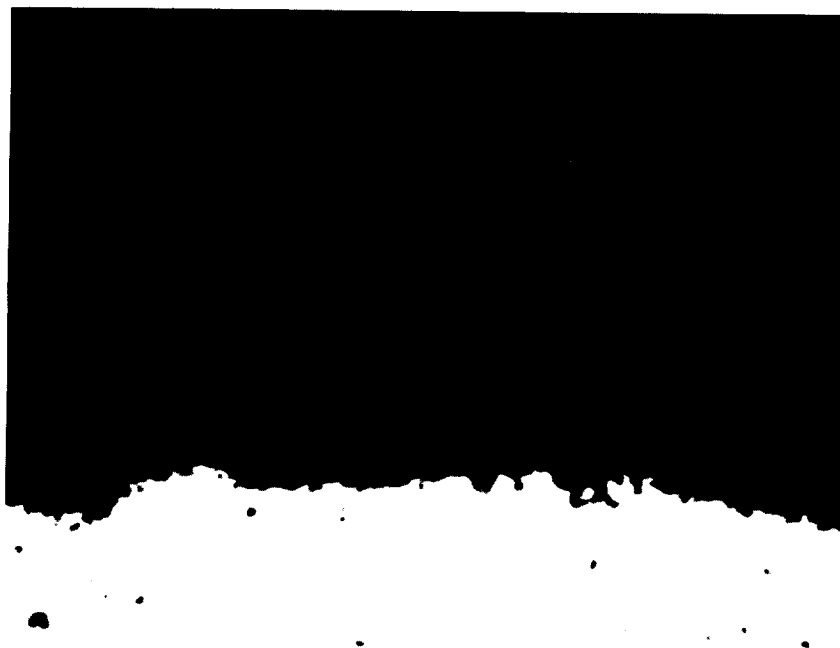
3.1.1 Task IA- Experimental Design

The objectives of this subtask were to review the TBC literature and Pratt & Whitney experience with thermal barrier coated turbine components, and based on this review, to establish an experimental program to determine the relative importance of various TBC degradation mechanisms as they relate to coating service life.

Early work on thermal barrier coatings described numerous material and process developments and identified several potential degradation and failure modes (Refs. 1-14). These modes included thermomechanically induced structural failure of the ceramic coating layer, oxidative degradation of the underlying metallic bond coating, thermochemically (hot corrosion) induced ceramic degradation, foreign object damage (FOD), and erosion.

ORIGINAL PAGE
BLACK AND WHITE PHOTOGRAPH

Examination of experimental and flight serviced engine components indicates the first of these degradation modes to be the predominant cause of coating failure, resulting in spallation of the ceramic coating layer due to formation of a dominant crack in the ceramic parallel and adjacent to the metal-ceramic interface (Figure 2). Laboratory test results reported in the literature suggest that this thermomechanical spallation mode is accelerated by time/temperature dependent interfacial oxidation of the metallic bond coat (Refs. 15-16). The examination of engine exposed components indicates that hot corrosion, FOD, and erosion do not represent life-limiting modes of degradation in engine service. Based on these observations, an experimental program was designed to separately assess and quantify the relative contributions of mechanical and oxidation degradation to TBC failure. While hot corrosion was not identified as a major failure mode in commercial engine service, experimental tests were included in the program to identify the threshold contaminant level for corrosion damage, thus providing a basis for prediction of flight environments where this degradation mode might be important. Details of findings from the literature and engine component review and of the experimental program designed to assess critical mode importance, are provided in the following paragraphs.



200X

Figure 2 Typical Thermal Barrier Coating Engine Failure Mode

In reviewing the available literature, laboratory data, and engine hardware, there was general agreement that the major TBC failure mode is thermomechanical ceramic coating spallation due to dominant crack propagation parallel to but not coincident with the ceramic-metal interface. Crack driving forces are presumed due to thermal expansion differences between the ceramic and metal components of the system, with the coefficient of thermal expansion of the ceramic being significantly lower than that of the underlying metallic system. It is also hypothesized that the stresses resulting from thermal expansion mismatch during thermal cycling are augmented by oxidation of the NiCoCrAlY bond coat, which has an irregular roughened surface topology (Refs. 15, 16, 17, 18). Miller and Lowell (see Ref. 15) were the first to discuss the role of the irregular bond coat/ceramic interface on oxidation related failure.

Despite the observation that the predominant thermal barrier coating failure mode involves thermomechanical spalling, resulting from thermal cycle induced stresses, some laboratory evidence exists which indicates a time and environmental dependence of the mechanical failure mode. Early evidence of time dependence was provided by McDonald & Hendricks (Ref. 19). They showed, at least for some compositions, a substantial decrease in the number of thermal-cycle caused ceramic spallation failures as cycle duration increased from 7 minutes to 60 minutes. Similar results have been obtained at Pratt & Whitney. Gedwill (Ref. 20) confirmed this effect with a more durable coating of similar composition. Miller & Lowell (see Ref. 15) postulated time dependent changes of "stress-free temperature," resulting from time dependent bond coat flow, as being responsible at least in part for interaction between thermal exposure and thermal cycling effects, but also noted that exposure in an oxidizing atmosphere was much more damaging than exposure on a non-oxidizing environment. Early results from Pratt & Whitney also indicate a cyclic life reduction for both oxidizing and non-oxidizing pre-exposure, with the oxidizing atmosphere being much more deleterious. A preliminary thermal barrier coating oxidation/thermal stress life prediction model has been proposed by Miller (see Ref. 18).

Andersson (Ref. 21) analyzed the stresses of typical thermal barrier coated heat engine components and found that the stresses are tensile in directions parallel to metal-ceramic interface for elevated temperature steady state operating conditions and during the cool down portion of the cycle, and in tangential compression during the heat-up portion of the cycle.

The stresses induced in coatings are hypothesized to be dependent not only on material properties but also heat flux or degree of thermal loading. The latter was addressed by Miller and Berndt (Ref. 22). They reported that "good" ZrO_2 -8 w/o Y_2O_3 coatings have remarkable tolerance to an extremely high heat flux plasma torch test.

The geometry of the component and the coating thickness are also important life variables. For thinner coatings (≤ 0.125 mm (0.005 in)), the stresses due to temperature gradients in the coating have been shown to be less severe so that increased service life can be expected (Ref. 23). Normal stresses are introduced in the coating of a curved surface by the tangential compressive stresses present resulting in ceramic spallation. In coated airfoil applications this is seen at the leading and trailing edges where the convex radii of curvature are minimized. (It should be noted that even a flat surface would have radial stresses due to surface roughness.)

Ceramic thermal stability is an important characteristic effecting coating life. Thermal stability refers to the ability of the ceramic layer to endure prolonged high temperature exposure without the occurrence of damaging morphological, chemical, or phase changes. Ceramic sintering is a thermally activated processes which can also limit cycle life. However, it has not been observed in laboratory/engine testing. Phase studies have determined that the presence of large amounts of monoclinic phase correlate to poor performing coatings (Refs. 24,25,26 also Ref 8).

Room temperature x-ray diffraction studies of 7YSZ coatings indicate a two phase structure consisting primarily of the cubic and metastable tetragonal phases together with 0 to 5% monoclinic. Because of the extremely rapid cooling rates associated with deposition of the ceramic coating layer, the tetragonal phase formed in the coating contains a relatively high percentage of Y_2O_3 , and is not readily transformed to monoclinic. With prolonged exposure at elevated temperature in the cubic plus tetragonal phase field, yttrium diffusion occurs and the high Y_2O_3 tetragonal phase transforms to cubic plus low Y_2O_3 tetragonal, with the low Y_2O_3 tetragonal phase being readily transformed to monoclinic upon cooling (Refs. 24, 25, see also Ref. 27).

Stecura (28) studied TBC systems and hypothesized that compositional changes in various bond coats and substrates play a more important role in coating durability than does the coefficient of thermal expansion of the substrate material. It was hypothesized that yttrium, aluminum and chromium in the bond coat critically affect the TBC life. Aluminum, chromium and yttrium oxides are formed at the interface during thermal testing. Yttrium diffuses toward the bond coat-ceramic interface, chromium diffuses towards the substrate and molybdenum into the bond coat. These events are considered to have an adverse effect on coating life. It has been shown that yttria in the bond coat moves coating failure location from the bond coat-substrate interface to just above the ceramic-bond coat interface (see Ref. 16). It is hypothesized that the location of major crack initiation, whether within the bond coat oxide layer or in the ceramic, is dependent on the stress state at the roughened interface which is at the very least changed by oxide growth.

Other degradation modes noted in several studies include secondary failure modes i.e., hot corrosion, erosion, FOD. Results from several laboratories (Refs. 29-34) have demonstrated an apparent susceptibility of thermal barrier coatings to fail in hot corrosion environments. The responsible mechanism appears to involve infiltration of the porous ceramic with liquid corrodent deposited on the coating surface at intermediate exposure temperatures and subsequent "mechanical" spalling resulting from alternate freezing and thawing of the infiltrated corrodent (see Refs. 34,32,30,14).

Some evidence has been reported which supports "thermochemical" ceramic spallation in hot corrosion environments; i.e., the infiltrated (Na_2SO_4) reacts with the ceramic at high SO_3 partial pressures (Refs. 35,36, also Refs. 34,30), resulting in destabilization of ZrO_2 . This degradation is attributed to acid leaching of yttrium from the ceramic.

Thermal barrier coating degradation and failure modes and mechanisms observed in prior Pratt & Whitney laboratory tests were found to be in general agreement with analysis from the literature. The major mode of failure in PWA264 is spallation of the ceramic layer resulting from in-plane cracking adjacent to but not coincident with the metal-ceramic interface. Prior or concurrent bond coat oxidation appears to play a major role in cyclic thermal stress induced spallation cracking. The Task IB testing was designed to identify the relative importance of these two degradation modes and to provide the quantitative data required to develop a preliminary model to predict spalling life under varying exposure conditions.

While the Task IA study included reviews of TBC literature and prior laboratory experience, primary emphasis was placed on the evaluation of failure mode as observed on ground based experimental engine and field service exposed components. Engine exposed PWA 264 coated parts have been evaluated from the commercial engines; JT9D-7R4G2, -7R4D -7R4D1, 7R4E1, 7R4H and PW2037, and the military engines; F-100, ATEGG (F-100) and TF-30. Details of the reviewed parts are documented in Table II. Where available, components representing the unexposed coating in each of the engine exposed components also have been examined to identify changes which occurred in coating structure during engine test. Significant observations from this review of engine exposed components are as follows:

- a) Ceramic sintering was not observed in any case
- b) Oxidation of the low pressure chamber sprayed PWA276 bond coat contributed to coating failure to a lesser degree than as seen in the laboratory
- c) Coating failure due to oxidation of substandard, air plasma sprayed bond coat was a major life limiting factor found in PW2037 first vane platforms
- d) Geometry effects were considered to play a significant role in coating degradation.

Examination of numerous engine tested components indicated that thermal barrier failures are almost exclusively of the "thermomechanical" type shown in Figure 2. In only one case has engine component thermal barrier coating failure been attributable directly to bond coat oxidation alone. That particular failure occurred on a vane airfoil which was operated under unusually severe thermal conditions and was, for reasons of processing convenience, coated with an air sprayed bond coat.

TABLE II
EVALUATION OF ENGINE EXPOSED PWA 264 COATED COMPONENTS

Date	Engine Type	Part Name	Engine #	Operator	Material	Remarks
12/02/83	2037	1st Vane Paired Platform	X-666-1C	P&W	647/264 modified bond coat	265.89 hrs/1500 cycles endurance testing. APS/LPCS bond coat - APS severely oxidized. Spalling at A.P.S. - LPCS bond coat interface. Ceramic thick in some areas.
09/01/82	2037	1st Vane Platform N/C	X-664-1A			36.97 hrs/136 cycles endurance testing. Limited spallation of the ceramic on O.D. T.E., ceramic microstructure meets specifications.
09/01/82	2037	1st Vane Platform N/C	X-664-1A			36.97 hrs/136 cycles endurance testing. Limited spallation of the ceramic on O.D. T.E., ceramic microstructure meets specifications.
01/10/84	2037	1st Vane Paired Platform	X-662-6			Ceramic spallation on ID platform bond coat oxidation of the A.P.S. layer.
05/10/84	2034	1st Turbine Vane Platform	X-671-5		647/264	485 cycles limited ceramic spallation. Ceramic structure meets specification.
10/25/82	TF30	2nd Vane	P-559-4 1B		633/264	1000 F.H./2171 A/B squirts. Ceramic thickness; 0.4 - 0.5 mm (0.016 - 0.020 in). Spallation around most of C.V. side of airfoil, C.C. L.E. In plane cracking. Metal bond coat has thin oxide layer ceramic microstructure meets specifications.
10/25/82	TF30	2nd Vane	P-559-4 1B	P&W (FAA)	633/264	1000 F.H./2171 A/B squirts. Spallation at L.E.
01/17/83	F-100 (ATEGG)	1st Vane	P-686-2		1422/264	910 TAC cycles/53.7 hot time. Spallation at I.D. L.E. only; due to specimen geometry and thermal cycling stress. Coating structure meets specifications. Bond coat has very thin oxide layer.
01/17/83	F-100 (ATEGG)	1st Blade	P-686-2		1422/264	910 TAC cycles/53.7 hot time. Spallation at I.D. L.E. only due to specimen geometry and thermal cycling stress. Coating microstructure meets specifications. Bond coat has very thin oxide layer.
05/18/83	F100	1st Vane	-		1480/264 modified bond coat	2000 TAC cycles ceramic spalled L.E.; bond coat failures.
04/20/82	JT9D-7R4D	1st Vane Platform	X-491-45	P&W	647/264	246.9 hrs/1500 cycles spalled after engine run. Spalling location - corners of platforms. Ceramic structure meets specifications. Very thin oxide layer/thin Beta depleted zone. Some segmentation and in plane cracking in ceramic. *(Rec'd vacuum H.T./1079°C (1975°F) F/4 hrs.)

TABLE II (Continued)
EVALUATION OF ENGINE EXPOSED PWA 264 COATED COMPONENTS

Date	Engine Type	Part Name	Engine #	Operator	Material	Remarks
04/20/82	JT9D-7R4D	1st Vane Platform	X-491-45	P&W	647/264	246.9 hrs/1500 cycles spalled after engine run. Spalling location - corners of platforms. Ceramic structure meets specifications. Some segmentation and in plane cracking in ceramic. Ceramic thickness 0.4 - 0.45 mm (0.016 - 0.018 in.)
04/21/82	JT9D-7R4D	1st Vane Platform	X-491-45			Ceramic not distressed after engine run. Ceramic structure meets specifications (Rec'd Ar H.T./1079°C (1975°F)/4hrs). Ceramic thickness 0.20 mm (0.008 in.).
04/19/82	JT9D-7R4G2	Wide Chord 1st Vane Platform	X-579-29			FAA 1000 cycle Test (Bond Coat - A.P.S./L.P.C.S.) A.P.S. portion is severely oxidized. In plane cracking of the ceramic. Ceramic structure meets specification.
05/82	JT9D-7R4G2	Wide Chord 1st Vane Platform	X-579-29A			114 hrs./19 cycles, substantial spallation on OD/ID. Good ceramic porosity but layered in - plane cracking. Spallation due to oxidizable inclusions; ZrCN ₂ (Starck #5399 + Union Carbide 1365-1).
01/12/83	2037	1st Vane (Paired) Platform	X-666-1C			265.89 hrs/1500 cycles endurance testing. Limited spallation on O.D. T.E. and I.D.L.E. due to F.O.D. - (not apparent from microstructure). Spallation adjacent to areas where ceramic thickness 0.18 mm (0.007 in.). Some in plane cracking. A.P.S./L.P.C.S. bond layer-thick A.P.S. 0.13 mm (0.005 in.). Microstructure adjacent to spalled areas was acceptable.
01/07/83	2037	1st Vane Paired Platform/Airfoil coated also	X-667-1A		647/264 (modified bond coat)	325.3 hrs/1500 cycles endurance testing. Spallation on O.D.T.E. and I.D.L.E. (A.P.S./L.P.C. - bond coat) also hidden pressure airfoil. Metallic thickness specifications not met. Spallation - chipping documented as FOD. Some areas of thick ceramic.
01/12/83	2037	1st Vane Paired Platform/Airfoil coated also	X-667-1A			325.3 hrs/1500 cycles endurance testing. Spallation on O.D.T.E. and I.D.L.E. (A.P.S./L.P.C. - bond coat) also hidden pressure airfoil. Metallic thickness specifications not met. Spallation - chipping documented as FOD. Some areas of thick ceramic. Note: layer of engine debris
09/06/83	2037	1st Vane Paired Platform/Airfoil coated also	X-667-1A,B 2,3, X-670-2A			593.6 hrs/1947 cycles endurance testing. Spallation limited but did occur in bond coat at APS/LPCS bond coat interface due to bond coat oxidation. Some in plane cracking some cracking at bond coat - ceramic interface also ceramic thick in some areas. O.D., I.D., T.E. hidden pressure airfoil. FOD.
09/11/84	JT9D-7R4E1	1st Vane Platform	716102	Airbus A-310	264	2355 hrs/411 cycles coating looks excellent.
09/13/84	JT9D-7R4D	1st Vane Platform	709643	TW	264	227 hrs/868 cycles coating looks excellent.
5/1/85	JT9D-7R4D	1st Vane	708603	SR	264	9300 hrs/2328 cycles coating looks excellent.
10/25/85	JT9D-7R4D1	1st Vane Platform	707714	SR	264	4978 hrs/4109 cycles coating looks excellent.

3.1.2 Task IB. 1 Conduct Critical Experiments

The objective of this subtask was to conduct a series of critical experiments and tests designed in Task IA to determine the relative importance of various thermomechanical and thermochemical coating degradation modes. Failure life data from these tests was also used to develop a preliminary life prediction model in Task IC. The test program included clean fuel and salted burner rig tests as well as static furnace testing of thermal barrier coated specimens to establish the relative importance of thermal stress cycling versus thermal and thermochemical degradation in determining thermal barrier coating life. The overall Task I test plan is shown in Figure 3.

The specimen used for all static and cyclic exposure testing in this subtask is illustrated in Figure 4. For cyclic burner rig testing, this specimen was thermal barrier coated on all surfaces except for the butt end, where coating was optional but not required. For static furnace exposure testing, the application of a tapered coating to only the cylindrical portion of the bar was employed to minimize the possibility of premature coating failure at the edge of the ceramic layer.

Prior to use in this task, all raw materials were thoroughly characterized and tested to ensure acceptability. Table III presents ceramic and metallic powder analysis which include: chemistry, particle size distribution and x-ray diffraction results.

Following raw material qualification, all burner rig standard erosion bars used in Task I testing were LPCS with NiCoCrAlY metallic bond coat (AMI Lot No. 6192). Low pressure chamber spray conditions and parameters are presented in Table IV. Sample tip sections were taken from selected specimens from each batch of bars for verification of thickness and microstructure.

The test bars were air plasma sprayed with $ZrO_2-7w/o\ Y_2O_3$. Air plasma spray deposition parameters are given in Table V. A statistical program designed to randomize coating sequence, and hence any uncontrolled variability of deposition parameters, was used to coat and select test bars.

To document uniformity of structure, a pre-test sample was obtained from every specimen tested in this program. Selected samples (about 10%) were examined metallographically using a statistically designed selection plan. The balance of the samples remained available for metallographic examination if needed.

3.1.2.1 Furnace Exposure Tests

These tests were performed to determine the influence of static thermal exposure on TBC degradation and failure. Specimens were furnace exposed at two temperatures for various times in various combinations of oxidizing and non-oxidizing environments as shown in Figure 5 and described below. Baseline tests designated "A" were conducted at 1149°C (2100°F) in oxidizing and non-oxidizing environments. These tests involved furnace exposure of two thermal barrier coated specimens per test condition for times sufficient to cause failure of the ceramic coating. Failure in this context is defined as development of "delamination" cracking over a significant area. In order to observe delamination damage, specimens were infrequently cycled to room temperature. Cycle frequency/inspection intervals are presented in Table VI.

T E M P E R A T U R E °C (°F)	EXPOSURE		STATIC		CYCLIC		FRACTIONAL EXPOSURE					
	TEST		FURNACE		BURNER RIG		FURNACE		BURNER RIG			
	ATMOSPHERE		OXIDIZING	NON-OXIDIZING	OXIDIZING	HOT CORROSION	OXIDIZING	NON-OXIDIZING	OXIDIZING	HOT CORROSION		
	CYCLE LENGTH				SHORT	LONG			SHORT	LONG		
	HEATING RATE				F S A T	L O W			F S A T	L O W		
	CORRODENT LEVEL						LOW	HIGH			LOW	HIGH
899 (1650)							J	H				K
1094 (2000)					D ₂							
1149 (2100)			A ₁	A ₂	D ₁	E F		C		G		
1204 (2200)			B									

CYCLIC OXIDATION BURNER RIG TEST SPECIMEN SET FOR CONDITIONS D1, D2, E & F-12 SPECIMENNS PER TEST

CERAMIC
COATING
THICKNESS

NUMBER OF TEST BARS	THICKNESS
4	0.25mm (0.010 in) AS-SPRAYED CERAMIC ("BASELINE" COATING)
2	0.13mm (0.005 in) AS-SPRAYED CERAMIC
2	0.38mm (0.015 in) AS-SPRAYED CERAMIC
2	0.25mm (0.101 in) AIR PRE-EXPOSED FOR APPROXIMATELY ½ ESTIMATED BURNER RIG HOT TIME LIFE
2	0.25mm (0.010 in) Ar PRE-EXPOSED FOR APPROXIMATELY ½ ESTIMATED BURNER RIG HOT TIME LIFE

SHORT: 6 MINUTE CYCLE = 4 MINUTES IN THE FLAME + 2 MINUTES FORCE AIR COOLED

LONG: 60 MINUTE CYCLE = 57 MINUTES IN THE FLAME + 3 MINUTES FORCE AIR COOLED

CYCLE RATE

FAST: NOMINAL 60 SECOND HEAT-UP TO MAXIMUM TEMPERATURE

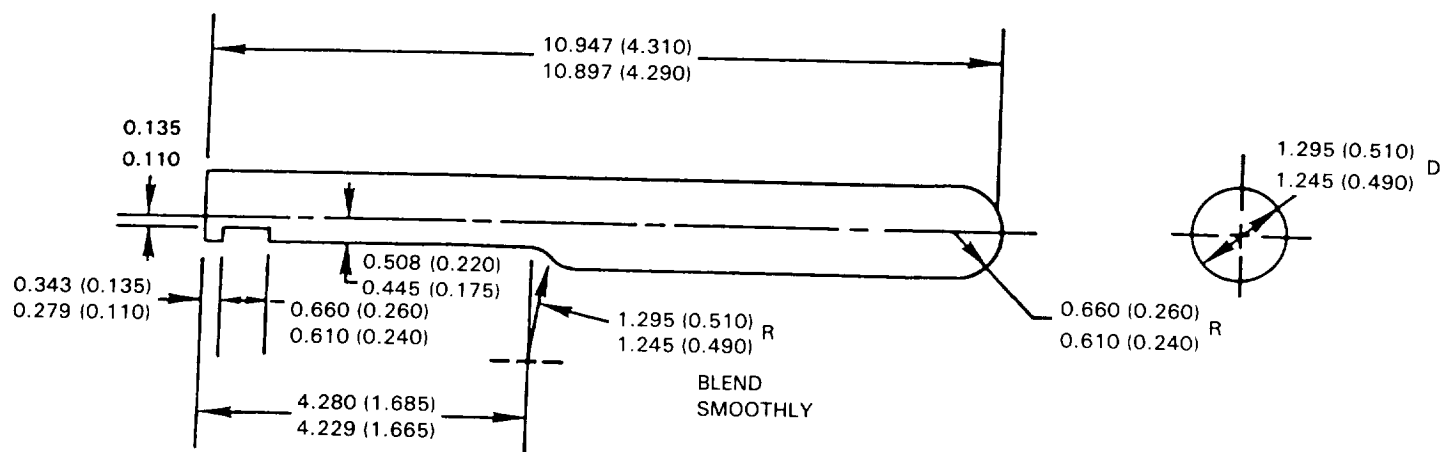
SLOW: NOMINAL 180 SECOND HEAT-UP TO MAXIMUM TEMPERATURE

CORRODENT LEVEL

LOW: 10 PPM % SYNTHETIC SEA SALT

HIGH: 35 PPM % SYNTHETIC SEA SALT

Figure 3 Task I Test Plan to Evaluate Thermal Barrier Coating Failure Life



ALL DIMENSIONS SHOWN IN CM (INCHES)

Figure 4 Burner Rig Coating Evaluation Specimen

TABLE III
METALLIC AND CERAMIC POWDER ANALYSES

Material	Chemical Analysis	Particle Size Analysis	
		Cumulative % Finer	Microns
NiCoCrAlY (Alloy Metals Lot #6192)	21.60 w/o Co	100	176
	17.50 w/o Cr	100	125
	13.00 w/o Al	100	88
	0.66 w/o Y	100	62
	Bal. - Ni	93	44
		72.2	31
		41.5	22
		21.9	16
		11.8	11
		5.5	7.8
		2.3	5.5
		0.7	3.9
		0.0	2.8
7 w/o Y ₂ O ₃ -ZrO ₂ 176 (Zircoa Lot #30656)	7.2 w/o Y ₂ O ₃	100%	
	1.7 w/o HfO ₂	94.7%	125
	0.1 w/o CaO	86.1%	88
	0.2 w/o TiO ₂	63.7%	62
	0.1 w/o Fe ₂ O ₃	39.4%	44
	0.3 w/o Al ₂ O ₃	29.0%	31
	Bal. -ZrO ₂	11.8%	22
		5.3%	16
		2.7%	11
		1.3%	7.8
		0.5%	5.5
		0.5%	3.9
		0%	2.8

X-RD Results

80-85 v/o fcc ZrO₂
20-15 v/o monoclinic ZrO₂

TABLE IV
LOW PRESSURE PLASMA SPRAY CONDITIONS

Standard erosion bar specimens coated using an Electroplasma High Energy Gun.

Gun Voltage (V)	58
Gun Current (A)	1500
Standoff	38.1 cm (15 in)
Workpiece Temperature	816 - 927°C (1500-1700°F)

Helium and Argon arc gases used

TABLE V
AIR PLASMA SPRAY CONDITIONS

Standard erosion bar specimens coated using a Plasmadyne SG-100 Gun.

Gun Voltage (V)	42
Gun Current (A)	900
Standoff	7.62 cm (3 in)
Workpiece Temperature	260°C (500°F)

Helium and Argon arc gases used.
He = 32 SCFH (100 psig) 0.91 m³/hr
Ar = 106 SCFH (50 psig) 3.0 m²/hr

TEMPERATURE °C (°F)	OXIDIZING ATMOSPHERE		NON-OXIDIZING ATMOSPHERE	
	STATIC FAILURE	FRACTIONAL EXPOSURE	STATIC FAILURE	FRACTIONAL EXPOSURE
HIGH 1204 (2200)	① B	②	③	④
INTERMEDIATE 1149 (2100)	⑤ A ₁	⑥ C	⑦ A ₂	⑧

MINIMUM OF TWO (2) COUPONS PER BLOCK


TEST CONDITIONS SHOWN THUS:  NOT TO BE EVALUATED

Figure 5 Task I Furnace Exposure Test Plan to Evaluate Thermal Barrier Coating Static Failure Life

TABLE VI
INSPECTION INTERVALS FOR TASK IB FURNACE TESTS

Test Code	Condition	Inspection Interval
A1.A	1149°C (2100°F)/Air	10 hrs.
A1.B	1149°C (2100°F)/Air	80 hrs.
A2	1149°C (2100°F)/Argon	80 hrs.
B	1204°C (2200°F)/Air	10 hrs.

Examination involved visual observation to detect areas of delaminated ceramic. To determine the influence of temperature on static coating failure life in air, an additional furnace exposure test designated "B" was conducted at 1204°C (2200°F). To evaluate progressive damage accumulation, a fractional exposure test designated "C" was conducted in the oxidizing environment at 1149°C (2100°F).

This fractional exposure test involved metallographic examination of specimens successively removed at approximate decile fractions of the "static failure" life as defined in the corresponding "A" test. The primary goal of the examination was to find evidence of incipient delamination cracking; in addition, specimens were examined to determine oxide scale growth at the interface between the metal and ceramic coating layers and beta phase depletion in the metallic coating layer.

3.1.2.1.1 Furnace Test Results and Microstructural Evaluation

Furnace exposure test results are summarized in Table VII and Figure 6. Note that independent of this program, data generated in-house for 1094°C (2000°F) has been included in Figure 6. Spallation failure of the ceramic coating layer did not occur during isothermal exposure; all specimen failures occurred upon cool-down, initiating at the tip area where there is a radius change. A photograph of a typical failed coating is shown in Figure 7. Weight gain measurements were made at each inspection interval for every specimen. Although the tapered coating scheme prevented premature coating failure, the design allowed for exposed substrate; thus, the weight gain data will only give a rough indication of oxide accumulation. These weight gain data are summarized in Appendix A.

Review of the failure time data in Table VII clearly shows the influence of temperature, exposure environment and cycle frequency on ceramic spallation life. The results show that thermal exposure in Argon does not cause coating failure for an extended period of time compared to air exposure. For furnace exposure conducted in air, frequent thermal cycling did not significantly decrease the total exposure time to failure, as shown by comparison of 1149°C (2100°F) air tests with 10 hour and 80 hour inspection intervals. Thermal barrier coating life was shown to be more dramatically dependent on "cyclic content" by previous work conducted by Miller (Ref. 37) and McDonald and Hendricks (Ref. 19).

TABLE VII
SUMMARY OF AIR AND ARGON FURNACE EXPOSURE TEST RESULTS

Specimen I.D. #	Code/ Condition	Exposure Time/(hrs) # of Cycles	Results	Metallographic Observations
TP07 TP08	A1.A/Air-1149°C (2100°F) (10 hr inspection)	140/14 160/16	Failed	Major crack just above interface within ceramic oxide layer
TP01 TP02	A1.B/Air-1149°C (2100°F) (80 hr inspection)	240/3 160/2	Failed	Major crack just above interface within ceramic
TP05 TP06	A2/Ar-1149°C (2100°F) (80 hr inspection)	1040/13 1040/13	No Failure No Failure	Incipient cracking near interface noted
TP03 TP04	B/Air-1204°F (2200°F) (10 hr inspection)	40/4 60/6	Failed	Major crack just above interface within ceramic
TP16	C/Air-1149°C (2100°F) Fractional	90/1	No Failure	(60%)No major cracking; some incipient cracking near the ceramic oxide interface
TP19	C/Air-1149°C (2100°F) Fractional	135/1	No Failure	(90%)No major cracking; some incipient cracking near the ceramic oxide interface
TP20	C/Air-1149°C (2100°F) Fractional	150/1	No Failure	Incipient failure observed at suspected bond coat defect; Major cracking extending from "blister" through aligned Kirkendall voids
TP21	C/Air-1149°C (2100°F) 165/1 Fractional		Failed	Major cracking/ delamination
TP22	C/Air-1149°C (2100°F) 180/1 Fractional		Failed	Major cracking/ delamination
TP23	C/Air-1149°C (2100°F) 120/12 (10hr inspection)		Failed	Incipient cracking at the tip
TP24	C/Air-1149°C (2100°F) 150/15 (10hr inspection)		Failed	Major cracking with some delamination at tip

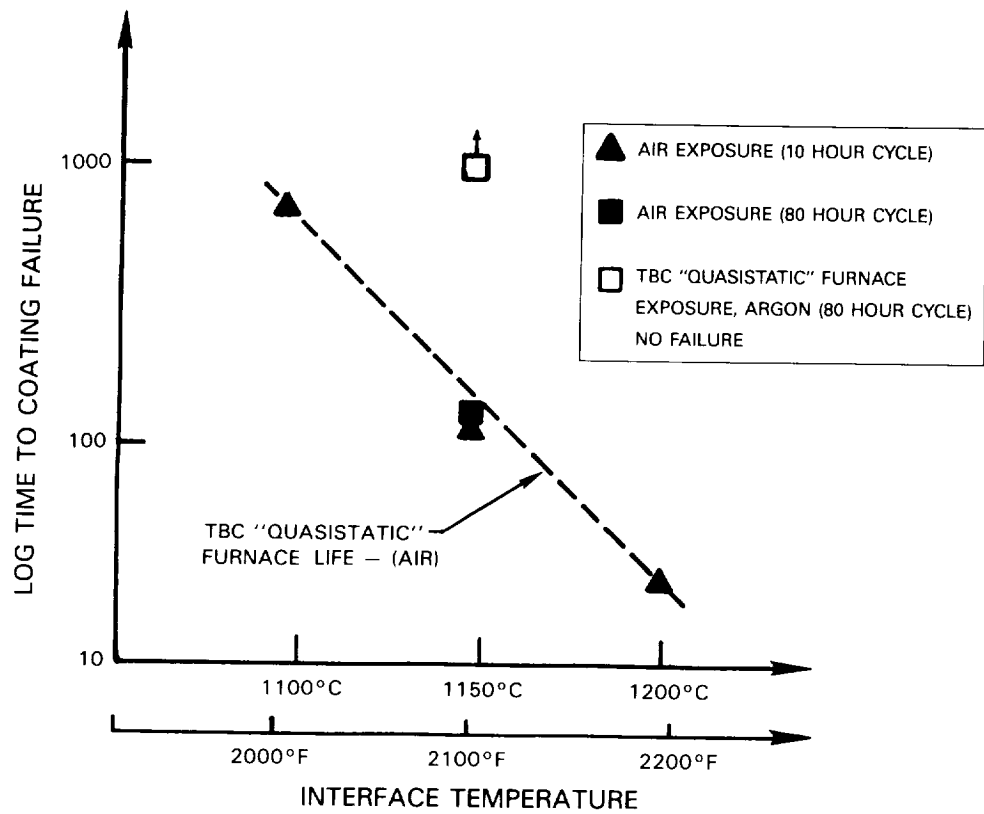
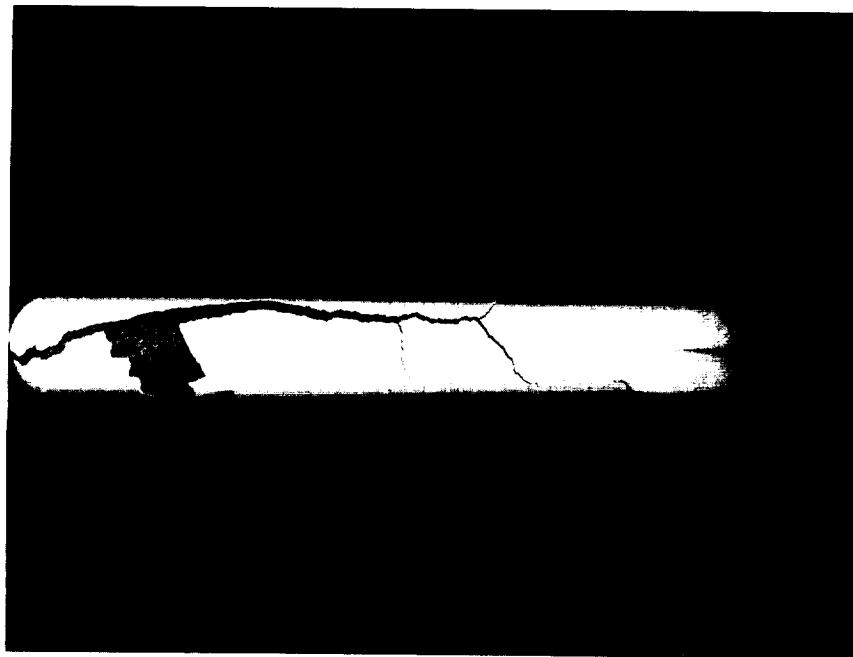


Figure 6 Test Data Showing Thermal Exposure Atmosphere Effects on Coating Durability



0.9X

Figure 7 Photomicrograph of Typical Furnace Tested Failed Coating

The high temperature (1204°C (2200°F) in air) furnace exposure results show a significant decrease in TBC life. This life decrease is attributed to a combination of more rapid oxidation at the high temperature and larger thermal strain excursion on cooling to ambient from the higher temperature. The Argon environment significantly reduced the weight gain (oxidation) rate as compared to an air environment so that exposure time and cycle life increased dramatically without causing ceramic spallation.

To aid in interpretation of static furnace exposure results, metallographic and x-ray diffraction analyses were conducted on pre- and post-exposure specimens. X-ray diffraction results are summarized in Figure 8. In the air exposed specimens, the v/o of monoclinic ZrO_2 increases with increasing exposure time. In individual comparisons between these tested specimens and the pre-test specimen, there is an apparent decrease in the tetragonal phase which accompanies the increase in the monoclinic phase and a slight increase in the FCC phase, suggesting that existing metastable tetragonal phase is undergoing transformation. In looking at the two specimens tested at 1149°C (2100°F) (different cycle lengths; 80 hrs. and 10 hrs.), one failing at 160 hours and the other at 240 hours, there appears to be not only an increase in the v/o monoclinic phase with time but an associated decrease in the v/o FCC phase and no change in the v/o tetragonal phase with increasing time.

These observations are consistent with those presented by Miller (Ref. 24), suggesting that homogenization resulting from heat treatment may have resulted in an increase in both the low Y_2O_3 transformable tetragonal and the high Y_2O_3 cubic phase. Upon cooling, the transformable tetragonal then would transform to the monoclinic phase, while the cubic phase is retained.

X-ray diffraction analysis of the Argon exposed specimen revealed 100% FCC ZrO_2 . This result is consistent with other studies which suggested that the equilibrium phase distribution may be sensitive to oxygen partial pressure (Ref. 38).

Thermal exposure effects including oxidation, beta (NiAl) depletion, bond coat substrate interdiffusion, and ceramic structure were metallographically studied. Electron Microprobe analyses were conducted to study time dependent chemical changes occurring in the substrate-bondcoat-ceramic system. Table VIII presents a summary of the metallographic evaluation of selected post-test furnace exposed specimens which are shown in Figures 9 through 15. Thermal barrier coating failure was observed to be associated with increased time at temperature which resulted in increased beta depletion, average oxide thickness, interdiffusion zone width and average void size. An increase in Kirkendall void population is seen with the high exposure temperature. Specific examples of these various changes are discussed in the following paragraphs.

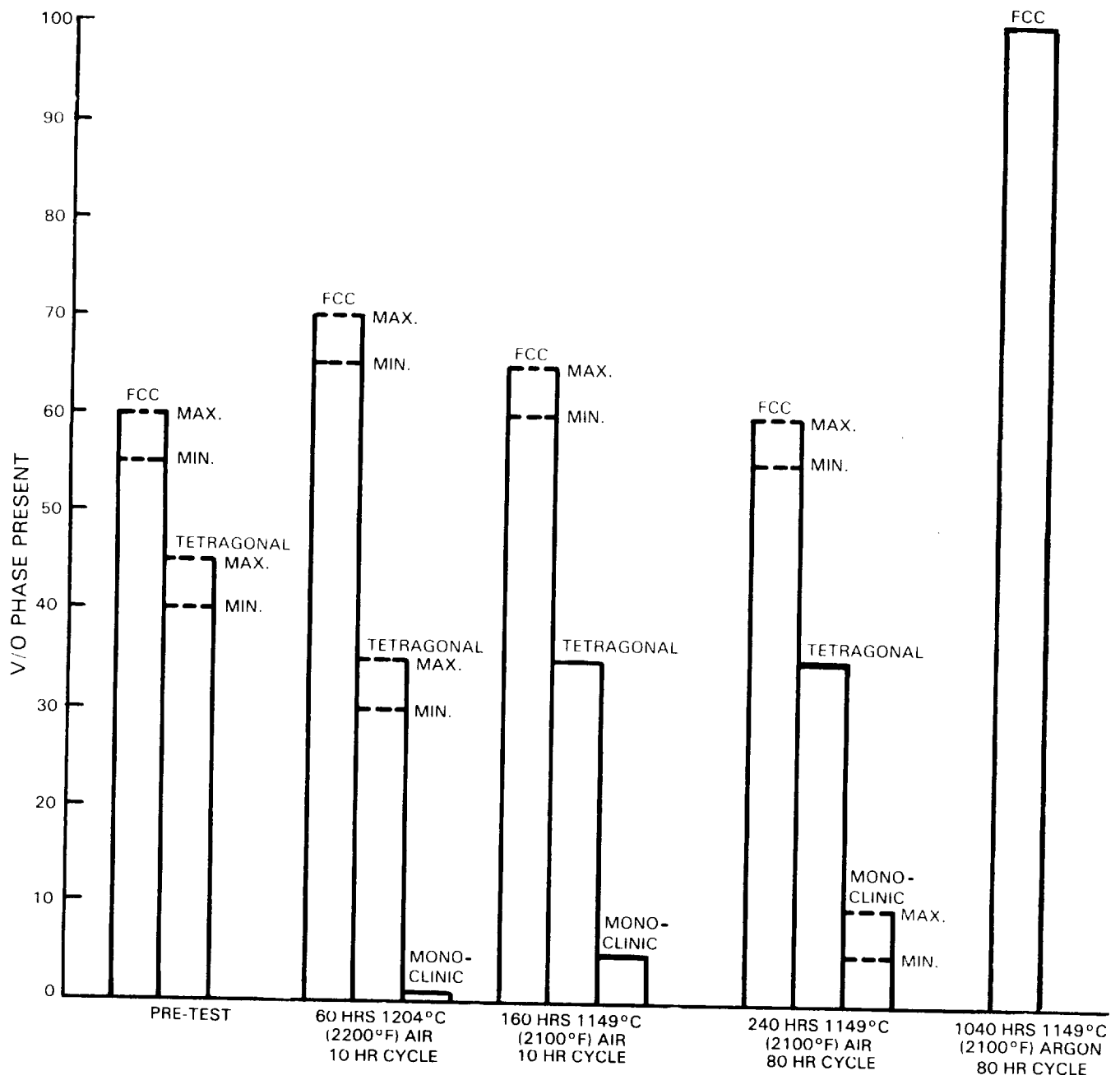
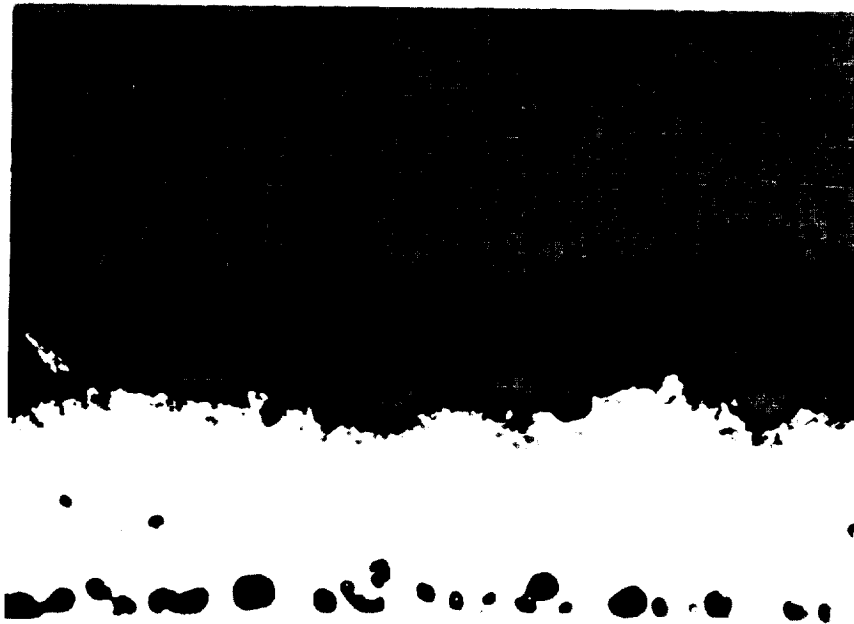


Figure 8 X-Ray Diffraction Results of Furnace Exposed Test Specimens

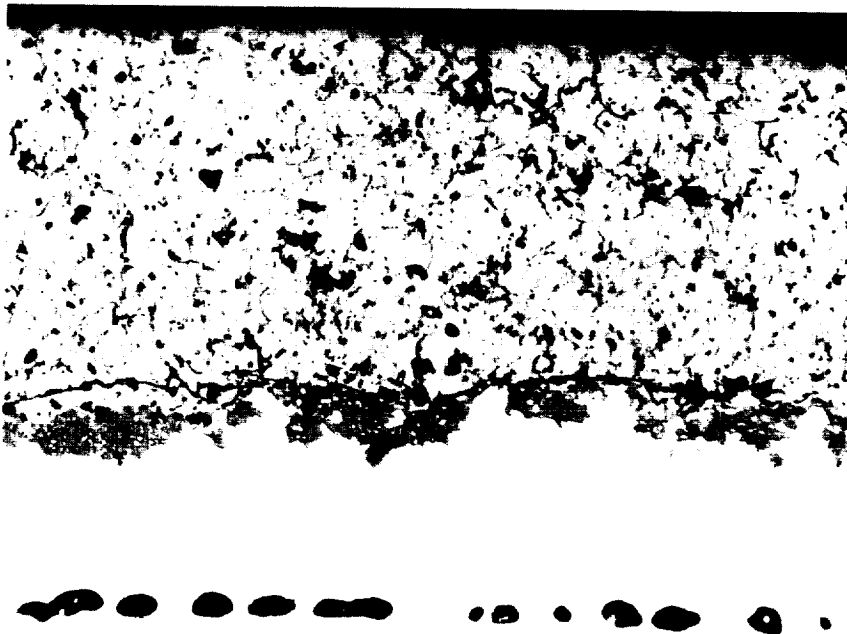
TABLE VIII
METALLOGRAPHIC EVALUATION OF SELECTED FURNACE EXPOSURE SPECIMENS AFTER EXPOSURE

Specimen I.D.#	Test Code/ Conditions	Average Oxide Thickess. Microns (in)	Beta (NiAl) Depletion	Interdiffusion Zone. Microns (in)	Average Void Width Microns (in)
TP01	A1.A/240 hrs. in Air 1149°C (2100°F)/3 80 hr. inspections	6.4 - 12.7 (0.00025 - 0.0005)	100%	102 (0.004)	12.7 - 25.4 (0.0005 - 0.001)
TP08	A1.B/160 hrs. in Air 1149°C (2100°F)/16 10 hr. inspections	6.35 - 12.7 (0.001 - 0.00125)	100%	76 (0.003)	12.7 (0.0005)
TP05	A2/1040 hrs. in Argon 1149°C (2100°F)/13 80 hr. inspections	25.4 - 31.8 (0.001 - 0.00125) *very irregular discontinuous	100%	178 (0.007)	19.1 - 25.4 (0.00075 - 0.001)
TP04	B/60 hrs. in. Air 1204°C (2200°F)/6 10 hr. inspection	6.4 (0.00025)	Overall 60 - 70% 40-50 depleted MCrAlY to ceramic 10-25% depleted MCrAlY to sub- strate interface	114 - 127 (0.0045 - 0.005)	12.7 - 19.1 (0.0005 - 0.00075) * void population is high
TP16	C/90 hrs. in Air 1149°C (2100°F) 60%	6.5 - 12.7 (0.00025 - 0.0005)	Overall 80 - 100% 60 - 70% depleted MCrAlY to ceramic interface 10-20% depleted MCrAlY to sub- strate interface	64 - 76 (0.00025 - 0.003)	6.4 - 19.1 (0.00025 - 0.00075)
TP19	C/135 hrs. in Air 1149°C (2100°F) 90%	6.4 - 12.7 (0.00025 - 0.0005)	100%	64 - 76 (0.0025 - 0.003)	6.4 - 12.7 (0.00025 - 0.0005)
TP20	C/150 hrs. in Air 1149°C (2100°F)	6.4 (0.00025)	100%	64 - 76 (0.0025 - 0.003)	6.4 - 12.7 (0.00025 - 0.0005)



200X

Figure 9 Light Photomicrograph of Post-Test Microstructure. Failed After Furnace Exposure in Air at 1149°C (2100°F) with 80 Hour Inspection Intervals (240 hrs/3 cycles)



200X

Figure 10 Light Photomicrograph of Post-Test Microstructure. Furnace Exposure in Argon at 1149°C (2100°F) with 80 Hour Inspection Intervals (1040 hrs/13 Cycles)

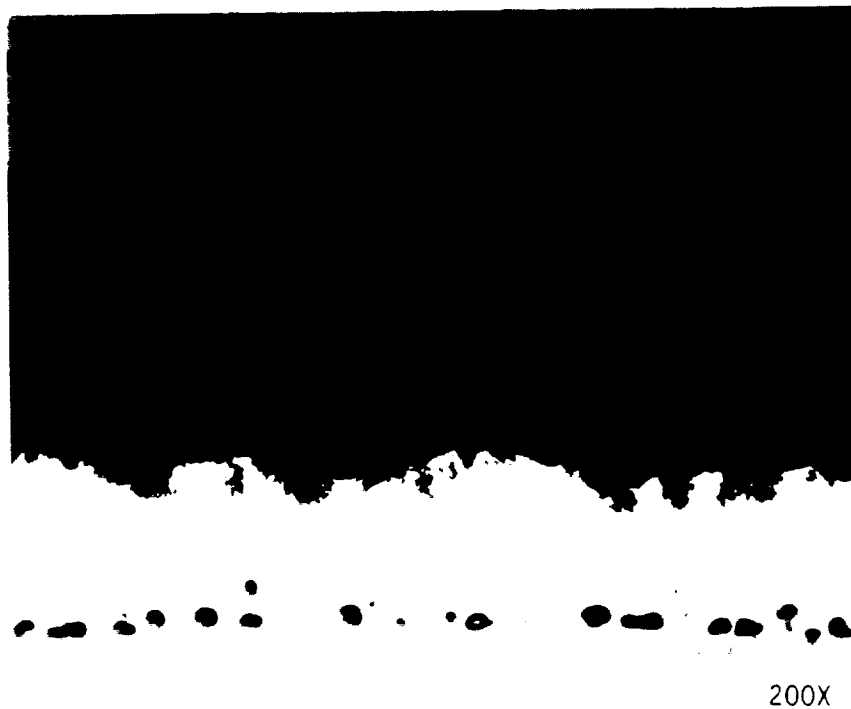


Figure 11 Light Photomicrograph of Post-Test Microstructure. Failed Furnace After Exposure in Air at 1149°C (2100°F) with 10 Hour Inspection Intervals (160 hrs/16 cycles)

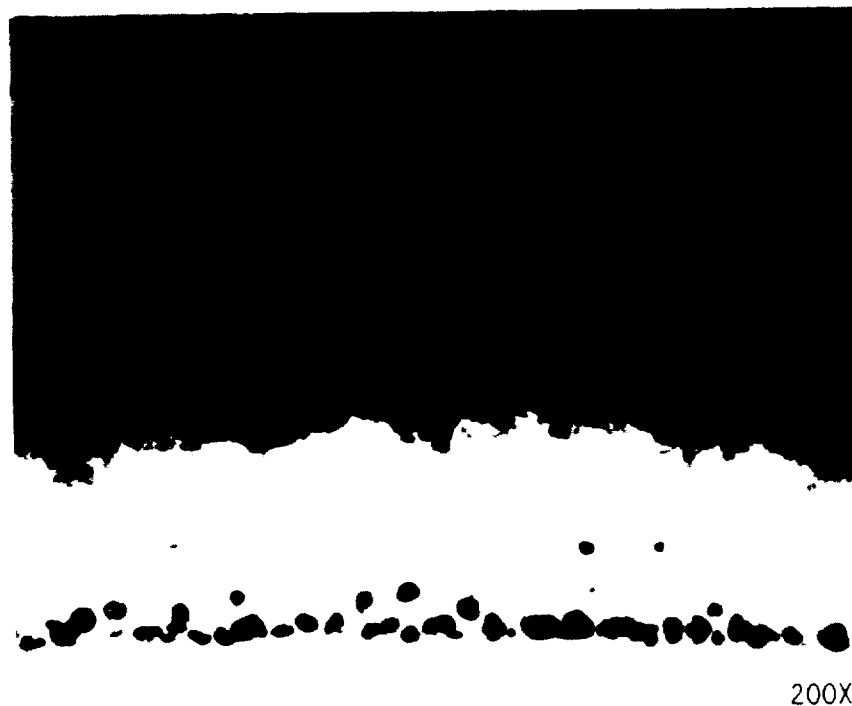
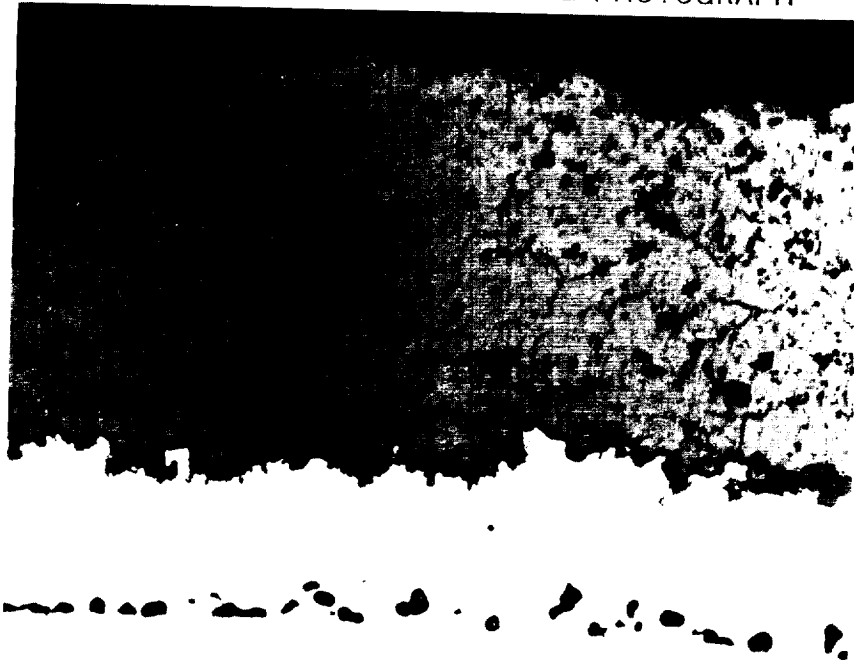


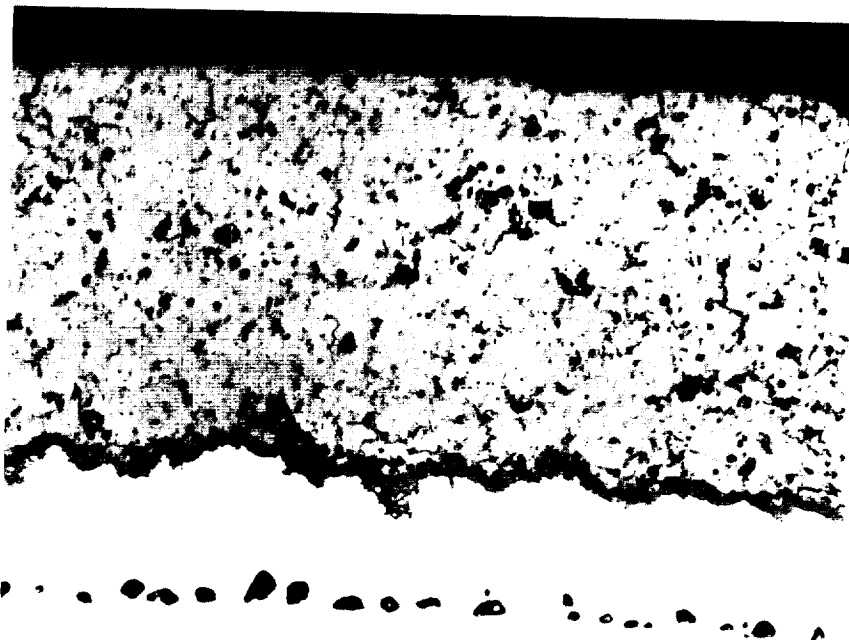
Figure 12 Light Photomicrograph of Post-Test Microstructure. Failed After Furnace Exposure in Air at 1204°C (2200°F) with 10 Hour Inspection Intervals (60 hrs/6 cycles)

ORIGINAL PAGE
BLACK AND WHITE PHOTOGRAPH



200X

Figure 13 Light Photomicrograph of Post-Test Microstructure After Furnace Exposure in Air (90 hrs/1149°C (2100°F)/1 cycle 60%)



200X

Figure 14 Light Photomicrograph of Post-Test Microstructure After Fractional Furnace Exposure in Air (135 hrs/1149°C (2100°F)/1 cycle 90%)

ORIGINAL PAGE
BLACK AND WHITE PHOTOGRAPH



Figure 15 Light Photomicrograph of Post-Test Microstructure After a 150 Hr Fractional Exposure at 1149°C (2100°F) in Air

Figures 16a through 16c show the back scatter image photomicrographs of the post-test microstructure for the specimen furnace tested in Argon for 1040 hours at 1149°C (2100°F). Although thermal exposure in Argon did not result in TBC failure, the microstructure reveals major crack formation at near-interface locations. Some bond coat oxidation was observed indicating that the chamber oxygen partial pressure may not have been low enough to prevent alumina formation. In addition, it is implied, from the color of the coating, that the ceramic outer layer became oxygen deficient. It is possible that the loss of oxygen in the 745Z coating was in part due to alumina formation at the interface. Upon examination of the Back Scatter Image (BSI) photomicrographs, dark and light regions appear at the interface. Bond coat oxide is observed to be the darker, discontinuous region. The light areas in the oxide, are believed to be unoxidized bond-coat evident by the polishing marks which are visible in Figure 16c. Figures 16d through 16h show the energy dispersion spectragraphs for the various elements present, corresponding to the locations marked 1-5 on Figure 16b. Figures 17a through 17j show the X-ray maps for various elements present. It becomes clear from these maps that the dark interface phase is predominantly Al_2O_3 . Cobalt, Ni, and Cr are the major bond-coat elements and show a strong x-ray image, while Molybdenum, Hf, Ti and Ta are substrate elements which have clearly diffused into the bond coat. Some Ti and Hf enrichment is occurring at the bond coat-ceramic interface and many Hf enriched phases are also visible.

Figures 18a through 18c show back scatter images for the post-test microstructure for the specimen furnace tested in air for 240 hours at 1149°C (2100°F). The figures show a thick, well defined, continuous, dual oxide layer. The dual layer oxide consists of a light oxide region and a dark oxide region. The light oxide seems almost porous and shows a network of extensions reaching into the ceramic. The darker phase however is very dense but with some secondary phases or "islands". A previous analysis showed that they seem to be either Hf-rich oxides or spinel-type oxide particles. Figures 18d through 18k, show the energy dispersion spectrographs for the various elements present corresponding to the locations marked 1-8 on Figure 18c. Figures 19a through 19j show the X-ray maps for the various elements present. The maps show clearly that the "dark" portion of the oxide is Al_2O_3 . Kirkendall voids are present at the substrate-bond coat interface. The x-ray map for Al shows a strong image of Al picked up in the void area. This is assumed to be an artifact resulting from entrapment of Al_2O_3 polishing media. The "light" portion of the oxide appears to consist of spinel i.e., Ni or Co chromates. Hafnium, Ti and Ta appear to have diffused into the bond coat but do not appear to have greatly enriched any particular area at the bond coat-ceramic interface.

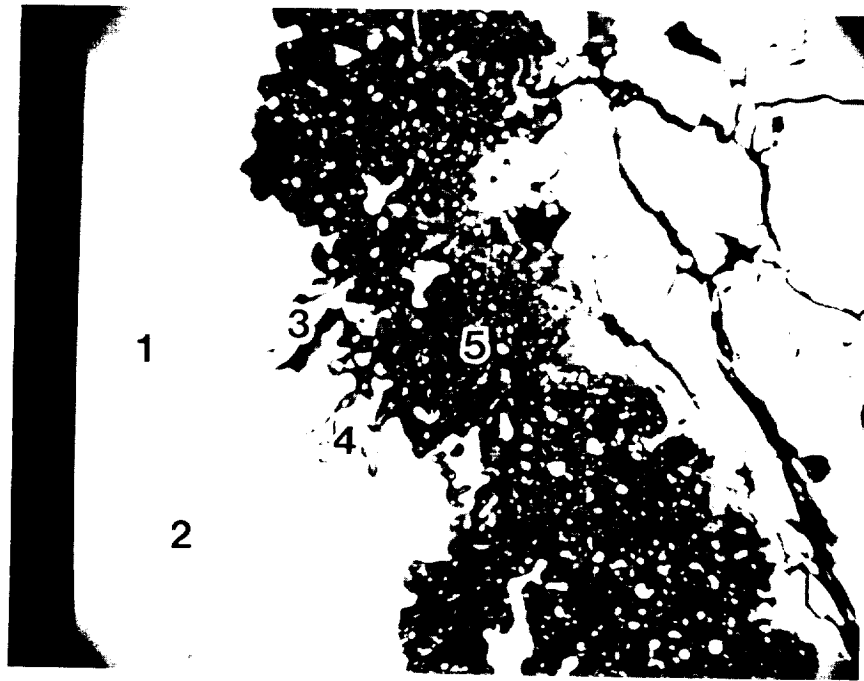
As shown previously, Figures 13 and 14 represent the "fractional" exposure test specimen microstructures after exposure for 60% and 90% of the total exposure time. These specimens were not cycled periodically for inspection as were those discussed previously. Presumably as a consequence, they show less microcracking than the cycled specimens. Figure 15 shows the post-test specimen microstructure in cross-section through a blister which developed during the high temperature exposure for 100% of the total life time, 150 hours. It is highly probable that this blister was caused by an initial bond coat defect.

Two additional specimens were tested at 1149°C (2100°F) in air for 165 hours and 180 hours with one thermal cycle achieved upon removal from the furnace. These additional tests were conducted in order to verify the single cycle ceramic spalling life in terms of hours exposed in the furnace. Both of these specimens exhibited ceramic spallation after a single thermal cycle.



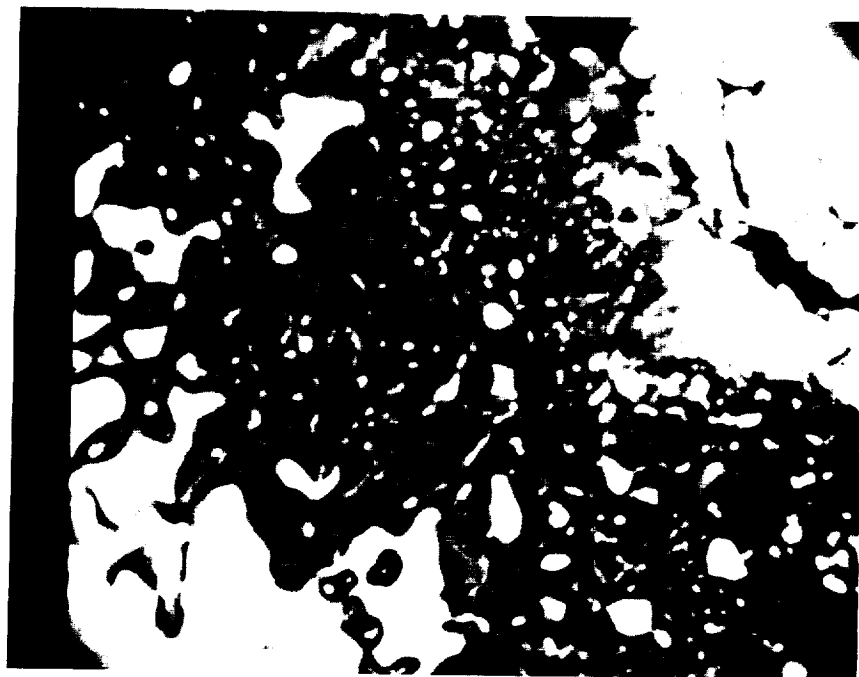
500X

Figure 16a Back Scatter Image of Post-Test Microstructure. Furnace Exposure in Argon at 1149°C (2100°F) for 1040 Hours (80 hour cycles - 13 cycles)



(b)

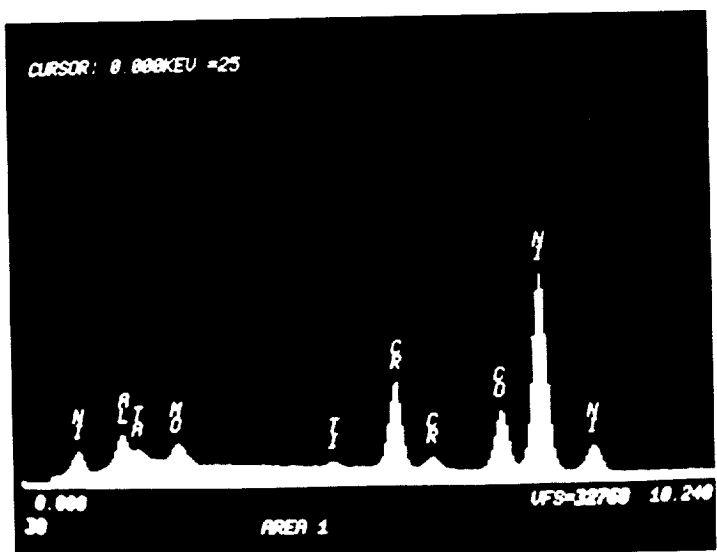
1200X
(BSI)



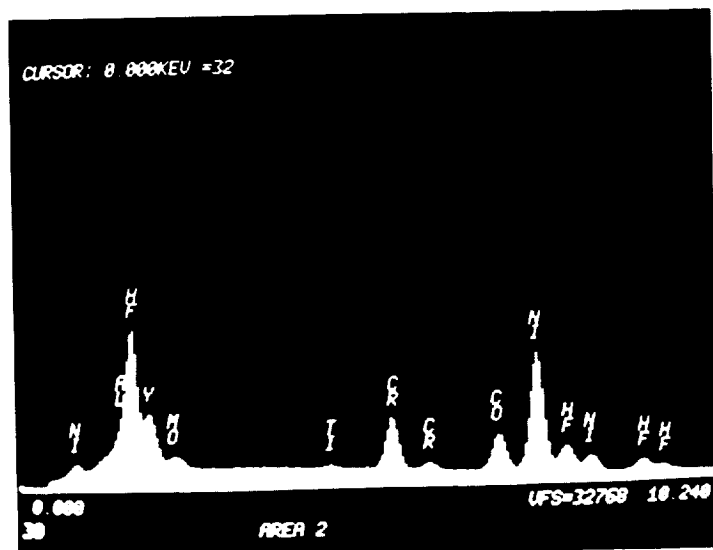
(c)

3000X
(BSI)

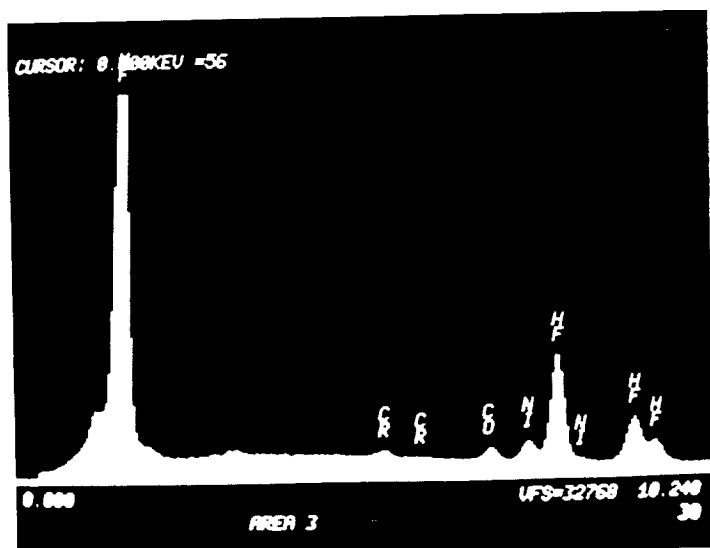
Figure 16 (b-c) Back Scatter Images of Post-Test Microstructure. Furnace Exposure in Argon at 1149°C (2100°F) for 1040 Hours (80 hour cycles - 13 cycles)



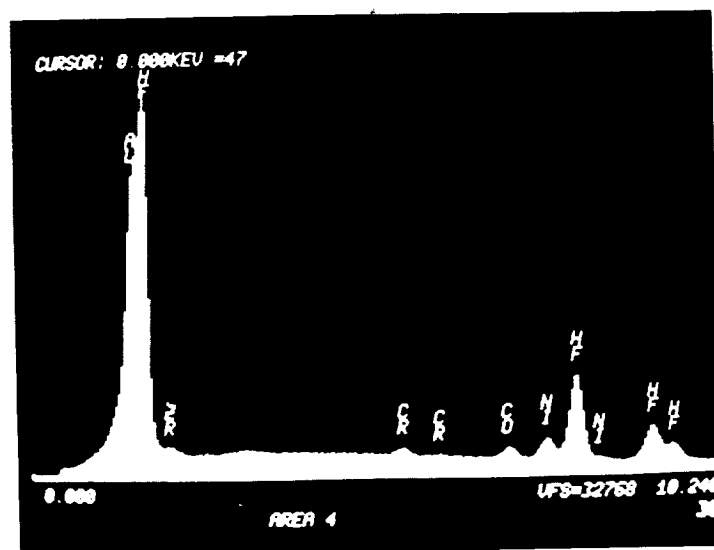
(d)



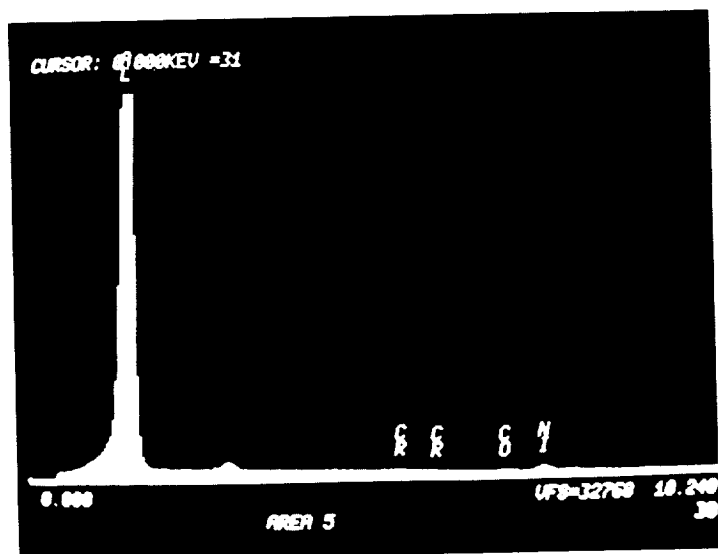
(e)



(f)



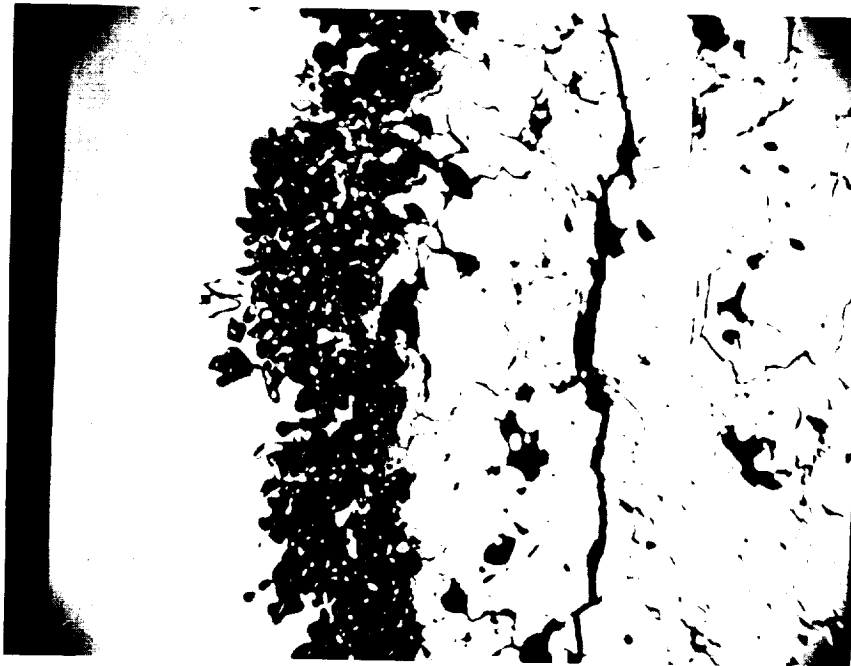
(g)



(h)

Figure 16 (d thru h) Energy Dispersion Spectrographs for Elements Present at Various Locations Corresponding to Figure 16b. Argon Exposed 1149°C (2100°F) for 1040 Hours 80 hour cycles - 13 cycles)

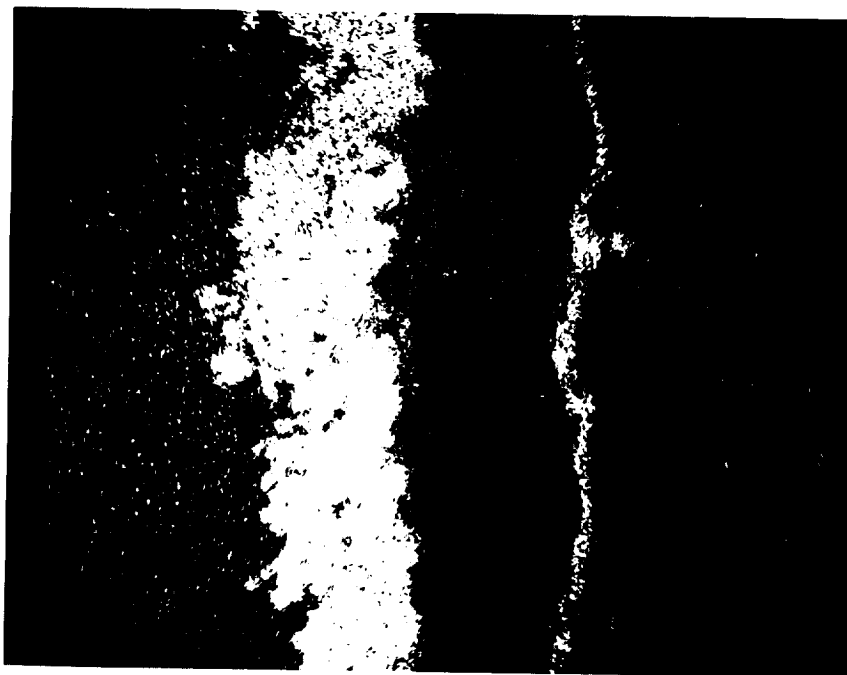
ORIGINAL PAGE
BLACK AND WHITE PHOTOGRAPH



BACK SCATTER IMAGE

(a)

800X

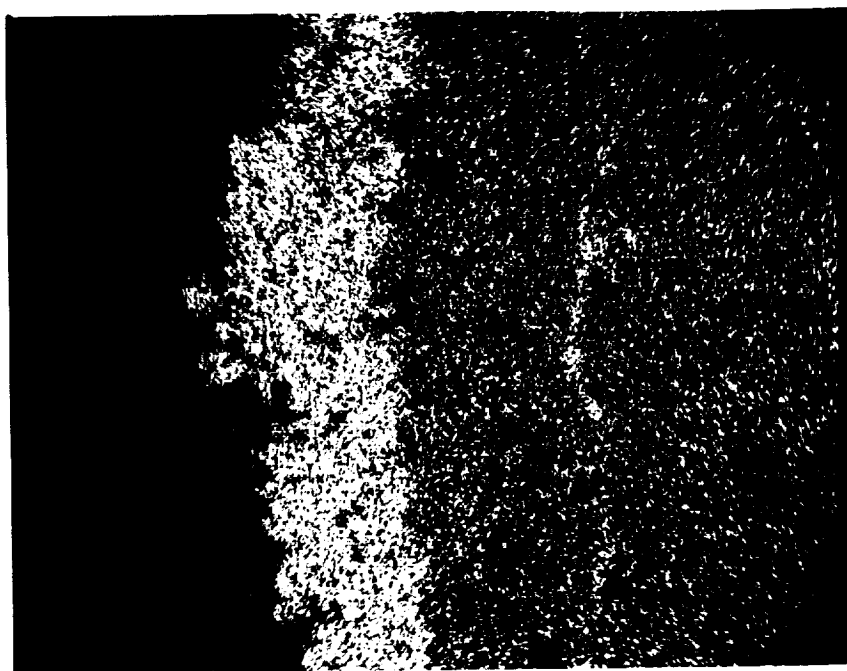


Al X-ray Map

(b)

800X

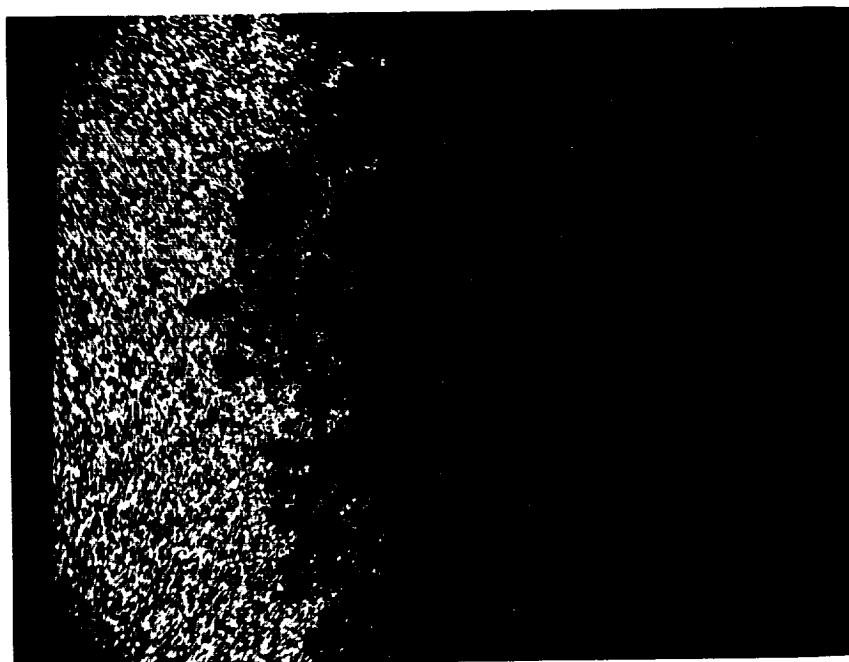
Figure 17 (a-j) Post-Test Microstructure. Furnace Exposure in Argon at 1149°C (2100°F) for 1040 Hours (80 hour cycles - 13 cycles)



O X-ray Map

(c)

800X



Co X-ray Map

(d)

800X

Figure 17 (continued)

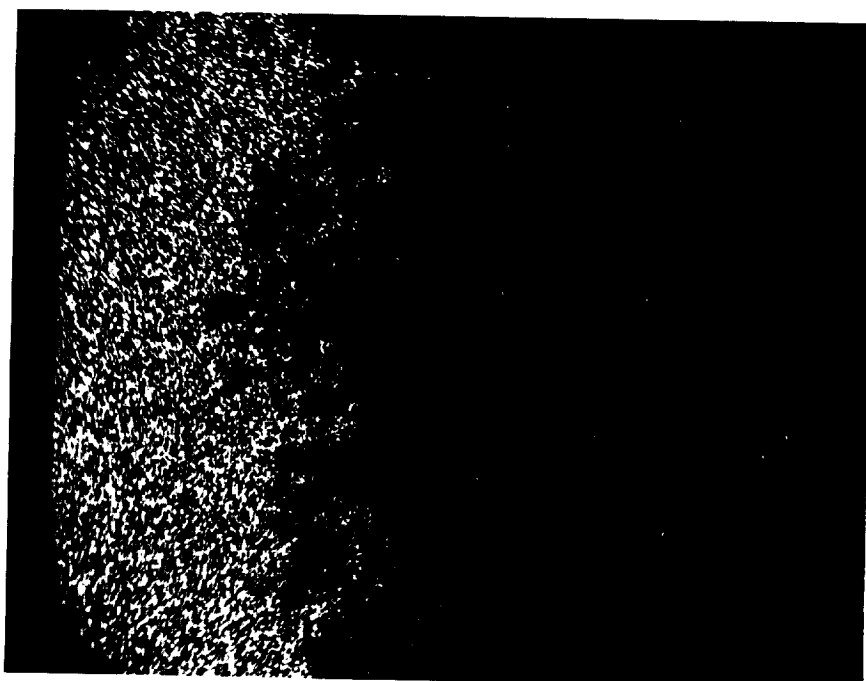
ORIGINAL PAGE
BLACK AND WHITE PHOTOGRAPH



Ni X-ray Map

(e)

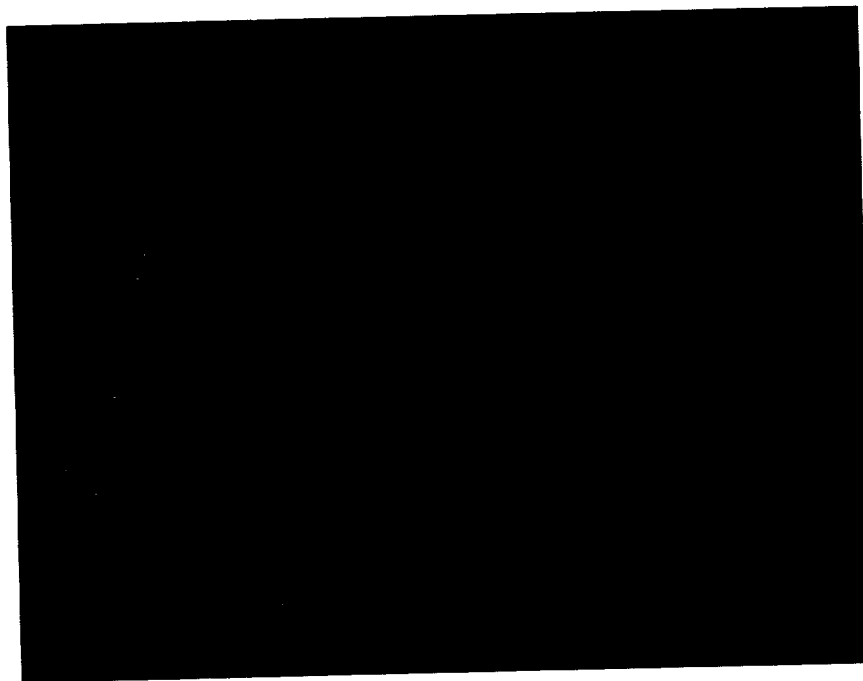
800X



Cr X-ray Map

(f)

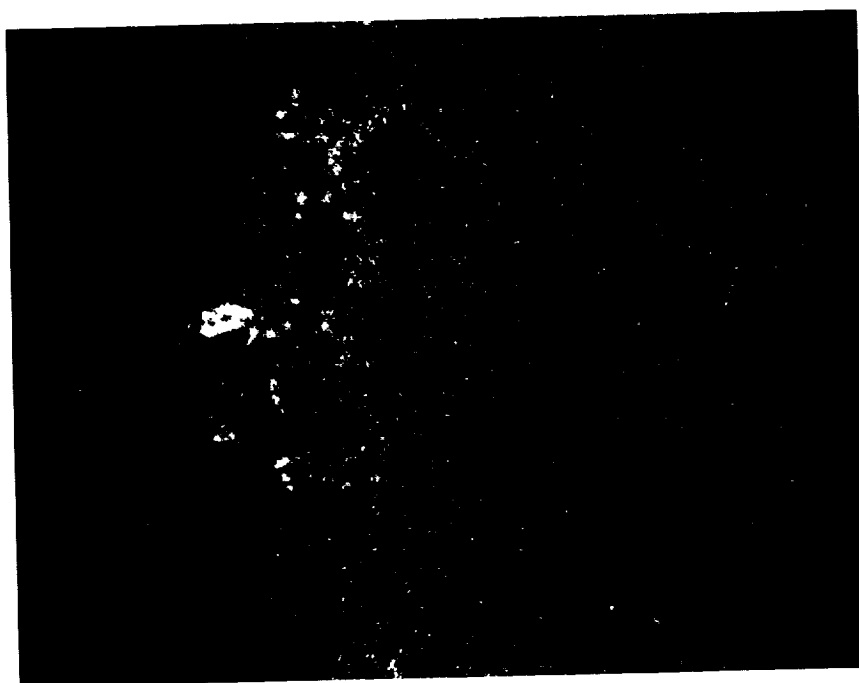
800X



Mo X-ray Map

(g)

800X



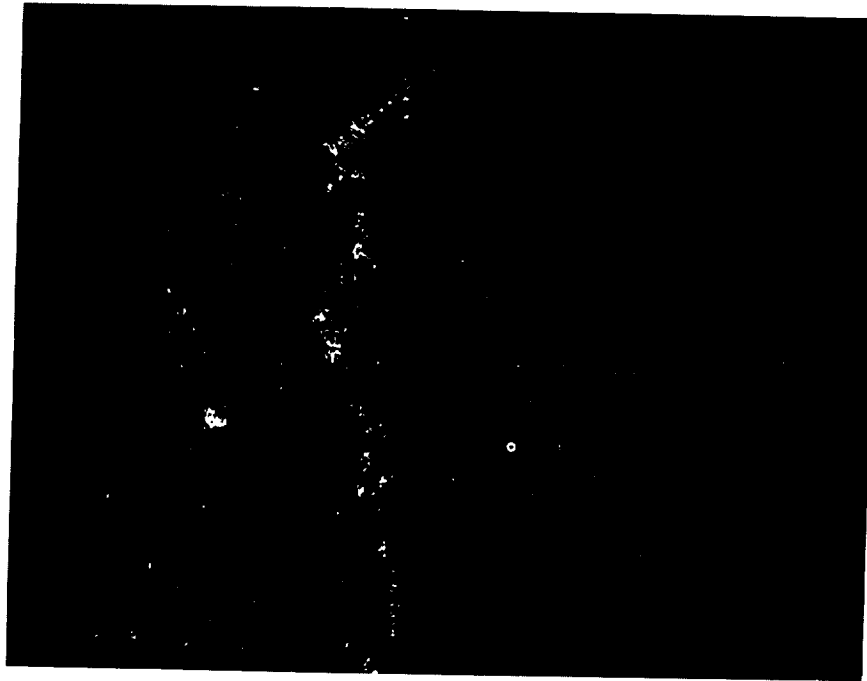
Hf X-ray Map

(h)

800X

Figure 17 (continued)

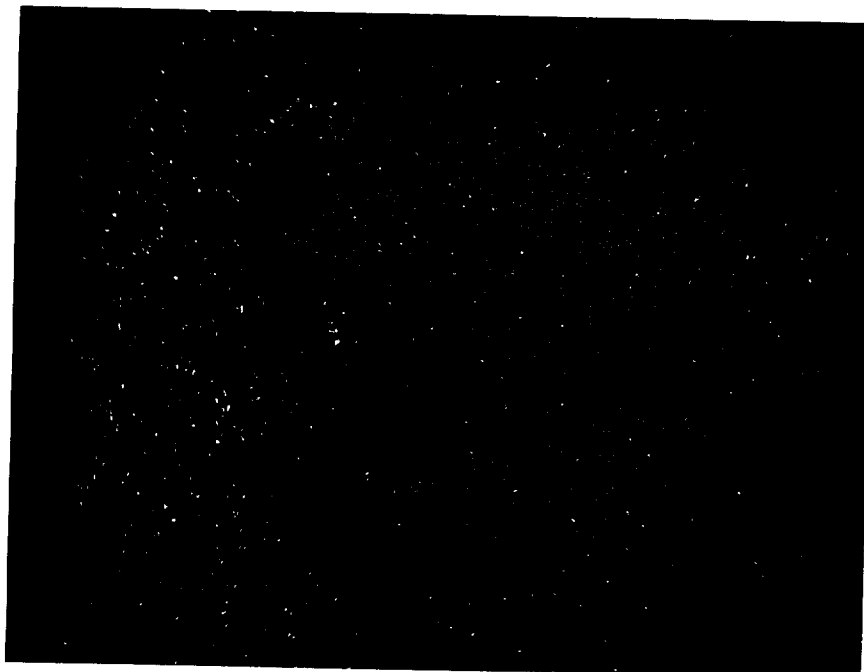
ORIGINAL PAGE
BLACK AND WHITE PHOTOGRAPH



Ti X-ray Map

(i)

800X



Ta X-ray Map

(j)

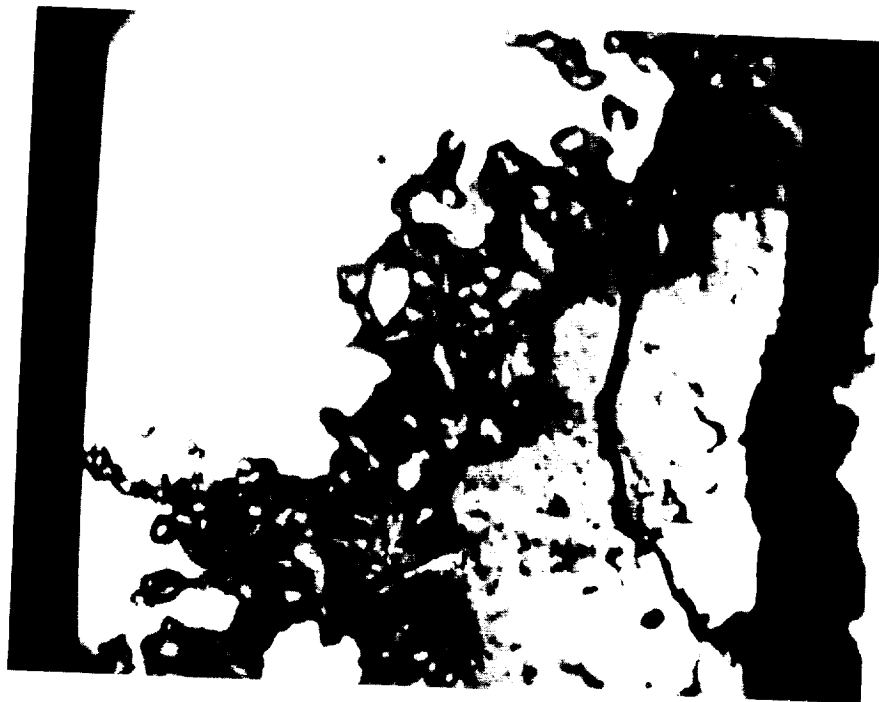
800X

Figure 17 (continued)



500X

Figure 18a Back Scatter Image of Post-Test Microstructure. Furnace Exposure
in Air at 1149°C (2100°F) for 240 Hours (80 hour cycles - 3
cycles)



(BSI)

(b)

2000X

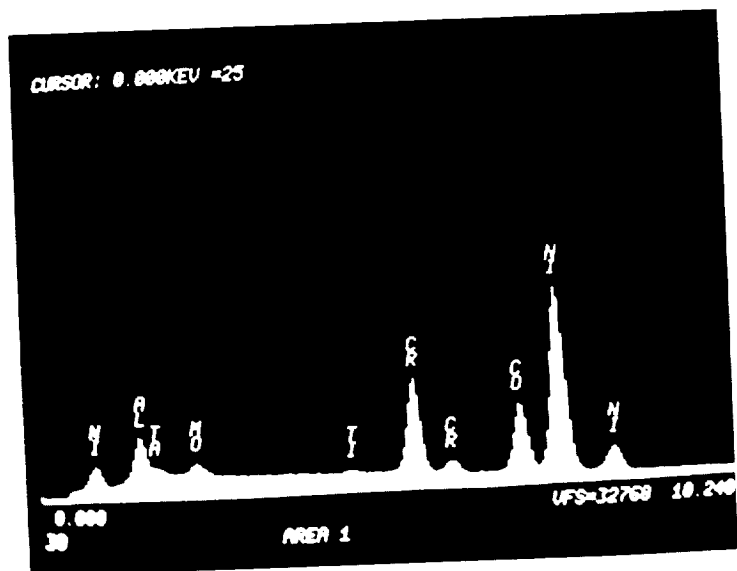


(BSI)

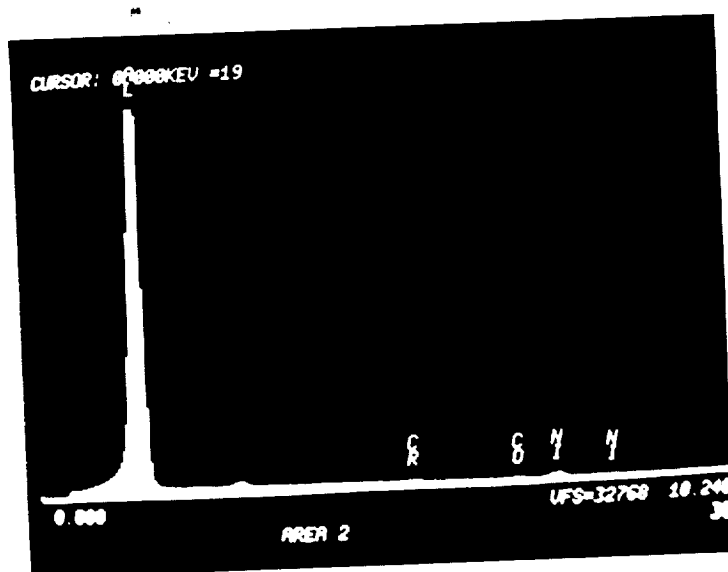
(c)

2000X

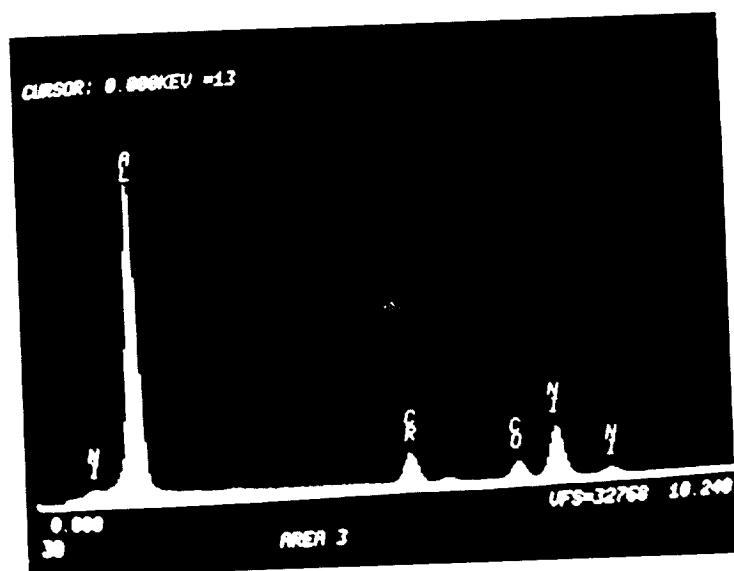
Figure 18 (b-c) Back Scatter Image of Post-Test Microstructure. Furnace Exposure in Air at 1149°C (2100°F) for 240 Hours (80 hour cycles - 3 cycles)



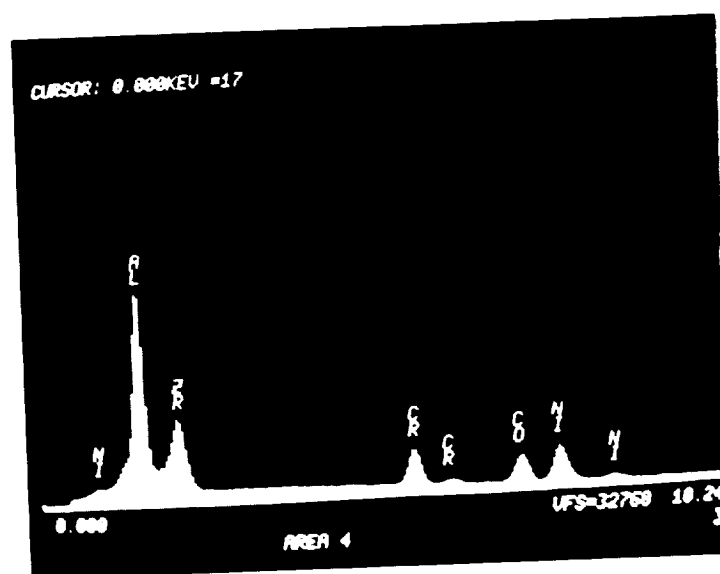
(d)



(e)



(f)

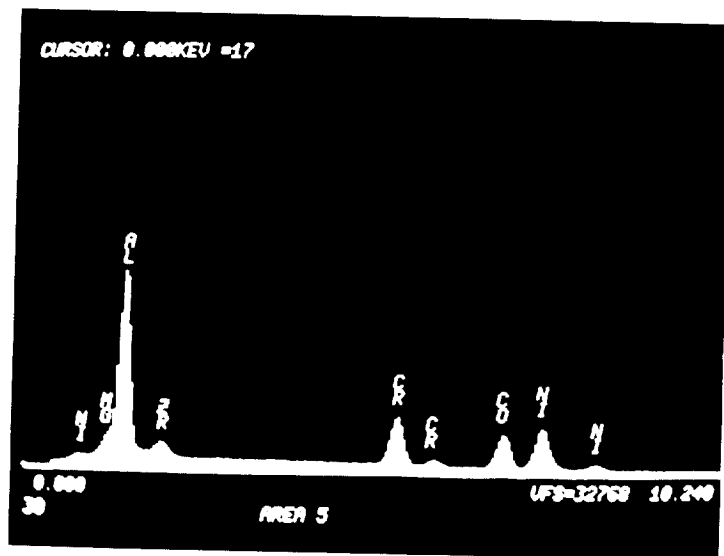


(g)

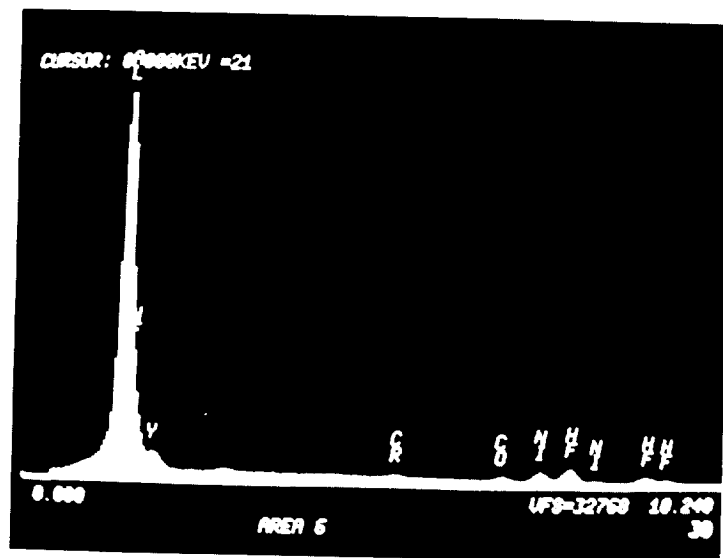
Figure 18 (d-g) Energy Dispersion Spectrographs for Elements Present at Various Locations Corresponding to Figure 18b. Air Exposed 1149°C (2100°F) for 240 Hours (80 hour cycles - 3 cycles)

ORIGINAL PAGE
BLACK AND WHITE PHOTOGRAPH

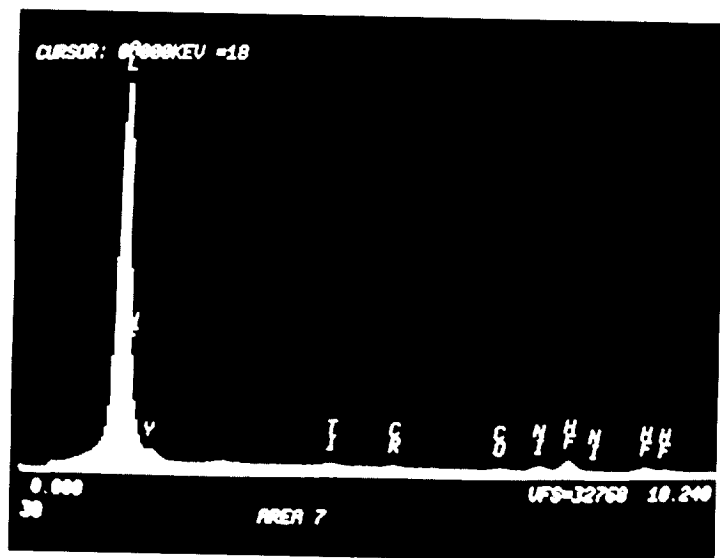
ORIGINAL PAGE
BLACK AND WHITE PHOTOGRAPH



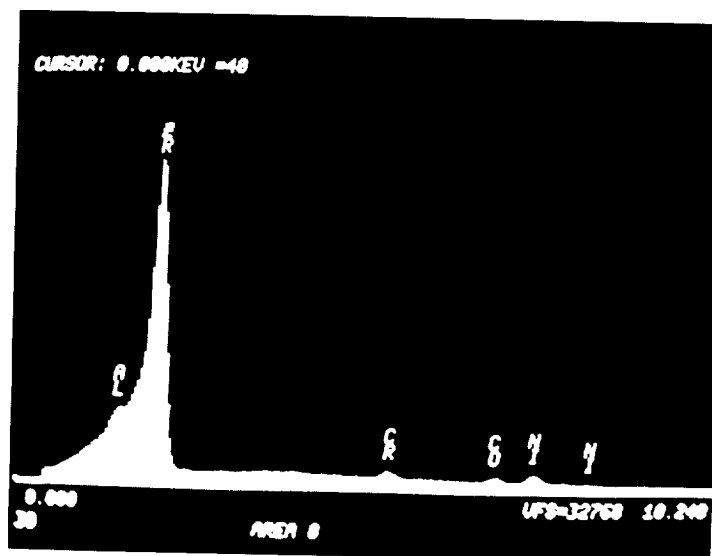
(h)



(i)



(j)



(k)

Figure 18 (h-k) Energy Dispersion Spectrographs for Elements Present at Various Locations Corresponding to Figure 18b. Air Exposed at 1149°C (2100°F) for 240 Hours (80 hour cycles - 3 cycles)

ORIGINAL PAGE
BLACK AND WHITE PHOTOGRAPH

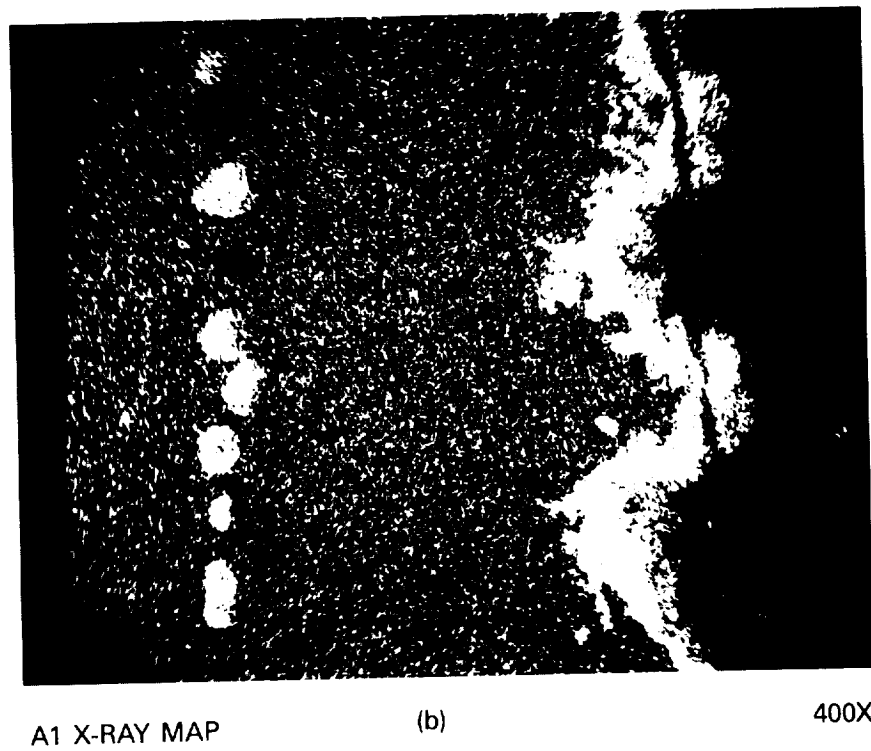
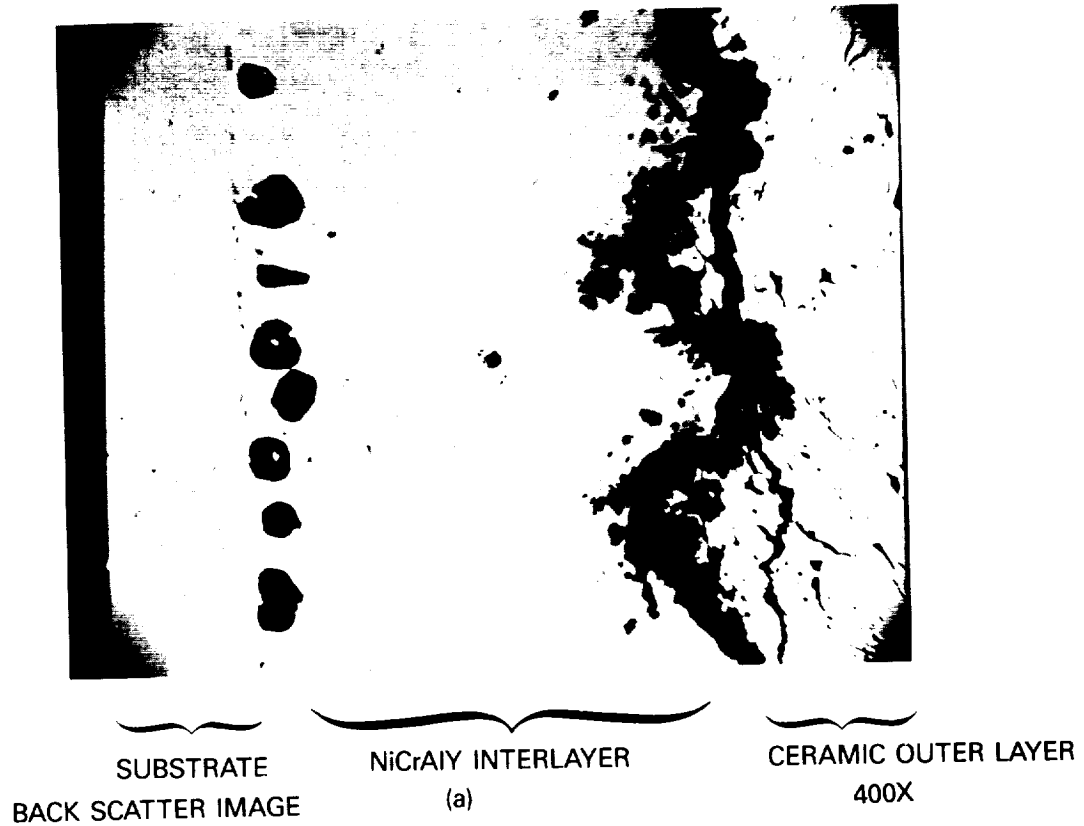
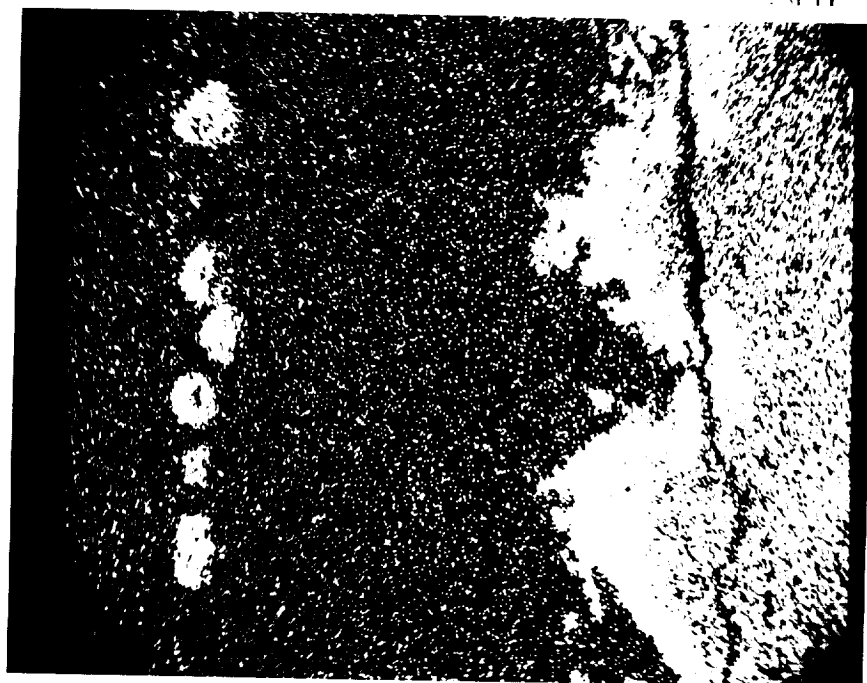


Figure 19 (a-j) Back Scatter Image of Post-Test Microstructure. Furnace Exposure in Air at 1149°C (2100°F) for 240 Hours (80 hour cycles - 3 cycles)

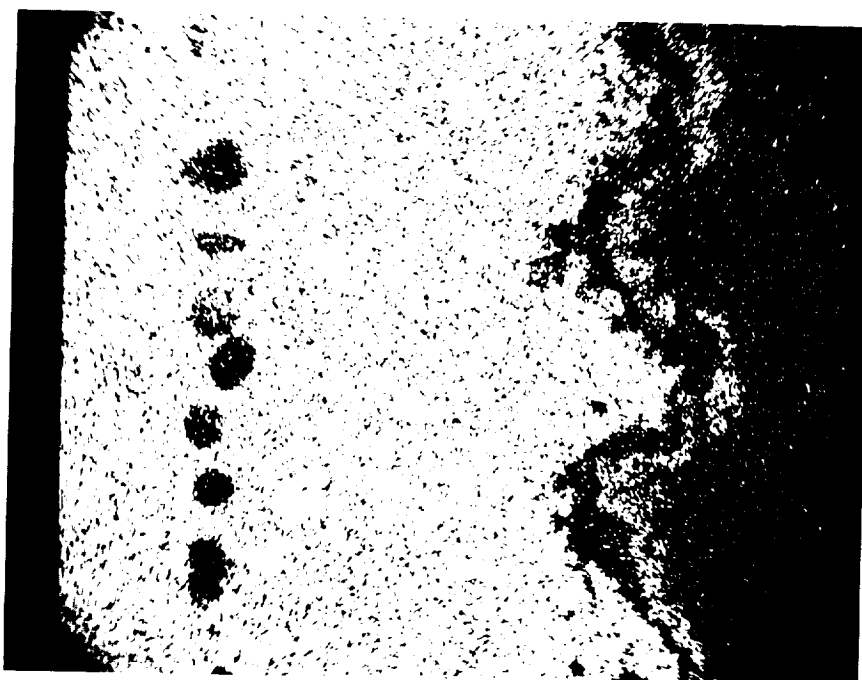
ORIGINAL PAGE
BLACK AND WHITE PHOTOGRAPH



O X-RAY MAP

(c)

400X



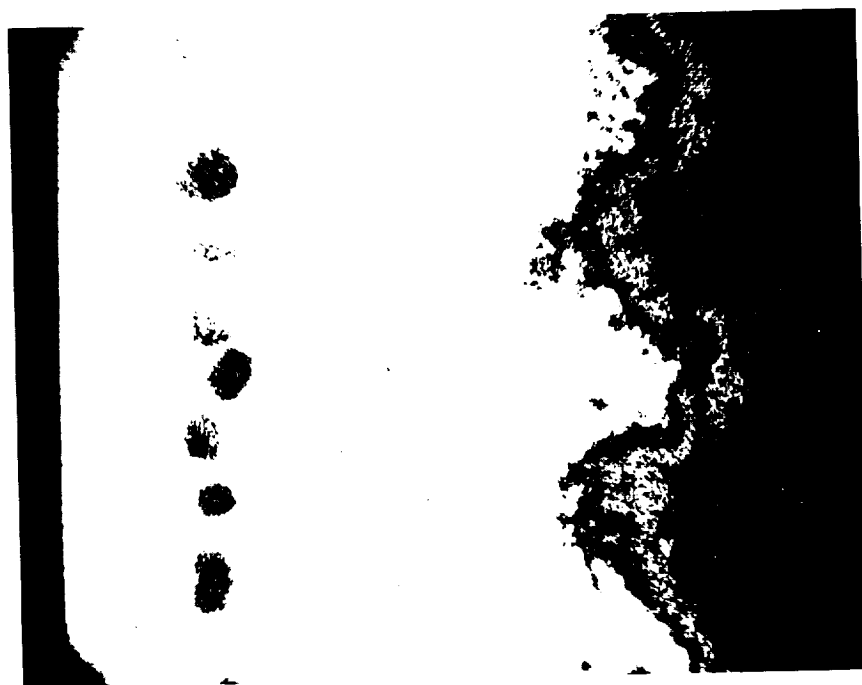
Co X-RAY MAP

(d)

400X

Figure 19 (continued)

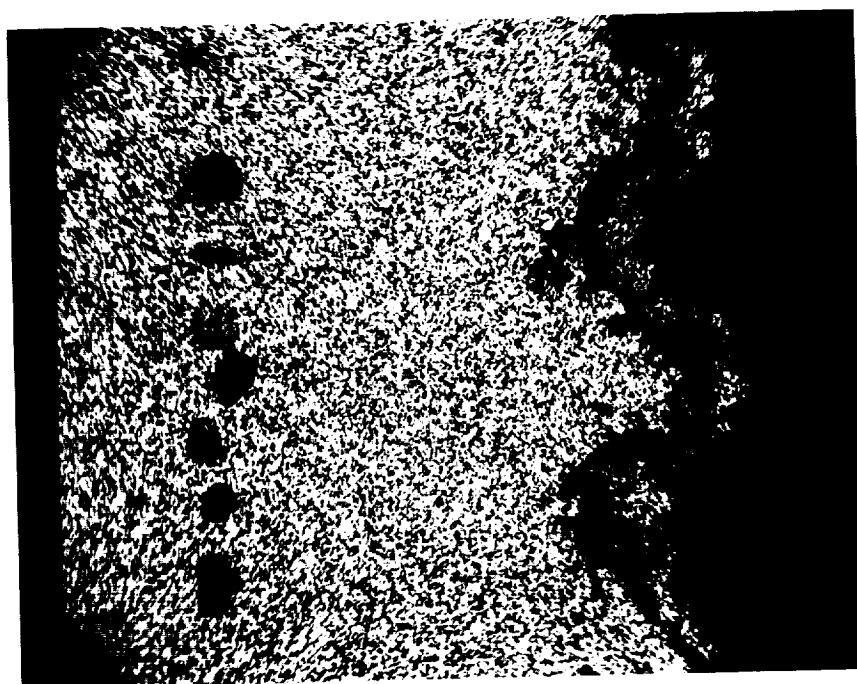
ORIGINAL PAGE
BLACK AND WHITE PHOTOGRAPH



Ni X-RAY MAP

(e)

400X



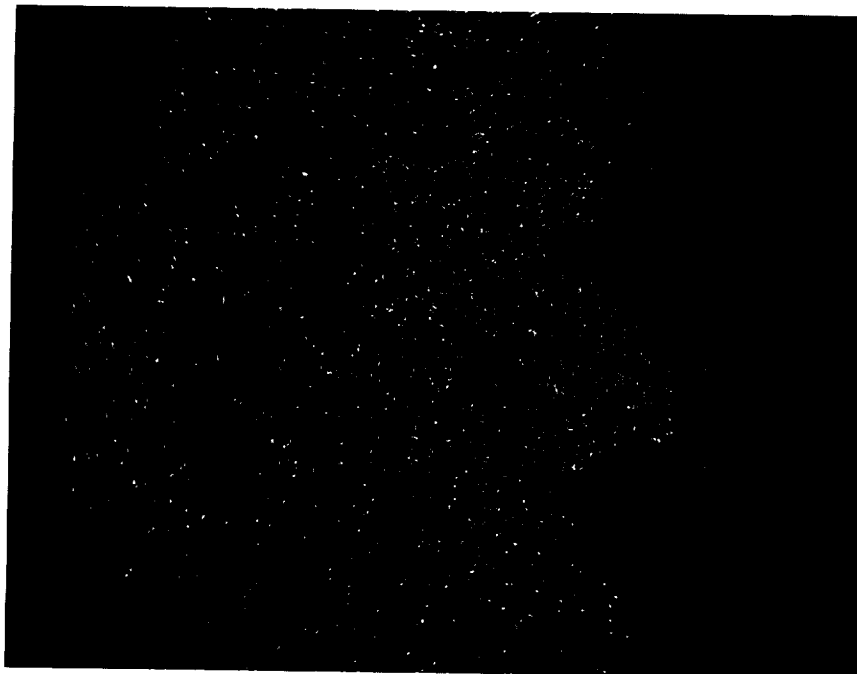
Cr X-RAY MAP

(f)

400X

Figure 19 (continued)

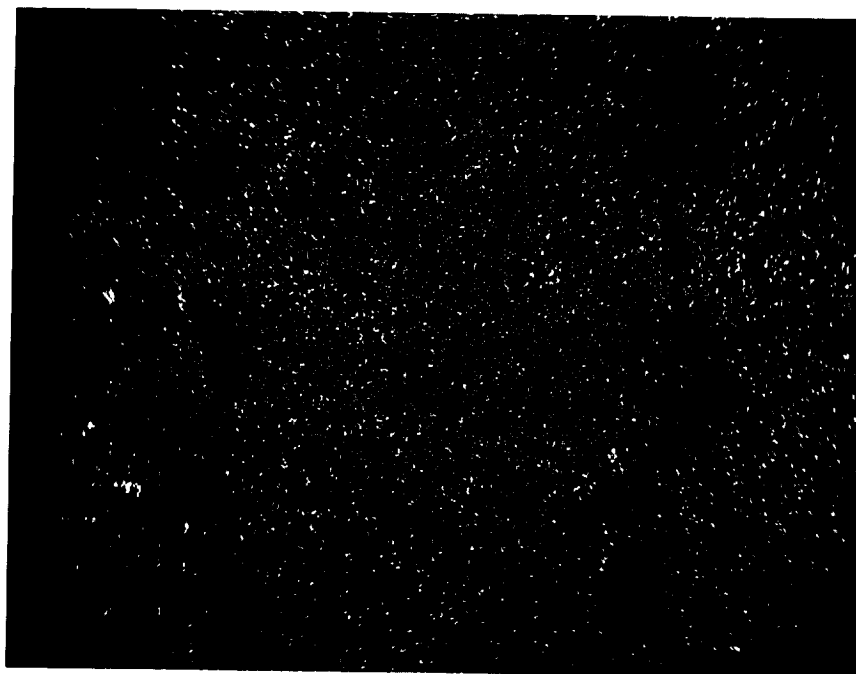
ORIGINAL PAGE
BLACK AND WHITE PHOTOGRAPH



Mo X-RAY MAP

(g)

400X

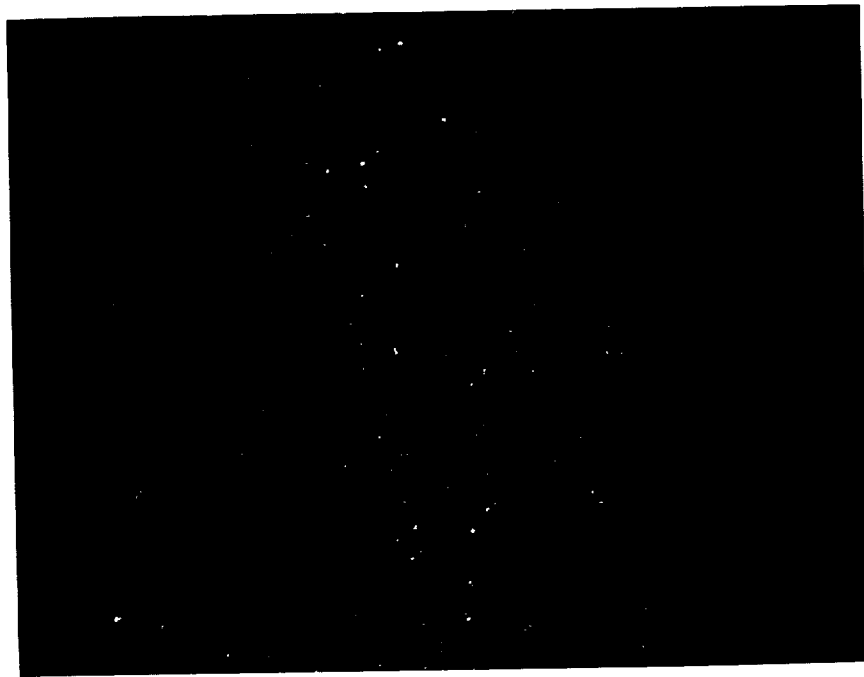


Hf X-RAY MAP

(h)

400X

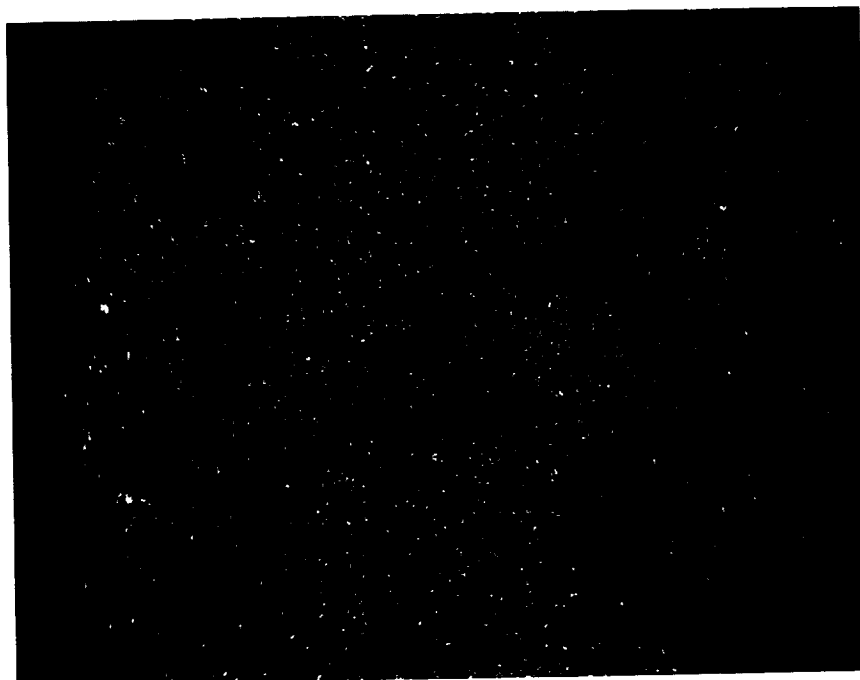
Figure 19 (continued)



Ti X-RAY MAP

(i)

400X



Ta X-RAY MAP

(j)

400X

Figure 19 (continued)

As noted in Table VII, cracking occurred at the tip location for the 80% (120 hrs) specimen and major cracking and delamination was observed for the 100% (150 hrs) specimen. The metallographic results of the fractional exposure furnace test specimens showed near interface cracking was occurring at exposure times which are relatively short as compared with the total exposure lifetime of the coating. These "incipient" cracks appear to be a direct physical result of oxidation of the bond coat asperities. The subcritical cracks seen are short, fine and directly linked to bond coat asperities. However, no "dominant" major subcritical cracking is observed, nor is the gradual growth of singularly large cracks, which may result in spallation, seen.

3.1.2.2 Cyclic Thermal Exposure Tests

A partial factorial test program shown in Figure 20 was conducted to determine the influence of temperature, cycle rate, coating thickness and static pre-exposure on coating cyclic thermal failure life and to provide preliminary information concerning interactions between static and cyclic thermal failure modes.

MAXIMUM CYCLE TEMPERATURE °C (°F)	TRANSIENT HEATING RATE	SHORT CYCLE		LONG CYCLE	
		CYCLE TO FAILURE	FRACTIONAL EXPOSURE	CYCLE TO FAILURE	FRACTIONAL EXPOSURE
1149 (2100)	FAST	① D ₁	⑩ G	① F	⑩
	SLOW	② E	⑬	⑬	⑬
1094 (2000)	FAST	⑦ D ₂	⑫	⑫	⑫
	SLOW	④	④	④	④

NUMBER OF TEST BARS	CERAMIC COATING THICKNESS	
4	0.25mm (0.010 in) AS-SPRAYED CERAMIC ("BASELINE" COATING)	} 40 HR AT 1149°C (2100°F) FOR 1149°C (2100°F) TESTING 100 HR AT 1094°C (2000°F) FOR 1094°C (2000°F) TESTING
2	0.13mm (0.005 in) AS-SPRAYED CERAMIC	
2	0.38mm (0.015 in) AS-SPRAYED CERAMIC	
2	0.25mm (0.101 in) AIR PRE-EXPOSED CERAMIC	
2	0.25mm (0.010 in) ARGON PRE-EXPOSED CERAMIC	

CONDITION G:

FRACTION EXPOSURE TEST, DESCRIBED IN TEXT

Figure 20 Task I Clean Fuel Cyclic Burner Rig Test Program

The test method used to measure cyclic coating life involved uncooled cyclic burner rig testing as described in Appendix B. The Jet A fueled burner employed in this test simulates the clean fuel combustor environment in which most hot section components operate. The primary method of temperature control in this test involved optical measurement of specimen surface temperature. To ensure consistent test conditions, a thermocoupled specimen was employed at all times during testing to monitor/calibrate the test temperature. To provide specimen temperature distributions required for subsequent preliminary life prediction modeling (Task IC), instrumented specimens were tested, to characterize specimen temperature distributions; see Figure 21.

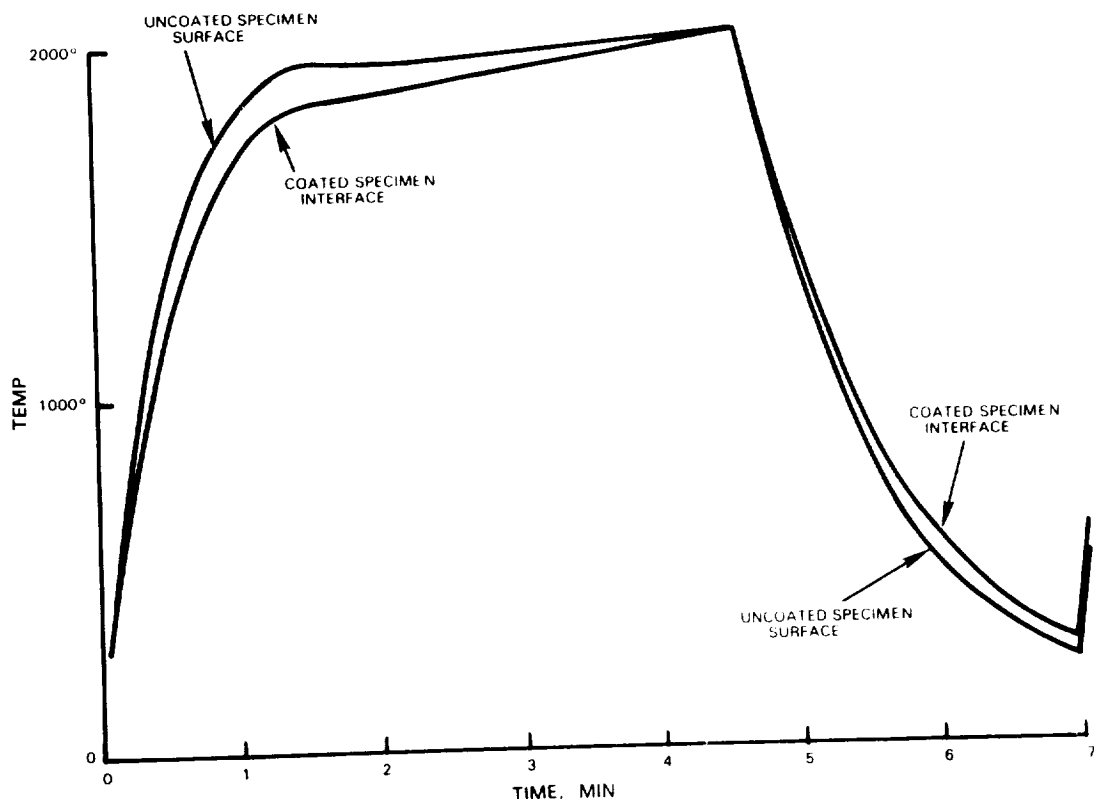
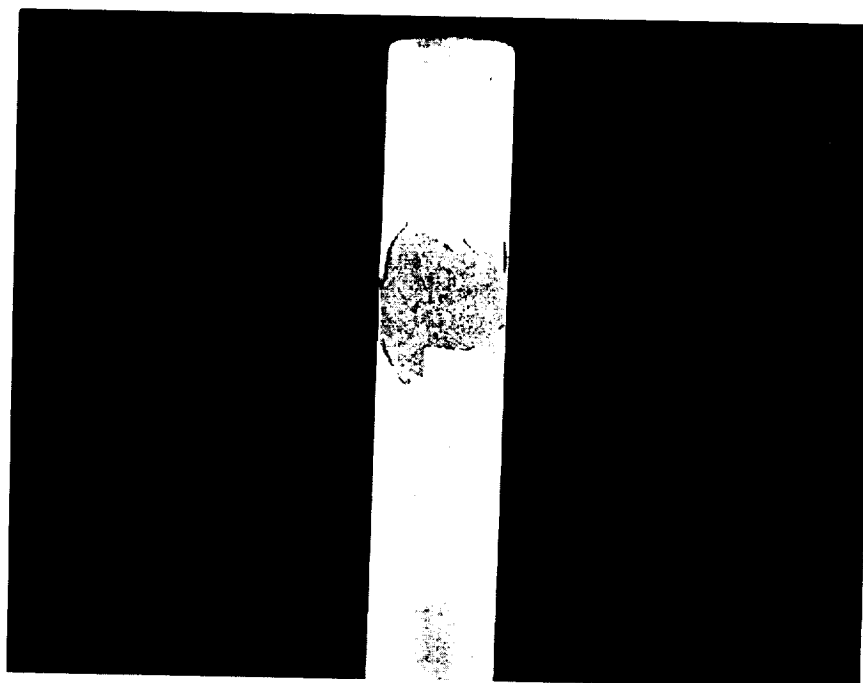


Figure 21 Typical Burner Rig Cycle Thermocouple Data

Baseline cyclic life of the TBC was determined as a function of maximum substrate temperature by exposure of eight baseline coated burner rig test specimens to the test condition identified as "D1" and five baseline coated specimens to test condition "D2" in Figure 20. Cycle duration in these tests was 6 minutes, with 4 minutes of flame immersion (1 - 1.5 minutes to temperature and 2.5 - 3 minutes at temperature) and 2 minutes forced air cooling. Each specimen was cycled to failure, with failure being defined as spallation of the TBC over approximately 50% of the specimen hot zone which amounts approximately to a 1.27cm x 1.27cm (0.5 in x 0.5 in) size patch. A photograph of a typical failed burner rig test specimen is shown in Figure 22.



~1.5 X

Figure 22 Photomicrograph of Typical Burner Rig Failed Specimen

To provide information on the influence of transient heating rate on thermal barrier coating spalling life, six specimens were tested to failure at a transient heating rate which was approximately three minutes instead of one minute. Results of these tests, identified as "E" (3 minute heat-up + 1 minute maximum temperature + 2 minutes cool down) in Figure 20, were used in Task IC and subsequent life prediction modeling analyses.

Two approaches were employed to evaluate interaction(s) between thermal exposure and cyclic degradation modes. The first of these involved cyclic exposure as defined above with a longer cycle duration (identified as "long cycle" in Figure 20). The long cycle employed was 60 minutes, involving 57 minutes flame immersion (approximately 1 - 1.5 minutes to temperature and 55.5 - 56 minutes at temperature) and 3 minutes forced air cooling. Four "baseline" thermal barrier coated specimens were cycled to failure at the condition identified as "F" in Figure 20.

A second approach to evaluate interactions between cycling and thermal exposure involved cyclic testing of furnace pre-exposed specimens at the same cyclic conditions as the baseline specimens. The test plan involved pre-exposure of test specimens in air and in argon to approximately one-half of the estimated total hot times (hot time = total cycle time-transient heat-up + transient cool down time), which were anticipated for failure of the baseline coating in the corresponding test. Pre-exposure durations were selected on the basis of prior experience. The actual pre-exposure "life fraction" was calculated from baseline test results after testing was completed. Four pre-exposed specimens, two each exposed in oxidizing and non-oxidizing environments, were tested at each of the test conditions identified in Figure 20.

To determine the influence of ceramic thickness on coating life, two specimens coated with a nominal 0.13 mm (0.005 in) thick ceramic and two specimens coated with a nominal 0.38 mm (0.015 in) thick ceramic were included in each of the four burner rig tests identified as 9, 11, 13, and 17 in Figure 20.

To provide information concerning the nature and rate of accumulation of coating damage, a fractional exposure test, identified as "G" was conducted. In this test, two groups of specimens were exposed to approximate decile fractions of the cyclic failure life and examined metallographically to identify possible progressive damage mode(s) which cause ceramic spalling failure. In the first group, specimens were cycled to each of the approximately 10%, 20%, 30%, 40%, 50%, 60%, 70%, 80%, and 90% fractions of the estimated cyclic failure life defined in the "D1" test. A single specimen was included in this first group which was tested until failure and then life fractions of the other specimens in this group were adjusted accordingly. The second group of specimens were cycled to life fractions of exposure times which were chosen to focus on giving better resolution to the actual failure time.

3.1.2.2.1 Cyclic Thermal Exposure Test Results

A comparative summary of the Task IB burner rig test results is presented in Table IX. Detailed results for each test are listed in Table X.

TABLE IX
COMPARATIVE SUMMARY OF TASK IB BURNER RIG TEST RESULTS
TOTAL HOURS TO FAILURE/CYCLES TO FAILURE/
ESTIMATED HOURS OF HOT TIME TO FAILURE*

TEST CODE/ CONDITION	STANDARD "BASELINE" AVERAGE	THIN AVERAGE	ARGON PRE-EXPOSED AVERAGE	THICK AVERAGE	AIR PRE-EXPOSED AVERAGE
D1/2100°F I.D., Short Cycle - Fast Heat Up Rate	186/1860/77	238/2380/99	215/2150/130	132/1320/55	50/500/61
D2/2000°F I.D., Short Cycle - Fast Heat Up	471/4710/235	525/5250/263	694/6940/447	470/4700/235	205/2050/203
E/2100°F I.D., Short Cycle - Slow Heat Up	135/1350/22	162/1620/27	142/1420/64	121/1210/20	29/290/45
F/2100°F I.D., Long Cycle - Fast Heat Up	72/72/67	119/119/110	98/98/162	59/59/55	16/16/55

*Estimated hours of hot time to failure include time for Air and Argon thermal exposure prior to burner rig testing.

TABLE X
BURNER RIG TEST RESULTS

TEST CODE/ TEST CONDITION	"BASELINE" STANDARD	AIR PRE-EXPOSED	ARGON PRE-EXPOSED	THICK CERAMIC	THIN CERAMIC
D1/2100°F, Short Cycle Fast Heat Up Rate	182 } 172 } 213 } 175 } 172 } 193 } 182 } 198 } AVG = 186	50 } 50 } AVG = 50	75 } 67 } 279 } 279 } 279 } 221 } 199 } 199 } 271 } AVG = 215	104 } 160 } AVG = 132	243 } 232 } AVG = 238
D2/2000°F, Short Cycle Fast Heat Up Rate	386 } 443 } 435 } 557 } 536 } AVG = 471	194 } 215 } AVG = 205	679 } 708 } AVG = 694	515 } 425 } AVG = 470	557 } 492 } AVG = 525
E1/2100°F, Short Cycle Fast Heat Up Rate	156 } 129 } 142 } 142 } 121 } 121 } AVG = 135	39 } 18 } AVG = 29	142 } 142 } AVG = 142	121 } 121 } AVG = 121	162 } 162 } AVG = 162
F1/2100°F, Long Cycle Fast Heat Up Rate	70 } 60 } 59 } 98 } AVG = 72	16 } 16 } AVG = 16	93 } 102 } AVG = 98	54 } 64 } AVG = 59	116 } 122 } AVG = 119

Review of these data clearly indicates exposure temperature to have a strong influence on spallation life. Comparison of baseline coating lives at 1094°C (2000°F) and 1149°C (2100°F) (D2 versus D1 results in Table IX) indicates approximately 60 percent reduction in life for a 55°C (100°F) increase in exposure temperature. This temperature effect is shown graphically in Figure 23, where estimated total hot time to failure is plotted versus exposure temperature for the D1 and D2 baseline tests together with results from other tests conducted on internal programs. Also included for comparison in Figure 23 are results of the quasi-static failure tests shown previously in Figure 6. This comparison clearly shows the influence of thermal cycling on spallation life. The reason for the apparent curvature of the cyclic data in Figure 23, as opposed to the apparently linear behavior of the static data, is not presently understood.

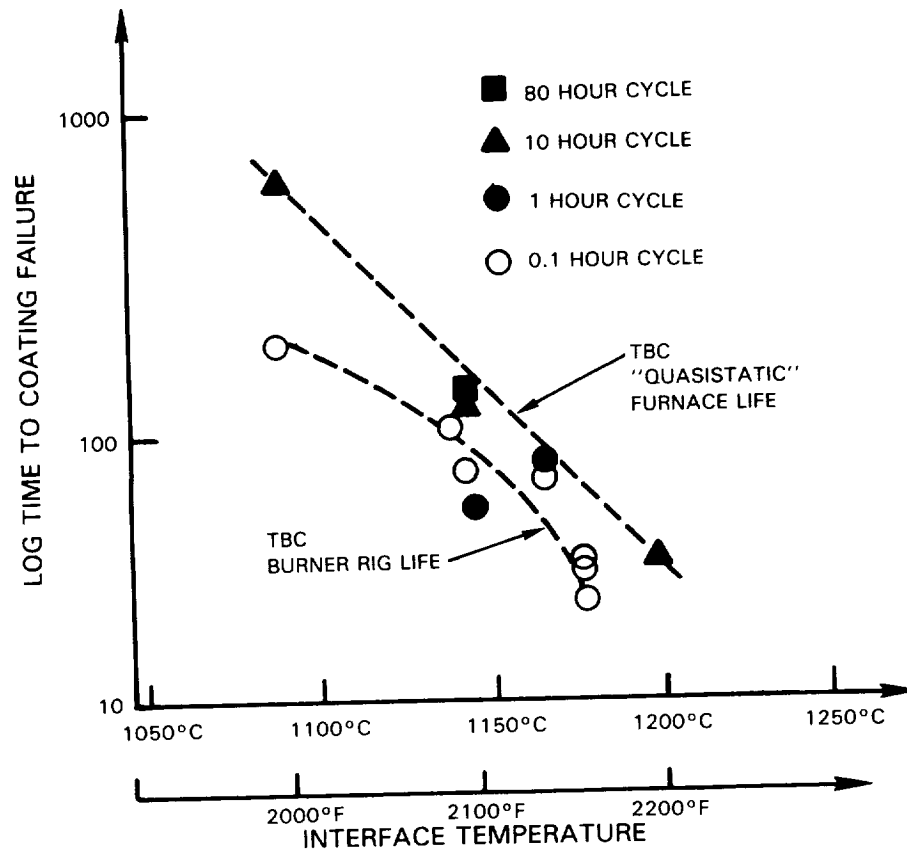


Figure 23 Test Data Showing Coating Life Dependent on Temperature, "Cyclic Content"

The effect of cycle frequency on spallation life is shown by comparison of the D1 and F test results in Table IX. When compared on the basis of cycles to failure, a dramatic life reduction is seen; however, when compared on the basis of estimated time at maximum exposure temperature, cyclic frequency is seen to have relatively little influence on life in the frequency range and at the temperature studied, as seen in Figure 23. This latter observation must be interpreted with some caution, as the 1149°C (2100°F) temperature where the frequency effect was studied is, by coincidence, the temperature of closest approach of the cyclic and quasi-static life data. It is possible that, had the effect of frequency been measured at a lower or higher temperature, a more significant influence on life might have been seen.

As described previously, Test E was conducted to assess the influence of transient heating rate on spallation life. It was expected that the slower transient and reduced time at temperature would increase life; however, as seen in Table IX, spallation life appears to have been slightly reduced by this change of test parameters. This result is not fully understood at the present time; however, evaluation of this data set by the subsequently discussed preliminary prediction system indicates that the difference of life between the baseline and reduced transient results could be accounted for by a temperature error of less than 5.6°C (10°F), which is within the inherent accuracy of the thermocouple based instrumentation system used to establish

temperature for these two tests. Based on this observation, it seems reasonable to conclude at this point that the reduction of transient heating rate appears to have no significant influence on life within the range of scatter inherent in the burner rig test.

In an effort to assess the influence of thermal exposure on spallation life and to separate thermal from environmental effects, coated specimens which were thermally pre-exposed in both oxidizing and non-oxidizing environments were included in several of the burner rig tests discussed above. As illustrated in Figures 24 and 25, results of these tests indicate that isothermal pre-exposure in air caused a significant reduction of subsequent cyclic spalling life, while pre-exposure in a non-oxidizing environment did not reduce life. It is interesting to note in Figure 24 that the total time at temperature for spallation of the air pre-exposed specimens is roughly comparable to hot time to failure for cyclically tested baseline specimens. This observation, coupled with the absence of a life debit for non-oxidizing pre-exposure, strongly suggests that oxidization is a primary thermal barrier coating degradation mechanism.

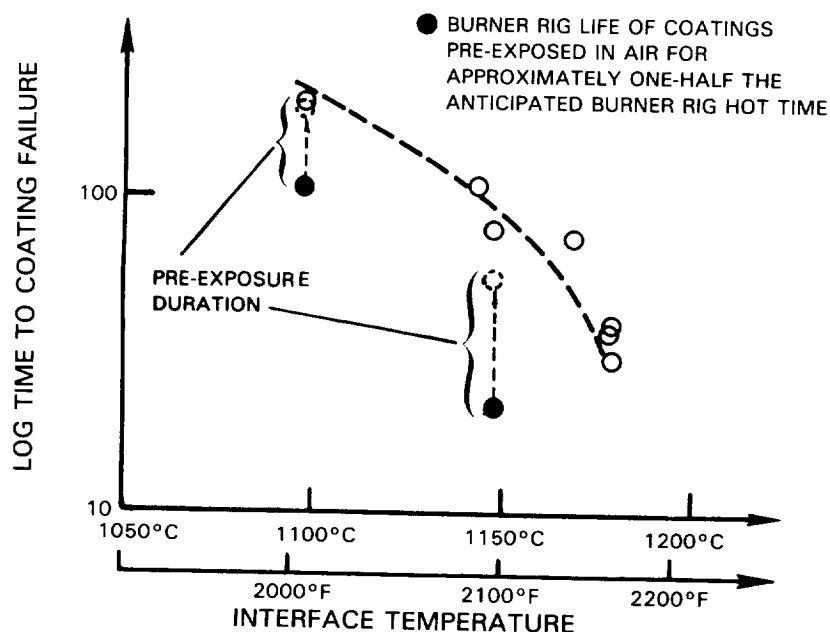


Figure 24 Test Data Showing Air Pre-Exposure Degrades Cyclic Life

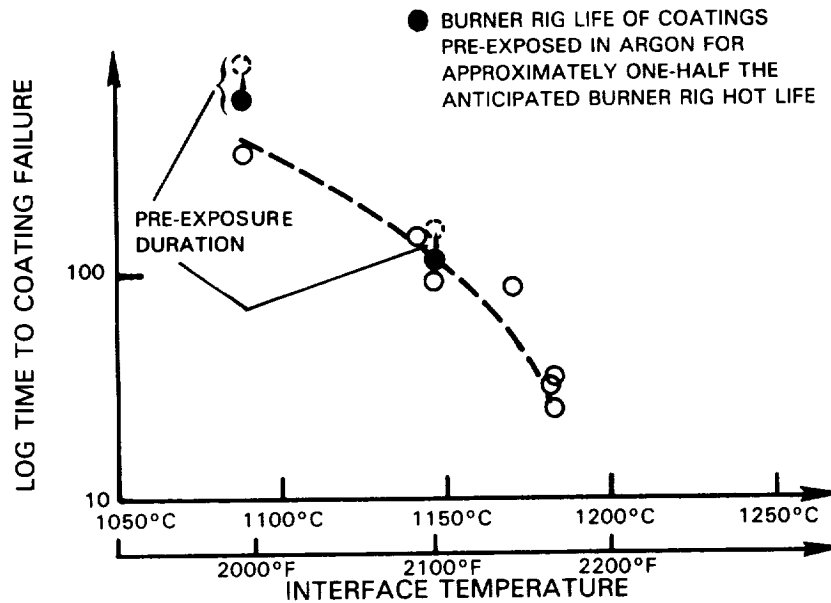


Figure 25 Test Data Showing "INERT" Pre-Exposure Does Not Effect Coating Performance

The influence of ceramic thickness on baseline test spallation life is illustrated in Figure 26. As expected, reducing ceramic thickness provided a small increase of life, while increasing thickness reduced life. Examination of the data in Table IX indicates that this effect is consistent for the various test parameters investigated.

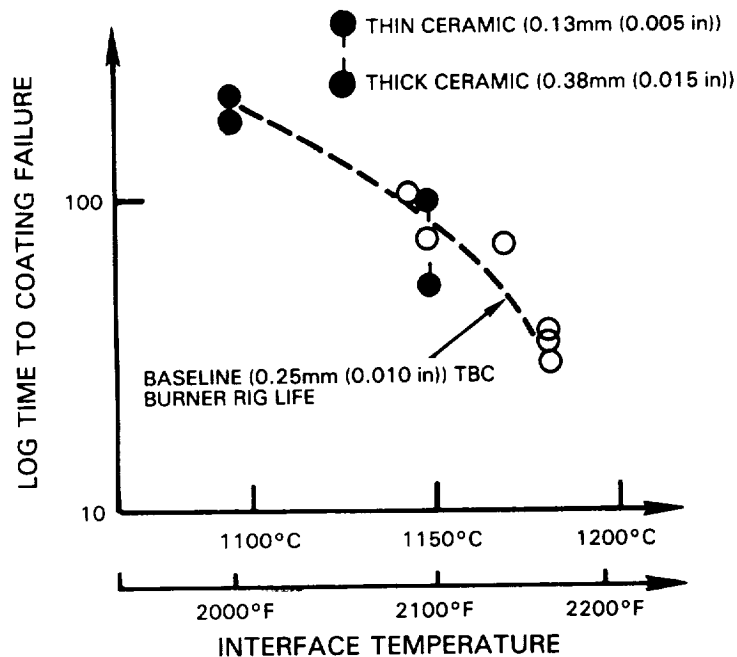


Figure 26 Test Data Showing Ceramic Thickness Effects

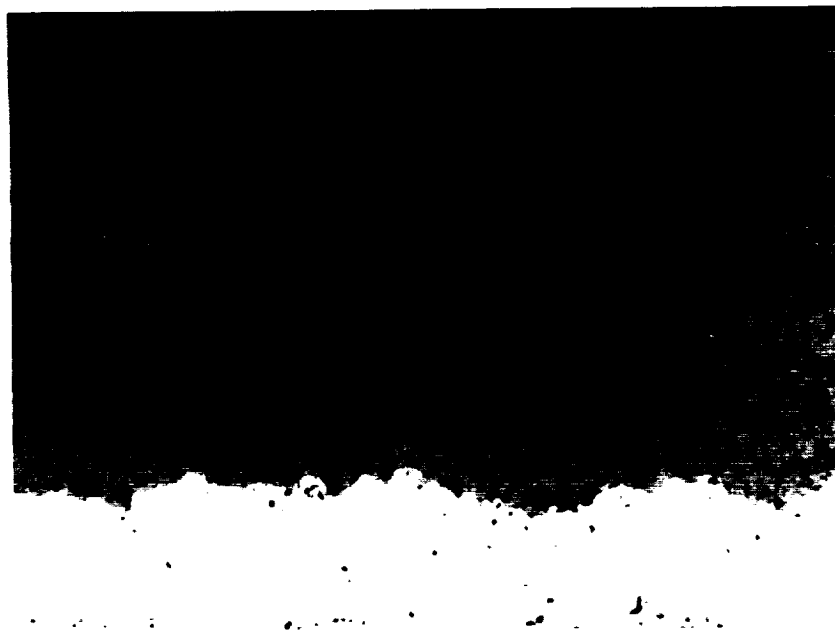
3.1.2.2.2 Microstructural Evaluation for Cyclic Thermal Exposure Tests

In an effort to better understand the phenomenological observations discussed above, failed burner rig specimens were examined metallographically. All burner rig specimens exhibited "typical" near interface ceramic spallation, with a thin layer of ceramic remaining adherent to the bond coat after failure.

Figures 27 through 30 show representative baseline pre-test and post-test microstructures for all four burner rig test conditions. In comparing the baseline laboratory post test microstructures with engine exposed failures, "oxidation damage" (oxide thickness) appeared to be somewhat greater for the laboratory test specimens. This is attributed to the relatively high interface temperatures employed in the accelerated laboratory spallation life testing. Oxide thickness was on the order of 7.6 microns (0.0003 in) for all of the tests except for the long cycle 1149°C (2100°F) test in which oxide thickness was estimated to be twice as thick. The microstructures also show Kirkendall void alignment at the original bond coat- substrate interface suggesting bond-coat/substrate compositional changes. Kirkendall voids have not generally been observed to a great extent in revenue engine service hardware.

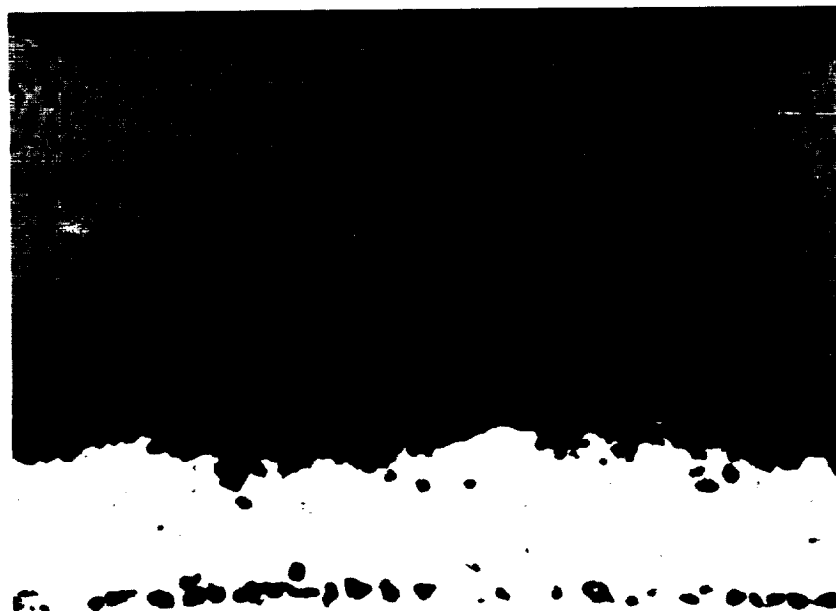
In the laboratory test conducted to study environmental effects, results suggested that oxidation damage contributed significantly to thermomechanical cracking in the ceramic layer. Figures 31 through 34 show the pre-test (post furnace exposure) and post burner rig test microstructures of representative air pre-exposed specimens for each test condition. Figures 35 through 38 show the pre-test (post-furnace exposure) and post burner rig test microstructures for representative argon pre-exposed specimens. Evaluation of the specimen microstructures pre-exposed in air and in argon, prior to burner rig testing, showed that the former has a well defined thick oxide layer at the metal ceramic interface which the latter does not. The air pre-exposed specimen oxide layer is on the order of 7.6 microns (0.0003 in) thick prior to laboratory testing. The air pre-exposed microstructures also show a beta (NiAl) depleted zone in the bond coat about 38.1 microns (0.0015 in) wide directly below the oxide layer, suggesting that the composition of the oxide may be predominantly Al_2O_3 or alumina spinel. This near-interface beta depletion is clearly absent in those specimens which were argon heat treated. Coarsening of the beta phase was observed for both types of pre-exposure.

The air and argon pre-exposed microstructures, exhibited an interdiffusion zone at the area adjacent to and below the bond coat-substrate interface, marked by Kirkendall void alignment. This suggests that the bond coat and substrate composition has changed. It is possible that the slight increase in coating life found with the argon pre-exposed specimens is due to these compositional changes which may result in changes in the bond coat strength properties. For the air pre-exposed specimens, any benefits obtained due to these compositional changes would be overridden by the thick oxide developed at the interface.



200X
Unetched

Figure 27a Light Photomicrograph of Baseline Pre-Test Microstructure (D1 Test)

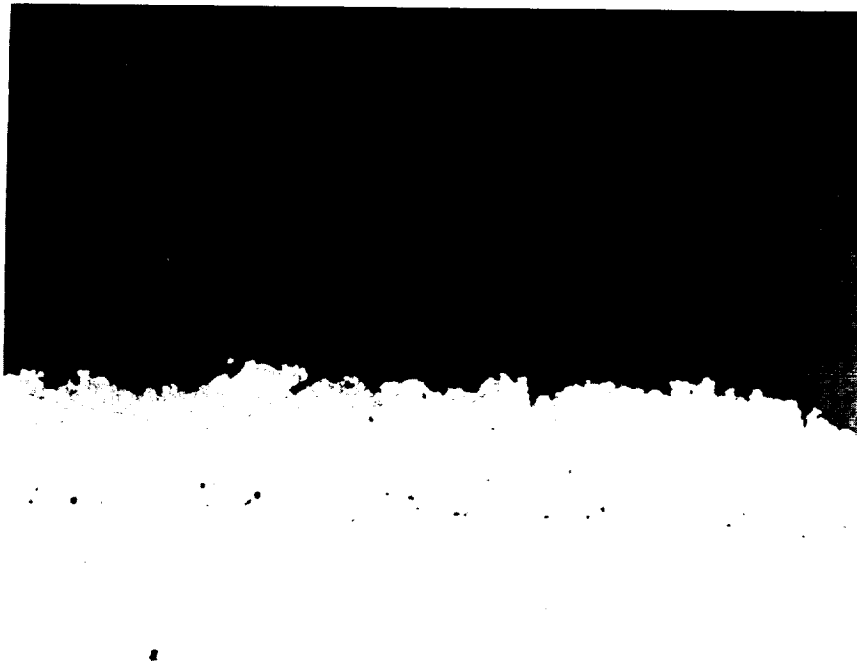


D1 Baseline Post-Test
175 hrs/2100°F - I.D./Short Cycle
HST 004 (85-18)

200X
Etched - AG 21

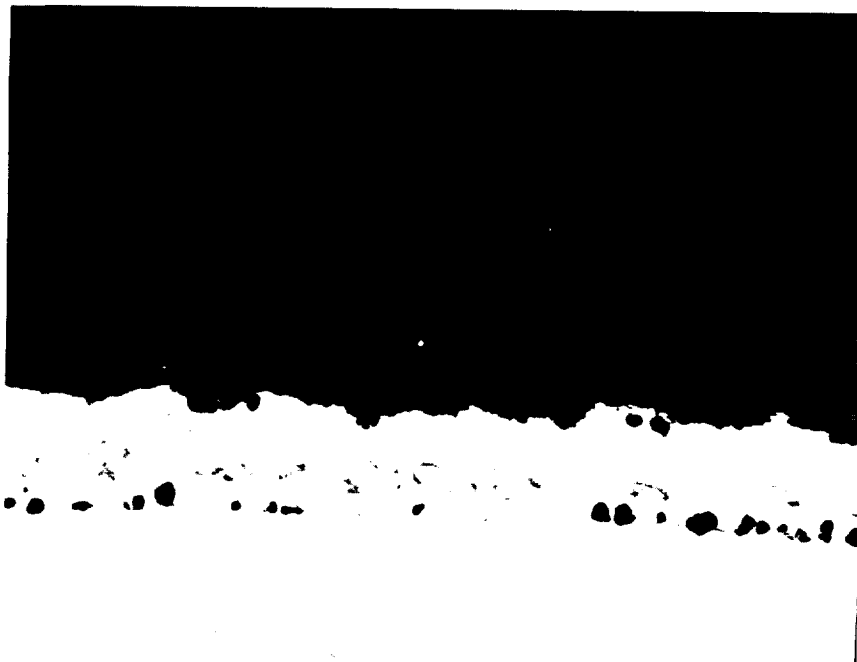
Figure 27b Light Photomicrograph of Baseline Post-Test Microstructure (D1 Test) After 175 hrs at 1149°C (2100°F)/Short Cycle/Fast Heat-Up Rate

ORIGINAL PAGE
BLACK AND WHITE PHOTOGRAPH



Etched - AG 21 200X

Figure 28a Light Photomicrograph of Baseline Pre-Test Microstructure (D2 Test)



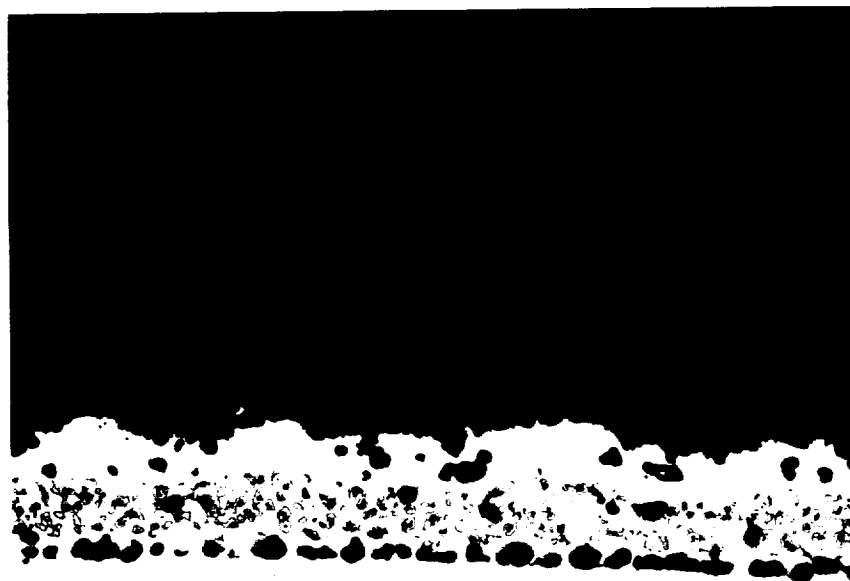
Etched - AG 21 200X

Figure 28b Light Photomicrograph of Baseline Post-Test Microstructure (D2 Test) After 435 hrs at 1094°C (2000°F)/Short Cycle/Fast Heat-Up Rate



Etched - AG 21 200X

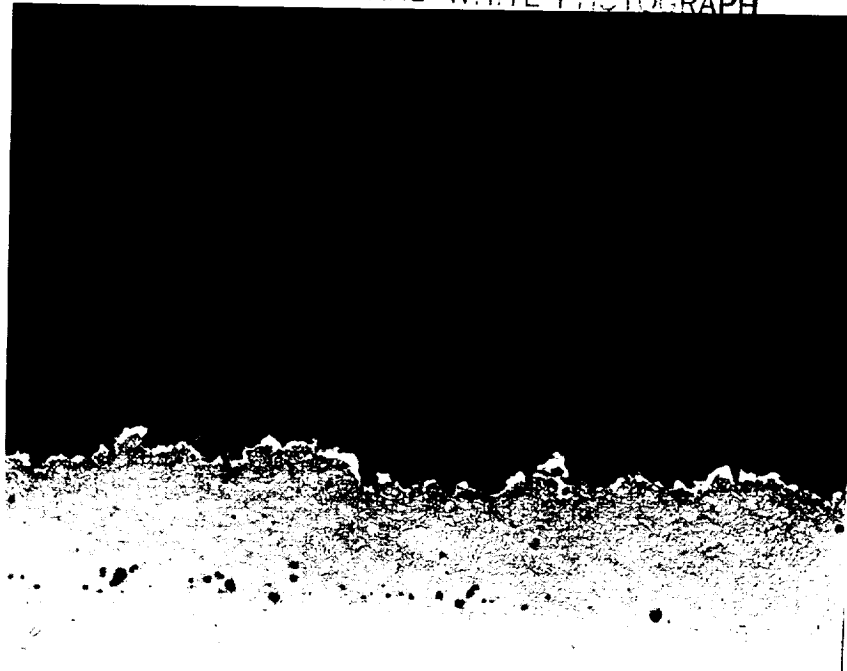
Figure 29a Light Photomicrograph of Baseline Pre-Test Condition (E Test)



Etched - AG 21 200X

Figure 29b Light Photomicrograph of Baseline Post-Test Microstructure (E Test)
After 142 hrs at 1149°C (2100°F)/Short Cycle/Slow Heat-Up Rate

ORIGINAL PAGE
BLACK AND WHITE PHOTOGRAPH



Etched - AG 21 200X

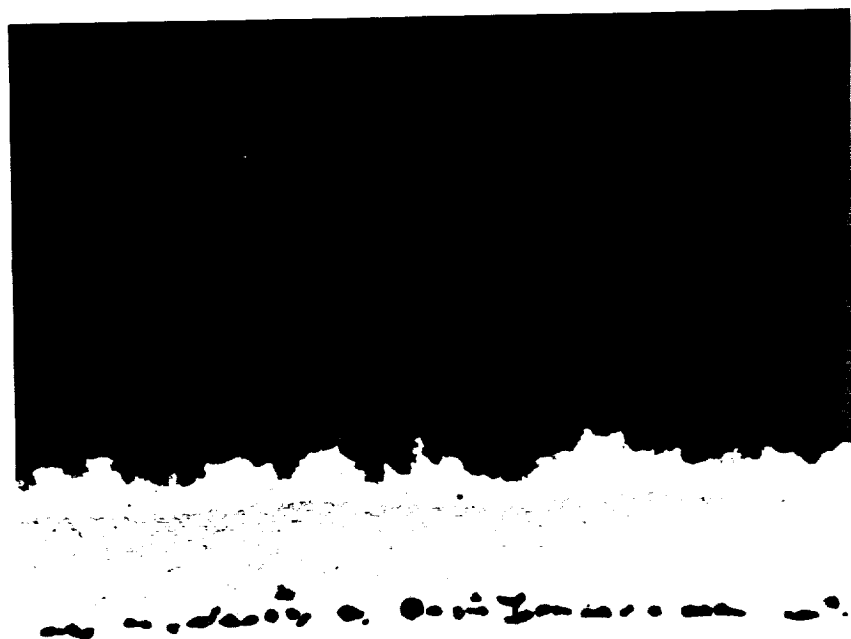
Figure 30a Light Photomicrograph of Baseline Pre-Test Microstructure (F Test)



Etched - AG 21 200X

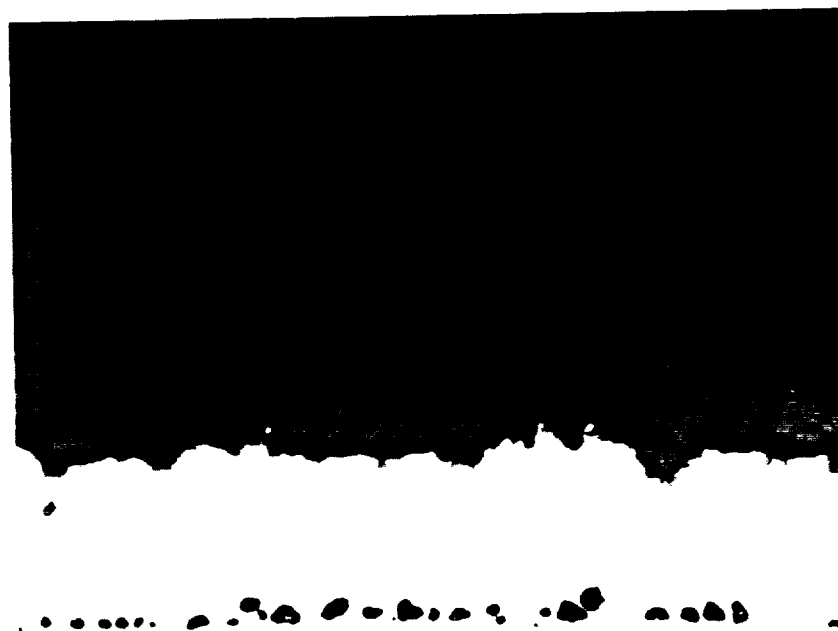
Figure 30b Light Photomicrograph of Baseline Post-Test Microstructure (F Test)
After 70 hrs at 1149°C (2100°F)/Long Cycle/Fast Heat-Up Rate

ORIGINAL PAGE
BLACK AND WHITE PHOTOGRAPH



Etched - AG 21 200X

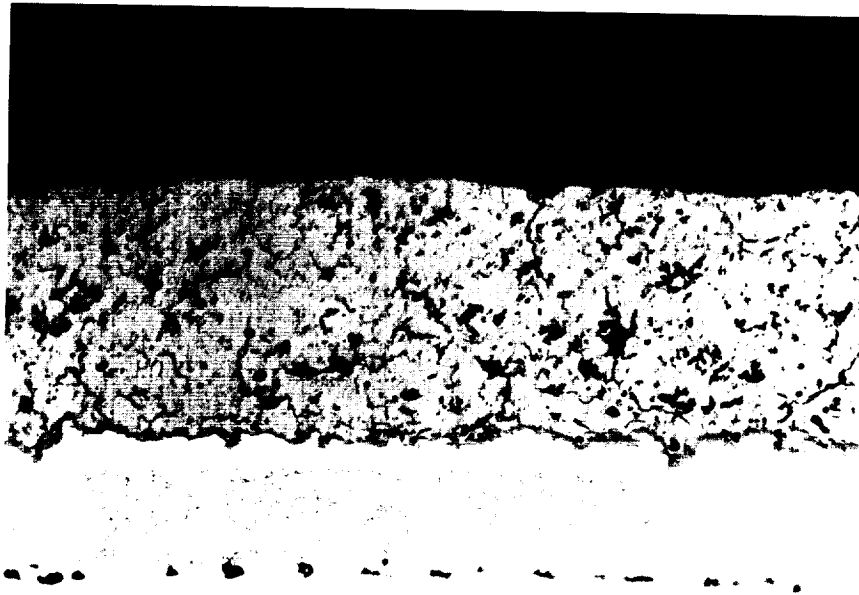
Figure 31a Light Photomicrograph of Pre-Burner Rig Microstructure (D1 Test)
for Air Pre-Exposed Specimen (1149°C (2100°F)/40hrs)



Etched - AG 21 200X

Figure 31b Light Photomicrograph of Post-Burner Rig Microstructure (D1 Test)
for Air Pre-Exposed Specimen (1149°C (2100°F)/40 hrs) After 50 hrs
at 2100°F/Short Cycle/Fast Heat-Up Rate

ORIGINAL PAGE
BLACK AND WHITE PHOTOGRAPH



Etched - AG 21 200X

Figure 32a Light Photomicrograph of Pre-Burner Rig Microstructure 56 (D2 Test)
for Air Pre-Exposed Specimen (1149°C (2000°F)/100hrs)



Etched - AG 21 200X

Figure 32b Light Photomicrograph of Post-Burner Rig Microstructure (D2 Test)
for Air Pre-Exposed Specimen (1149°C (2100°F)/100 hrs) After 215
hrs at 1094°C (2000°F)/Short Cycle/Fast Heat-Up Rate

ORIGINAL PAGE
BLACK AND WHITE PHOTOGRAPH



Etched - AG 21 200X

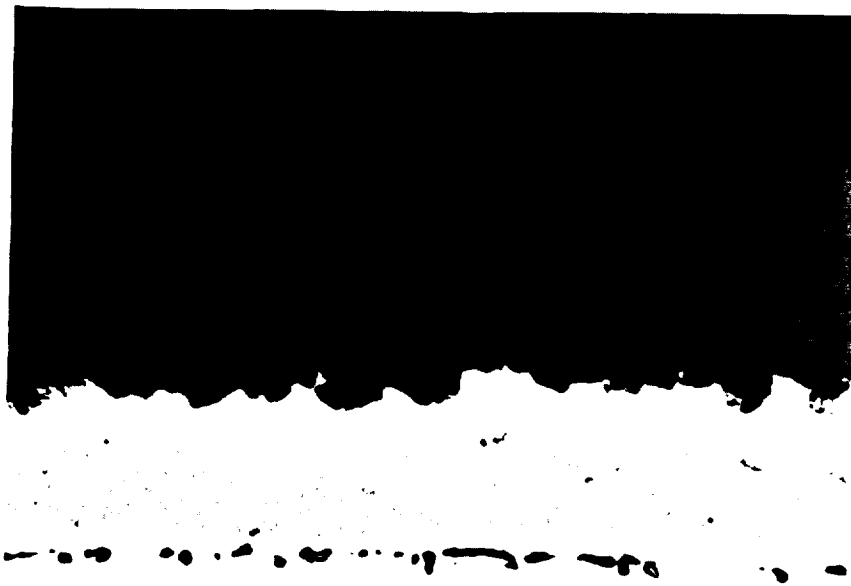
Figure 33a Light Photomicrograph of Pre-Burner Rig Microstructure (E2 Test)
for Air Pre-Exposed Specimen (1149°C (2100°F)/40 hrs)



Etched - AG 21 200X

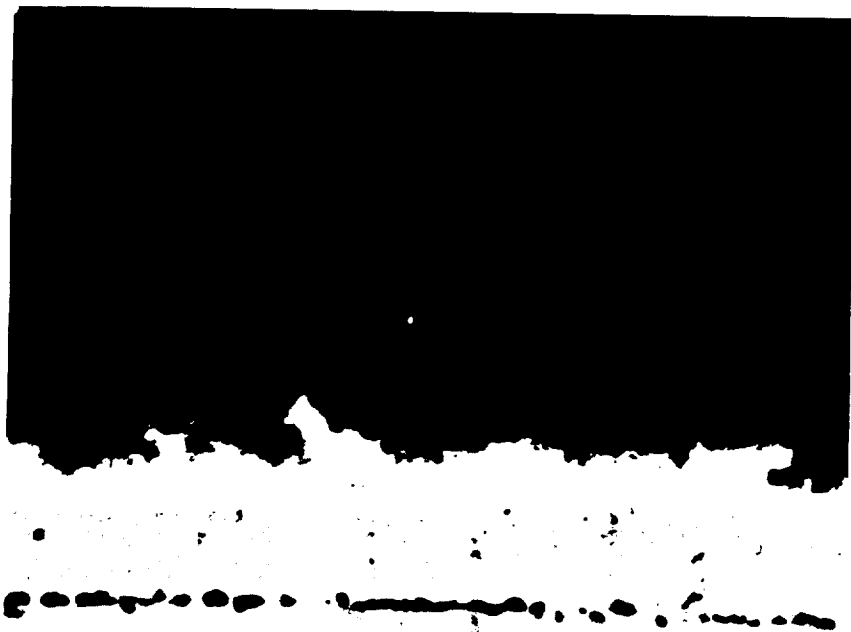
Figure 33b Light Photomicrograph of Post-Burner Rig Microstructure (E2 Test)
for Air Pre-Exposed Specimen (1149°C (2100°F)/40 hrs) After 39 hrs
at 1094°C (2000°F)/Short Cycle/Slow Heat-Up Rate

ORIGINAL PAGE
BLACK AND WHITE PHOTOGRAPH



Etched - AG 21 200X

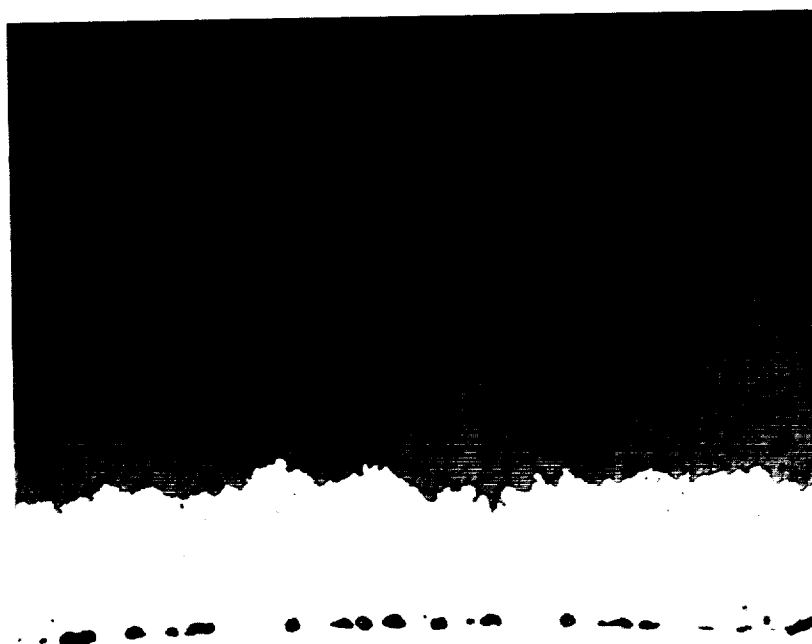
Figure 34a Light Photomicrograph of Pre-Burner Rig Microstructure (F1 Test)
for Air Pre-Exposed Specimen (1149°C (2100°F)/40 hrs)



Etched - AG 21 200X

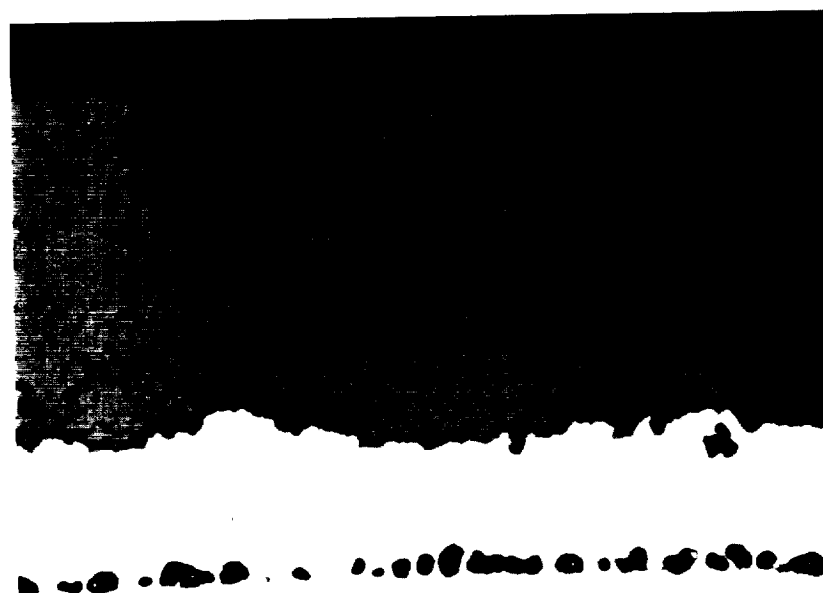
Figure 34b Light Photomicrograph of Post-Burner Rig Microstructure (F1 Test)
for Air Pre-Exposed Specimen (1149°C (2100°F)/40 hrs) After 16 hrs
at 2100°F/Long Cycle/Fast Heat-Rate.

ORIGINAL PAGE
BLACK AND WHITE PHOTOGRAPH



Etched - AG 21 200X

Figure 35a Light Photomicrograph of Pre-Burner Rig Microstructure (D1 Test)
for Argon Pre-Exposed Specimen (1149°C (2100°F)/40 hrs)



Etched - AG 21 200X

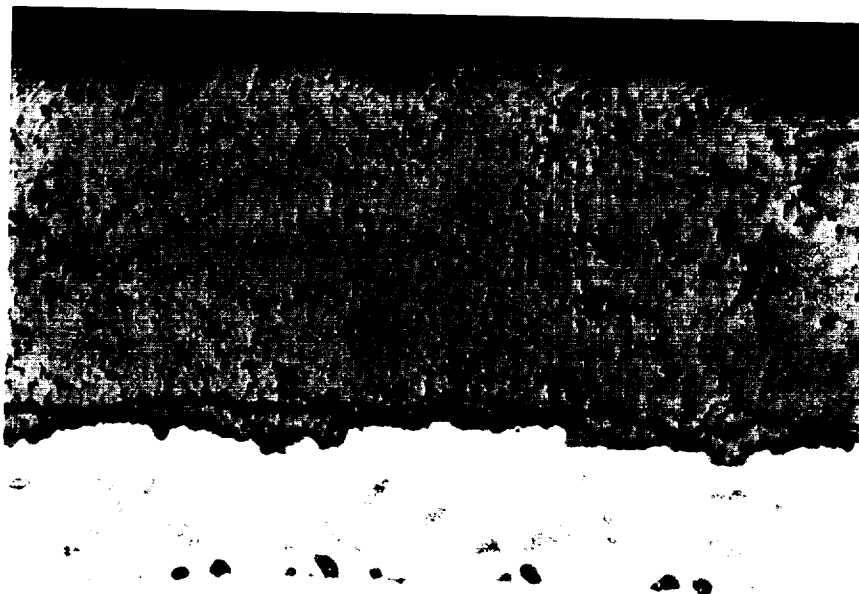
Figure 35b Light Photomicrograph of Post-Burner Rig Microstructure (D1 Test)
for Argon Pre-Exposed Specimens After 67 hrs at 1149°C
(2100°F)/Short Cycle/Fast Heat-Up Rate

ORIGINAL PAGE
BLACK AND WHITE PHOTOGRAPH



Etched - AG 21 200X

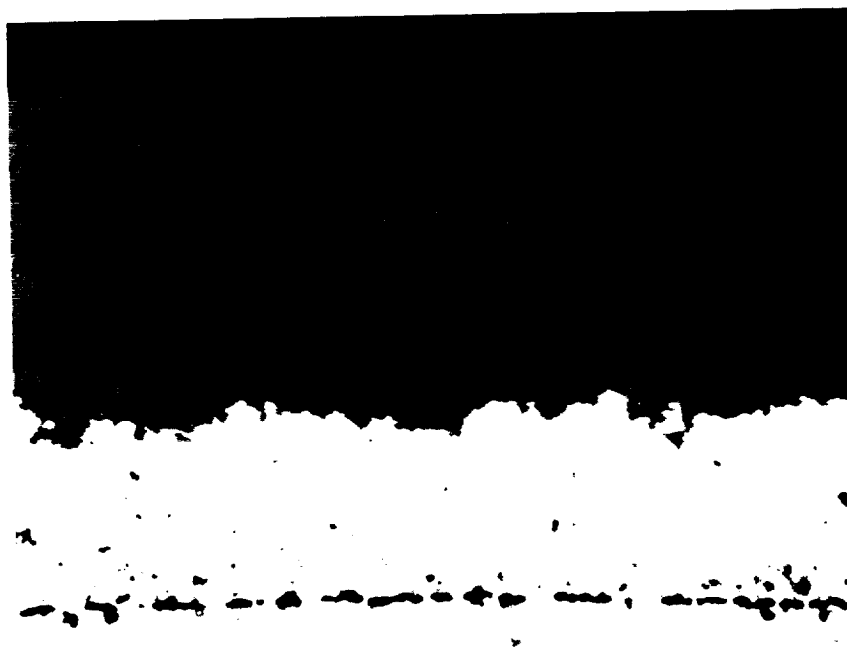
Figure 36a Light Photomicrograph for Pre-Burner Rig Microstructure (D2 Test)
for Argon Pre-Exposed Specimen (1094°C (2000°F)/100 hrs)



Etched - AG 21 200X

Figure 36b Light Photomicrograph of Post Burner Rig Microstructure (D2 Test)
for Argon Pre-Exposed Specimen (1094°C (2000°F)/100 hrs) After 708
hrs at 1094°C (2000°F)/Short Cycle/Fast Heat-Up Rate

ORIGINAL PAGE
BLACK AND WHITE PHOTOGRAPH



Etched - AG 21 200X

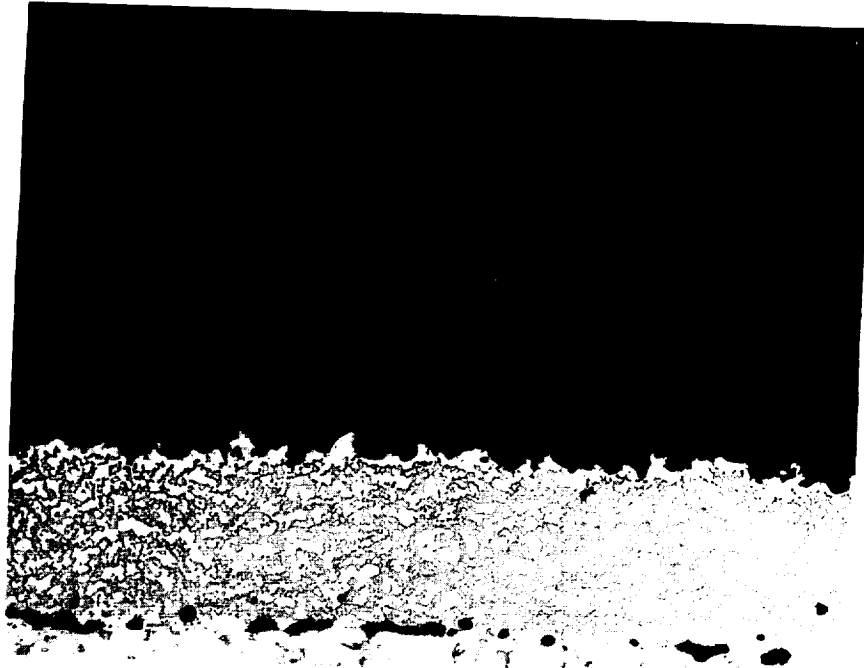
Figure 37a Light Photomicrograph for Pre-Burner Rig Microstructure (E Test)
for Argon Pre-Exposed Specimen (1194°C (2100°F)/40 hrs)



Etched - AG 21 200X

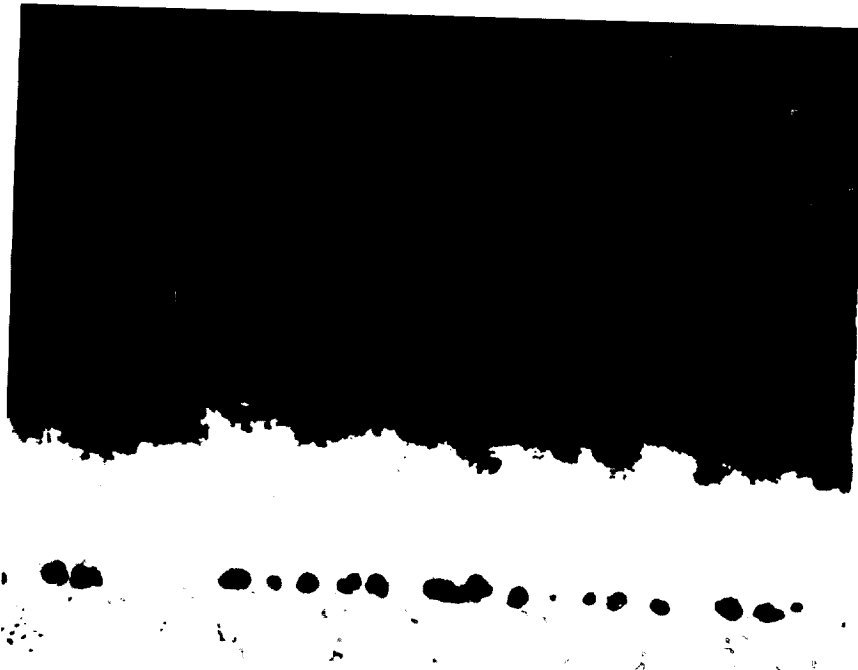
Figure 37b Light Photomicrograph of Post Burner Rig Microstructure (E Test)
for Argon Pre-Exposed Specimen (1194°C (2100°F)/40 hrs) After Short
Cycle/Slow Heat-Up Rate

ORIGINAL PAGE
BLACK AND WHITE PHOTOGRAPH



Etched - AG 21 200X

Figure 38a Light Photomicrograph for Pre-Burner Rig Microstructure (F Test)
for Argon Pre-Exposed Specimen (1194°C (2100°F)/40 hrs)



Etched - AG 21 200X

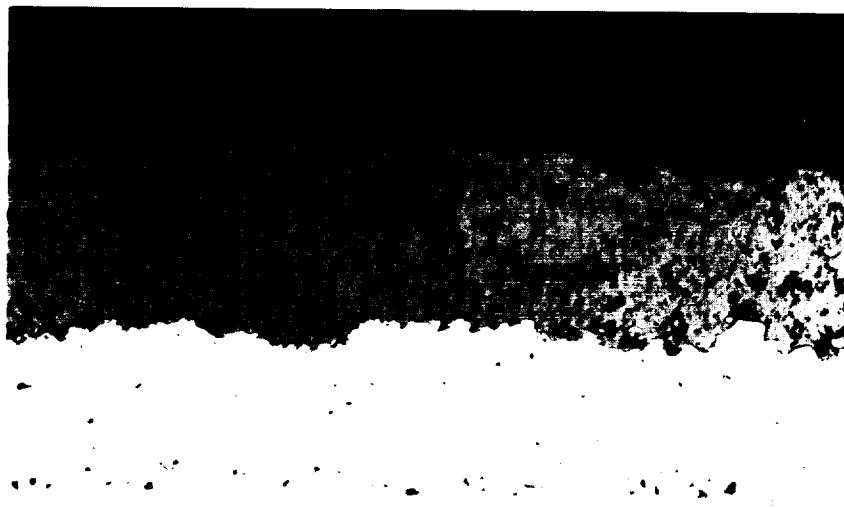
Figure 38b Light Photomicrograph of Post Burner Rig Microstructure (F Test)
for Argon Pre-Exposed Specimen (1194°C (2100°F)/40 hrs) After Long
Cycle/Fast Heat-Up Rate

Figures 39 through 42 show the pre-test and post-test microstructures for representative thin ceramic coated specimens. The post-test microstructures all show wide beta (NiAl) depleted zones and substrate interdiffusion layers as compared with baseline coating microstructures. This is attributed to the greater exposure time experienced by these specimens. Bond coat oxide thickness ranged from 5.1 microns (0.0002 in) to 15.2 microns (0.0006 in) for the D1 (1149°C (2100°F), short cycle, fast heat-up) and F (1149°C (2100°F), long cycle, fast heat-up) test specimens, respectively. Figures 43 through 46 show the pre-test and post-test microstructures for representative thick ceramic coated specimens. The microstructures shown in these figures show distinct differences in bond coat oxide growth and beta depletion as well as the degree of beta phase coarsening. The D2 (1094°C (2000°F)/short cycle/fast heat-up) test specimen microstructure shows a larger degree of beta phase coarsening as compared with the other specimen microstructures. The F (1149°C (2100°F)/long cycle/fast heat-up) test specimen microstructure shows the greatest oxide scale thickness as seen earlier. The bond coat microstructure from the specimen in the E test (1149°C (2100°F)/short cycle/slow heat-up) shows excessive porosity, believed to be due to poor bond coat deposition. No differences in the ceramic microstructures are observed in either the pre-test or post-test condition as compared with the other microstructures which have been discussed in preceding paragraphs.

X-ray diffraction analyses for all representative post-test specimens are presented in Table XI. It is believed that no significant amount of monoclinic ZrO_2 was formed. Although, it should be noted that for most cases 1 v/o monoclinic phase was present adjacent to the spall and absent away from the spalled location.

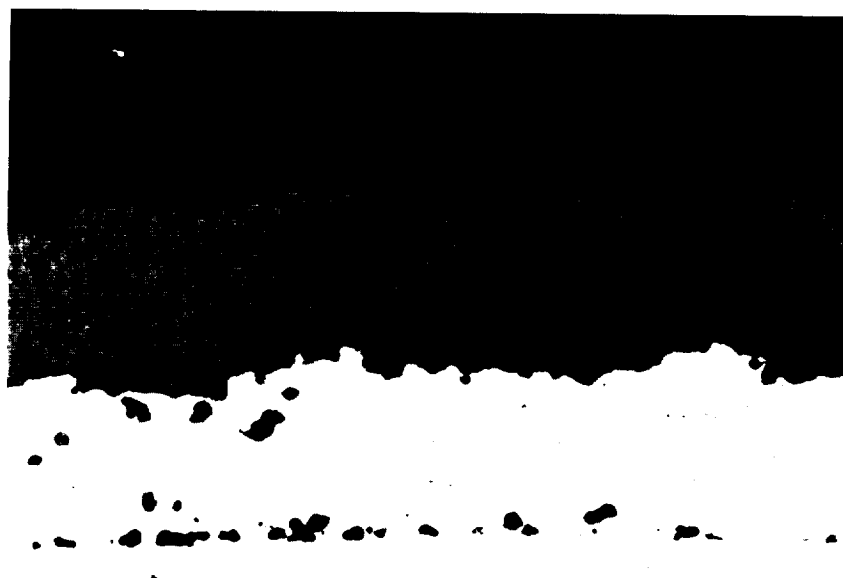
In summary, the comparative post-test specimen evaluation has shown that increased exposure time results in: 1) increased MCrAlY oxide scale thickness, 2) increased beta depletion and/or coarsening, 3) some increase in Kirkendall void population and size occurring at the original bond coat-substrate interface, 4) no significant phase changes in the ceramic, and 5) no gross microstructural changes in the ceramic. Also, it is clear from the post-test microstructures studied that more bond coat oxidation has occurred for the long cycle (F) test than for the more rapid cycle tests, even though total "hot" life was similar.

ORIGINAL PAGE
BLACK AND WHITE PHOTOGRAPH



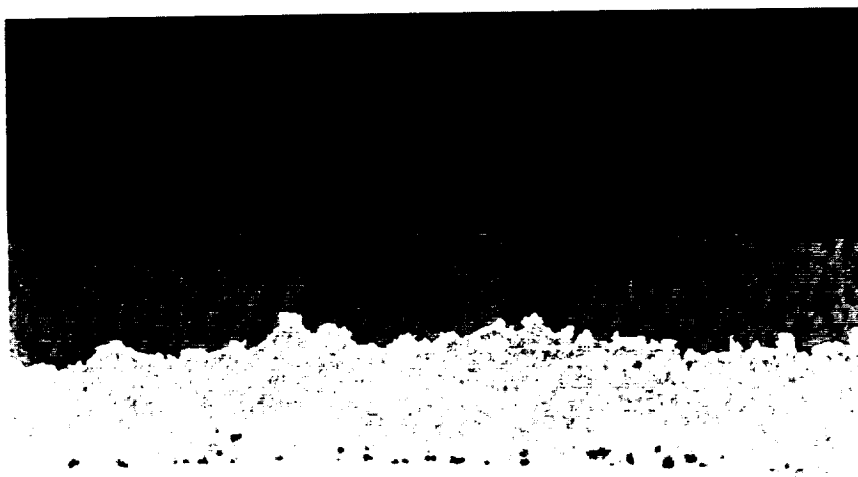
Etched 200X

Figure 39a Light Photomicrograph of Pre-Test Microstructure (DI Test) for a Thin Ceramic Specimen



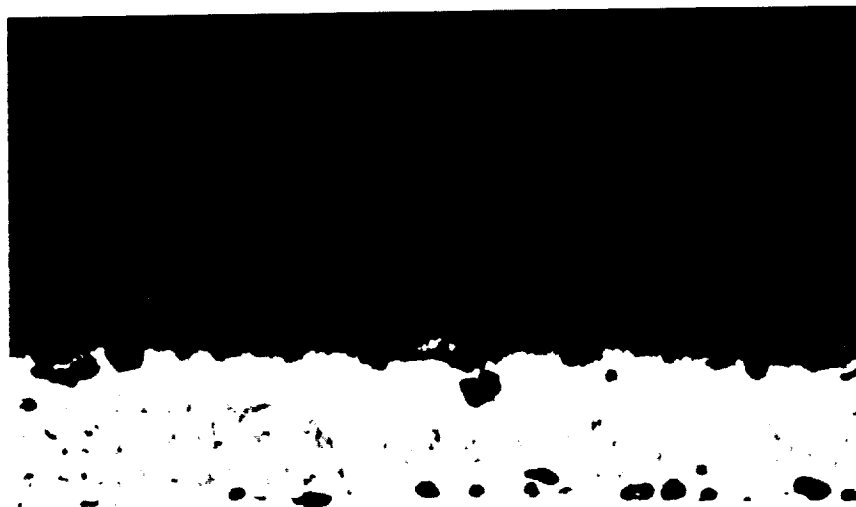
Etched - AG 21 200X

Figure 39b Light Photomicrograph of Post-Test Microstructure (DI Test) for a Thin Ceramic Specimen After 243 hrs at 1194°C (2100°F)/Short Cycle/Fast Heat-Up Rate



Etched - AG 21 200X

Figure 40a Light Photomicrograph of Pre-Test Microstructure (D2 Test) for a Thin Ceramic Specimen



Etched - AG 21 200X

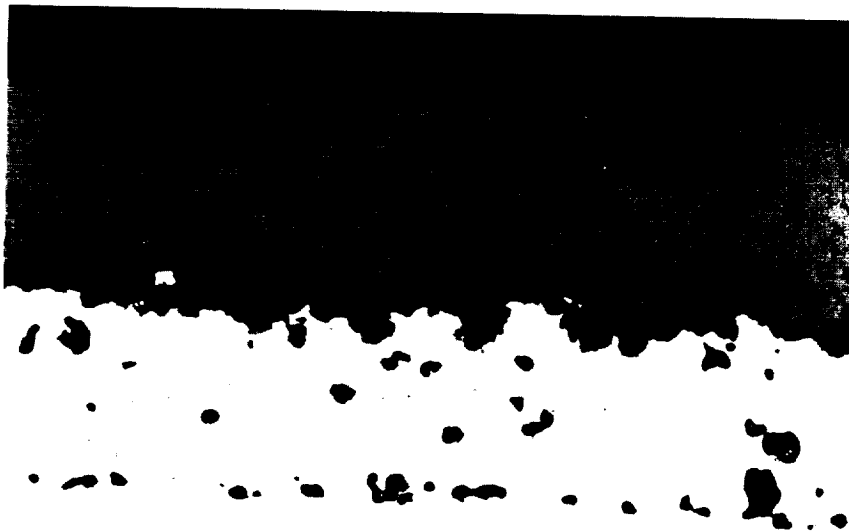
Figure 40b Light Photomicrograph of Post-Test Microstructure (D2 Test) for a Thin Ceramic Specimen After 492 hrs at 1094°C (2000°F)/Short Cycle/Fast Heat-Up Rate

ORIGINAL PAGE
BLACK AND WHITE PHOTOGRAPH



Etched - AG 21 200X

Figure 41a Light Photomicrograph of Pre-Test Microstructure (E Test) for a Thin Ceramic Specimen



Etched - AG 21 200X

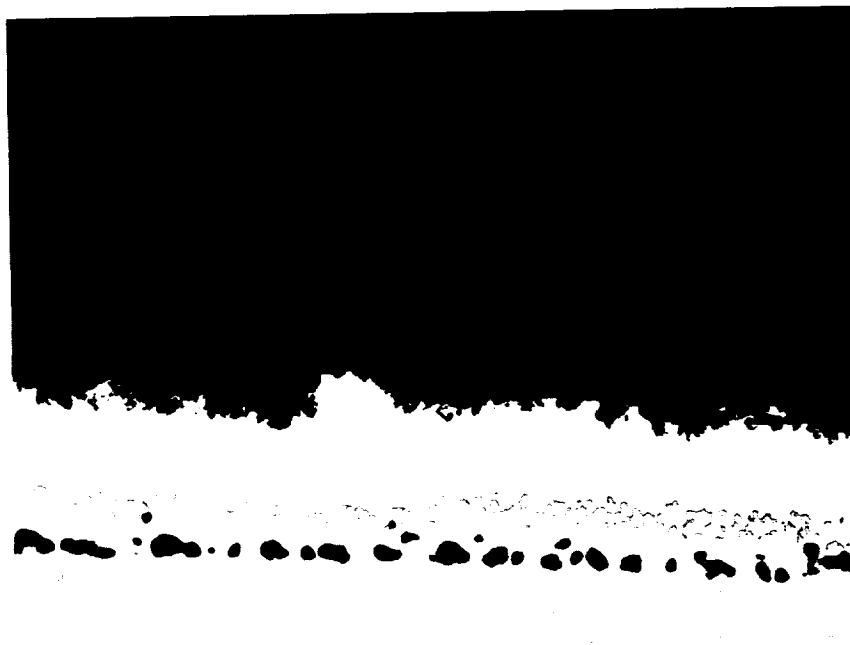
Figure 41b Light Photomicrograph of Post Burner Rig Test Microstructure (E Test) for a Thin Ceramic Specimen After 162 hrs at 1149°C (2100°F)/Short Cycle/Slow Heat-Up Rate

ORIGINAL PAGE
BLACK AND WHITE PHOTOGRAPH



Etched - AG 21 200X

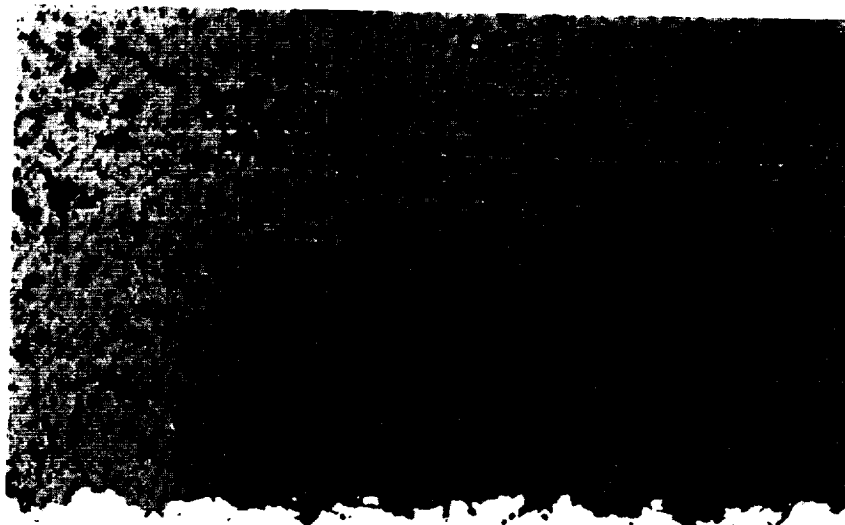
Figure 42a Light Photomicrograph of Pre-Test Microstructure (F Test) for a Thin Ceramic Specimen



Etched - AG 21 200X

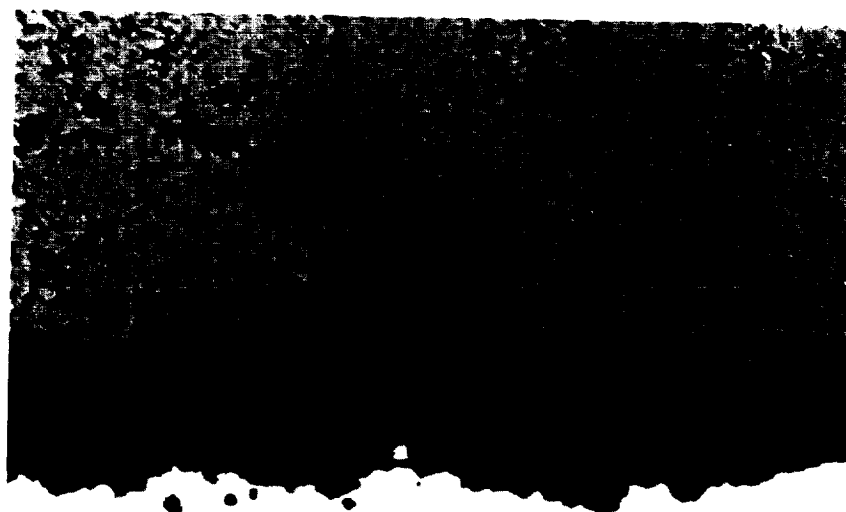
Figure 42b Light Photomicrograph of Post Burner Rig Test Microstructure (F Test) for Thin Ceramic Specimen After 116 hrs at 1149°C (2100°F)/Long Cycle/Fast Heat-Up Rate

ORIGINAL PAGE
BLACK AND WHITE PHOTOGRAPH



Unetched 200X

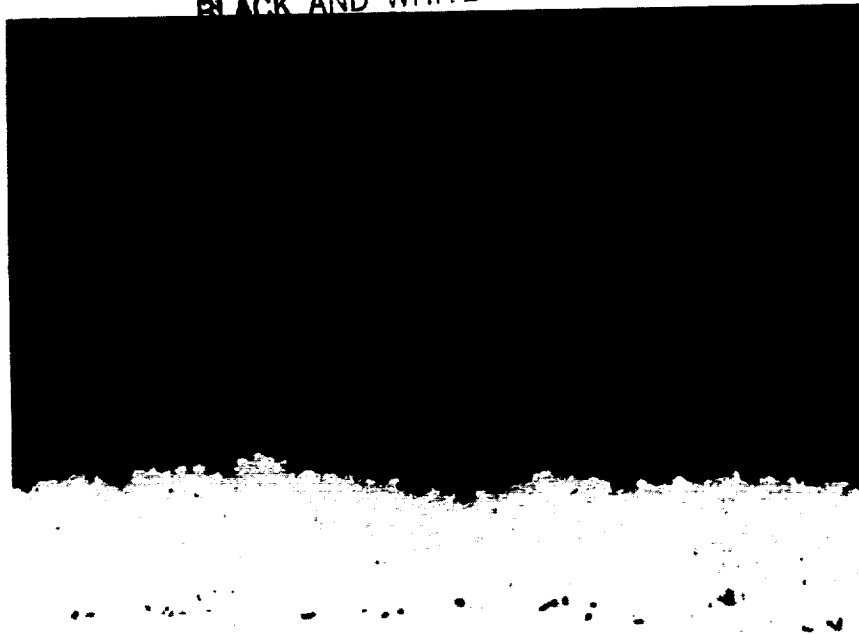
Figure 43a Light Photomicrograph of Post Burner Rig Test Microstructure (D1 Test) for a Thick Ceramic Specimen



Etched - AG 21 200X

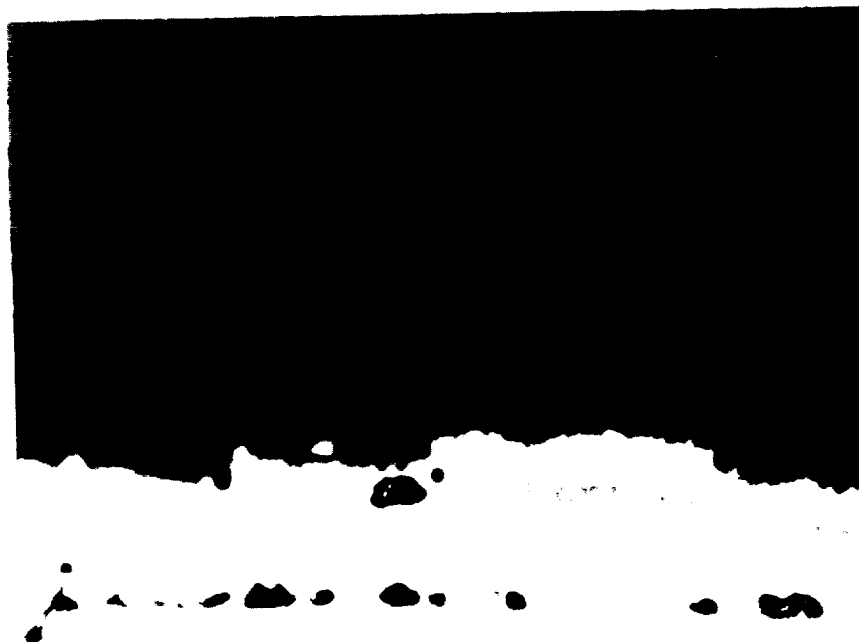
Figure 43b Light Photomicrograph of Post Burner Rig Test Microstructure (D1 Test) for a Thick Ceramic Specimen After 160 hrs at 1149°C (2100°F)/Short Cycle/Fast Heat-Up Rate

ORIGINAL PAGE
BLACK AND WHITE PHOTOGRAPH



Unetched 200X

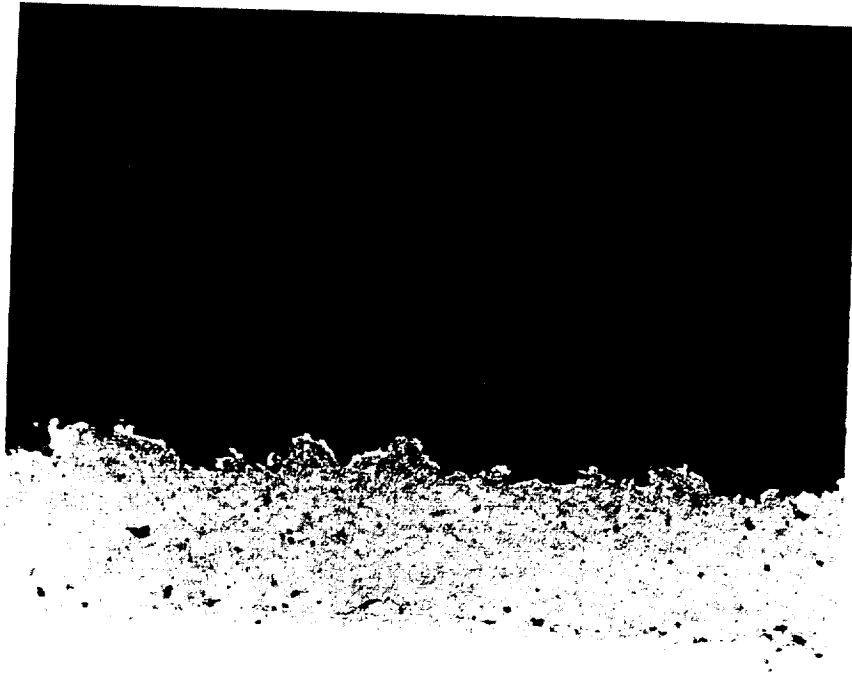
Figure 44a Light Photomicrograph of Pre-Test Microstructure (D2 68 Test) for a Thick Ceramic Specimen



Etched - AG 21 200X

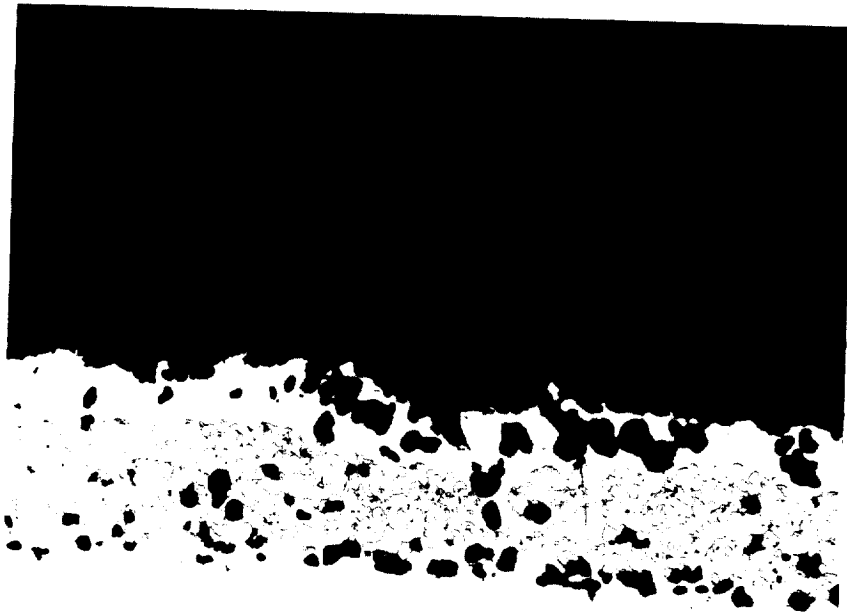
Figure 44b Light Photomicrograph of Post Burner Rig Test Microstructure (D2 Test) for a Thick Ceramic Specimen After 454 hrs at 1149°C (2100°F)/Short Cycle/Fast Heat-Up Rate

ORIGINAL PAGE
BLACK AND WHITE PHOTOGRAPH



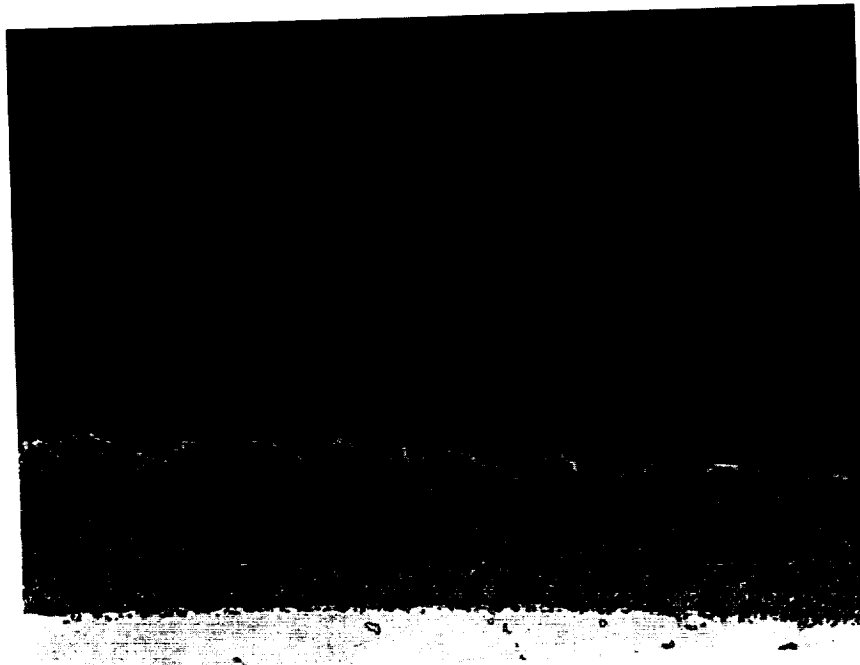
Etched - AG 21 200X

Figure 45a Light Photomicrograph of Pre-Test Microstructure (E Test) for a Thick Ceramic Specimen



Etched - AG 21 200X

Figure 45b Light Photomicrograph of Post Burner Rig Test Microstructure (E Test) for a Thick Ceramic Specimen After 121 hrs at 1149°C (2100°F)/Short Cycle/Slow Heat-Up Rate



Etched - AG 21 200X

Figure 46a Light Photomicrograph of Pre-Test Microstructure (F Test) for a Thick Ceramic Specimen



Etched - AG 21 200X

Figure 46b Light Photomicrograph of Post Burner Rig Test Microstructure (F Test) for Thick Ceramic Specimen After 54 hrs at 1149°C (2100°F)/Long Cycle/Fast Heat-Up Rate

ORIGINAL PAGE
BLACK AND WHITE PHOTOGRAPH

TABLE XI
X-RAY DIFFRACTION ANALYSIS OF SOME REPRESENTATIVE POST-TEST SPECIMENS

Specimen/ Location	v/o FCC ZrO ₂	v/o Tetragonal ZrO ₂	v/o Monoclinic ZrO ₂	Failure Time (hours)
<u>1149°C (2100°F) Short Cycle, Fast Heat-Up Test (D1)</u>				
Baseline Pre-test	60-55 ($a_0 = 5.122 \times 10^{-8}$ cm) (5.122A)	40-45 ($a_0 = 5.1172 \times 10^{-8}$ cm (5.1172A) $c_0 = 5.1646 \times 10^{-8}$ cm (5.1646A)	Not detected	N/A
Baseline: adjacent to spall	60-65 ($a_0 = 5.13263 \times 10^{-8}$ cm (5.13263A))	35-30	5	175
180° from spall	55-60 ($a_0 = 5.3575 \times 10^{-8}$ cm (5.3575A))	45-40	1	
Air pre-exposed: adjacent to spall	60-65 (5.13907×10^{-8} cm) (5.13907A)	35-30	5	
180° from spall	55-60 (5.13910×10^{-8} cm) (5.13910A)	45-40	Not detected	50
Thick: adjacent to spall	60-65 ($a_0 = 5.13762 \times 10^{-8}$ cm (5.13762A))	40-35	Not detected	
adjacent to spall (other side)	60-65 ($a_0 = 5.14152 \times 10^{-8}$ cm (5.14125A))	40-35	--	104
<u>1149°C (2100°F) Short Cycle, Fast Heat-Up Test (D2)</u>				
Air pre-exposed: adjacent to spall	65-70	35-30	1	194
Argon pre-exposed: adjacent to spall	60-65	35-30	1 (Possibly mono- clinic ZrO ₂ or hexagonal Y ₂ O ₃)	679
Thick ceramic: adjacent to spall	50-70	45-40	Not detected	443
Thin ceramic: adjacent to spall	50-55	50-45	Not detected	557

TABLE XI (continued)
X-RAY DIFFRACTION ANALYSIS OF SOME REPRESENTATIVE POST-TEST SPECIMENS

Specimen/ Location	v/o FCC ZrO ₂	v/o Tetragonal ZrO ₂	v/o Monoclinic ZrO ₂	Failure Time (hours)
<u>1149°C (2100°F) Short Cycle, Slow Heat-Up Test (E)</u>				
Baseline: Away from Spall	60-65	40-35	Not detected	142
Spalled Area	60-65	40-35	1	
Air Pre-Exposed: Away from Spall Area	60-65	40-35	1	18
Spalled Area	60-65	40-35	1	
Argon Pre-Exposed: Away from Spall Area	60-65	40-35	Not detected	142
Spalled Area	65-70	35-30	1	
Thick: Away from Spall	55-60	45-40	Not detected	121
Spalled Area	60-65	40-35	1	
Thin: Away from Spall	55-60	45-40	Not detected	121
Spalled Area	60-65	40-35	Not detected	
<u>1149°C (2100°F) Short Cycle, Fast Heat-Up Test (F)</u>				
Baseline: Away from Spall	55-60	45-40	Not detected	98
Spalled Area	65-70	35-30	1	
Air Pre-Exposed: Away from Spall Area	55-60	45-40	Not detected	18
Spalled Area	60-65	40-35	1	
Argon Pre-Exposed: Away from Spall Area	55-60	45-40	Not detected	102
Spalled Area	60-65	40-35	1	
Thick: Away from Spall	55-60	45-40	Not detected	64
Spalled Area	65-70	35-30	1	
Thin: Away from Spall	55-60	45-40	Not detected	122
Spalled Area	60-65	40-35	1	

3.1.2.2.3 Fractional Exposure Burner Rig Test Results

The purpose of this test was to investigate the occurrence and accumulation of microstructural damage resulting from cyclic thermal burner rig exposure for various fractions of spalling life. The approach involved burner rig exposure of test bars for various fractions of life as measured in the D1 (1149°C (2100°F)/short cycle/fast heat-up) test. There were two series of tests conducted. The first set provided a broad survey of damage throughout life, with the specimens being exposed for approximate decile fractions of the average D1 test life (180 hours). The second set focused more closely on high life fractions, with the specimens being exposed at life fractions in the range of 58% - 100%.

Both series of tests were conducted at the D1 test (1140°C, short cycle, fast heat-up) conditions. At least one specimen was tested to failure in each group to assure the validity of the estimated life. Specific exposure times are listed in Table XII, together with estimates of life fractions represented by each exposure. In the first group, the control specimen failed very close to the D1 test average. In the second group, life fraction estimates were less exact; two specimens exceeded the D1 baseline average and the control specimen failed at 130% of the average, suggesting test conditions may have shifted slightly. As calculated by the preliminary life prediction model discussed in succeeding sections, the 30% shift in life for Group II specimens would correspond to a temperature shift of 10°. Table XII shows two Group II calculated life fractions. The first is based on the nominal 180 hour life at 1149°C (2100°F) and the second is based on the observed failure life of the reference bar in the Group II test.

Microstructural examination of fractionally exposed specimens shows incipient/subcritical cracking as early as 20-30 percent of the burner rig test life (Figure 47). Examination of crack morphology at successively increasing life fractions suggests that ceramic spallation may result from progressive link-up of adjacent subcritical cracks, as opposed to subcritical growth of a single dominant crack. Quantitative measurement of average crack length shows a progressive increase with increasing exposure. "Young" specimens, (<30%) contain cracks on the order of 0.05-0.08 mm (0.002-0.003 in.); longer exposure times yield average crack sizes of 0.16-0.26 mm (0.006-0.010 in.). The number of cracks also appears to increase with exposure time. "Old" specimens, (>60%) show large isolated cracks on the order of 0.33 mm (0.0125 in.), together with shorter 0.05-0.08 mm (0.002-0.003 in.) cracks. The "oldest" unfailed specimen, (90% exposure) evaluated showed one major crack 0.97 mm (38 mils) long and some 0.15-0.18 mm (0.006-0.007 in.) cracks.

Because previously discussed phenomenological evidence clearly indicated a significant influence of oxidative environment on coating "damage" accumulation, substantial effort was devoted to investigation of the relationship between incipient cracking and the growing oxide scale. Most of the observed ceramic cracking occurred parallel to and about 0.03-0.05 mm (0.001-0.002 in.) above the zirconia-oxide scale interface with no obvious linkage between cracks and oxide. While scanning electron microscope studies, discussed below, did show a few isolated cases of scale initiated cracking, these examples were sufficiently difficult to find as to lead to the conclusion that this is not the major mode of crack initiation in the ceramic

layer. It is interesting to note that examples of scale initiated cracking were easier to find in older specimens, occurring in the same structure together with larger numbers of well-developed longer cracks which appeared to be isolated from the interface. The observation could suggest that the thicker oxide scale developed at larger exposure times can initiate cracks, but that this is not the "critical" damage mode in the sense that those cracks which propagate to failure are initiated early in life and appear to be isolated from the interface.

TABLE XII
FRACTIONAL EXPOSURE TEST (Condition G) RESULTS
(1149°C (2100°F)/Short Cycle/Fast Heat-Up Rate)

Specimen Identification Number	Total Test Hours (TTH)	(TTH/180 X 100)	Percent Life 1(TTH/235 X 100)
<u>GROUP I</u>			
214	15	8%	
215	30	17%	
216	45	25%	
217	60	33%	
218	75	42%	
219	90	50%	
220	105	58%	
221	120	67%	
227	135	75%	
223	150	83%	
224	165	92%	
225	180	100% Failed	
<u>GROUP II</u>			
290	136	76%	58%
292	143	80%	61%
296	145	81%	62%
297	151	84%	64%
298	171	95%	73%
299	174	97%	74%
300	177	98%	75%
301	180	100%	77%
303	215	120%	91%
302	235	130%	100% - Failed

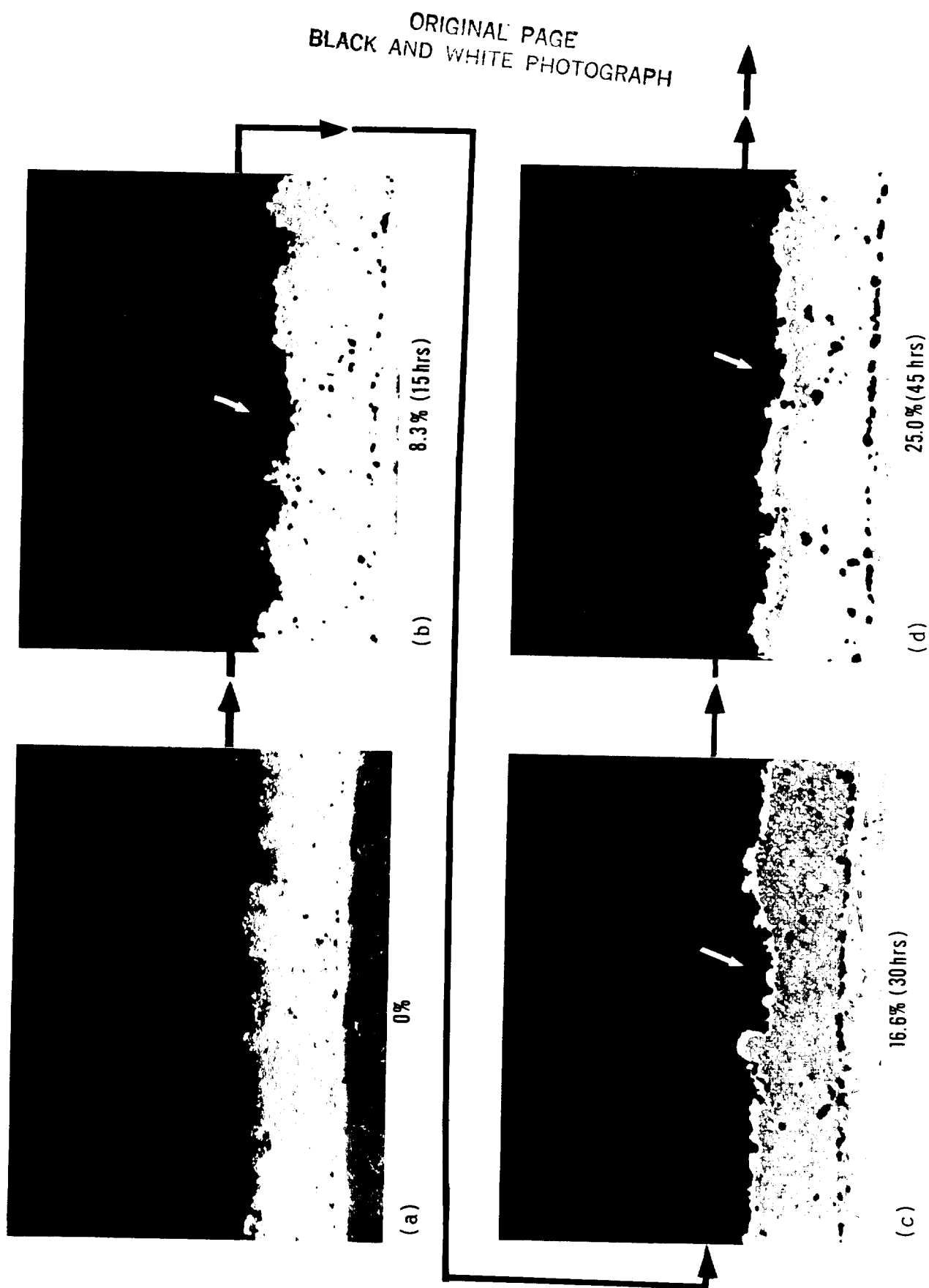
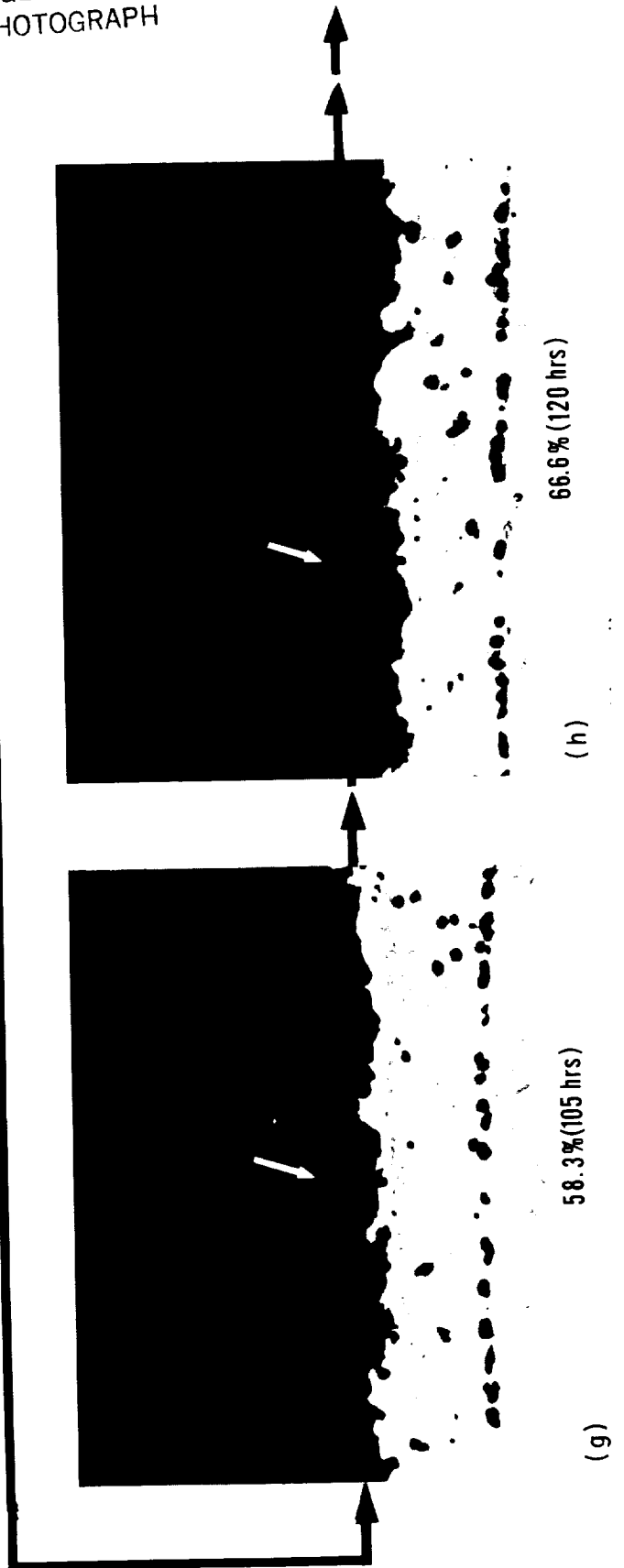
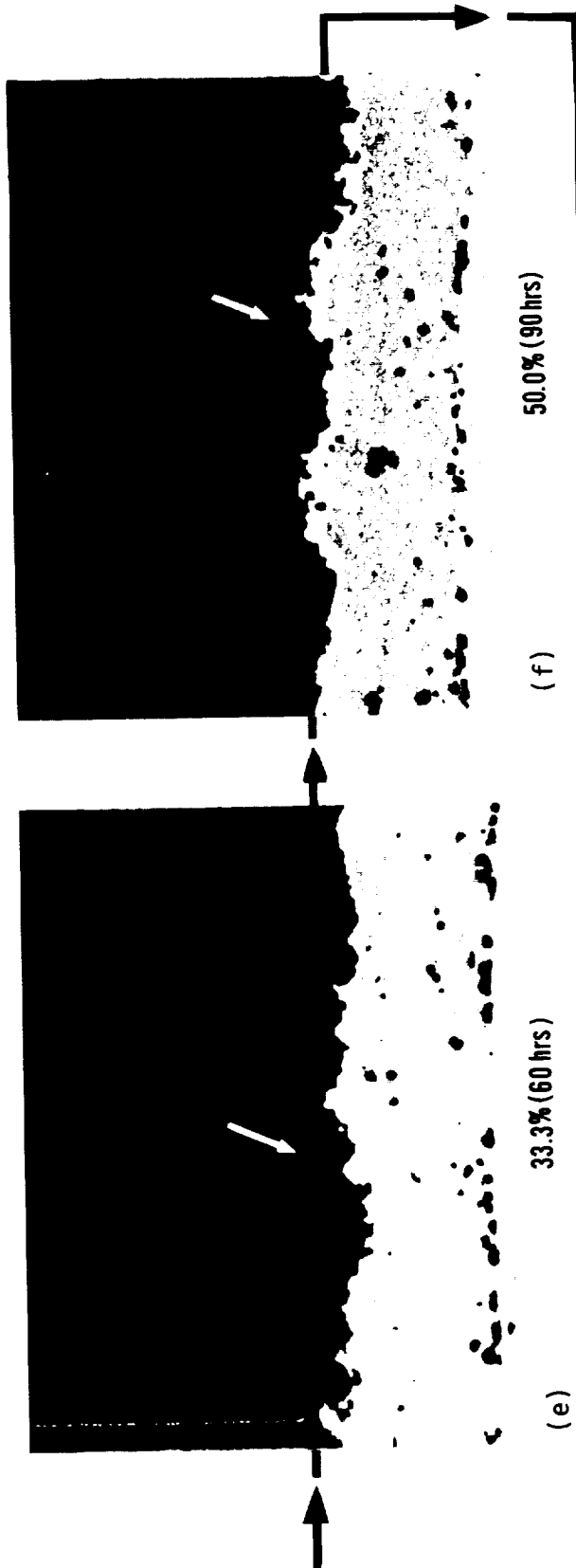


Figure 47 Thermal Barrier Coating Damage Progression (200X)

ORIGINAL PAGE
BLACK AND WHITE PHOTOGRAPH



ORIGINAL PAGE
BLACK AND WHITE PHOTOGRAPH

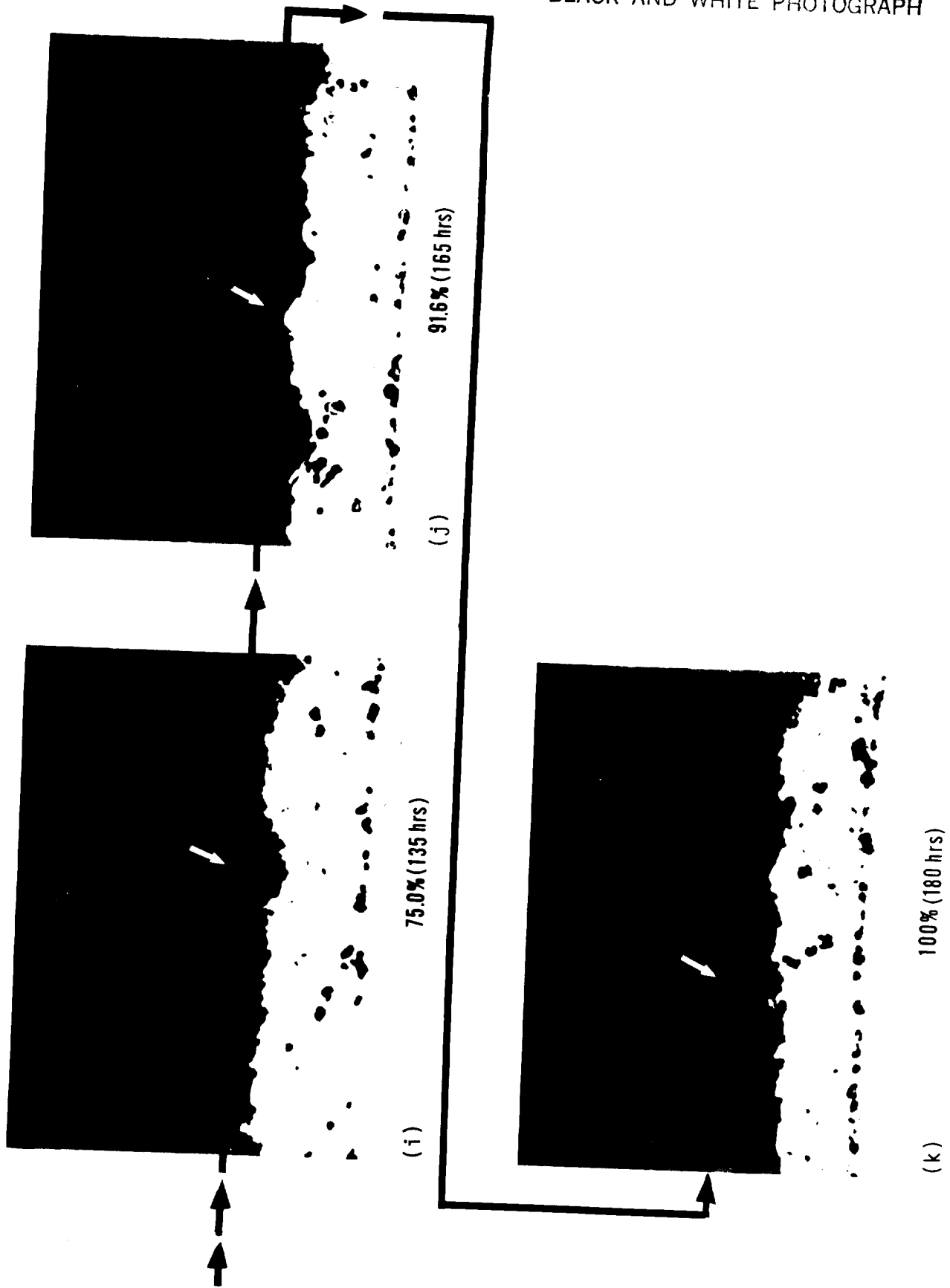


Figure 47 (Continued)

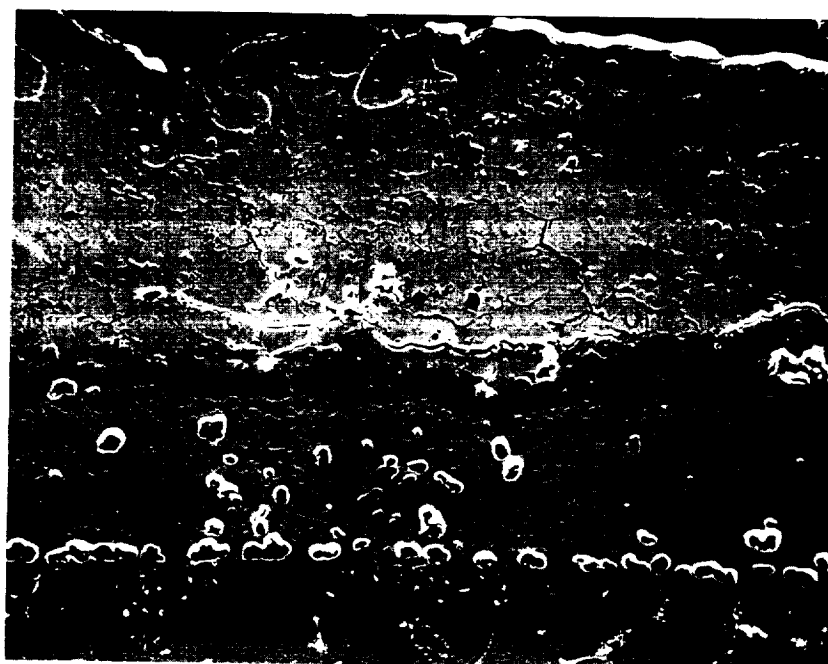
Scanning electron micrographs of typical crack structures are shown in Figures 48 through 51. Shown in Figure 48 is the structure found in a specimen exposed for 90 hours (50% life), in which subcritical cracks are noted in the vicinity of (but not clearly initiated at) the bond coat peaks. Figure 50 is the same specimen as seen in Figure 49 but shows a different area; fine layered cracking in the bond coat oxide is noted at higher magnifications. "Older" specimens with more oxide accumulation frequently showed this type of layered type cracking within the oxide, but these cracks were, in general, not associated with the major subcritical cracks seen in Figure 47. Figure 49 shows the BSI for the specimen exposed for 105 hours, and two large cracks are observed to extend from either edge of a particular bond coat asperity. Figure 51 shows the BSI for the specimen exposed for 135 hours. This figure also shows a subcritical crack extending from the edge of a bond coat peak with cracking observed in the bond coat oxide.

Another interesting structural feature observed in "older" specimens was an apparent increase in the amount of near-interface porosity, usually associated with major cracks. Critical examination of this porosity indicates that it is an artifact, resulting from pull-out in polishing rather than being an inherent feature of the structure. This apparent increased sensitivity of the ceramic to pull-out suggests that the ceramic may be somewhat "weakened" in the vicinity of the interface. It appears that the suggested near-interface weakening may correspond physically to a progressive increase of localized near-interface microcrack density. Additional metallographic studies are required to further investigate this phenomenon.

3.1.2.3 Cyclic Hot Corrosion Tests

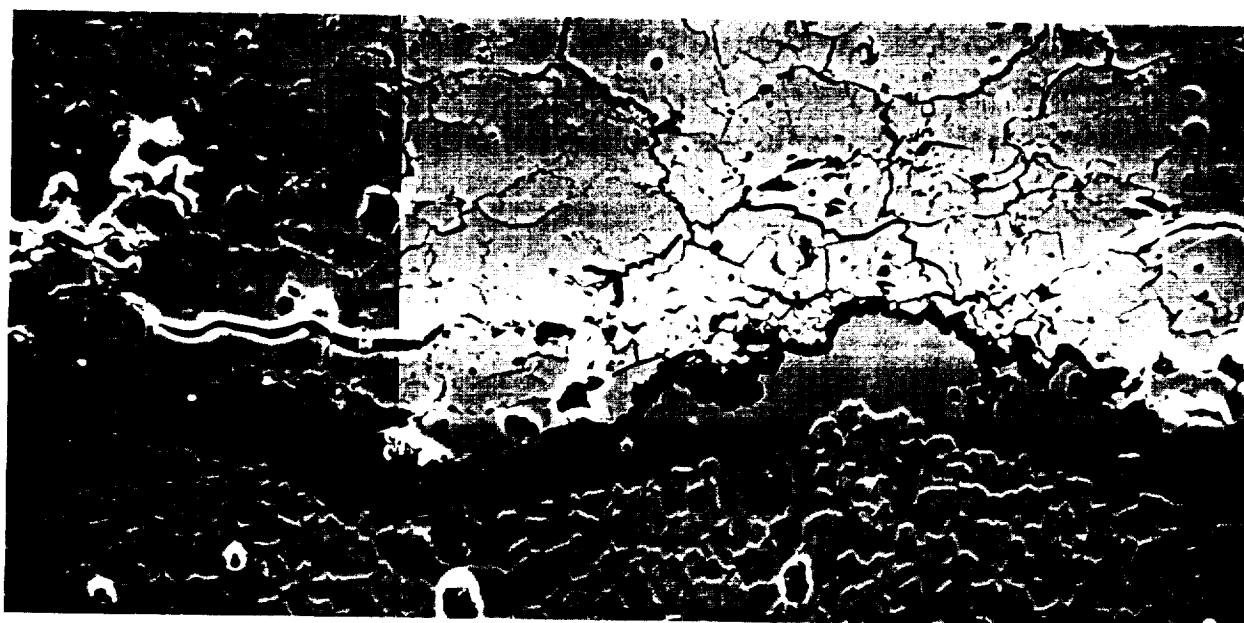
This subtask was designed to determine the relative importance of hot corrosion as a thermal barrier coating failure mechanism and provided test data from which a preliminary life prediction model might be developed. Nine specimens were exposed to a high corrodent level and six specimens were exposed to a low corrodent level. Twenty additional specimens were then exposed to various cyclic life fractions.

The test method involved ducted burner rig testing as described in Appendix C. To maximize the potential for hot corrosion damage, these tests were conducted with a surface temperature of 899°C (1650°F). A partial factorial test program is shown in Figure 52. Testing to spallation failure was conducted at a "high" corrodent level (35 ppm synthetic sea salt, condition "H" in Figure 52) and at a lower corrodent level (10 ppm synthetic sea salt identified as "J" in Figure 52). To provide information concerning the nature and rate of accumulation of hot corrosion damage, a fractional exposure test, identified as "K" in Figure 52 also, was conducted. In this test, specimens exposed to decile fractions of the high corrodent level hot corrosion life were examined metallographically to identify and characterize progressive damage mode(s) which cause thermal barrier coating hot corrosion failure. Two specimens were cycled to each of the approximate 10%, 20%, 30%, 40%, 50%, 60%, 70%, 80%, and 90% fractions of the average cyclic failure life defined in the "H" test. Two additional specimens were cycled to 100% of the "H" test life; however, after 1000 hrs of exposure no failures occurred.



85-196

200X



85-196

500X

Figure 48 Back Scatter Image of Thermal Barrier Coating After 90 Hours of Burner Rig Test Time 1149°C (2100°F)/Short Cycle/Fast Heat-Up Rate

ORIGINAL PAGE
BLACK AND WHITE PHOTOGRAPH

ORIGINAL PAGE
BLACK AND WHITE PHOTOGRAPH

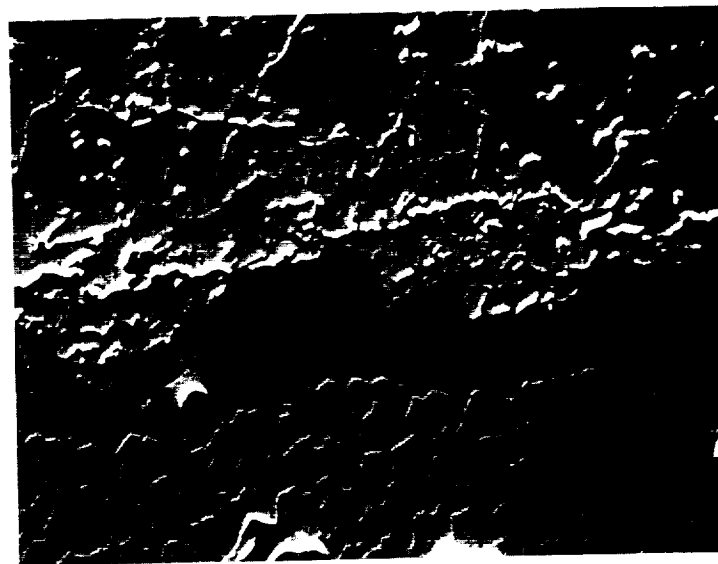
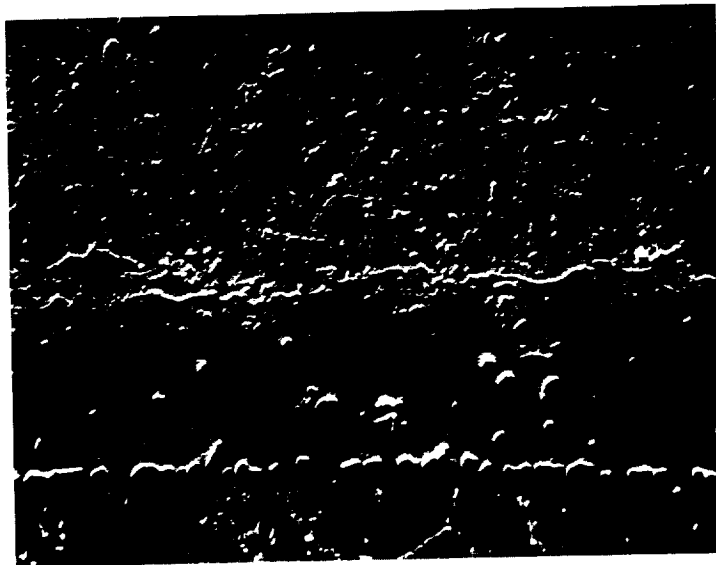


Figure 49 Back Scatter Image of Thermal Barrier Coating After 105 Hours of Burner Rig Test Time at 1149°C (2100°F)/Short Cycle/Fast Heat-Up Rate

ORIGINAL PAGE
BLACK AND WHITE PHOTOGRAPH

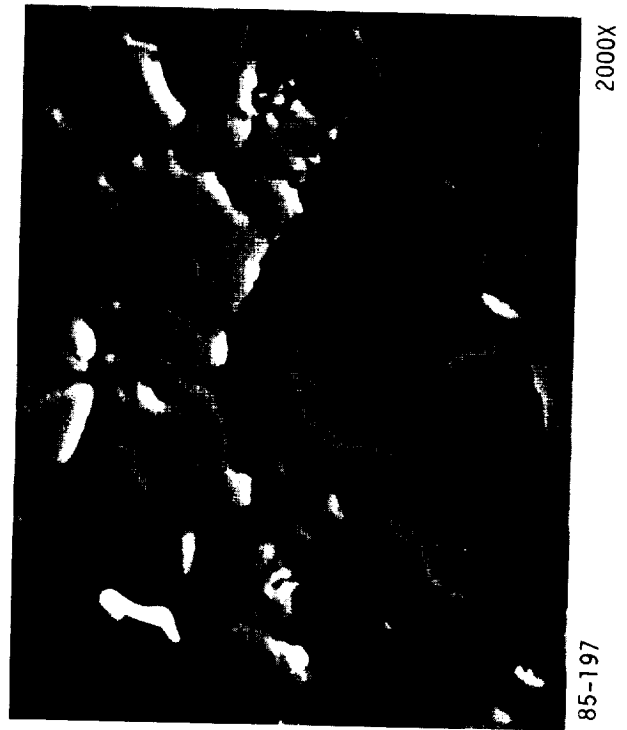
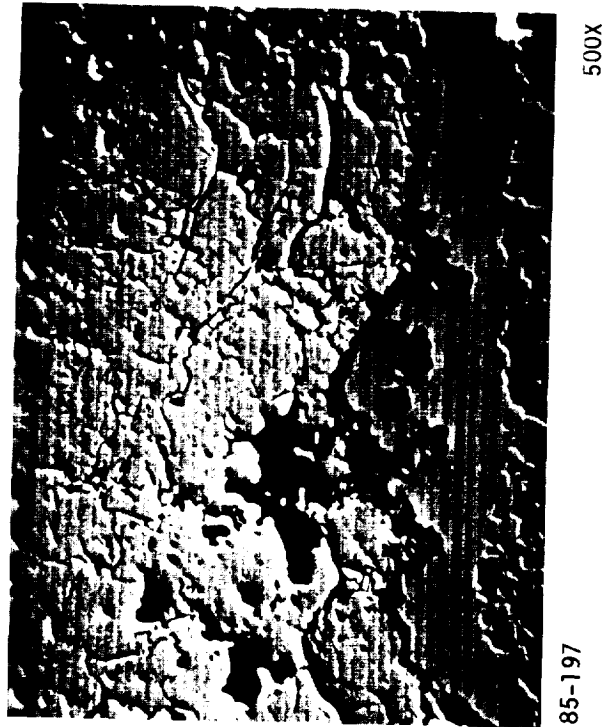
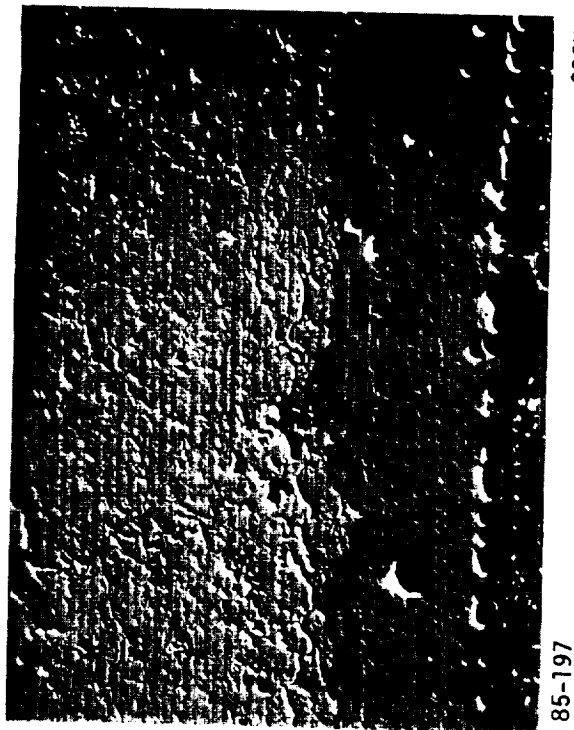
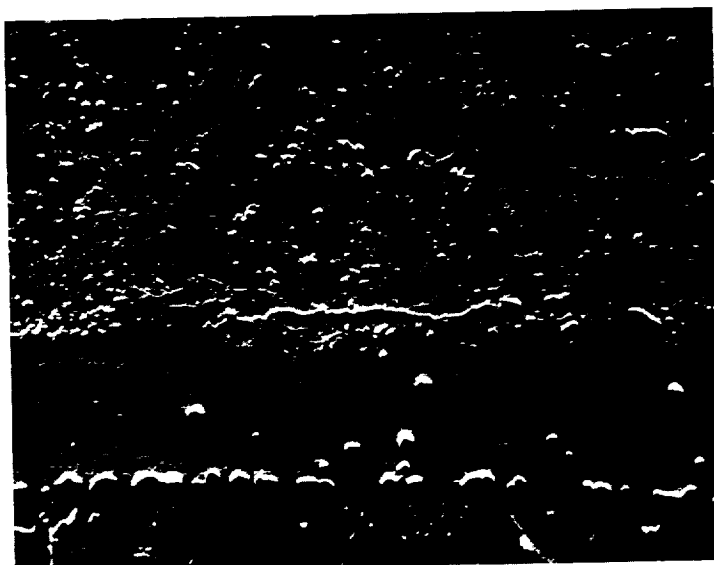
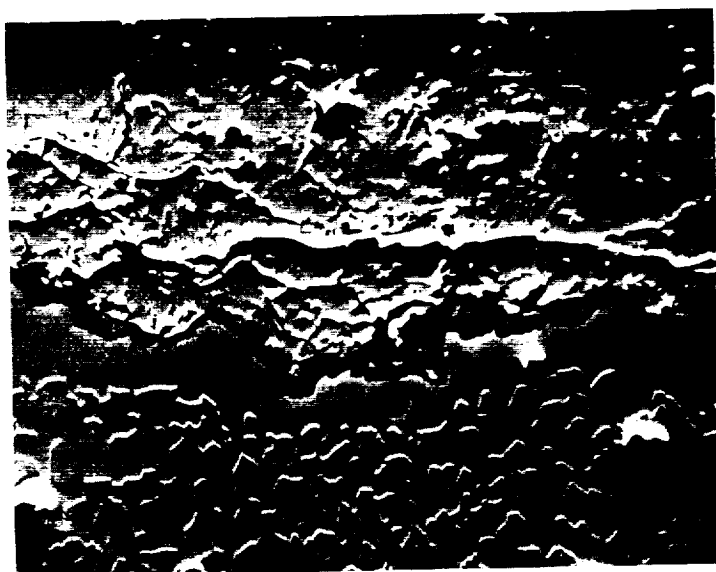


Figure 50 Back Scatter Image of Thermal Barrier Coating After 105 Hours of
Burner Rig Test Time at 1149°C (2100°F)/Short Cycle/Fast Heat-Up
Rate

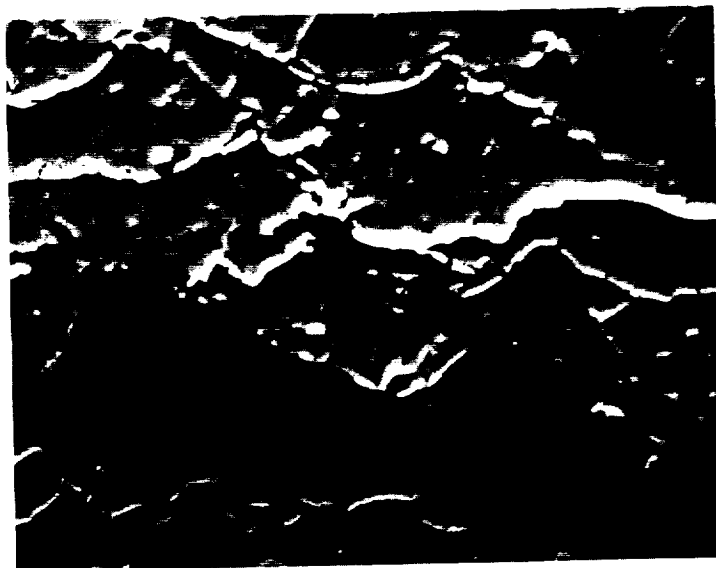
ORIGINAL PAGE
BLACK AND WHITE PHOTOGRAPH



85-199
200X



85-199
500X



85-199
1000X

Figure 51 Back Scatter Image of Thermal Barrier Coating After 135 Hours of Burner Rig Test Time at 1149°C (2100°F)/Short Cycle/Fast Heat-Up Rate

	LOW CORRODANT LEVEL, 10 PPM	HIGH CORRODANT LEVEL, 35 PPM
CYCLE TO FAILURE	(29) J	(29) H
FRACTIONAL EXPOSURE	(27) X	(28) K

Figure 52 Task I Hot Corrosion Test Program

3.1.2.3.1 High Corrodent Level Test Results

Results of the high corrodent level test (899°C (1650°F), 35 ppm artificial sea salt, 1.3%SO₃, 1 hour cycle (57 minutes in the flame + 3 minutes FAC)) are summarized in Table XIII. These results contain significant scatter with five specimens failing between six and seven hundred hours, and two specimens surviving to 1000 hours, when testing was terminated with no failure.

A photograph of a typical high corrodent level failure is shown in Figure 53. Failures occurred well above the ceramic-metallic interface with large amounts of ceramic remaining adherent. Small visually observable cracks grew in length as testing continued until discrete patches of ceramic spalled around the bar, favoring leading edge locations.

Figures 54 and 55(a and b) show the pre-test and post-test microstructures of specimens tested 693 and 1000 hours, respectively. The ceramic spallation mode seen in these structures clearly is different from that observed in clean fuel burner rig test failures, exhibiting multi-level in-plane, ceramic cracking and flaking, as opposed to the predominant near-interface cracking seen in clean fuel failure.

Figures 56(a-c), and 57(a-d) show post-test surface structure and transverse microstructure for a test specimen exposed for 450 hours in the high corrodent level test (Condition H). The EMP results, as seen in the x-ray maps, clearly show the infiltration of sodium and sulfur in the pores and microcracks.

Further post corrosion test specimen evaluations have confirmed infiltration of sodium and sulfur in localized areas of porosity and microcracking throughout the thickness of the ceramic coating. Increased exposure time shows increased infiltrant concentration in these areas. Magnesium, contained in synthetic sea salt as MgCl₂ (see Table XIV), was generally not detected in the zirconia layer but was found concentrated at the oxide layer between the ceramic/bond coat interface. As shown in Figures 58(a-g), x-ray maps for Al and Mg may suggest the predominance of the formation of MgAl₂O₄ spinel.

Table XV shows x-ray diffraction analysis for representative post test high corrodent level test specimens (condition H). It is noted that "higher" time specimens show a significant increase in v/o monoclinic and also up to 10 v/o of other phases; i.e., fcc NiO, the orthorhombic NiCrO₄ or Ca₂SiO₄. This increase in monoclinic phase (destabilization of ZrO₂) is believed to influence coating spalling life.

TABLE XIII
CYCLIC HOT CORROSION TEST RESULTS (Condition H) HIGH CORRODENT LEVEL
(1650°F/Long Cycle/35ppm Artificial Sea Salt/1.3% SO₃)

Failure Time (Hrs)	
693	Avg = 618
693	
638	
615	
450	
1000	No Failure
1000	Observed
1000	



Figure 53 Cyclic Hot Corrosion Test Specimen Showing Multi-Level Flaking of the Ceramic

ORIGINAL PAGE
BLACK AND WHITE PHOTOGRAPH

ORIGINAL PAGE
BLACK AND WHITE PHOTOGRAPH

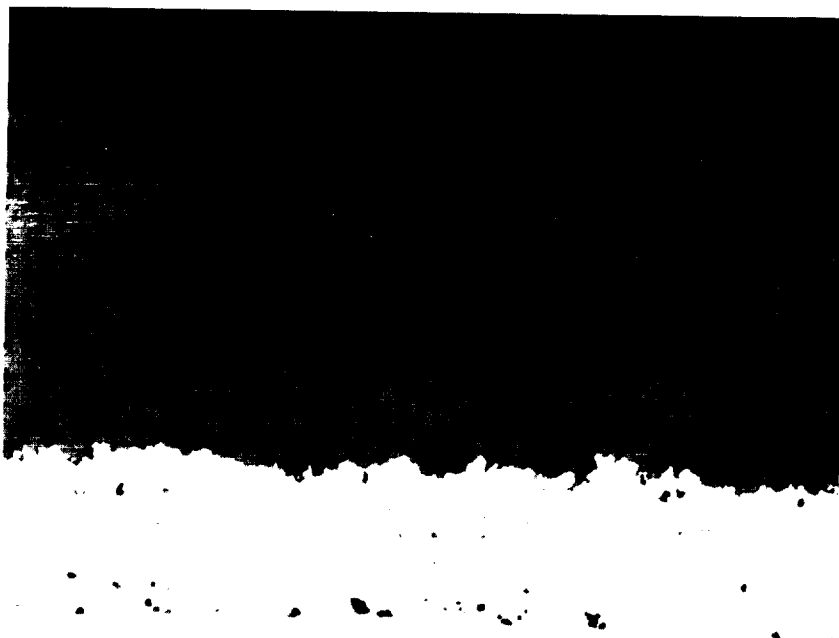


Figure 54a Pre-Test Hot Corrosion Test Specimen; 35 ppm Artificial Sea Salt/
899°C (1650°F)/1 Hour Cycle

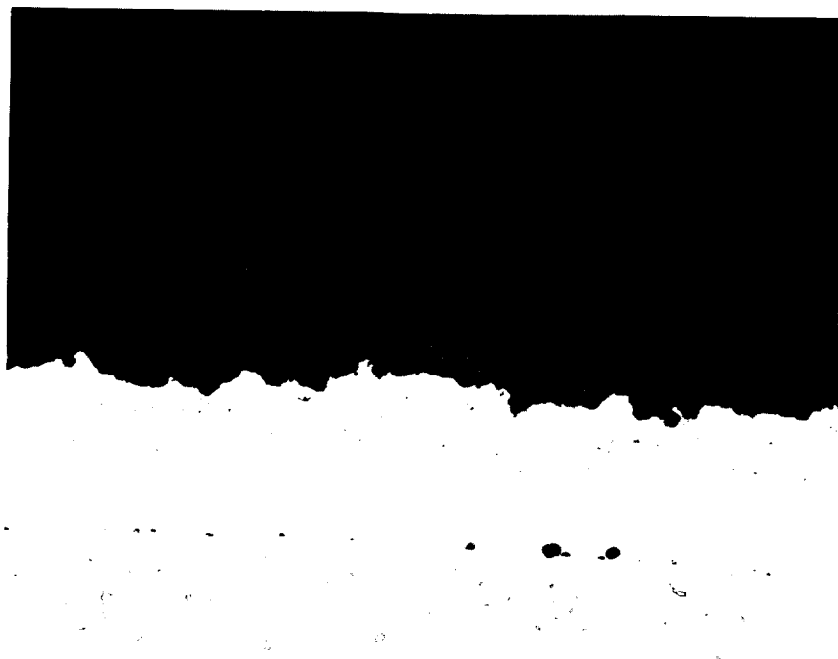


Figure 54b Post-Test Hot Corrosion Test Specimen Showing In-Plane Ceramic
Cracking in Central and Upper Portions of Ceramic Layer After 693
hrs at 35 ppm Artificial Sea Salt/899°C (1650°F)/1 Hour Cycle



Figure 55a Pre-Test Hot Corrosion Test Specimen; 35 ppm Artificial Sea Salt/899°C (1650°F)/1 Hour Cycle

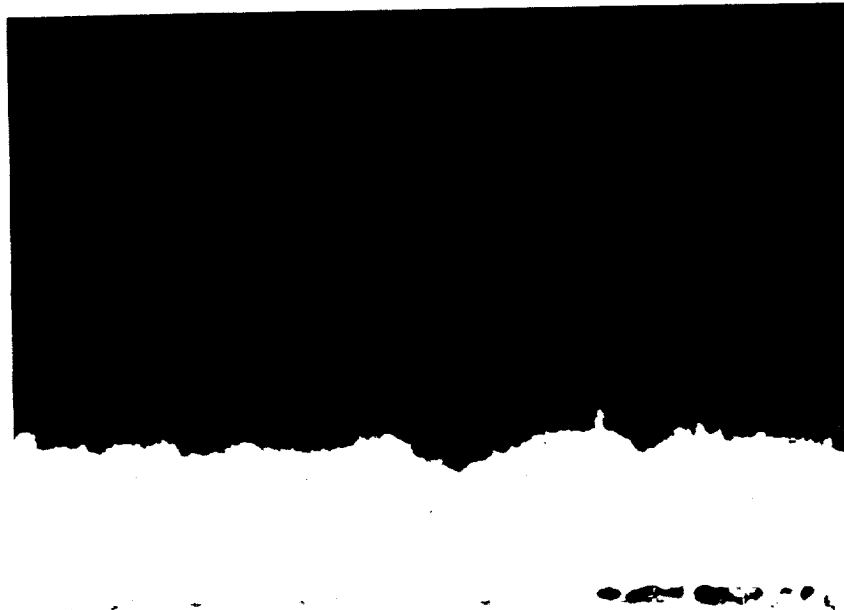
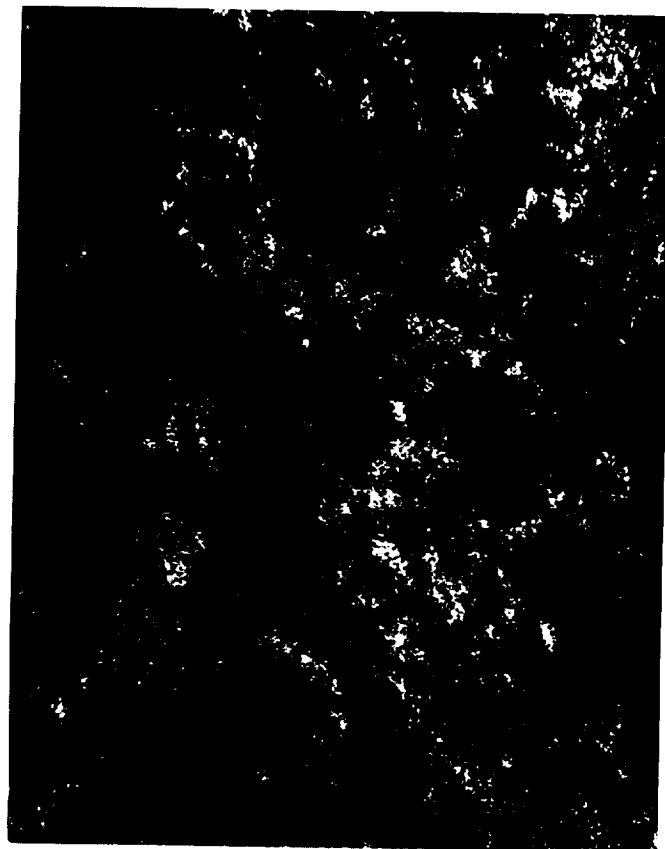


Figure 55b Post-Test Hot Corrosion Test Specimen After 1000 hrs at 35 ppm Artificial Sea Salt/899°C (1650°F)/1 Hour Cycle

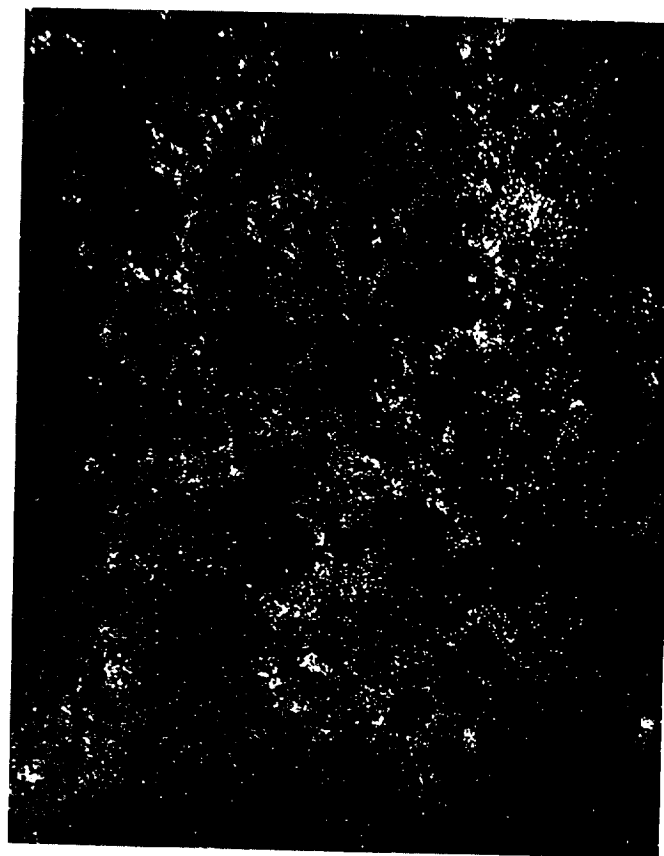
Figure 56
Cyclic Hot Corrosion Test
Specimen Surface (HST-086)
After 450 Hrs/899°C (1650°F)
High Corrodent Level Test



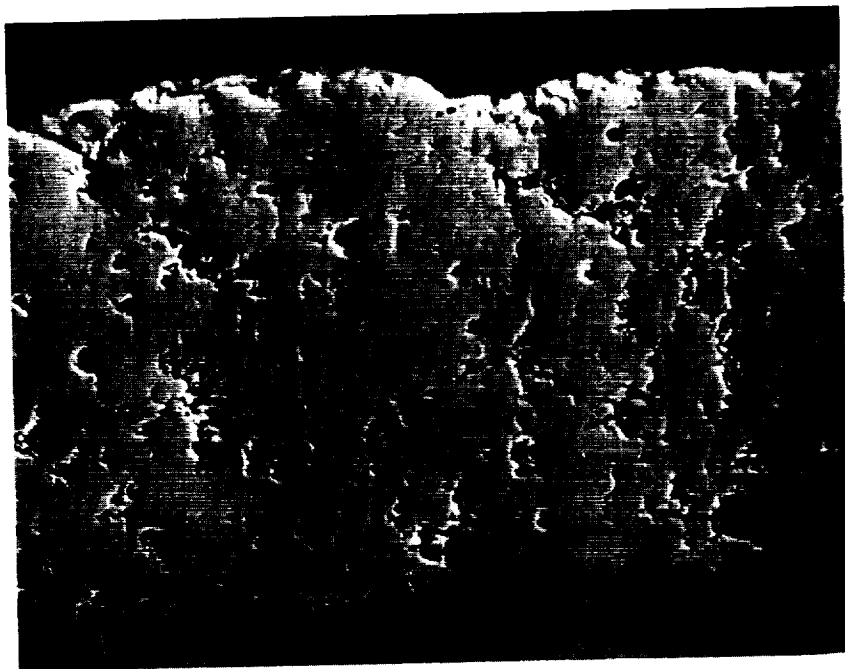
a) SEI Detailed Image Of Coating On Test Bar Surface 800X



b) Na X-Ray Map 800X

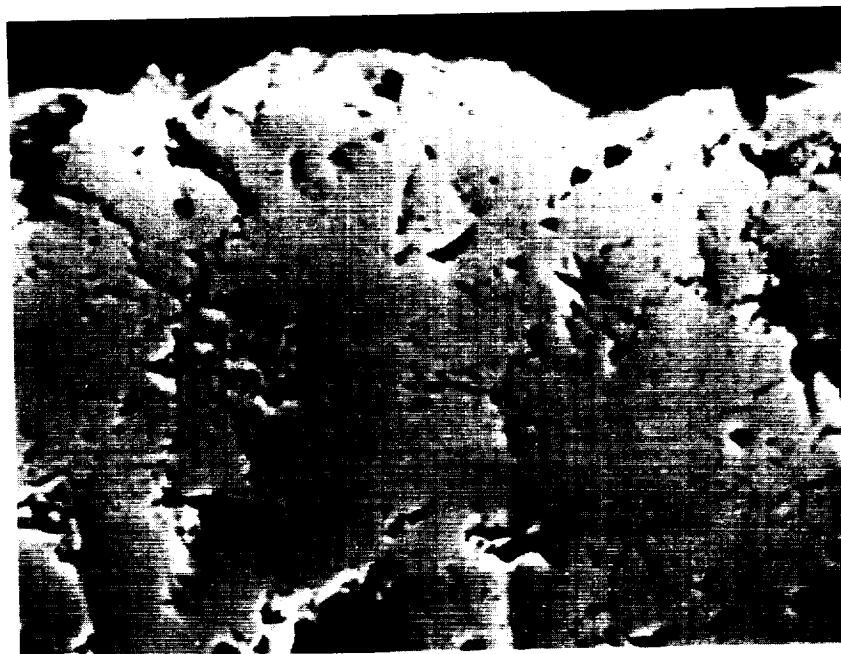


c) Sulfur X-Ray Map 800X



a) BEI

300X

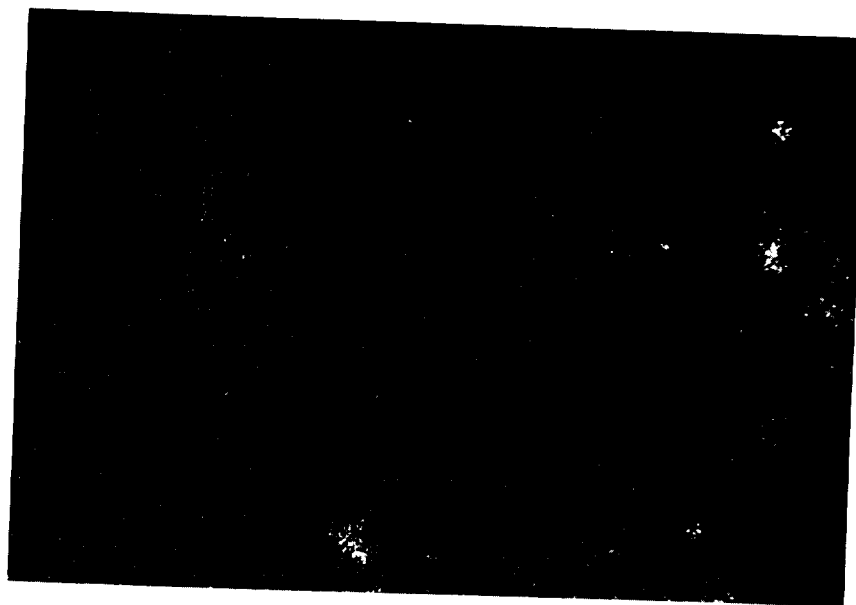


b) BEI Detailed Image Of Outer Surface Of Coating

1000X

Figure 57 Cyclic Hot Corrosion Test Specimen After 450 Hrs at 899°C (1650°F). High 35 ppm Corrodent Level in Area Near Failure.

ORIGINAL PAGE
BLACK AND WHITE PHOTOGRAPH



c) Na X-Ray Map

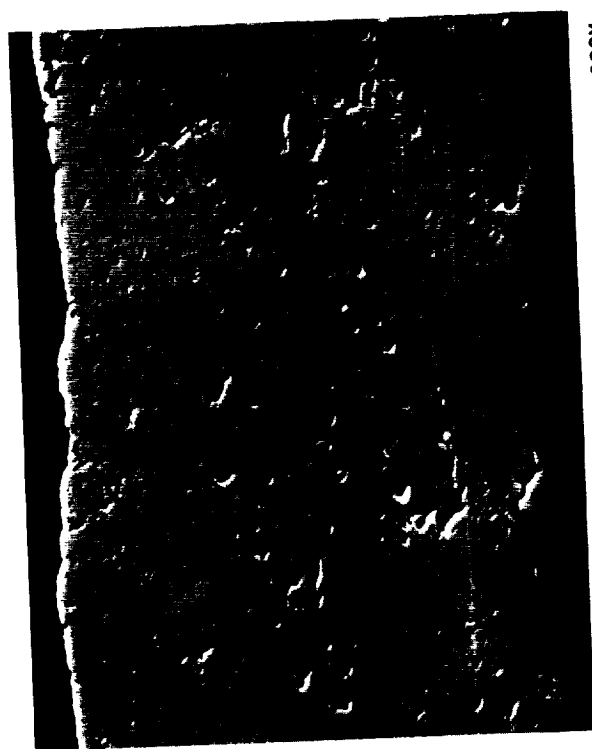
1000X



d) Sulfur X-Ray Map

1000X

Figure 57 (Continued)



a) BEI

300X



b) BEI Detailed Image of Oxide Layer

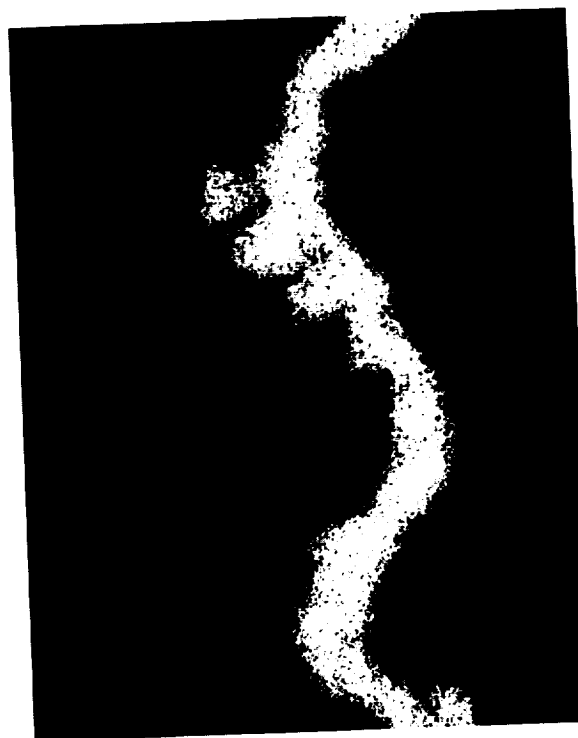
2000X



c)

Al X-Ray Map

2000X



d)

Mg X-Ray Map

2000X

Figure 58 Cyclic Hot Corrosion Post-Test Specimen After 1000 hrs at 899°C
in 1.3% SO₂ / 98.7% Air

ORIGINAL PAGE
BLACK AND WHITE PHOTOGRAPH

Figure 58 (Continued)



Cr X-Ray Map

2000X

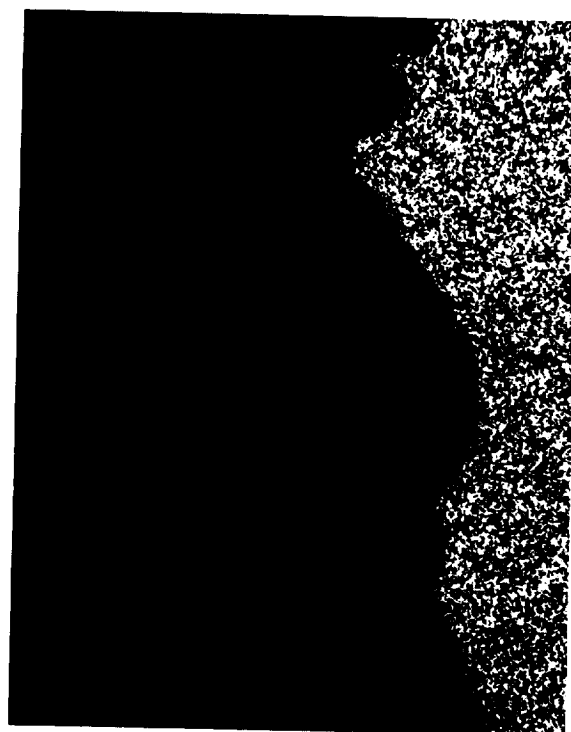
e)



Ni X-Ray Map

2000X

f)



Co X-Ray Map

2000X

g)

TABLE XIV
ARTIFICIAL SEA SALT COMPOSITION

NaCl	58.4%
MgCl ₂	26.4
Na ₂ SO ₄	9.7
CaCl ₂	2.7
KCl	1.6
NaHCO ₃	.4
KBr	.23
H ₃ BO ₃	.07
SrCl ₂	.09
Na F	.007

TABLE XV
X-RAY DIFFRACTION ANALYSIS FOR SOME REPRESENTATIVE CYCLIC
HOT CORROSION POST-TEST SPECIMENS
(High Corroderent Level)

Specimen/ Location	v/o fcc ZrO ₂	v/o Tetragonal ZrO ₂	v/o Monoclinic ZrO ₂	Other	Failure Time (hrs)
(HST #086) Spalled Area	60-65	35-40	5	1 v/o Unidentified	450
(HST #088) Spalled Area	50	25-35	15-10	10 v/o fcc and /or MgO 1 v/o orthorhombic NiCrO ₄	615
(HST #091) Spalled Area	45-50	45-50	10	1 v/o fcc NiO, MgO and/or Ca ₂ SiO ₄	693

3.1.2.3.2 Low Corroderent Level Test Results

The low corroderent level test (Condition J) 10 ppm artificial sea salt, 1.3% SO₃, was terminated after completing 1000 hrs of test time, with none of the six specimens tested exhibiting any evidence of coating degradation. The specimens did show, however, a dark brown surface appearance. Figure 59 shows a photomicrograph of one of these specimens after over 1000 hours of exposure.

ORIGINAL PAGE
BLACK AND WHITE PHOTOGRAPH



HST-125

Leading Edge

2.5X

Figure 59 Light Photomacrograph of Test Specimen After 1000 hrs at 899°C (1650°F)/ Long Cycle/10 ppm Synthetic Sea Salt/1.3% SO₃ - Condition J

Electron microprobe analysis conducted on the cross-sectional microstructure of an unfailed low corrodent level specimen indicated less corrodent infiltration than found in high corrodent level specimens. As seen in Figures 60a through 60d, low levels of Na and S were detected in areas of porosity and microcracking. Magnesium was detected not only within pores and cracks, but also at the ceramic-bond coat interface. It appears that this element is in the form of an oxide and at the interface forms spinel; MgAl₂O₄, as shown in Figures 61a through 61d.

Table XVI presents X-ray diffraction data for two representative low corrodent level samples. The phase distribution as shown is not consistent for these two specimens exposed for the same length of time. It was observed that for at least one specimen, a high v/o monoclinic ZrO₂ (20-25 v/o) was detected.

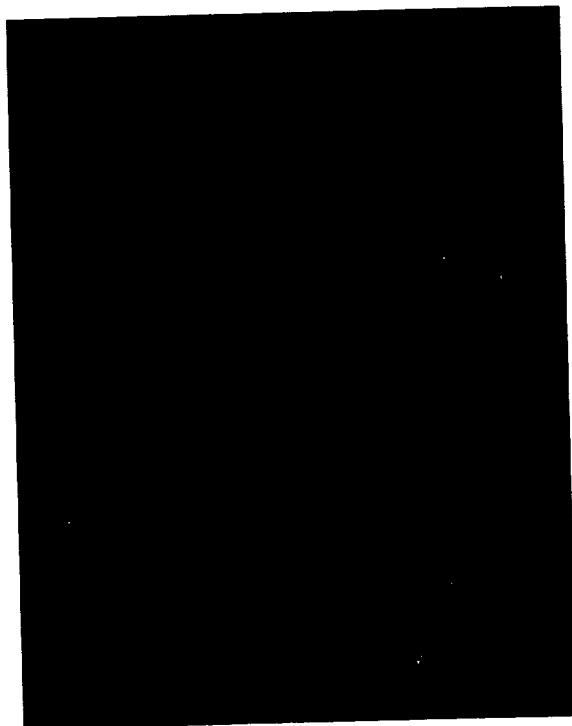
3.1.2.3.3 Fractional Exposure Hot Corrosion Test Results

The fractional exposure corrosion test K (35ppm artificial sea salt, 899°C (1650°F), long cycle) was terminated with over 1000 hours of test time accumulated. Two of the twenty specimens planned for this test were to be reference specimens taken to failure to confirm the previously determined average test life from the H test: 35ppm artificial sea salt, long cycle, 899°C (1650°F). The other 18 specimens were to be tested to decile fractions of this life. However, these two specimens did not fail after over 1000 hours of testing and, in accordance with the Statement of Work, this test was terminated. Thus, there is an uncertainty as to the actual life fractions of the eighteen specimens evaluated.



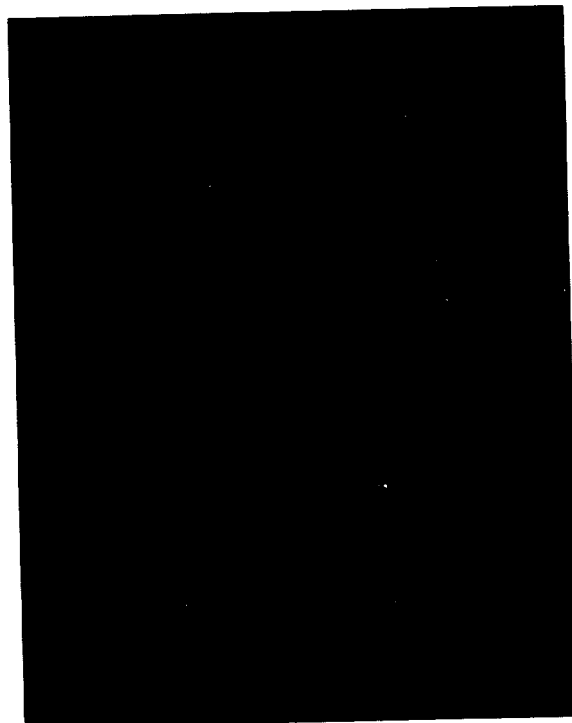
(a) Detailed Image of Coating

800X



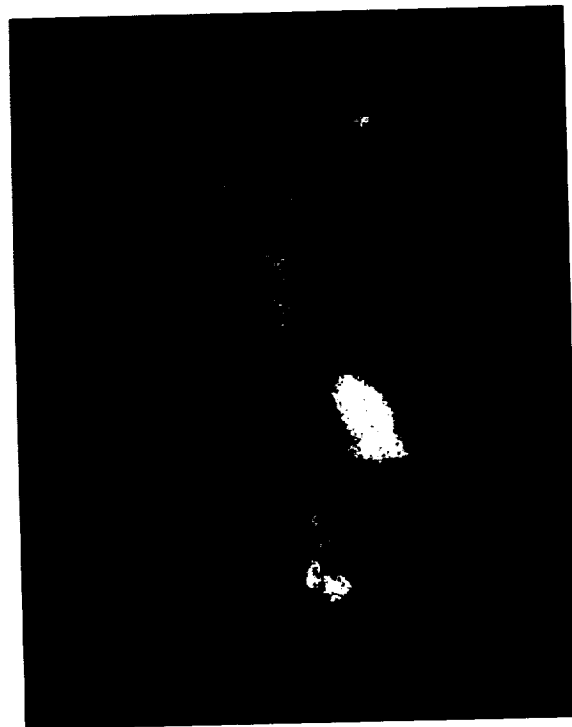
(b) Na X-ray Map

800X



(c) Sulfur X-ray Map

800X



(d) Ag X-ray Map

800X

Figure 60 Post Test Specimen Microstructure After 1000 hrs with Artificial Sea Salt 10ppm and 899°C (1650°F)-Host Test "J"

ORIGINAL PAGE
BLACK AND WHITE PHOTOGRAPH



(a) BEI

300X



(b) BEI

Detailed Image of Oxide Layer 2000X



(c)

Al X-ray map

2000X



(d)

Al X-ray map

2000X

Figure 61 Post Test Specimen Microstructure After 1000 hrs with Artificial Sea Salt 10ppm and 899°C (1650°F)-Host Test "J"

TABLE XVI
X-RAY DIFFRACTION ANALYSES OF SOME REPRESENTATIVE POST-TEST SPECIMENS,
CYCLIC HOT CORROSION TEST (Low Corrodent Level)

Specimen/ Exposure Time	v/o FCC ZrO ₂	v/o Tetragonal ZrO ₂	v/o Monoclinic ZrO ₂	v/o Other
HST 113/ 1000 hrs	42-45	32-35	5	10-7 fcc NiCr ₂ O ₄ and/or NiFe ₂ O ₄ spinel), 5 fcc NiO and and/or MgO, 3-1 hexagonal NiS, 2-1 bcc Y ₂ O ₃ , 1 tetragonal TiO ₂ , and possibly 1 hexagonal - Al ₂ O ₃
HST 131/ 1000 hrs	30-35	25-20	25-20	5 fcc NiFe ₂ O ₄ and/or NiFe ₂ O ₄ (spinel), 5 hexagonal NiS, 10-15 fcc (Fe,Ni)S ₂

Post-test metallographic analysis was conducted for one of the specimens exposed to each fraction of the coating life. Figures 62a through 62i show the typical post-test microstructures for specimens exposed to the estimated 10%-90% of TBC life. These specimens were polished using standard procedures except that an oil-based polishing slurry replaced water to prevent leaching of infiltrated corrodent. This metallographic analysis was conducted to look for subcritical crack development. Fractionally exposed specimen metallography showed some accumulated damage after 515 - 585 test hours; large in-plane cracks with several minor extensions were noted above the "typical" failure location. Note that the large crack in Figure 62i has several smaller extensions. Also, this crack is far from the interface in comparison with the typical clean fuel burner rig test failure mode. Figure 62h shows what may be considered the start of microcrack "link-up" at the center of the ceramic. Also, note the patch of ceramic which has flaked off at the outer surface. Most of the remaining photomicrographs show some segmentation cracking which is thought to have developed during exposure.

The results of the X-ray diffraction analysis for the fractionally exposed specimens are included in Table XVII. It is apparent from the data that increased exposure times show increased v/o monoclinic ZrO₂.

ORIGINAL PAGE
BLACK AND WHITE PHOTOGRAPH



200X

Figure 62a Post-Test Fractional (10% Life) Hot Corrosion Specimen
Microstructure, 65 hrs/899°C (1650°F)/35 ppm Na₂SO₄



200X

Figure 62b Post-Test Fractional (20% Life) Hot Corrosion Specimen
Microstructure, 130 hrs/899°C (1650°F)/35 ppm Na₂SO₄



200X

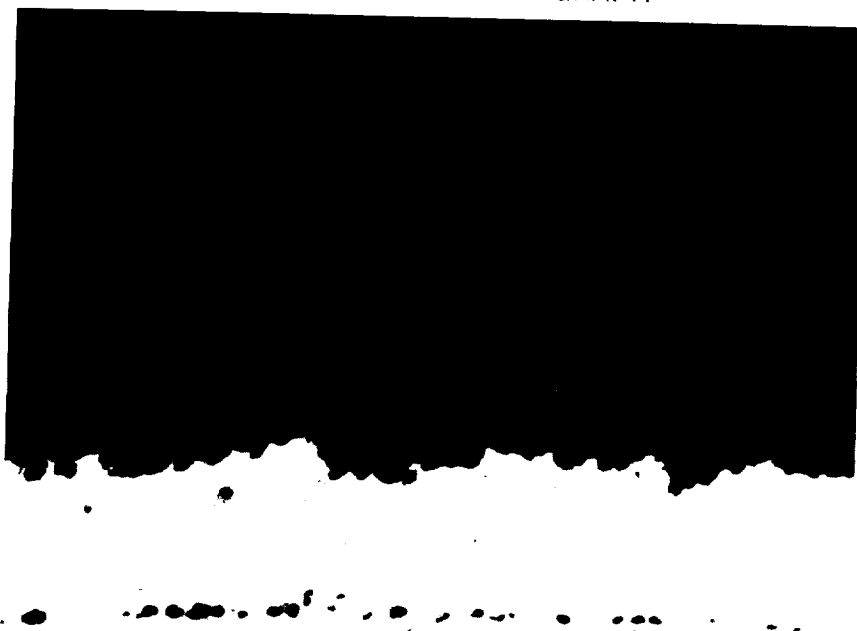
Figure 62c Post-Test Fractional (30% Life) Hot Corrosion Specimen
Microstructure, 185 hrs/899°C (1650°F)/35 ppm Na₂SO₄



200X

Figure 62d Post-Test Fractional (40% Life) Hot Corrosion Specimen
Microstructure, 250 hrs/899°C (1650°F)/35 ppm Na₂SO₄

ORIGINAL PAGE
BLACK AND WHITE PHOTOGRAPH



200X

Figure 62e Post-Test Fractional (50% Life) Hot Corrosion Specimen
Microstructure, 315 hrs/899°C (1650°F)/35 ppm Na₂SO₄



200X

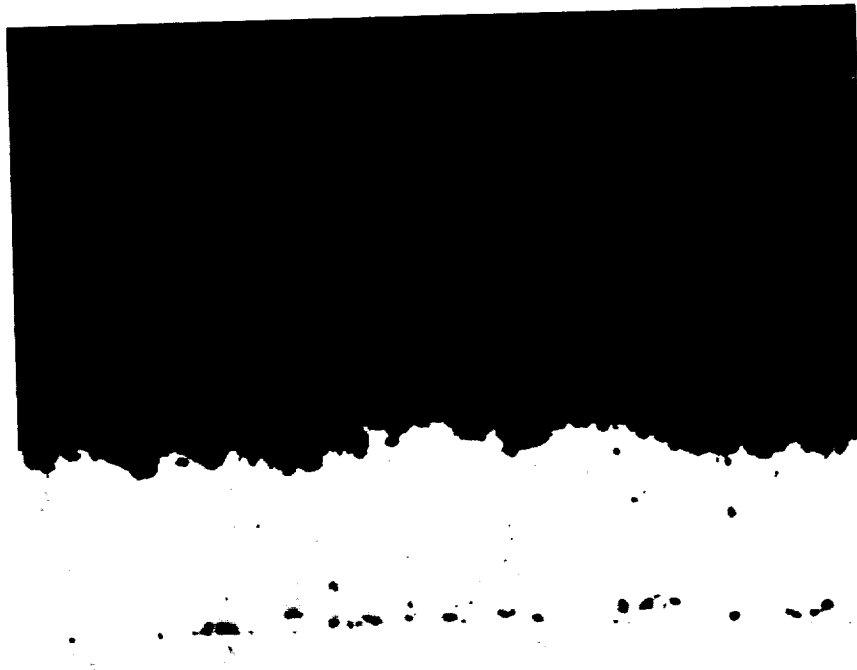
Figure 62f Post-Test Fractional (60% Life) Hot Corrosion Specimen
Microstructure, 380 hrs/899°C (1650°F)/35 ppm Na₂SO₄

ORIGINAL PAGE
BLACK AND WHITE PHOTOGRAPH



200X

Figure 62g Post-Test Fractional (70% Life) Hot Corrosion Specimen
Microstructure, 445 hrs/899°C (1650°F)/35 ppm Na_2SO_4



200X

Figure 62h Post-Test Fractional (80% Life) Hot Corrosion Specimen
Microstructure, 510 hrs/899°C (1650°F)/35 ppm Na_2SO_4

ORIGINAL PAGE
BLACK AND WHITE PHOTOGRAPH



200X

Figure 62i Post-Test Fractional (90% Life) Hot Corrosion Specimen
Microstructure, 575 hrs/899°C (1650°F)/35 ppm Na₂SO₄

The analysis of the fractionally exposed specimens (10% - 90%) removed from the test showed a minimum of 5 v/o monoclinic ZrO₂ for smaller fractions of exposure and up to 9 v/o monoclinic ZrO₂ for higher fractions of exposure. This result is consistent with earlier suggestions of thermochemical interaction of the corrodent with the ceramic (Ref. 30, 34, 35, 36), i.e., selective "leaching" of Y₂O₃ by the corrodent.

In summary, the results of the contaminated fuel burner rig test conducted showed that 7YSZ is extremely spall resistant in hot corrosion environments. When TBC failure did occur (only in high corrodent level testing), the TBC failure mode consisted of multilevel flaking of the ceramic. This mode is unique to cyclic hot corrosion testing and has not been seen in clean fuel burner rig tests, in furnace tests, or more importantly in any of the engine exposed hardware examined to date. X-ray diffraction analysis has shown higher levels of monoclinic ZrO₂ forming upon cool down; however, ceramic spallation was unobserved. Thus, a predominant failure mechanism may more likely involve mismatch between infiltrate and ceramic as reported in earlier studies (Ref. 14, 30, 32, 34) than selective leaching of Y₂O₃ causing destabilization (Ref. 35, 36). Although the latter is occurring, there seems to be no correlation to actual failure life. However, failure life of the ceramic is most probably governed by the interaction of these two mechanisms.

TABLE XVII
X-RAY DIFFRACTION ANALYSES OF FRACTIONAL EXPOSURE, CYCLIC HOT CORROSION TEST SPECIMENS

SPECIMEN ID/ EXPOSURE TIME	V/O PHASE PRESENT			OTHER
	FCC ZrO ₂	TETRAGONAL ZrO ₂	MONOCLINIC ZrO ₂	
HST-004A - 65 hrs	55-53	40-42	5	1 unidentified (possibly fcc NiO)
HST-007A - 130 hrs	54-56	39-37	6-4	1-2 NiO and 1fcc (Ni, Fe) S ₂
HST-009A - 185 hrs	54-56	39-37	6-4	1 Hexagonal Na ₂ SO ₄ and/or Hexagonal - NaFeO ₂
HST-012A - 250 hrs	53-55	38-36	5-3	2-4 fcc NiO, 2-1 tetragonal - Fe ₂ O ₃ 1 fcc FeS ₂
HST-017A - 315 hrs	53-55	37-35	4-6	2 Tetragonal - Fe ₂ O ₃ 2-1 Hexagonal - NaFeO ₂ , 2-1 fcc (Ni, Fe) S ₂
HST-019A - 380 hrs	43-45	45-43	7-9	3-1 fcc (Ni, Fe) S ₂ , 2 Tetragonal - Fe ₂ O ₃ 1 fcc NiO
HST-022A - 445 hrs	52-54	38-36	6-8	2-1 Tetragonal - Fe ₂ O ₃
HST-025A - 510 hrs	Poor, Profile trace, major phase-fcc ZrO ₂ , minor phases-tetragonal ZrO ₂ , monoclinic ZrO ₂ and hexagonal Na ₂ SO ₄			
HST-027A - 575 hrs	Poor profile trace major phase hexagonal Na ₂ SO ₄ , fcc ZrO ₂ - trace			
HST-032A - 1000 hrs	30	45-50	15-10	10 2 (Mg ₉₆ Fe _{0.04}) 0. SiO ₂ 1 NiAl 1 NiO
HST-032A - 1000 hrs	30	45-50	15-10	10 2 (Mg ₉₆ Fe _{0.04}) 0. SiO ₂ 1 NiAl 1 NiO

3.1.3 Task IB.2 Determine Physical/Mechanical Properties

The purpose of this subtask was to measure values of physical and mechanical properties required for subsequent analytical and life modeling. Measured physical properties include thermal conductivity, specific heat, and thermal expansion of bulk porous zirconia and dense NiCoCrAlY specimens fabricated to simulate structures found in the respective TBC coating layers. Mechanical tests were conducted only on bulk porous zirconia and included fracture toughness, uniaxial tension and compression, tensile and compressive creep, and "derived" tensile fatigue in the range of ambient to 1204°C (2200°F). All needed base alloy properties and mechanical properties of the metallic coating were available from prior internally funded programs and were not remeasured in this program. All physical property testing was conducted by Dynatech Corporation, Cambridge, Mass. With the exception of an ambient temperature four point bend test conducted early in the program to gain needed preliminary insight into basic ceramic constitutive behavior, all mechanical property tests were conducted at Southwest Research Institute, San Antonio, Texas.

Bulk ceramic and metallic property test specimens were fabricated by plasma deposition using the same parameters as used to make the respective TBC coating layer. Coating thickness of up to 1.27cm (0.5") were accumulated on mild steel panels and then the test specimens were machined off and ground to required dimensions. Shown in Figure 63 is a bulk ceramic specimen microstructure which can clearly be seen to quite closely simulate the microstructure of the 0.25mm (0.010 in.) ceramic coating.

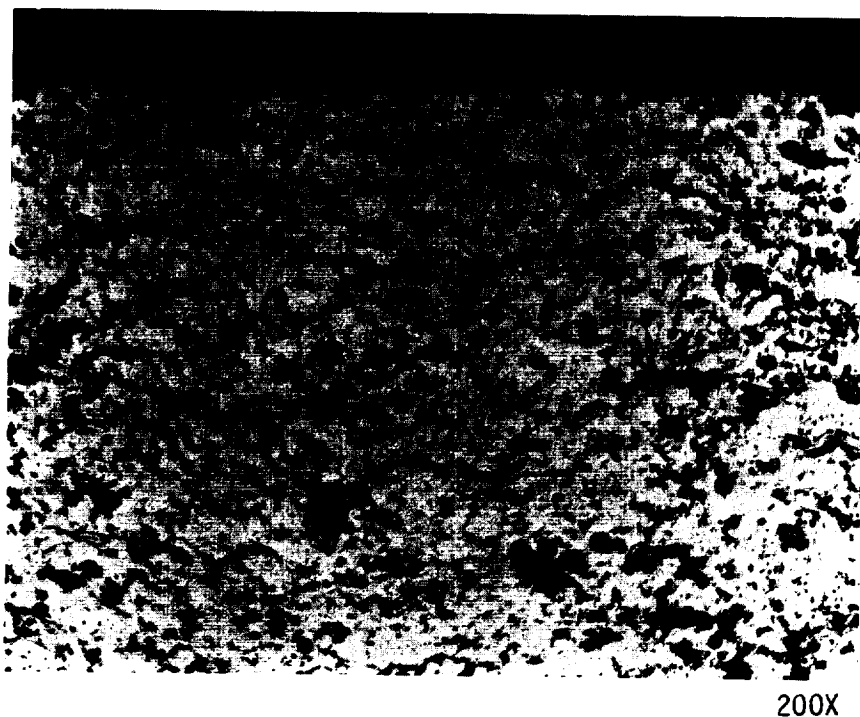


Figure 63 Bulk Ceramic Microstructure Used for Physical/Mechanical Property Tests

3.1.3.1 Physical Property Tests

Procedures used by Dynatech to measure physical properties are summarized in Appendix D. Specific numbers of physical tests conducted and the corresponding temperature ranges investigated are summarized in Table XVIII. Results of these tests are presented in Tables XIX through XXIV.

TABLE XVIII
COATING PROPERTY TESTS

	Ceramic (Bulk Specimen)	Bond Coat (Bulk Specimen)
o Thermal Conductivity	3 Tests: 538°C (1000°F), 871°C (1600°F), 1149°C (2100°F)	3 Tests: 538°C (1000°F), 871°C (1600°F), 1149°C (2100°F)
o Thermal Expansion	2 Tests: 538°C (1000°F), 1149°C (2100°F)	2 Tests: 538°C (1000°F), 1149°C (2100°F)
o Specific Heat	3 Tests: 538°C (1000°F), 871°C (1600°F), 1149°C (2100°F)	3 Tests: 538°C (1000°F), 871°C (1600°F), 1149°C (2100°F)

TABLE XIX
THERMAL CONDUCTIVITY OF 7 w/o Y₂O₃ -ZrO₂

Temperature (°C/°F)	Thermal Conductivity	
	(W/mK)	(Btu in/hr ft ² °F)
538/1000	0.645	4.47
871/1600	0.675	4.68*
1100/2012	0.660	4.58

*The accuracy of these measurements ranges from +8-10% and, therefore, the apparent peak at 817°C (1600°F) is not considered to be significant. This judgment is based in part on previous work done at Dynatech for Pratt & Whitney, which showed no thermal conductivity peaks at intermediate temperatures.

TABLE XX
SPECIFIC HEAT OF 7 w/o Y₂O₃ -ZrO₂

Temperature (°C/°F)	Specific Heat	
	(J/g °C)	(Btu/lb °F)
538/1000	0.582	0.139
871/1600	0.593	0.142
1149/2100	0.603	0.144

TABLE XXI
THERMAL EXPANSION OF 7 w/o Y₂O₃ -ZrO₂

Temperature (°C/°F)	Thermal Expansion T. E. x 10 ⁴	Coefficient of* Thermal Expansion x 10 ⁶ (°C ⁻¹)
25/77	0	-
100/212	7.26	9.68
200/392	17.53	10.02
300/572	27.00	9.82
400/752	36.39	9.70
500/932	45.77	9.64
600/1112	56.25	9.78
700/1292	66.72	9.88
800/1472	77.64	10.02
900/1652	89.15	10.19
1000/1832	100.82	10.34
1100/2012	110.64	10.29
1175/2147	116.12	10.10

*Average-from ambient temperature to temperature indicated

TABLE XXII
THE THERMAL CONDUCTIVITY OF NiCoCrAlY

Sample thickness = 9.47mm (.373 inch)

Temperature (°C/°F)	Thermal Conductivity (W/mK) (Btu in/hr ft ² °F)	
538/1000	20.5	142
871/1600	24.3	168
1100/2012	34.2	237

TABLE XXIII
THE SPECIFIC HEAT OF NiCoCrAlY

Temperature (°C/°F)	Specific Heat (J/G°C) (Btu/lb °F)	
538/1000	0.628	.150
871/1600	0.674	.161
1149/2100	0.712	.170

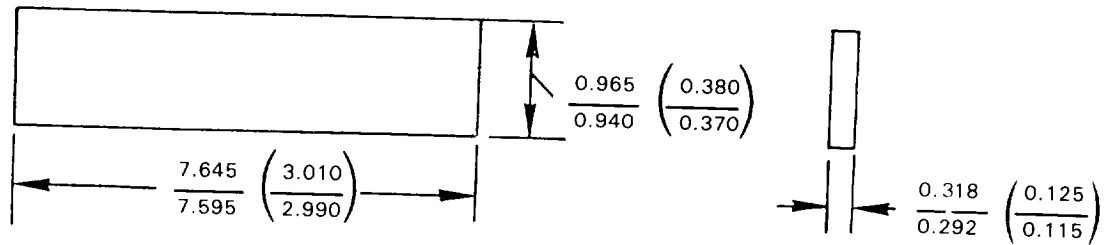
TABLE XXIV
THERMAL EXPANSION OF NiCoCrAlY

Temperature (°C/°F)	Thermal Expansion TE x 10 ⁴	Coefficient of Thermal Expansion [1/°C]/[1/°F] x10 ⁶
25/77	0	12.75 / 6.94
100/212	2.56	12.67 / 7.03
200/392	22.17	13.39 / 7.40
300/572	36.83	13.97 / 7.76
400/752	52.38	14.22 / 7.90
500/932	67.53	14.81 / 8.23
600/1112	85.15	15.5 / 8.60
700/1292	104.62	16.29 / 9.05
800/1472	126.27	16.93 / 9.41
900/1652	148.15	17.30 / 9.60
1000/1832	168.72	17.78 / 9.87
1100/2012	191.13	17.96 / 9.97
1175/2150	202.02	

3.1.3.2 Preliminary Mechanical Testing

As mentioned previously, a preliminary room temperature four point bend test was conducted at the United Technologies Research Center to gain early insight into the constitutive behavior of the strain tolerant ceramic. The geometry of the test specimen is illustrated in Figure 64. A plot of outer fiber tensile stress (calculated from applied load using classical elastic bending relationships) vs. outer fiber tensile strain (measured by bonded strain gage) is shown in Figure 65a. The stress-strain relationship differs dramatically from the completely elastic ambient temperature behavior typically observed for fully dense structural ceramic materials. The strain tolerant ceramic deformation appears to be nonlinear even at very low stress levels, with no clearly definable linear elastic segment of the stress-strain curve. Unloading of another partially loaded specimen showed substantial permanent offset with no observable microcracking on the tensile side, indicating that the curvature seen in Figure 65a represents truly inelastic behavior.

Despite the occurrence of significant inelastic deformation, the ultimate strength and fracture strain of the strain tolerant ceramic are quite low, 47.6 MPa (6.9 ksi) and 0.26% respectively. The material also is highly compliant with an initial stiffness of 4.0x10 MPa (5.8x10⁶ psi). Measurements from multiply oriented strain gages indicate a relatively small Poisson's ratio of 0.091. An interesting fractograph from the tensile side of a broken specimen shows a highly columnar structure with "splats" of the plasma deposited ceramic (Figure 65b).



All Dimensions Shown in cm (inches)

Figure 64 Bulk Four Point Bend Specimen Geometry

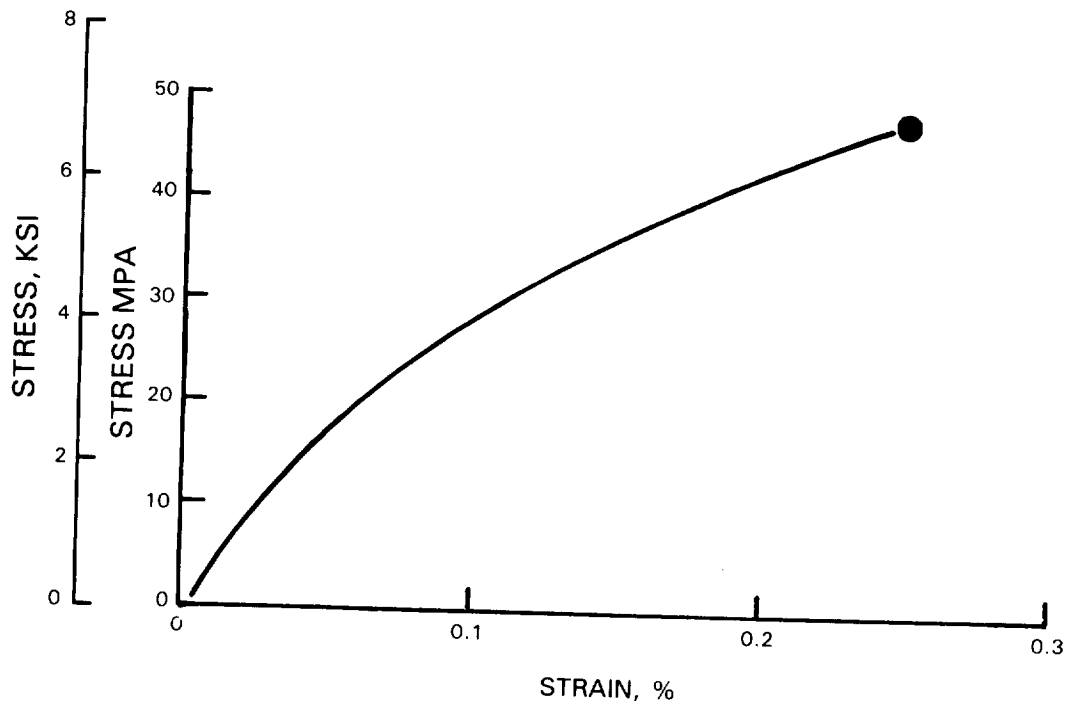
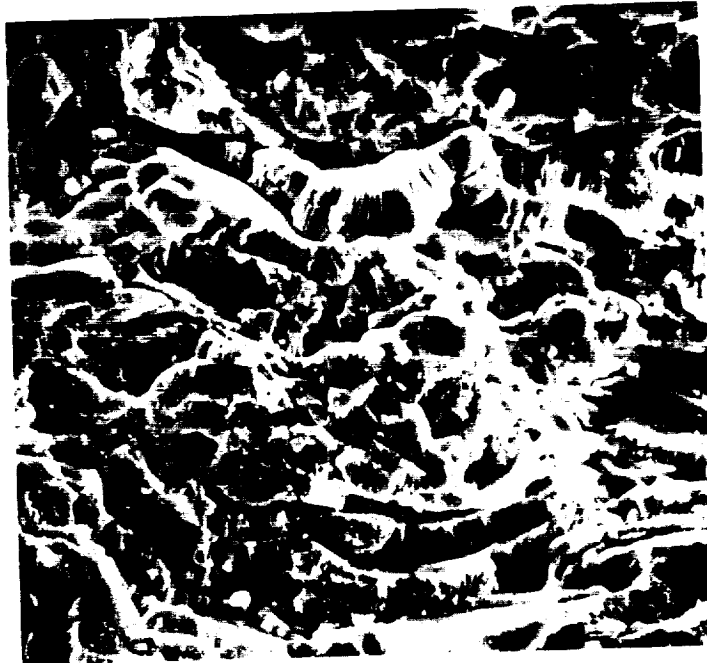


Figure 65a Room Temperature Four Point Bend Test Results for Bulk Plasma Sprayed 7 w/o $Y_2O_3 - ZrO_2$



1000X

Figure 65b Fracture Surface of Four Point Bend Test Specimen

3.1.3.3 Southwest Research Institute Mechanical Test Program

The mechanical test program conducted by Southwest is summarized in Figure 66. Test methods and results are described in the following paragraphs. All tests were conducted with the primary loading axis in the plane of the splat structure.

Uniaxial compression tests were conducted on right circular cylinders (Figure 67) loaded along the cylinder axis between flat and parallel alumina anvils having self locking tapered ends mounted in water cooled adapters (Figure 68). A 227 Kg (500 pound) capacity load cell was used to provide good resolution (0.02 Kg (.05 lb)) at the relatively small loads involved in this testing. Loading of the specimens was performed under displacement control of the actuator shaft at a constant displacement rate approximating a strain rate of 1×10^{-3} cm/cm/sec (1×10^{-3} in/in/sec). Displacement was measured to an accuracy of 12.7 microns (0.0005 inches) on the actuator shaft near the loading fixture attachment point. A machine compliance calibration was obtained at each test temperature by measuring the load-deflection characteristics of the compression apparatus without the test specimen. All data was corrected by subtracting the appropriate calibration values from the recorded displacement. Alignment of the system was confirmed by plastically deforming aluminum rodlets and measuring the resulting height variation around the circumference; this variation was less than 0.005 mm (0.0002 inches). Compression specimens were heated inductively with a cylindrical graphite susceptor. To prevent rapid deterioration of the susceptor, a water cooled copper jacket with a viewing port was placed over the specimen and flooded with Argon gas (Figure 69). Test temperature was determined from the averaged output of two thermocouples located adjacent to the opposing loading platens.

Test Temperature	Number of Tests Planned (Conducted)				
	1000°F 538°C	1600°F 871°C	1800°F 982°C	2000°F 1093°C	2200°F 1204°C
Test Type					
Stress-Strain Response Test					
Tension	1(3)	1(2)		1(2)	1(2)
Compression	0(1)	1(1)			1(2)
Creep/Stress Rupture Test					
Tension	1(1)		1(2)		1(1)
Compression			1(3)		1(4)
Fatigue (Wafer) Test	3(5)	3(5)			
Fracture Toughness Test	2(2)	2(2)			

Figure 66 Mechanical Property Test Plan for Bulk Ceramic

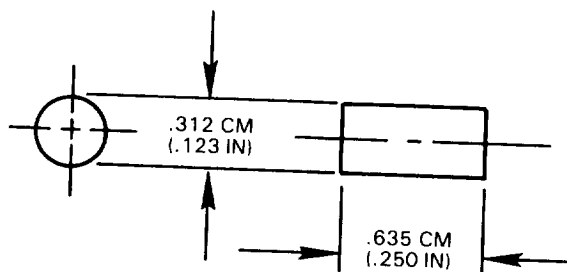


Figure 67 Compression Specimen

ORIGINAL PAGE
BLACK AND WHITE PHOTOGRAPH

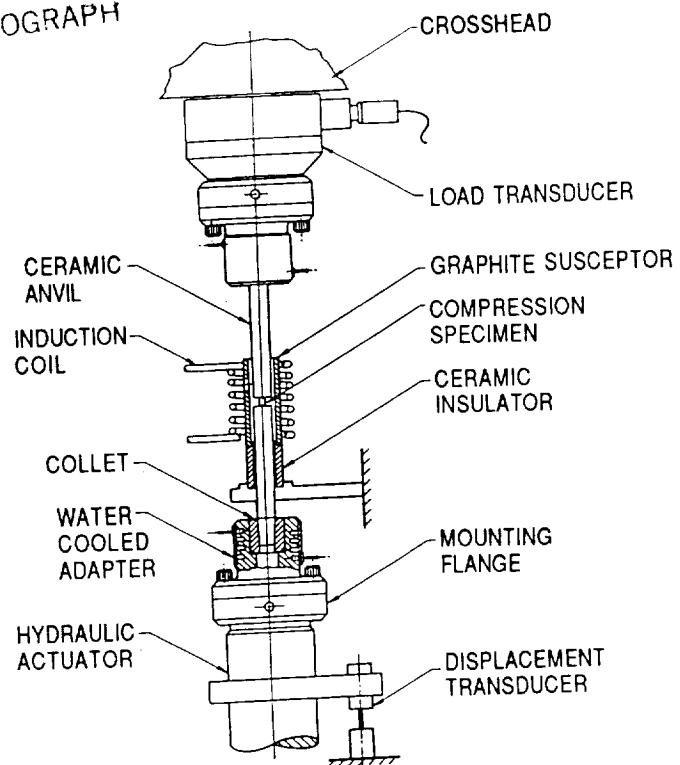


Figure 68 Compression Test Apparatus



Figure 69 Test Rig

The configuration of the specimen used for testing with uniaxial tensile loading is shown in Figure 70. The tapered portion of this specimen was gripped with boron nitride coated split ceramic collets constrained with a superalloy shield and loaded by superalloy shear pins (Figure 71). Specimen strain was inferred from actuator displacement using machine compliance corrections generated from a strain gaged tensile specimen loaded to failure at room temperature. A static pre-loading apparatus was used to seat the grip section without application of significant preload to the gage section of the specimen.

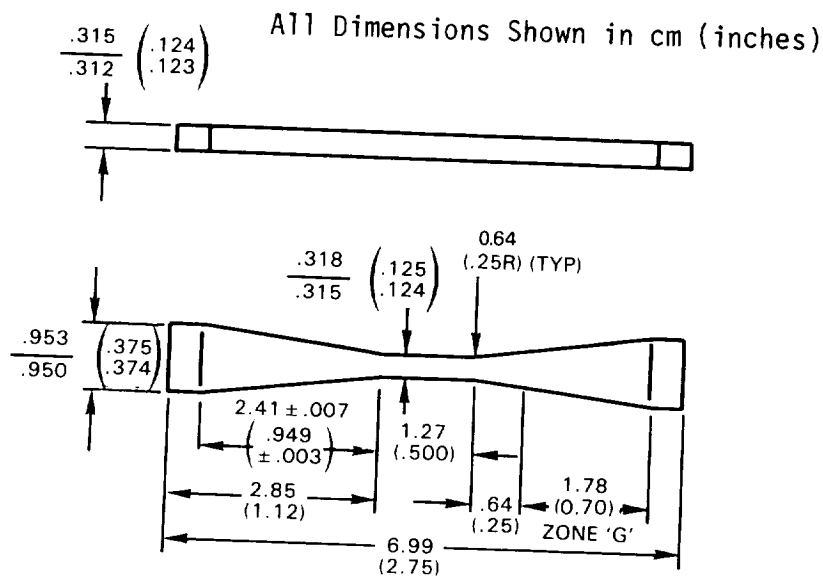


Figure 70 Tensile Specimen Geometry

Fracture toughness was measured by single edge notching the tensile specimen to a depth of about 0.5 mm (0.020 in.) using a 0.24 mm (0.009 in.) diameter diamond coated wire. While plane strain conditions were not fully satisfied in this test, it is felt to provide a reasonable indication of the general toughness capability of the material.

Derived tensile fatigue testing was conducted in the previously described compression test apparatus by compressive edge loading of the wafer geometry specimen illustrated in Figure 72. Based on the analysis of Shaw, Braiden, and DeSalvo, (Ref. 39: on Figure 73), this loading produced a biaxial stress state with a low level of tensile loading in the plane of the disk perpendicular to the compression axis (Figure 73). For materials such as ceramics where the tensile strength is substantially less than the compressive strength, tensile failure will occur in the center of the disk at loads below the compressive strength of the material. By cyclically loading this specimen, tension-tension fatigue testing was conducted on the ceramic, using a small positive R ratio (0.1) to maintain the specimen firmly between the anvils at all times.

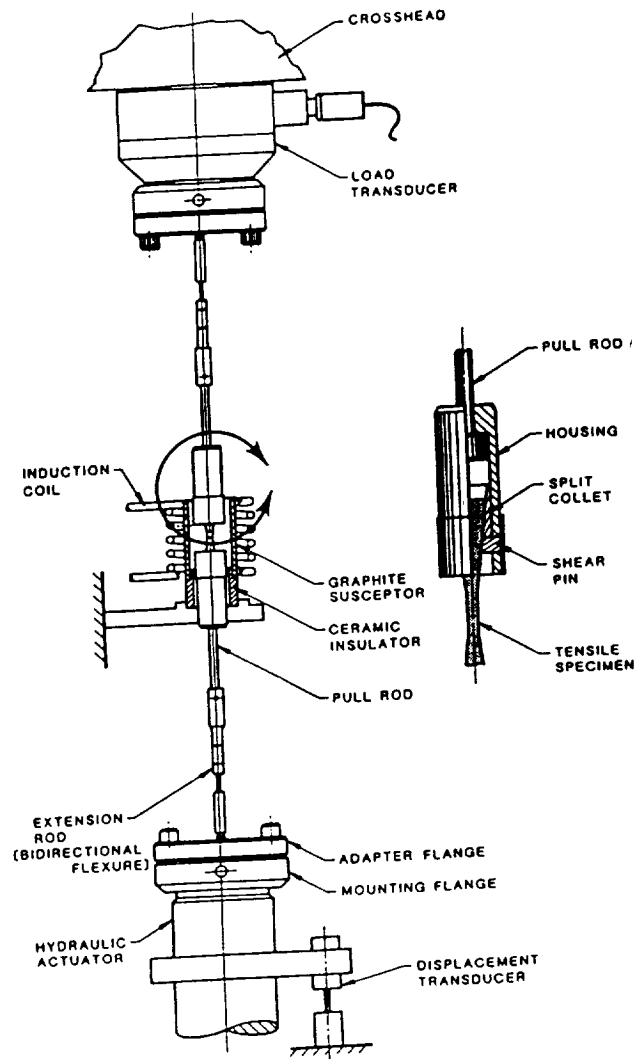


Figure 71 Tensile Test Apparatus

All Dimensions Shown in cm (Inches)

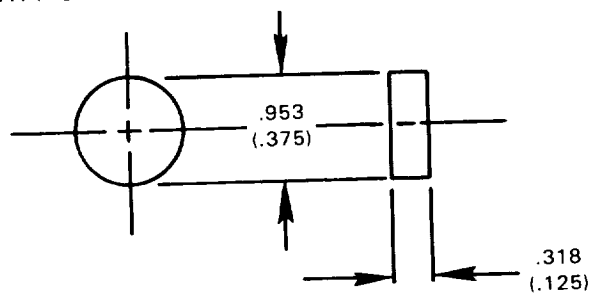
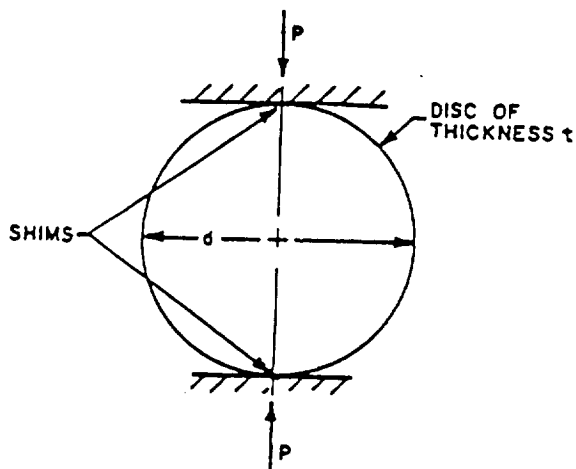
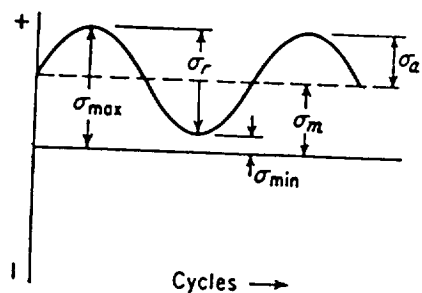


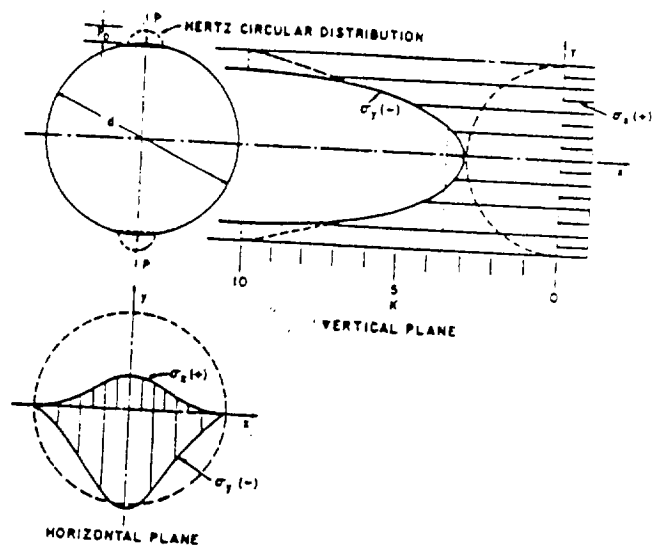
Figure 72 Wafer Specimen



a Diametral Compression Specimen



c Fatigue Stress Cycle: Repeated Stress



b Stress Distribution for Transversely Loaded Disk

Figure 73 Fatigue Stress Cycle

3.1.3.3.1 SWRI Test Results

Results of mechanical property tests are summarized in Tables XXV through XXX. Stress-strain and creep curves for each test are included in Appendix E.

3.1.3.3.1.1 Uniaxial Tension and Compression Test Results

The most significant result of these property tests is confirmation of the non-linear deformation behavior observed in the previously discussed preliminary bend testing. Shown in Figure 74 is a room temperature tensile stress-strain curve generated from the strain gauged machine calibration specimen mentioned earlier. As with the previously discussed bend test, the strain tolerant ceramic exhibits non-linear deformation behavior throughout the loading history. Because of this non-linear behavior, it is difficult to define an "elastic modulus"; "initial stiffness" values, noted in Table XXVI, are graphical estimates of the tangent to the stress strain curve near zero load. Because elevated temperature stiffness values are based on crosshead displacement, some caution must be used in interpreting these data despite all of the precautions taken in testing to minimize seating and machine compliance effects. For example, the slight upward curvature seen in the initial portion of most of the elevated temperature curves is assumed to be an artifact and has been ignored in measurement of initial slopes.

TABLE XXV
UNIAXIAL COMPRESSION PROPERTY TEST DATA

Specimen Identification Number	Test Temperature °C (°F)	Ultimate Compressive Strength MPa (Ksi)	Strain Ultimate (%)	Strain at Fracture (%)	Initial Stiffness E GPa (PSI x 10 ⁶)
-2-CP-27-1	871 (1600)	303 (44.0)			11.31 (1.64)
	1191 (2175)	198 (28.7)		2.46	21.72 (3.15)
-2-CP-27-11	538 (1000)	376 (54.6)	2.61	2.61	13.51 (1.96)
-2-CP-27-3	871 (1600)	274 (39.7)	1.90	1.90	12.41 (1.80)
-2-CP-27-2	1204 (2200)	218 (31.6)	3.54	4.38	13.44 (1.95)
-2-CP-27-4	1202 (2196)	273 (39.6)	4.32	5.14	10.34 (1.50)

TABLE XXVI
UNIAXIAL TENSION PROPERTY TEST DATA

Specimen Identification Number	Test Temperature °C (°F)	Initial Stiffness, E GPa (PSI x 10 ⁶)	Ultimate Tensile Strength MPa (Ksi)	Apparent ¹ Failure Strain, %
EC-1	24 (75)	19.99 (2.90)	1.350 (3.08)	0.196 ²
EC-2	538 (1000)	21.24 (3.08)	1.089 (2.65)	0.158
EC-10	538 (1000)	Data Unavailable	(2.60)	Data Unavailable
CP-24	538 (1000)	43.51 (6.31)	0.386 (2.58)	0.056
CP-13	871 (1600)	43.51 (6.31)	0.531 (2.58)	0.077
CP-14	871 (1600)	12.41 (1.80)	1.950 (2.68)	0.283
CP-21	1094 (2000)	21.24 (3.08)	1.481 (3.08)	0.215
CP-23	1094 (2000)	25.72 (3.73)	1.295 (3.18)	0.188
EC-4	1204 (2200)	27.65 (4.01)	2.039 (2.45)	0.296
EC-5	1204 (2200)	27.65 (4.01)	1.826 (2.32)	0.265

¹ Except as noted, measured from crosshead displacement at failure, compensated for machine stiffness

² Measured from strain gage

³ Tangent slope at zero load

TABLE XXVII
COMPRESSION-CREEP PROPERTY TEST DATA

Specimen Identification Number	Test Temperature °C (°F)	Applied Stress MPa (ksi)	Accumulated Strain (%)	Creep Time (Minutes)	Comments
-2-CP-27-5	982 (1800)	264.6 (38.4)	2.22	5.9	Same Specimen No Failure
		279.7 (40.6)	2.48	4.6	
		293.5 (42.6)	2.82	6.3	
-2-CP-27-12	982 (1800)	89.6 (13.0)	1.88	295.2	No Failure, Minimum Creep Rate = 0.24% /hrs
-2-CP-27-6	982 (1800)	276.3 (40.1)	2.32	8.8	Minimum Creep Rate = 1.27 % /hr, Same Specimen Minimum Creep Rate = 0.62 % /hr, No Failure
		292.1 (42.4)	2.76	20.0	
-2-CP-27-7	1204 (2200)	237.7 (34.5)	5.17	1.90	
					Initial Creep Rate = 68.5% /hr
-2-CP-27-8	1204 (2200)	217.0 (31.5)	6.35	3.40	Initial Creep Rate = 40.8% /hr
-2-CP-27-9	1204 (2200)	65.5 (9.5)	4.5	106.1	No Failure, Minimum Creep Rate = 1.42% /hr
-2-CP-27-10	1204 (2200)	68.6 (9.95)	6.34	111.4	No Failure, Minimum Creep Rate = 1.83% /hr

TABLE XXVIII
TENSION-CREEP PROPERTY TEST DATA

Specimen Identification Number	Test Temperature °C (°F)	Applied Stress MPa (ksi)	Accumulated Strain (%)	Creep Time (Minutes)	Comments
CP-12	538 (1000)	14.47 (2.10)	0.048	1.94	No failure, no creep response
CP-19	982 (1800)	14.95 (2.17)	0.140	3.75	Failed, M.C.R. 0.0038% /hr ¹
CP-20	982 (1800)	14.26 (2.07)	0.160	5.28	Failed, M.C.R. 0.0011% /hr ¹
EC-6	1204 (2200)	1350 (1.96)	0.80	0.61	Failed

¹ M.C.R = Minimum Creep Rate

TABLE XXIX
FATIGUE PROPERTY TEST DATA

Specimen Identification Number	Test Mode Mode	Test Temperature °C (°F)	Maximum Applied Stress MP _A (ksi)	R	Number of Cycles	
-2-CP-26-2	Fatigue	538 (1000)	17.2 (2.5)	0.1	20,000	No Failure
-2-CP-26-2*	"Tensile"	538 (1000)	23.4 (3.4)	---	1/4	
-2-CP-26-5	Fatigue	538 (1000)	17.9 (2.6)	0.1	307	
-2-CP-26-3	Fatigue	538 (1000)	18.6 (2.7)	0.1	410	
-2-CP-26-4	Fatigue	538 (1000)	18.6 (2.7)	0.1	195	
-2-CP-25-2	Fatigue	871 (1600)	14.6 (2.12)	0.1	60,000	Same Specimen No Failure
			18.4 (2.67)	0.1	10,000	
			20.2 (2.93)	0.1	10,452	
			21.7 (3.15)	0.1	11,000	
			22.7 (3.3)	0.1	10,050	
2 CP-25-5	Fatigue	871 (1600)	18.2 (2.64)	0.1	407	
-2-CP-26-1	Fatigue	871 (1600)	18.2 (2.64)	0.1	158	
2-CP-25-1	"Tensile"	871 (1600)	22.0 (3.2)	---	1/4	
2 CP-25-3	"Tensile"	871 (1600)	22.7 (3.3)	---	1/4	

*Specimen uploaded to failure

TABLE XXX
FRACTURE MECHANICS PROPERTY TEST DATA

Specimen Identification Number	Test Temperature °C (°F)	Failure Stress MP _A (ksi)	a cm (in.) ¹	b cm (in.) ²	K _Q MP _A √m (ksi√in) ³	
CP-22	538 (1000)	12.13 (1.76)	0.0444 (0.0175)	0.315 (0.124)	0.634 (0.578)	3.98
CP-9	538 (1000)	10.27 (1.49)	0.0462 (0.0182)	0.310 (0.122)	0.499 (0.454)	3.13
CP-15	871 (1600)	13.09 (1.90)	0.0465 (0.0183)	0.315 (0.124)	0.636 (0.579)	3.99
CP-18	871 (1600)	10.40 (1.51)	0.0538 (0.0212)	0.315 (0.124)	0.567 (0.517)	3.56

Notes:

1. Crack (notch) depth
2. Total specimen depth
3. Apparent (not valid) critical stress intensity factor

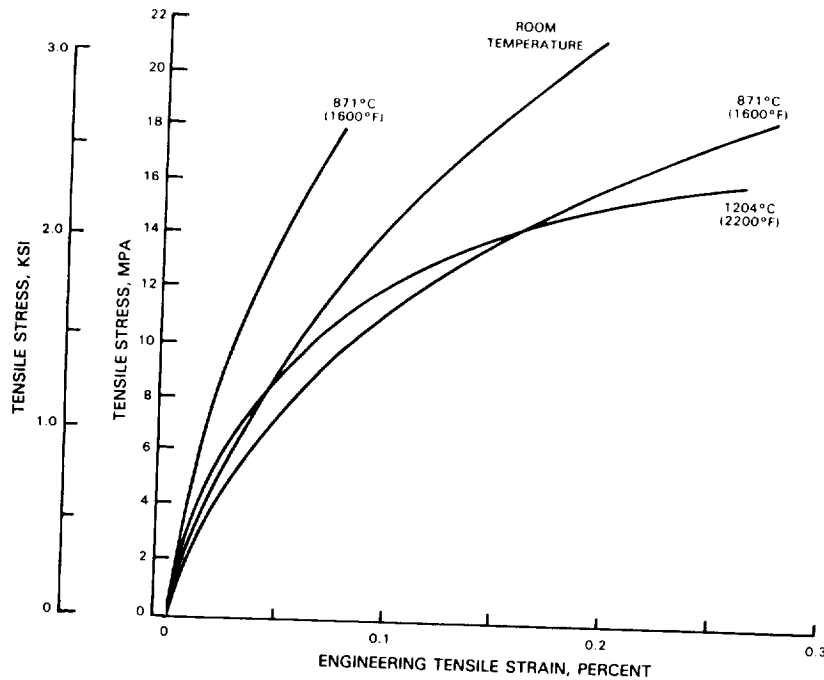


Figure 74 Representative Strain Tolerant Ceramic Tensile Stress Strain Curves at Various Temperatures. Room temperature strain data measured by strain gauge; temperature curves obtained from corrected cross head displacement.

Examination of the elevated temperature tensile curves included in Appendix E indicates that while there is substantial variability of initial and overall stiffness, the basic non-linear shape of the stress-strain curve is similar at all temperatures up to 1094°C (2000°F). Both the shape similarity and the stiffness variability are illustrated by comparison of the room temperature and the two 871°C (1600°F) curves reproduced in Figure 74. At 1204°C (2200°F) there is substantially more curvature than at the lower temperatures, as shown by the high temperature curve reproduced in Figure 74.

Both ultimate tensile strength and tensile failure strains are relatively low at all temperatures. As shown in Figure 75, strength appears to exhibit a slight decreasing trend between room temperature and 538°C (1000°F), rising again to about room temperature levels at 1094°C (2000°F), and again decreasing at 1204°C (2200°F). The reason for this apparent increase at 1094°C (2000°F) is not presently understood and may reflect data scatter, although reproducibility at each temperature appears to be quite good. It is possible that this strength peak is related to subtle phase changes (very slight monoclinic to tetragonal transformation) in this temperature range, but such interpretation must be viewed as highly speculative at the present time.

Because of substantial data scatter, it is difficult to identify any trend for temperature dependence of tensile failure strain. It should be noted that all tensile failures occurred in the fillet region of the specimen where stress concentration is calculated to be on the order of 1.15, suggesting that some caution should be exercised in interpretation of the strength and "ductility" data discussed above.

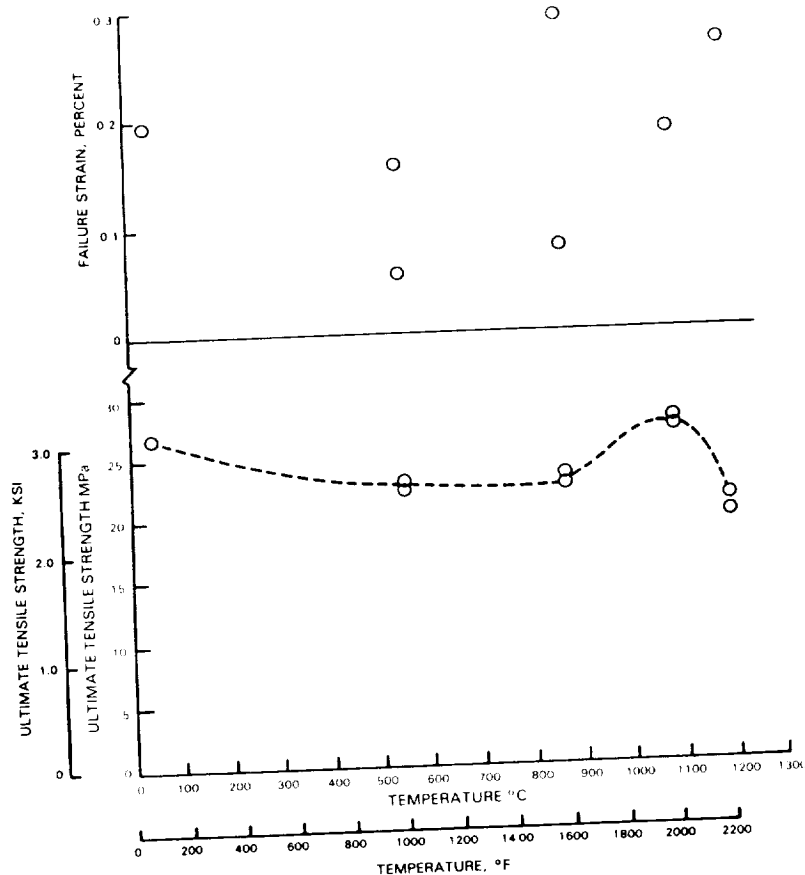


Figure 75 In-plane Temperature Elevated Tensile Properties of Strain Tolerant Ceramic

Compressive stress-strain behavior, summarized in Figure 76 and Table XXV, differs significantly from tensile behavior; compressive strengths are much higher than tensile strengths, and there appear to be distinct linear and non-linear segments to the stress-strain curves. Because corrected crosshead displacement was used to measure strain, with attendant seating effects at low loads, this latter observation is made with some reservation. This reservation notwithstanding, the 538°C (1000°F) and 871°C (1600°F) compressive stress-strain curves clearly are shaped differently than corresponding tensile stress-strain curves. At 1204°C (2200°F), compressive deformation begins to resemble tensile deformation, departing from linearity at relatively low stress levels. Within accuracy limits imposed by use of corrected crosshead displacement, initial stiffness appears to be essentially independent of temperature in the range studied.

The compressive failure mode was observed to be of the classical shear type (Figure 77). Compressive stresses and strains at failure are plotted in Figure 78. Because compressive tests were not conducted at 1094°C (2000°F), the occurrence of a strength peak, such as that seen at this temperature in tensile loading, could not be verified.

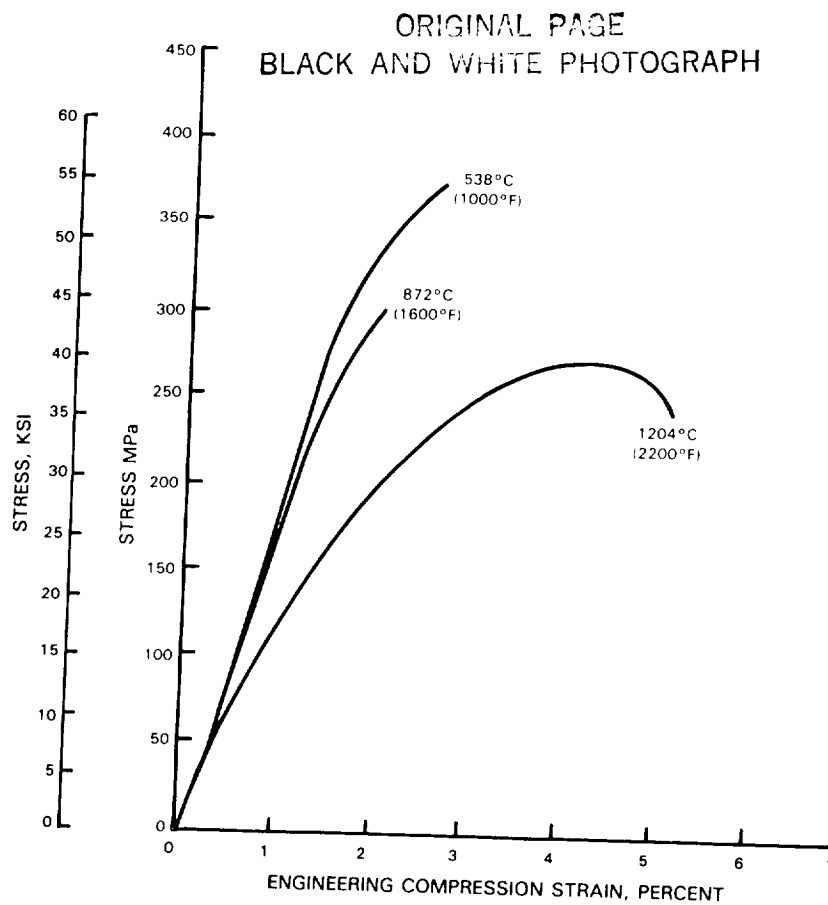


Figure 76 Representative Strain Tolerant Ceramic Compressive Stress-Strain Curves at Various Temperatures. Compressive strains calculated from corrected crosshead displacement.



Figure 77 Typical Compressive Failure Mode

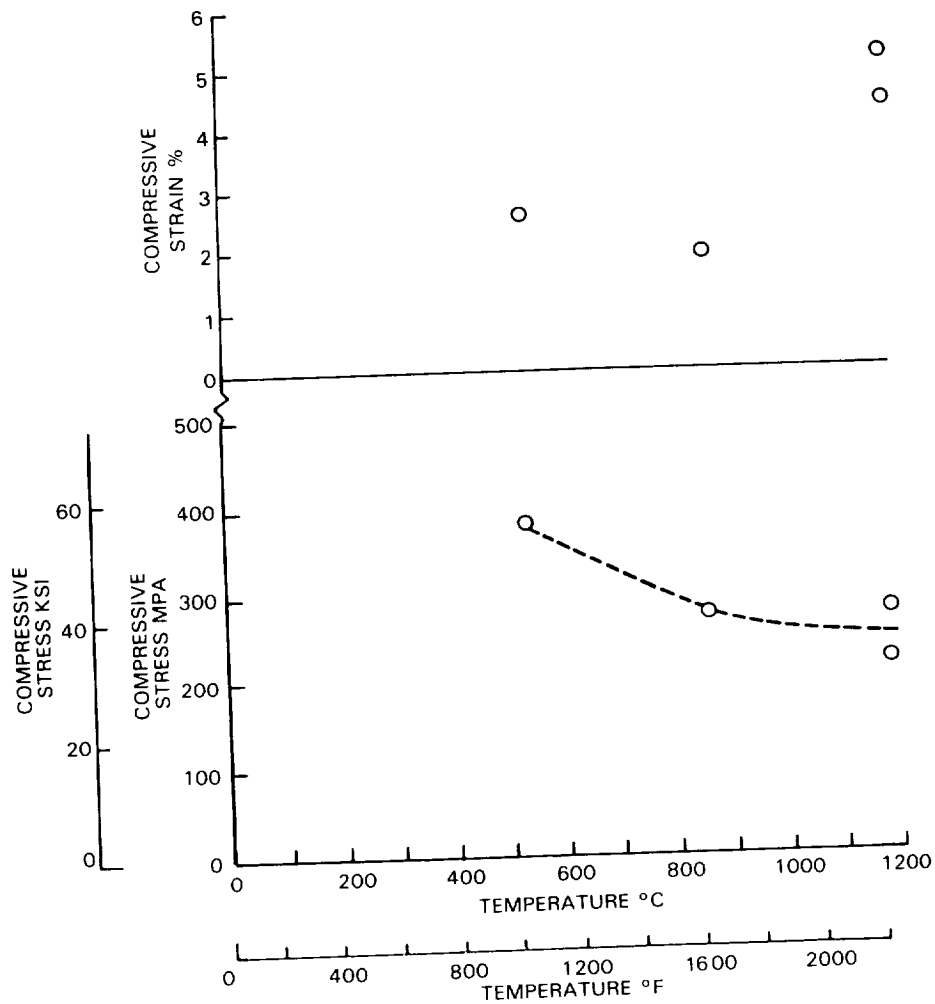


Figure 78 In-plane Elevated Temperature Compressive Properties of Strain Tolerant Ceramic

3.1.3.3.1.2 Creep Behavior

The creep test results are listed in Tables XXVII and XXVIII for compression and tension, respectively. All strain-time curves for these tests are presented in Appendix E. As shown in Table XXVII, uniaxial compression-creep tests were conducted for two stress levels at 982°C (1800°F) and 1204°C (2200°F), on a total of seven specimens.

Compression-creep tests showed a strong creep response at 982°C (1800°F) and 1204°C (2200°F) for low and high stress levels. At 982°C (1800°F) a larger amount of compressive straining occurred in the higher stress level test.

Compression-creep tests conducted at 1204°C (2200°F) showed a significant increase in creep response as compared with the 982°C (1800°F) test results. In both the low stress and high stress level tests at 1204°C (2200°F), the initial creep rates are very high, but in the lower stress level tests, the creep rates diminish significantly with time. However, the high stress level tests at 1204°C (2200°F) reach very large compressive strain values very quickly.

Uniaxial tension-creep tests were conducted for high stress levels ($\approx 80\%$ UTS) at 538°C (1000°F), 982°C (1800°F) and 1204°C (2200°F) on a total of four specimens.

No tension-creep response was seen at 538°C (1000°F) after testing for over two hours. However, test data at 982°C (1800°F) and 1204°C (2200°F) revealed a significant tensile-creep response.

Minimum creep rates were estimated graphically for a significant portion of the compression-creep and tensile-creep data. The minimum compression creep rate values were much higher than those calculated for tension and were seen to be strongly dependent on stress level and temperature. At 982°C (1800°F), minimum creep rates for compression at the lower stress level were on the order of $2.5 \times 10^{-3} \text{hr}^{-1}$ and at higher stress levels were greater than 10^{-2}hr^{-1} . Tensile minimum creep rate values averaged $\approx 7 \times 10^{-5} \text{hr}^{-1}$ at 982°C (1800°F).

At 1204°C (2200°F), minimum creep rate values for compression approached $2 \times 10^{-2} \text{hr}^{-1}$ at low stress levels. At higher stress levels, it appears as though only primary creep occurred and creep rates were $\approx 5 \times 10^{-1} \text{hr}^{-1}$ for compression and $1 \times 10^{-3} \text{hr}^{-1}$ for tension. Minimum creep rates are plotted versus stress in Figure 79; Figure 80 shows the creep rate-temperature dependence.

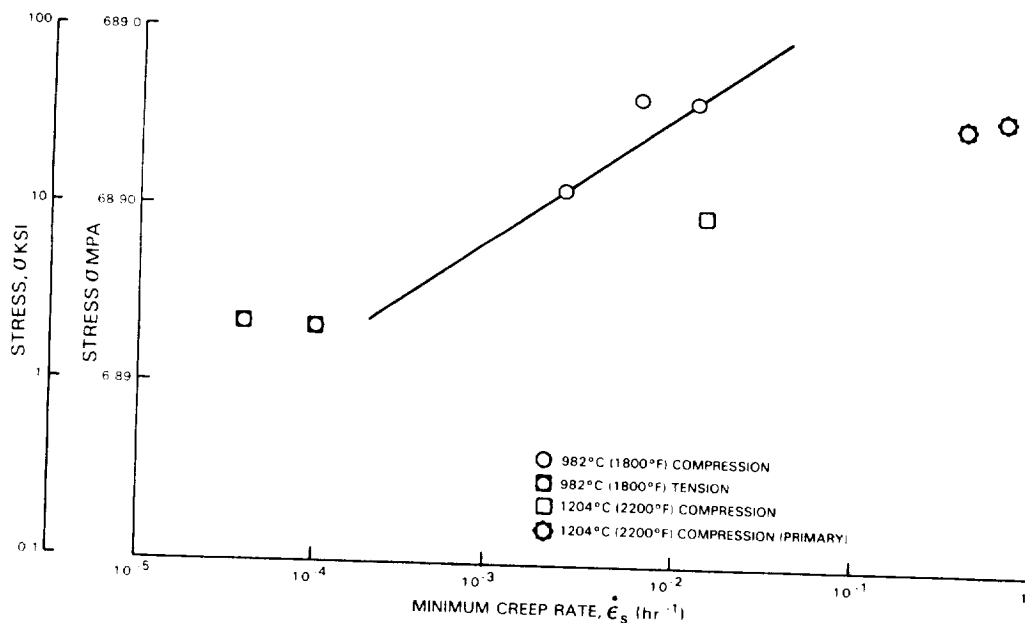


Figure 79 Stress Versus Creep Rate

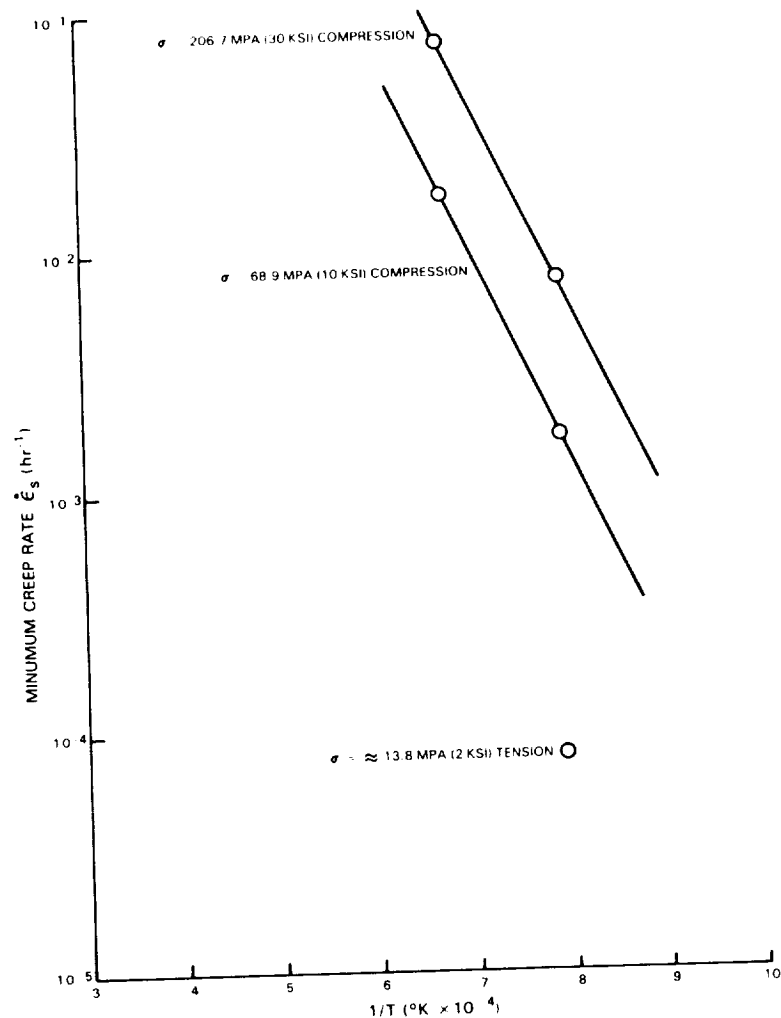


Figure 80 Creep Rate Versus Temperature

3.1.3.3.1.3 Fatigue Behavior

Fatigue test results are listed in Table XXIX and plotted in S-N form in Figure 81. As shown in the table, five specimens were cycled directly to failure: three at 538°C (1000°F) and two at 871°C (1600°F). Three additional specimens were failed in monotonic loading to compare tensile strength as measured in the wafer test with previous uniaxial results and to provide a "one quarter cycle" data point. One of these specimens was exposed to 20,000 cycles at an intermediate stress prior to uploading to failure at 538°C (1000°F).

Comparison of the "quarter cycle" strength values with those plotted in Figure 75 indicates reasonably good agreement between the two test methods, despite the highly biaxial stress state in the wafer specimen. This observation adds a significant level of confidence to the fatigue test results plotted in Figure 81.

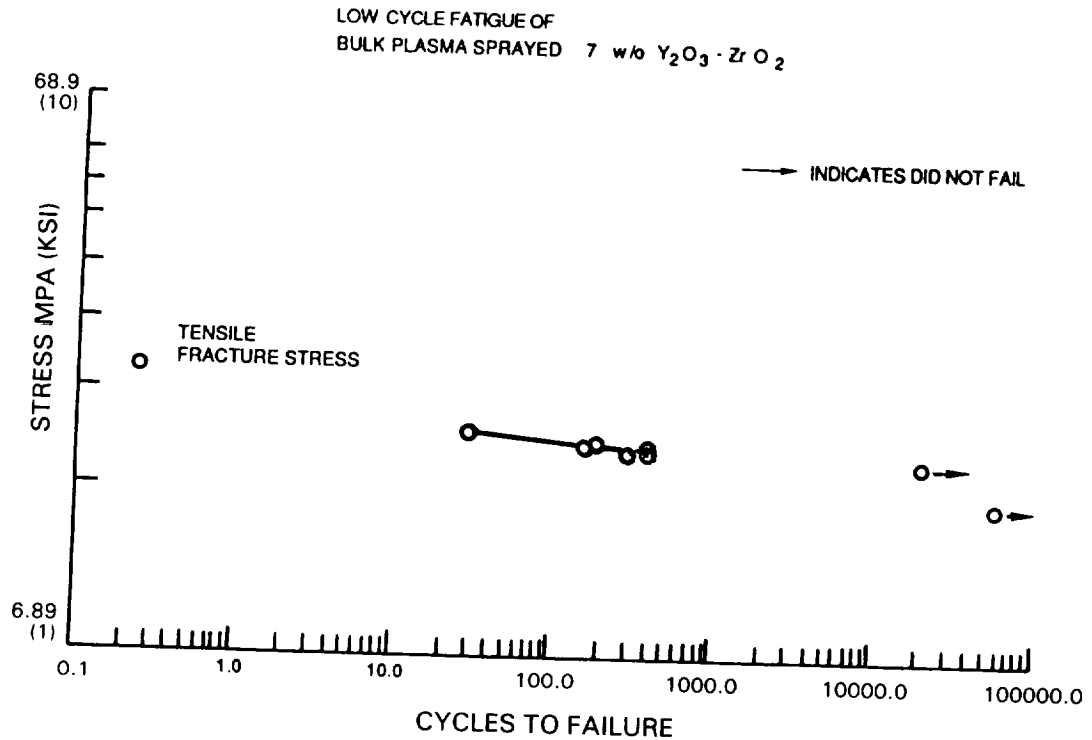


Figure 81 S-N Curve for 7YSZ (538°C (1000°F) and 871°C (1600°F) data plotted together)

The data plotted in Figure 81 show an apparently real fatigue response in the strain tolerant ceramic, but with a stress dependence substantially different from that observed in metals. Whereas metallic materials typically exhibit slopes ranging from ≈ -1.5 with reversed plasticity to ≈ -8 in the fully elastic range, the data in Figure 81 appears to have a slope on the order of -50 . Specific degradation and failure mechanisms responsible for this very stress sensitive fatigue behavior are not presently understood.

A very surprising result was obtained on a specimen which was incrementally uploaded at 871°C (1600°F). As seen in Table XXIX, this specimen (O-2-CP-25-2) was uploaded five times, with 10,000 run-out cycles being applied after the fifth upload to the quarter cycle failure stress. This apparent "coaxing" behavior is not understood.

3.1.3.3.1.4 Fracture Toughness

Results of four fracture toughness tests at 538°C (1000°F) and 871°C (1600°F) are presented in Table XXX. While plane strain conditions were not fully satisfied in these tests, the values presented are believed to provide some indication of the inherent toughness of the strain tolerant ceramic and would probably serve as upper limit values. Inspection of the data indicates that the toughness is on the order of 0.55 MPa (0.50 ksi \sqrt{in}) in the temperature range investigated. It should be noted that this toughness was measured with the plane and direction of propagation of the crack perpendicular to the ceramic splat structure; it is expected that toughness in the plane of the splat structure, where predominant failure cracks are located in the cyclic thermal exposure specimen, would be lower than the value measured in these tests.

3.1.4 Task IC - Predominant Mode Determinations

Based on the information generated in Tasks 1A and 1B, the relative importance of the thermomechanical and thermochemical failure modes were determined. An empirically based correlative life prediction model was developed to independently predict life for the predominant failure modes. Three predominant failure mode verification tests were conducted to determine the applicability and limits of the preliminary life prediction model.

3.1.4.1 Task IC. 1 Develop Preliminary Life Prediction System

The objective of this subtask was to develop a preliminary thermal barrier coating life prediction system based on coating life test results generated in Task 1B. These results identified two important modes of coating degradation. The first of these is mechanical and is assumed to involve an accumulation of fatigue damage resulting from thermally induced cyclic strains. The second degradation mode involves prolonged thermal exposure and appears, on the basis of phenomenological evidence, to involve oxidative degradation of the metal coating system component. The approach described below to accomplish the objective of this subtask was developed at Southwest Research Institute under the direction of Dr. T. A. Cruse.

Following the approach of Miller (Ref. 18), an existing fatigue life correlation model was selected as the basis for the thermal barrier coating life model. The specific analytical form used is based on a Manson-Coffin type relationship, where the number of inelastic strain cycles to failure (N_f) is linearly related to applied inelastic strain range ($\Delta\epsilon_f$) raised to a power (b):

$$N = A (\Delta\epsilon_f)^b$$

where A is a constant of proportionality. The exponent, (b), typically has a value on the order of -1.5 for metallic materials. The use of inelastic strain range as a mechanical damage driver in the ceramic coating layer is justified on the basis of substantial inelasticity observed in the previously discussed mechanical test program.

To facilitate incorporation of an environmental damage driver in the Manson-Coffin relationship, the proportionality constant is expressed in the form:

$$A = \frac{1}{(\Delta\epsilon_f)^b}$$

with $\Delta\epsilon_f$ (the inelastic strain range which causes failure in a single cycle) being made dependent on accumulated oxide thickness:

$$\Delta\epsilon_f = \Delta\epsilon_{f_0} (1 - \delta/\delta_c)^c + \Delta\epsilon_f (\delta/\delta_c)^d$$

The constant $\Delta\epsilon_{f_0}$ is failure strain in the absence of oxidation, δ_c is a constant representing the "critical" oxide thickness which would cause ceramic spallation failure in a single thermal cycle, and c and d are empirically determined constants. For the preliminary analysis, these two constants were set equal to unity. (In one run of the subsequently discussed correlation program, the coefficients c and d were allowed to vary; the "optimized" values of these coefficients did not deviate significantly from the initially assigned value of unity.)

To establish values of the constants b , $\Delta\epsilon_{ro}$, and δc , the spallation life data generated in Task IB were correlated with the preliminary model. To accomplish this, it was necessary to establish analytical relationships between the two independent model variables (oxide thickness and inelastic strain range) and physically measurable test parameters such as time (t), temperature (T), and cycles (N). For the preliminary analysis, oxide scale thickness was calculated from the classical exponential temperature and parabolic time relationship:

$$\delta \cong c (Kpt)^{1/2}$$

where Kp is the parabolic rate constant:

$$Kp = A e^{-\Delta H/RT}$$

Best estimate values of the constants A , c , and ΔH based on prior Pratt & Whitney and literature data were used for this initial analysis:

$$A = 0.06760 \text{ gm}^2/\text{cm}^4\text{-sec}$$

$$c = 0.5358 \text{ cm}^3/\text{gm}$$

$$\Delta H = 66,430 \text{ cal/mole}$$

As discussed in a later section, actual oxide accumulation data obtained on the PWA 264 system at the NASA Lewis Research Center were used for the Task II improvement on this preliminary model.

The most difficult and complex value to obtain for this analysis is inelastic strain range for each of the tests conducted in Task IB. To calculate this value, relatively coarse finite element thermal and stress-strain analyses of the TBC coated test bar configuration were conducted. The finite element break-up for this analysis is shown in Figure 82.

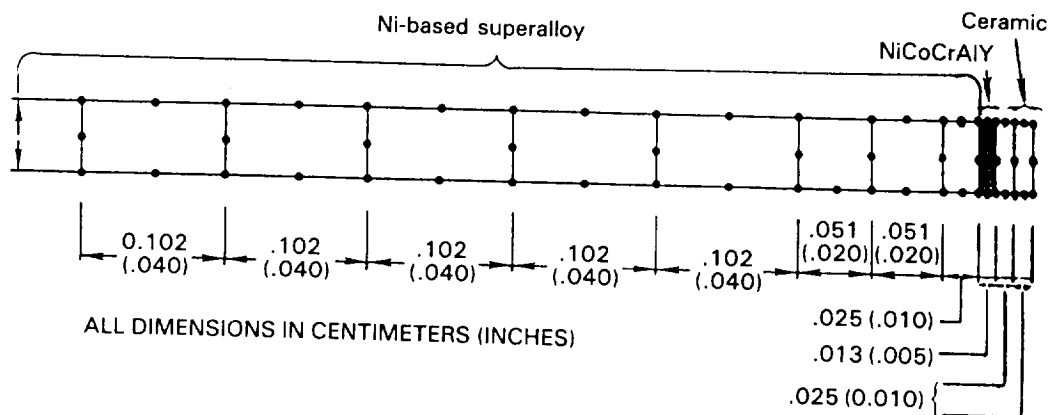


Figure 82 Axisymmetric Finite Element Model Breakup of Substrate, Bond Coat, and Thermal Barrier Coating

To approximate the non-linear tensile and compressive stress-strain behavior discussed previously, the ceramic material was modeled as being ideally inelastic, as illustrated in Figure 83. This material model assumes elastic behavior up to the yield point, followed by inelastic deformation with zero strain hardening. Because this model was formulated prior to testing which showed a large difference in tensile and compressive strength, both tensile and compressive yield strengths were assumed equal to 37.9 MPa (5.5 ksi) and independent of temperature. Results of the SWRI tension and compression tests, which show a significant dependence of yield stress on stress state, were incorporated to refine the model in Task II (as discussed in Section 3.2).

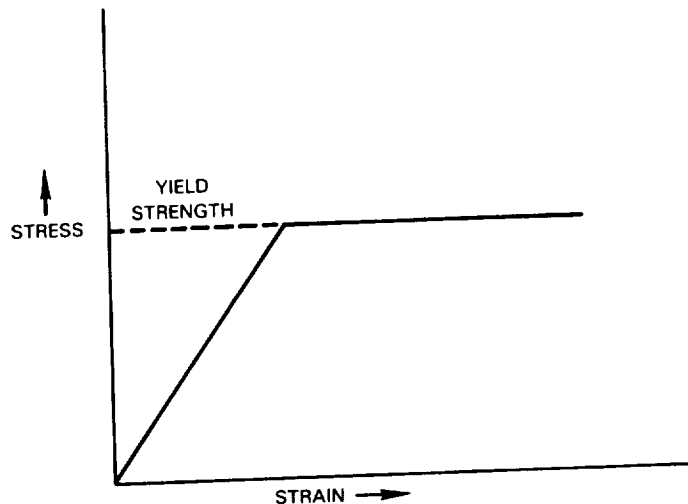


Figure 83 Ideally Inelastic Behavioral Model Initially Used to Represent Ceramic Stress-Strain Behavior

Using the assumption of ideal inelasticity, results of the thermal and stress-strain analyses predict a ceramic hysteresis loop as illustrated in Figure 84. Initially the ceramic is assumed to be in slight compression as a result of the fabrication process (point 1 in Figure 84). During the initial portion of the thermal cycle the ceramic heats more rapidly than the underlying metallic layer; since it is constrained from expanding by the much stiffer metallic substrate, the ceramic deforms compressively, elastically at first and then inelastically as thermally imposed strain exceeds the assumed compressive yield point (Point 2 on Figure 84). As the underlying metal begins to heat and the substrate temperature begins to "catch-up" with the ceramic temperature, differential expansion reverses the ceramic deformation and forces it toward tension, elastically until the tensile yield point is reached (point 3 to point 4), then inelastically until the entire system equilibrates at the maximum exposure temperature (point 4 to point 5). Upon initial cool down, as the ceramic cools (and shrinks) more rapidly than the underlying metal, additional tensile going inelastic strain is accumulated in the ceramic (point 5 to point 6 in Figure 84). As the metal starts to cool and the transient through-ceramic-thickness gradient decreases, differential contraction forces the ceramic into compression, elastically at first (point 6 to point 7), and then inelastically until the entire system approaches equilibrium at the minimum exposure temperature (point 8), thus completing the thermal cycle. It should be noted in Figure 84 that at completion of the

initial thermal cycle the ideally inelastic hysteresis loop does not close. While multiple cycles were not modeled analytically for this preliminary analysis, it is assumed that multiple cycling would result in the development of a stable hysteresis loop shifted laterally along the strain axis from that illustrated in Figure 84.

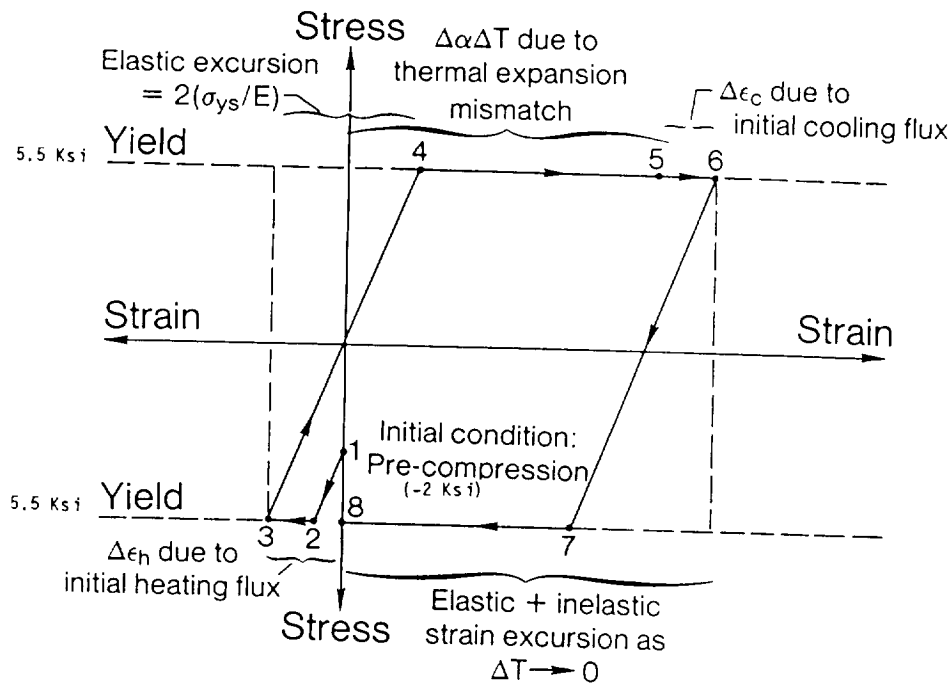


Figure 84 Conceptual Model of Thermally Driven Ceramic Stress-Strain Cycle Under Initial Elastic/Perfect Plastic Model

The total inelastic strain range for the hysteresis loop illustrated in Figure 84 may be analytically expressed as follows:

$$\Delta \epsilon_i = \Delta(\alpha \Delta T) + \Delta \epsilon_h + \Delta \epsilon_c - 2(\sigma_{y.s.} / E)$$

where $\Delta \epsilon_h$ is the inelastic strain resulting from the heating transient and $\Delta \epsilon_c$ is that resulting from the cooling transient. It is important to note that, depending on the severity of the transients, the total inelastic strain range can be larger than the nominal $\Delta(\alpha \Delta T)$ driving force.

To establish values of the constants b , $\Delta \epsilon_{ro}$, and δ_c in the preliminary model, life data from the Task IB cyclic burner rig tests were correlated with values of $\Delta \epsilon_i$ and δ calculated for each set of test conditions. The approach to computation involved computerized linear summation of fractional mechanical and oxidative damage accumulated in successive "blocks" of exposure at specific conditions. Results of this correlation are shown in Figure 85 together with best fit values of the three constants. Based on a computed correlation coefficient, 0.9, the fit of the experimental data must be considered quite good for this initial model. It is reassuring to note that the best-fit critical oxide thickness and oxide-free failure strain constants have physically reasonable values, on the order of 0.01 mm (0.0003 in.) and 1% strain, respectively. It is of interest to note that the slope of the correlation (b) is extremely high when compared to typical metal values discussed previously. This observation is consistent with the previously mentioned isothermal fatigue slope, which was estimated to be on the order of 50 (Figure 81).

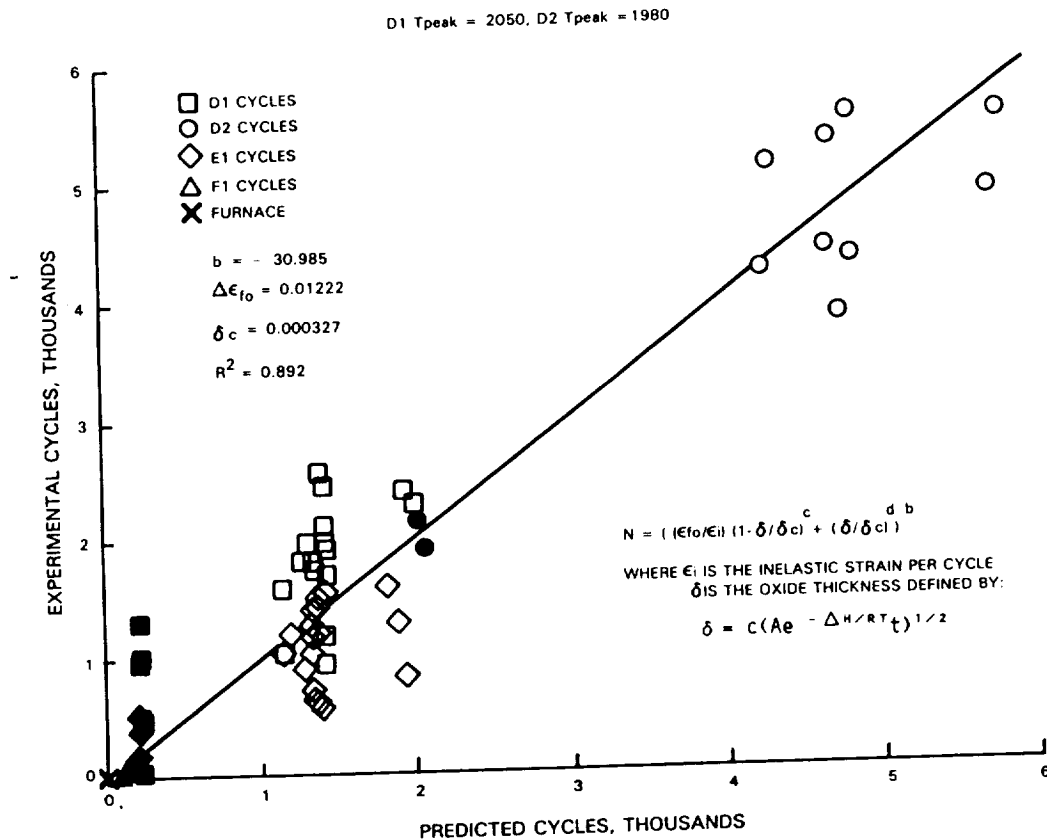


Figure 85 Preliminary Life Model Correlation

3.1.4.2 Task IC.2 Verification Tests

The objective of this subtask was to experimentally verify the preliminary life prediction model described in the previous section. The approach to verification testing involved cyclic burner rig testing as conducted in Task IB, modified as described below to more closely simulate engine operation conditions. Three tests were conducted at three sets of exposure conditions which were different from one another and from the conditions used to establish the correlation in Task IB.

The test method used for life model verification involved clean fuel, cyclic burner rig testing with a single, internally cooled hollow specimen. This specimen permitted exposure of the ceramic with a steady state through-thickness gradient to more closely simulate engine exposure of the coating, and also allowed more precise instrumentation and control of the thermal environment. As shown in Figure 86, the hollow verification test specimen is twice the diameter of the previously utilized specimen and rotates about its own axis to assure circumferential temperature uniformity. These substantial changes from the Task IB experimental condition assured that the preliminary model was effectively challenged by the verification testing.

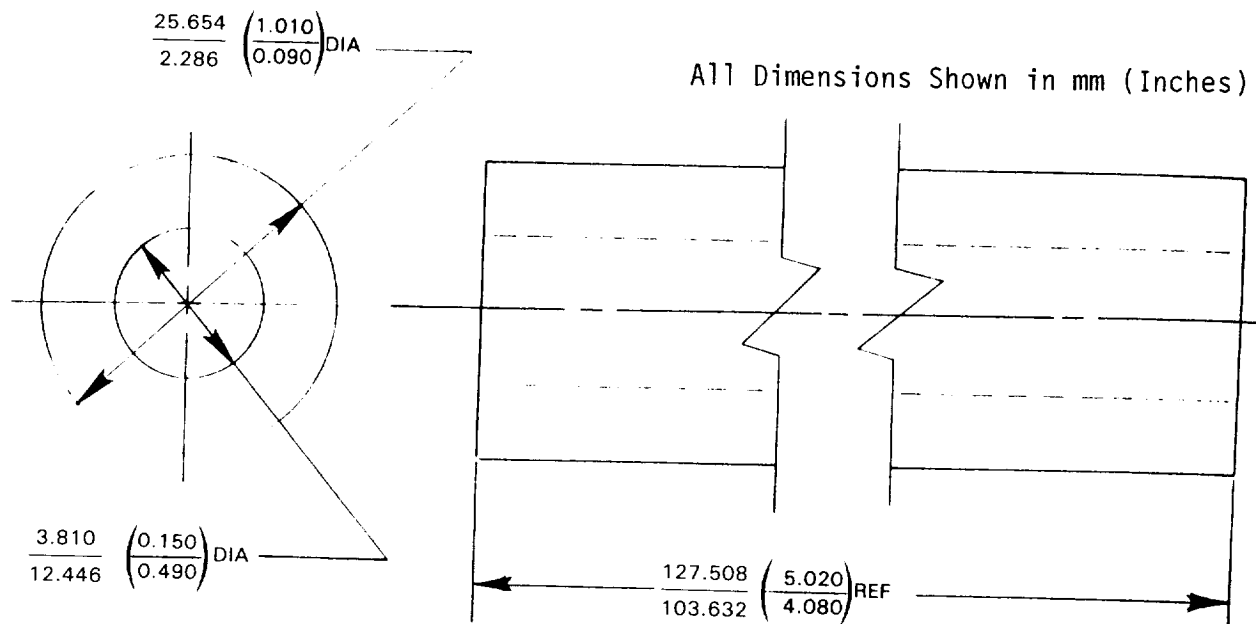


Figure 86 Single Rotating, Internally-Cooled Tube Test Specimen Geometry

Specific test conditions and results of the verification tests are presented in Table XXXI; comparisons between observed and predicted cyclic life are made graphically in Figure 87. It is clear from this plot that the model predicts the uncooled test result more accurately than the two cooled test results. Prediction of the uncooled test indicates that the radial stress model accurately accounts for changes associated with the change in specimen radius from 0.35 mm to 12.7 mm. Also, the relatively accurate prediction for the uncooled verification test indicates that for tests emphasizing cyclic strain damage, the fatigue based model is a good functional form for life prediction.

Two possible explanations for the inaccuracy of cooled test predictions are: 1) the model is inadequate to account for the complex stress distribution which would result from the through-thickness ΔT , and 2) the inaccuracy of the relatively simple instrumentation used. Task II results from much more sophisticated instrumentation indicated possible errors in the temperature readings taken in Task I. Both of the above mentioned sources of error were addressed in Task II. Consistent with the purpose of this Task, the model was upgraded and much better instrumentation was used for Task II testing.

It is of interest to examine damage predictions versus number of cycles for the three verification tests. Figure 88 indicates that for the verification test conditions, the model predicts very little mechanical damage early in life, with damage accumulating rapidly for the last few hundred cycles. This result is really a reflection of the steep slope being used in the model. It should be noted that on Figure 88, the inflections in the two uncooled verification test curves have no physical meaning but are merely a result of how temperature data blocks were sequenced and inputted. A plot of the predicted oxide thickness ratio versus number of cycles, shown in Figure 89, indicates that the uncooled test is accumulating oxide damage at a greater rate than the two cooled tests, presumably because of the higher interface temperature.

TABLE XXXI
VERIFICATION TEST RESULTS

Specimen Identification Number	T.C. Temperature	Interface Temperature (Calculated)	Ceramic Surface Temperature (Estimated)	Test Condition	Test Hours	Hot Hours (Estimated)	Experimental Number of Cycles Accumulated	Predicted Number of Cycles	Predicted Cycles/Experimental Cycles
HT-05	1057°C (1935°F)	1096°C (2005°F)	1174°C (2145°F)	12 min. cycle - Cooled I.D.	105.87	70.58	524	1907	3.6
HT-06	1071°C (1960°F)	1113°C (2035°F)	1191°C (2175°F)	6 min. cycle - Cooled I.D.	88.37	29.45	884	4290	4.9
HT-12	1121°C (2050°F)	1121°C (2050°F)		12 min. cycle - Uncooled I.D.	138.00	97.75	686	619	0.9

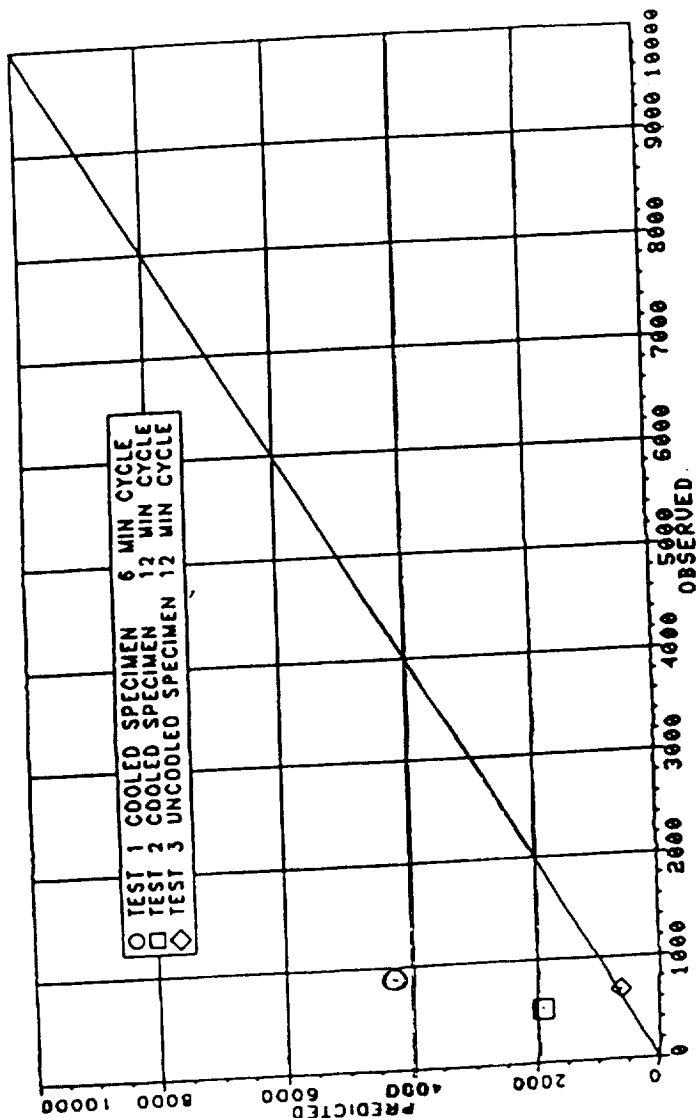
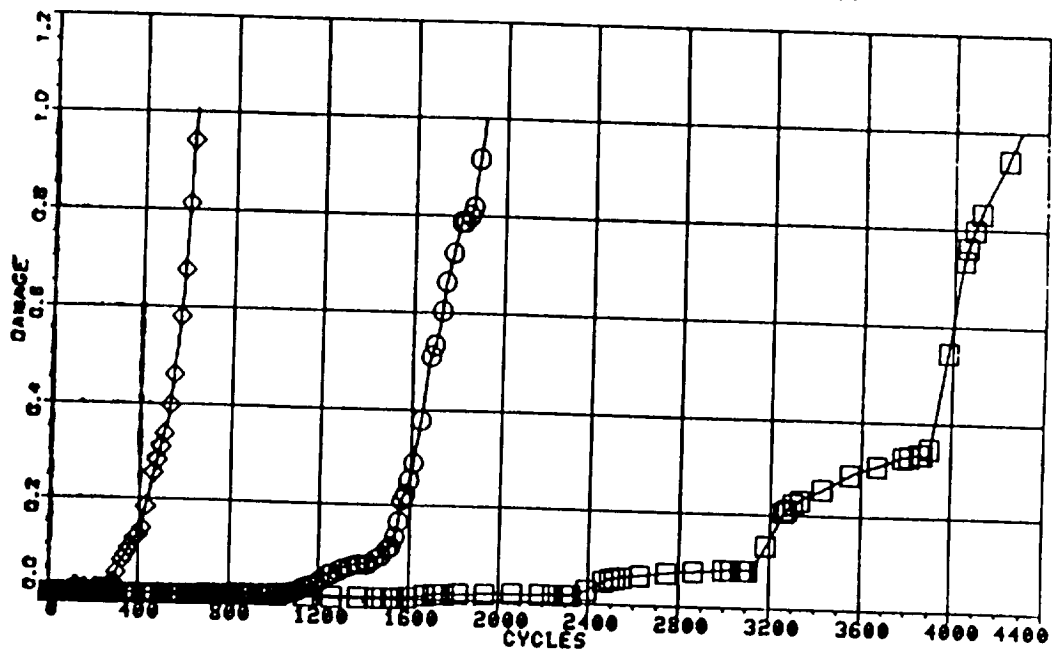


Figure 87 Predicted Cycles Versus Observed Cycles for the Task IC Verification Tests

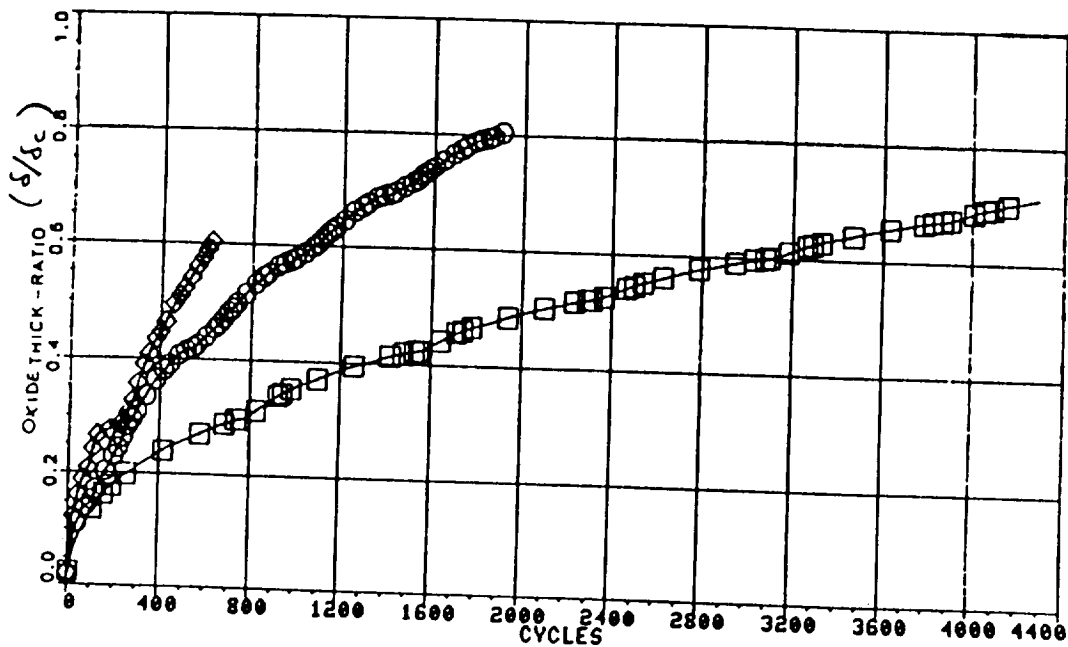
PRATT & WHITNEY
 1 ○ VERIFICATION TEST COOLED 12 MIN CYCLE LOWER TEMP FIT ST
 2 □ VERIFICATION TEST COOLED 6 MIN CYCLE LOWER TEMP FIT ST
 3 ◇ UNCOOLED VERIFICATION TEST UNCOOLED DURING WHOLE FIT ST



03/26/86 12:26:03

Figure 88 Damage Versus Number of Cycles Showing All Three Verification Tests

PRATT & WHITNEY
 1 ○ VERIFICATION TEST COOLED 12 MIN CYCLE LOWER TEMP FIT ST
 2 □ VERIFICATION TEST COOLED 6 MIN CYCLE LOWER TEMP FIT ST
 3 ◇ UNCOOLED VERIFICATION TEST UNCOOLED DURING WHOLE FIT ST



03/26/86 12:27:51

Figure 89 Critical Oxide Thickness Ratio Versus Number of Cycles for the Three Verification Tests

Failure modes were examined for comparison with those observed on the smaller, solid bar specimens and on engine parts. All three specimens exhibited typical, near interface spallation. The crack morphology was, in general, similar except in one case, described below where more fine cracks are seen. Specific metallographic observations are described in the succeeding paragraphs, and the post-test microstructures are presented in Figures 90 through 92.

Figures 90a and 90b show the post-test specimen and microstructure after 105.87 test hours/524 cycles. This specimen was tested in the burner rig using a 12-minute cycle with internal cooling. The specimen exhibited ceramic spallation completely around the bar in the hot zone. The specimen microstructure shown in Figure 90b is of the upper portion of the hot zone on the test bar, including an area where the ceramic had not been spalled. Two types of near interface cracks are observed in the area where the ceramic remains adherent. There are some very large cracks which do not appear to be directly associated with the bond coat oxide but which do appear to follow the general bond coat topology. The other type of crack is directly associated with the bond coat oxide. These are finer, smaller cracks which are either extending from the oxidized bond coat asperity or are within the bond coat oxide layer itself. These cracks do not appear to directly result in ceramic spallation because they are still present in the area where spalling has occurred.

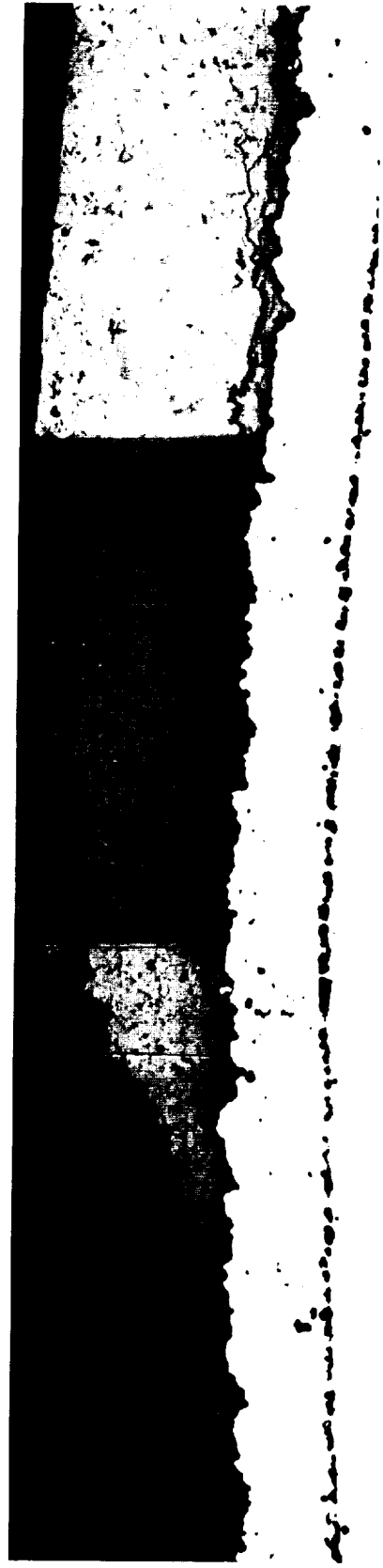
Another interesting observation in Figure 90b is that there is a very large crack 0.0762-0.1016 mm (0.003-0.004 in.) down from the ceramic surface. This crack may well be consequential damage i.e., a crack started by the large chip spalling off.

Figures 91a and 91b show the post-test specimen for the second verification test and its microstructure. This specimen had accumulated 88.37 hours of test time/884 cycles. The burner rig cycle was 6 minutes, and the specimen was internally cooled. The microstructure of the specimen shows less "subcritical" cracking than the 12-minute cycle, internally cooled test specimen. While it survived less time at the peak temperature than the latter specimen, it did accumulate a greater number of cycles. The microstructure shows some oxidized islands of NiCoCrAlY at the interface that are not apparent in the other internally cooled specimen, but these areas do not appear to be associated with any major cracks.

Figures 92a and 92b show the post-test specimen and microstructure of the uncooled test specimen after 138 test hours/686 cycles. A 12-minute burner rig cycle was used. This specimen spalled in two areas in the hot zone of the bar approximately 90° apart. In the area where ceramic is still adherent, the microstructure shows a large number of subcritical cracks such that if exposed for a longer period of time, ceramic spalling may have occurred 360° around the bar. These cracks appear to follow the bond coat topology. In the spalled area the bond coat topology does not seem to be as complex as in the area where the ceramic is still adherent. Perhaps localized changes in the bond coat geometry caused the ceramic to spall in that particular area first.



(a) .64X



(b) 128X

Figure 90 (a) Post-Test Specimen After 105.87 Test Hours/524 Cycles, 12 Minute Burner Rig Cycle, Cooled I.D. (b) Post-Test Microstructure Near Spalled Area

ORIGINAL PAGE
BLACK AND WHITE PHOTOGRAPH



(a) .64X

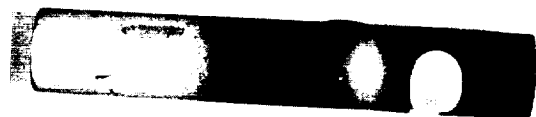


128X

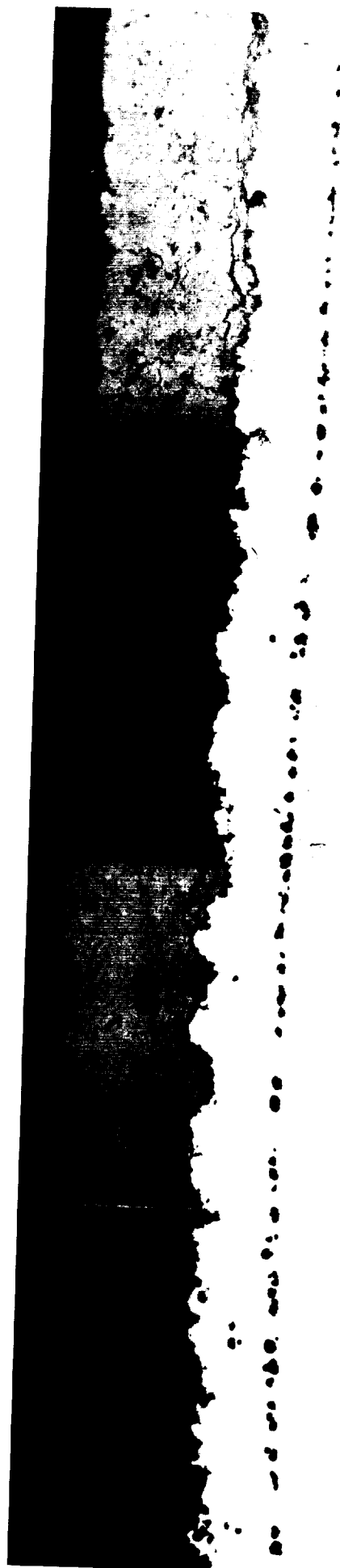
(b)

Figure 91 (a) Post-Test Specimen After 88.37 Test Hours/884 Cycles, 6 Minute
Burner Rig Cycle, Cooled I.D. (b) Post-Test Microstructure Near
Spalled Area

ORIGINAL PAGE
BLACK AND WHITE PHOTOGRAPH



(a) .64X



(b)

128X

Figure 92 (a) Post-Test Specimen After 138 Test Hours/686 Cycles, 12 Minute
Burner Rig Cycle, Uncooled I.D. (b) Post-Test Microstructure Near
Spalled Area

3.2 Task II - Major Mode Life Prediction Model

The objective of this task was refinement of the preliminary life prediction model developed in Task I. The approach involved refinement of both the analytical and the experimental approaches utilized to develop the preliminary model. Analytical enhancements involved better modeling of the ceramic constitutive and time dependent mechanical behavior, as well as refinement of the finite element calculation of temperature and stress-strain distribution. Improvements to the experimental approach involved improved simulation of engine exposure conditions and expansion of the parameter envelope to cover a broader range of mechanical and oxidation forcing functions. The improved test method involved well-characterized testing of the single internally cooled specimen used for Task IC verification testing.

3.2.1 Task IIA - Experimental Design

The objective of Task IIA was to design experiments to obtain data for the major mode life prediction model. Selection of the test program parameters was based on results obtained in Task I testing. The test parameters were varied as appropriate for the failure mode(s) being modeled to cover the range of parameters anticipated in thermal barrier coated turbine components.

The Task II, twenty-test matrix is shown in Table XXXII. These tests were designed to cover the widest possible range of damage. The damage range includes that induced by bond coat oxide growth as well as by mechanical strain. The critical oxide thickness and cycle strain ratio, as calculated by the model, are shown in Table XXXII for each test. Using the planned test parameters as input into the model, life predictions (cycles/hours) were also made for each test as designated. Shown in Figure 93 are the relative mechanical and oxidation damage fractions calculated for each of these twenty tests. Tests 1 through 6 minimize mechanical damage and emphasize oxidation damage by reducing the cycle temperature range. Tests 7 through 12 emphasize mechanical damage while minimizing oxide growth by minimizing exposure to the maximum cycle temperature. Tests 13 through 18 are mixed mode tests designed to improve capability of the model to handle interactive effects. Tests 19 and 20 duplicate test 7 and 8 conditions using a smaller specimen diameter, 21.34 mm (0.84 in.) versus 25.4 mm (1.0 in.) to assess the effect of component geometry on life.

The experiments were designed to minimize the temperature gradient along the length of the tube by enclosing the test specimen in a metal box. The enclosure has a port on one side for the burner and another port on the opposite side for the gas to exit. This enclosure has the effect of "flattening" the burner gas temperature profile and reducing radiant heat loss of the specimen to the surrounding room.

To obtain accurate thermal histories for each test, all Task II specimens were instrumented with a single axially routed thermocouple located 3.18mm (.125") below the bond coat substrate interface. Thermocouple output was continuously monitored via radio telemetry using a computerized data acquisition system.

Prior to conducting the Task II test program, a more elaborately instrumented specimen was fabricated and tested to characterize the variation of temperature with time at various locations in the specimen. This information was used together with thermal conductivities obtained in Task I to calculate the external and internal heat transfer coefficients and to measure the transient temperature response of the specimen. This information also permitted characterization of the axial temperature gradient.

TABLE XXXII
TASK II PLANNED TEST MATRIX

Test	Emphasis	Interface Temp		Cycle		Purpose of Test is to Establish	
		Max °C	°F	Min °C	°F		Time (Min)
1	Oxide	1107	2025	427	800	6	Critical Oxide Thickness
2	↓		↓	↓	↓	6	
3						12	
4						12	
5						24	
6						24	
7	Strain	1121	2050	21	70	6	Static Failure Strain
8	↓	1121	2050				
9		1149	2100				
10		1149	2100				
11		1177	2150				
12		1177	2150				
13	Mixed Mode	1079	1975	57	135	6	Rate of Oxide Growth
14	↓		↓			6	
15						12	
16						12	
17		1107	2025			6	
18		1107	2025			12	
19	10.67mm (0.42") Radius	1121	2050	21	70	6	Direct Effect of Radial Stress
20	10.67mm (0.42") Radius	1121	2050	21	70	6	

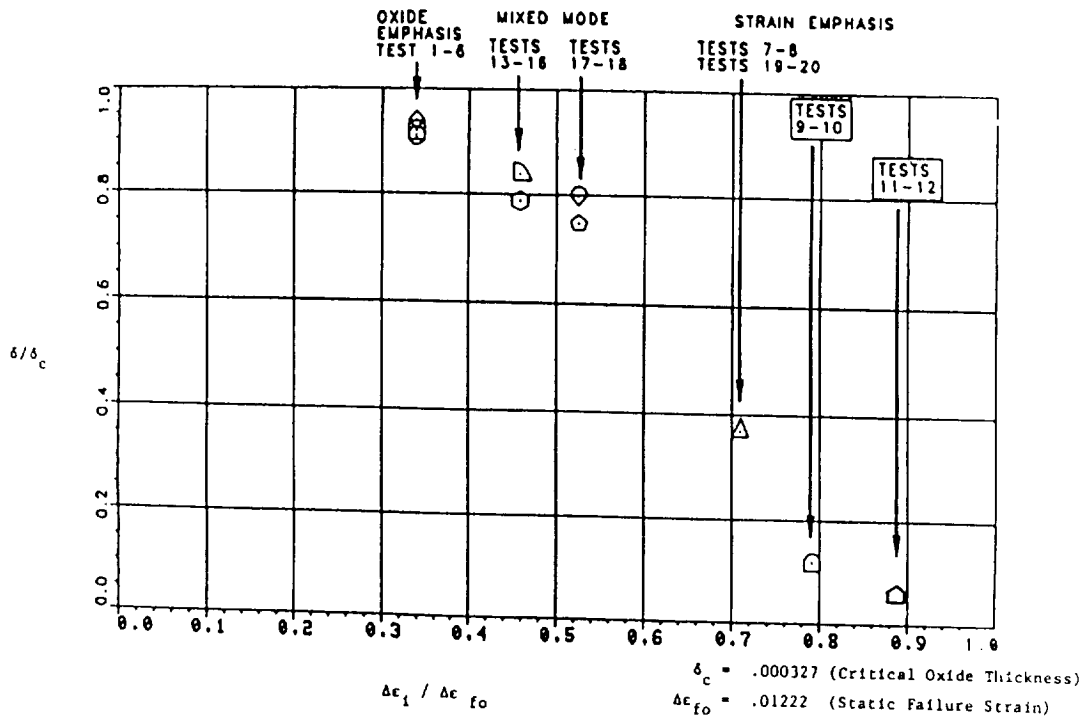


Figure 93 Task II Predictions: Oxide Thickness Ratio at Failure Versus Strain Ratio

As shown in Figure 94, the instrumented specimen had nine axially routed metal sheathed thermocouples: four on the inner diameter (I.D.), and five on the substrate outer diameter (O.D.), just below the substrate-bond coat interface. To assure accurate metal temperature measurement on the I.D., the specimen was split axially and the I.D. thermocouples were buried just below the metal surface. After I.D. thermocouple installation, the specimen was electron beam re-welded. O.D. thermocouples were similarly buried and oversprayed with bond coat and ceramic.

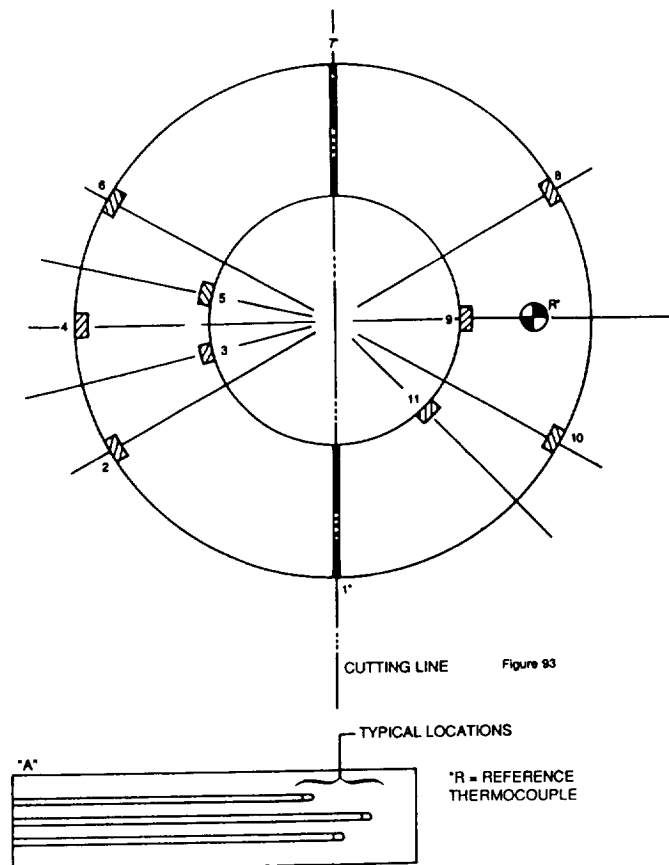


Figure 94 2.54 cm (One-Inch) Diameter Instrumented Specimen Design

The measured axial temperature gradient in the hot zone of the specimen is very small ($<5.5^{\circ}\text{C}$ ($<10^{\circ}\text{F}$)). This is due to the test conditions which flatten the gas temperature profile. Also, this reduces the uncertainty in monitoring the test conditions due to the location of the reference thermocouple present in all test specimens.

Results of instrumented testing indicate an external gas heat transfer coefficient in the range of 80 to 90 $\text{BTU}/\text{ft}^2\text{-hr}^{\circ}\text{F}$. This value was established by putting the instrumented specimen into the burner gas path without internal cooling. A finite element, transient heat transfer analysis was then conducted to select the external gas heat transfer coefficient that produced the best match between calculated and observed transient metal temperature response. The match produced, using this procedure, is shown in Figure 95. Shown in Figure 96 is a comparison of the measured temperature gradient through the metal wall during heat-up with the predicted values from the finite element analysis. Also seen in this figure is the maximum

temperature gradient (88°C (190°F)) across the substrate during heating. This value is critical in the sense that the way the model bookkeeps inelastic ceramic strain at the metal-ceramic interface is based on the temperature gradient through the substrate during the heating portion of the cycle. Figure 97 shows the predicted transient temperature gradient through the ceramic. The maximum temperature gradient across 0.254mm (0.010 in.) of $7\text{ w/o } \text{Y}_2\text{O}_3\text{-ZrO}_2$ is calculated to be 121°C (250°F); this maximum occurs very early in the cycle.

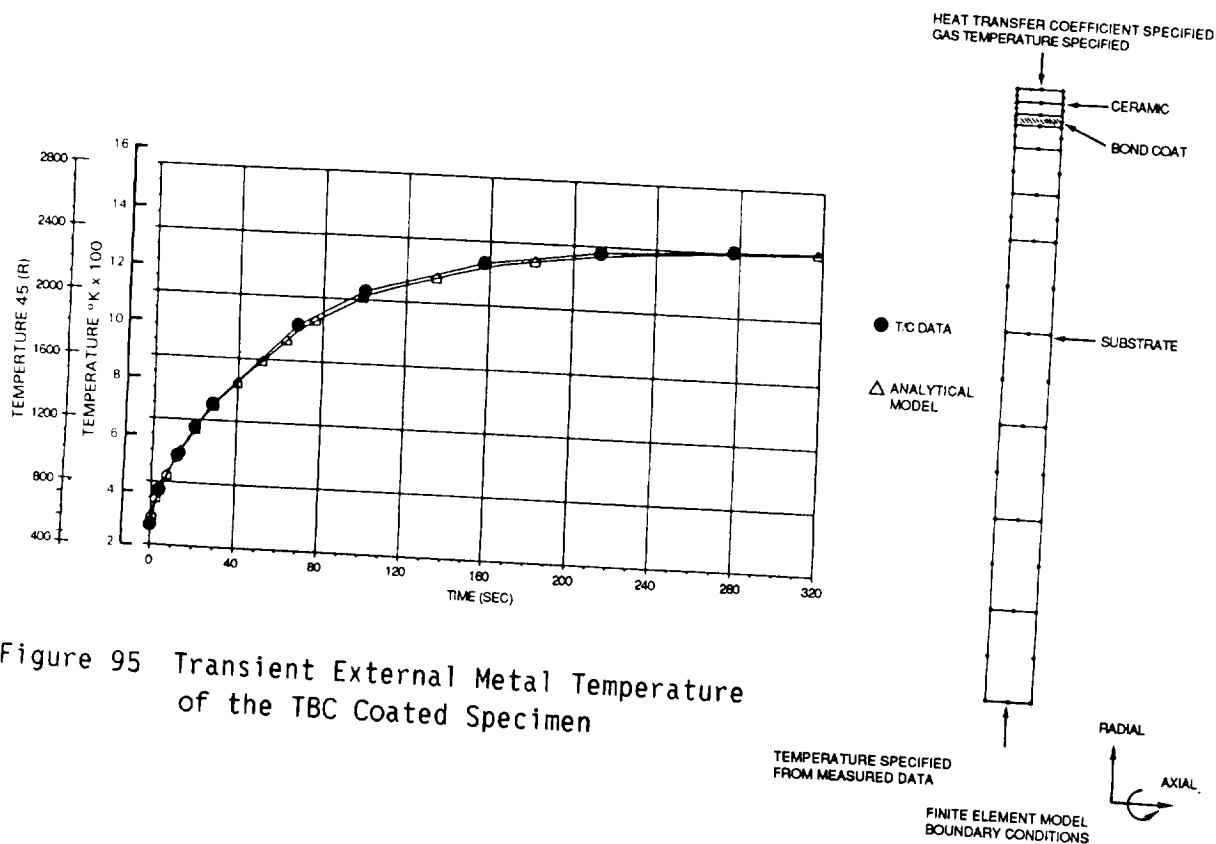


Figure 95 Transient External Metal Temperature of the TBC Coated Specimen

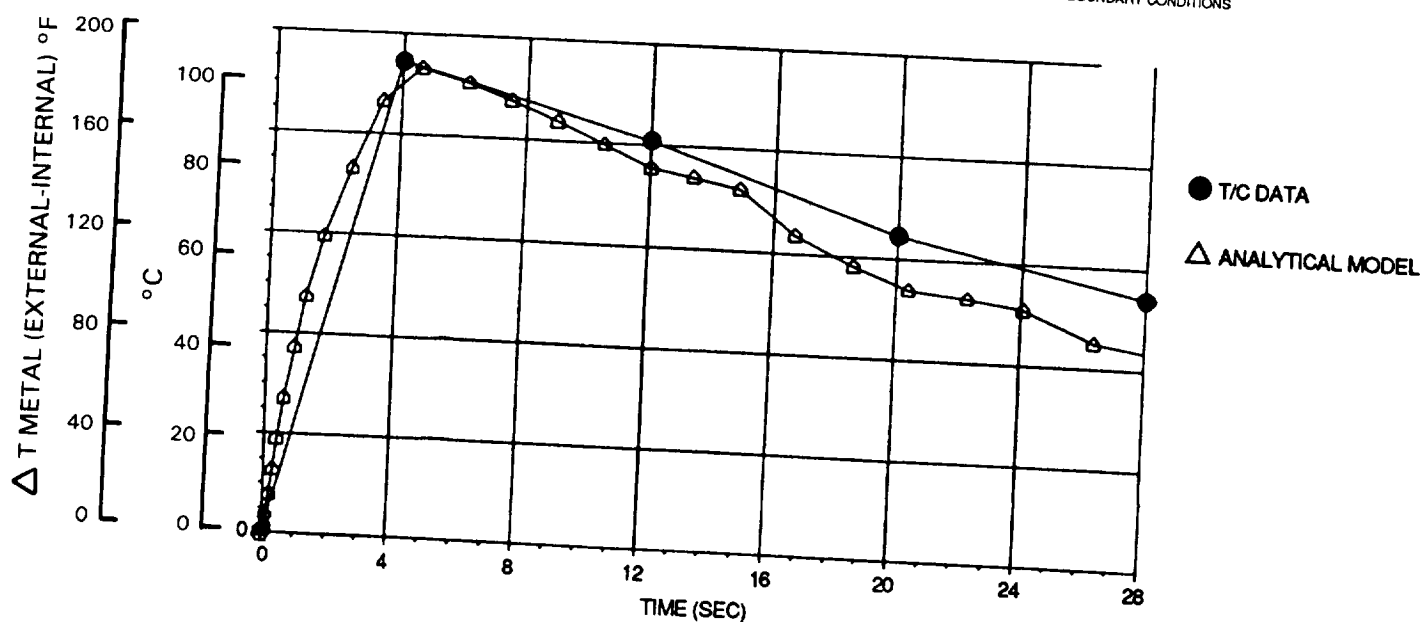


Figure 96 Transient Metal Temperature Response During Initial Heat-up

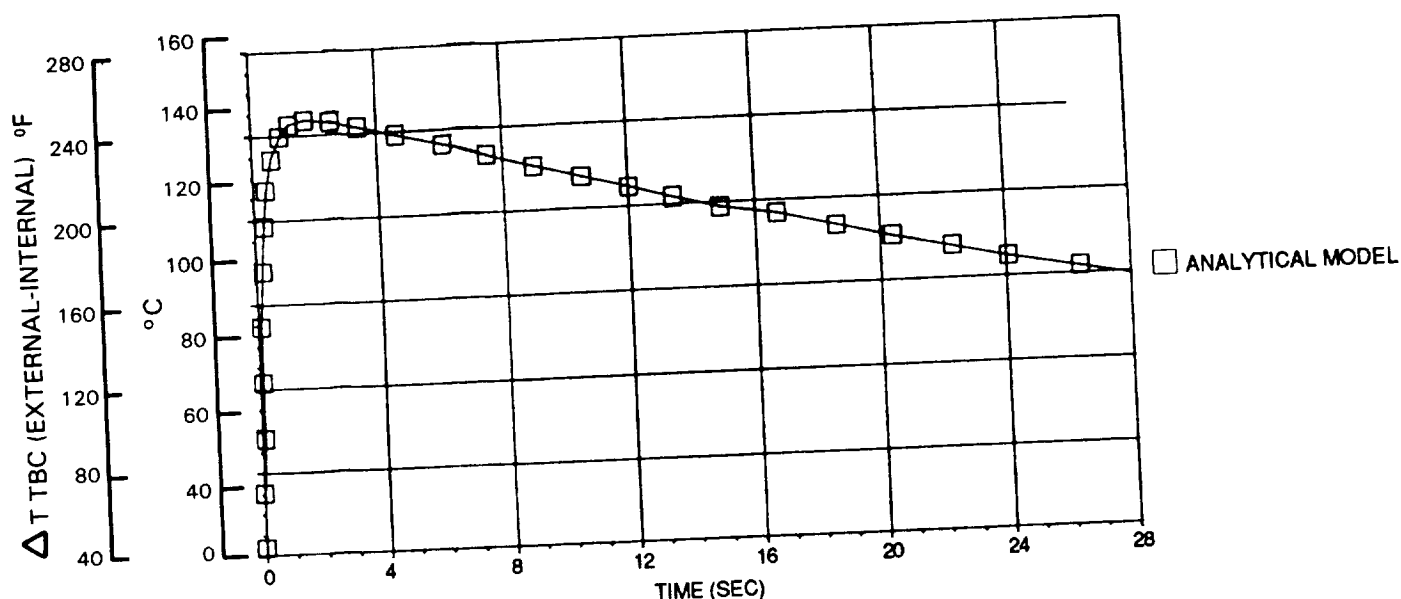


Figure 97 Transient TBC Temperature Response During Initial Heat-up

During steady-state conditions using internal cooling air, the temperature gradient through the metal wall of the specimen was measured at 33°C (60°F). This corresponds to an estimated internal cooling heat transfer coefficient of 25 to 28 BTU/ft²-hr°F. This is much smaller than the 78°C (140°F) temperature gradient assumed in the previous life prediction for Task IC.2.

3.2.2 Task IIB - Experiments/Analysis and Model Development

The objective of Task IIB was to conduct experiments designed in Task IIA to obtain data for major mode life prediction model development. The Task II experiments presented in Table XXXII established a data base for correlating a major mode life prediction model. The modeling effort was based on refinement of Task I preliminary analysis. Refinements focused on thermal strain and oxidation effects as well as other time-at-temperature dependent effects such as creep. The stress analysis was upgraded by including all mechanical property test results, including inelastic behavior, in the finite element analysis for the ceramic.

3.2.2.1 Cyclic Thermal Exposure Test Results and Microstructural Analysis

Results of the twenty Task IIA tests are presented in Table XXXIII. Because of the variability of the burner rig optical temperature measurement and control system, most of the Task II experiments did not run precisely at the planned temperatures. The average maximum and minimum cycle temperature recorded from the thermocouple installed in each specimen is shown in Table XXIII. These actual temperatures were used in the subsequently described life modeling analysis.

Figures 98-117 show the post-test microstructures for each specimen. The photomicrographs shown were taken in an effort to focus on bond coat oxide development. Bond coat oxide thicknesses, representing averages of 18 measurements made in groups of three at 6 intervals around the circumference of each specimen, are presented in Table XXXIII. Figures 98 through 103 and 103 through 108 show the post-test, hot zone, cross-sectional microstructures for the oxide emphasis and the strain emphasis tests respectively. Although the failure mode for all oxide and strain emphasis conditions was the same, there are clearly some very distinct features found relative to the two groups in the microstructures. The oxide emphasis group shows much greater bond coat oxide development as compared with the strain emphasis test; oxide thickness for the oxide emphasis group tests was on the order of 0.00635mm (0.00025"), whereas the oxide thickness for the strain emphasis group tests was less than 0.00254mm (0.0001"). Correspondingly significant differences between the two groups are seen in the bond coat microstructure in terms of Beta phase (NiAl) depletion. In addition, in-plane ceramic cracking appears to be more closely related to bond coat oxide growth in the oxide emphasis group tests than in the strain emphasis group tests.

Figures 110 through 117 show the post-test, hot zone, cross-sectional microstructures for the mixed mode group and small radius group tests respectively. The mixed mode group test microstructures (Figures 110-115) show bond coat oxide development to be on the order of 0.00508mm (0.0002"). In this respect they are more closely related to the oxide emphasis group microstructures. The small radius group tests (Figures 116, 117) show oxide thickness similar to that for the strain emphasis tests; this result is not unexpected since the test conditions were designed to emphasize strain. The small radius group tests exhibited test lives on the order of the corresponding one-inch diameter, strain emphasis tests (numbers 7 and 8) 1121°C T_{max} (2050°F T_{max}), even though the radial stress was increased by ~15% as a result of the radius change. This result suggests that radial stress is not a first order driver on ceramic spalling life.

TABLE XXIII
TASK II - EXPERIMENTAL RESULTS AND NEW MODEL PREDICTIONS

Test No.	Spec. No.	Test Emphasis	Interface Temperature Max°C Min°F	Planned Cycle	Actual Cycles/Hour	Actual Test Hours	Estimated Hot Hours	T Strain (10 ⁻²)	AVG. Walker Strain (10 ⁻²)	Measured Oxide Thickness in.	Predicted Cycle Life
1	HT-61	Oxide	1119 2407 407 764	1.5 minutes heat-up 4.0 minutes at T max 0.5 minutes cool down	9.74 2,036	208.9	153.0	0.5984	0.1246	0.000206	0.00523 3748
2	HT-58	Oxide	1134 2073 487 909	1.5 minutes heat-up 4.0 minutes at T max 0.5 minutes cool down	9.76 3,065	314.1	230.0	0.5887	0.1231	0.000230	0.00584 3050
3	HT-52	Oxide	1116 2040 399 750	1.5 minutes heat-up 10.0 minutes at T max 0.5 minutes cool down	4.90 818	167.1	143.0	0.5921	0.1240	0.000205	0.00521 22428
4	HT-51	Oxide	1139 2082 417 783	1.5 minutes heat-up 10.0 minutes at T max 0.5 minutes cool down	4.92 1,574	320.4	75.0	0.6279	0.1314	0.000200	0.00508 1184
5	HT-59	Oxide	1121 2049 389 733	1.5 minutes heat-up 22.0 minutes at T max 0.5 minutes cool down	2.45 784	319.8	294.0	0.6062	0.1262	0.000270	0.00686 1077
6	HT-60	Oxide	1172 2142 389 733	1.5 minutes heat-up 22.0 minutes at T max 0.5 minutes cool down	2.44 798	327.1	299.0	0.8715	0.1531	0.000240	0.00610 482
7	HT-33	Strain	1103 2017 48 119	1.5 minutes heat-up to T max 4.0-4.5 minutes cool down	10.61 2,387	224.9	20.0	0.7256	0.1640	0.000072	0.00183 4063
8	HT-35	Strain	1104 2019 41 106	1.5 minutes heat-up to T max 4.0-4.5 minutes cool down	10.83 2,079	192.4	17.3	0.7301	0.1659	0.000087	0.00221 1893
9	HT-32	Strain	1114 2037 34 93	1.4 minutes heat-up to T max 4.0-4.6 minutes cool down	10.39 414	35	3.5	0.7464	0.1773	0.000053	0.00135 1462
10	HT-36	Strain	1140 2084 36 96	1.6 minutes heat-up to T max 4.0-4.4 minutes cool down	10.09 484	48	4.0	0.7953	0.2113	0.000082	0.00208 277
11	HT-08	Strain	1187 2168 23 74	1.8 minutes heat-up to T max 4.0-4.2 minutes cool down	28	2.9	0.23	0.8891	0.3199	0.000079	0.00201 20
12	HT-34	Strain	-- -- --	1.8 minutes heat-up to T max 4.0-4.2 minutes cool down	260	52	2.17	-----	-----	0.000074	0.00188 ----
13	HT-62	Mixed	1083 1982 195 383	1.4 minutes heat-up 2.6 minutes at T max 2.0 minutes cool down	9.74 4,198	430.9	2.17	0.7659	0.1272	0.000163	0.00414 12306
14	HT-64	Mixed	1080 1976 67 153	1.4 minutes heat-up 2.6 minutes at T max 2.0 minutes cool down	9.76 4,177	428.4	216.0	0.7923	0.1340	0.000210	0.00533 11660
15	HT-56	Mixed	1088 1991 58 136	1.4 minutes heat-up 8.6 minutes at T max 2.0 minutes cool down	4.92 2,563	521.4	384.0	0.6540	0.1394	0.000169	0.00429 857
16	HT-63	Mixed	1102 2016 80 176	1.4 minutes heat-up 8.6 minutes at T max 2.0 minutes cool down	4.92 2,332	474.1	354.0	0.7038	0.1615	0.000204	0.00518 215
17	HT-37	Mixed	1104 2019 53 128	1.5 minutes heat-up 2.5 minutes at T max 2.0 minutes cool down	9.74 2,474	254.4	127.0	0.6800	0.1559	0.000133	0.00338 4392
18	HT-35	Mixed	1149 2101 61 141	1.5 minutes heat-up 8.5 minutes at T max 2.0 minutes cool down	4.88 468	96.1	70.0	0.7613	0.2001	0.000179	0.00455 287
19	HT-13	Small Radius	1112 2033 36 96	1.5 minutes heat-up to T max 4.0-4.5 minutes cool down	9.82 2,754	250.5	23.0	-----	0.1753	0.000070	0.00178 2978
20	HT-15	Small Radius	1124 2055 24 76	1.5 minutes heat-up to T max 4.0-4.5 minutes cool down	9.93 2,090	131.1	17.4	-----	0.1911	0.000082	0.00208 949

ORIGINAL PAGE
BLACK AND WHITE PHOTOGRAPH

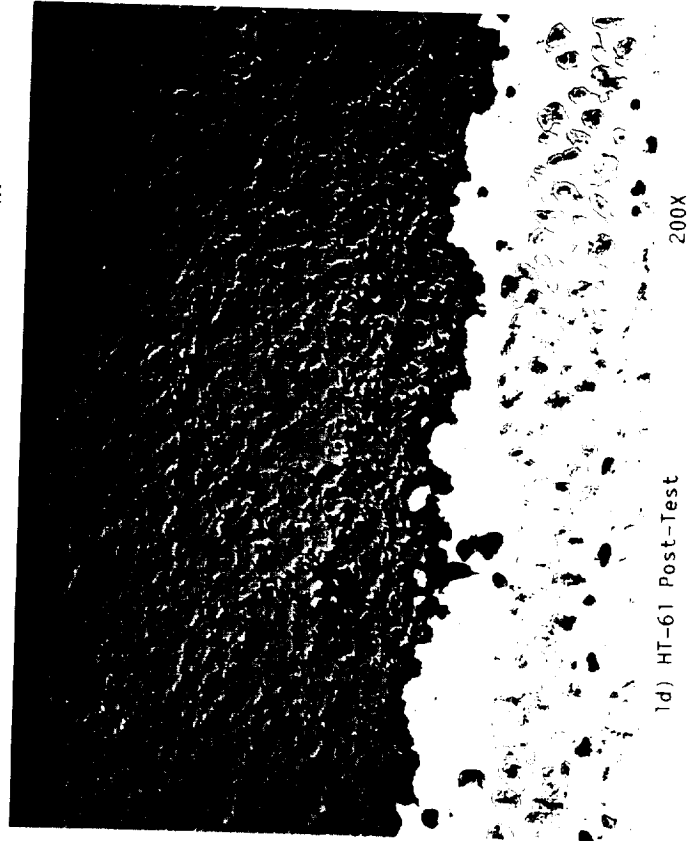
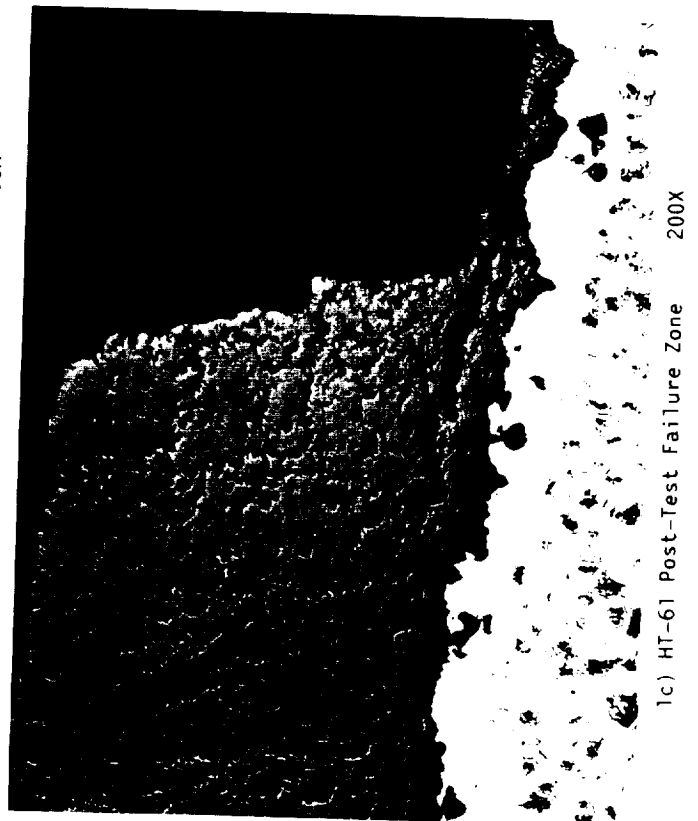
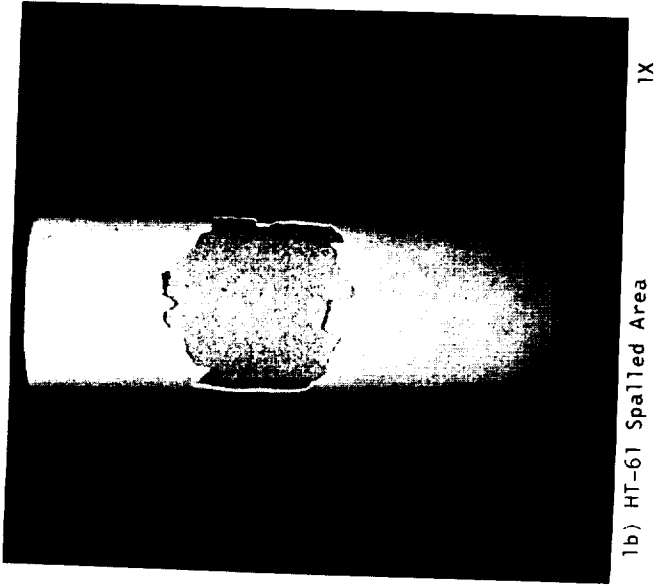
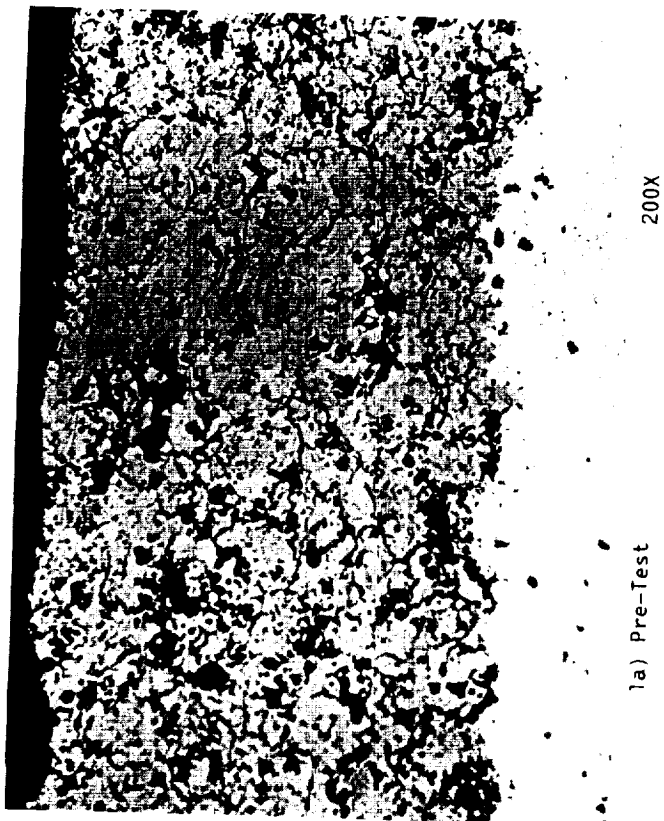
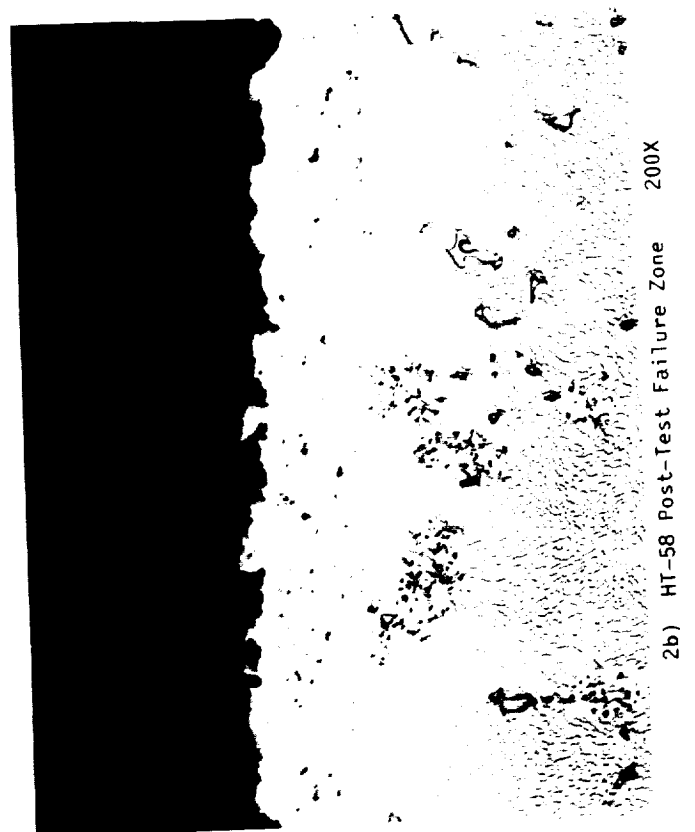
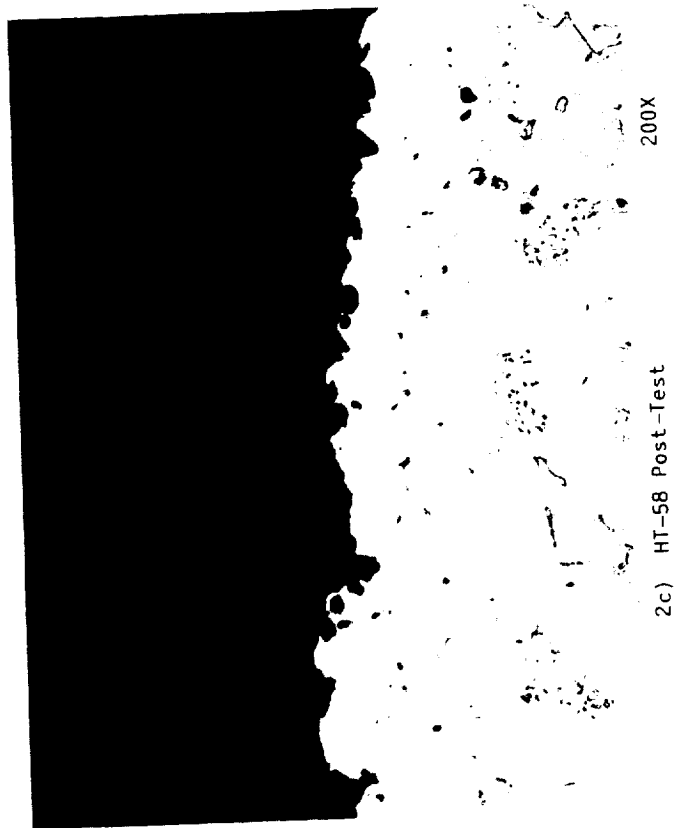
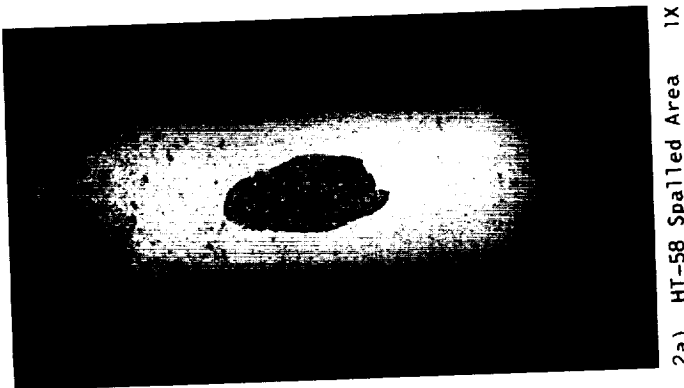


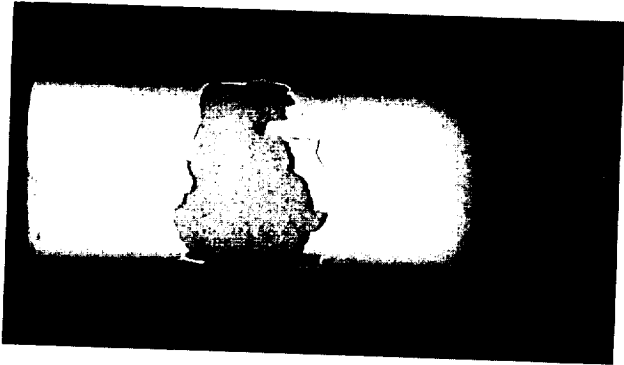
Figure 98 Oxide Emphasis Test #1 Post-Test Specimen Microstructure

Figure 99 Oxide Emphasis Test #2 Post-Test
Specimen Microstructure



ORIGINAL PAGE
BLACK AND WHITE PHOTOGRAPH

Figure 100 Oxide Emphasis Test #3 Post-Test
Specimen Microstructure



3a) HT-52 Spalled Area 1X

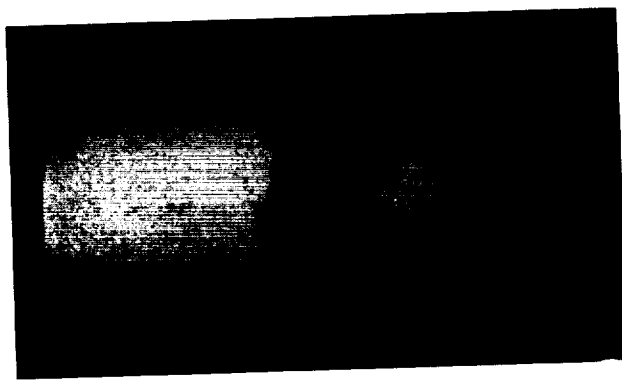


3b) HT-52 Post-Test Failure Zone 200X



3c) HT-52 Post-Test 200X

ORIGINAL PAGE
BLACK AND WHITE PHOTOGRAPH



4a) HT-51 Spalled Area 1X



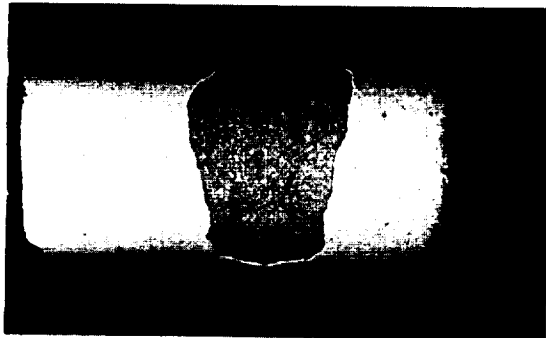
4b) HT-51 Post-Test Failure Zone 200X

Figure 101 Oxide Emphasis Test #4 Post-Test
Specimen Microstructure

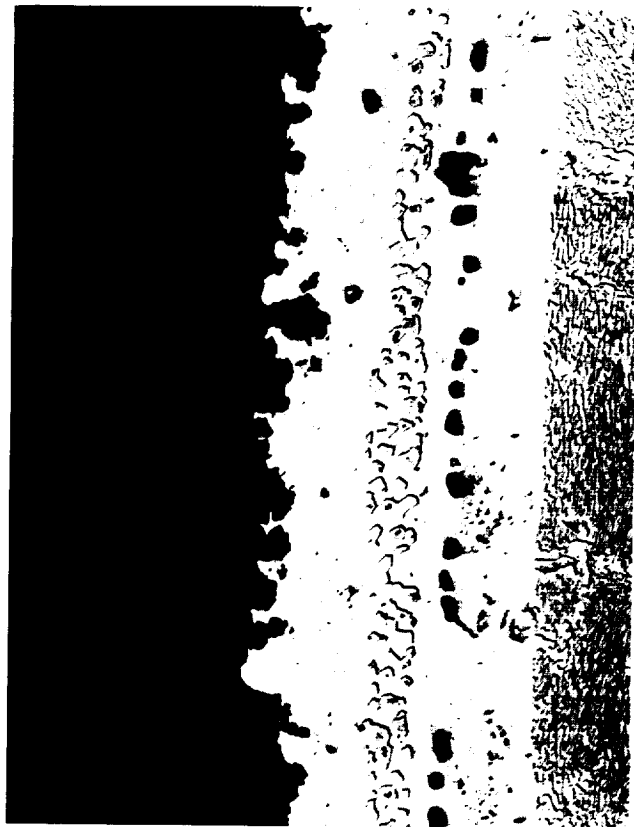


4c) HT-51 Post-Test 200X

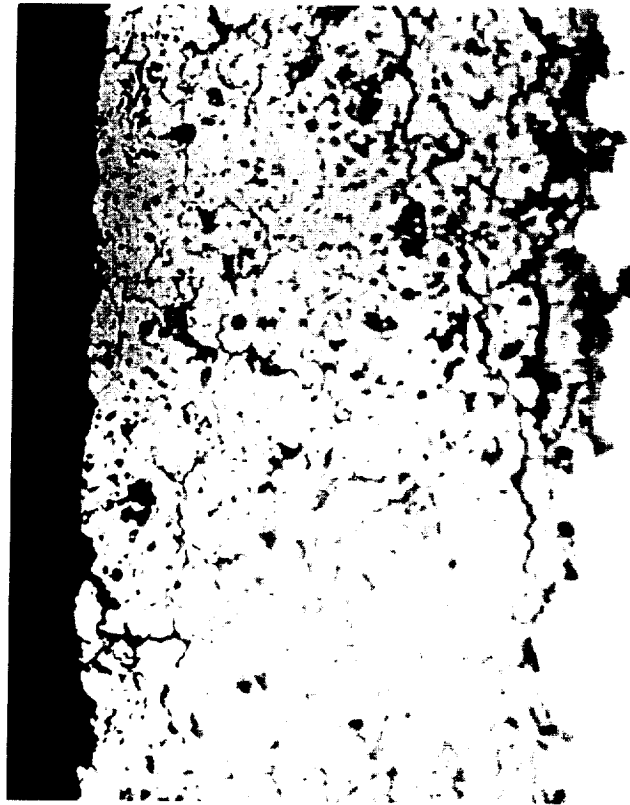
Figure 102 Oxide Emphasis Test #5 Post-Test
Specimen Microstructure



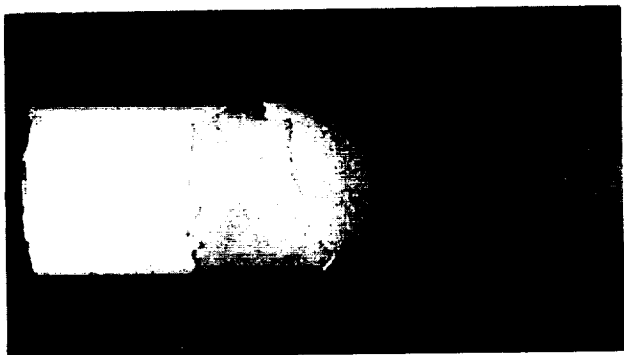
5a) HT-59 Spalled Area 1X



5b) HT-59 Post-Test Failure Zone 200X

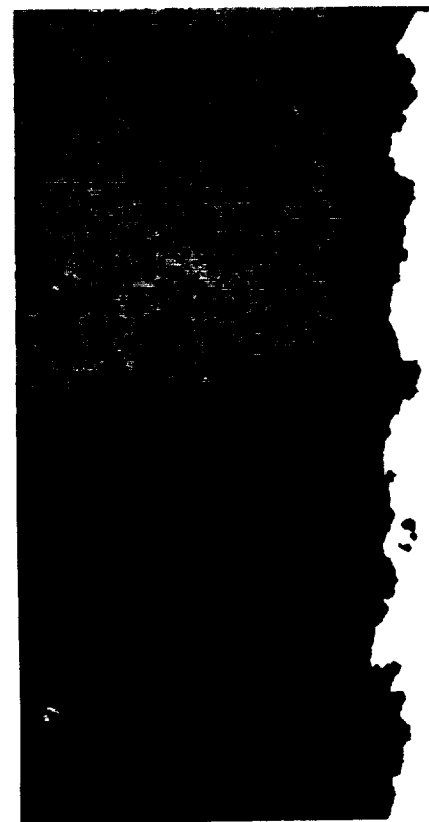


5c) HT-59 Post-Test 200X



6a) HT-60 Spalled Area 1X

Figure 103 Oxide Emphasis Test #6 Post-Test
Specimen Microstructure



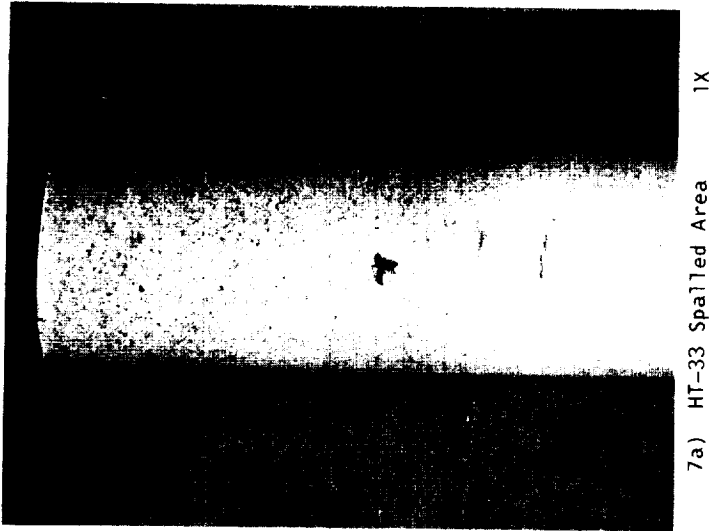
6b) HT-60 Post-Test Failure Zone 200X



6c) HT-60 Post-Test 200X

ORIGINAL PAGE
BLACK AND WHITE PHOTOGRAPH

Figure 104 Oxide Emphasis Test #7 Post-Test
Specimen Microstructure



ORIGINAL PAGE
BLACK AND WHITE PHOTOGRAPH

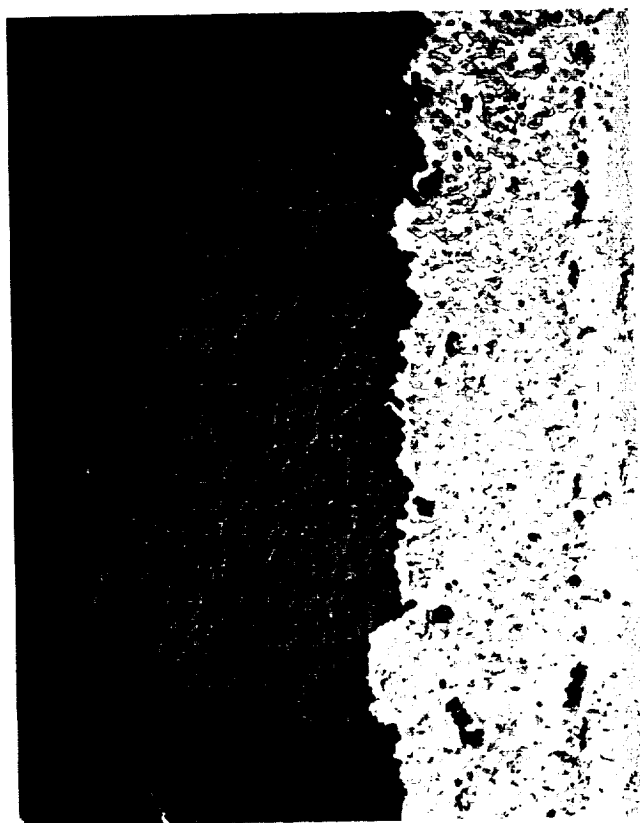


8a) HT-35 Spalled Area 1X

Figure 105 Oxide Emphasis Test #8 Post-Test
Specimen Microstructure

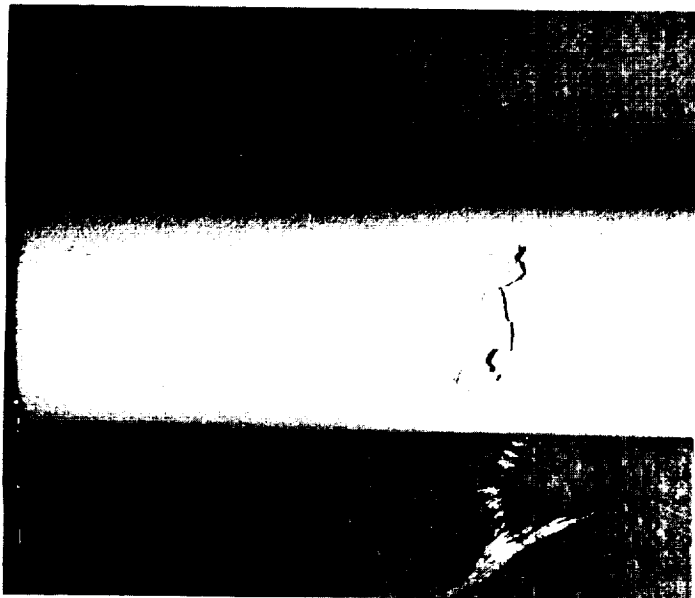


8b) HT-35 Post-Test Failure Zone 200X



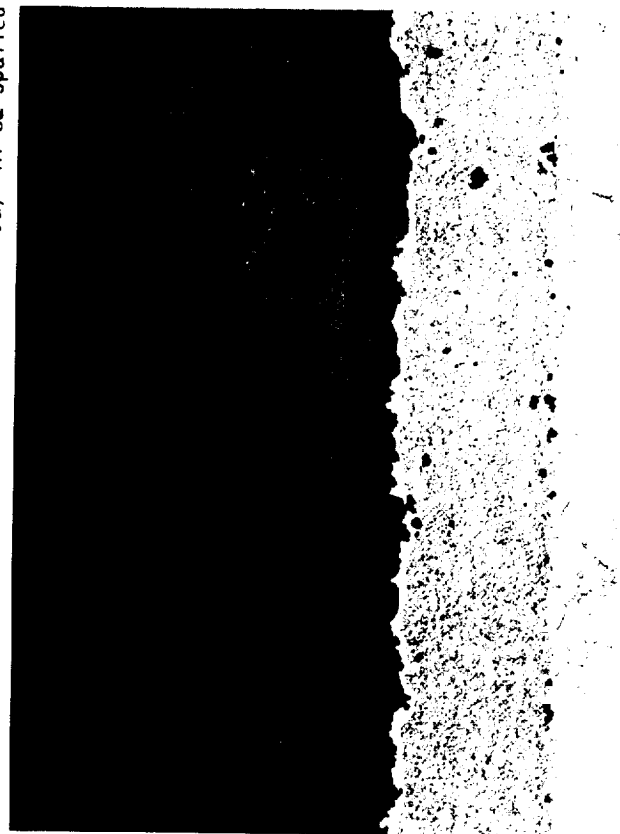
8c) HT-35 Post-Test

200X

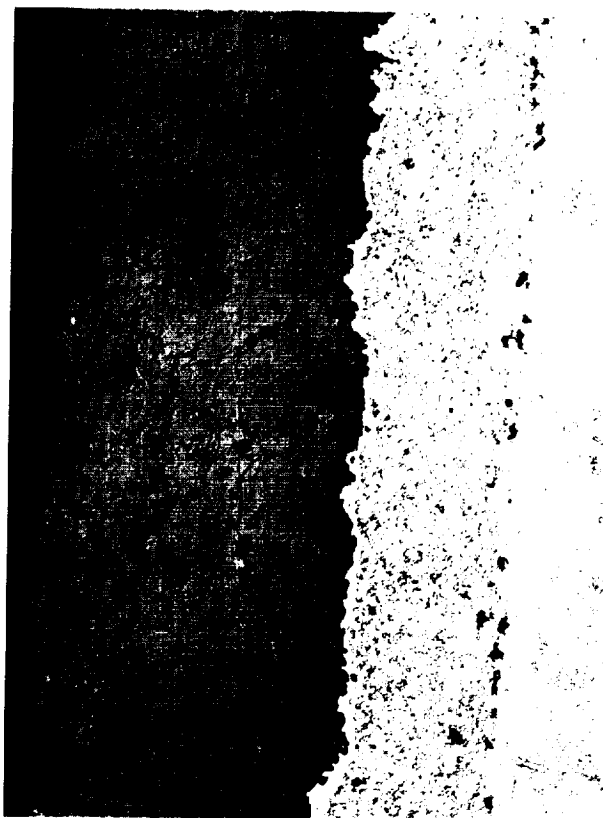


9a) HT-32 Spalled Area 1X

Figure 106 Oxide Emphasis Test #9 Post-Test Specimen Microstructure



9b) HT-32 Post-Test Failure Zone 200X



9c) HT-32 Post-Test 200X

ORIGINAL PAGE
BLACK AND WHITE PHOTOGRAPH

ORIGINAL PAGE
BLACK AND WHITE PHOTOGRAPH

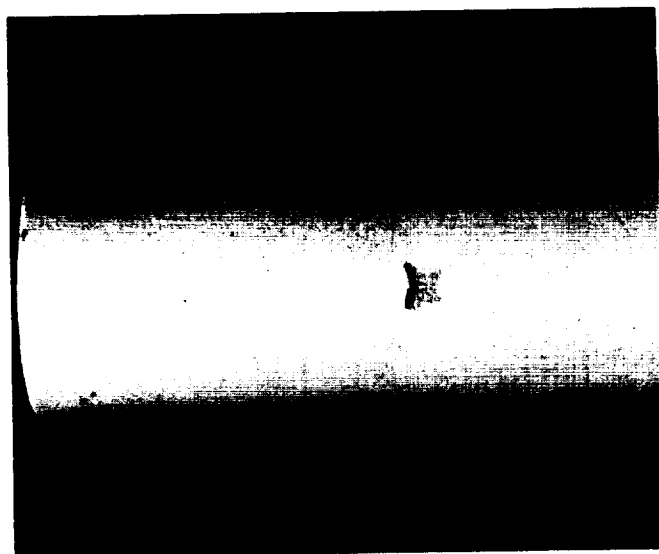


Figure 107 Oxide Emphasis Test #10
Post-Test Specimen Microstructure



ORIGINAL PAGE
BLACK AND WHITE PHOTOGRAPH

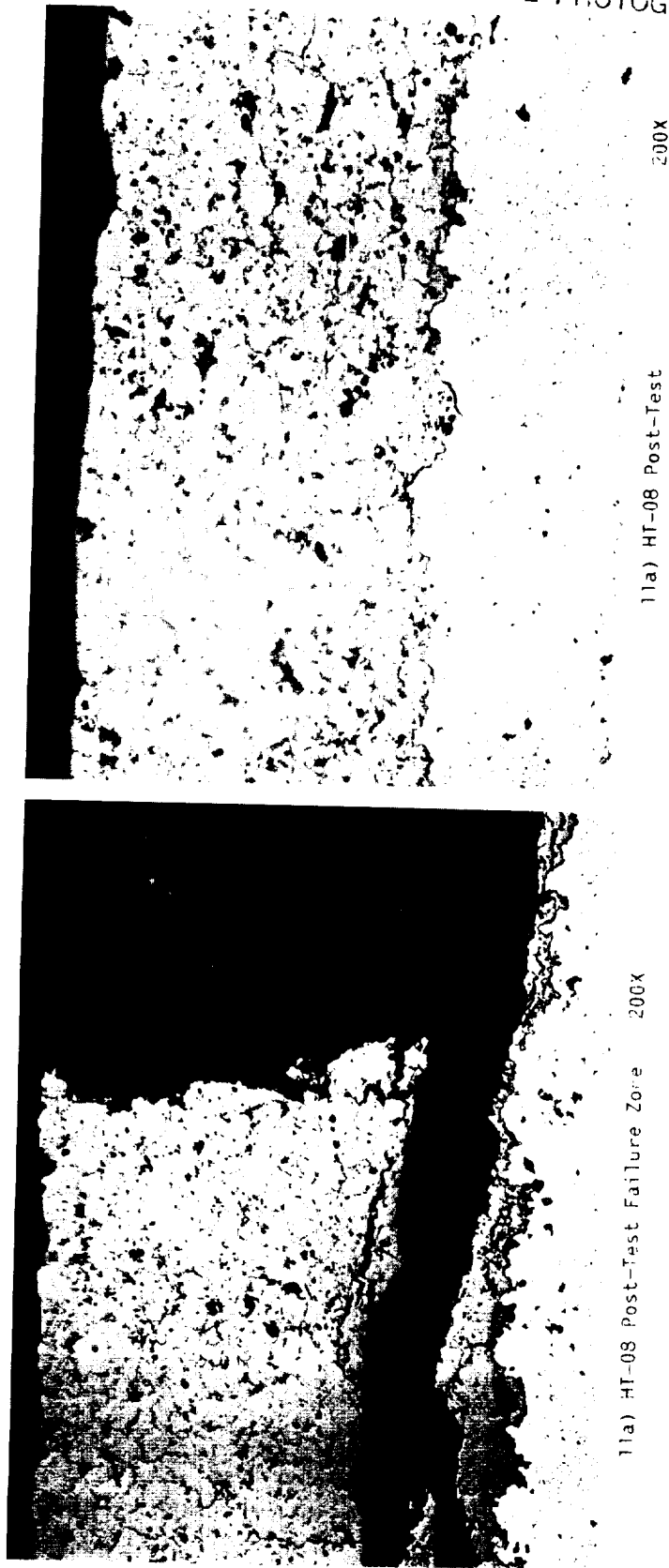
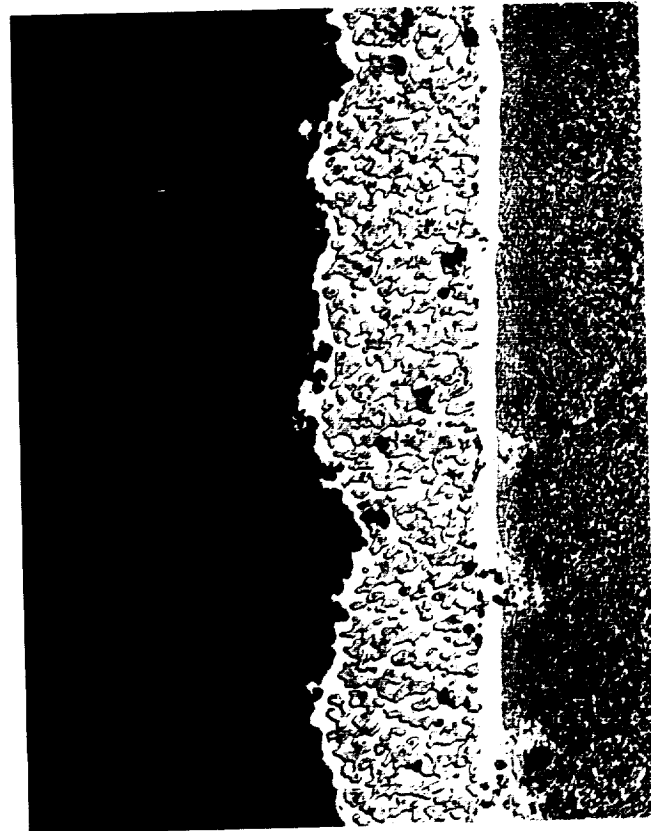


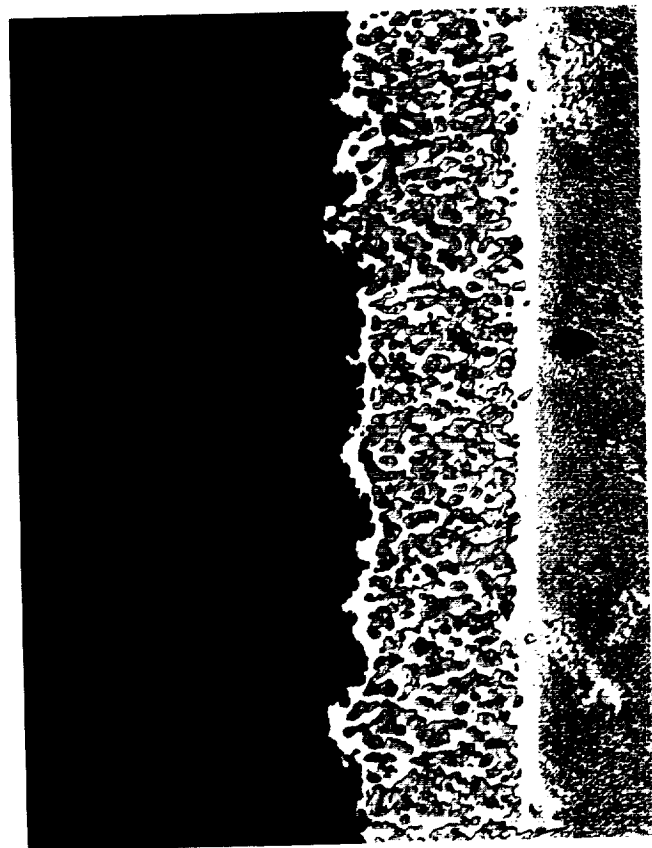
Figure 108 Oxide Emphasis Test #11 Post-Test Specimen Microstructure



12a) HT-34 Spalled Area 1X



12c) HT-34 Post-Test 200X



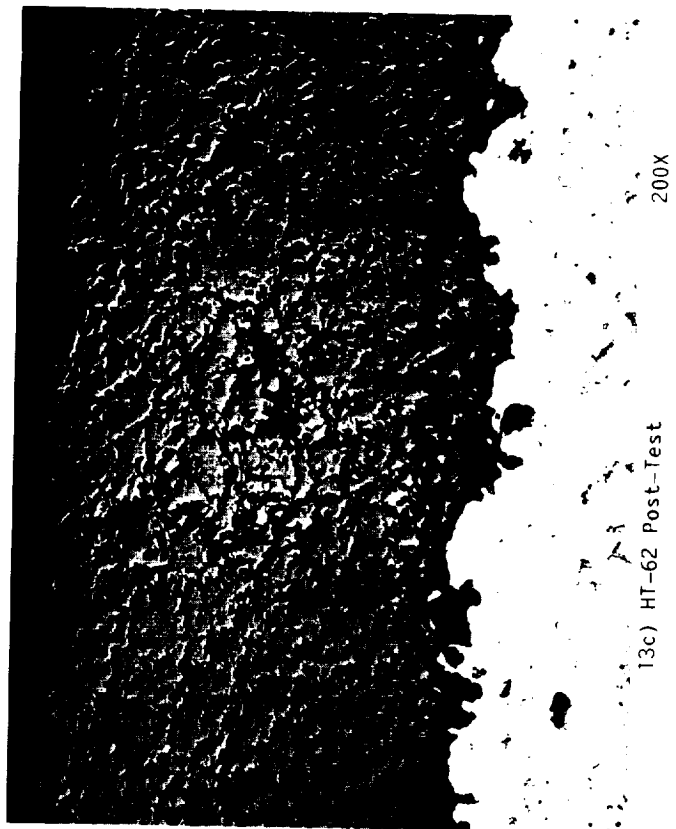
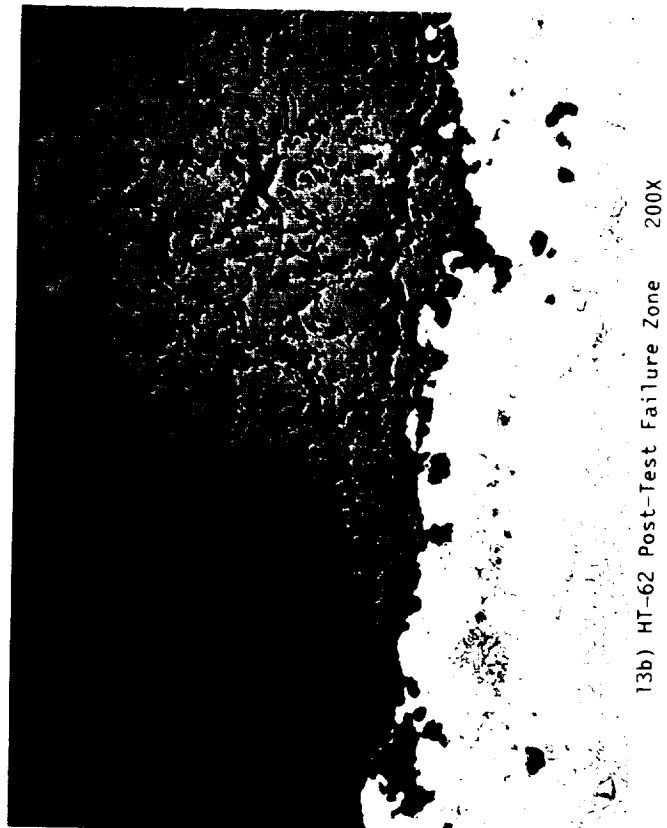
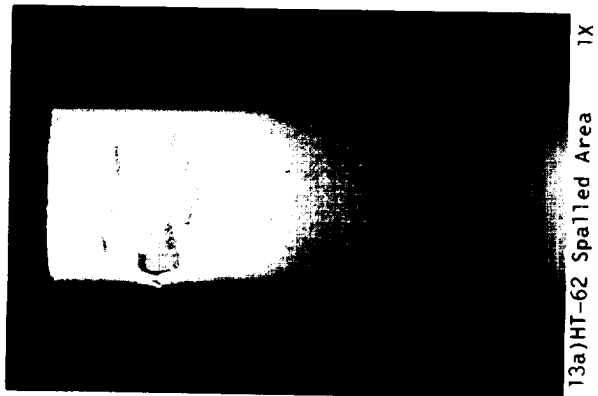
12b) HT-34 Post-Test Failure Zone 200X

Figure 109 Oxide Emphasis Test #12
Post-Test Specimen Microstructure

ORIGINAL PAGE
BLACK AND WHITE PHOTOGRAPH

ORIGINAL PAGE
BLACK AND WHITE PHOTOGRAPH

Figure 110 Mixed Mode Oxide Emphasis Test
#13 Post-Test Specimen
Microstructure

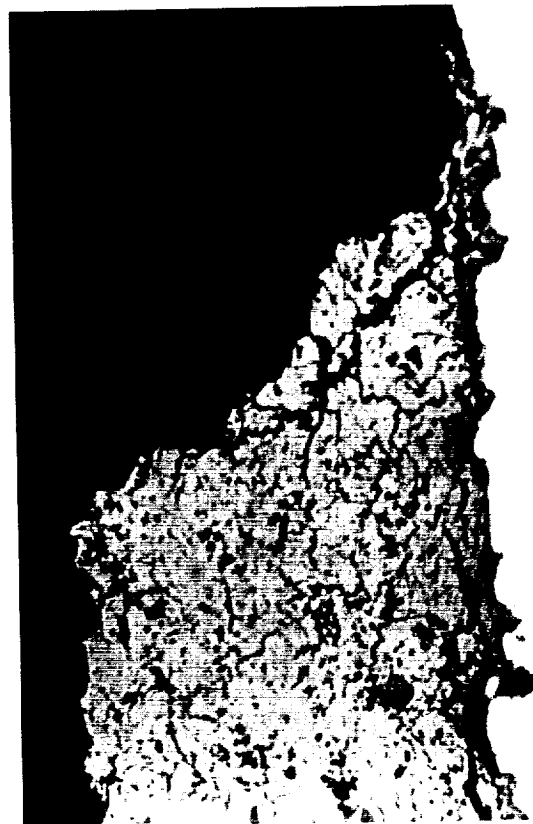


ORIGINAL PAGE
BLACK AND WHITE PHOTOGRAPH

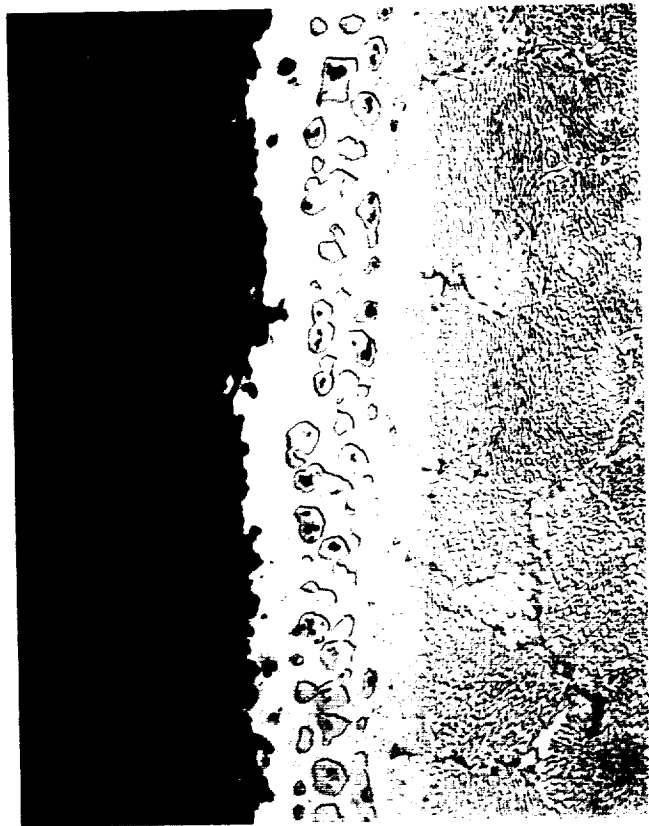


14a) HT-64 Spalled Area 1X

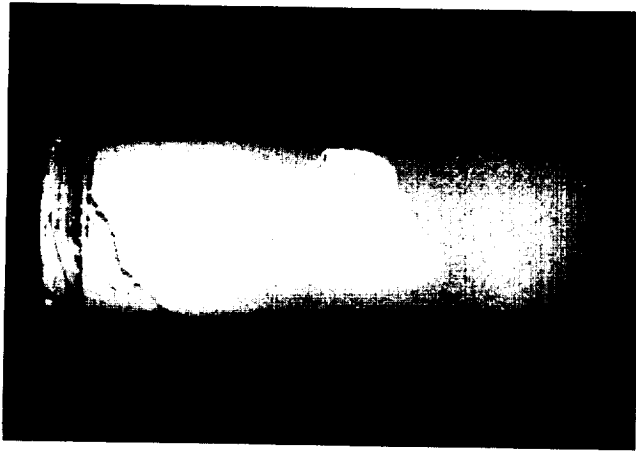
Figure 111 Mixed Mode Oxide Emphasis Test
#14 Post-Test Specimen
Microstructure



14b) HT-64 Post-Test Failure Zone 200X



14c) HT-64 Post-Test 200X



15a) HT-56 Spalled Area 1X

Figure 112 Mixed Mode Oxide Emphasis Test
#15 Post-Test Specimen
Microstructure

ORIGINAL PAGE
BLACK AND WHITE PHOTOGRAPH



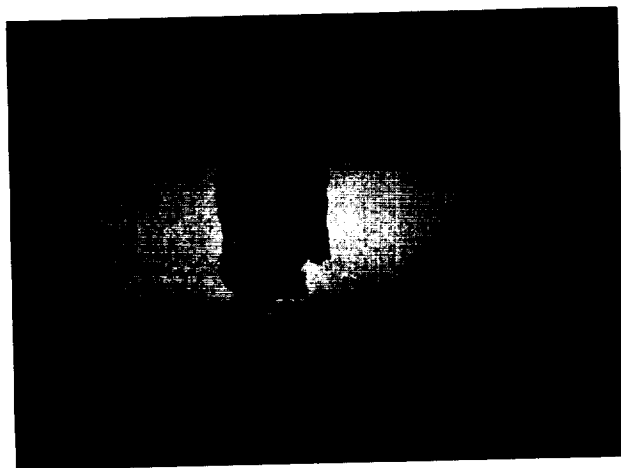
15b) HT-56 Post-Test Failure Zone 200X



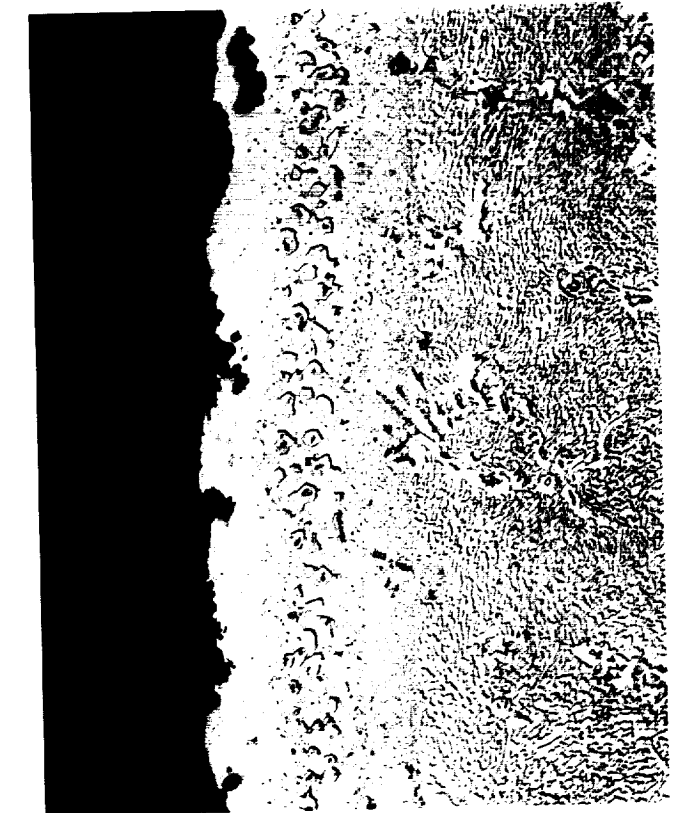
15c) HT-56 Post-Test 200X

Figure 113 Mixed Mode Oxide Emphasis Test
#16 Post-Test Specimen
Microstructure

ORIGINAL PAGE
BLACK AND WHITE PHOTOGRAPH



16a) HT-63 Spalled Area 1X

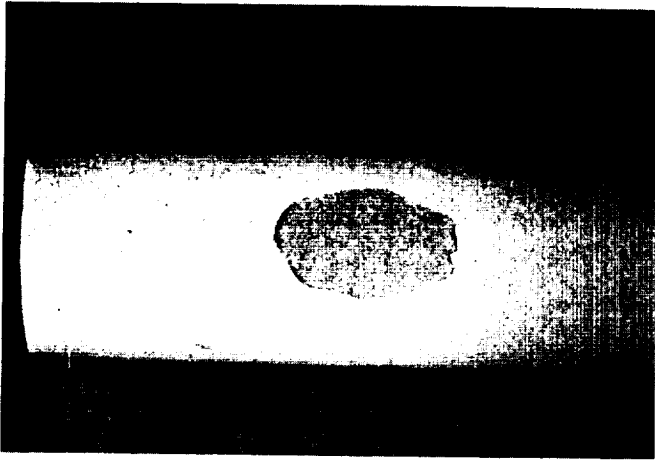


16b) HT-63 Post-Test Failure Zone 200X



16c) HT-63 Post-Test 200X

Figure 114 Mixed Mode Oxide Emphasis Test
#17 Post-Test Specimen
Microstructure



17a) HT-37 Spalled Area 1X

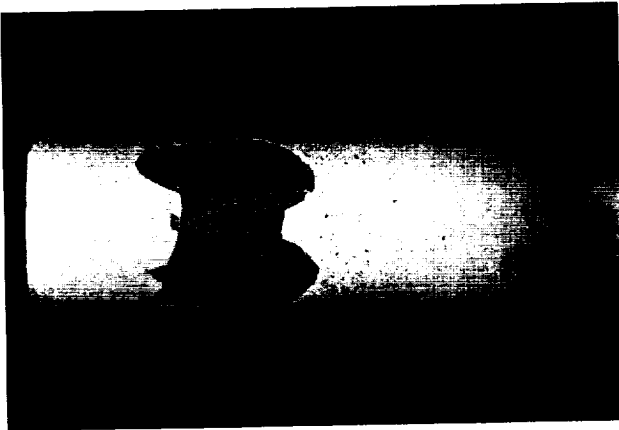


17b) HT-37 Post-Test Failure Zone 200X



17c) HT-37 Post-Test 200X

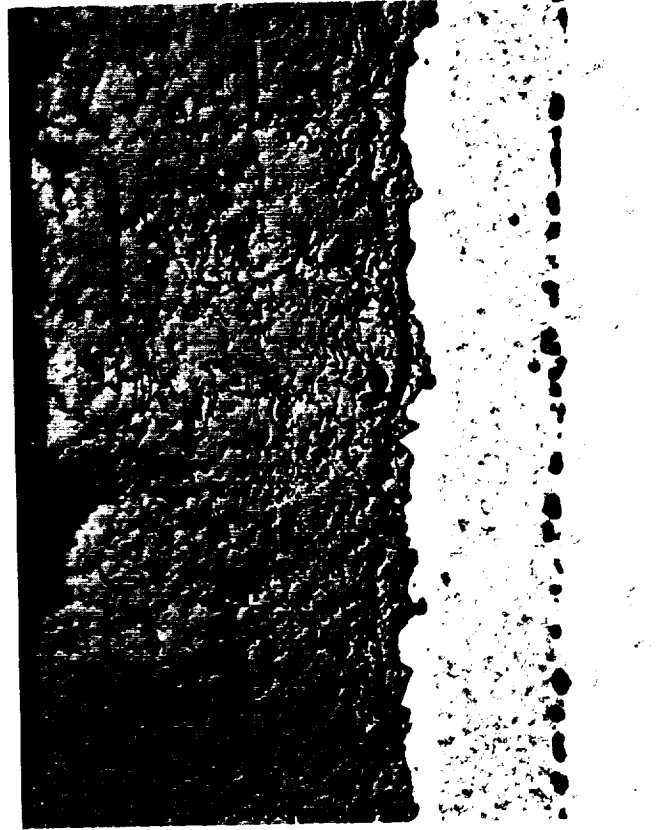
Figure 115 Mixed Mode Oxide Emphasis Test
#18 Post-Test Specimen
Microstructure



18a) HT-39 Spalled Area 1X

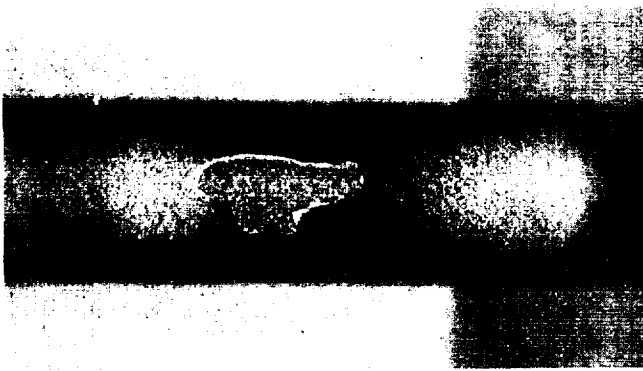


18b) HT-39 Post-Test Failure Zone 200X

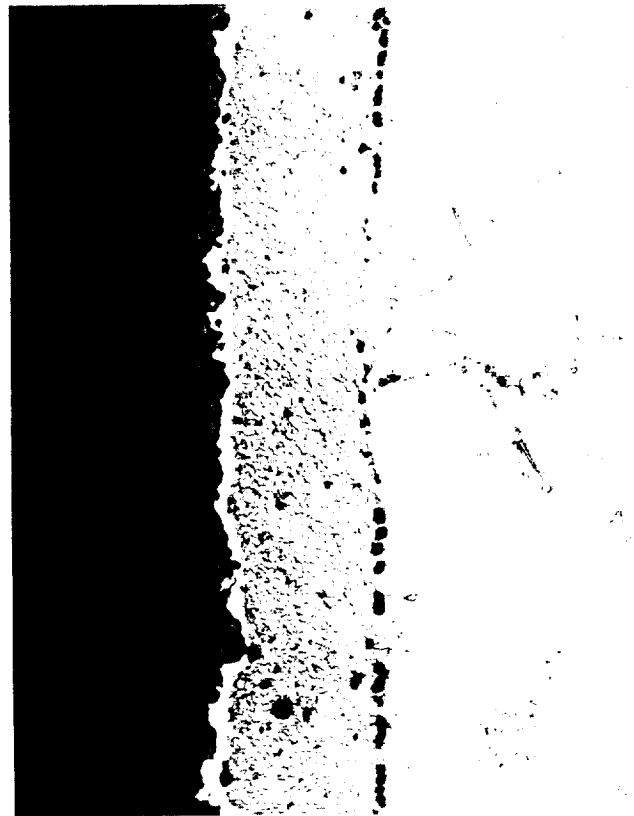


18c) HT-39 Post-Test 200X

Figure 116 Small Radius Test #19 Post-Test
Specimen Microstructure



19a) HT-13 Spalled Area 1X



19b) HT-13 Post-Test Failure Zone 200X



19c) HT-13 Post-Test 200X

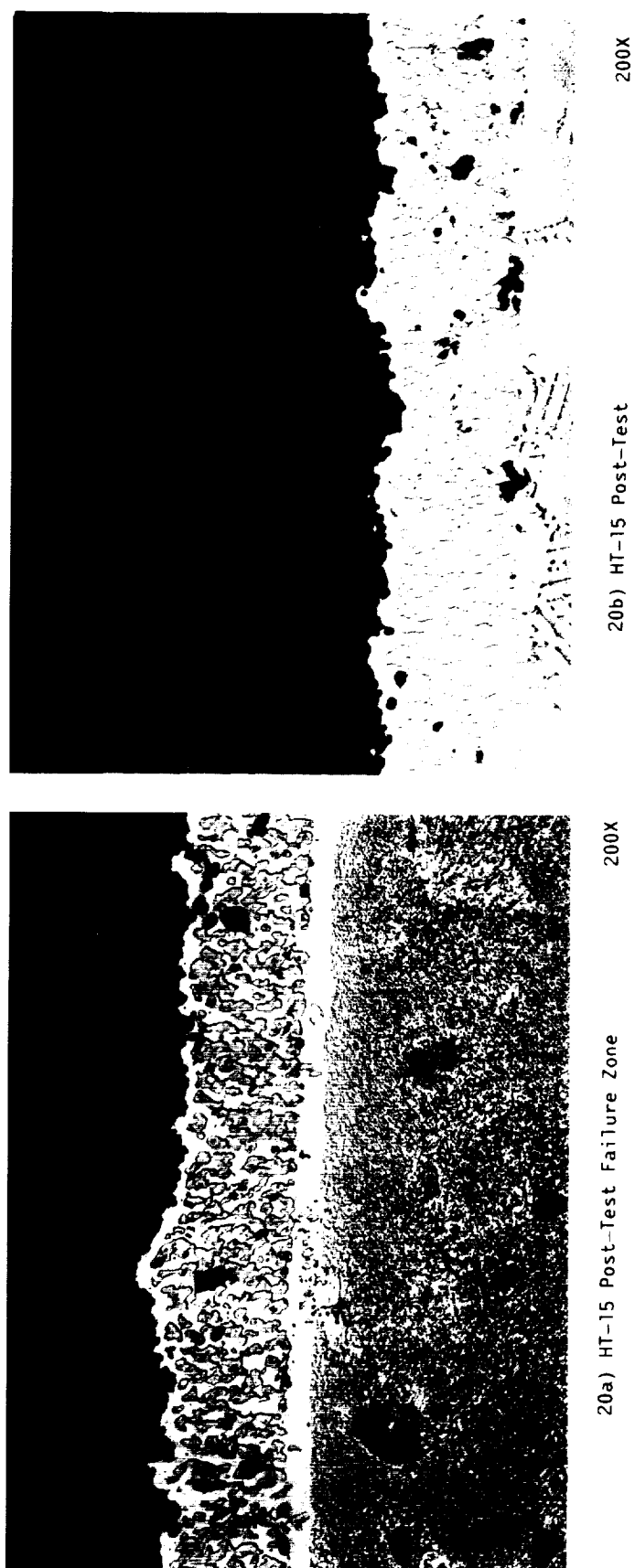


Figure 117 Small Radius Test #20 Post-Test Specimen Microstructure

3.2.2.2 Advanced Life Prediction Model Development

Constitutive Property Model Analysis

In the advanced life prediction model developed under this task, the prediction of the ceramic inelastic strain range ($\Delta \epsilon_i$) (eq. 4, section 3.1.4.1) has been improved. Analytical enhancements involved more accurate modeling of the TBC's ceramic outer layer constitutive and time dependent behavior including: non-linear stress-strain characteristics, asymmetric tensile and compressive response, and time dependent inelastic deformation. This was accomplished by using a time dependent one-dimensional constitutive model developed by Walker (Ref. 40). The Walker model considers all non-linear behavior as time dependent inelasticity such that no distinction between plastic and creep deformation is made. The governing equation for inelastic strain is given by:

$$\dot{\epsilon}_{\text{inelastic}} = \left(\frac{\sigma - \Omega}{K} \right)^n \quad (1)$$

where n is a constant, Ω is the back stress, and K is the instantaneous drag stress. The back stress term is a quantity which physically corresponds to the asymptotic stress state under relaxation conditions. Qualitatively, the evolutionary expression for back stress is a sum of opposing hardening and thermal and dynamic recovery components which can be characterized as:

$$\dot{\Omega} = \underbrace{f(\epsilon_{in}, \dot{\epsilon}_{in}, T, t)}_{\text{Hardening}} - \underbrace{f(\Omega, \dot{\epsilon}_{in}, T, t)}_{\text{Recovery}} \quad (2)$$

The one-dimensional form of the Walker model was used to regress tensile, compression and creep data to obtain the equation constants. Some modifications to the constitutive relationships were required to match the TBC's mechanical behavior. These modifications are noted below:

$$\dot{\epsilon}_t = \dot{\epsilon}_e + \dot{\epsilon}_{in} \quad (3)$$

$$\dot{\epsilon}_{in} = \left(\frac{\sigma - \Omega}{k} \right)^n \quad (4)$$

$$\dot{\Omega} = (n_1 + n_2) \dot{\epsilon}_{in} + \dot{\epsilon}_{in} \frac{\delta n_1}{\delta \Theta} \dot{\Theta} - (\Omega - \Omega_{-n_1} \epsilon_{in}) \left(\dot{G} - \frac{1}{n_2} \frac{\delta n_2}{\delta \Theta} \delta \dot{\Theta} \right) \quad (5)$$

$$\dot{G} = (n_3 + n_4 \exp(-n_5 R)) \dot{R} + n_6 \Omega^{m-1} \quad (6)$$

$$\dot{R} = |\dot{\epsilon}_{in}| \quad (7)$$

$$K = k_1 - K_2 \text{ATAN}(\sigma_e/n_7) \quad (8)$$

$$\sigma_{e_{i+1}} = E(\epsilon_{t_i} - \epsilon_{in_i} - \Delta \epsilon_{in_i} \times \Delta t_{i+1}/\Delta t_i) \quad (9)$$

$$\Omega_{i+1} = \Omega_i + d\Omega \quad (10)$$

$$\epsilon_{in_{i+1}} = \epsilon_{in_i} + d\epsilon_{in} \quad (11)$$

$$\epsilon_{t_{i+1}} = \epsilon_{t_i} + d\epsilon_{t_{i+1}} \quad (12)$$

$$\sigma_{i+1} = E (\epsilon_{t_{i+1}} - \epsilon_{in_{i+1}}) \quad (13)$$

ϵ_t = total mechanical strain
 ϵ_e = elastic strain
 ϵ_{in} = inelastic strain
 σ = stress
 Ω = back stress
 K = drag stress
 E = Elastic Modules
 t = time

$n_1, n_2, n_3, n_4, n_5, n_6, n_7, K_1, K_2, \Omega, m, n, E$ depend on temperature.

The drag stress (K) was modified to reflect the asymmetry between tension and compression. The value of " K " alternates between $(K_1 + K_2 \cdot \pi/2)$ in compression and $(K_1 - K_2 \cdot \pi/2)$ in tension as shown in Figure 117A. An estimated value of stress (σ_e) is used to determine what value of K is used during a specific time increment.

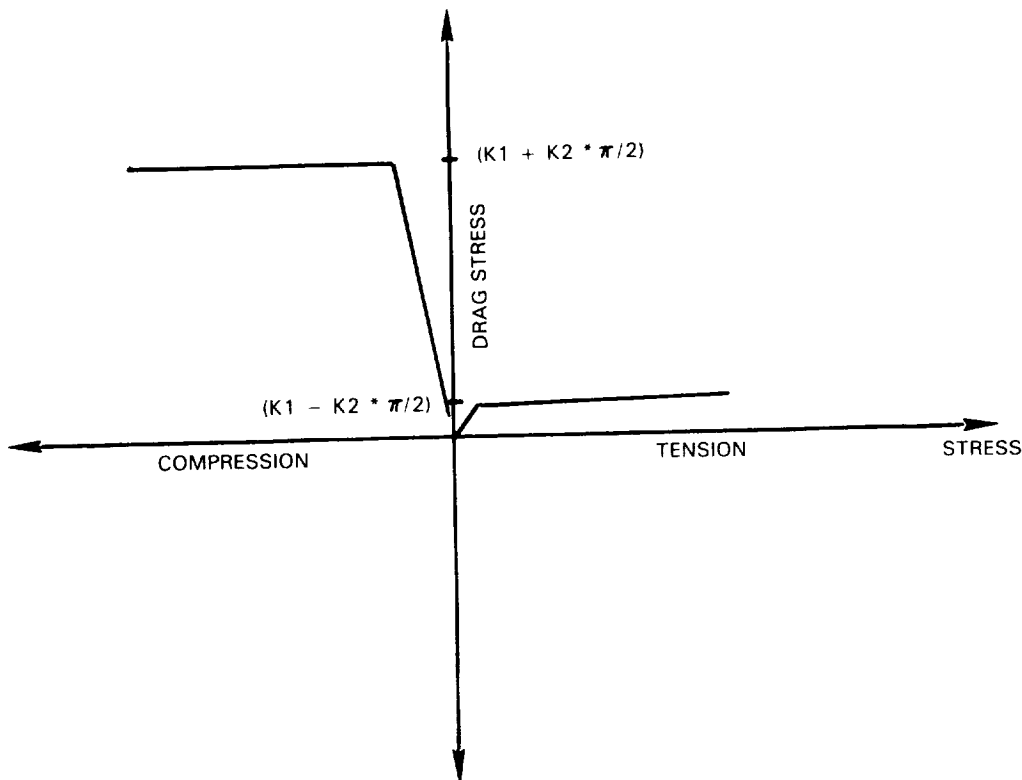


Figure 117A Drag Stress (K) in Thermal Barrier Coating Walker Model

The constitutive model for the TBC appears to reasonably reflect the most important features of the mechanical behavior of the insulating ceramic layer, i.e., asymmetric tensile and compressive stress/strain response, non-linear stress-strain response in tension and compression, and creep behavior. The coefficients to the constitutive model were selected to reflect the most important characteristics of the material at each temperature. These coefficients were regressed using a computer code developed by D. Nissely under the NASA (HOST) Contract; "Life Prediction and Constitutive Models for Hot Section Anisotropic Materials Program, NAS3-23939."

At high temperatures the TBC is in tension because the metal it is adhered to has a higher thermal expansion; therefore, at high temperatures the tensile behavior was matched. At lower temperatures the compressive uniaxial and creep data was matched. Figures 118 through 123 show the Walker model predictions for ceramic mechanical behavior in tension, compression, and creep. These plots show that the modified Walker model is simulating the uniaxial data relatively well. While the secondary creep rate is also simulated relatively well, the actual level of creep tends to be overpredicted.

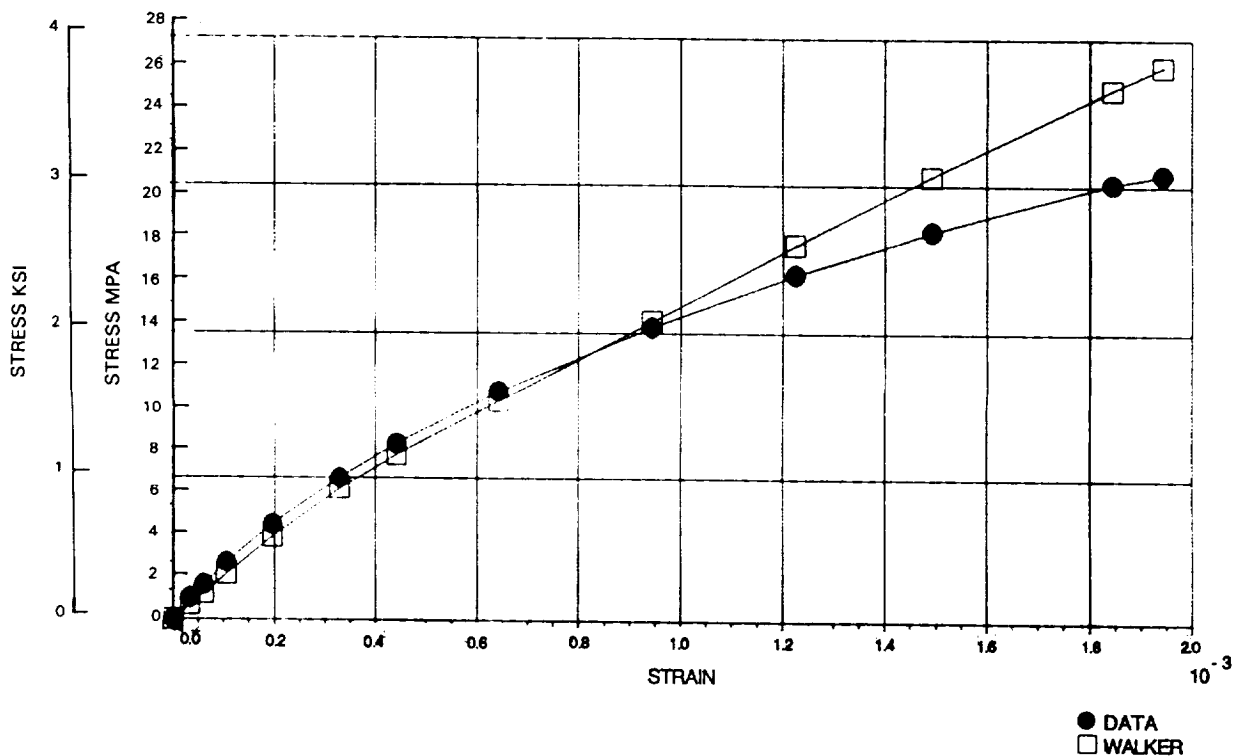


Figure 118 Comparison of Uniaxial Tensile Data (Room Temperature) and Modified Walker Model Predictions

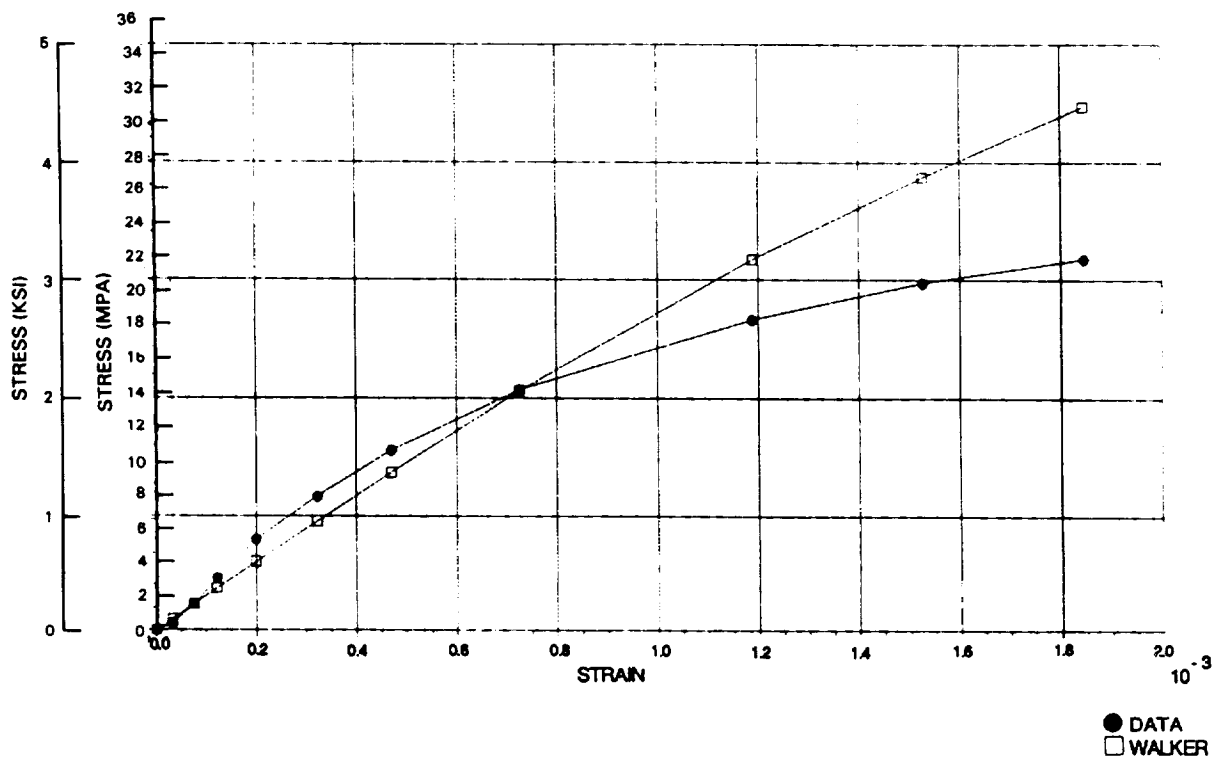


Figure 119 Comparison of Uniaxial Tensile Data 1094°C (2000°F) and Modified Walker Model Predictions

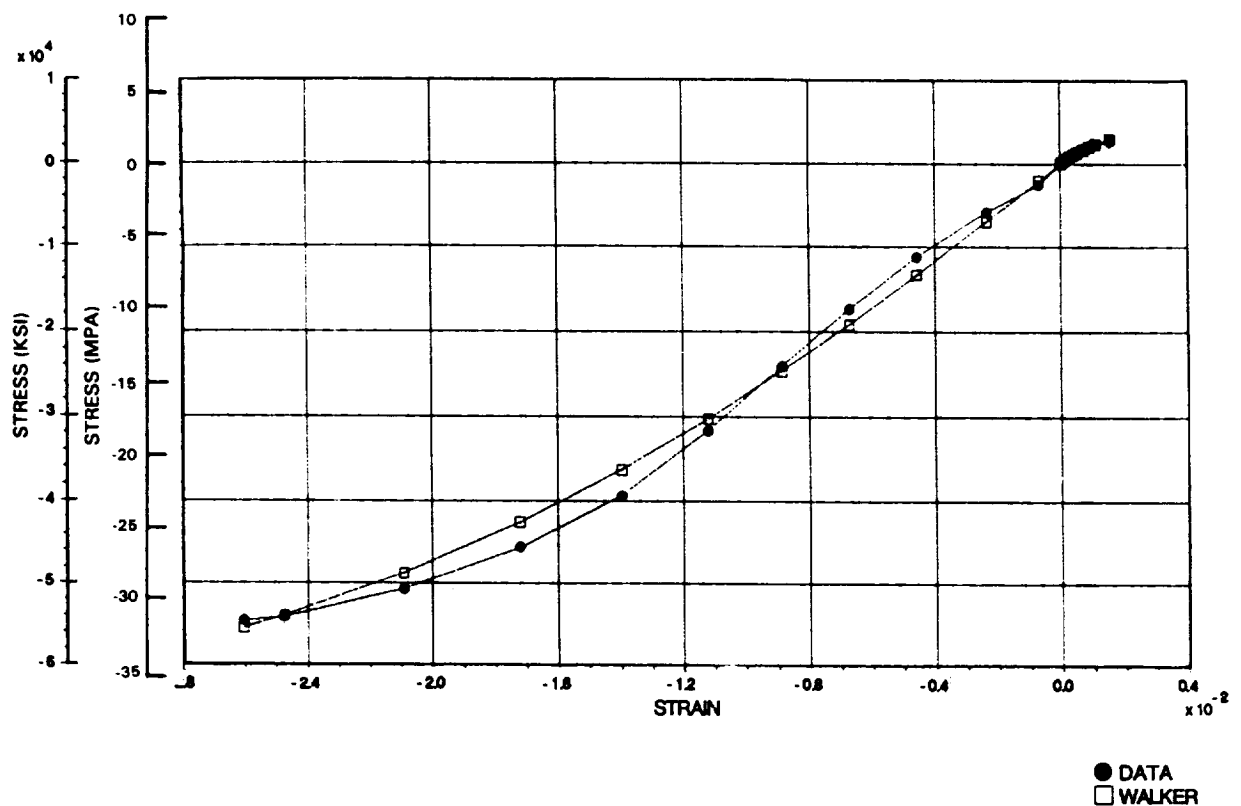


Figure 120 Comparison of Uniaxial Tensile Data and Compressive Data 538°C (1000°F) and Modified Walker Model Predictions

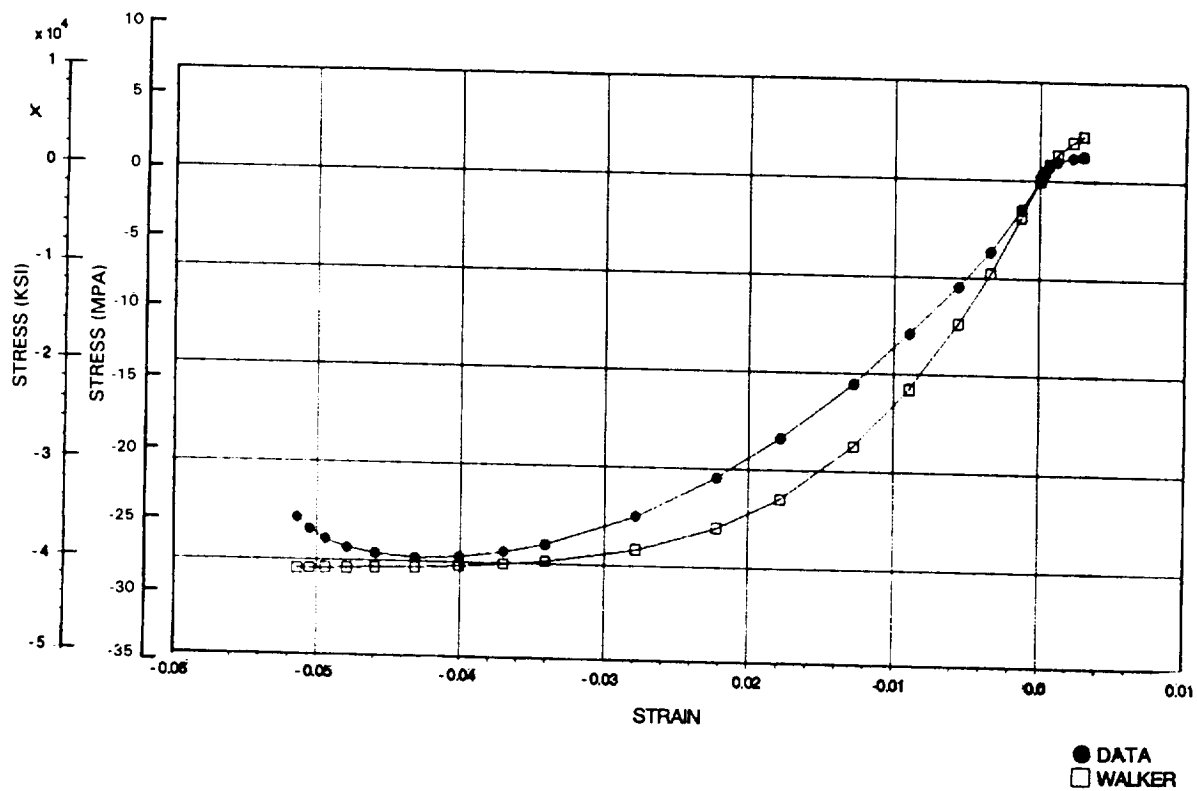


Figure 121 Comparison of Uniaxial Tensile Data and Compressive Data 1094°C (2200°F) and Modified Walker Model Predictions

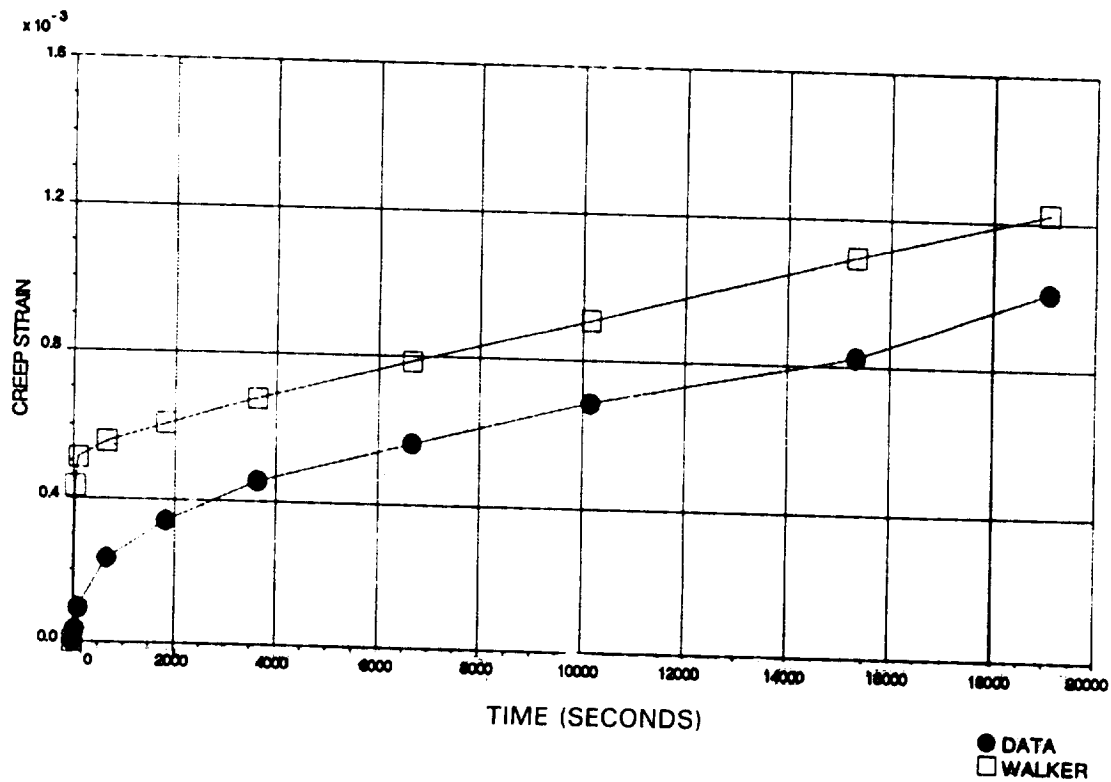


Figure 122 Comparison of Uniaxial Tensile-Creep Data 982°C (1800°F) and Modified Walker Model Predictions

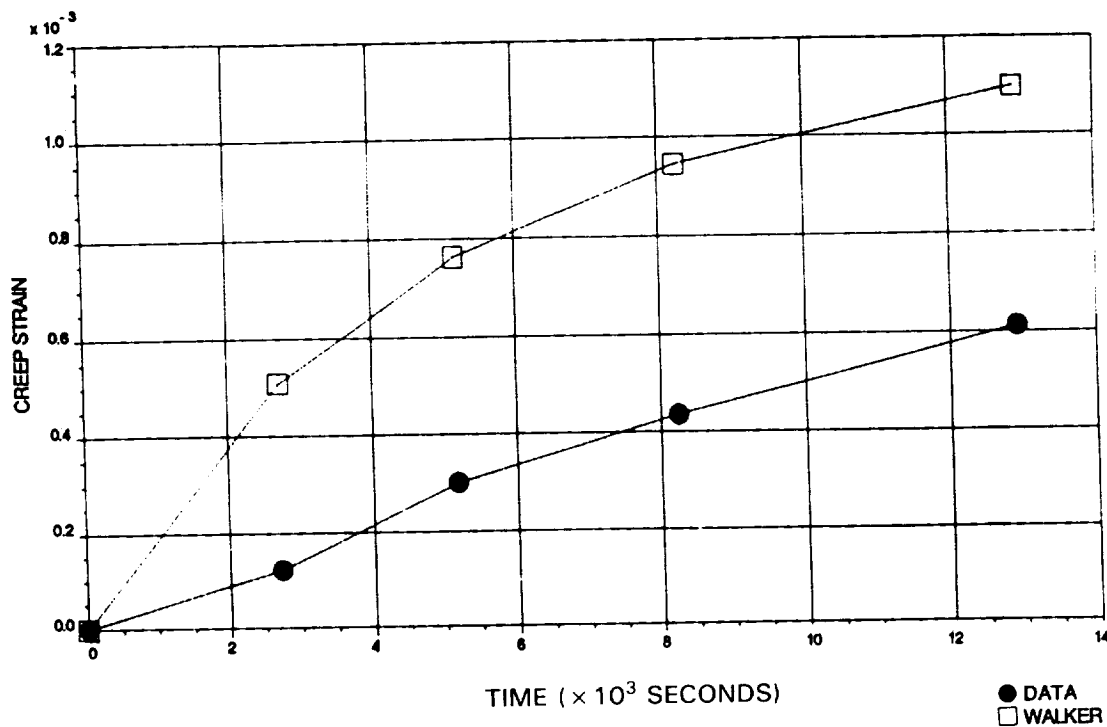


Figure 123 Comparison of Uniaxial Tensile-Creep Data 982°C (1800°F) and Modified Walker Model Prediction

To obtain thermal displacements for thermal stress-strain analysis, heat transfer analyses were completed for all the Task II experiments. An average cycle temperature was established for each test based on the average of the monitored thermocouple minimum and maximum cycle temperatures. An elastic finite element stress analyses then was made for each test using the thermal boundary condition computed from the heat transfer analysis. The mechanical strain of the specimen metal O.D. surface is the applied boundary condition to the TBC constitutive model. The TBC stress is then calculated based on the TBC constitutive relationships. The maximum width of the resulting stress/strain hysteresis loop is $\Delta\epsilon$, which is used to correlate the life prediction model.

A typical hysteresis loop calculated for a "strain emphasis" type burner rig cycle is shown in Figure 124. It should be noted that the predicted hysteresis loop includes extended tensile ductility i.e., it allows for inelastic straining past the bulk material property tensile failure strain ($\approx 0.3\%$). The physical hypothesis put forth for this phenomenon is that a thin coating having excellent adherence to the underlying substrate is able to accommodate greater inelastic straining than a bulk specimen which fails from the first crack. This is manifested in the microstructure as segmentation type, micro/macro, cracks.

In the mature, thermally driven ceramic stress-strain cycle, the ceramic is in compression at point 1. When the ceramic layer begins to heat up initially, and the metal substrate is still cold, the TBC is driven further into compression non-linearly (points 1-2). As the metal substrate also begins to heat up the ceramic layer is driven into tension linearly, initially, and then non-linearly when the ceramic layer is in an actual tensile state. When the TBC reaches the steady state maximum cycle temperature, point 3, a certain amount of linear stress relaxation occurs, the amount of which depends on how

long the TBC remains at the maximum temperature (points 3-4). When the ceramic is initially cooled, while the metal substrate is still hot, additional non-linear tensile straining occurs due to the initial external cooling flux, (points 4-5). Upon cool down, when the metal subsystem begins to cool, the ceramic layer is driven back into compression, initially linearly. At higher stress levels in compression the unloading becomes nonlinear. At still lower temperatures some stress relaxation or stress recovery is dictated by the model as the ceramic returns to point 1.

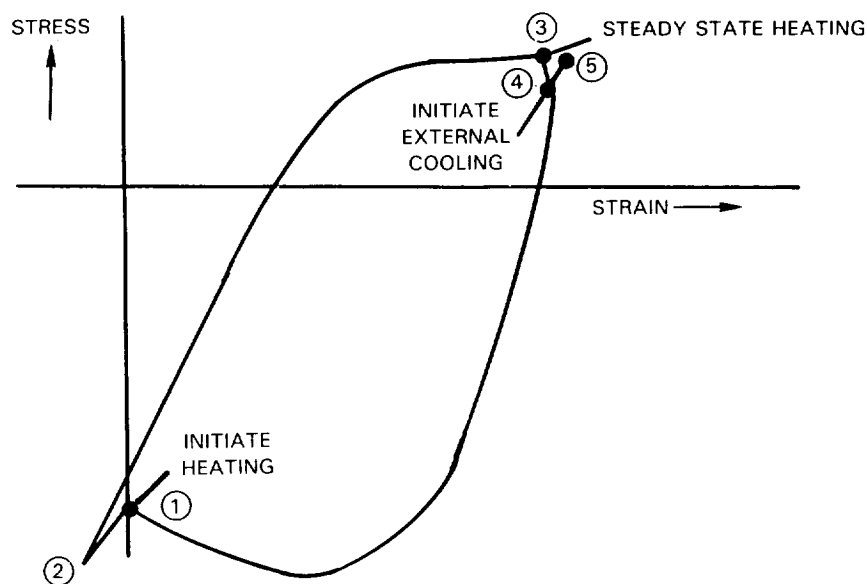


Figure 124 One-dimensional Walker Model Prediction of Stress-Strain Cycle for Burner Rig Experiment At Cracking Location Just Above Interface In Ceramic

The model predicts a very open loop with a quite large reversed plastic strain range to drive ceramic fatigue damage. Predictions for all of the experimental burner rig cycles were made with this model for correlation of the improved life prediction system.

Figures 125 through 127 show the predicted stress-strain hysteresis loops for representative oxide emphasis, strain emphasis and mixed mode group tests respectively. Figures 126 and 127 show that, for the strain emphasis and mixed mode tests, the hysteresis loop "ratchets" to a stable cycle after a relatively small number of cycles. The oxide emphasis, stress-strain hysteresis loop requires a larger number of cycles before it becomes stable. This is because this type of test allows the specimen to cool only to 427°C (800°F) instead of 38°C (100°F); thus, very little cooling time is accumulated, resulting in less stress-relaxation per cycle. In comparison the strain-emphasis type test requires much more cooling, so that the specimen returns almost to ambient temperature, thus resulting in greater stress-relaxation and the loop stabilizes after 4-5 cycles.

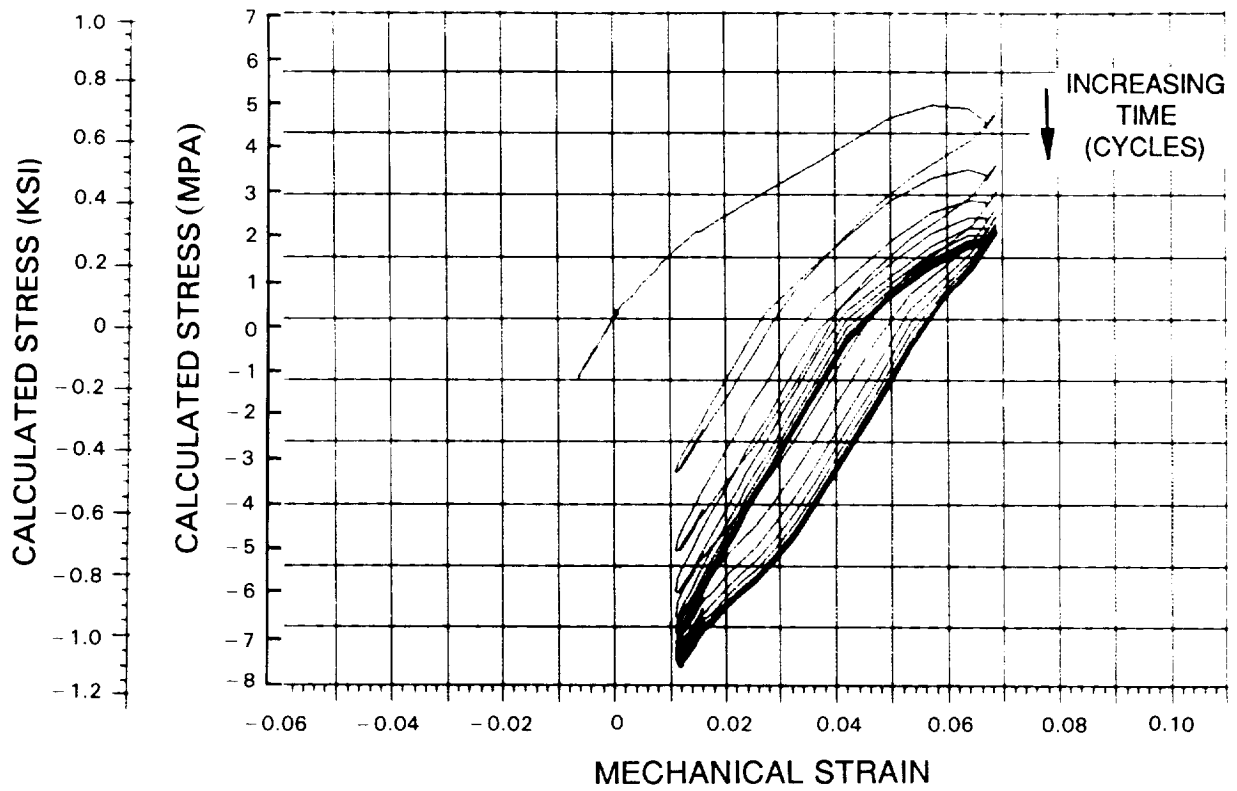


Figure 125 Predicted Stress-Strain Hysteresis Loop for Oxide Emphasis Loop for Oxide Emphasis Test #1

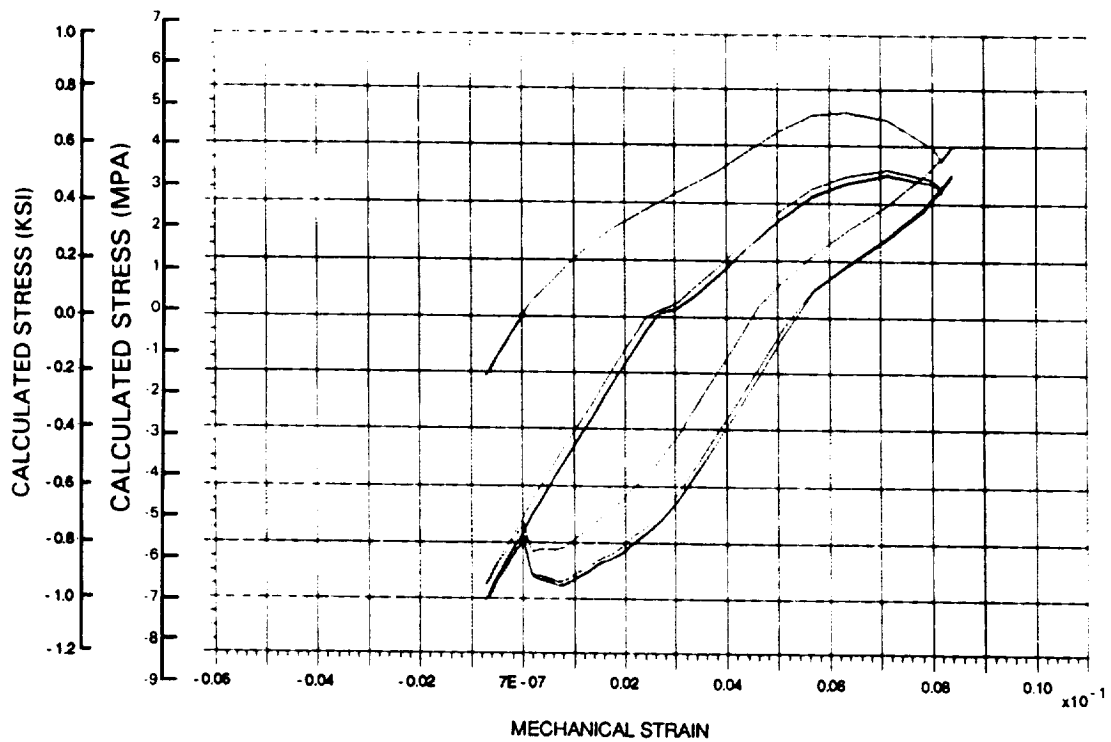


Figure 126 Predicted Stress-Strain Hysteresis Loop for Strain Emphasis Test #12

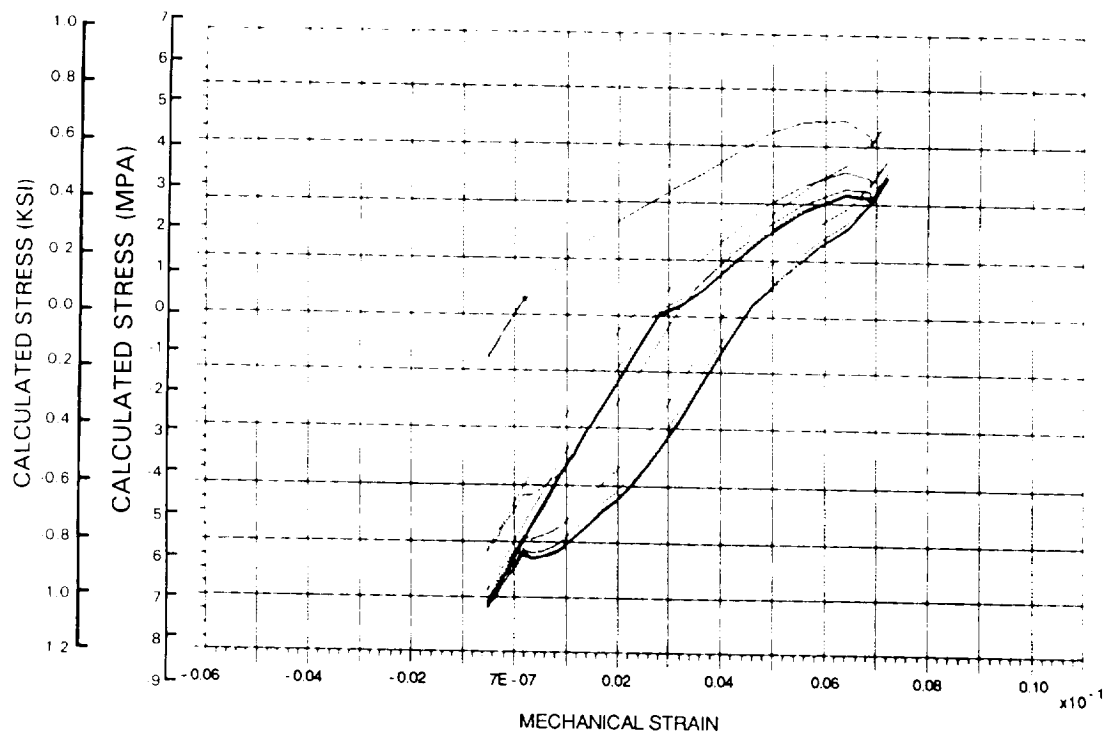


Figure 127 Predicted Stress-Strain Hysteresis Loop for Mixed Mode Test #16

Oxidation Model Development

To improve the bond coat oxide growth rate model developed in Task I of this phase, oxidation experiments were conducted using the program's Substrate-TBC System, at the NASA Lewis Research Center. Dr. Robert Miller used his data to develop a more accurate oxidation fit for the improved life prediction system. Oxidation data from furnace experiments was obtained at two temperatures: 1100°C (2012°F) and 1200°C (2192°F). From this experimental data a new oxide growth rate expression was developed based on the average of the two tests. The oxide thickness expression is shown below:

$$\frac{W}{A} = \left[2.057 \times 10^{15} e^{-(-52771/T)} t \right]^{0.2952} \quad (14)$$

where: W = weight to change in mg
A = area in cm²
t = time in hours
T = temperature °K

An oxide thickness expression may be obtained using the weight gain data if it is assumed that only Al₂O₃ growth occurs:

$$\frac{W}{A} = \phi \rho_{Al_2O_3} \Delta X_{Al_2O_3} \quad (15)$$

where ϕ = average weight fraction of oxygen in Al₂O₃ scale
 $\rho_{Al_2O_3}$ = density of Al₂O₃ scale
 $\Delta X_{Al_2O_3}$ = thickness of Al₂O₃ scale

The oxide thickness expression obtained based on the NASA furnace data is:

$$\Delta X_{Al_2O_3} = 5.35 \times 10^{-4} [2.057 \times 10^{15} e^{(-52771/T)} t]^{0.2952} \quad (16)$$

Using this oxide growth rate expression, bond coat oxide thickness at failure was predicted for each of the Task II single-specimen tests. As shown in Figure 128, the predicted oxide thickness is ~2X greater than measured.

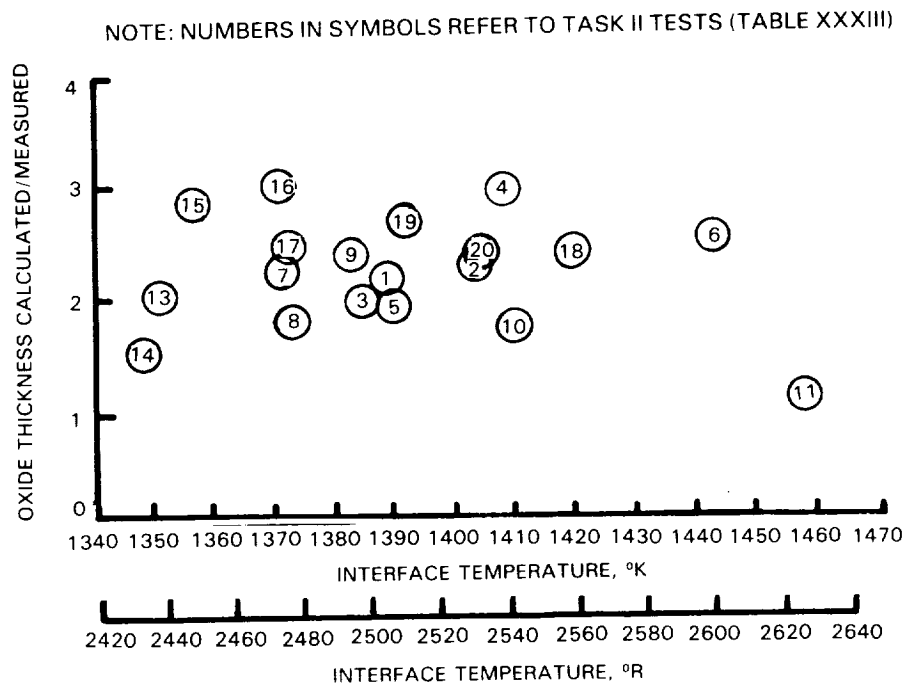


Figure 128 Calculated vs Measured Oxidation Thickness for Burner Rig Specimens

To improve the correspondence between calculated and measured oxide thickness values, the measured thickness values were empirically curve-fit using the Miller value for activation energy and allowing the exponent and pre-exponential constants to vary.

While the current oxide thickness correlation better represents the measured data, appreciable scatter is still evident. The type of cycle affects the prediction of oxide thickness as depicted in Figure 129. This discrepancy will be addressed in Phase II, Task VI; Empirical Oxidation Model. Results of this correlation are shown in Figure 129. The resulting oxide thickness expression used in the subsequent life correlation is:

$$\delta = 1.20 \times 10^{-4} (5.714 \times 10^{11} e^{-104856/RT} t)^{0.5} \quad (17)$$

$R = 1.987$, $\delta = (\text{CM})$
 $T = (^\circ\text{K})$
 $t = (\text{SEC})$

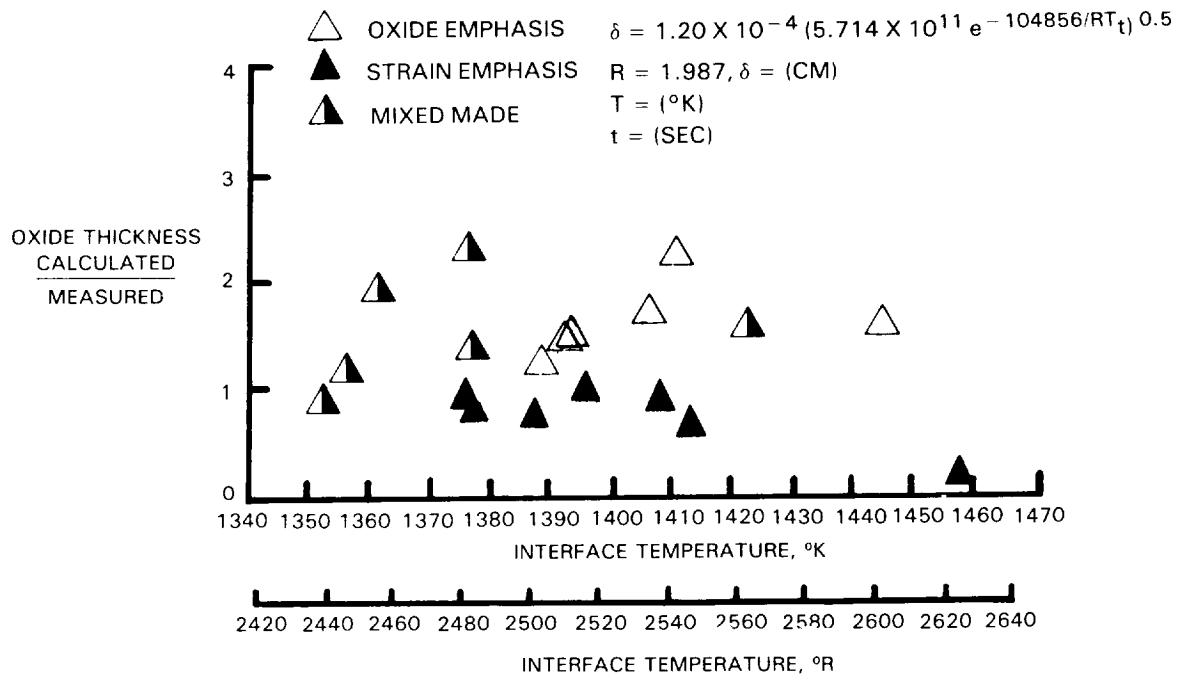


Figure 129 Oxide Thickness Ratio Used in Life Correlation

Advanced Model Correlation

Task II modeling employed the functional form developed in Task I which is reproduced below:

$$N = (\Delta\epsilon_i / \Delta\epsilon_r)^b \quad (18)$$

$$\Delta\epsilon_r = \epsilon_{r0} (1 - \delta/\delta_c) + \Delta\epsilon_i (\delta/\delta_c) \quad (19)$$

$\Delta\epsilon_i$ = total inelastic strain of the ceramic determined by the maximum width of the stress-strain hysteresis loop (see Figure 129A).

$$\delta = A(Ce^{-\Delta H/RT} t)^n \quad (20)$$

Where:

- N = Number of Cycles to Failure
- ϵ_r = failure strain range
- ϵ_i = inelastic strain range
- ϵ_{r0} = static failure strain = 0.004
- δ = oxide thickness
- δ_c = critical oxide thickness
- T = Temperature
- t = time
- ΔH = activation energy
- R = gas constant
- A, C, n, b = constant

c-3

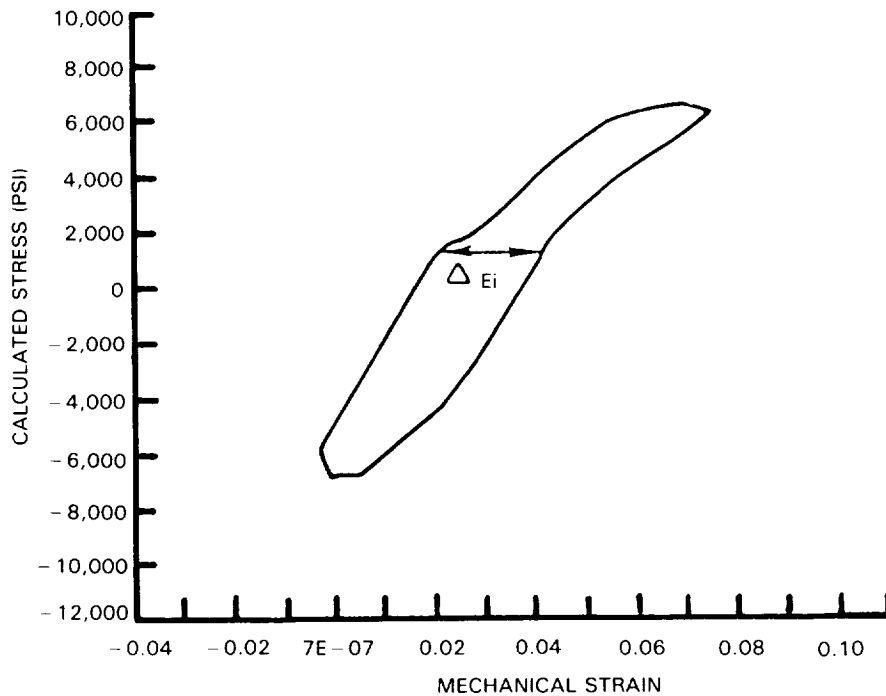


Figure 129A Predicted Stress Strain Hysteresis Loop Using Walker Model (section 3.2.2.2)

Results of the twenty Task II tests were fit to this equation using the values for A, C, ΔH , and n discussed in the last section (Figure 129). The strain range exponent (b) was derived by recorrelating the Task I data with the preliminary life model (section 3.1.4.1) with the oxide thickness equation based on the NASA data (equation 1b, section 3.2.2.2). Best fit values of the critical oxide thickness (δ_c) and static failure strain ($\Delta \epsilon_{f_0}$) are shown in Figure 130 together with the correlation achieved with these constants. Specific values of predicted life are listed in Table XXXIII. A computer code was developed under this NASA contract to make these life predictions. The computer code along with a Users Manual is shown in Appendix E. With the exception of test 16, which was a maverick in all correlation attempts, the model provides predictions which are within $\pm 3x$ of observed life for the remaining test specimens.

While no specific goal was established regarding accuracy of prediction capability for this program, it generally is accepted that, to be useful as a design tool, a turbine design life prediction system should predict life within a factor of ± 2 for life critical components. Because the subject coating (PWA 264) currently is being used for life extension rather than as an integral element of component structural design, the factor of ± 3 is judged adequate for purposes of Phase I of this program. A primary goal of Phase II will be to improve this capability to ± 2 on life for "life critical" application of an improved TBC. This will be a challenging goal; prediction with $\pm 2x$ generally is considered a "good fit" for a single failure mode (such as fatigue or creep). In situations such as TBC failure, where two separate but interactive degradation modes are involved, ± 2 fit will indeed be a challenge.

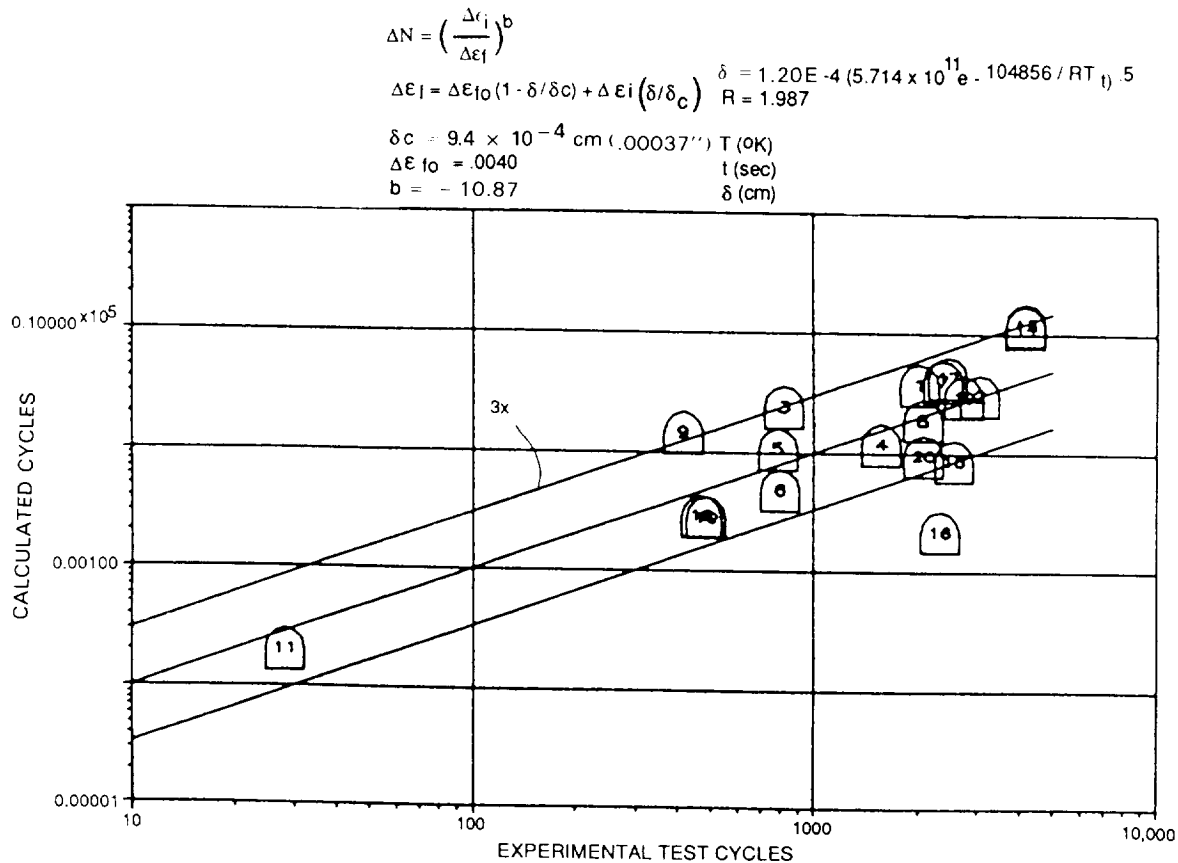


Figure 130 Life Prediction Model Correlation Using Optimized Oxide Growth Rate Model: Calculated vs Experimental Cycle Life

To assess sources of inaccuracy in the Task II prediction system, the data were re-correlated using metallographically measured rather than calculated oxide thickness values. Results of this correlation, shown in Figure 131, indicate only a modest improvement in prediction accuracy, from $\pm 3X$ to $\pm 2.6X$ on life. This observation suggests that the primary source of error in the prediction system is in the mechanical rather than the environmental part of the interactive model.

Another approach employed to seek sources of error was to look at the degree of correlation of life with each of the primary degradation drivers. Figure 132 shows a correlation of cyclic life with plastic strain range and in Figure 133 is shown a correlation of estimated time at maximum temperature with maximum cycle temperature. Examination of these two figures shows cyclic life to correlate with strain range much better than temporal life correlates with temperature ($\pm 4.3X$ scatter for $\Delta \epsilon$, vs $\pm 70X$ scatter for temperature), suggesting that mechanical fatigue may be the predominant driver with environmental degradation playing a secondary role. This observation is consistent with the fatigue driver being the primary source of scatter in the interactive model predictions.

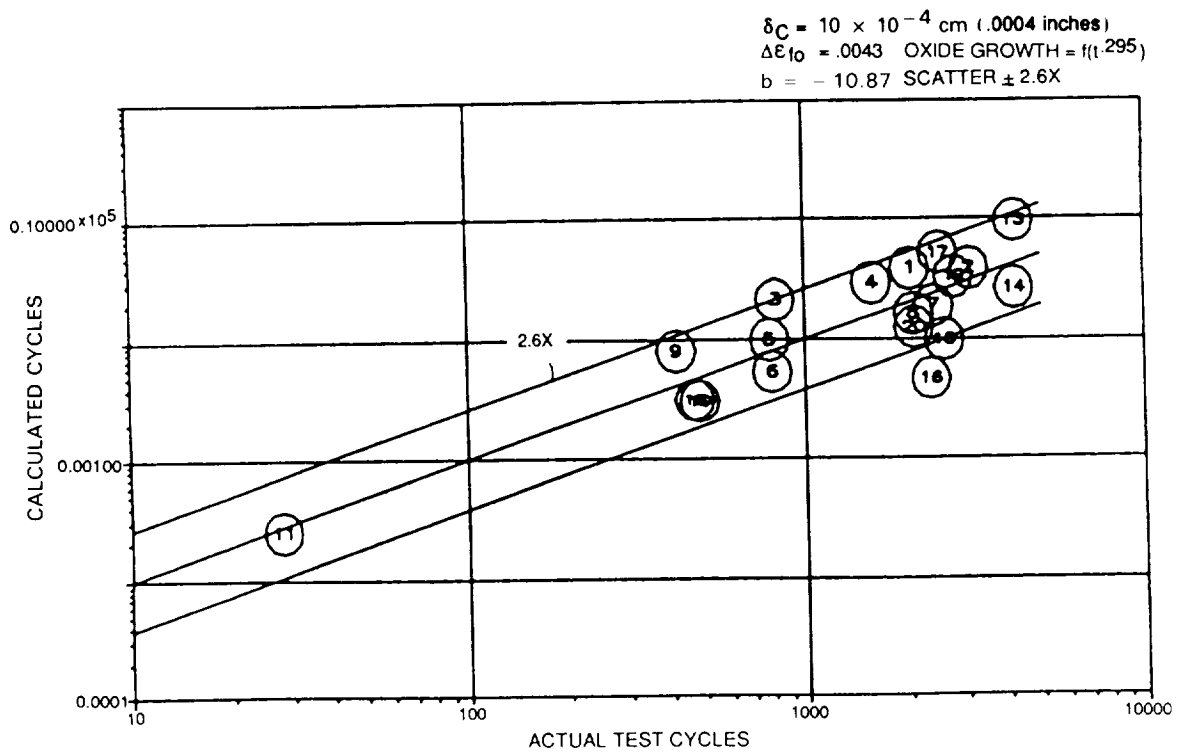


Figure 131 Calculated vs Experimental Cycle Life Using Measured Oxide Thickness

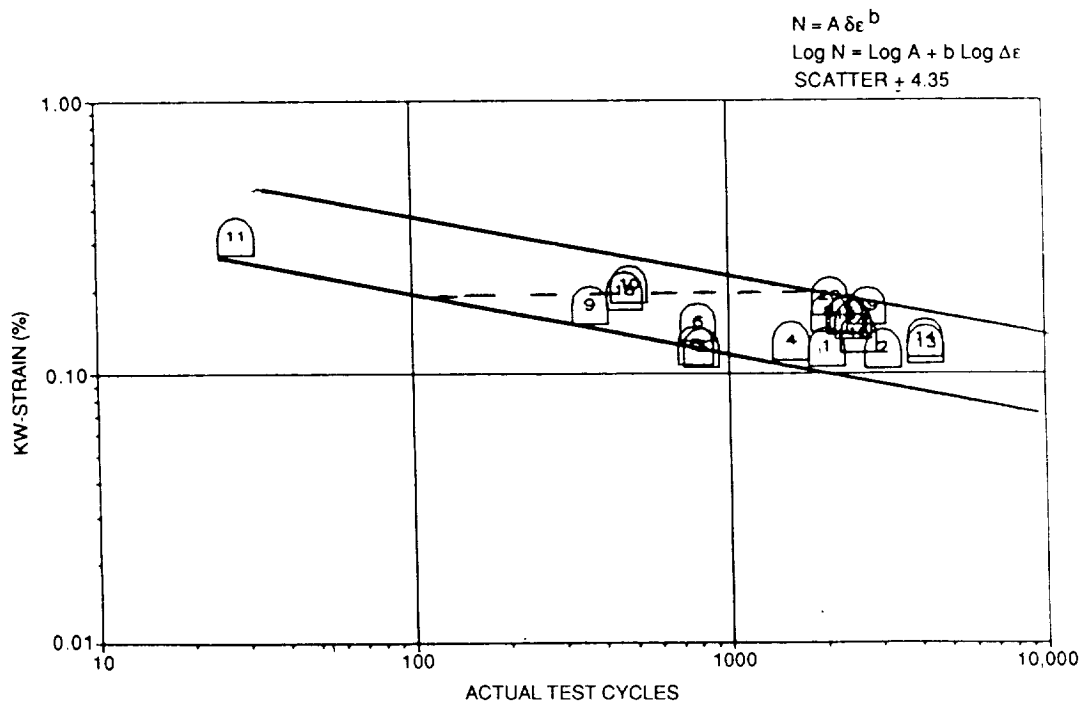


Figure 132 Cyclic Life vs Inelastic Strain Range for Task II Tests

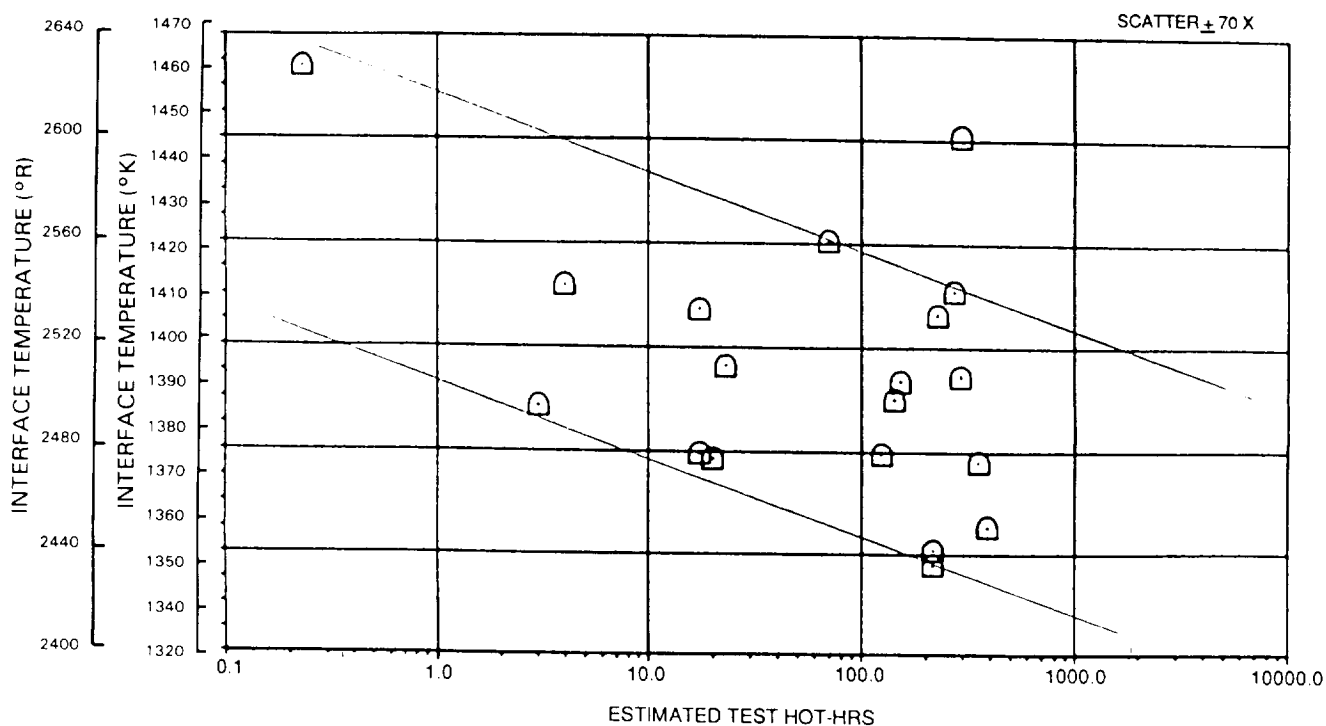


Figure 133 Time at Maximum Cycle Temperature vs. Maximum Cycle Temperature for Task II Tests

3.3 Task III - Model Verification

The objective of this task was to experimentally challenge and verify the life prediction model developed in Task II. The approach involved Task II type cyclic burner rig testing using parameters that were different from those employed in Task II as well as testing in a higher heat flux quartz lamp rig. The basis of verification involved comparison between experimental results and predictions of the Task II model.

3.3.1 Task IIIA - Experimental Design

The objective of Task IIIA was to design a set of four experiments that would test the validity of the model developed in Task I and refined in Task II. Test parameters were selected as appropriate to simulate the failure mode of interest.

The basic test matrix designed for Task III involved four verification experiments (Table XXXIV). This plan included: (1) a baseline strain emphasis type test (2) an oxide emphasis test and (3) and (4) two mixed strain emphasis cycle tests in which two different strain cycles were imposed in an alternate sequence to determine if the linear damage accumulation form of the model is appropriate.

TABLE XXXIV
PLANNED CONDITIONS FOR TASK III EXPERIMENTS
MODEL VERIFICATION TESTS

Test	Emphasis	Maximum Cycle Temperature Interface		Minimum Cycle Temperature Interface		Time To Tmax	Time At Tmax	Time To Tmin	Total Cycle Time	Comments
1	Baseline - Strain Emphasis	1149°C	2100°F	38°C	100°F	1.5 min	0	4.5 min	6.0 min	No Internal Cooling
2	Oxide Emphasis	1149°C	2100°F	427°C	800°F	1.5 min	6 min	0.5 min	8.0 min	Internal Cooling Required
3	Mixed Strain Cycle									
	Type I Cycle	1093°C	2000°F	38°C	100°F	1.5 min	0 min	4.5 min	6.0 min	Type I 1500 cycles
	Type II Cycle	1149°C	2100°F	38°C	100°F	1.5 min	0 min	4.5 min	6.0 min	Type II - To Failure
4	Mixed Strain Cycle									
	Type II Cycle	1149°C	2100°F	38°C	100°F	1.5 min	0 min	4.5 min	6.0 min	Type II Same Number of Cycles as in test #3
	Type I Cycle	1093°C	2000°F	38°C	100°F	1.5 min	0 min	4.5 min	6.0 min	Type I - To Failure

Two additional tests were conducted to nominally reproduce the conditions of Tests 1 and 2 but with flat specimen geometry and quartz lamp heating. The key differences between these tests and the burner rig tests were the specimen radius of curvature and heat flux. Heat flux sensors employed to calibrate the quartz lamp heaters indicated a capability of 360 KBTU/hr-ft² at 90% power; this is on the order of 3 1/2 times the capability of the burner rigs employed in this program (but still only about 1/3 typical maximum heat flux in the engine). To improve thermal coupling between the quartz heaters and the specimen and to avoid edge failures, black nickel oxide paint was applied to the central area of the flat panel specimen.

3.3.2 Task IIIB - Verification Test Results/Analysis/Recommendations

Results of the six verification tests are included in Table XXXV and are plotted vs. the Task II model predictions in Figure 134. These results may be considered to verify the Task II model will experimental lives being within $\pm 3X$ of predicted values.

In contrast with the Task II data, where no systematic life deviations were observed, the model appears to be systematically under-predicting the fatigue driven failures and over-predicting environmentally driven failures for the Task III results. Currently, there is no clear evidence as to whether this apparent systematic deviation is real or is the result of random chance.

TABLE XXXV
TASK III MODEL VERIFICATION - EXPERIMENTAL AND PROJECTED RESULTS

Test	Emphasis	Average T/C Maximum Cycle Temperature	Average T/C Minimum Cycle Temperature	Hours To Failure	Cycles To Failure	Total Cycles	Predicted Cycles to Failure
1	Baseline Strain	1127°C 2060°F	23°C 73°F	157.7	1513		663
2	Oxide	1138°C 2081°F	481°C 897°F	52.8	431		1296
3	Mixed: Type I Type II	1077°C 1970°F 1154°C 2110°F	28°C 83°F 27°C 80°F	140.4 67.4	1310 665	1975	1380
4	Mixed: Type I Type II	1137°C 2078°F 1102°C 2015°F	29°C 85°F 28°C 83°F	64.2 29.7	602 267	869	286
5	Baseline Strain (Quartz Lamp Heater)	1149°C 2100°F	<38°C <100°F	57	570		223
6	Oxide (Quartz Lamp Heater)	1136°C 2077°F	217°C 963°F	91.6	1000		2900

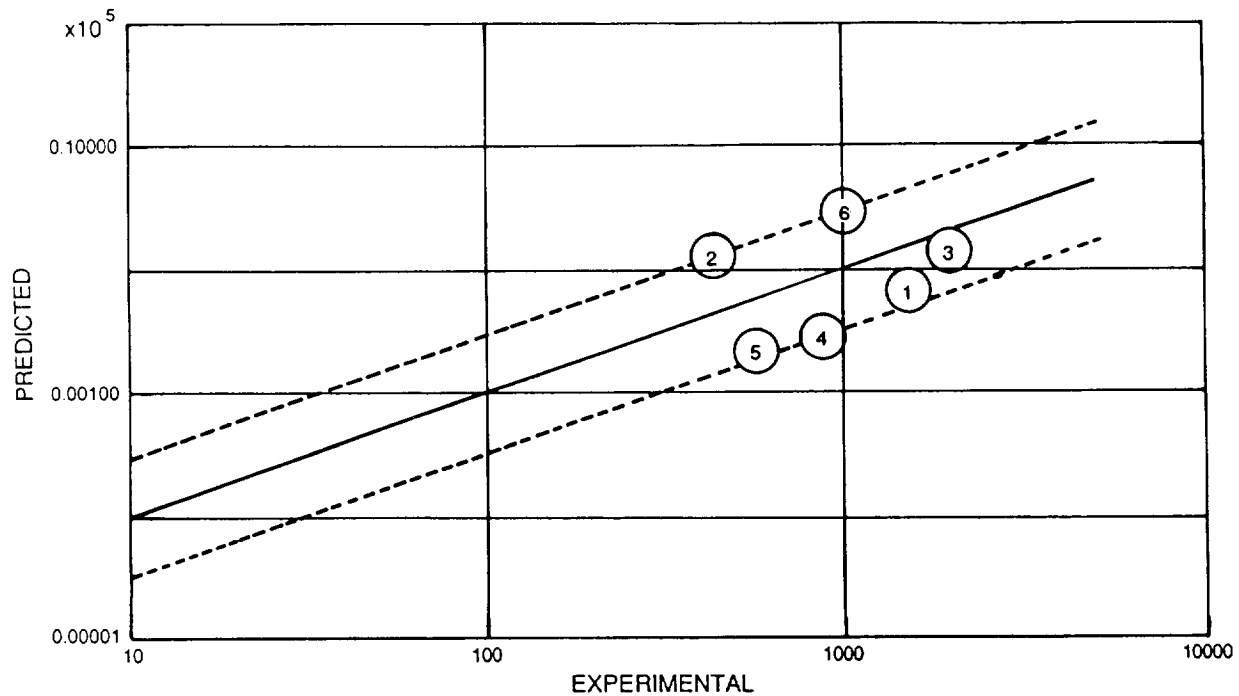


Figure 134 Task II Verification Test Results Predicted Using the Advanced Model Correlation (section 3.2.2.2)

Of particular significance in the Task III results is the ability of the model to predict results of the quartz lamp tests with accuracy comparable to predictions for the burner rig tests upon which data the model is based. Two significant differences of the quartz lamp tests are the specimen geometry (flat vs cylindrical for burner rig) and the heat flux. The significance of the geometrical difference is its affect on the difference in radial stress state in the ceramic layer. Whereas the cylindrical geometry is expected to develop a small radial stress component resulting from differences in expansion between concentric circular cylinders, the flat specimen, ideally, should be free of this stress component. Apparently, this difference has little influence on the ceramic spallation life. The difference of heat flux results in two differences in thermal conditions between the quartz lamp and burner rig specimens. First, transient heating rates are substantially different, with the quartz lamp heating rate being about three times faster than that achieved in the burner rig. Second, the thermal gradient through the ceramic thickness is about four times larger $\approx 139^{\circ}\text{C}$ ($\approx 250^{\circ}\text{F}$) in the quartz lamp specimen. The ability of the model to predict the higher heat flux test with accuracy equal to that achieved in the burner rig is highly encouraging since the quartz lamp test is a much better simulation of engine conditions than the burner rig.

As mentioned previously, Tests 3 and 4 were conducted to determine if sequence of damage accumulation influenced life and the predictive capability of the model. In Test 3, the specimen accumulated damage at a low rate (low strain range) for approximately 1400 cycles and then was "uploaded" to a higher strain range by increasing peak temperature from 1093°C (2000°F) to 1149°C (2100°F). Specimen 4, on the other hand, accumulated damage at a high strain then range initially and then was "downloaded" from 1149°C (2100°F) to 1093°C (2000°F) peak temperature and cycled to failure, which occurred shortly after downloading. While the two specimens did not run at exactly the same nominally corresponding temperatures because of non-optimum temperature control, the comparison of results shown in Figure 135 is nonetheless interesting. First, consistent with the earlier observation that the model consistently under-predicted the strain emphasis tests in this task, both tests ran longer than predicted. More importantly, however, an apparent sequence effect was observed, with the uploaded specimen having a substantially longer life than the downloaded specimen, despite the difference of actual test temperatures. This result indicates that further modeling refinement would be desirable to account for sequence-of-damage effects.

3.3.2.1 Task IIIB - Microstructural Evaluation

Figures 136-140 present selective photo macro/micrographs from post-verification test specimens. Figure 136 shows the baseline strain emphasis test microstructure. It is apparent that after ~ 1500 cycles only a small amount of the bond coat, Beta (NiAl) phase, has been exhausted to create a very thin $< 0.00254\text{mm}$ ($0.00010''$) continuous Al_2O_3 layer. One unusual observation is that spalling had occurred in two separate locations.

Figure 137 shows the oxide emphasis test which after < 500 cycles exhibits nearly complete exhaustion of the Beta phase in the bond coat near the spalled location. A very thick bond coat surface oxide layer has been formed, and fine in-plane cracks are observed within the Al_2O_3 layer itself.

Figures 138 and 139 show the mixed strain cycle microstructures. As expected, the specimen with greater accumulation of test hours to failure exhibits thicker bond coat scale and a higher degree of Beta phase coarsening.

Figure 140 shows the strain emphasis test specimen microstructure after exposure for ≈ 570 cycles in the quartz lamp heater. Sections were made through the ceramic blister. The microstructure exhibits some segmentation cracking. In the oxide emphasis quartz lamp heater test, ceramic blister formation was also observed in the hot zone location. This blister, which formed early in life, eventually initiated ceramic spallation of 40% of the hot zone location. However, the failure mode is similar to burner rig specimen failure in that ceramic spalling occurs just above the metal-ceramic interface such that a thin layer of remnant ceramic is still adherent to the bond coat when the bulk of ceramic has spalled away.

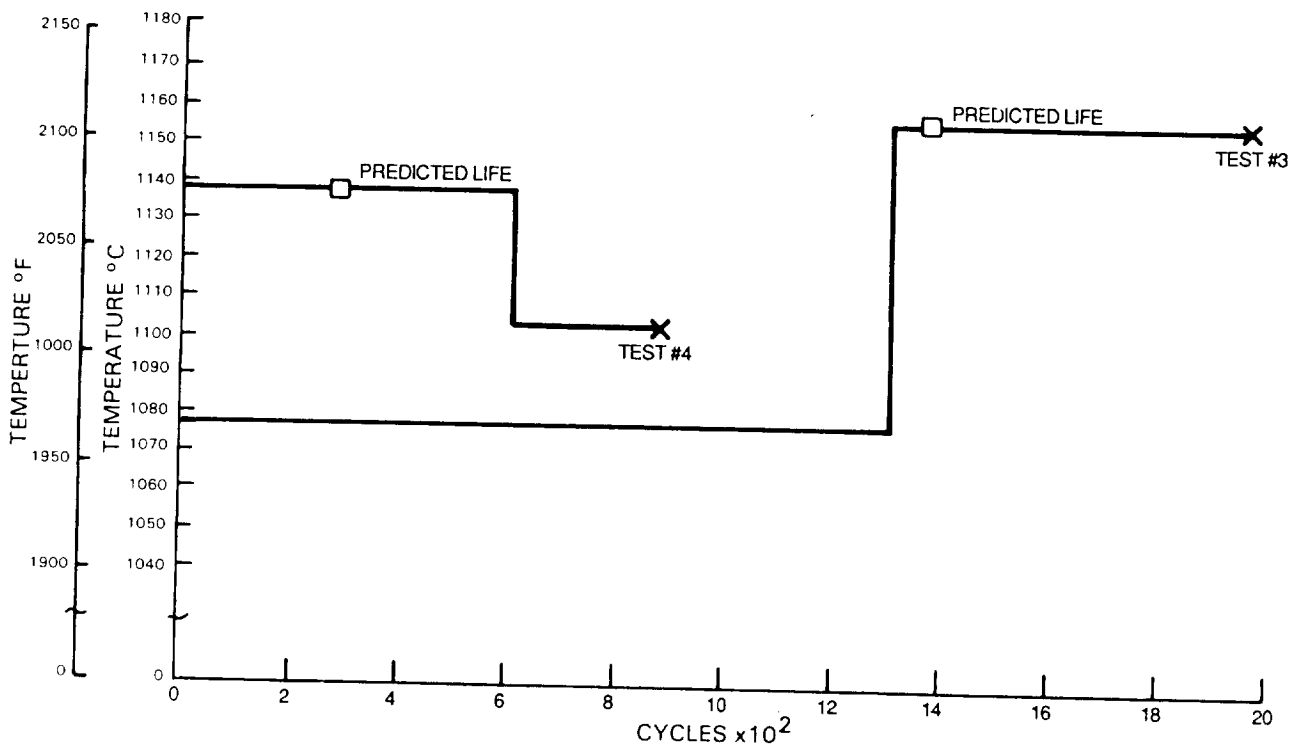


Figure 135 Temperature vs. Cycles to Failure for Task III Mixed Strain Emphasis Tests

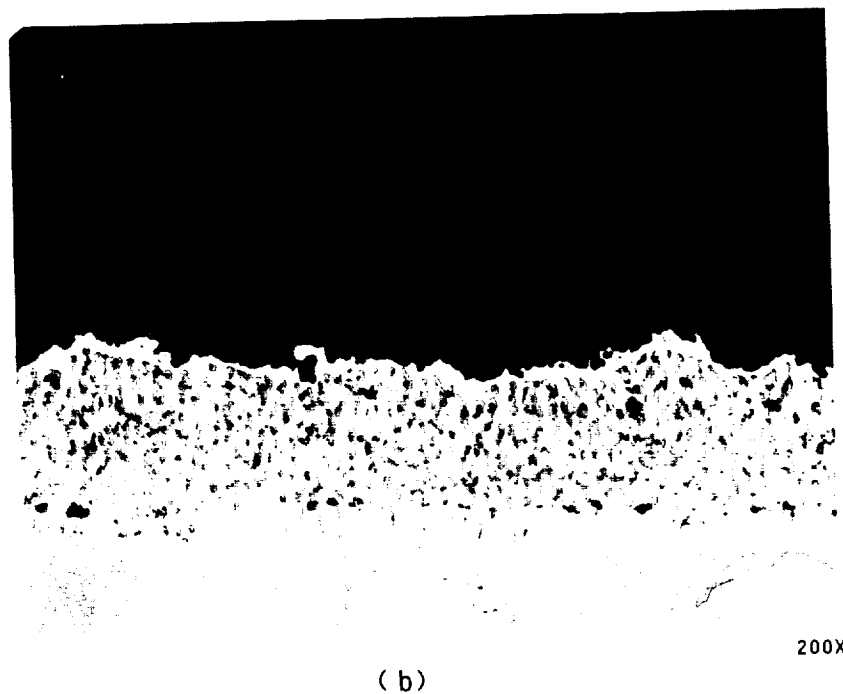
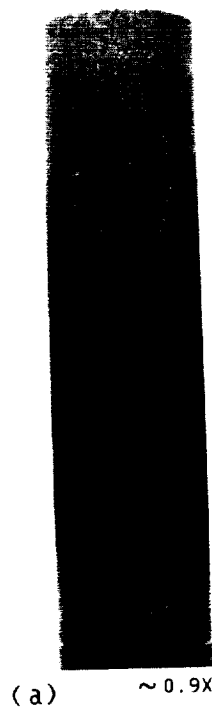
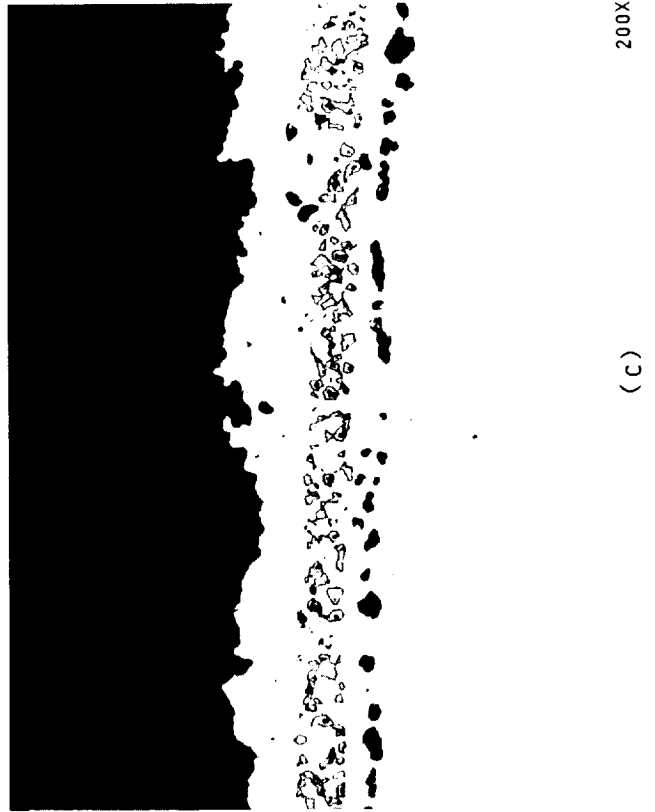
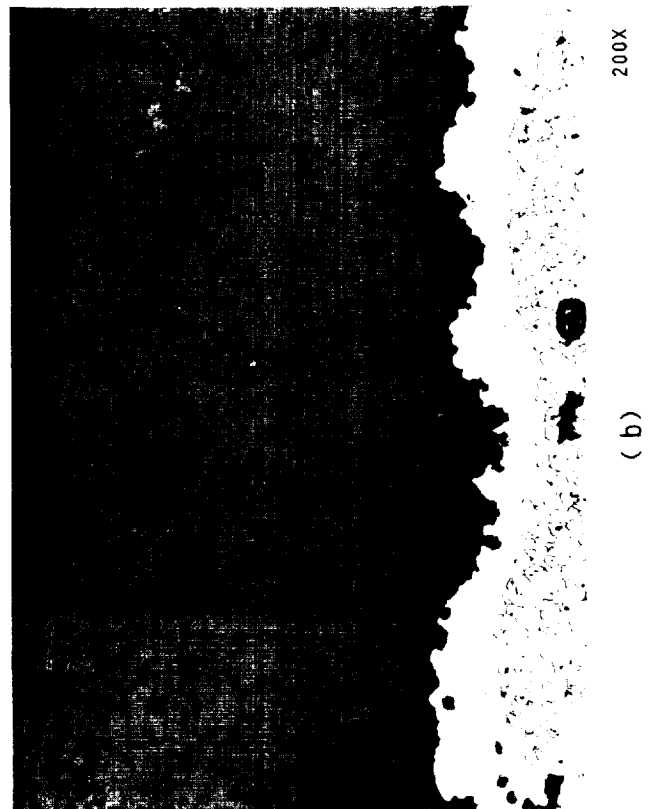


Figure 136 HT-46 Strain Emphasis Burner Rig Verification Test #1
(a) Photomacrograph of Failed Specimen
(b) Post-Test Microstructure

ORIGINAL PAGE
BLACK AND WHITE PHOTOGRAPH

Figure 137 HT-66 Oxide Emphasis Burner Rig
Verification Test #2. 52.8
Hours/396 Cycles, 8 Min. Cycle
(a) Photomacrograph of Failed
Specimen
(b) Post-Test Microstructure
(c) Post-Test Microstructure in
Failure Zone



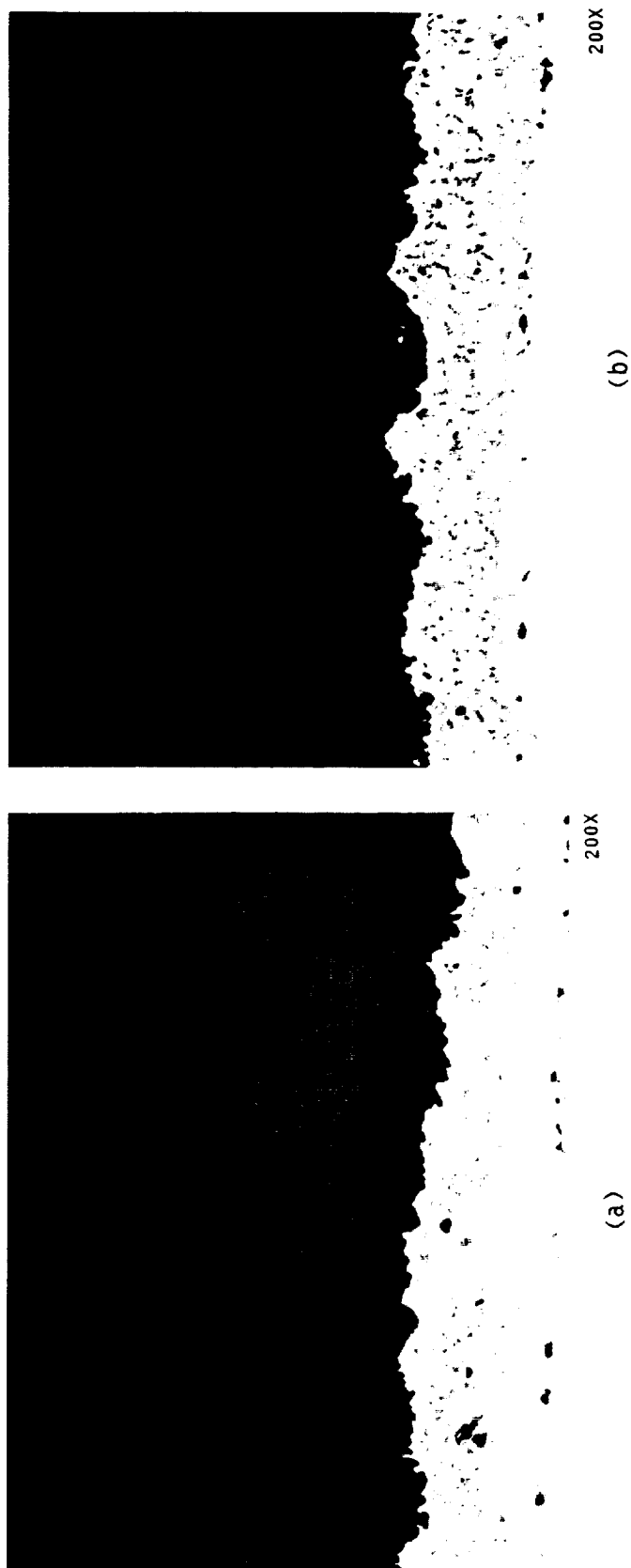


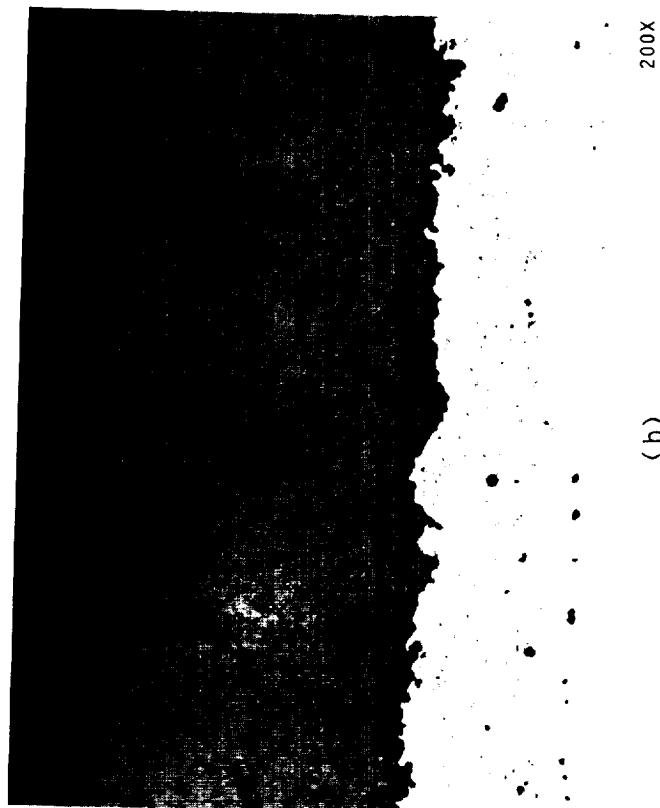
Figure 138 HT-49 Mixed Strain Emphasis Burner Rig Verification Test #3
(a) Post-Test Microstructure
(b) Post-Test Microstructure in Failure Zone

ORIGINAL PAGE
BLACK AND WHITE PHOTOGRAPH

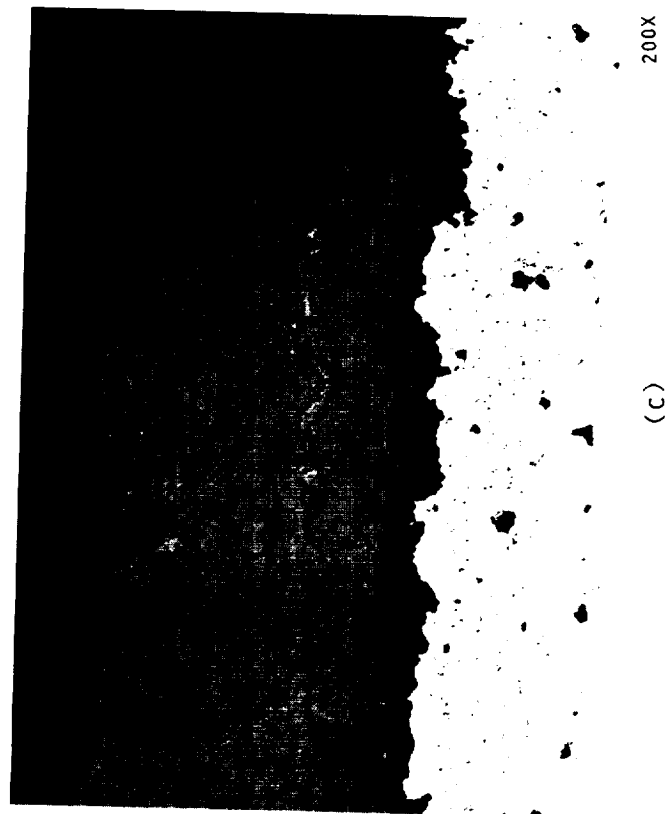
Figure 139 HT-54 Mixed Strain Emphasis
Burner Rig Verification Test #4
(a) Photomacrograph of Failed Specimen
(b) Post-Test Microstructure
(c) Post-Test Microstructure in Failure Zone



1X
(a)



200X
(b)



(c)

200X

ORIGINAL PAGE
BLACK AND WHITE PHOTOGRAPH

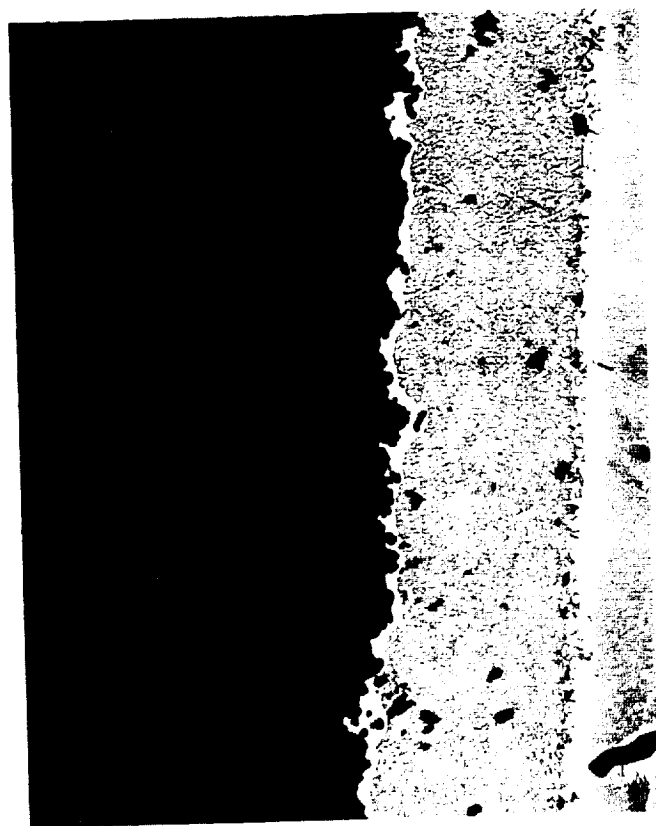


(a) 1X



(b)

200X



(c)

200X

Figure 140 6-124-2 Strain Emphasis Quartz
Lamp Heater Verification Test #5
(a) Photomicrograph of Post Test
Specimen
(b) Post-Test Microstructure
(c) Post-Test Microstructure

4.0 CONCLUSIONS

This final report covers the work accomplished in Phase I of the program. This phase was directed towards identification and modeling of predominant TBC failure modes. It consisted of three technical tasks, the conclusions of which are discussed below.

The objective of Task I was to identify predominant TBC failure modes and develop a preliminary life prediction model. A series of critical experiments were designed and conducted to accomplish this task. Results of these experiments are listed below.

Task I Conclusions:

- o NiCrAlY oxidation is a significant life driver. Low cycle rate furnace testing in air and argon showed a dramatic increase in spalling life for exposure in a nonoxidizing environment. Elevated temperature pre-exposure of the TBC in air caused a proportionate reduction in post-exposure cyclic thermal spalling life, whereas TBC pre-exposure in argon did not.
- o TBC spallation results from progressive damage. Interrupted burner rig tests showed that the predominant ceramic failure mode, near interface ceramic spallation, results from subcritical microcrack link up to form a dominant near-interface, in-plane crack. Bond coat oxidation was not conclusively shown to initiate these subcritical cracks.
- o Ceramic thickness affects coating longevity. Thin coatings (0.127mm (0.005")) showed an increase in spalling life while thick (0.138mm (0.015")) coatings showed a decrease as compared to baseline thickness of 0.254mm (0.010").
- o Cyclic Hot Corrosion was found to be a secondary failure mode. The TBC was shown to be highly resistant to thermochemical degradation in contaminated fuel burner rig experiments.
- o Mechanical Properties of the bulk ceramic were shown to be highly uncharacteristic of classical ceramic materials. The plasma sprayed ceramic exhibits a nonlinear ambient and elevated temperature stress-strain response in uniaxial tension and compression, a strong creep response and extremely stress sensitive fatigue behavior.
- o A preliminary life model was developed. This model focused on two life driving parameters: thermomechanical and oxidation. Environmental damage was analytically accounted for in the model by influencing the intensity of the mechanical driving force.
- o Verification tests showed that the an environmentally modified Manson-Coffin type fatigue model was a good functional form for life prediction of the TBC.

The objective of Task II was to build an advanced TBC life prediction model. Experiments designed, conducted, and analyzed covered a wide range of damage parameter intensities in order to provide a data base for correlation of the life prediction model developed in Task I. The advanced model was established through improved bond oxidation and bulk ceramic behavior modeling.

Task II Conclusions:

- o Twenty critical experiments were designed by using the Task I preliminary life prediction model to predict range of damage and hence dictate testing parameters.
- o Twenty single specimen design data tests were conducted and successfully used to identify the life prediction model constants, δ_c and $\Delta E_{r,o}$.
- o The Kevin Walker Constitutive Model was successfully adapted and used to predict stress-strain hysteresis loops for the bulk ceramic outer layer in the life prediction mode.
- o Oxidation test data obtained from the NASA program manager was used to create an improved bond coat oxide growth rate equation.
- o The advanced life prediction model correlated all the Task II data which represented an extremely wide damage parameter space. This data was correlated within a factor of $\pm 3X$.

The objective of Task III was to design and conduct verification experiments which challenged the advanced, synergetic life prediction model developed.

- o Six experiments were designed and conducted to verify the validity of the life prediction model. The experimental data was predicted within a factor of $\pm 3X$. Two of these six experiments were conducted at heat flux levels substantially closer to engine conditions than those used to generate the model.

REFERENCES

1. Stecura, S., "Effects of Plasma Spray Parameters on Two-Layer Thermal Barrier Coating System Life," NASA TM 81724, 1981.
2. Summer, I. E., "Development of Improved-Durability Plasma Sprayed Ceramic Coatings for Gas Turbine Engine," AIAA/SAE/ASME 16th Joint Propulsion Conference, AIAA-80-1193, 1980.
3. Cassenti, B. N., Brickley, A. M., "Thermal and Stress Analysis of Thermal Barrier Coatings," AIAA-81-1402, 1981.
4. Grot, A. S., Martin, J. K., "Behavior of Plasma Sprayed Ceramic Thermal Barrier Coating for Gas Turbine Engines," American Ceramic Society Bulletin, 60 (8) pp. 807-811, 1981.
5. Anderson, N. P., Sheffler, K. D., "Development of Stain Tolerant Thermal Barrier Coating Systems" Final Report, Tasks I-III, Contract No. NAS3-22548, NASA CR 168251, PWA-5777-29, 1983.
6. Miller, R. A., Levine, S. R., Stecura, S., "Thermal Barrier Coatings for Aircraft Gas Turbines," AIAA 80-0302, 1980.
7. Sheffler, K. D., Graziani, R. A., Sinko, G. C., "JT9D Thermal Barrier Coated Vanes," Final Report, Contract No. NAS3-20630, NASA CR 167964, 1982.
8. Becher, P. F., Rice, R. W., Wu C. Cm., Jones, R. L. "Factors in the Degradation of Ceramic Coating for Turbine Alloys," Thin Solid Films, 53, pp. 225-232, 1978.
9. Gladden, H. J., "Thermal Performance of a Ceramic Coated Turbine Vane Under Transient Gas Conditions," SAE preprint N810205, presented at International Congress and Exposition, Detroit, Michigan Feb. 23-27, 1981.
10. Duvall, D. S., Ruckle, D. L., "Ceramic Thermal Barrier Coatings for Turbine Engine Components," ASME International Gas Turbine Conference and Exhibit, ASME Paper 82-GT-322, 27th, London, England, Apr. 18-22, 1982.
11. Ruckle, D. L., "Plasma-Sprayed Ceramic Thermal Barrier Coatings for Turbine Vane Platforms," Thin Solid Films, 73, pp. 455-461, 1980.
12. Stecura, S., "Two-Layer Thermal Barrier Coating for Turbine Airfoils - Furnace and Burner Rig Test Results," NASA TM X-3425, Sept. 1976.
13. Stecura, S., "Two-Layer Thermal Barrier Coating for High Temperature Components," American Ceramic Society Bulletin, 56 (12), pp. 1082-1089, 1977.
14. Levine S. R., Miller, R. A., Hodge, P. E., "Thermal Barrier Coatings for Heat Engine Components," SAMPE Quarterly, pp. 20-26, 1980.

15. Miller, R. A., Lowell C. E., "Failure Mechanisms of Thermal Barrier Coatings Exposed to Elevated Temperatures," Thin Solid Films, 95, pp. 265-273, 1982.
16. Stecura, S., "Effects of Yttrium, Aluminum and Chromium Concentrations in Bond Coatings on the Performance of Zirconia-Yttria Thermal Barriers," Thin Solid Films, 73, pp. 481-489, 1980.
17. Andersson, C. A., Lau, S. K., Bratton, R. J., Lee, S. Y., Rieke, K. L., "Advanced Ceramic Coating Development for Industrial/Utility Gas Turbine Applications," Final Report DOE/NASA 0110-1, NASA CR-165619, 1982.
18. Miller, R. A., "Oxidation - Based Model for Thermal Barrier Coating Life," J. Am. Cer. Soc., 67 (8), pp. 517-521, 1984.
19. McDonald, G., Hendricks R. C., "Effects of Thermal Cycling on ZrO_2 - Y_2O_3 Thermal Barrier Coatings," Thin Solid Films, 72 (2), pp. 491-496, 1980.
20. Gedwill, M. A., "Burner Rig Evaluation of Thermal Barrier Coating Systems for Nickel Base Alloys", NASA TM 81685, Feb. 1981.
21. Andersson, C. A., "Thermal Stress Fracture of Ceramic Coatings", Fracture Mechanics of Ceramics, Vol. 6: Measurements, Transformation, and High Temperature Fracture, N.Y., Plenum Press, pp. 497-509, 1983.
22. Miller, R.A., Berndt, C.C., "Performance of Thermal Barrier Coatings in High Heat Flux Environments," Thin Solid Films, 119, pp. 195-202, 1984.
23. Harding, A. G., Adam, T. "Thermal Stress in Ceramics Applied as Thermal Barrier Layers to Turbine Blades," British Ceramic Society Transactions, 65 (5), pp. 289-307, 1965.
24. Miller, R. A., Smialek, J. L., Garlick, R. G., "Phase Stability in Plasma Sprayed Partially Stabilized Zirconia-Yttria" Advances in Ceramics, Vol. 3, pp. 241-253, 1981.
25. Miller, R. A., Garlick, R. G., Smialek, J. L., "Phase Distributions in Plasma Sprayed Zirconia-Yttria," American Ceramic Society Bulletin, 62 (12), pp. 1355-1358, 1983.
26. Rice, R. W., Pahanke, R. C., McDonough, W. J., "Effect of Stresses from Thermal Expansion Anisotropy, Phase Transformation and Second Phases on the Strength of Ceramics," J. Am. Cer. Soc., 63 (11-12), pp. 703-710, 1980.
27. Berndt, C. C., Herman, H., "Anisotropic Thermal Expansion Effects in Plasma Sprayed ZrO_2 -8% Y_2O_3 Coatings," Ceramic Engineering and Science Proceedings, Vol. 4, pp. 792-801, 1983.

28. Stecura, S., "Two-Layer Thermal Barrier Systems for Ni-Al-Mo Alloy and Effects of Alloy Thermal Expansion on System Life," American Ceramic Society Bulletin, 61 (2), pp. 256-262, 1982.
29. Bevan, C. E., "Development of Advanced Plasma Sprayed Ceramic Coatings for Industrial Gas Turbine Engines" Final Report, DOE/Batelle Subcontract B-A0747-A-Z, PWA 5906, 1982.
30. Miller, R. A., "Analysis of the Response of a Thermal Barrier Coating to Sodium and Vanadium Doped Combustion Cases," DOE/NASA 2593-79/7, NASA TM 79205, 1979.
31. Hodge, P. E., Stecura, S., Gedwill, M. A., Zaplatynsky, I., Levine, S. R., "Thermal Barrier Coating: Burner Rig Hot Corrosion Test Results," J. Materials for Energy Systems, 1, pp. 47-58, March 1980.
32. Hodge, P. E., Miller, R. A., Gedwill, M. A., "Evaluation of Hot Corrosion Behavior of Thermal Barrier Coatings", Thin Solid Films, 73 (2), pp. 447-453, 1980.
33. Pettit, F. S., Goward, G. W., "High Temperature Corrosion and use of Coatings for Protection," Metallurgical Treatises, Metallurgical Society of AIME, pp. 603-619, 1983.
34. Lau, S. K., Bratton, R. J., "Degradation Mechanisms of Ceramic Thermal Barrier Coatings in Corrosion Environments," High Temperature Protective Coatings Proceedings of the Symposium, Atlanta, Georgia, March 7, 8, 1983 Metallurgical Society of AIME, pp. 305-317, 1984, .
35. Barkalow, R. H., "Hot Corrosion of Ceramic Coating Materials for Industrial/Utility Gas Turbines," DOE No.DE-AC-03-78ET15236, Ref. No. 81-200-7003-FR, Jan. 1981.
36. Hamilton, J. C., Nagelberg, A. S., "In Situ Raman Spectroscopic Study of Yttria-Stabilized Zirconia Attack by Molten Sodium Vanadate," J. Am. Cer. Soc., 67 (10), pp. 686-690, 1984.
37. Miller, R. A., Argarwal, P., Duderstadt, E. C., "Life Modelling of Atmospheric and Low Pressure Plasma Sprayed Thermal Barrier Coatings," Ceramic and Engineering Science Proceedings, 5 (7-8), pp. 470-478, July-Aug. 1984.
38. Shankar, R. N., Berndt, C. C., Herman, H., "Phase Analysis of Plasma Sprayed Zirconia-Yttria Coatings," Ceramic Engineering and Science Proceedings, Vol. 4, pp. 784-787, 1983.
39. Shaw, M. C., Braiden, P. M., DeSalvo, G. J., "The Disk Test for Brittle Materials". Transactions of the ASME, Journal of Engineering for Industry Paper No. 73-WA/Prod-17, pp. 1-11, 1973.
40. Walker, K. P., "Research and Development Program for Nonlinear Structural Modeling With Advanced Time-Temperature Dependent Constitutive Relationships," NASA CR-165533.

APPENDIX A

SUMMARY OF WEIGHT GAIN DATA FOR FURNACE EXPOSED SPECIMENS

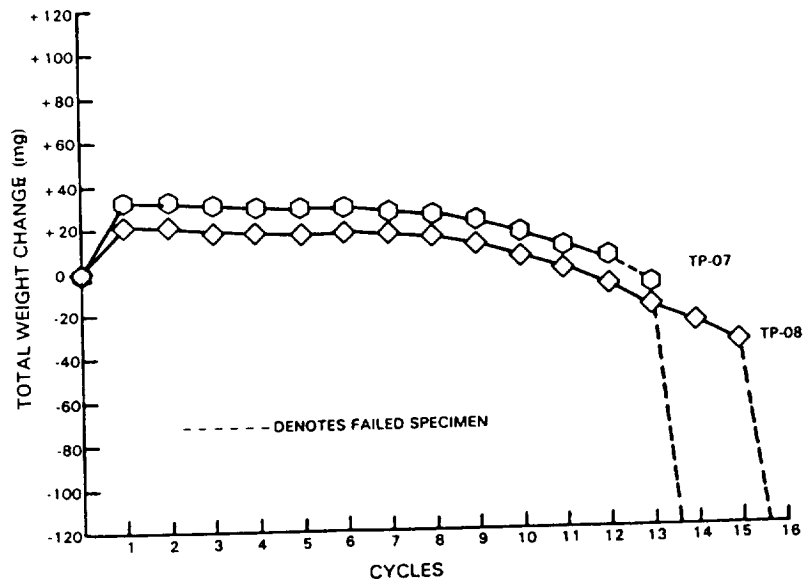


Figure A-1 Task I Furnace Test Results: Weight Change Versus Cycles for 1149°C (2100°F), Air, 10 Hour Cycle

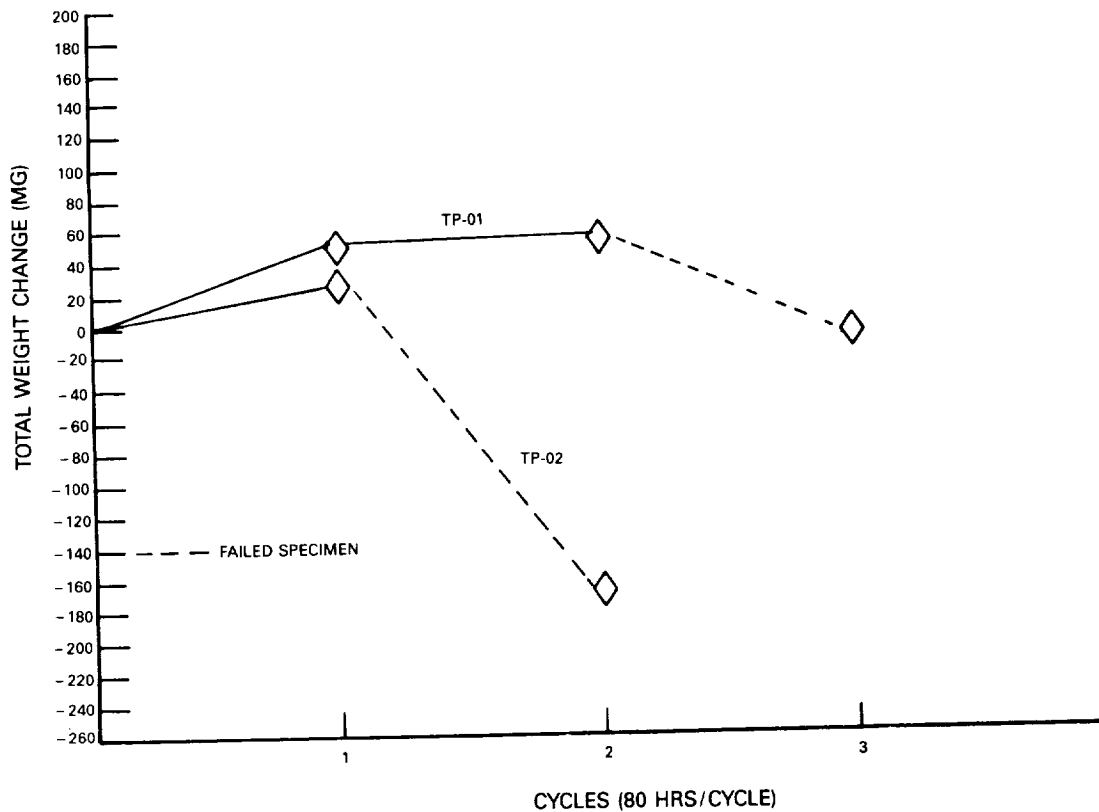


Figure A-2 Task I Furnace Test Results: Weight Change Versus Cycles for 1149°C (2100°F), Air, 80 Hour Cycle

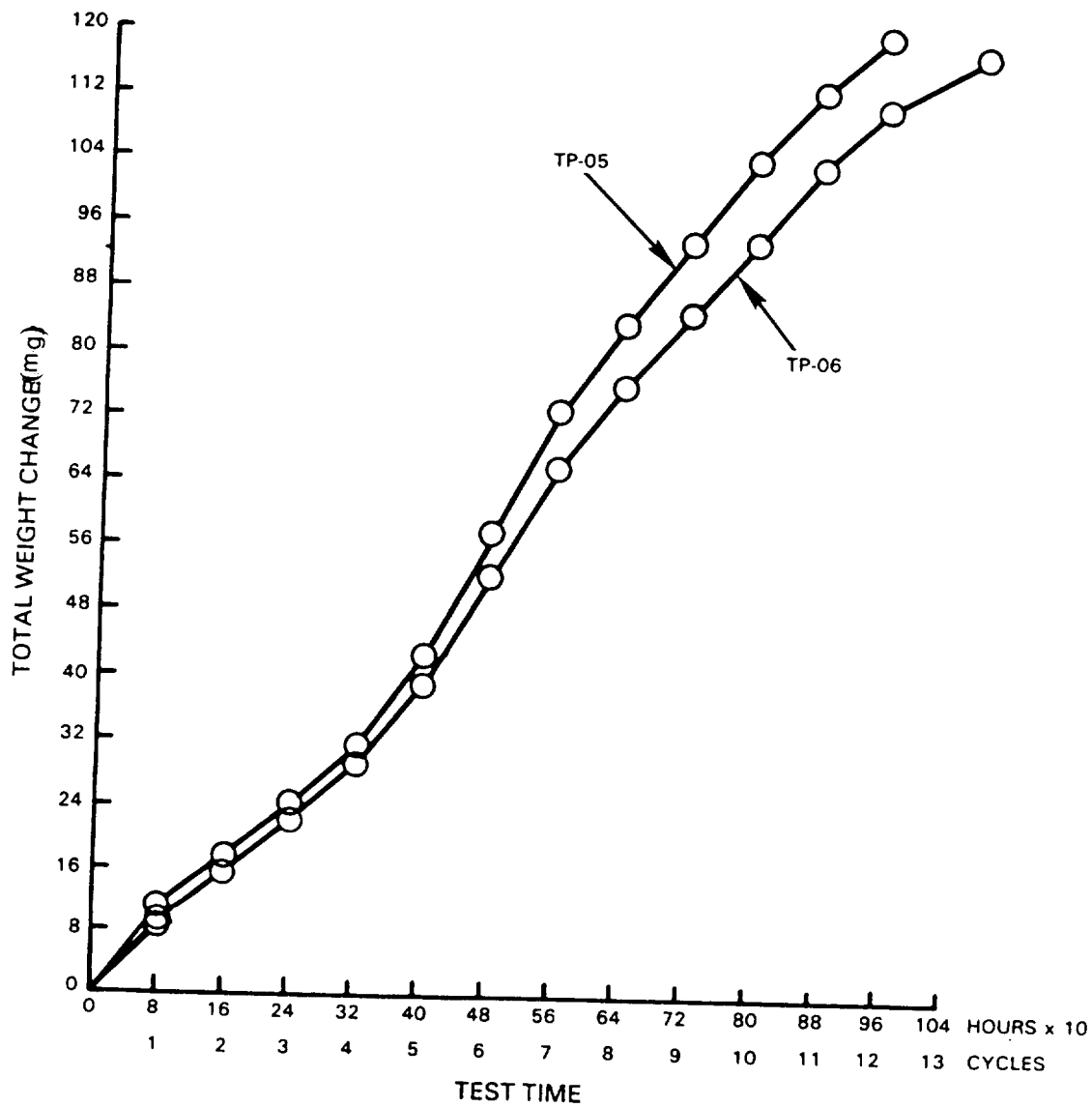


Figure A-3 Task I Furnace Test Results; Weight Change Versus Cycles for 1149°C (2100°F), Argon, 80 Hour Cycle

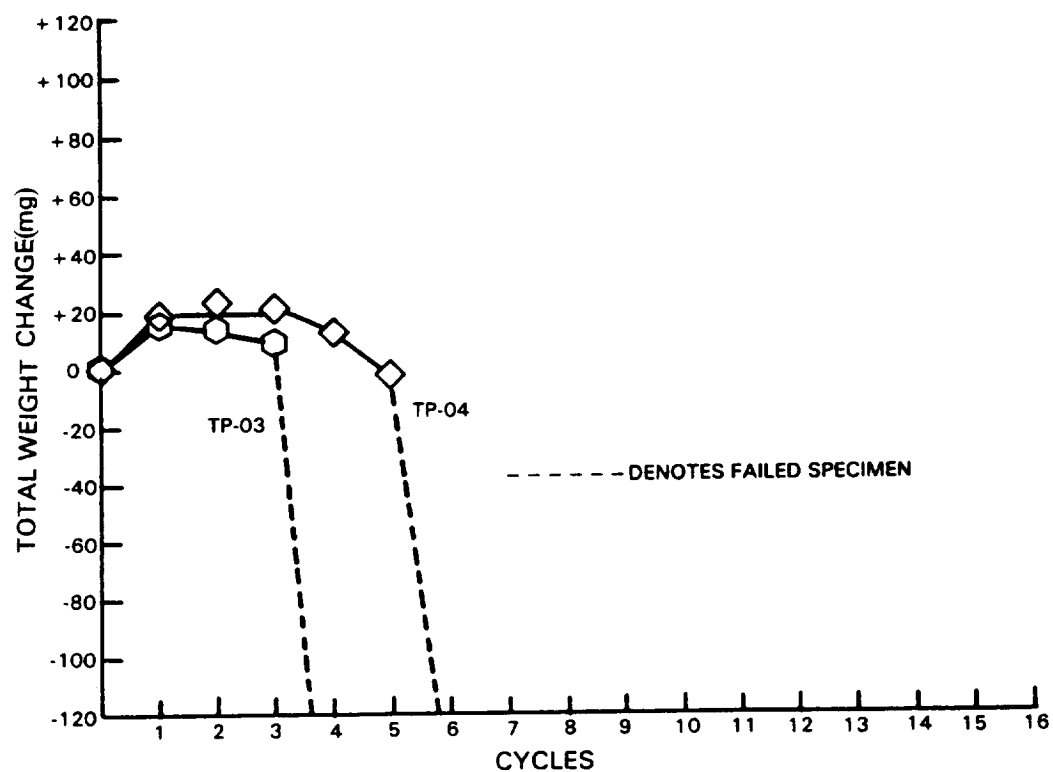


Figure A-4 Task I Furnace Test Results; Weight Change Versus Cycles for 1204°C (2200°F), Air, 10 Hour Cycle

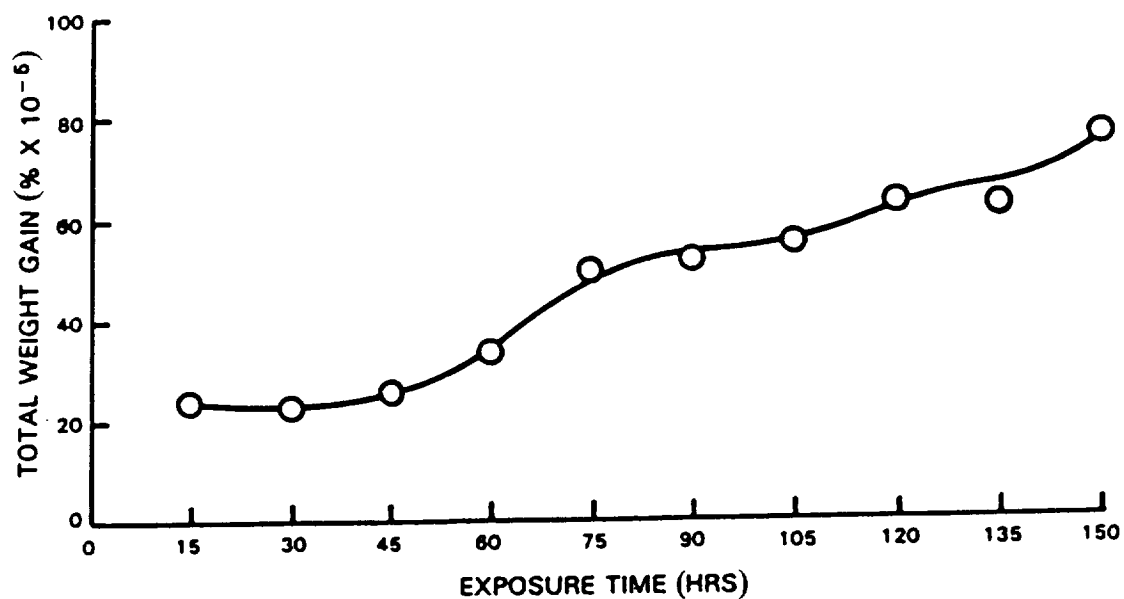


Figure A-5 Task I Furnace Test Results; Weight Change Exposure Time for Fractional Exposure Test, 1149°C (2100°F), Air, 15 Hour Cycle

APPENDIX B

CYCLIC BURNER RIG TEST DETAILS

The uncooled burner rig test employed in Task I involves cyclic flame heating and forced air cooling of coated cylindrical test specimens. A set of 12 specimens are installed on a spindle per test set at one time. These bars are rotated in the exhaust gases of a jet fuel burner rig to provide a uniform temperature for all specimens. The exhaust gases are the combustion products of Jet A fuel and air, with a velocity of Mach 0.3. Specimen temperature is controlled using an optical pyrometer and automatic feedback controller.

During rig operation the fuel pressure is regulated automatically to maintain the desired temperature. To provide cyclic cooling, the burner is automatically moved away from the specimens for the cool-down portion of the cycle, during which a compressed air blast is applied to the specimens. The test rig is shown in Figure B-1. Testing is interrupted approximately every 20 hours to allow for visual examination of the specimens. Failure is considered to have occurred when spallation occurs over approximately 50 percent of the "test" zone of the bar. The "test" zone includes an area which is approximately 2.5 cm (1 inch) long at the center of the exposed portion of the bar, having a uniform temperature during testing. This failure criterion recognizes that some ceramic loss may occur without severe degradation of the protective nature of the ceramic. It should be noted that, once initiated, spallation failure propagates relatively rapidly so that, the stated coating life is not highly sensitive to end point definitions.

In order to further maintain of reliable test temperatures with good repeatability, one of the twelve 12.7mm (0.5") diameter test bars was replaced with a coated specimen with two internal passages for the routing of thermocouple sensors. One passage was an axial hole 4.318mm (0.170") diameter through the entire length of the specimen. The other hole also penetrated the bar parallel to the axis but was located 50% of the distance between the circumference of the aforementioned 4.138mm (0.170") hole and the outside diameter of the specimen. This passage extended approximately 31.75mm (1.25") down from the tip of the bar and was of 1.016mm (0.040") diameter to accept a 0.8128mm (0.032") thermocouple sensor. The specimen geometry is shown in Figure B-2. This specimen is installed in the test cluster with the sensor located in the trailing edge or inside diameter wall of the bar. Thermocouple leads are routed down the specimen drive unit through a slip-ring and finally to a recording device.

By correlating optical pyrometer values with thermocouple readings, optical controller set points are established daily with the thermocouple, thus, avoiding drift of the test specimen temperature resulting from gradual ceramic emissivity changes.

An alternate specimen was also designed and has seen limited application. Essentially, this specimen is utilized similar to the previously described type, except there is no 4.138mm (0.170") I.D. center hole, and there are three, rather than one, thermocouple holes, each terminating within different longitudinal points in the specimen/cluster hot zone.

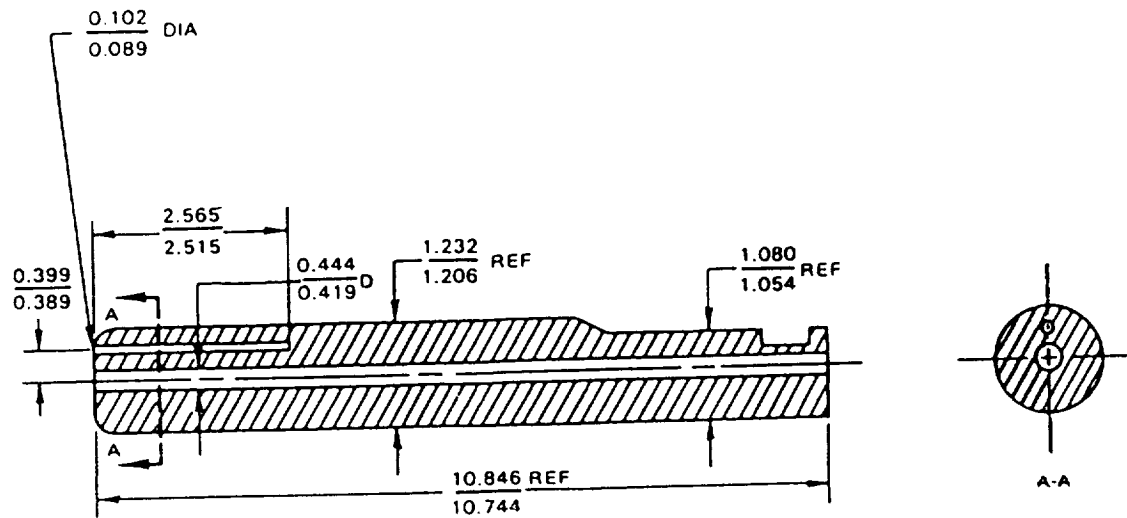


Figure B-1 Diagram of Thermocoupled Specimen Used for Burner Rig Testing. Dimensions are expressed in centimeters.

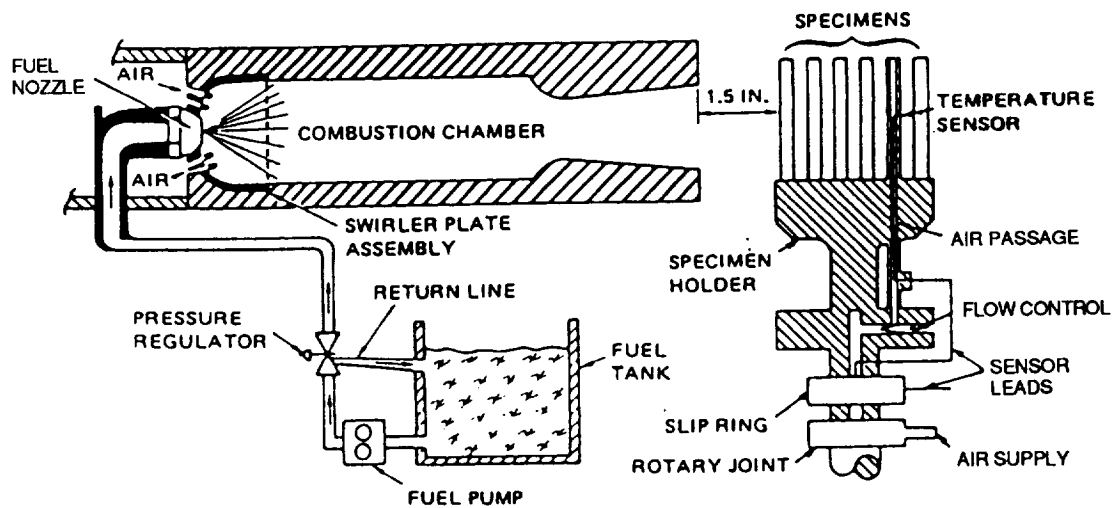


Figure B-2 Schematic Diagram of Cyclic Burner Rig Test Apparatus for Task I

APPENDIX C

CORROSION BURNER RIG TEST DETAILS

A cyclic hot corrosion test was utilized in Task I to aid in defining the capability of the coating system under simulated field service conditions. Specific test conditions were selected to model a mixed oxidation-hot corrosion type of exposure encountered in relatively high temperature aircraft turbine exposure with "clean" fuels and moderate atmospheric contaminants.

Intensive study of hot corrosion phenomena at Pratt & Whitney has shown that the primary contaminants responsible for hot corrosion attack in aircraft turbine engines operating on clean fuels are sea salt from near ground level air (ingested during take-off) and sulfur trioxides from the combustion gases. A comprehensive analysis of hot corrosion mechanisms has shown conclusively that acidification of contaminant salt deposits by sulfur trioxide is critically related to turbine hot corrosion and that meaningful laboratory hot corrosion testing requires that the activity of SO_3 be maintained at levels characteristic of turbine operation. Accordingly, the hot corrosion test rig used in Task I provides for control of both salt contaminant loading and for control of combustion gas composition by effectively limiting excess dilution air.

The test rig used in the hot corrosion exposure evaluation was specifically designed for evaluation of turbine materials in contaminated environmental conditions. The rig is similar to that previously described in Appendix A for oxidation test evaluation in that it maintains full automatic control of test temperature and cooling cycles and features a special rotating specimen mounting fixture with internal specimen cooling air. This fixture provides for simultaneous testing of twelve air-cooled specimens. There is also provision for metered injection of contaminants to allow accurate simulation of aircraft turbine environments. Temperature control of the hot corrosion test rig is conducted in the same manner as previously discussed for oxidation test rigs.

The major modification in the hot corrosion test rig is that the cooled specimen cluster is operated inside a burner exhaust gas duct as shown schematically in Figure C-1. This duct exhaust allows specific restriction of ambient air dilution and consequently provides for optimum control of the level of exhaust gas sulfur and air contaminants.

The hot corrosion test conditions used in Task I simulate typical hot corrosion conditions encountered in near ground aircraft engine operation. Selection of the 899°C (1650°F) ceramic surface temperature was based on conditions that exist where major salt loading from atmosphere contamination occurs. The test cycle was the same as that used for cyclic oxidation testing, i.e., 57 minutes in the flame and 3 minutes for air cooling.

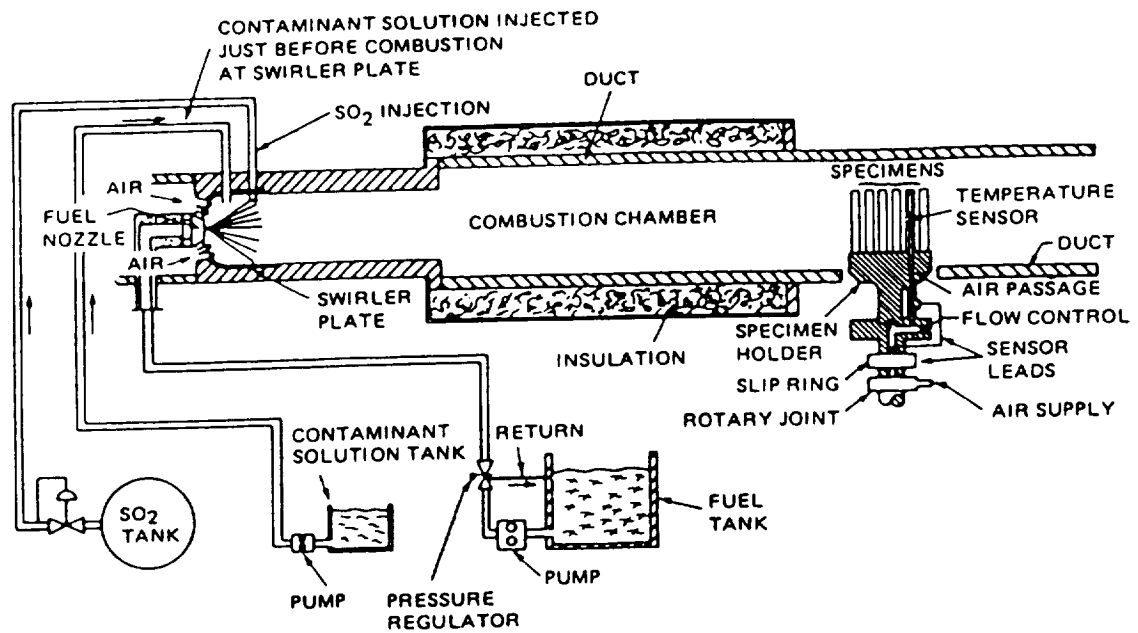


Figure C-1 Schematic Diagram of Ducted Burner Rig Test Apparatus for Task I Hot Corrosion Exposure. Test specimens are enclosed to allow precise control of SO_3 and other contaminants.

APPENDIX D

EXPERIMENTAL PROCEDURES USED TO MEASURE PHYSICAL PROPERTIES

Thermal Conductivity - A comparative method was used to determine thermal conductivity. The sample was instrumented with thermocouples and placed between two instrumented reference standards of identical geometry to the sample. The composite stack was fitted between an upper heater and lower heater, and the complete system was placed on a liquid cooled heat sink. A load was applied to the top of the system and a thermal guard which could be heated or cooled was placed around the system.

A temperature gradient was established in the stack; radial heat loss was minimized by establishing a similar gradient in the guard tube. The system reached equilibrium after which successive readings of temperatures at various points were averaged and evaluated. From this data, heat flux was determined and specimen thermal conductivity was calculated. The results are shown in Tables XIX and XXII of the main body of this report for the bulk ceramic and metallic specimens, respectively.

Specific Heat - The specific heat was determined using a high temperature calibrated copper drop calorimeter. The sample was attached to a 3mm platinum support wire and suspended vertically at the center of a three-zone controlled temperature furnace with the sample resting upon the receiver below it. Thermocouples were attached such that junctions touched the sample near the top and bottom.

The sample was allowed to attain a selected equilibrium temperature for a period of time on the order of 1-2 hours then regular readings of the thermocouple were taken. At a given time, the radiation shields moved to allow the sample to fall and come to rest in the receiver. When the sample came to rest, these shields returned to the original position to reduce any radiation heat transfer from the furnace to the receiver or convective and radiant heat transfer from the receiver to the outside. The temperature of the copper receiver was taken regularly. Following a drop, the receiver system was allowed to come to equilibrium on the order of two hours. The specific heat was calculated at selected temperature by differentiation and substitution and is shown in Tables XX and XXIII of the main body of this report for the bulk ceramic and metallic specimens, respectively.

Thermal Expansion - The room temperature length of each specimen was measured before the test. The specimen was then placed in an electronic automatic recording dilatometer and a thermocouple placed in contact with the center of the sample. An environmental chamber which controlled the temperature at constant rates surrounded the system. The dilatometer was allowed to run with length and the temperature recorded continuously and autographically. The results tested are given in Tables XXI and XXIV of the main body of this report for the bulk ceramic and metallic specimens, respectively.

APPENDIX E

STRESS-STRAIN AND CREEP CURVES FOR ALL MECHANICAL PROPERTY
TESTS CONDUCTED AT SOUTHWEST RESEARCH INSTITUTE

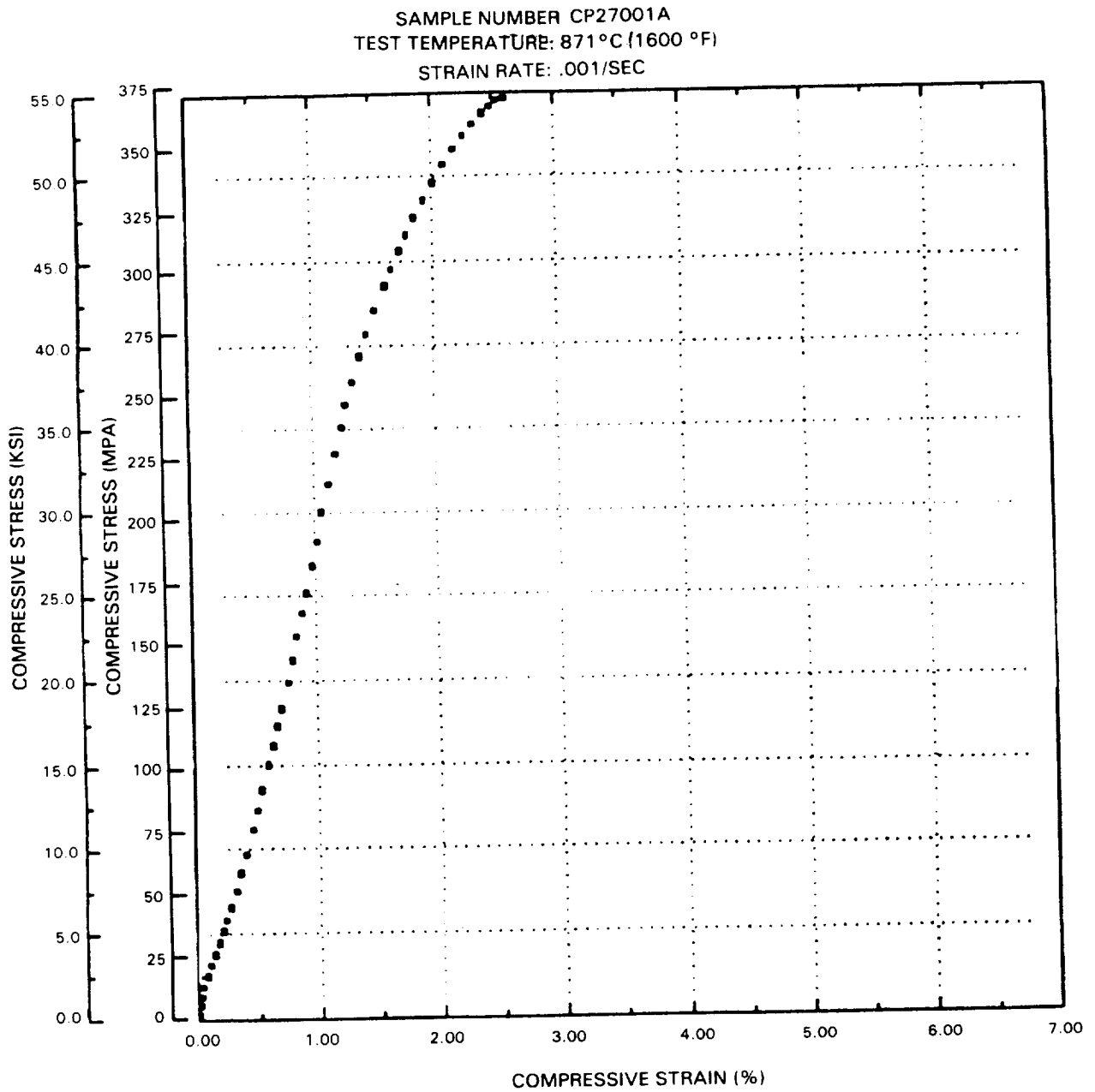


Figure E-1 Compression Stress-Strain (538°C (1000°F))

SAMPLE NUMBER CP27001A
TEST TEMPERATURE: 871°C (1600 °F)
STRAIN RATE: .001/SEC

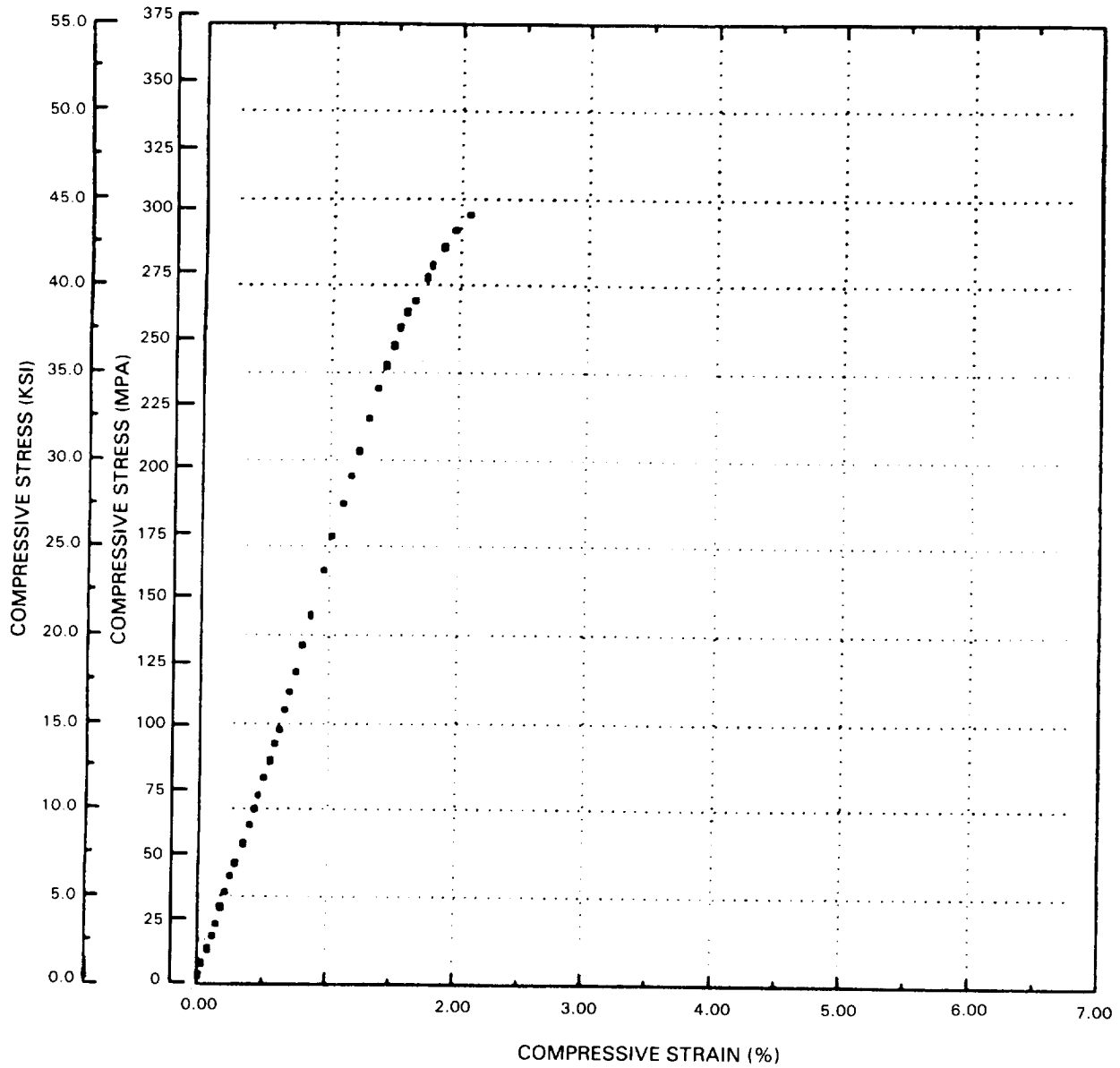


Figure E-2 Compression Stress-Strain (871°C (1600°F))

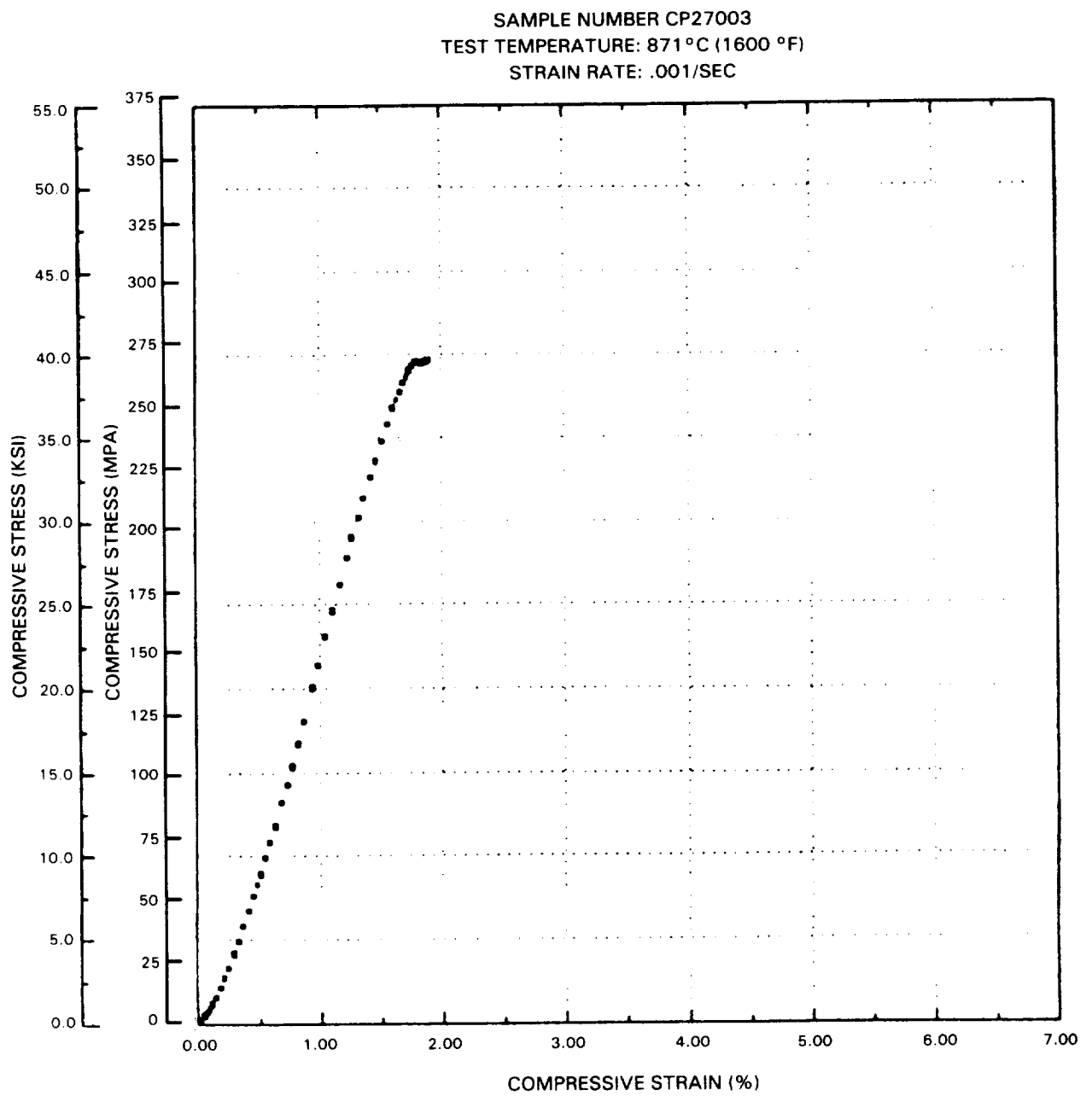


Figure E-3 Compression Stress-Strain (871°C (1600°F))

SAMPLE NUMBER CP27001B
TEST TEMPERATURE: 1204°C (2200 °F)
STRAIN RATE: .001/SEC

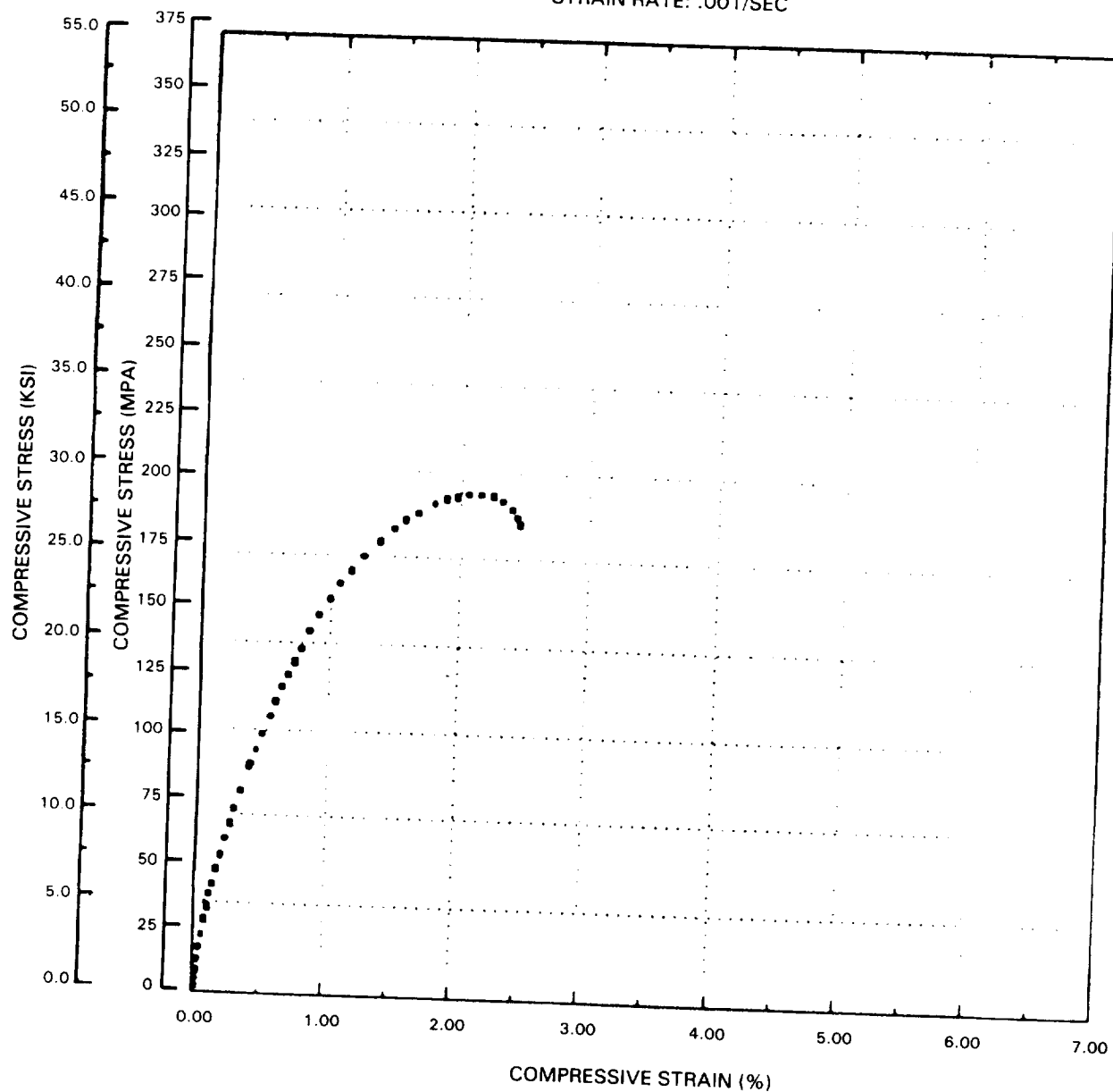


Figure E-4 Compression Stress-Strain (1204°C (2200°F))

SAMPLE NUMBER CP27002
TEST TEMPERATURE: 1204°C (2200 °F)
STRAIN RATE: .001/SEC

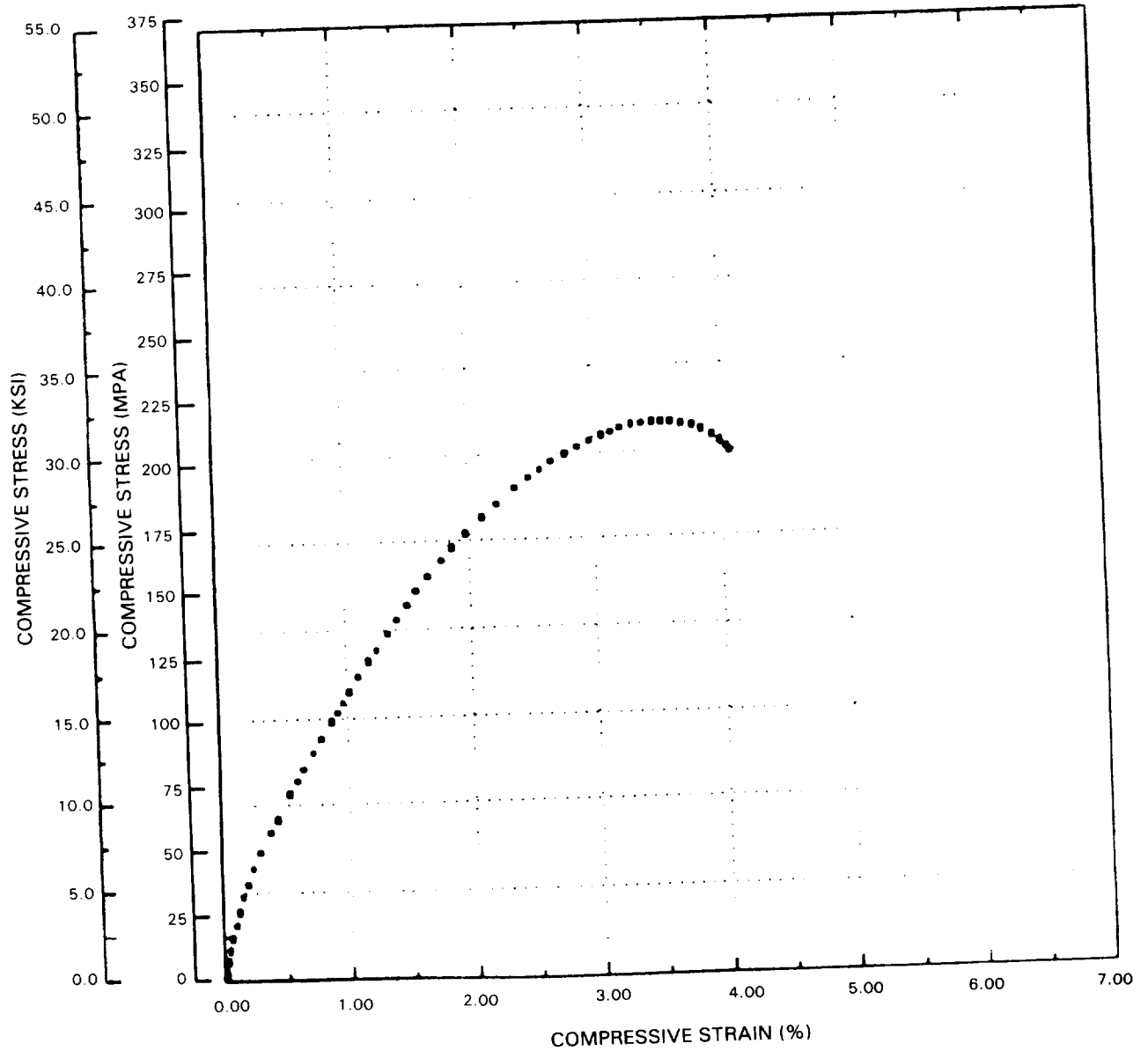


Figure E-5 Compression Stress-Strain (1204°C (2200°F))

SAMPLE NUMBER CP27004
TEST TEMPERATURE: 1204°C (2200 °F)
STRAIN RATE: .001/SEC

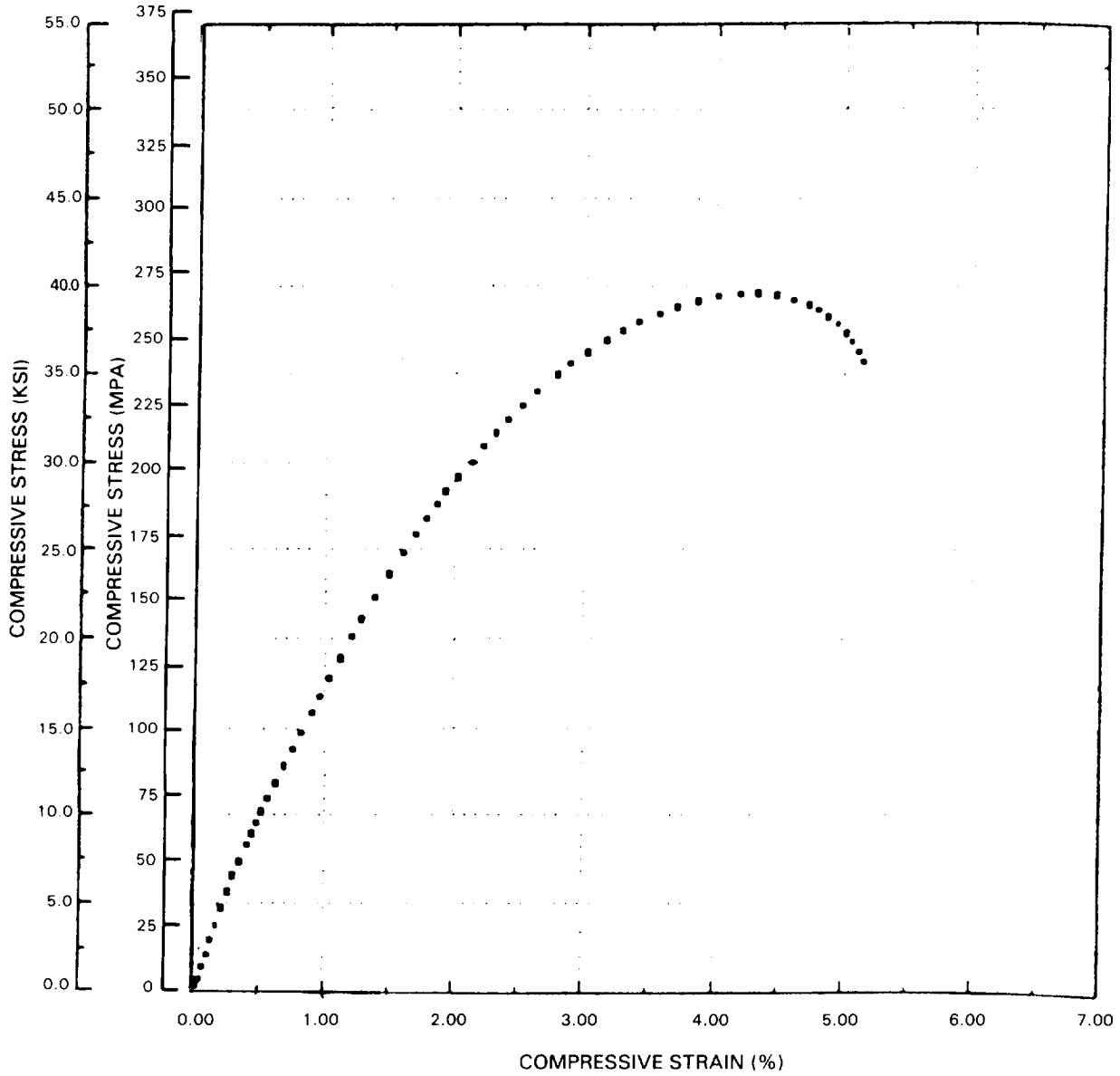


Figure E-6 Compression Stress-Strain (1204°C (2200°F))

SAMPLE NUMBER EC1
TEST TEMPERATURE: 24°C (75°F)
STRAIN RATE: .001/SEC

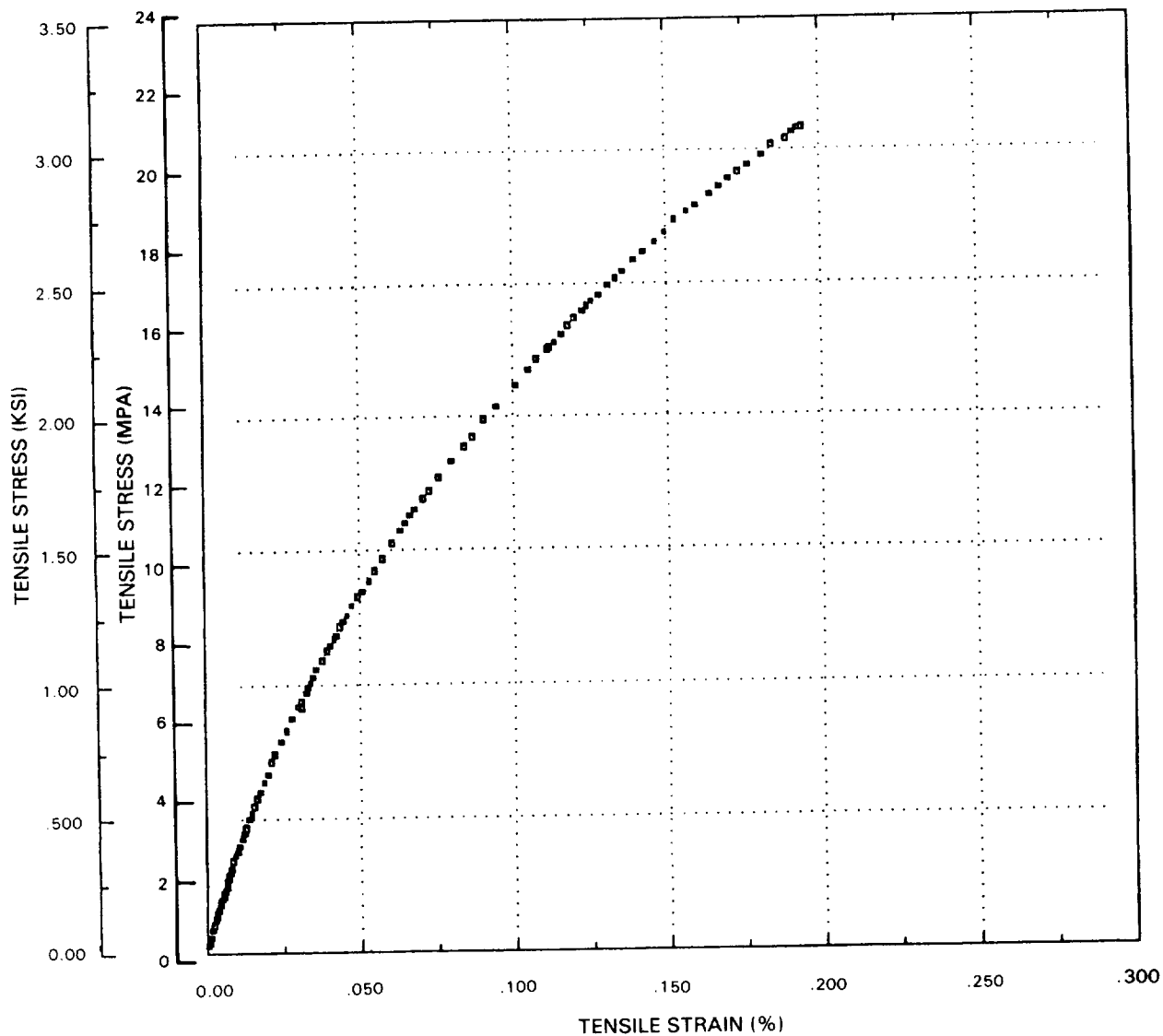


Figure E-7 Tension Stress-Strain (24°C (75°F))

SAMPLE NUMBER CP24
TEST TEMPERATURE: 538°C (1000 °F)
STRAIN RATE: .001/SEC

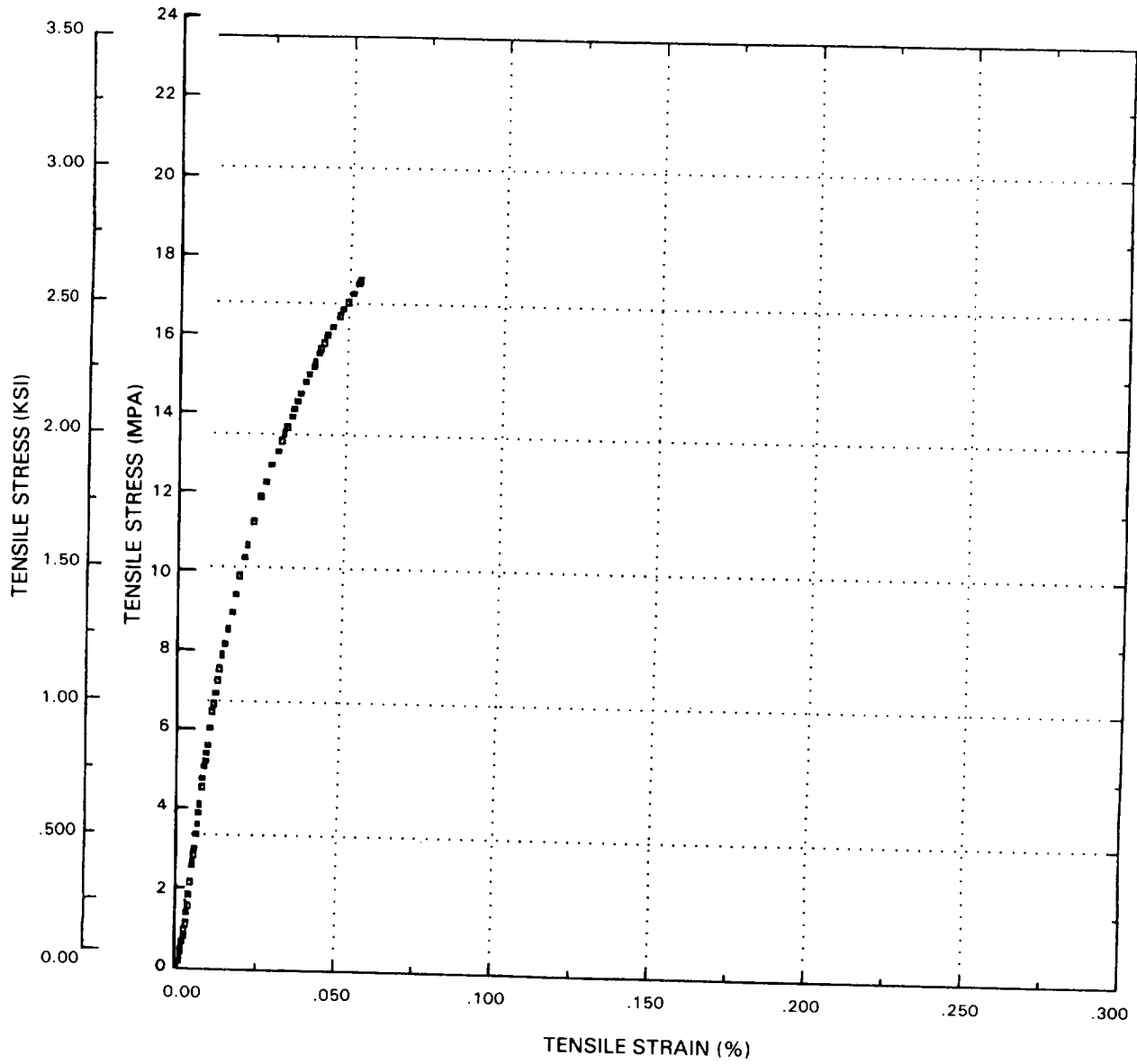


Figure E-8 Tension Stress-Strain (538°C (1000°F))

SAMPLE NUMBER EC2
TEST TEMPERATURE: 538°C (1000 °F)
STRAIN RATE: .001/SEC

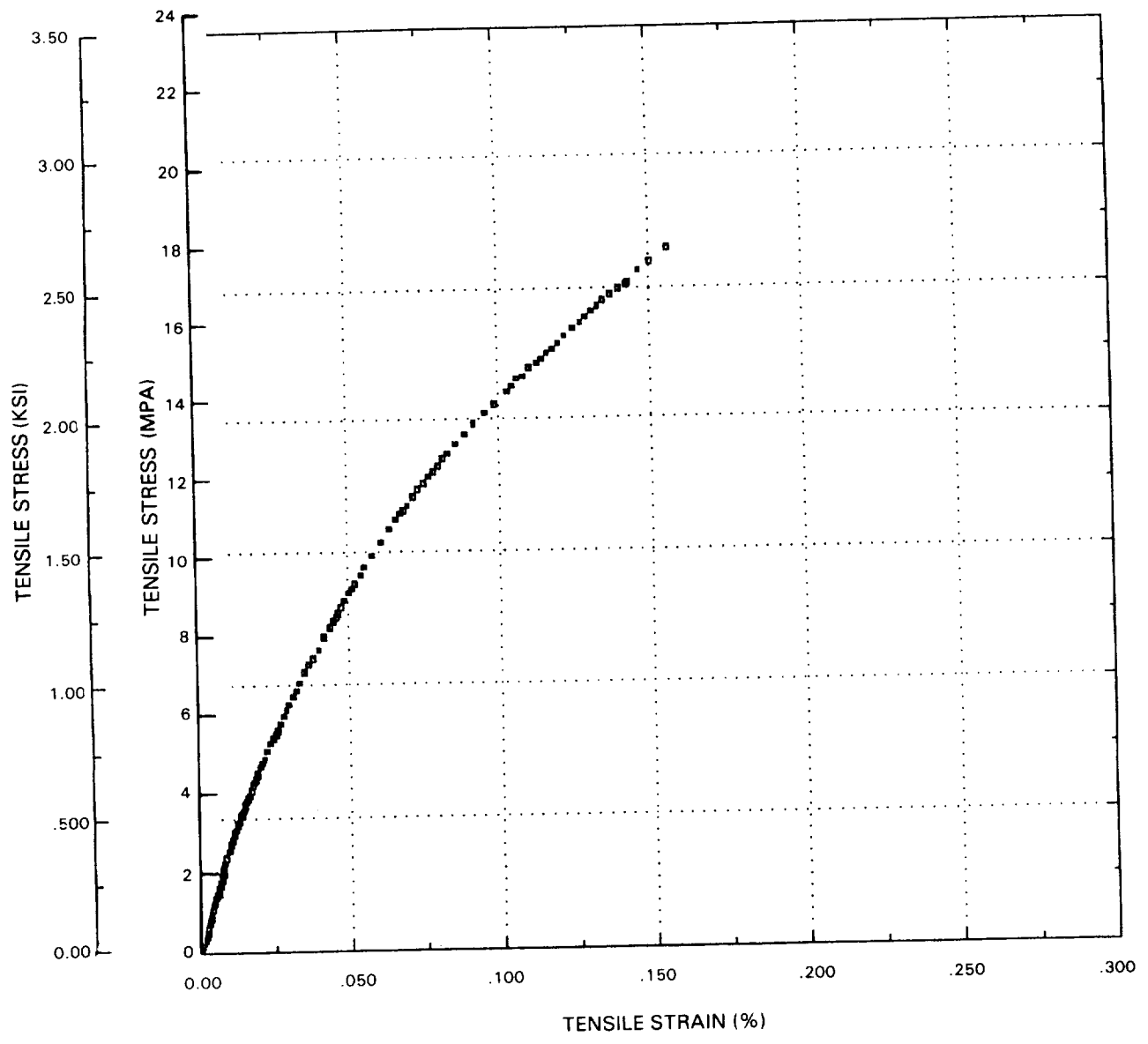


Figure E-9 Tension Stress-Strain (538°C (1000°F))

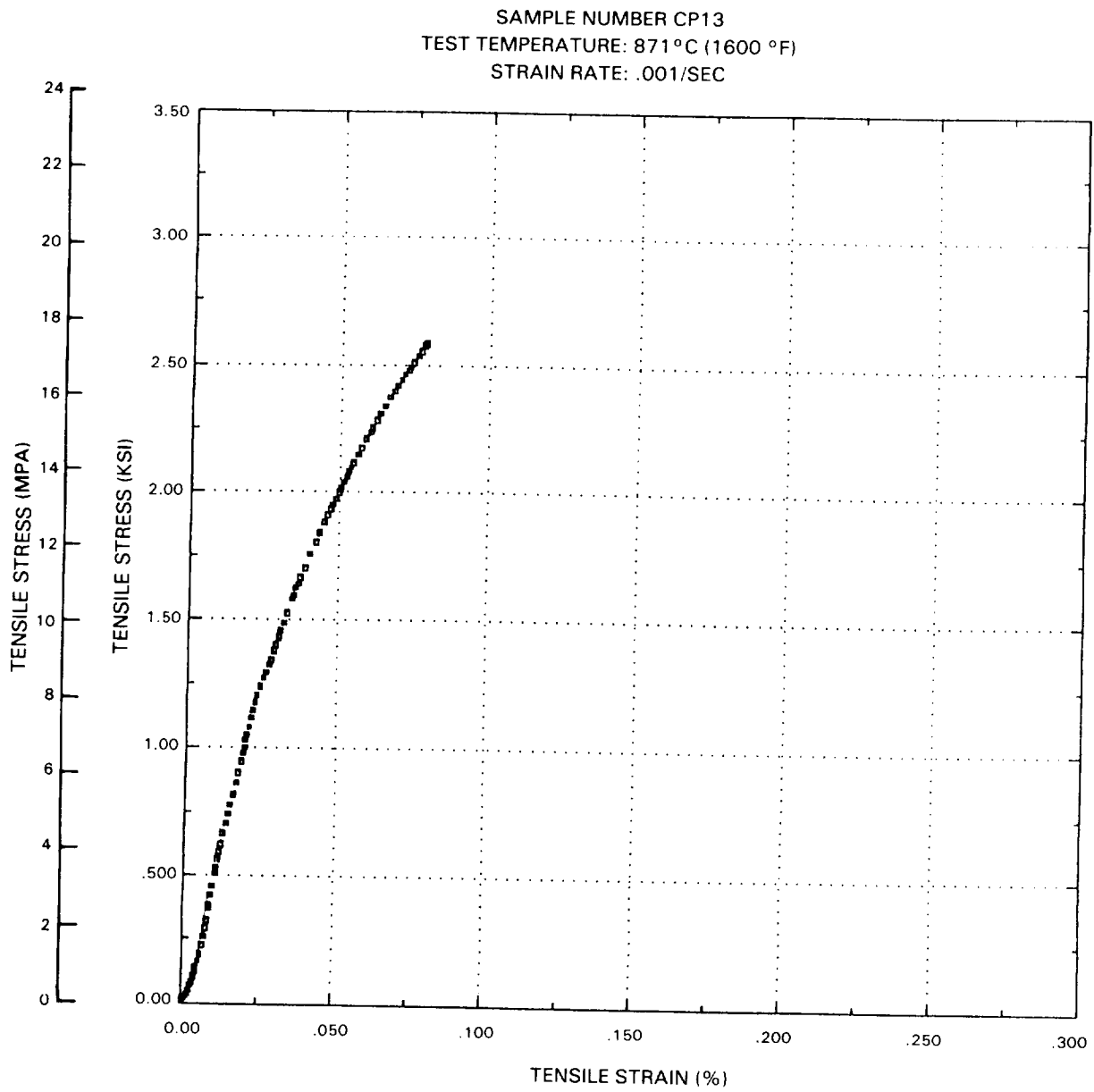


Figure E-10 Tension Stress-Strain (871°C (1600°F))

SAMPLE NUMBER CP14
TEST TEMPERATURE: 871°C (1600 °F)
STRAIN RATE: .001/SEC

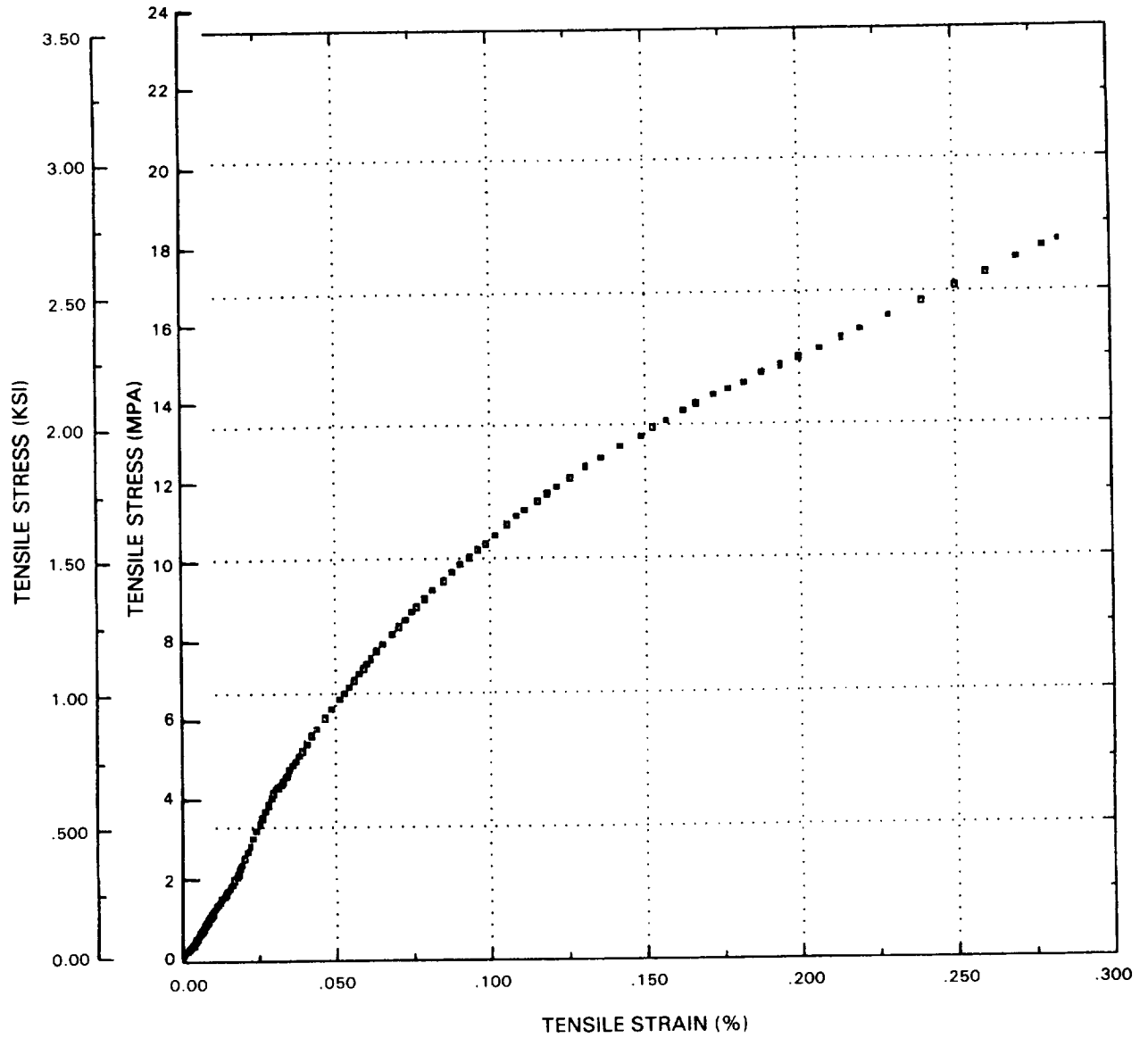


Figure E-11 Tension Stress-Strain (871°C (1600°F))

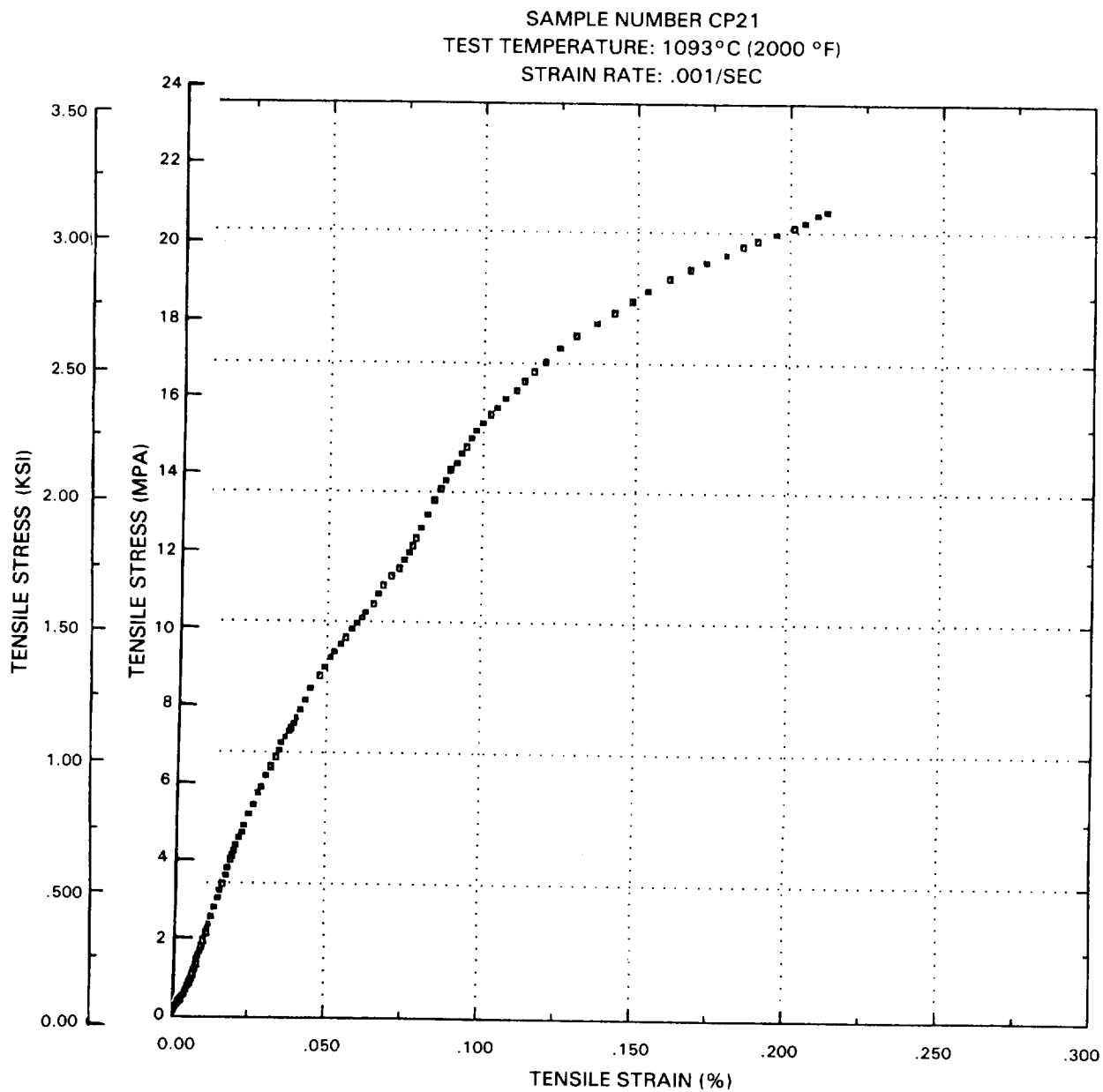


Figure E-12 Tension Stress-Strain (1093°C (2000°F))

SAMPLE NUMBER CP23
TEST TEMPERATURE: 1093°C (2000 °F)
STRAIN RATE: .001/SEC

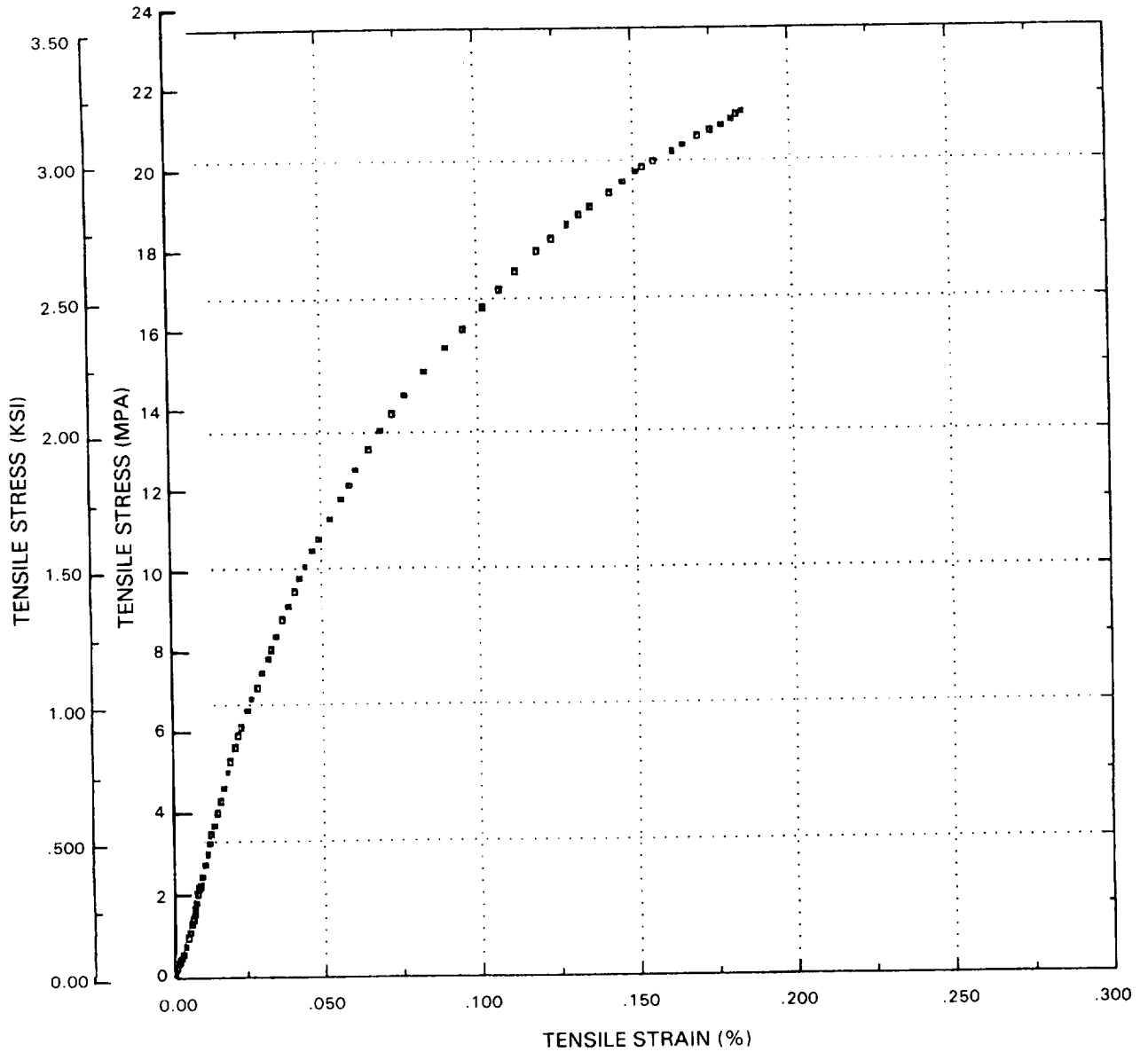


Figure E-13 Tension Stress-Strain (1093°C (2000°F))

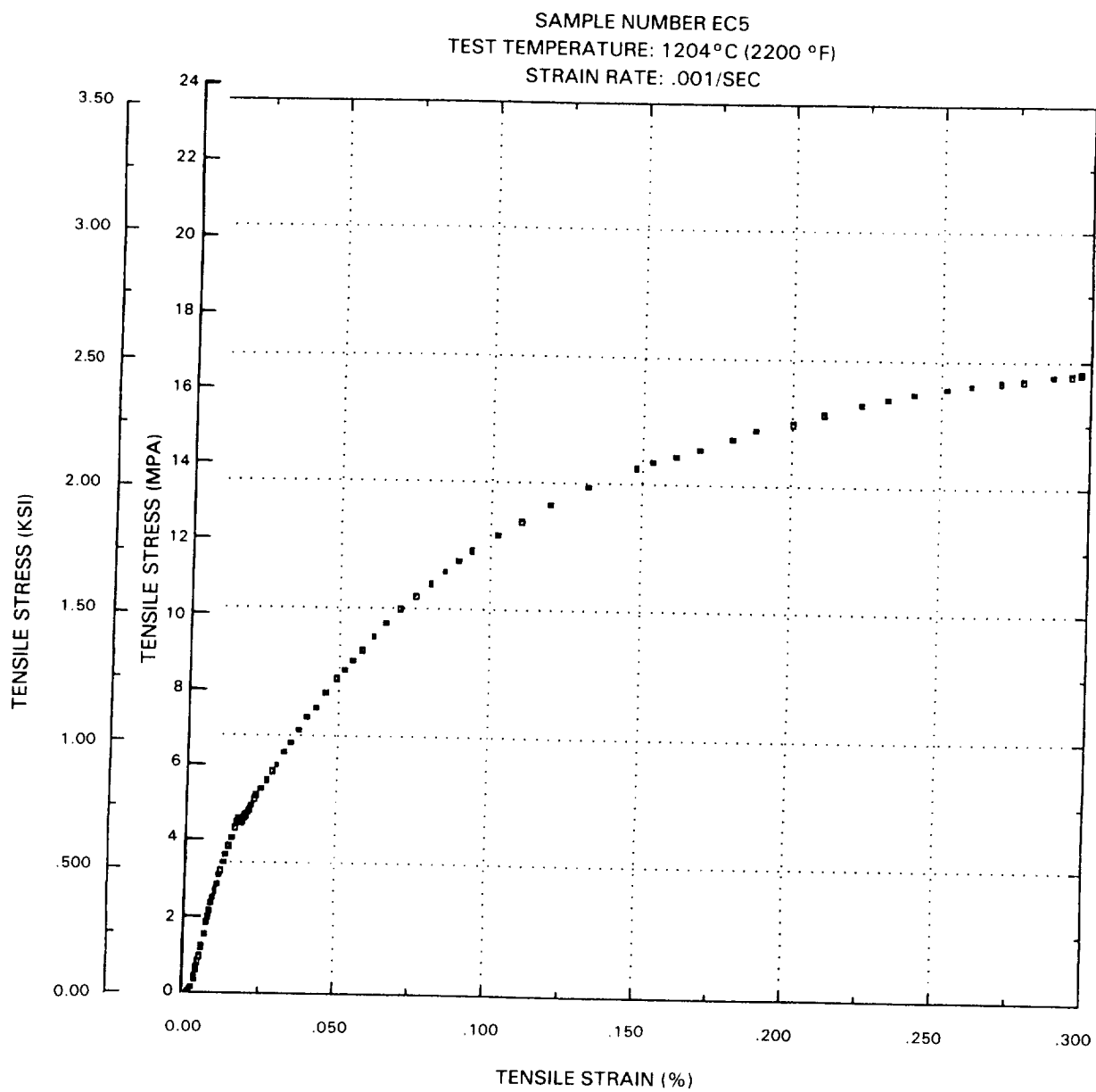


Figure E-14 Tension Stress-Strain (1204°C (2200°F))

SAMPLE NUMBER EC4
TEST TEMPERATURE: 1204°C (2200 °F)
STRAIN RATE: .001/SEC

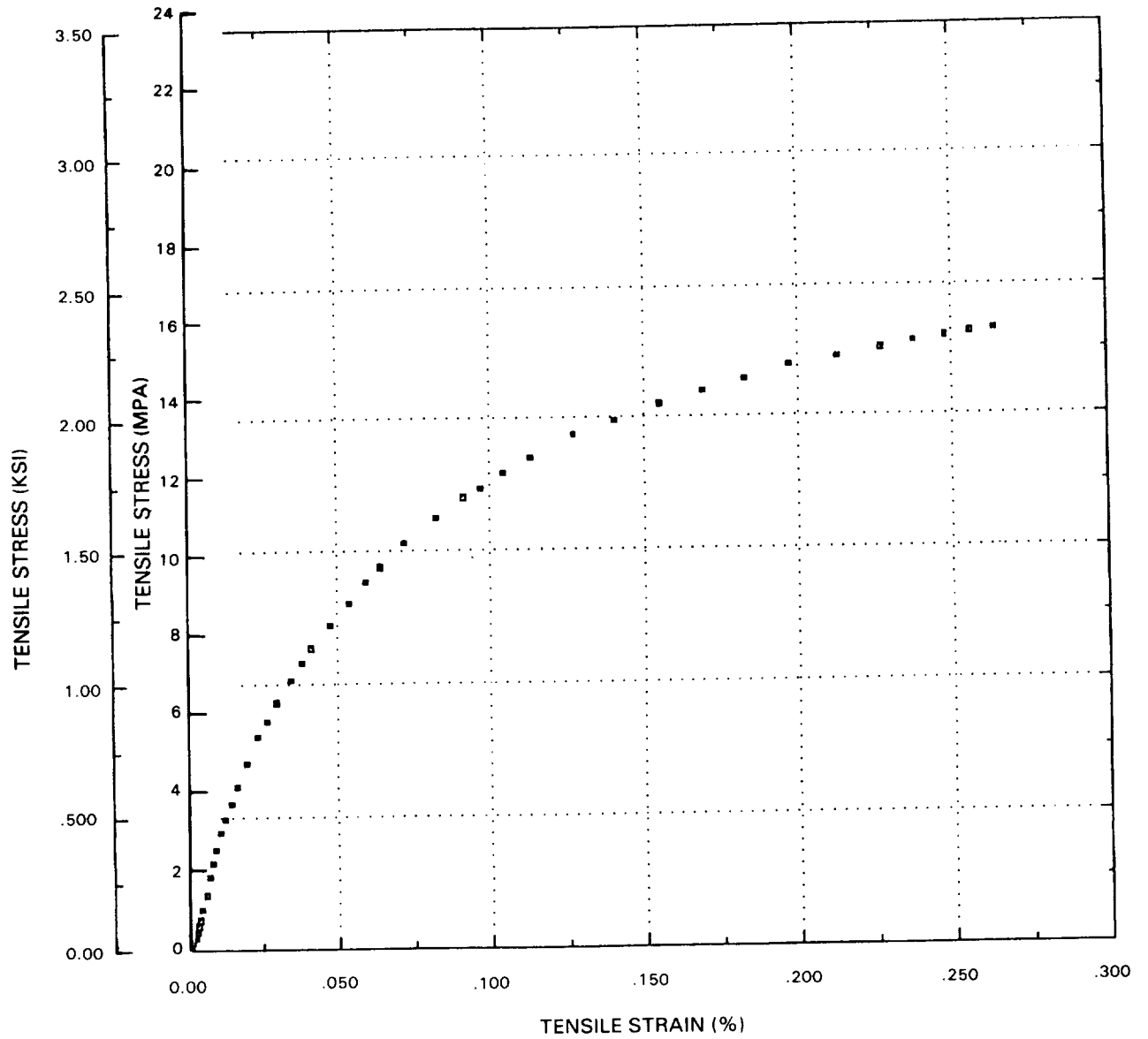


Figure E-15 Tension Stress-Strain (1204°C (2200°F))

SAMPLE NUMBER CP27006
TEST TEMPERATURE: 982°C (1800 °F)
STRAIN RATE: CREEP/SEC

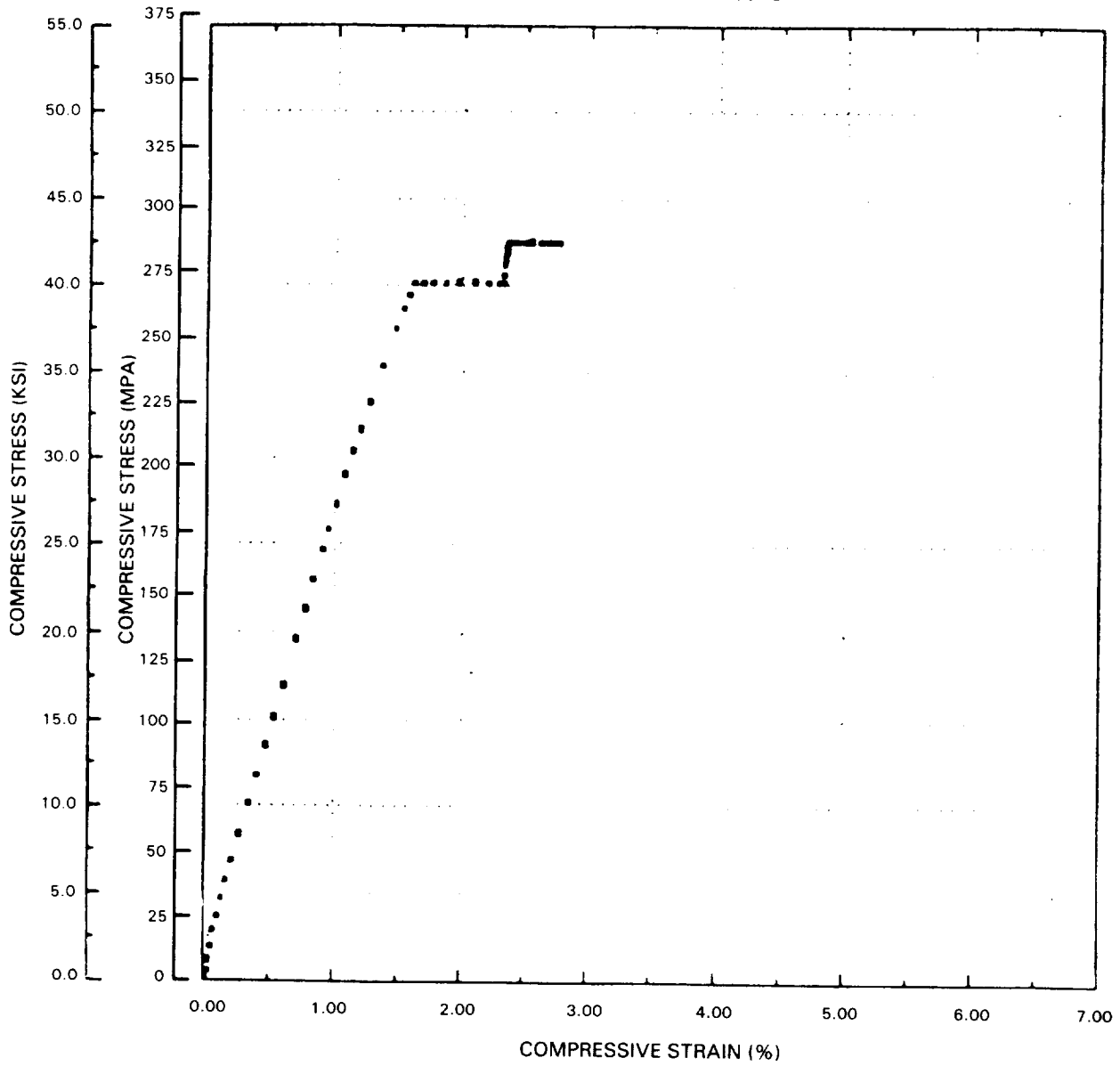


Figure E-16 Compression Creep (982°C (1800°F))

SAMPLE NUMBER CP27006TM
TEST TEMPERATURE: 982°C (1800°F)
STRAIN RATE: CREEP/SEC

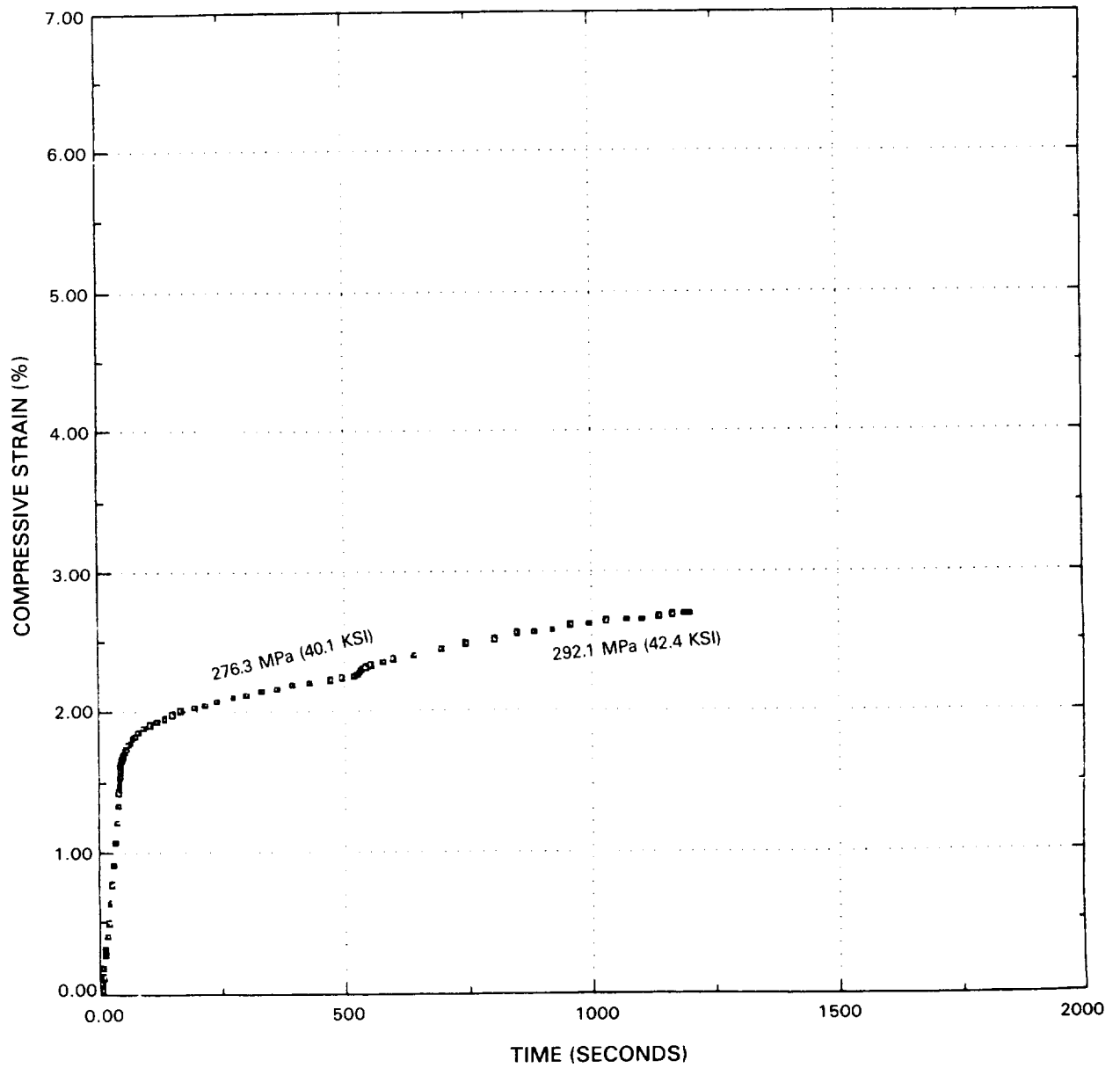


Figure E-17 Compression Creep Strain-Time (982°C (1800°F))

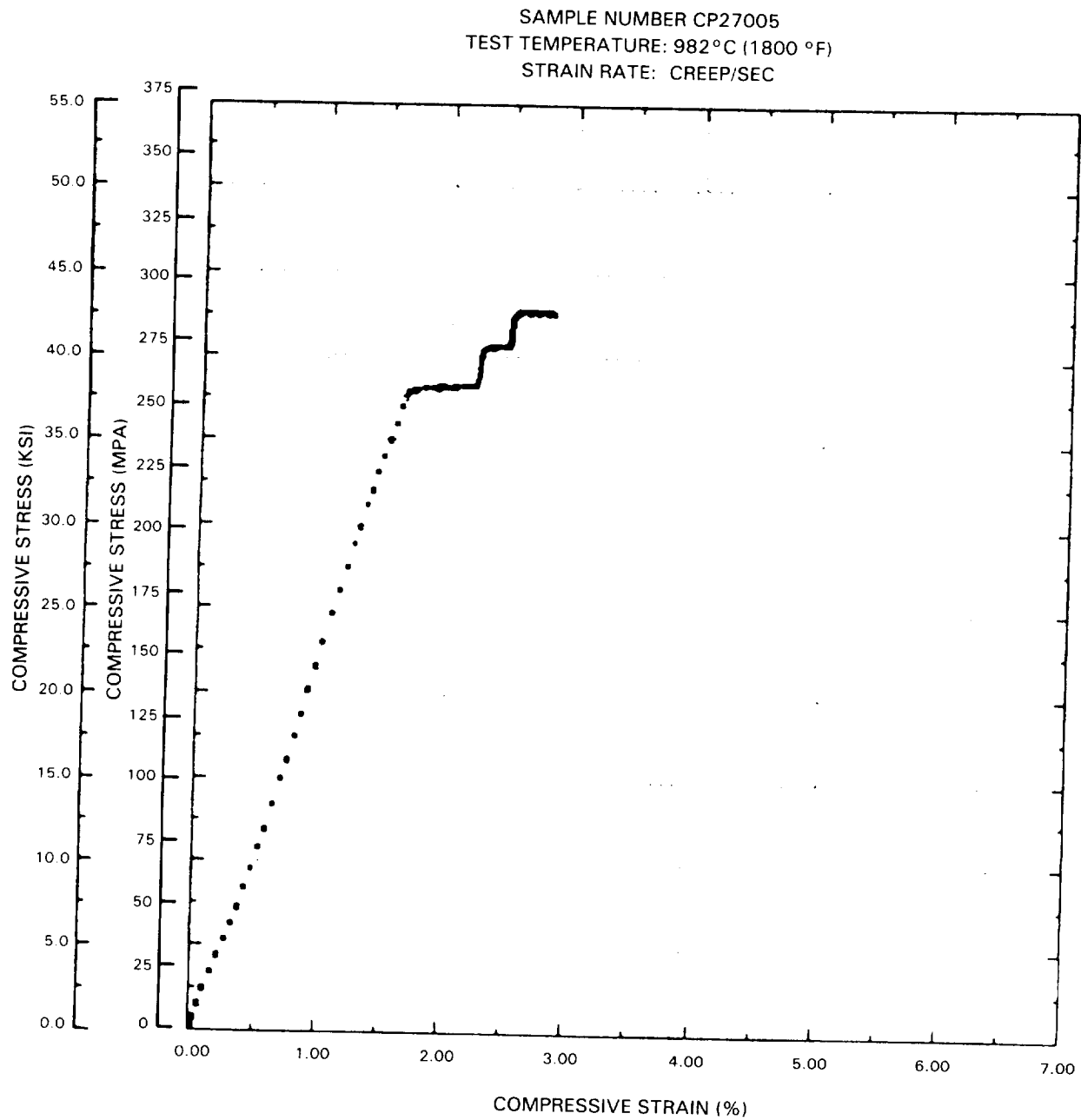


Figure E-18 Compression Creep Stress-Strain (982°C (1800°F))

SAMPLE NUMBER CP270012
TEST TEMPERATURE: 982°C (1800 °F)
STRAIN RATE: CREEP/SEC

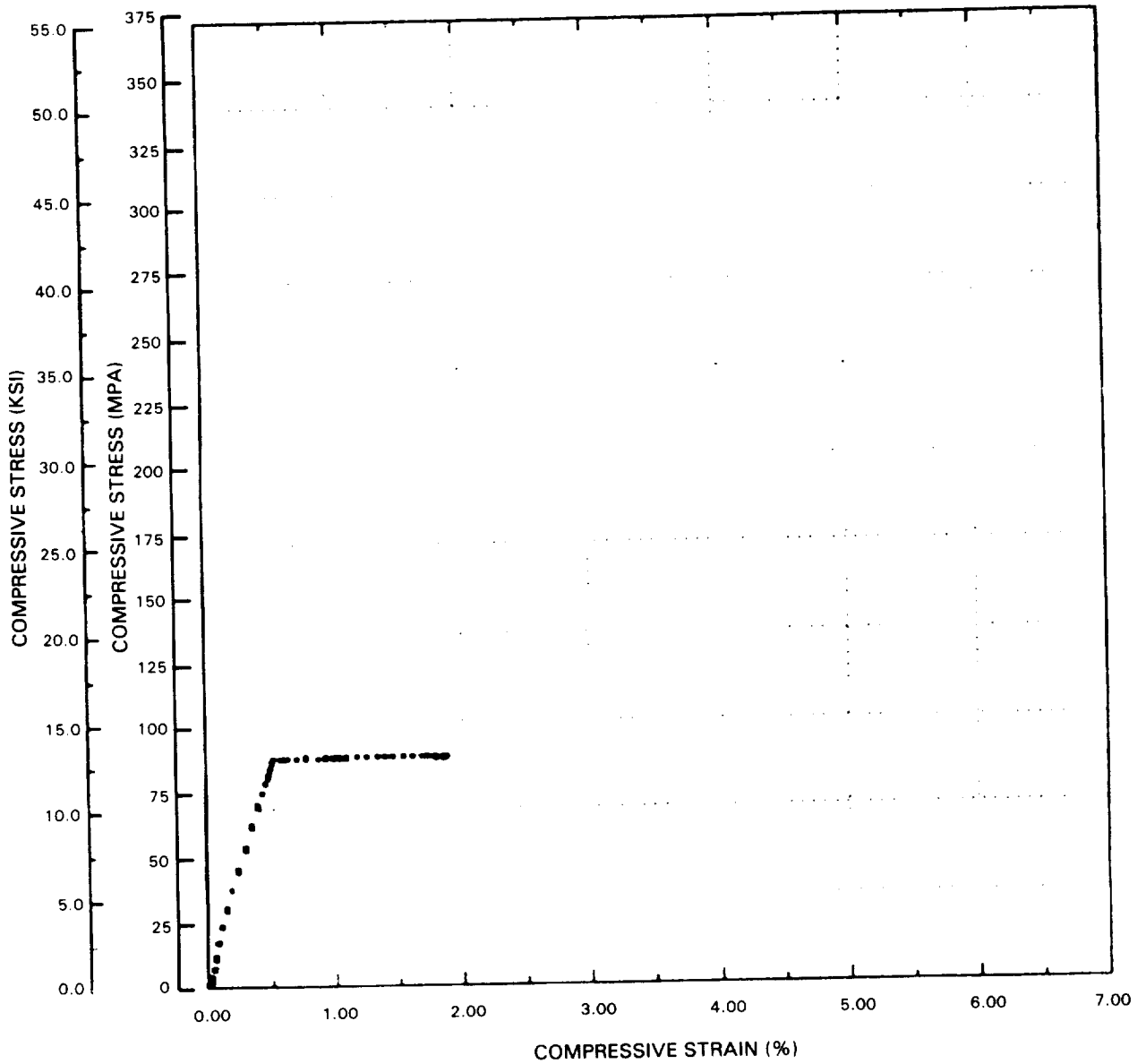


Figure E-19 Compression Creep (982°C (1800°F))

SAMPLE NUMBER CP27012TM
TEST TEMPERATURE: 982°C (1800 °F)
STRAIN RATE: CREEP/SEC

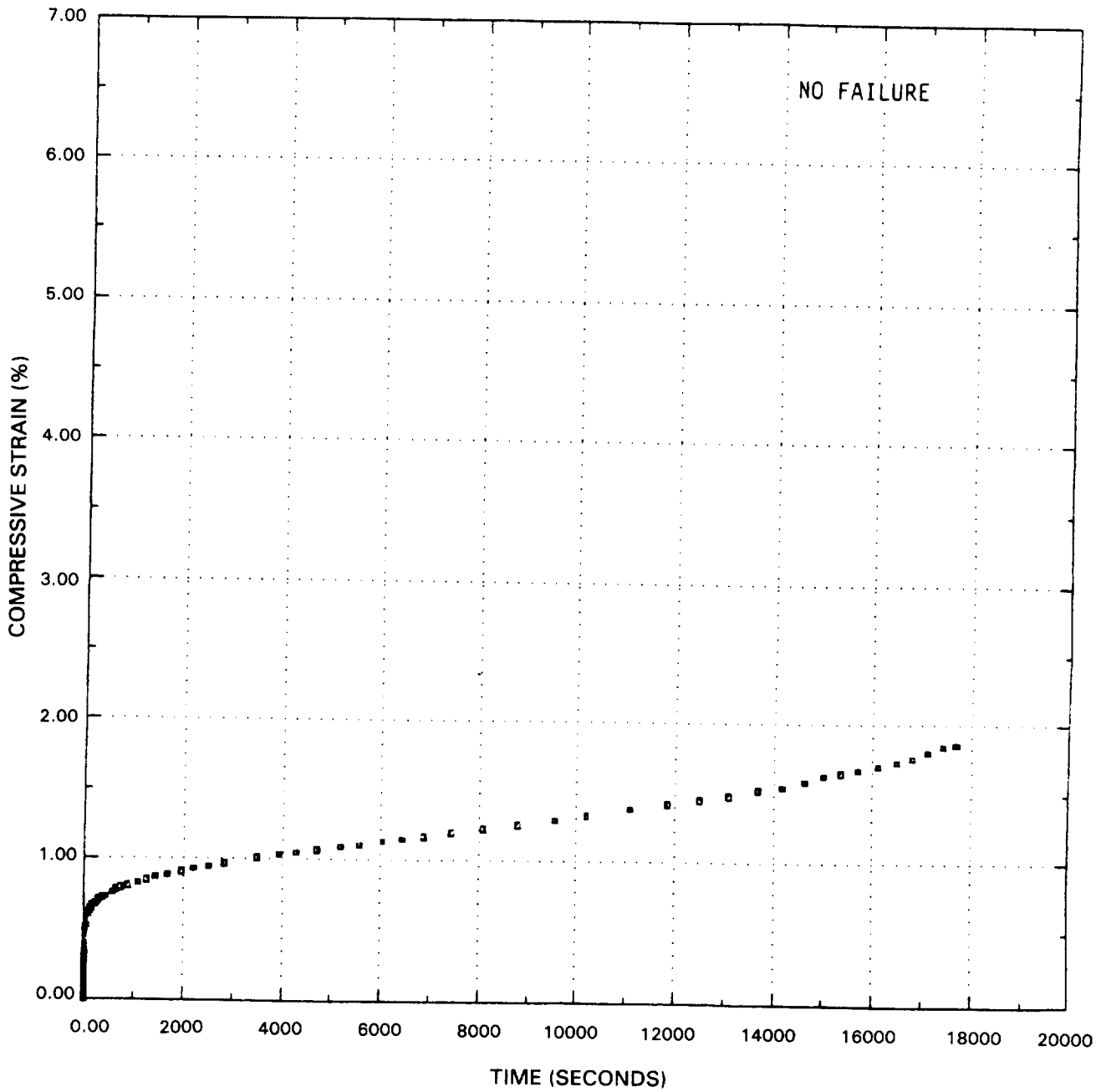


Figure E-20 Compression Creep Strain-Time (982°C (1800°F))

SAMPLE NUMBER CP27007
TEST TEMPERATURE: 1204°C (2200 °F)
STRAIN RATE: CREEP/SEC

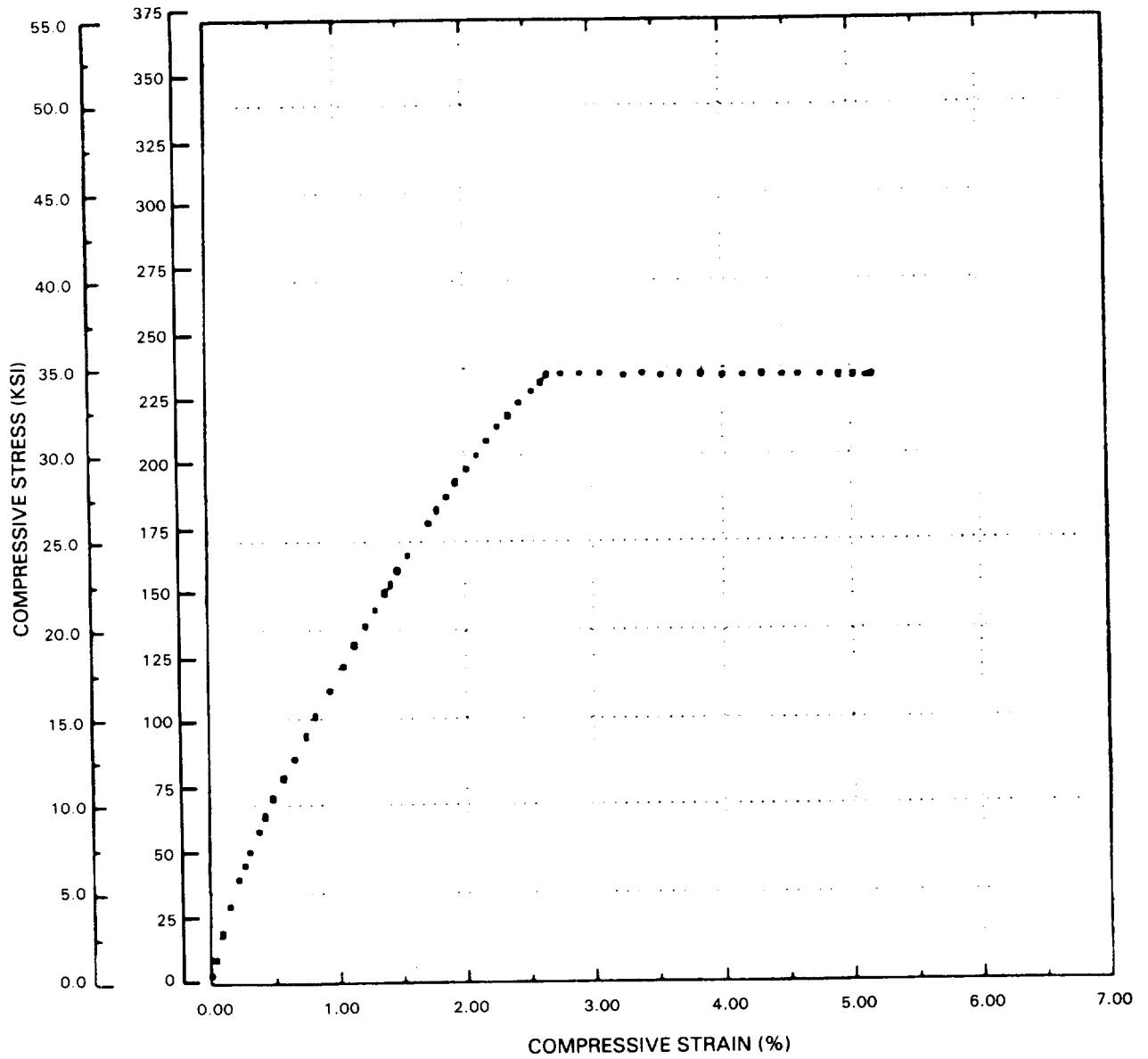


Figure E-21 Compression Creep (1204°C (2200°F))

SAMPLE NUMBER CP27007TM
TEST TEMPERATURE: 1204°C (2200 °F)
STRAIN RATE: CREEP/SEC

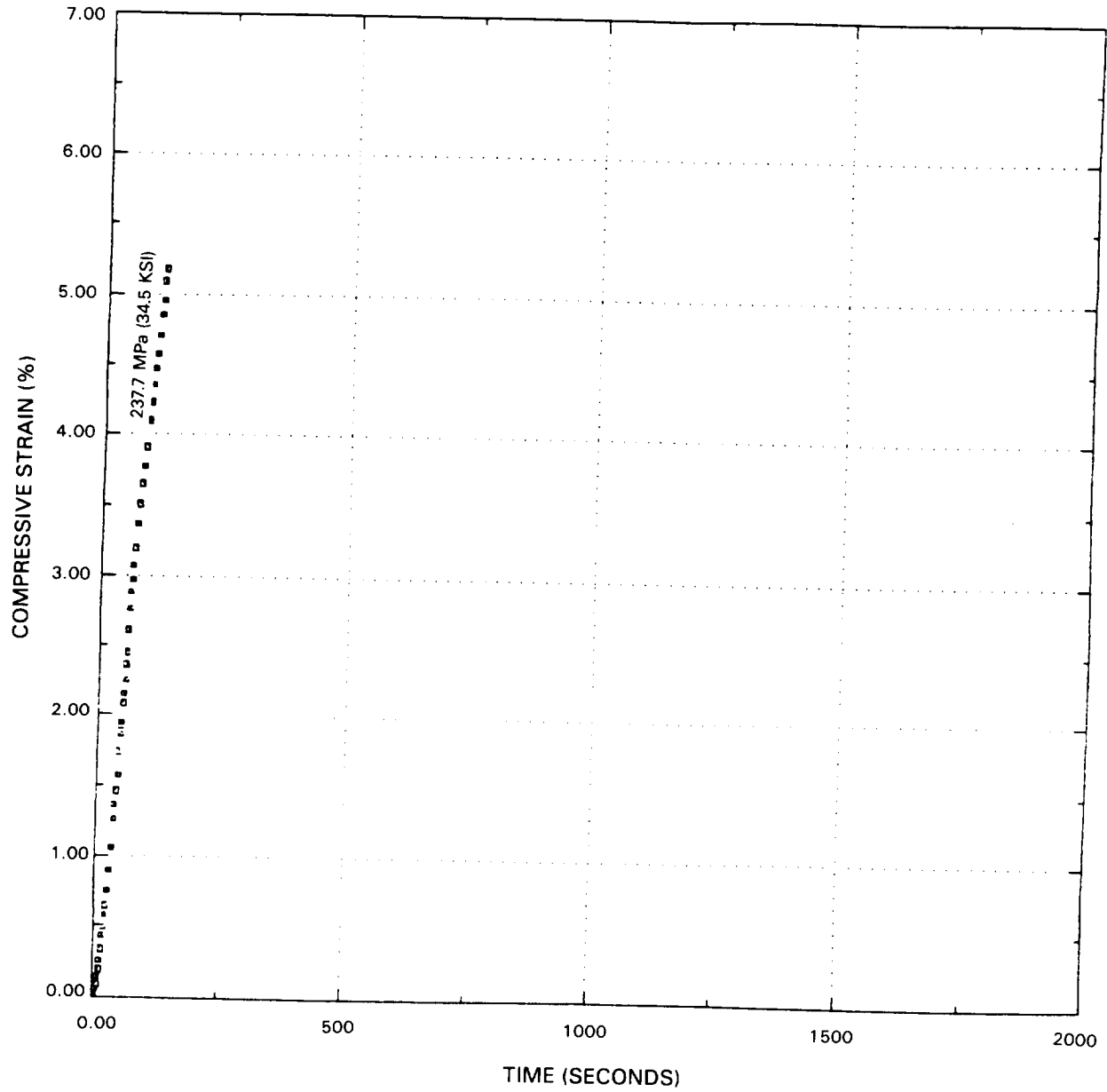


Figure E-22 Compression Creep Strain-Time (1204°C (2200°F))

SAMPLE NUMBER CP27008
TEST TEMPERATURE: 1204°C (2200 °F)
STRAIN RATE: CREEP/SEC

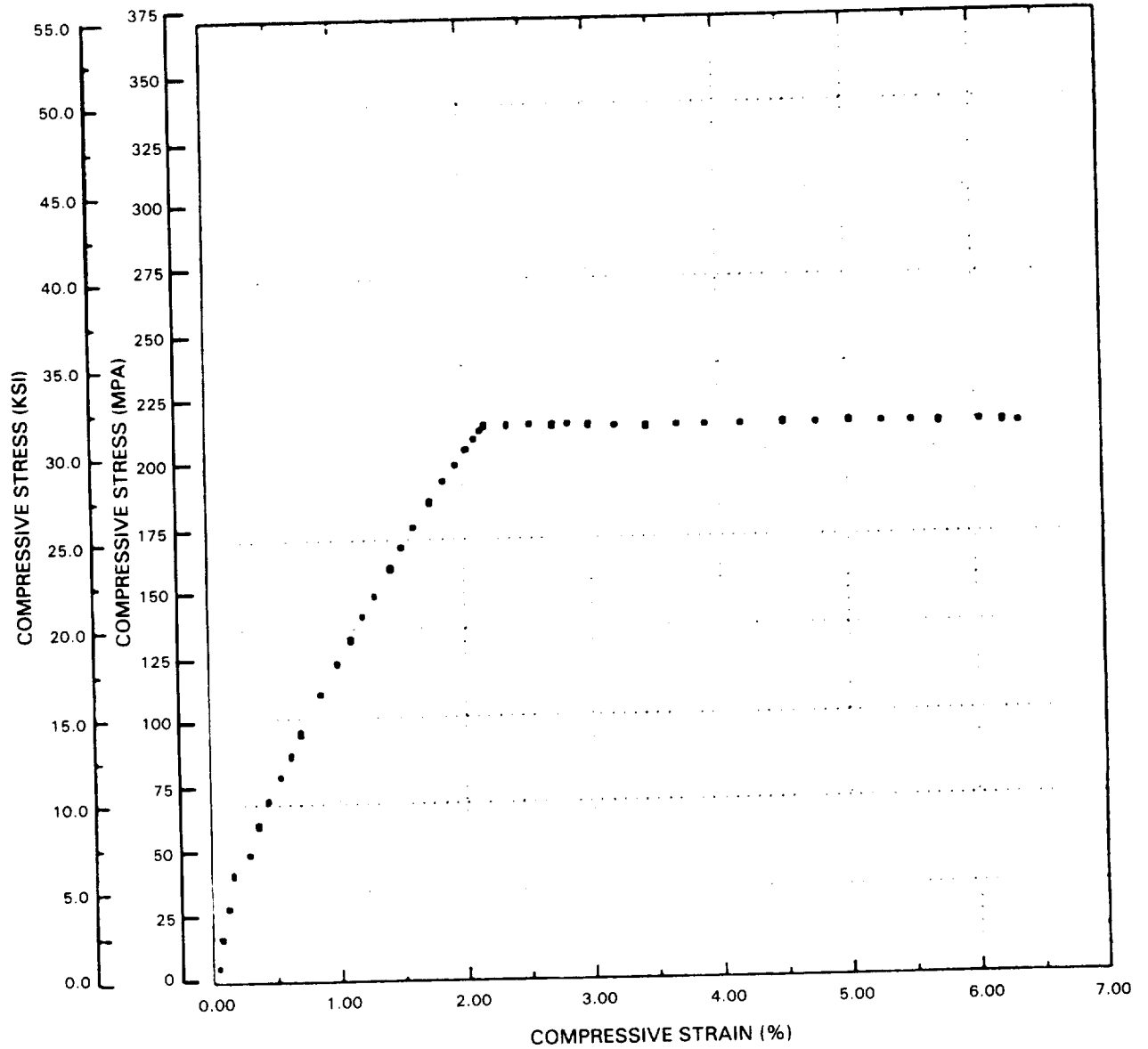


Figure E-23 Compression Creep (1204°C (2200°F))

SAMPLE NUMBER CP27008TM
TEST TEMPERATURE: 1204°C (2200 °F)
STRAIN RATE: CREEP/SEC

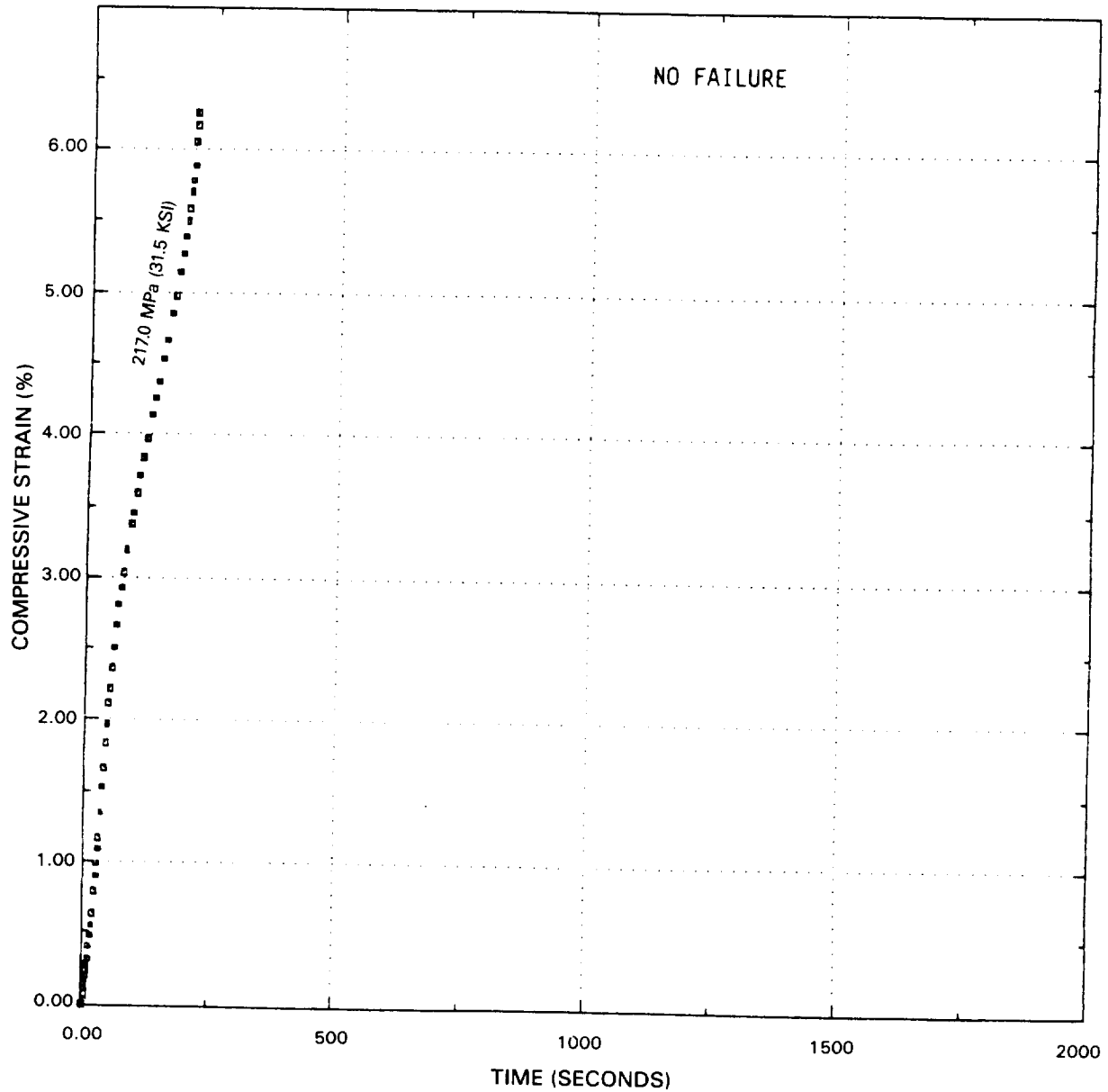


Figure E-24 Compression Creep Strain-Time (1204°C (2200°F))

SAMPLE NUMBER CP27009
TEST TEMPERATURE: 1204°C (2200 °F)
STRAIN RATE: CREEP/SEC

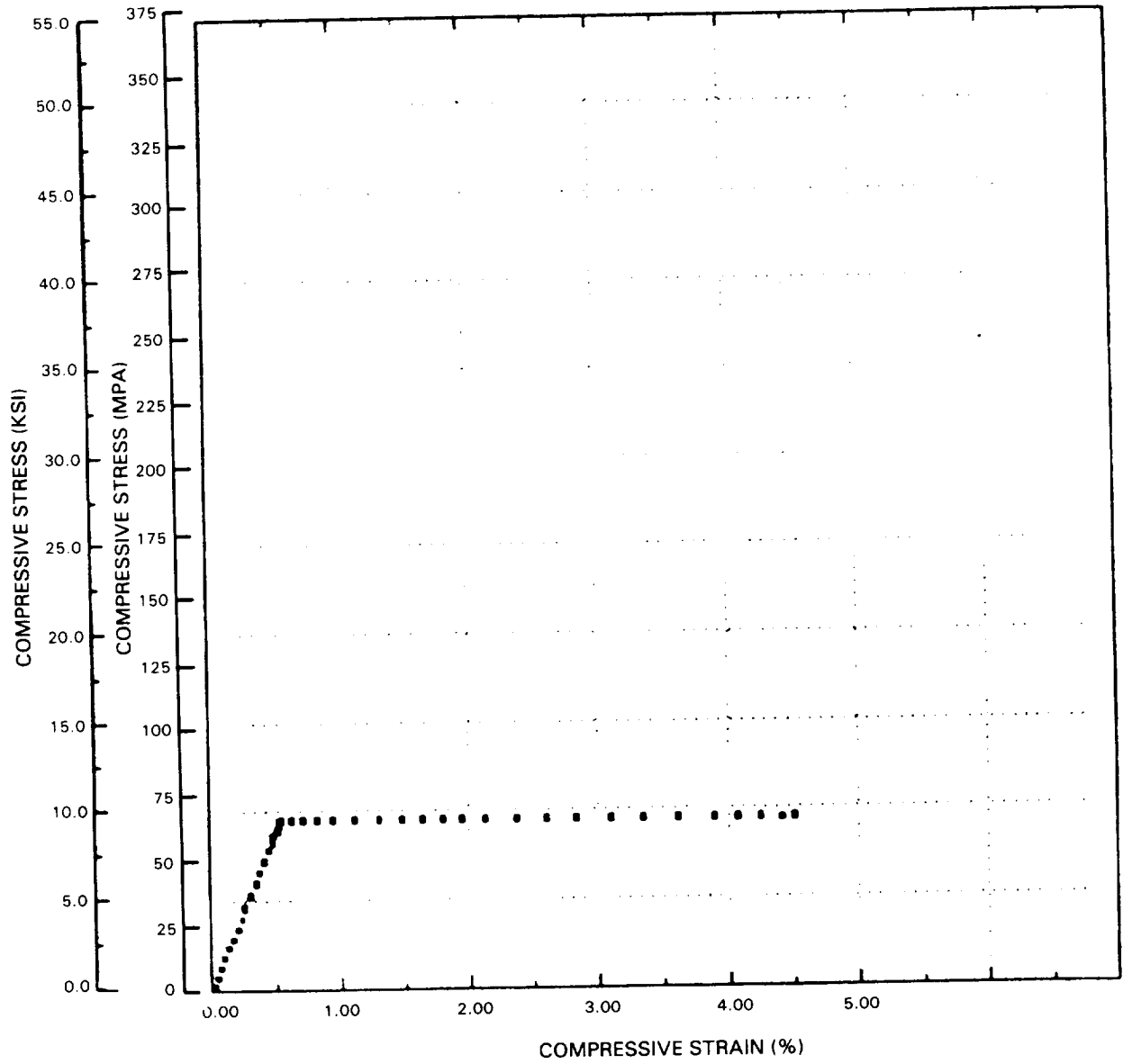


Figure E-25 Compression Creep (1204°C (2200°F))

SAMPLE NUMBER CP27009TM
TEST TEMPERATURE: 1204°C (2200 °F)
STRAIN RATE: CREEP/SEC

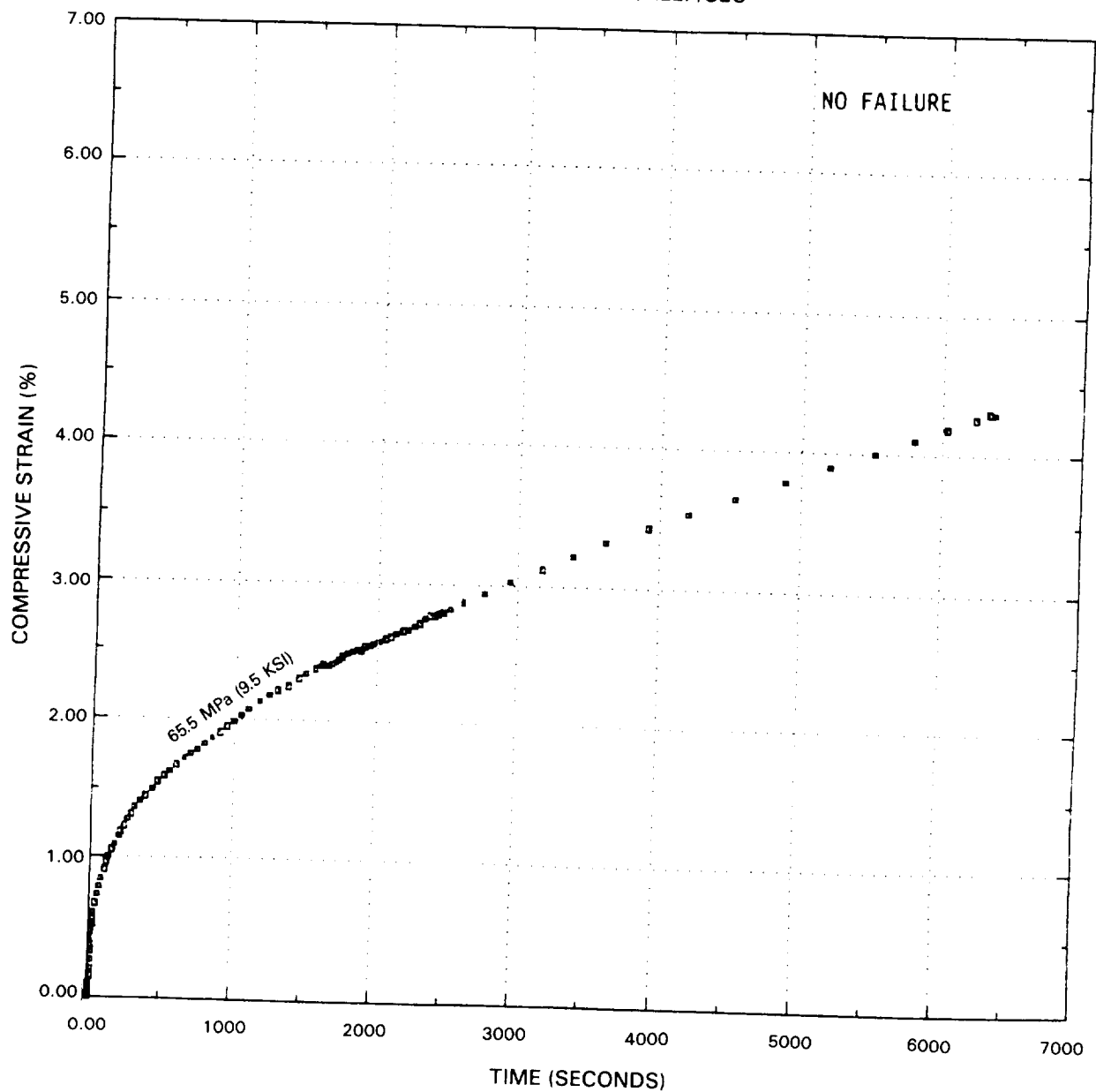


Figure E-26 Compression Creep Strain-Time (1204°C (2200°F))

SAMPLE NUMBER CP27010
TEST TEMPERATURE: 1204°C (2200 °F)
STRAIN RATE: CREEP/SEC

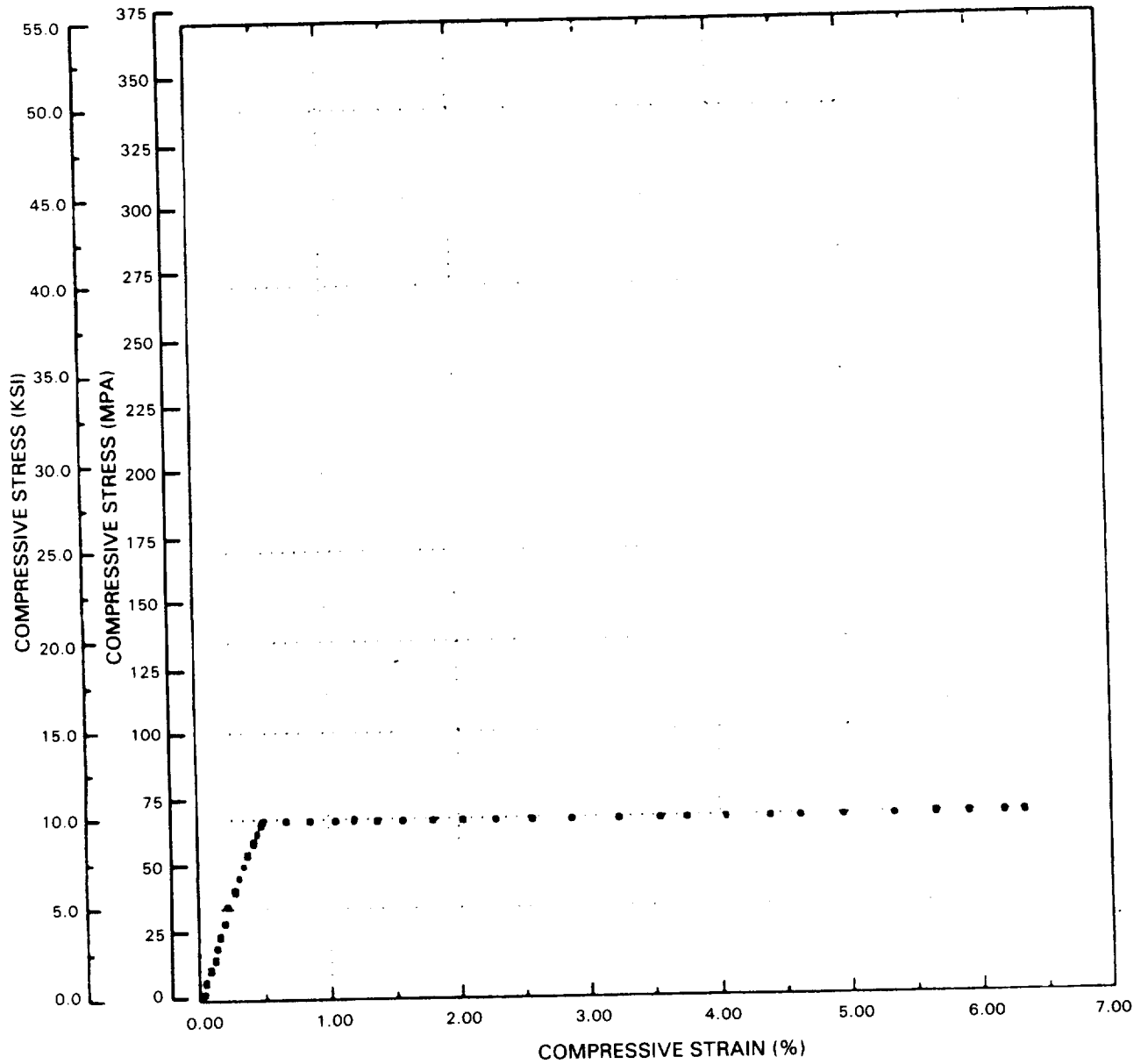


Figure E-27 Compression Creep (1204°C (2200°F))

SAMPLE NUMBER CP270100TM
TEST TEMPERATURE: 1204°C (2200°F)
STRAIN RATE: CREEP/SEC

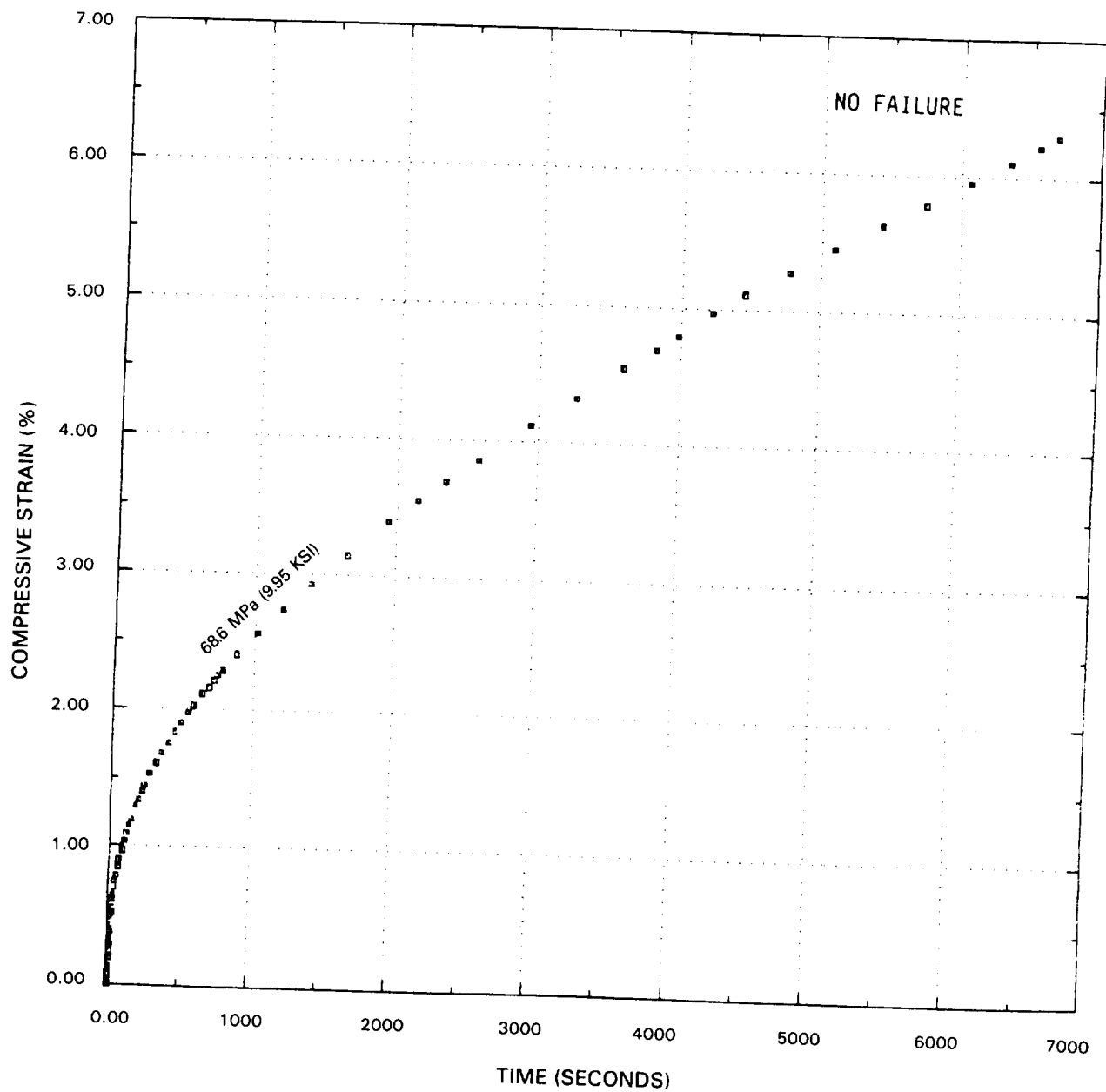


Figure E-28 Compression Creep Strain-Time (1204°C (2200°F))

SAMPLE NUMBER CP12A
TEST TEMPERATURE: 538°C (1000 °F)
STRAIN RATE: CREEP/SEC

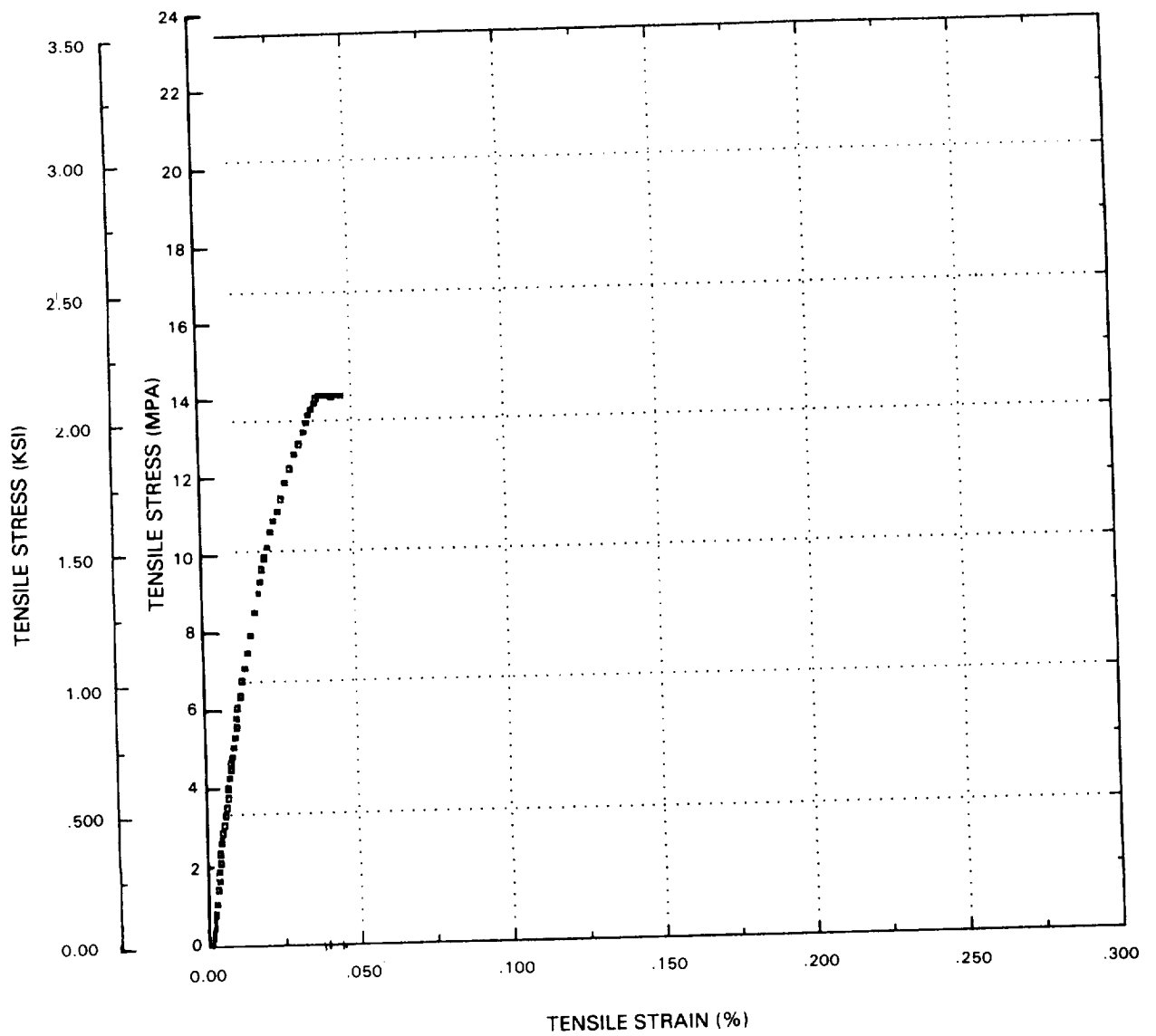


Figure E-29 Tension Creep (538°C (1000°F))

SAMPLE NUMBERCP12TM
TEST TEMPERATURE: 538°C (1000 °F)
STRAIN RATE: CREEP/SEC

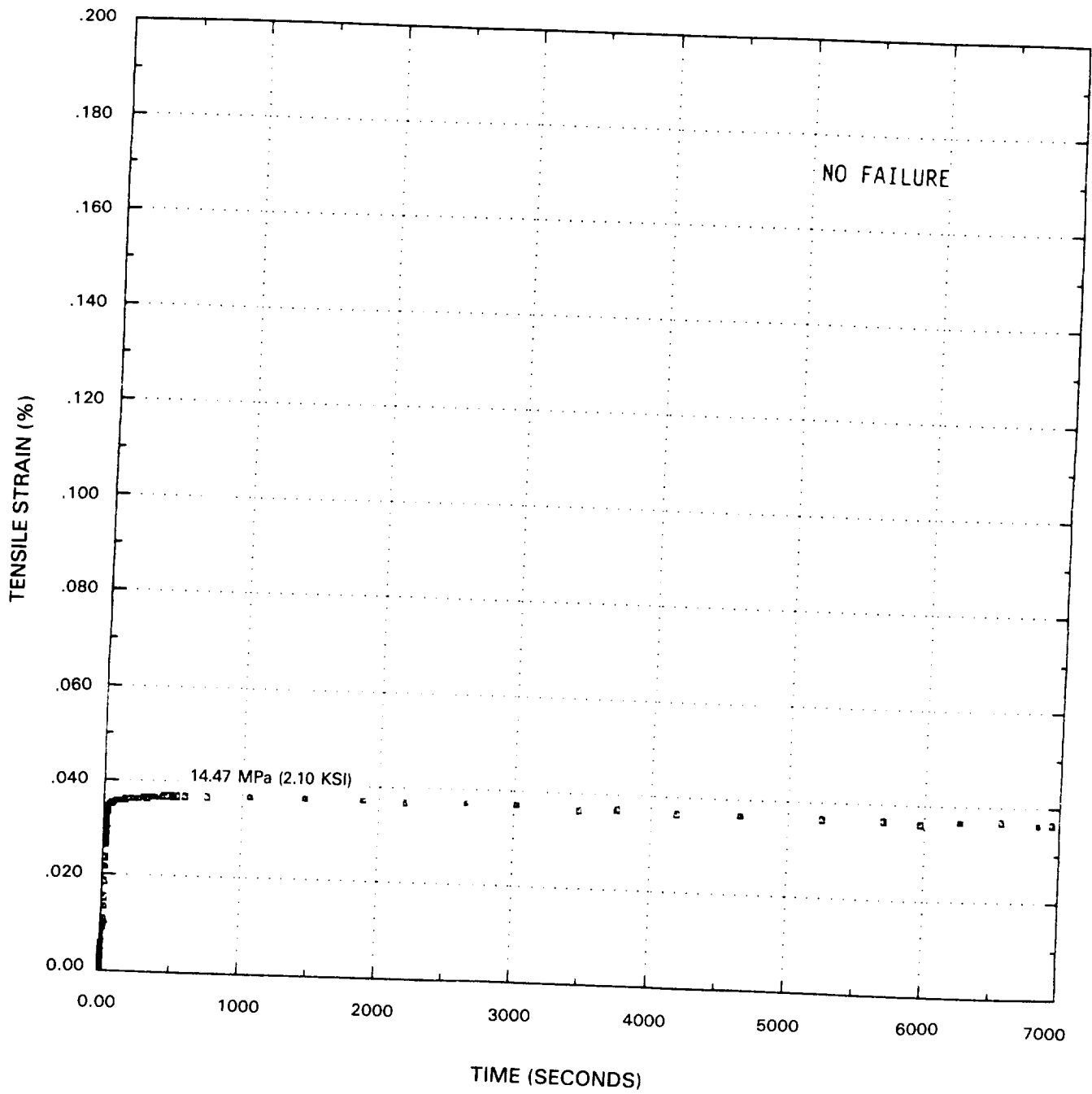


Figure E-30 Tension Creep Strain-Time (538°C (1000°F))

SAMPLE NUMBER CP19
TEST TEMPERATURE: 982°C (1800 °F)
STRAIN RATE: CREEP/SEC

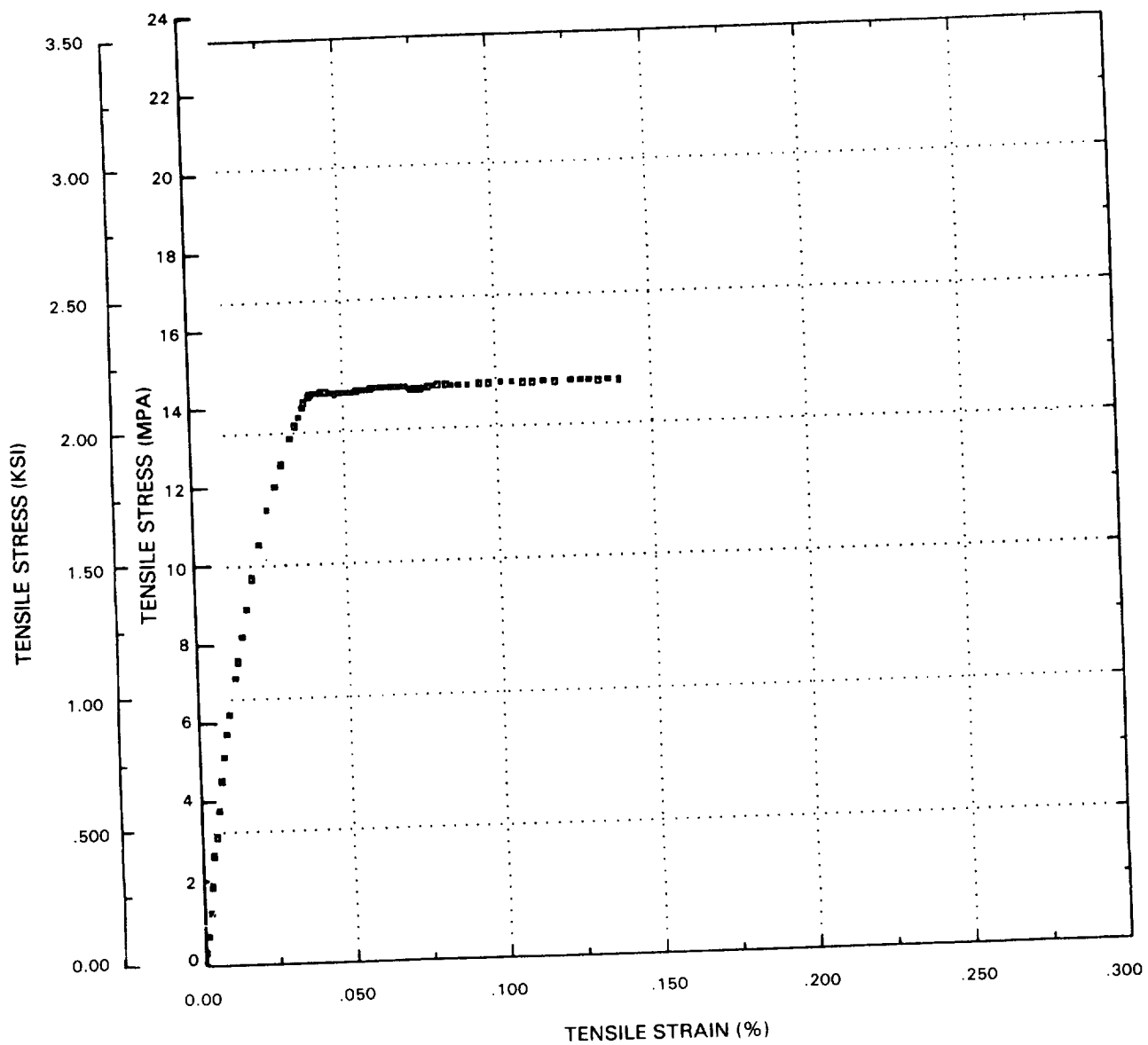


Figure E-31 Tension Creep (982°C (1800°F))

SAMPLE NUMBER CP19TM
TEST TEMPERATURE: 982°C (1800 °F)
STRAIN RATE: CREEP/SEC

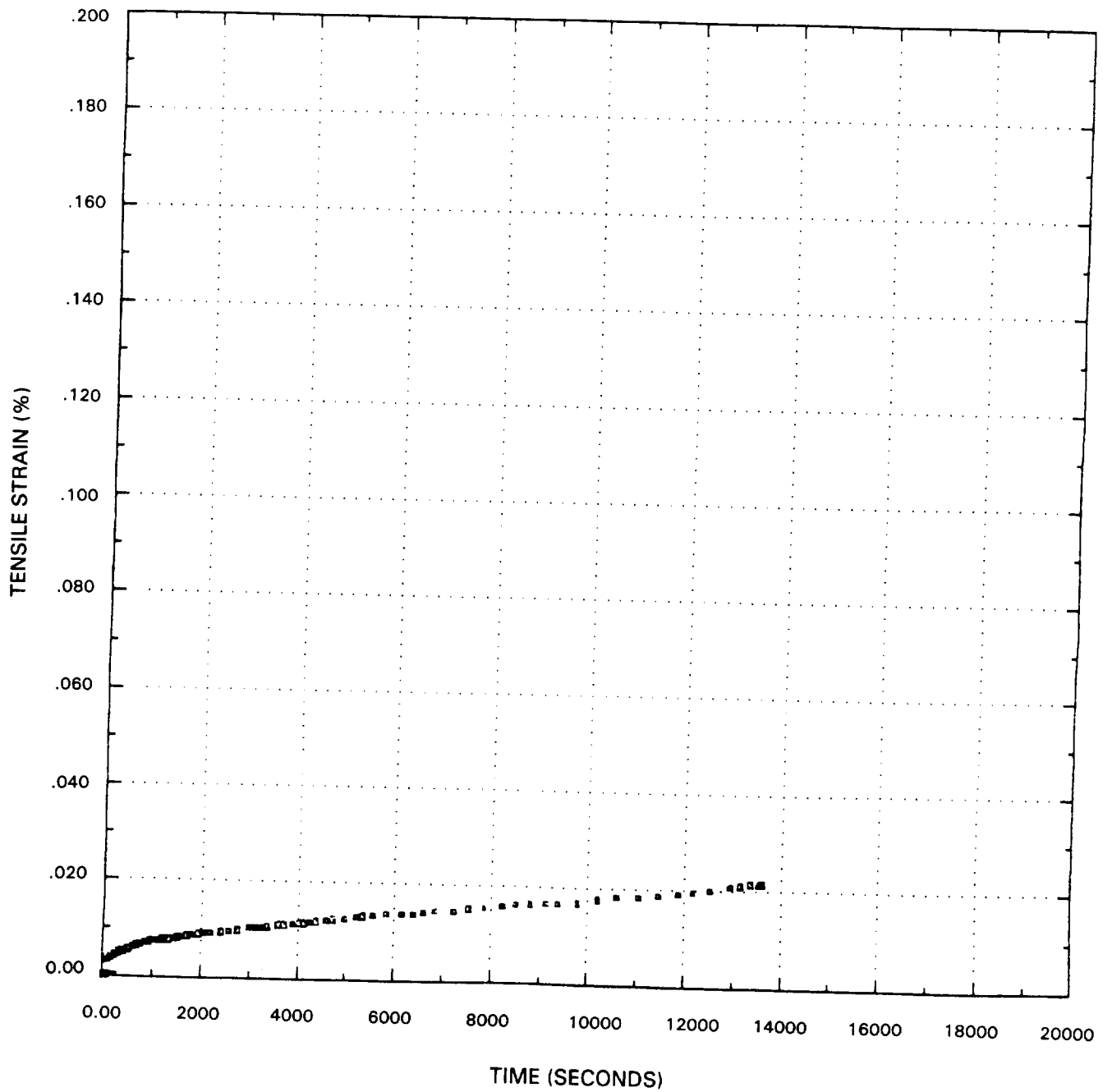


Figure E-32 Tension Creep Strain-Time (982°C (1800°F))

SAMPLE NUMBER CP20
TEST TEMPERATURE: 982°C (1800 °F)
STRAIN RATE: CREEP/SEC

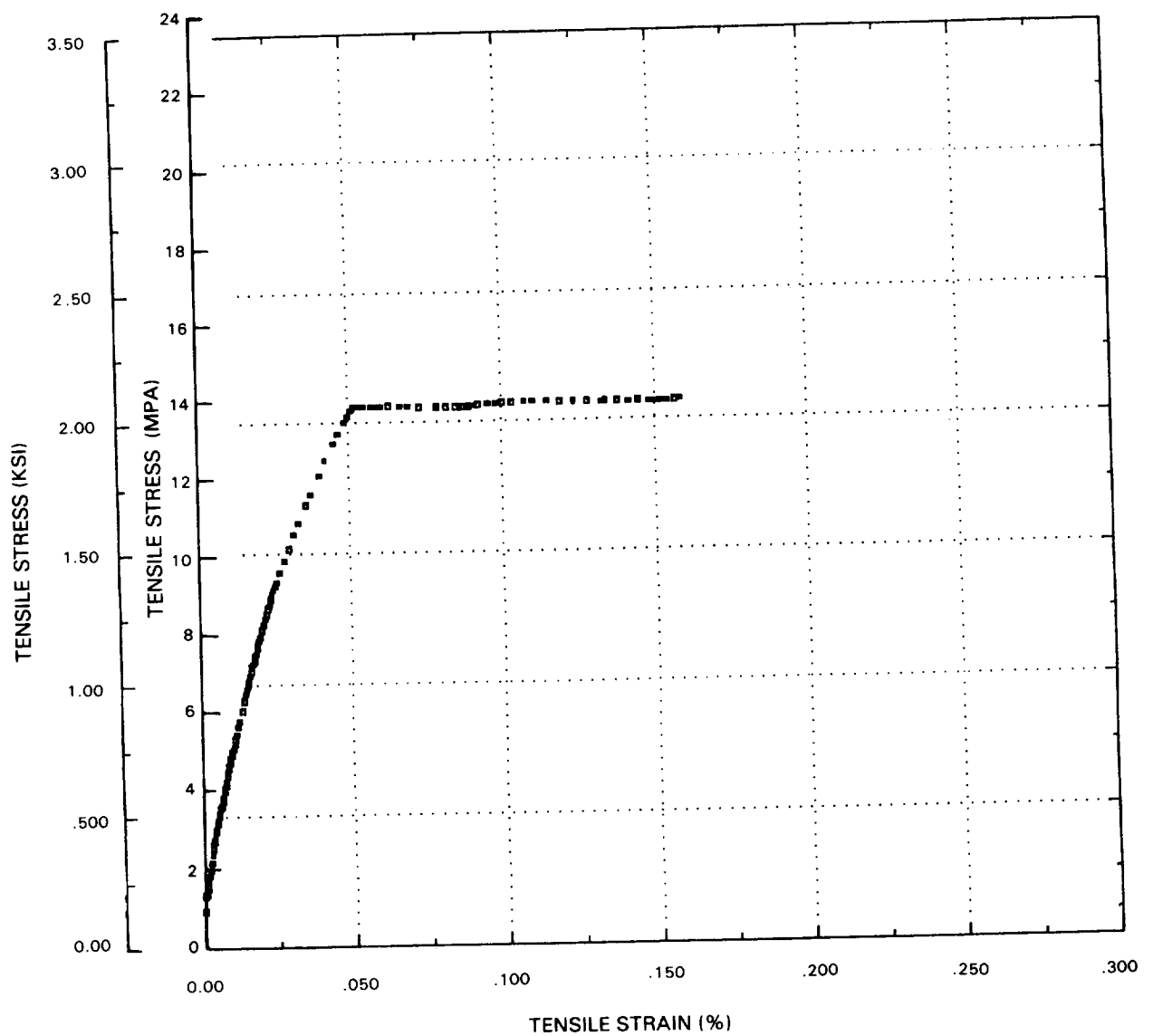


Figure E-33 Tension Creep (982°C (1800°F))

SAMPLE NUMBER CP20TM
TEST TEMPERATURE: 982°C (1800 °F)
STRAIN RATE: CREEP/SEC

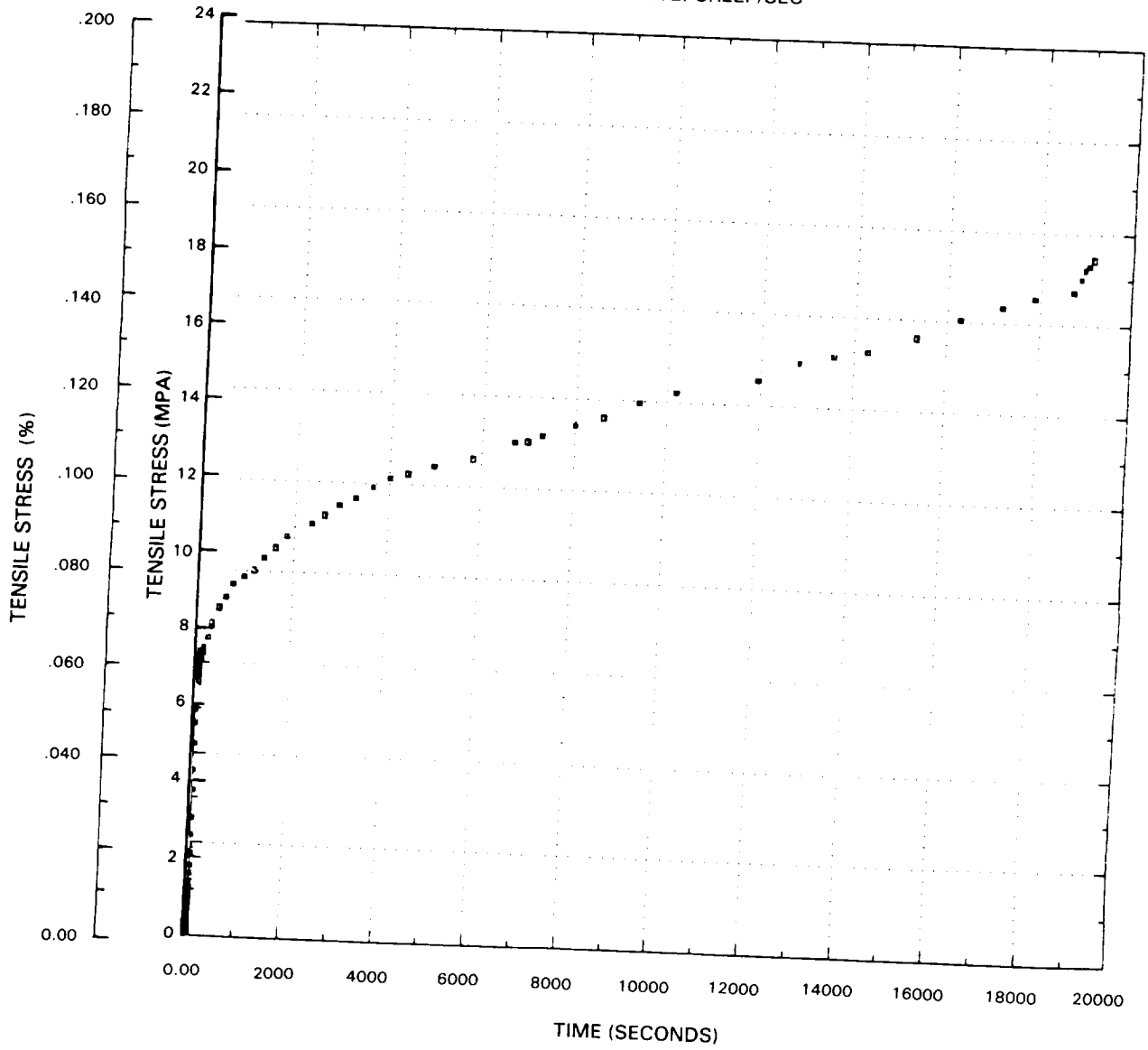


Figure E-34 Tension Creep (982°C (1800°F))

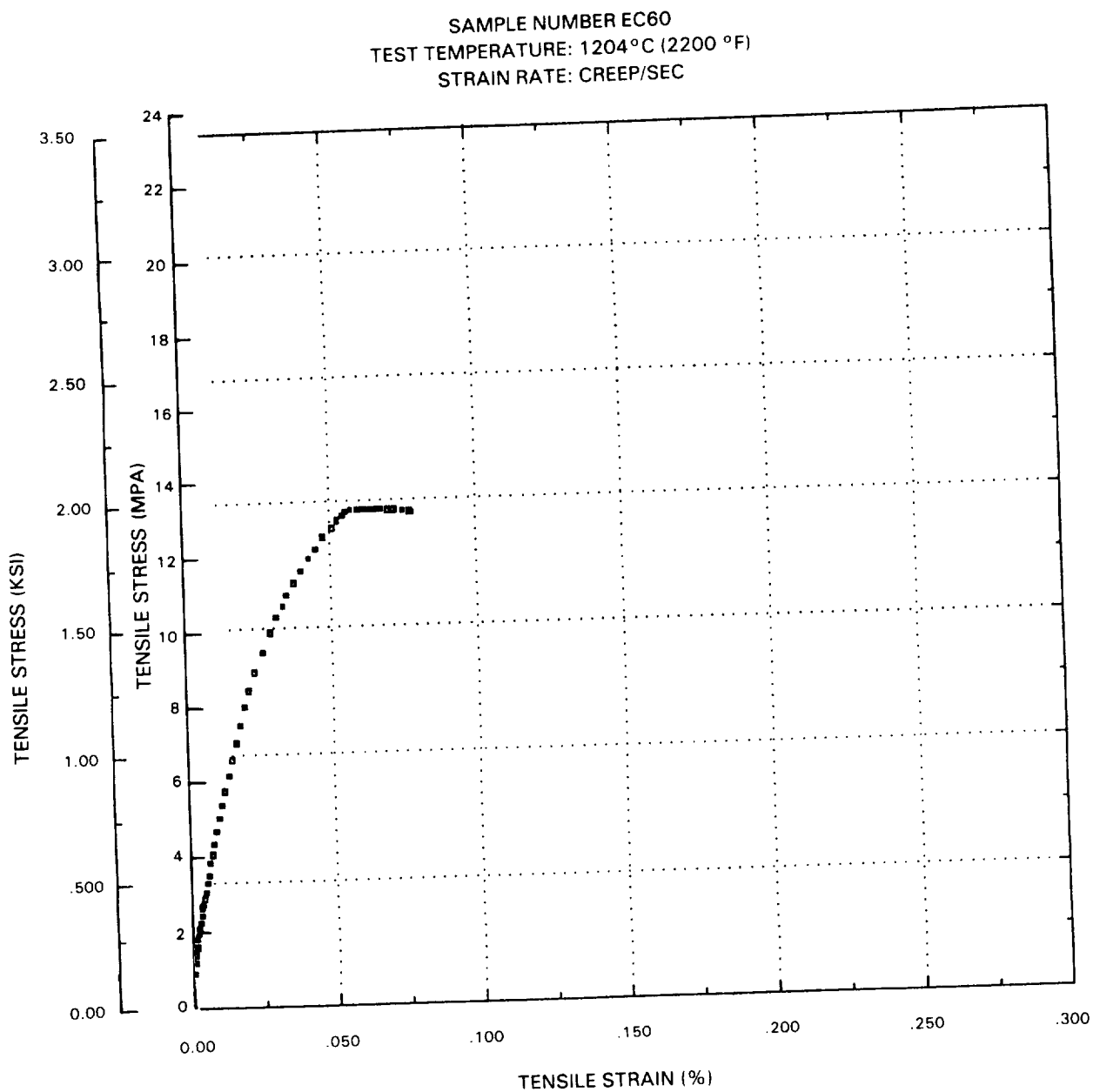


Figure E-35 Tension Creep (1204°C (2200°F))

SAMPLE NUMBER EC6TM
TEST TEMPERATURE: 1204°C (2200 °F)
STRAIN RATE: CREEP/SEC

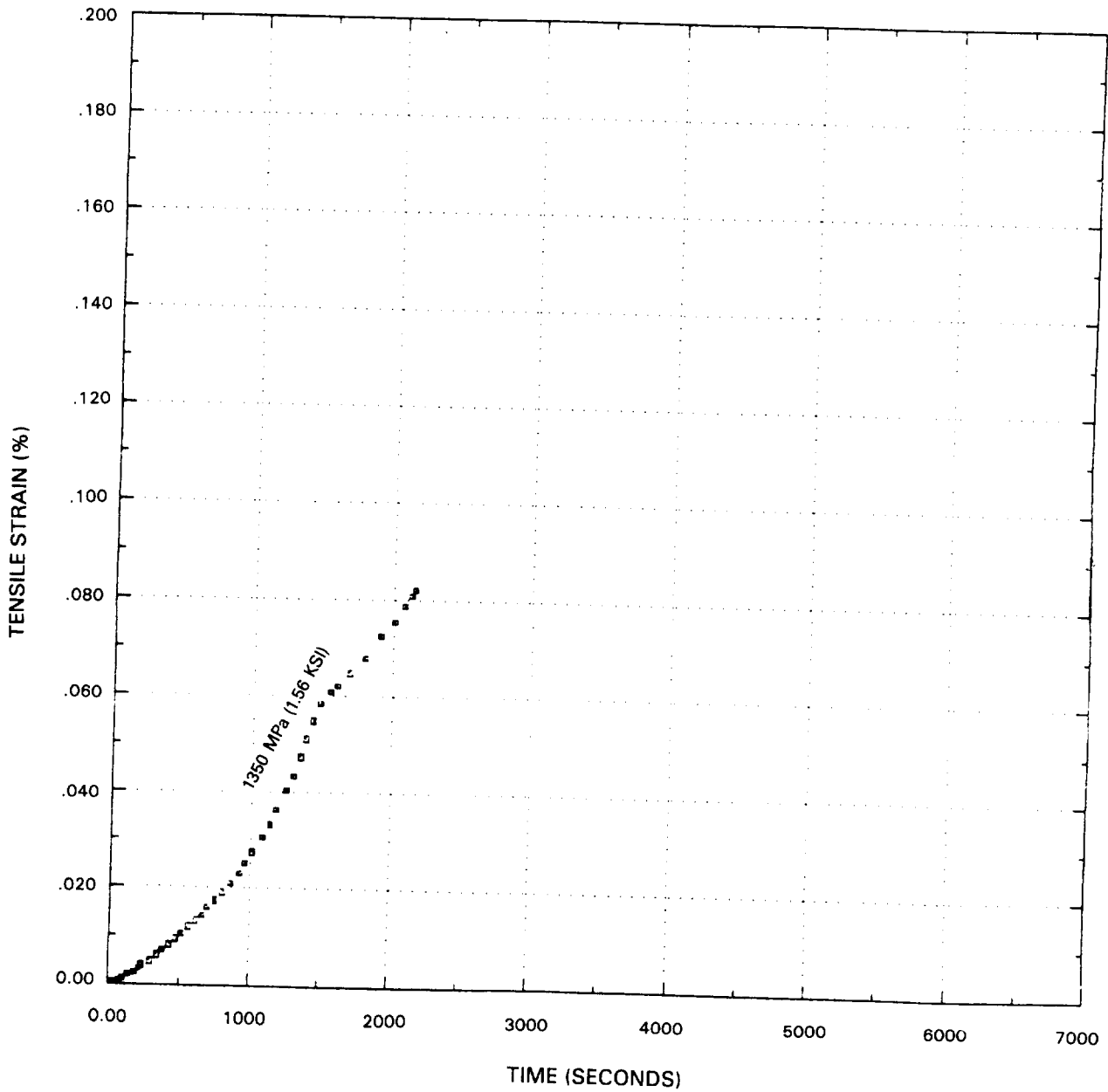


Figure E-36 Tension Creep Strain-Time (1204°C (2200°F))

APPENDIX F

USER'S AND PROGRAMMER'S GUIDE TO TBCLIF

1.0 INTRODUCTION

TBCLIF is a computer code written by the Southwest Research Institute (SwRI) for Pratt & Whitney Engineering (PWED). The code analytically predicts the life (in terms of thermal cycles) of components coated with PWED's metallic bond-ceramic thermal barrier coating system, known as PWA 264.

TBCLIF was written in partial fulfillment of Task IC1 of PWED's contract NAS3-23944 with NASA. The program and its documentation were written in accordance with PWED's guidelines for externally generated software. It is written entirely in FORTRAN IV and has been executed on an IBM 4340 series computer using the CMS operating system.

The thermal barrier coating TBC life prediction model used in TBCLIF was developed during the summer of 1985. The model is preliminary, additions and improvements may be added later. The life prediction model considers TBC failure to be a function of two processes: oxide growth at the bond coat and cyclic plastic strain damage. Life of TBC systems is predicted by calculating, on a cycle-by-cycle basis, the cumulative "damage" accrued by the TBC system. (One defines "damage" in this context as the percentage of life used during the cycle.) Such damage is accumulated using Miner's Rule, i.e. if the damage in one cycle is

$$d = 1/N_i \quad (1)$$

then the cumulative damage is

$$D = \sum_i 1/N_i \quad (2)$$

At any point in the thermo-mechanical load history of the TBC system, the value of N_f is a non-linear function of the current oxide thickness and the cyclic plastic strain.

In this guide, the details of TBC life prediction are described from the technical/theoretical, programmer's and user's perspectives. A principal objective of this report, however, is to describe TBCLIF's organization and use. Hence, emphasis has been placed on sections dealing with these topics. For further details regarding theoretical/technical aspects of TBC failure, consult references [1-6].

2.0 LIFE PREDICTION METHODOLOGY IN TBCLIF

Failure of the thermal barrier coating is currently believed to be the result of the two independent processes: bond oxidation and plastic work. The bond coat oxidation process results in a net gain in material at the bond-ceramic interface. The oxide forces the bond coat radially outwards and creates asperities (stress concentrations) along the ceramic-bond interface. Growth of oxide clearly affects the lives of TBC experimental specimens [7]; TBC systems in environments conducive to high oxide growth rates are significantly shorter than those in inert environments. Exactly how oxide reduces the life of the barrier coatings is not totally clear. Plastic work, on the other hand, is believed to cause micro-crack formation and growth, reducing the strength capacity of the ceramic coating. The life prediction algorithm developed by SwRI states that the coating life is proportional to the thickness of the oxide at the bond coating and the cyclic plastic strain. The model follows the form of the Coffin-Manson equation

$$N = (\Delta\epsilon_p / \Delta\epsilon_f)^{-b} \quad (3)$$

In (3), $\Delta\epsilon_f$ is the failure strain of the TBC and $\Delta\epsilon_p$ is the plastic strain per cycle. The magnitude of the failure strain, $\Delta\epsilon_f$, is influenced by the amount of oxide present, and the magnitude of the cyclic plastic strain. Cyclic plastic strain, $\Delta\epsilon_p$, is given by the total of all cyclic plastic strain effects

$$\Delta\epsilon_p = \Delta\epsilon_{DADT} + \Delta\epsilon_H + \Delta\epsilon_C \quad (4)$$

where $\Delta\epsilon_{DADT}$ is the total plastic thermal mismatch strain for a mature cycle, and $\Delta\epsilon_H$ and $\Delta\epsilon_C$ are additional plastic strains, perhaps due to heating and cooling which are not included in $\Delta\epsilon_{DADT}$.

The failure strain in (3), $\Delta\epsilon_f$, is represented as a combination of the single cycle (static) failure strain, and the applied plastic strain

$$\Delta\epsilon_f = \Delta\epsilon_{f0}(1 - t/t_c)^C + \Delta\epsilon_p(t/t_c)^d \quad (5)$$

Substituting (5) into (3) results in the life algorithm used in TBCLIF

$$N = [(\Delta\epsilon_{f0}/\Delta\epsilon_p)(1-t/t_c)^C + E(t/t_c)^d]^b \quad (6)$$

The first term in the square brackets can be considered the cyclic damage term, while the second can be considered the damage done by oxidation of the bond coat. Because bond coat oxidation occurs during thermal cycling, the value of t in (6) changes with time. Miner's Rule must be used in conjunction with (6) to assess the life of the TBC system.

The magnitudes of the single cycle failure strain, $\Delta\epsilon_{f0}$, and the exponents b , c , d and E in (6) are TBC system dependent. They are empirically derived by fitting the life model to experimental data. A difference minimization technique is typically used to establish model variables that have the least sum of squared differences between predicted and experimental lives. Variables $\Delta\epsilon_{f0}$, b , c , and d are hereinafter referred to as the model parameters.

The current thickness of the bond coat oxide layer, t , in (6) is computed using the PWED oxide growth model for uniform exposure time τ (secs.).

$$t = A(K_p \tau)^{x_{PON}} \quad (7)$$

where K_p is the parabolic rate constant, and is given by a function containing the activation energy, ΔH , gas constant R , and ceramic temperature, T .

$$K_p = B \exp(-\Delta H/RT) \quad (8)$$

Bond coat oxidation thickness is updated after the completion of every thermal cycle in TBCLIF.

In experimental work performed at PWED, many TBC specimens were pre-exposed to an oxygen environment with a high, but constant temperature. Such experiments induced an oxidation layer on the bond coat before thermal cycling began. Lives of such specimens were uniformly lower than those of nonpre-exposed specimens undergoing identical thermal cycles. In TBCLIF such pre-exposure must be accounted for to accurately predict the lives of such specimens. Because the exposure temperature is constant, the oxide thickness at the end of the exposure period is calculable directly from equations (7) and (8).

To obtain a predicted life for the thermal barrier coating system, the cyclic plastic strain, single cycle failure strain and the critical thickness for the ceramic coating must be known, as well as the oxidation characteristics (coefficients of equations 7 and 8) of the bond coat. The amount of damage to the TBC system is computed at the end of every thermal cycle in TBCLIF. When the cumulative damage equals or exceeds 1.0, failure is presumed to occur and the total number of completed thermal cycles at that point is taken as the predicted life.

3.0 THE PROGRAMMER'S GUIDE TO TBCLIF

Figures F-1 and F-2 indicate the structure and logic of execution of TBCLIF. As can be seen from the charts, TBCLIF is highly modularized, "top down" code, with all major computations performed in subroutine programs, the main program consisting primarily of subroutine calls. All real variables and arrays in TBCLIF are double precision, i.e. eight bytes long on IBM mainframes.

Execution in TBCLIF proceeds in three phases: reading of input data and preliminary calculations, calculations of oxide thickness and TBC damage, and finally, results presentation. Subroutines INPUT, PREXPO, BLKDAT, INCREM and PLSTRN, constitute the first program phase; GROWTH, DAMAGE and CHECK make up the calculational phase; and the PRINT and MESAG subroutines present results and error messages. Execution flow during the input phase is illustrated in Figure F-1; the logic of computing oxide growth, damage, and TBC failure are somewhat more complex so these subroutines have been illustrated separately in Figure F-2.

INPUT and BLKDAT read the problem constants and thermal cycle characteristics, respectively, from the local file attached to logical unit NIN. These two subroutines also echo the input data on the file attached to

logical unit NOUT. Note that INPUT is called only once during program execution, while BLKDAT is called once for each block of thermal cycles. Thermal Cycles within a block are presumed to be identified. Table F-I lists the variables and constants passed to and from these subroutines via the subroutine argument list and common blocks.

PREXPO, INCREM, and PLSTRN subroutines compute the bond coating oxide thickness at the end of the pre-exposure period, constants controlling the printing of intermediate results, and the total cyclic plastic strain. Table F-I lists the variable and constants passed to and from these subroutines via common blocks or the subroutine argument list.

The calculation subroutines, GROWTH, DAMAGE and CHECK, are called within a program loop that repeats until TBC failure is predicted, or the total number of cycles associated with the current block has been applied (See Figure F-2. This loop is, in turn, nested inside another program loop beginning with the call to BLKDAT (See Figure F-1). Program control passes to the "BLKDAT" loop when multiple blocks of cycles are to be applied; if failure of the TBC has not occurred during the current set of cycles, another set of cycle characteristics is read from the input file and the additional damage calculated.

GROWTH integrates the oxide thickness growth model with respect to pre-exposure time and returns the current thickness at the end of each thermal cycle. This information is then passed to subroutine DAMAGE, along with the cyclic plastic strain. DAMAGE computes the additional damage done by the new thermal cycle. CHECK sums this additional damage to the cumulative damage value and compares the new total to 1.0. Table F-I summarizes variables and common blocks associated with these routines.

Figure F-3 illustrates the integration process used in GROWTH. The user supplies the thermal cycle time/temperature history. GROWTH then computes the parabolic rate constant, K_p , for a temperature at the beginning of a time interval. Using this K_p , the oxide thickness at the beginning and the end of the time interval is found from the expression for oxide growth (7). In this equation, τ is an effective time, t^* . t^* is equal to the time required to generate the accumulated oxide thickness with the parabolic rate constant, K_p computed at the beginning of the time interval. The difference in oxide thickness at the beginning and end of the time interval is found and added to the previous oxide thickness. This process is repeated for all time intervals in the thermal cycle, thus determining the oxide thickness during the cycle.

DAMAGE uses the current value of oxide thickness, model parameters and the cyclic plastic strain to compute a life, N_i , (see equations (1) and (2)) for these conditions. Since one cycle has elapsed, the TBC damage accrued during the cycle is $1/N_i$. CHECK sums this value to the cumulative damage from previous cycles ($\sum_i 1/N_i$) and compares the result with 1.0. If the total damage equals or exceeds 1.0 execution halts and appropriate error messages are printed in the output file.

The PRINT subroutine presents the current value of TBC damage, oxide thickness, critical thickness ratio, and the number of elapsed cycles (both total and within the current block of cycles) in tabular format. Table F-I indicates the variables, constants and common blocks associated with this routine.

4.0 THE USER'S GUIDE TO TBCLIF

Using TBCLIF is straightforward. Because TBCLIF is designed to run in the batch execution mode, two files must be created by the TBCLIF user: a job control file and the data input file. No other action is required of the user to run TBCLIF.

The job control file must make the data input file available for reading by TBCLIF, call TBCLIF for execution, and save the output in permanent storage if required. An example job control file for CMS operating systems is provided in Appendix A. Note that the input file is attached to logical unit five, and output/results file to unit six. These logical unit numbers are specified within the main program of TBCLIF and can be changed, if necessary.

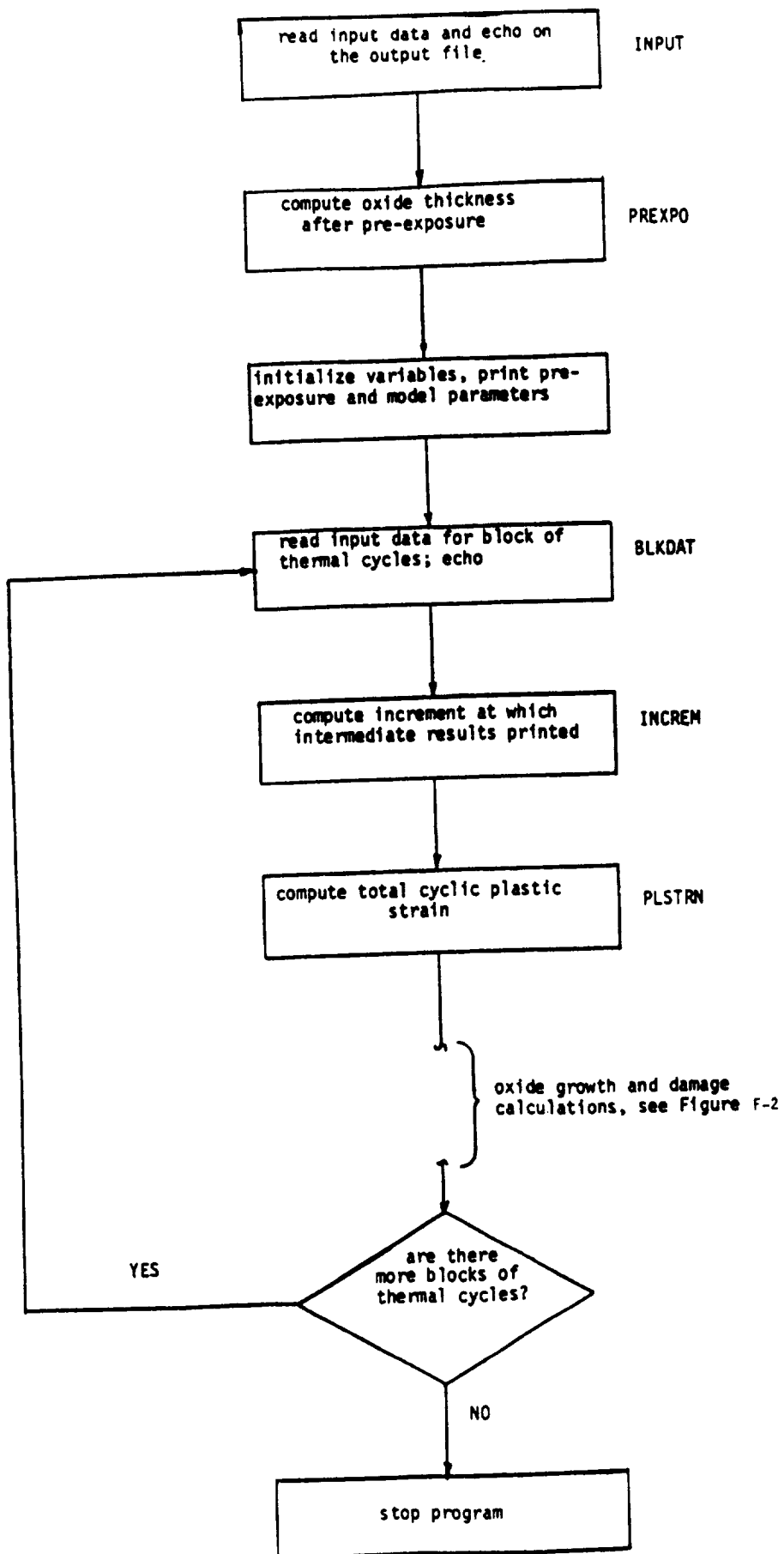
The input data file consists of two portions: the first nine records of data contain analysis type and pre-exposure data; the remaining cards contain thermal cycle data for each of the blocks of cycles to be applied to the TBC system. Six cards are required to describe each block of thermal cycles. The last card in the data file must be a *END card. Table F-2 is reproduced from the TBCLIF listing and describes in detail the structure of the input data file.

Output from TBCLIFE consists of four parts: 1) an echo of the analysis and pre-exposure characteristics, 2) a statement of the life equation parameters, 3) an echo of the temperature-time histories of the applied thermal cycles, and 4) a table of the final and intermediate results. Figures F-4 through F-6 illustrate typical program output.

Appendix A provides the user with a program listing, job control file, input and output from a typical TBCLIF run. The analysis and pre-exposure conditions for the example are given in Figure F-4.

References

1. T.E. Strangman, "Development of Thermomechanical Life Prediction Models for Thermal Barrier Coatings," Thermal Barrier Coatings Workshop, NASA Lewis Research Center, May 21-22, 1985, 1-8.
2. R.A. Miller, "Oxidation-Based Model for Thermal Barrier Coating Life," Journal of the American Ceramic Society, 67(8), 517-521 (1984).
3. G.C. Chang and W. Phucharoen, "Finite Element Analysis of Thermal Barrier Coatings," Thermal Barrier Coatings Workshop, op. cit., 111-126.
4. Letter from S.E. Stewart (SwRI) to F. Kopper (PWED) summarizing thermal and structural analyses of PWED carousel specimen, June 25, 1985.
5. Letter from S.E. Stewart (SwRI) to F. Kopper (PWED) reviewing preliminary life prediction model, July 31, 1985.
6. Letter from S.E. Stewart, "Thermal Barrier Coating Preliminary Life Prediction Model," sent to F. Kopper (PWED) as progress letter of August 20, 1985.
7. J.T. DeMasi and K.D. Sheffler, "Thermal Barrier Coating Life Prediction Model Development," HOST conference proceedings, NASA-Lewis Research Center, October 22 and 23, 1985.



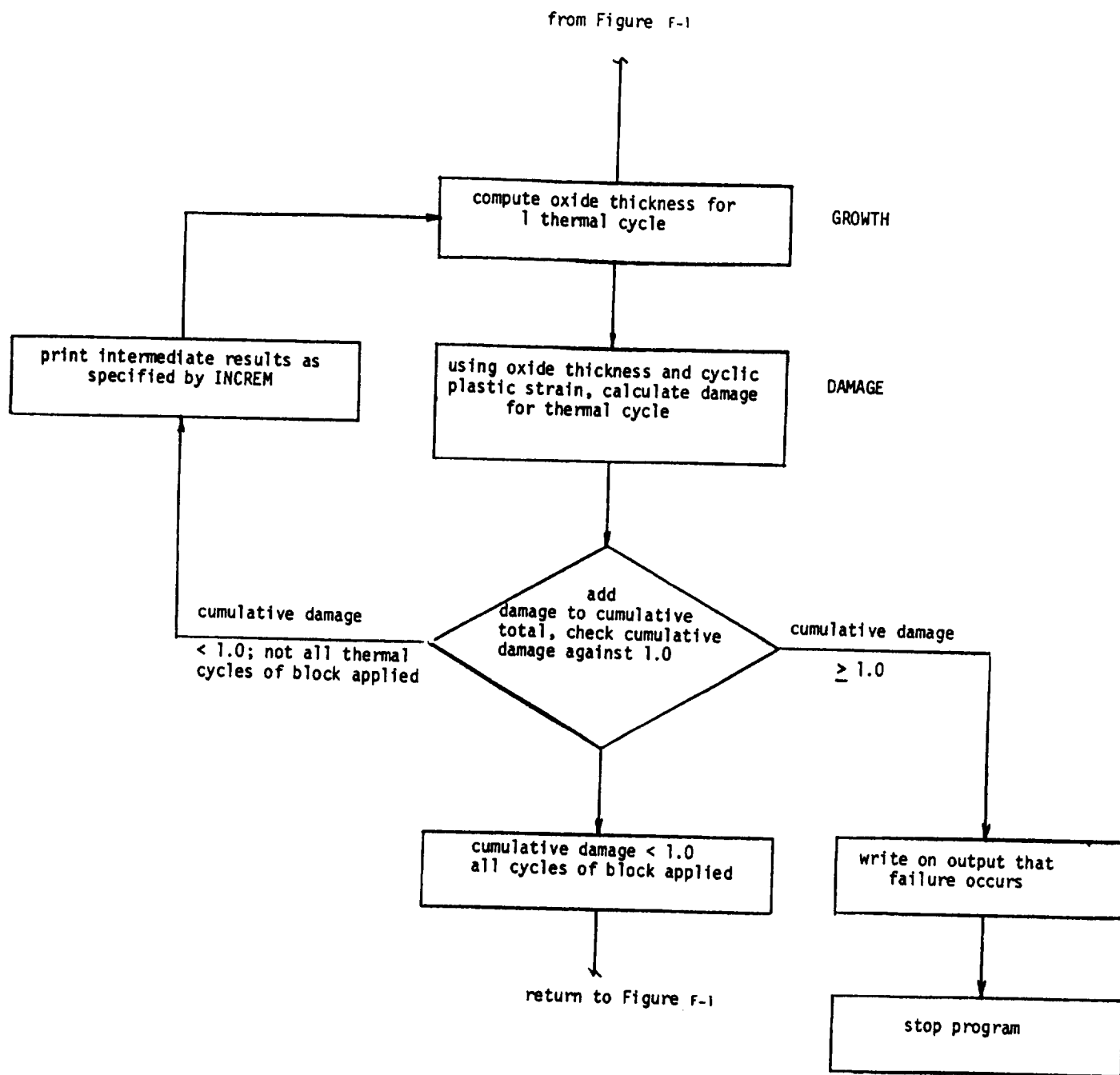


Figure F-2 Execution Flow During Calculational Phase

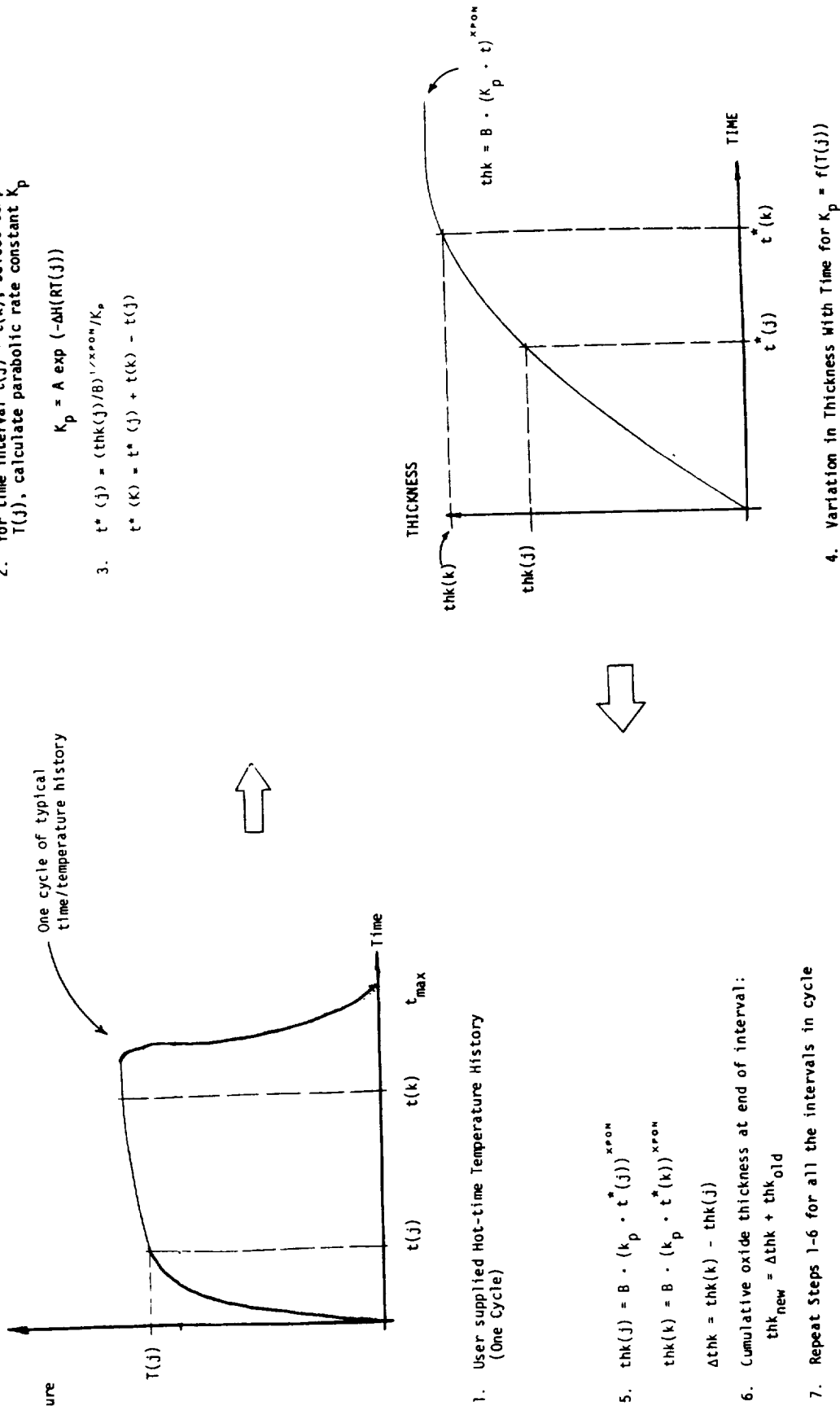


Figure F-3 Integration of Oxide Growth Equations in TBCLIF

TOTAL NUMBER OF BLOCKS (NUMBLK) = 6

NUMBER OF THERMAL CYCLES IN EACH BLOCK (CYCBLK) = 1202 202 1002 502 3000 1500

COEFFICIENT OF ARHENIUS EQUATION (GM2/CM4-SEC) (A) = 0.5714E+12

ACTIVATION ENERGY (CAL/MOLE) (DELH) = 0.1049E+06

GAS CONSTANT (CAL/DEG K-MOLE) (R) = 0.1987E+01

OXIDE GROWTH EQUATION COEFFICIENT (CM3/GM) (C2) = 0.1780E-03

OXIDE GROWTH EQUATION COEFFICIENT (XPON) = 0.3850E+00

CRITICAL THICKNESS (INCHES) (THKCRT) = 0.4000E-03

PRE-EXPOSURE TIME IN THE FURNACE (SEC) (TIMFUR) = 0.3600E+05

FURNACE TEMPERATURE (DEGREES RANKINE) (TMPFUR) = 0.2460E+04

FURNACE PRE-EXPOSURE THICKNESS (IN) (THKFUR) = 0.4677E-04

L I F E M O D E L P A R A M E T E R S

N = ((DELEPP/DELEPP) * (1 - THKNES/THKCRT)**C) + E * (THKNES/THKCRT)**D)**B

WHERE DELEPP = DELEPP + DELEPH + DADT

THKNES = C2 * ((KP * TIME) ** XPON)

KP = A * EXP(-DELH / (R * TEMP))

TIME(SEC)

TEMP(KELVIN)

SINGLE CYCLE FAILURE PLASTIC STRAIN (DELEPP) = 0.4300E-02

LIFE EQUATION EXPONENT (B) = 0.1088E+02

LIFE EQUATION EXPONENT (C) = 0.1000E+01

LIFE EQUATION EXPONENT (D) = 0.1000E+01

LIFE EQUATION COEFFICIENT (E) = 0.1000E+01

PLASTIC STRAIN DUE TO COOLING FLUX (DELEPC) = 0.0000E+00

PLASTIC STRAIN DUE TO HEATING FLUX (DELEPH) = 0.0000E+00

PLASTIC STRAIN DUE TO THERMAL MISMATCH .. (DADT) = 0.1258E-02

TIME STEP	CYCLE TIME (SEC)	INTERFACE TEMP (DEG R)
1	0.0000E+00	0.1163E+04
2	0.4000E+01	0.1331E+04
3	0.8000E+01	0.1448E+04
4	0.1500E+02	0.1634E+04
5	0.3100E+02	0.1911E+04
6	0.4600E+02	0.2112E+04
7	0.7300E+02	0.2341E+04
8	0.9200E+02	0.2434E+04
9	0.1190E+03	0.2492E+04
10	0.1390E+03	0.2500E+04
11	0.6820E+03	0.2500E+04
12	0.6860E+03	0.2350E+04
13	0.6900E+03	0.2155E+04
14	0.6970E+03	0.1844E+04
15	0.7090E+03	0.1556E+04
16	0.7200E+03	0.1163E+04

Figure F-5 Output File Echo of Thermal Cycle of Temperature History

ORIGINAL PAGE IS
OF POOR QUALITY

TOTAL CYCLES	NUMBER OF CYCLES IN THIS BLOCK	CURRENT VALUE OF OXIDE LAYER (IN.)	THK/THKCR	CYCLIC PLASTIC STRAIN (IN/IN)	CURRENT VALUE OF DAMAGE
1444	40	0.214469E-03	0.5362E+00	0.1372E-02	0.14994
1484	80	0.218976E-03	0.5474E+00	0.1372E-02	0.17398
1524	120	0.223339E-03	0.5583E+00	0.1372E-02	0.20139
1564	160	0.227570E-03	0.5689E+00	0.1372E-02	0.23255
1604	200	0.231679E-03	0.5792E+00	0.1372E-02	0.26789
1644	240	0.235675E-03	0.5892E+00	0.1372E-02	0.30789
1684	280	0.239565E-03	0.5989E+00	0.1372E-02	0.35307
1724	320	0.243357E-03	0.6084E+00	0.1372E-02	0.40402
1764	360	0.247057E-03	0.6176E+00	0.1372E-02	0.46137
1804	400	0.250670E-03	0.6267E+00	0.1372E-02	0.52583
1844	440	0.254202E-03	0.6355E+00	0.1372E-02	0.59816
1884	480	0.257658E-03	0.6441E+00	0.1372E-02	0.67924
1924	520	0.261041E-03	0.6526E+00	0.1372E-02	0.76999
1964	560	0.264355E-03	0.6609E+00	0.1372E-02	0.87146
2004	600	0.267604E-03	0.6690E+00	0.1372E-02	0.98477
>> << CURRENT DAMAGE IS GREATER THAN OR EQUAL TO 1.0.					
2010	606	0.268086E-03	0.6702E+00	0.1372E-02	1.00287
*** END OF PROGRAM ***					

Figure F-6 Tabulated Output From TBCLIF

Table F-I
Variables and Arrays Used in Subroutines

VARIABLE OR ARRAY	USED IN SUBROUTINE	PASSED VIA
A	Input, Preexpo, Growth	Cnst
B	Input, Damage	Inpt
C	Input, Damage	Inpt
C2	Input, Preexpo, Growth	Cnst
CMMENT	Blkdat	Internal
CURCYC	Print	Internal
CYCBLK(I)	Input, Print	*Arg. list
CYTIME(I)	Blkdat, Growth	Tmiv
D	Input, Damage	Inpt
DADT	Blkdat, Plstrn	Arg. list
DAMCYC	Check	Arg. list
DAMISN	Check, Print	Arg. list
DELEPC	Blkdat, Plstrn	Arg. list
DELEPF	Input, Damage	Inpt
DELEPH	Blkdat, Plstrn	Arg. list
DELEPP	Plstrn, Damage, Print	Arg. list
DELGRW	Growth	Internal
DELH	Input, Preexpo, Growth	Cnst
FLAG	Blkdat	Arg. list
HEADNG	Input	*Internal
ICODE	Message	Arg. list
ICYCLE	Growth, Print	Arg. list
IDUM	Blkdat, Growth	Internal
INCR	Increment	Arg. list
KP	Preexpo, Growth	Internal
N	Damage	Internal
NBLK	Print	Arg. list
NBLOCK	Blkdat	Arg. list
NCYC	Increment	Arg. list
NIN	Input, Blkdat, Check, Print, Message	Ioun
NOUT	Input, Blkdat, Check, Print, Message	Ioun
NT	Growth	Internal
NTIME	Blkdat	Tmiv
NUM	Increment, Message	Arg. list
NUMBLK	Input	Arg. list
R	Input, Preexpo, Growth	Cnst
REMAIN	Increment	Arg. list
STOP	Check	Internal
TEMP	Preexpo, Growth	Internal
THK1	Growth	Internal
THK2	Growth	Internal
THKCRT	Input, Damage, Print	Arg. list
THKFUR	Preexpo	Arg. list
THKNES	Growth, Damage, Print	Arg. list
TIMFUR	Input, Preexpo	Furn
TMAX	Growth	Internal
TMNEW1	Growth	Internal
TMNEW2	Growth	Internal
TMPFUR	Input, Preexpo	Furn
TMPINF(I)	Blkdat, Growth	Temp
XPON	Input, Preexpo, Growth	Cnst

*Note: "Arg. list" and "Internal" refer to subroutine argument list and internally generated variables, respectively.

Table F-2

Characteristics of Input Data

C INPUT DATA: TEM00160
 C TEM00170
 C THERE ARE TWO PORTIONS OF INPUT DATA. THE FIRST PORTION TEM00180
 C CONTAINS THE GENERAL INFORMATION FOR THE PROGRAM. THE SECOND TEM00190
 C PORTION HAS SETS OF REPETITIVE DATA ARRANGED IN DATA BLOCKS. TEM00200
 C EACH BLOCK DATA SET BEGINS WITH A COMMENT CARD, *BLOCKN. AN TEM00210
 C *END CARD IS USED TO TERMINATE THE EXECUTION OF THE PROGRAM TEM00220
 C AND DESIGNATES THE END OF THE INPUT DATA. DATA INPUT IS IN TEM00230
 C FREE FORMAT, SEPARATE MULTIPLE ENTRIES IN A RECORD WITH COMMAS TEM00240
 C OR BLANKS. TEM00250
 C TEM00260
 C PORTION I. TEM00270
 C TEM00280
 C

CARD #	ITEMS	DATA TYPE	REMARKS	TEM00290
1	HEADNG	CHARACTER STRING	GENERAL PROBLEM DESCRIPTION (UP TO 80 CHARACTERS)	TEM00300 TEM00310 TEM00320
2	NUMBLK	INTEGER*4	TOTAL NUMBER OF BLOCKS (UP TO 7000)	TEM00330 TEM00340 TEM00350 TEM00360
3	CYCBK(I) (I=1,NUMBLK)	INTEGER*4	NUMBER OF THERMAL CYCLES IN EACH (COULD BE MORE THAN ONE CARD	TEM00370 TEM00380
4	A, DELH, R,	REAL*8	ARRHENIUS EQUATION COEFFICIENTS (DELH > 0.0)	TEM00390 TEM00400 TEM00410 TEM00420
5	C2, XPON	REAL*8	OXIDE GROWTH EQUATION COEFFICIENTS	TEM00430 TEM00440 TEM00450
6	THKCRT	REAL*8	CRITICAL OXIDE THICKNESS	TEM00460 TEM00470
7	TIMFUR	REAL*8	PRE-EXPOSURE TIME IN THE FURNACE (SEC)	TEM00480 TEM00490
8	TMPFUR	REAL*8	PRE-EXPOSURE FURNACE TEMPERATURE	TEM00500

LEVEL 2.1.1 (SEPT 1986)

VS FORTRAN

DATE: JUL 29, 1987

TIME: 12:42:39

NAME: MAIN

PAGE: 2

IF DO ISN *.....1.....2.....3.....4.....5.....6.....7.....8

C (DEGREES RANKINE) TEM00510
 C TEM00520
 C 9 DELEPF,B,C,D,E REAL*8 FIVE CONSTANTS OF LIFE EQUATION TEM00530
 C PORTION II. TEM00540
 C TEM00550
 C 10 *BLOCKN CHARACTER COMMENT CARD TEM00560
 C STRING (N IS THE BLOCK NUMBER.) TEM00570
 C TEM00580
 C 11 DELEPC,DELEPH REAL*8 HEATING AND COOLING CYCLIC PLATE TEM00600
 C STRAIN COMPONENTS FOR CURRENT TEM00610
 C TEM00620
 C 12 DADT REAL*8 PLASTIC STRAIN DUE TO THERMAL TEM00630
 C MISMATCH OCCURRING DURING ONE TEM00640
 C TEM00650
 C 13 NTIME INTEGER*4 TOTAL NUMBER OF TIME STEPS IN TEM00660
 C THE THERMAL CYCLE TEM00670
 C IS DIVIDED TEM00680
 C (UP TO 50; FOR INTEGRATION OF TEM00690
 C GROWTH EQUATION) TEM00700
 C TEM00710
 C TEM00720
 C TEM00730
 C TEM00740
 C 14 CYTIME(L) REAL*8 VECTOR OF TIME POINTS INTO WHICH TEM00750
 C (L=1,NTIME) THERMAL CYCLE OF BLOCK IS DIVIDED TEM00760
 C (SECONDS; IN ORDER OF INCREASE TEM00770
 C TIME, TIME = 0 AT THE BEGINNING TEM00780
 C OF THE THERMAL CYCLE "HOT TIME") TEM00790
 C TEM00800
 C 15 TMPINF(L) REAL*8 VECTOR OF "HOT TIME" TEMPERATURE TEM00810
 C (L=1,NTIME) INTERFACE BETWEEN BOND AND CERAMIC TEM00820
 C (DEGREES RANKINE; TEMPERATURE TEM00830
 C THOSE ASSOCIATED WITH TIMES TEM00840
 C CYTIME) TEM00850
 C TEM00860
 C 16 *END LAST CARD OF INPUT DECK TEM00870
 C TEM00880
 C NOTE: TEM00890
 C CARDS 10, 11, 12, 13, 14 AND 15 COULD BE MORE THAN ONE CARD TEM00900
 C REPEAT CARDS 7 TO 15 NUMBLK TIMES. TEM00910
 C TEM00920
 C TEM00930

APPENDIX G
TBCLIF LISTING AND EXAMPLE PROBLEM

SAMPLE TEST CASE OUTPUT

TBCLIF

EXAMPLE PROBLEM

```

TOTAL NUMBER OF BLOCKS ..... (NUMBLK) = 6
NUMBER OF THERMAL CYCLES IN EACH BLOCK ..... (CYCBLK) =
1202 202 1002 502 3000 1500
COEFFICIENT OF ARHENIUS EQUATION (GM2/CM4-SEC) ..... ( A ) = 0.5714E+12
ACTIVATION ENERGY (CAL/MOLE) ..... ( DELH ) = 0.1049E+06
GAS CONSTANT (CAL/DEG K-MOLE) ..... ( R ) = 0.1987E+01
OXIDE GROWTH EQUATION COEFFICIENT (CM3/GM) ..... ( C2 ) = 0.1780E-03
OXIDE GROWTH EQUATION COEFFICIENT ..... ( XPON ) = 0.3850E+00
CRITICAL THICKNESS (INCHES) ..... (THKCRT) = 0.4000E-03
PRE-EXPOSURE TIME IN THE FURNACE (SEC) ..... (TIMFUR) = 0.3600E+05
FURNACE TEMPERATURE (DEGREES RANKINE) ..... (TMPFUR) = 0.2460E+04
FURNACE PRE-EXPOSURE THICKNESS (IN) ..... (THKFUR) = 0.4677E-04

```

L I F E M O D E L P A R A M E T E R S

```

N = ( (DELEPP/DELEPP) * (1 - THKNES/THKCRT**C) + E * (THKNES/THKCRT)**D )**B
WHERE  DELEPP = DELEPC + DELEPH + DADT
THKNES = C2 * (( KP * TIME ) ** XPON )
KP      = A * EXP( -DELH / (R * TEMP) )
TIME(SEC)
TEMP(KELVIN)

```

```

SINGLE CYCLE FAILURE PLASTIC STRAIN ..... (DELEPP) = 0.4300E-02
LIFE EQUATION EXPONENT ..... ( B ) = 0.1088E+02
LIFE EQUATION EXPONENT ..... ( C ) = 0.1000E+01
LIFE EQUATION EXPONENT ..... ( D ) = 0.1000E+01
LIFE EQUATION COEFFICIENT ..... ( E ) = 0.1000E+01

```

DATA FOR BLOCK NUMBER 1

PLASTIC STRAIN DUE TO COOLING FLUX (DELEPC) = 0.0000E+00
 PLASTIC STRAIN DUE TO HEATING FLUX (DELEPH) = 0.0000E+00
 PLASTIC STRAIN DUE TO THERMAL MISMATCH .. (DADT) = 0.1258E-02

TIME STEP	CYCLE TIME (SEC)	INTERFACE TEMP (DEG R)
1	0.0000E+00	0.1163E+04
2	0.4000E+01	0.1331E+04
3	0.8000E+01	0.1448E+04
4	0.1500E+02	0.1634E+04
5	0.3100E+02	0.1911E+04
6	0.4600E+02	0.2112E+04
7	0.7300E+02	0.2341E+04
8	0.9200E+02	0.2434E+04
9	0.1190E+03	0.2492E+04
10	0.1390E+03	0.2500E+04
11	0.6820E+03	0.2500E+04
12	0.6860E+03	0.2350E+04
13	0.6900E+03	0.2155E+04
14	0.6970E+03	0.1844E+04
15	0.7090E+03	0.1556E+04
16	0.7200E+03	0.1163E+04

RESULTS FOR BLOCK NO. 1

TOTAL CYCLES	NUMBER OF CYCLES IN THIS BLOCK	CURRENT VALUE OF OXIDE LAYER (IN.)	THK/THKCRIT	CYCLIC PLASTIC STRAIN (IN/IN)	CURRENT VALUE OF DAMAGE
48	48	0.657783E-04	0.1644E+00	0.1258E-02	0.00024
96	96	0.785906E-04	0.1965E+00	0.1258E-02	0.00058
144	144	0.887204E-04	0.2218E+00	0.1258E-02	0.00101
192	192	0.972761E-04	0.2432E+00	0.1258E-02	0.00154
240	240	0.104773E-03	0.2619E+00	0.1258E-02	0.00218
288	288	0.111498E-03	0.2787E+00	0.1258E-02	0.00294
336	336	0.117631E-03	0.2941E+00	0.1258E-02	0.00382
384	384	0.123292E-03	0.3082E+00	0.1258E-02	0.00484
432	432	0.128565E-03	0.3214E+00	0.1258E-02	0.00600
480	480	0.133514E-03	0.3338E+00	0.1258E-02	0.00732
528	528	0.138186E-03	0.3455E+00	0.1258E-02	0.00882
576	576	0.142618E-03	0.3565E+00	0.1258E-02	0.01049
624	624	0.146840E-03	0.3671E+00	0.1258E-02	0.01236
672	672	0.150877E-03	0.3772E+00	0.1258E-02	0.01445
720	720	0.154748E-03	0.3869E+00	0.1258E-02	0.01676
768	768	0.158471E-03	0.3962E+00	0.1258E-02	0.01931
816	816	0.162059E-03	0.4051E+00	0.1258E-02	0.02213
864	864	0.165524E-03	0.4138E+00	0.1258E-02	0.02523
912	912	0.168877E-03	0.4222E+00	0.1258E-02	0.02863
960	960	0.172127E-03	0.4303E+00	0.1258E-02	0.03235
1008	1008	0.175282E-03	0.4382E+00	0.1258E-02	0.03642
1056	1056	0.178348E-03	0.4459E+00	0.1258E-02	0.04085
1104	1104	0.181335E-03	0.4533E+00	0.1258E-02	0.04568
1152	1152	0.184241E-03	0.4606E+00	0.1258E-02	0.05093
1200	1200	0.187077E-03	0.4677E+00	0.1258E-02	0.05662
1202	1202	0.187194E-03	0.4680E+00	0.1258E-02	0.05687

D A T A F O R B L O C K N U M B E R 2

PLASTIC STRAIN DUE TO COOLING FLUX (DELEPC) = 0.0000E+00
 PLASTIC STRAIN DUE TO HEATING FLUX (DELEPH) = 0.0000E+00
 PLASTIC STRAIN DUE TO THERMAL MISMATCH .. (DADY) = 0.1367E-02

TIME STEP	CYCLE TIME (SEC)	INTERFACE TEMP (DEG R)
1	0.0000E+00	0.1203E+04
2	0.4000E+01	0.1372E+04
3	0.8000E+01	0.1490E+04
4	0.1500E+02	0.1678E+04
5	0.3100E+02	0.1957E+04
6	0.4600E+02	0.2160E+04
7	0.7300E+02	0.2390E+04
8	0.9200E+02	0.2484E+04
9	0.1190E+03	0.2542E+04
10	0.1390E+03	0.2550E+04
11	0.6820E+03	0.2550E+04
12	0.6860E+03	0.2399E+04
13	0.6900E+03	0.2202E+04
14	0.6970E+03	0.1889E+04
15	0.7090E+03	0.1599E+04
16	0.7200E+03	0.1203E+04

TOTAL CYCLES	NUMBER OF CYCLES IN THIS BLOCK	CURRENT VALUE OF OXIDE LAYER (IN.)	THK/THKCR1	CYCLIC PLASTIC STRAIN (IN/IN)	CURRENT VALUE OF DAMAGE
1210	8	0.188174E-03	0.4704E+00	0.1367E-02	0.05893
1218	16	0.189146E-03	0.4729E+00	0.1367E-02	0.06104
1226	24	0.190110E-03	0.4753E+00	0.1367E-02	0.06321
1234	32	0.191066E-03	0.4777E+00	0.1367E-02	0.06544
1242	40	0.192014E-03	0.4800E+00	0.1367E-02	0.06773
1250	48	0.192955E-03	0.4824E+00	0.1367E-02	0.07007
1258	56	0.193889E-03	0.4847E+00	0.1367E-02	0.07248
1266	64	0.194816E-03	0.4870E+00	0.1367E-02	0.07495
1274	72	0.195736E-03	0.4893E+00	0.1367E-02	0.07749
1282	80	0.196649E-03	0.4916E+00	0.1367E-02	0.08009
1290	88	0.197555E-03	0.4939E+00	0.1367E-02	0.08276
1298	96	0.198454E-03	0.4961E+00	0.1367E-02	0.08550
1306	104	0.199347E-03	0.4984E+00	0.1367E-02	0.08830
1314	112	0.200234E-03	0.5005E+00	0.1367E-02	0.09118
1322	120	0.201115E-03	0.5028E+00	0.1367E-02	0.09413
1330	128	0.201989E-03	0.5050E+00	0.1367E-02	0.09715
1338	136	0.202857E-03	0.5071E+00	0.1367E-02	0.10025
1346	144	0.203720E-03	0.5093E+00	0.1367E-02	0.10343
1354	152	0.204577E-03	0.5114E+00	0.1367E-02	0.10668
1362	160	0.205428E-03	0.5136E+00	0.1367E-02	0.11002
1370	168	0.206273E-03	0.5157E+00	0.1367E-02	0.11343
1378	176	0.207113E-03	0.5178E+00	0.1367E-02	0.11693
1386	184	0.207947E-03	0.5199E+00	0.1367E-02	0.12052
1394	192	0.208777E-03	0.5219E+00	0.1367E-02	0.12419
1402	200	0.209601E-03	0.5240E+00	0.1367E-02	0.12795
1404	202	0.209806E-03	0.5245E+00	0.1367E-02	0.12890

DATA FOR BLOCK NUMBER 3

PLASTIC STRAIN DUE TO COOLING FLUX (DELEPC) = 0.0000E+00
 PLASTIC STRAIN DUE TO HEATING FLUX (DELEPH) = 0.0000E+00
 PLASTIC STRAIN DUE TO THERMAL MISMATCH .. (DADT) = 0.1372E-02

TIME STEP	CYCLE TIME (SEC)	INTERFACE TEMP (DEG R)
1	0.0000E+00	0.1243E+04
2	0.4000E+01	0.1408E+04
3	0.8000E+01	0.1524E+04
4	0.1500E+02	0.1707E+04
5	0.3100E+02	0.1980E+04
6	0.4600E+02	0.2178E+04
7	0.7300E+02	0.2404E+04
8	0.9200E+02	0.2495E+04
9	0.1190E+03	0.2552E+04
10	0.1390E+03	0.2560E+04
11	0.6820E+03	0.2560E+04
12	0.6860E+03	0.2413E+04
13	0.6900E+03	0.2220E+04
14	0.6970E+03	0.1914E+04
15	0.7090E+03	0.1630E+04
16	0.7200E+03	0.1243E+04

TOTAL CYCLES	NUMBER OF CYCLES IN THIS BLOCK	CURRENT VALUE OF OXIDE LAYER (IN.)	THK/THKCR	CYCLIC PLASTIC STRAIN (IN/IN)	CURRENT VALUE OF DAMAGE
1444	40	0.214469E-03	0.5362E+00	0.1372E-02	0.14994
1484	80	0.218976E-03	0.5474E+00	0.1372E-02	0.17398
1524	120	0.223339E-03	0.5583E+00	0.1372E-02	0.20139
1564	160	0.227570E-03	0.5689E+00	0.1372E-02	0.23255
1604	200	0.231679E-03	0.5792E+00	0.1372E-02	0.26789
1644	240	0.235675E-03	0.5892E+00	0.1372E-02	0.30789
1684	280	0.239565E-03	0.5989E+00	0.1372E-02	0.35307
1724	320	0.243357E-03	0.6084E+00	0.1372E-02	0.40402
1764	360	0.247057E-03	0.6176E+00	0.1372E-02	0.46137
1804	400	0.250670E-03	0.6267E+00	0.1372E-02	0.52583
1844	440	0.254202E-03	0.6355E+00	0.1372E-02	0.59816
1884	480	0.257658E-03	0.6441E+00	0.1372E-02	0.67924
1924	520	0.261041E-03	0.6526E+00	0.1372E-02	0.76999
1964	560	0.264355E-03	0.6609E+00	0.1372E-02	0.87146
2004	600	0.267604E-03	0.6690E+00	0.1372E-02	0.98477
>> << CURRENT DAMAGE IS GREATER THAN OR EQUAL TO 1.0.					
2010	606	0.268086E-03	0.6702E+00	0.1372E-02	1.00287

*** END OF PROGRAM ***

TBCLIF

CMS JOB CONTROL LISTING

```

&TRACE OFF
&CONTROL OFF
&STACK HT EXEC USE VSFORT
-START &CONTINUE
&STACK RT
&BEGETYPE -T1

TBC LIFE PREDICTION MODEL

-T1
-INPUT &TYPE TYPE FN FT (FM) OF DATA FILE
&READ ARGS
&IF &INDEX EQ 3 &GOTO -IN3
&IF &INDEX NE 2 &GOTO -INPUT
&FN = &1
&FT = &2
&FM = &1
&GOTO -IN2
-IN3 &CONTINUE
&FN = &1
&FT = &2
&FM = &3
-IN2 &CONTINUE
&STACK HT
STATE &FN &FT &FM
&STACK RT
&IF &RETCODE NE 0 &GOTO -ERROR
&GOTO -FD
-ERROR &CONTINUE
&TYPE FILE NOT FOUND
-CONT &CONTINUE
&BEGETYPE -T2
CONTINUE? (YES NO)
-T2
&READ ARGS
&IF &INDEX NE 1 &GOTO -CONT
&IF &1 EQ NO &GOTO -GOHOME
&IF &1 EQ YES &GOTO -INPUT
&GOTO -CONT
-FD &CONTINUE

```

PAGIT

FI 07 TERMINAL
FI 5 DISK &FN &FT &FM
FI 6 DISK &FN OUT1 D (RECFM FB LRECL 132 BLKSIZE 132
LOAD TBCLIF (CLEAR START
&IF &RETCODE NE 0 &GOTO -ERRS
&GOTO -OPT1
-ERRS &CONTINUE
&BEGTYPE -LA2

ABNORMAL TERMINATION. PLEASE CHECK YOUR INPUT DATA.
HIT RETURN TO EDIT ERROR LISTING

-LA2
&READ &DUM
X ERROR LISTING D
&GOTO -GOHOME
-OPT1

-OUTPUT

PAGIT

&BEGTYPE -POST1

HOPM OPTIONS:		TYPE	MAIN OPTIONS
INPUT	1		XEDIT INPUT FILE
OUTPUT	2		XEDIT PRINT OUTPUT FILE
	3		PRINT OUTPUT FILE
RERUN	R		RERUN TBC
	99		TERMINATE

-POST1

```

-UP1Z  &CONTINUE
&BEGTYPE -POST2
TYPE OPTION. (HIT RETURN FOR OPTION LIST)
-POST2

&READ ARGS
&IF &1 EQ 99 &GOTO -GOHOME
&IF &1 EQ 1 &GOTO -DONE1
&IF &1 EQ 2 &GOTO -DONE2
&IF &1 EQ 3 &GOTO -DONE3
&IF &1 EQ R &GOTO -RUN
&GOTO -PRINT
-DONE1 &CONTINUE
&FNAME = &FN
&FTYPE = &FT
&FMODE = &FM
&GOTO -DON31
-DONE2
&FNAME = &FN
&FTYPE = OUT1
&FMODE = D
&GOTO -DON31
-DONE3
&FNAME = &FN
&FTYPE = OUT1
&FMODE = D
&GOTO -PRINT
-DON31
XEDIT &FNAME &FTYPE &FMODE
&GOTO -OUTPUT
-PRINT
PRINT &FNAME &FTYPE &FMODE
&GOTO -OUTPUT
-RUN
&GOTO -FD
-GOHOME
PAGEIT
&EXIT

```

ORIGINAL PAGE IS
OF POOR QUALITY

TBCLIF

PROGRAM LISTING

REQUESTED OPTIONS (EXECUTE): SOURCE XREF MAP

OPTIONS IN EFFECT: NOLIST MAP XREF GOSTMT NODUCK SOURCE TERM OBJECT FIXED TRMFLG NOSRCFLG NOSYM NORENT
 NOSDUMP AUTOOBL(NONE) NOSYM NOVECTOR IL NOTEST NODC NOINDIRECTIVE
 OPT(3) LANGVL(77) NOFIPS FLAG(I) NAME(MAIN) LINECOUNT(60) CHARLEN(500)

IF DO ISN *.....1.....2.....3.....4.....5.....6.....7.....8

C *****
 C C PURPOSE:
 C TEM00020
 C TEM00030
 C TEM00040
 C TEM00050
 C TEM00060
 C TEM00070
 C TEM00080
 C TEM00090
 C TEM00100
 C TEM00110
 C TEM00120
 C TEM00130
 C TEM00140
 C TEM00150
 C TEM00160
 C TEM00170
 C TEM00180
 C TEM00190
 C TEM00200
 C TEM00210
 C TEM00220
 C TEM00230
 C TEM00240
 C TEM00250
 C TEM00260
 C TEM00270
 C TEM00280
 C TEM00290
 C TEM00300
 C TEM00310
 C TEM00320
 C TEM00330
 C TEM00340
 C TEM00350
 C TEM00360
 C TEM00370
 C TEM00380
 C TEM00390
 C TEM00400
 C TEM00410
 C TEM00420
 C TEM00430
 C TEM00440
 C TEM00450
 C TEM00460
 C TEM00470
 C TEM00480
 C TEM00490
 C TEM00500

C INPUT DATA:

THERE ARE TWO PORTIONS OF INPUT DATA. THE FIRST PORTION
 CONTAINS THE GENERAL INFORMATION FOR THE PROGRAM. THE SECOND
 PORTION HAS SETS OF REPETITIVE DATA ARRANGED IN DATA BLOCKS.
 EACH BLOCK DATA SET BEGINS WITH A COMMENT CARD, *BLOCKN. AN
 *END CARD IS USED TO TERMINATE THE EXECUTION OF THE PROGRAM
 AND DESIGNATES THE END OF THE INPUT DATA. DATA INPUT IS IN
 FREE FORMAT, SEPARATE MULTIPLE ENTRIES IN A RECORD WITH COMMENTS
 OR BLANKS.

C PORTION I.

CARD #	ITEMS	DATA TYPE	REMARKS
1	HEADING	CHARACTER STRING	GENERAL PROBLEM DESCRIPTION CATEM00310 (UP TO 80 CHARACTERS)
2	NUMBLK	INTEGER*4	TOTAL NUMBER OF BLOCKS (UP TO 7000)
3	CYCBLK(I) (I=1,NUMBLK)	INTEGER*4	NUMBER OF THERMAL CYCLES IN EATEM00370 (COULD BE MORE THAN ONE CARD TEM00380
4	A, DELH, R,	REAL*8	ARRHENIUS EQUATION COEFFICIENTSTEM00400 (DELH > 0.0)
5	C2, XPON	REAL*8	OXIDE GROWTH EQUATION COEFFICIENTTEM00430
6	THKCR	REAL*8	CRITICAL OXIDE THICKNESS
7	TMFUR	REAL*8	PRE-EXPOSURE TIME IN THE FURNACETEM00470 (SEC)
8	TMPFUR	REAL*8	PRE-EXPOSURE FURNACE TEMPERATURETEM00500

IF DO ISN *.....1.....2.....3.....4.....5.....6.....7.....8

```

14      C      NUM = 25
      C
      C *** READ THE GENERAL DATA
      C
15      CALL INPUT(NUMBLK,CYCBLK,THKFUR)
16      IF (NUMBLK.GT. 7000) CALL MESSAGE(1,0)
18      IF (NUMBLK.GT. 7000) STOP
      C
      C *** CHECK VALUE OF GAS CONSTANT R
      C
20      IF(R.EQ. 0.) CALL MESSAGE(2,0)
22      IF(R.EQ. 0.) STOP
      C
      C *** COMPUTE THE SCALE GROWTH OF FURNACE PRE-EXPOSURE
      C
24      THKFUR = 0.
25      IF (TIMFUR.NE.0. .AND. TMPFUR.NE.0.) CALL PREXPO(THKFUR)
      C
      C *** INITIALIZE THE MISSION DAMAGE DAMISN, THE FLAG VARIABLE FLAG,
      C THE CYCLE COUNTER ICYCLE AND THE THICKNESS GAIN THKNES
      C
27      DAMISN = 0.
28      FLAG = 0
29      ICYCLE = 0
30      THKNES = THKFUR
      C
31      WRITE(NOUT,1008) THKFUR
32      WRITE(NOUT,1009) DELEPF,B,C,D,E
      C
      C *** REPEAT THE FOLLOWING CALCULATION FOR ALL THE BLOCKS
      C
33      DO 100 NBLK=1,NUMBLK
      C
      C *** READ THE DATA PERTAINING TO THIS BLOCK
      C
34      CALL BLKDAT(DELEPC,DELEPH,DADT,NBLK,FLAG)
35      IF (FLAG.EQ. 1) CALL MESSAGE(3,NBLK)
37      IF (FLAG.EQ. 1) STOP
39      IF (INTIME.GT. 50) CALL MESSAGE(4,0)
41      IF (INTIME.GT. 50) STOP
      C
      C *** COMPUTE THE INCREMENT AT WHICH INTERMEDIATE RESULTS ARE PRINTED
      C
43      CALL INCRCYCBLK(NBLK),NUM,INCR,REMAIN)
      C
      C *** COMPUTE DELEPP; THE PLASTIC STRAIN FOR ONE CYCLE
      C
44      CALL PLSTRN(DADT,DELEPC,DELEPH,DELEPP)
      C
      C *** PRINT THE HEADING FOR CURRENT BLOCK OUTPUT
      C
45      WRITE(NOUT,1010) NBLK
46      WRITE(NOUT,1020)

```

```

IF DO  ISN  *.....1.....2.....3.....4.....5.....6.....7.....8
C
1  47      NL = NUM
1  48      IF(INCR.EQ.1 .AND. REMAIN.EQ.0) NL = CYCBLK(NBLK)
C
1  50      DO 50 J=1,NL
2  51      DO 40 K=1,INCR
C
3  52      C *** COMPUTE THE THICKNESS GAIN FOR ONE THERMAL CYCLE OF BLOCK
C
C      CALL GROWTH(ICYCLE,THKNES)
C
C *** COMPUTE DAMAGE FOR THIS CYCLE
C
3  53      CALL DAMAGE(DELEPP,THKNES,THKCR,T,DAMCYC)
C
C *** CHECK THE MISSION DAMAGE
C
3  54      CALL CHECK(DAMCYC,DAMISN,STOP)
C
3  55      IF(STOP) GO TO 990
3  56      40 CONTINUE
C
2  57      CALL PRINT(NBLK,CYCBLK,ICYCLE,THKNES,THKCR,T,DELEPP,DAMISN)
2  58      50 CONTINUE
C
C *** COMPUTE DAMAGE FOR REMAINING CYCLES IN THE BLOCK
C
1  59      IF(REMAIN.EQ.0) GO TO 100
1  60      DO 80 J=1,REMAIN
C
2  61      CALL GROWTH(ICYCLE,THKNES)
2  62      CALL DAMAGE(DELEPP,THKNES,THKCR,T,DAMCYC)
2  63      CALL CHECK(DAMCYC,DAMISN,STOP)
C
2  64      IF(STOP) GO TO 990
2  65      80 CONTINUE
C
1  66      CALL PRINT(NBLK,CYCBLK,ICYCLE,THKNES,THKCR,T,DELEPP,DAMISN)
C
1  67      IND2 = 0
C
1  68      100 CONTINUE
69      IND2 = 1
C
70      60 TO 999
C
71      990 CONTINUE

```

TEM02190
 TEM02200
 TEM02210
 TEM02220
 TEM02230
 TEM02240
 TEM02250
 TEM02260
 TEM02270
 TEM02280
 TEM02290
 TEM02300
 TEM02310
 TEM02320
 TEM02330
 TEM02340
 TEM02350
 TEM02360
 TEM02370
 TEM02380
 TEM02390
 TEM02400
 TEM02410
 TEM02420
 TEM02430
 TEM02440
 TEM02450
 TEM02460
 TEM02470
 TEM02480
 TEM02490
 TEM02500
 TEM02510
 TEM02520
 TEM02530
 TEM02540
 TEM02550
 TEM02560
 TEM02570
 TEM02580
 TEM02590
 TEM02600
 TEM02610
 TEM02620
 TEM02630
 TEM02640
 TEM02650
 TEM02660
 TEM02670
 TEM02680
 TEM02690
 TEM02700
 TEM02710
 TEM02720
 TEM02730
 TEM02740

SYMBOL CROSS REFERENCE DICTIONARY

PROGRAM NAME: MAIN.

TAG: ARRAY(A) EQUIVALENCED(E) STATEMENT FUNCTION(F) GENERIC NAME(G) COMMON(C) PADDED(Q)		PROMOTED(P) DUMMY ARGUMENT(D) EXTERNAL SUBPROGRAM(X) NAMED CONSTANT(K) DYNAMIC COMMON(Y) SUBPROGRAM NAME(R)		ASSIGNED(S) INITIAL VALUE(V)		EXPLICITLY TYPED(T)		INTRINSIC FUNCTION(I) ENTRY(N)	
NAME	MODE	TAG	DECLARED REFS (F:REFD S:SET B:REFD/MAY BE SET)						
A	R*8	C	5	UNREFERENCED					
B	R*8	C	7	32F					
BLKDAT									
C	R*8	X	7	34					
CHECK	R*8	X	7	32F					
CYCBLK	I*4	AT	54	63					
CYTIME	R*8	AC	2	15B 43B	49F	57B	66B	73B	
C2	R*8	C	8	UNREFERENCED					
D	R*8	C	5	UNREFERENCED					
DADT	R*8	C	7	32F					
DAMAGE				34B 44B					
DAMCYC	R*8	X		53 62					
DANISN	R*8			53B 54B	62B	63B			
DELEPC	R*8			27S 54B	57B	63B	66B	73B	
DELEPF	R*8	C	7	34B 44B					
DELEPH	R*8			32F					
DELEPP	R*8			34B 44B					
DELH	R*8	C	5	UNREFERENCED					
E	R*8	C	7	32F					
FLAG	I*4	T	2	28S 34B	35F	37F			
GROWTH				52 61					
ICYCLE	I*4	X		29S 52B	57B	61B	66B	73B	
IDUM	I*4	C	8	UNREFERENCED					
INCR	I*4	C		43B 48F	51F				
INCREM				43					
IND1	I*4	X		9S					
IND2	I*4	X		10S	67S	69S	74S		
INPUT				15					
J	I*4	X		50B					
K	I*4	X		51B					
MESSAGE				17	21	36	40	72	
NBLK	I*4	C	4	33S 34B	36B	43F	45F	49F	57B 66B 73B
NIN	I*4	C		11S					
NL	I*4	C	4	47S 49S	50F	45F	46F	76F	
NOUT	I*4	C	4	13S 31F	32F				
NTERR	I*4	C	8	12S 39F	41F				
NTIME	I*4	C		14S 43B	47F				
NUM	I*4			15B 16F	18F	33F			
NUMBLK				44					
PLSTRN				26					
PREXPO				57	66	73			
PRINT				20F 22F					
R	R*8	C	5	43B 48F	59F	60F			
REMAIN	I*4	T	2	54B 55F	57B	62B	66B	73B	
STOP	L*1	T	3	15B 53B	26B	30F	31F	57B	
THKCR1	R*8			24S 52B	53B				
THKFLR	R*8			30S					
THKNES	R*8								

ORIGINAL PAGE IS
OF POOR QUALITY

NAME: MAIN
 TAG: ARRAY(A) EQUIVALENCED(E) STATEMENT FUNCTION(F) GENERIC NAME(G) COMMON(C) PADDED(Q)
 PROMOTED(P) DUMMY ARGUMENT(D) EXTERNAL SUBPROGRAM(X) NAMED CONSTANT(K) DYNAMIC COMMON(Y) SUBPROGRAM NAME(R)
 ASSIGNED(S) INITIAL VALUE(V) EXPLICITLY TYPED(T) INTRINSIC FUNCTION(I) ENTRY(N)

NAME MODE TAG DECLARED REFS (F:REFD S:SET B:REFD/MAY BE SET)

TIMEUR R*8 C 6 25F
 TIMEUR R*8 C 6 25F
 XPON R*8 C 5 UNREFERENCED

VARIABLES REFERENCED BUT NOT SET. (* POSSIBLY SET AS ARGUMENT.)

CYCBLK* DADT* DAMCYC* DELEPC* DELEPH* DELEPP* INCR* NUMBLK* REMAIN* STOP* THKCR*

LABEL CROSS REFERENCE DICTIONARY

TAG: FORMAT(F) NON-EXECUTABLE(N) USED AS ARGUMENT(A) OBJECT OF BRANCH(B) USED IN ASSIGN STATEMENT(S)

LABEL TAG DEFINED REFERENCES

LABEL	TAG	DEFINED	REFERENCES
40		56	51
50		58	50
80		65	60
100	B	68	33
990	B	71	55
999	B	75	70
1008	NF	78	31
1009	NF	79	32
1010	NF	80	45
1020	NF	81	46
1050	NF	82	76

STORAGE MAP

TAG: SET(S) ENTRY(IN) ASSIGNED(G) IN COMMON(C) EQUIVALENCED(E) INITIAL VALUE(V) INTRINSIC FCT(I) SUBPROGRAM(X) NAMED CONSTANT(K) STATEMENT FUNCTION(T) USED AS ARGUMENT(A) SUBPROGRAM NAME(R) PROGRAM NAME: MAIN. SIZE OF PROGRAM: 7838 HEX BYTES.

NAME	MODE	TAG	ADDR.	NAME	MODE	TAG	ADDR.	NAME	MODE	TAG	ADDR.
A	R*8	C	UNREFD	B	R*8	FCA	000008	BLKDAT	R*8	FX	007408
CHECK	FX	0074C8		CYCBULK	I*4	FA	000750	CYTIME	R*8	C	UNREFD
D	R*8	FCA	000018	DAOT	R*8	FA	000598	DAMAGE	FX	C	0074DC
DAMISN	R*8	SFA	0005A8	DELEPC	R*8	FA	0005B0	DELEPF	R*8	FCA	000000
DELEPP	R*8	FA	0005C0	DELH	R*8	C	UNREFD	E	R*8	FCA	000020
GROWTH	FX	0074E0		ICYCLE	I*4	SFA	000620	IDUM	I*4	C	UNREFD
INCREH	FX	0074E4		IND1	I*4	SF	0005F8	IND2	I*4	SF	0005FC
J	I*4	SF	0005E0	K	I*4	SF	0005E4	MESSAGE	FX	0074E8	NBLK
NIN	I*4	SFC	000000	NL	I*4	SF	0005E8	NOUT	I*4	SFCA	000004
NTIME	I*4	FC	000000	NLM	I*4	SFA	0005EC	NUNBLK	I*4	FA	000624
PREXPO	FX	0074F0		PRINT	R*8	FX	0074D0	R	R*8	FC	000010
STOP	L*1	FA	00062C	THKCR	R*8	FA	0005C8	THKFUR	R*8	SFA	0005D0
TIMEFUR	R*8	FC	000000	THPFUR	R*8	FC	000008	VFEES	FX	0074D4	THKNES
VFIXF#	FX	0074F8		VFNSEF#	FX	FX	0074FC	XPON	R*8	C	UNREFD

COMMON INFORMATION

NAME: IOUN. SIZE: 8 HEX BYTES. (E) - EQUIVALENCED

NAME	MODE	DISPL.	NAME	MODE	DISPL.
NIN	I*4	000000	NOUT	I*4	000004

NAME: CNST. SIZE: 28 HEX BYTES. (E) - EQUIVALENCED

NAME	MODE	DISPL.	NAME	MODE	DISPL.
A	R*8	000000	DELH	R*8	000008
XPON	R*8	000020	R	R*8	000010

NAME: FURN. SIZE: 10 HEX BYTES. (E) - EQUIVALENCED

NAME	MODE	DISPL.	NAME	MODE	DISPL.
TIMEFUR	R*8	000000	THPFUR	R*8	000008

NAME: INPT. SIZE: 28 HEX BYTES. (E) - EQUIVALENCED

NAME	MODE	DISPL.	NAME	MODE	DISPL.
DELEPF	R*8	000000	B	R*8	000008
E	R*8	000020	C	R*8	000010

NAME: TMIV. SIZE: 198 HEX BYTES. (E) - EQUIVALENCED

<u>NAME</u>	<u>MODE</u>	<u>DISPL.</u>	<u>NAME</u>	<u>MODE</u>	<u>DISPL.</u>	<u>NAME</u>	<u>MODE</u>	<u>DISPL.</u>
NTIME	T*4	000000	IDUM	I*4	000004	CYTIME	R*8	000008

282

LABEL INFORMATION.

LABEL	DEFINED	ADDR.	LABEL	DEFINED	ADDR.	LABEL	DEFINED	ADDR.	LABEL	DEFINED	ADDR.
40	56	00775C	50	58	00776E	80	65	00778C	100	68	0077CE
990	71	0077E4	999	75	007800	1008	78	000490	1009	79	000202
1010	80	0001CC	1020	81	0000D2	1050	82	0000A8			

```

*****
SOURCE STATEMENTS = 73.  PROGRAM SIZE = 30776 BYTES, PROGRAM NAME = MAIN
PAGE: 1.

```

STATISTICS NO DIAGNOSTICS GENERATED.

```

**MAIN** END OF COMPILATION I *****

```

ORIGINAL PAGE IS
OF POOR QUALITY

DATE: JUL 30, 1987 TIME: 15:24:13
VS FORIKAN
OPTIONS IN EFFECT: NOLIST MAP XREF GOSTMT NODCK SOURCE TERM OBJECT FIXED TRMFLG NOSRCFLG NOSYM NORENT
NOSLUMP AUTOOBL(NONE) NOSXM NOVECTOR IL NOTEST NODC NODIRECTIVE
OPT(3) LANGVL(77) NOFIPS FLAG(1) NAME(MAIN) LINECOUNT(60) CHARLEN(500)

```

IF DO  ISN  *.....1.....2.....3.....4.....5.....6.....7.....8
1  C  SUBROUTINE INPUT(NUMBLK,CYCBLK,THKCR)
C  C
C  C  PURPOSE:  READING OF THE GENERAL DATA AND PRINTING THE ECHO OF THE
C  C  INPUT
C  C  VARIABLES:
C  C
C  C  A  -- COEFFICIENT OF ARHENIUS EQUATION (SH2/CM%-SEC)
C  C  B  -- EXPONENT IN THE LIFE EQUATION
C  C  C  -- EXPONENT IN THE LIFE EQUATION
C  C  C2 -- OXIDE GROWTH EQUATION COEFFICIENT (CM3/GH)
C  C  CYCBLK(I) -- NUMBER OF CYCLES IN EACH BLOCK OF INPUT (INTEGER)
C  C  D  -- EXPONENT IN THE LIFE EQUATION
C  C  DELEPF -- STATIC PLASTIC STRAIN
C  C  DELH  -- ACTIVATION ENERGY (CAL/MOLE)
C  C  E  -- LIFE EQUATION COEFFICIENT
C  C  HEADNG -- PROBLEM DESCRIPTION
C  C  NIN  -- INPUT UNIT NUMBER
C  C  NOUT  -- OUTPUT UNIT NUMBER
C  C  NUMBLK -- TOTAL NUMBER OF BLOCKS OF INPUT ( UP TO 7000 )
C  C  R  -- GAS CONSTANT IN UNITS OF CAL/K-MOLE
C  C  THKCR -- CRITICAL OXIDE THICKNESS (IN)
C  C  TIMFUR -- PRE-EXPOSURE TIME IN THE FURNACE (SEC)
C  C  TMPFUR -- PRE-EXPOSURE FURNACE TEMPERATURE (DEGREES RANKINE)
C  C  XPON  -- EXPONENT IN THE ARHENIUS EQUATION
C  C *****
C  C  IMPLICIT REAL*8 (A-H,O-Z)
C  C  DIMENSION HEADNG(10)
C  C  INTEGER*4 CYCBLK(7000)
C  C  COMMON /IOUN/ NIN,NOUT
C  C  COMMON /CNST/ A,DELH,R,C2,XPON
C  C  COMMON /FURN/ TIMFUR,TMPFUR
C  C  COMMON /INPT/ DELEPF,B,C,D,E
C  C
C  C  DO 10 I=1,7000
C  C  10 CYCBLK(I) = 0
C  C
C  C  READ(NIN,1010) HEADNG
C  C  WRITE(NOUT,1020) HEADNG
C  C
C  C  READ(NIN,*) NUMBLK
C  C  READ(NIN,*) (CYCBLK(I),I=1,NUMBLK)
C  C  WRITE(NOUT,1030) NUMBLK
C  C  WRITE(NOUT,1040) (CYCBLK(I),I=1,NUMBLK)
C  C
C  C  READ(NIN,*) A,DELH,R
C  C  READ(NIN,*) C2,XPON

```

IF DO ISN *.....1.....2.....3.....4.....5.....6.....7.....8

```

19 READ(NIN,*) THKCRIT TEM03740
20 IF(DELF,LT.0.) DELH = -DELH TEM03750
21 WRITE(NOUT,1070) A TEM03760
22 WRITE(NOUT,1080) DELH TEM03770
23 WRITE(NOUT,1090) R TEM03780
24 WRITE(NOUT,1095) C2 TEM03790
25 WRITE(NOUT,1096) XPON TEM03800
26 WRITE(NOUT,1100) THKCRIT TEM03810
27 C TEM03820
28 READ(NIN,*) TIMFUR TEM03830
29 READ(NIN,*) THPFUR TEM03840
30 WRITE(NOUT,1110) TIMFUR TEM03850
31 WRITE(NOUT,1120) THPFUR TEM03860
32 C TEM03870
33 READ(NIN,*) DELEPF,B,C,D,E TEM03880
34 RETURN TEM03890
35 C TEM03900
36 C TEM03910
37 C TEM03920
38 C TEM03930
39 C TEM03940
40 C TEM03950
41 C TEM03960
42 C TEM03970
43 C TEM03980
44 C TEM03990
45 C TEM04000
46 C TEM04010
47 C TEM04020
48 C TEM04030
49 C TEM04040
50 C TEM04050
51 C TEM04060
52 C TEM04070
53 C TEM04080
54 C TEM04090
55 C TEM04100
56 C TEM04110
57 C TEM04120
58 C TEM04130
59 C TEM04140
60 C TEM04150
61 C TEM04160
62 C TEM04170
63 C TEM04180
64 C TEM04190

```

SYMBOL CROSS REFERENCE DICTIONARY

PROGRAM NAME: INPUT.

TAG: ARRAY(A) EQUIVALENCED(E) STATEMENT FUNCTION(F) GENERIC NAME(G) COMMON(C) PADDED(Q)
 PROMOTED(P) DUMMY ARGUMENT(D) EXTERNAL SUBPROGRAM(X) NAMED CONSTANT(K) DYNAMIC COMMON(Y) SUBPROGRAM NAME(R)
 ASSIGNED(S) INITIAL VALUE(V) EXPLICITLY TYPED(T) INTRINSIC FUNCTION(I) ENTRY(N)

NAME	MODE	TAG	DECLARED	REFS	(F:REFD	S:SET	B:REFD/MAY BE SET)
A	R*8	C	6	17S	22F		
B	R*8	C	8	32S			
C	R*8	C	8	32S			
CYCBLK	I*4	ADT	1	4	10S	16F	
C2	R*8	C	6	18S	25F		
D	R*8	C	8	32S			
DELEPF	R*8	C	8	32S			
DELH	R*8	C	6	17S	20F	21S	23F
E	R*8	C	8	32S			
HEADNG	R*8	A	3	11S	12F		
I	I*4			9S	10B	14S	16S 16B
INPUT	R		1				
NIN	I*4	C	5	11	13	17	18 19 28 29 32
NOUT	I*4	C	5	12F	15F	16F	22F 23F 25F 26F 27F 30F 31F
NURBLK	I*4	D	1	13S	14	15F	16F
R	R*8	C	6	17S	24F		
THKCR	R*8	D	1	19S	27F		
TIMFLR	R*8	C	7	28S	30F		
THPFUR	R*8	C	7	29S	31F		
XPON	R*8	C	6	18S	26F		

LABEL CROSS REFERENCE DICTIONARY

TAG: FORMAT(F) NON-EXECUTABLE(N) USED AS ARGUMENT(A) OBJECT OF BRANCH(B) USED IN ASSIGN STATEMENT(S)

LABEL	TAG	DEFINED	REFERENCES
10	NF	10	9
1010	NF	34	11
1020	NF	35	12
1021	NF	36	UNREFERENCED
1030	NF	37	15
1040	NF	38	16
1045	NF	39	UNREFERENCED
1070	NF	40	22
1080	NF	41	23
1090	NF	42	24
1095	NF	43	25
1096	NF	44	26
1100	NF	45	27
1110	NF	46	30
1120	NF	47	31

ORIGINAL PAGE IS
OF POOR QUALITY

STORAGE MAP

TAG: SET(S) ENTRY(N) ASSIGNED(G) IN COMMON(C) EQUIVALENCED(E) INITIAL VALUE(V) INTRINSIC FCT(I) REFERENCED(F) SUBPROGRAM(X) NAMED CONSTANT(K) STATEMENT FUNCTION(T) USED AS ARGUMENT(A) SUBPROGRAM NAME(R)

PROGRAM NAME: INPUT. SIZE OF PROGRAM: 982 HEX BYTES.

NAME	MODE	TAG	ADDR.	NAME	MODE	TAG	ADDR.	NAME	MODE	TAG	ADDR.	NAME	MODE	TAG	ADDR.
A	R*8	SFCA	000000	B	R*8	SFCA	000008	C	R*8	SFCA	000010	CYCBLK	I*4	SFA	000658
C2	R*8	SFCA	000018	D	R*8	SFCA	000018	DELEPF	R*8	SFCA	000000	DELH	R*8	SFCA	000008
E	R*8	SFCA	000020	HEADING	R*8	SFA	0005F8	I	I*4	SF	000460	INPUT	R		000000
NIN	I*4	FCA	000000	NOUT	I*4	FCA	000004	NURBLK	I*4	SFA	000660	R	R*8	SFCA	000010
THKCR	R*8	SFA	000664	TIMEFUR	R*8	SFCA	000000	TIMEFUR	R*8	SFCA	000008	VFFXL#	FX		000668
VFIXF#	FX		00066C	VFIXL#	FX		000670	VFRSF#	R*8	SFCA	000674	VFRSL#	FX		000678
VFSXF#	FX		00067C	VFWSF#	FX		000680	XPON	R*8	SFCA	000020				

COMMON INFORMATION

NAME: IOUN. SIZE: 8 HEX BYTES. (E) - EQUIVALENCED

NAME	MODE	DISPL.	NAME	MODE	DISPL.	NAME	MODE	DISPL.	NAME	MODE	DISPL.
NIN	I*4	000000	NOUT	I*4	000004						

NAME: CNST. SIZE: 28 HEX BYTES. (E) - EQUIVALENCED

NAME	MODE	DISPL.	NAME	MODE	DISPL.	NAME	MODE	DISPL.	NAME	MODE	DISPL.
A	R*8	000000	DELH	R*8	000008	R	R*8	000010	C2	R*8	000018
XPON	R*8	000020									

NAME: FURN. SIZE: 10 HEX BYTES. (E) - EQUIVALENCED

NAME	MODE	DISPL.	NAME	MODE	DISPL.	NAME	MODE	DISPL.	NAME	MODE	DISPL.
TIMEFUR	R*8	000000	TIMEFUR	R*8	000008						

NAME: INPT. SIZE: 28 HEX BYTES. (E) - EQUIVALENCED

NAME	MODE	DISPL.	NAME	MODE	DISPL.	NAME	MODE	DISPL.	NAME	MODE	DISPL.
DELEPF	R*8	000000	B	R*8	000008	C	R*8	000010	D	R*8	000018
E	R*8	000020									

LABEL INFORMATION.

LABEL	DEFINED	ADDR.	LABEL	DEFINED	ADDR.	LABEL	DEFINED	ADDR.	LABEL	DEFINED	ADDR.
10	10	0006AE	1010	34	0003BB	1020	35	0003AC	1021	36	000000
1030	37	000362	1040	38	000310	1045	39	000000	1070	40	0002C3
1080	41	000276	1090	42	000229	1095	43	0001DC	1096	44	00018F
1100	45	000142	1110	46	0000F5	1120	47	0000A8			

STATISTICS SOURCE STATEMENTS = 47, PROGRAM SIZE = 2482 BYTES, PROGRAM NAME = INPUT PAGE: 11.

STATISTICS NO DIAGNOSTICS GENERATED.

INPUT END OF COMPILATION 2 *****

ORIGINAL PAGE IS
OF POOR QUALITY

SYMBOL CROSS REFERENCE DICTIONARY

PROGRAM NAME: PREXPO.

TAG: ARRAY(A) EQUIVALENCED(E) STATEMENT FUNCTION(F) GENERIC NAME(G) COMMON(C) PADDED(Q)
 PROMOTED(P) DUMMY ARGUMENT(D) EXTERNAL SUBPROGRAM(X) NAMED CONSTANT(K) DYNAMIC COMMON(Y) SUBPROGRAM NAME(R)
 ASSIGNED(S) INITIAL VALUE(V) EXPLICITLY TYPED(T) INTRINSIC FUNCTION(I) ENTRY(N)

NAME	MODE	TAG	DECLARED	REFS	(F:REFD S:SET B:REFD/MAY BE SET)
A	R*8	C	4	8F	
C	R*8			7S	
C2	R*8	C	4	9F	8F
DELH	R*8	C	4	7F	
DEXP	R*8	I		8	
KP	R*8	T	3	8S	9F
PREXPO		R	1		
R	R*8	C	4	7F	
TEMP	R*8			6S	
THKFUR	R*8	D	1	9S	7F
TIMFUR	R*8	C	5	9F	10F 10S
TMPFUR	R*8	C	5	6F	
XPON	R*8	C	4	9F	

**** NO USER LABELS ****

ORIGINAL PAGE IS
 OF POOR QUALITY

STORAGE MAP

TAG: SET(S) ENTRY(N) ASSIGNED(G) IN COMMON(C) EQUIVALENCED(E) INITIAL VALUE(V) INTRINSIC FCT(I)
 REFERENCED(F) SUBPROGRAM(X) NAMED CONSTANT(K) STATEMENT FUNCTION(T) USED AS ARGUMENT(A) SUBPROGRAM NAME(R)

PROGRAM NAME: PREXPO. SIZE OF PROGRAM: 1FA HEX BYTES.

NAME	MODE	TAG	ADDR.	NAME	MODE	TAG	ADDR.	NAME	MODE	TAG	ADDR.
A	R*8	FC	000000	C	R*8	SFA	000130	C2	R*8	FC	000018
DEXP	R*8	FI	00015C	FDXPD#	R*8	FX	000160	KP	R*8	SF	000138
R	R*8	FC	000010	TEMP	R*8	SF	000140	THKFUR	R*8	SF	000164
TMPFUR	R*8	FC	000008	XPON	R*8	FC	000020				

COMMON INFORMATION

NAME: CNST. SIZE: 28 HEX BYTES. (E) - EQUIVALENCED

NAME	MODE	DISPL.	NAME	MODE	DISPL.	NAME	MODE	DISPL.
A	R*8	000000	DELH	R*8	000008	R	R*8	000010
XPON	R*8	000020						

NAME: FURN. SIZE: 10 HEX BYTES. (E) - EQUIVALENCED

NAME	MODE	DISPL.	NAME	MODE	DISPL.	NAME	MODE	DISPL.
TMPFUR	R*8	000000	TMPFUR	R*8	000008			

***** NO USER LABELS *****

STATISTICS SOURCE STATEMENTS = 12, PROGRAM SIZE = 506 BYTES, PROGRAM NAME = PREXPO PAGE: 16.

STATISTICS NO DIAGNOSTICS GENERATED.

PREXPO END OF COMPILATION 3 *****

IF DO ISN *.....1.....2.....3.....4.....5.....6.....7.*.....8

```

C
22      WRITE(NOUT,1040)
23      DO 50 I=1,NTIME
24      WRITE(NOUT,1050) I,CYTIME(I),TMPINF(I)
25      50 CONTINUE
C
26      99 CONTINUE
27      RETURN
C
C      FORMAT STATEMENTS
C
28      1010 FORMAT(A8)
29      1015 FORMAT(1H1,10X,' D A T A   F O R   B L O C K   N U M B E R ',I5,
30      $////)
31      1020 FORMAT(10X,'PLASTIC STRAIN DUE TO COOLING FLUX ..... (DELEPC) =',TEM05330,
32      $IX,E10.4,/)
33      1030 FORMAT(10X,'PLASTIC STRAIN DUE TO HEATING FLUX ..... (DELEPH) =',TEM05350,
34      $IX,E10.4,/)
35      1035 FORMAT(10X,'PLASTIC STRAIN DUE TO THERMAL MISMATCH .. ( D A O T ) =',TEM05370,
36      $IX,E10.4,/)
37      1040 FORMAT(10X,'TIME STEP',4X,'CYCLE TIME',2X,'INTERFACE TEMP',/,
38      $26X,'(SEC)',8X,'(DEG R)',/,
39      $10X,'-----',4X,10(' '),2X,14(' '),/)
40      1050 FORMAT(11X,15,5X,2X,E10.4,4X,E10.4)
C
END

```

SYMBOL CROSS REFERENCE DICTIONARY

PROGRAM NAME: BLKDAT.

TAG: ARRAY(A) EQUIVALENCED(E) STATEMENT FUNCTION(F) GENERIC NAME(G) COMMON(C) PADDED(Q)
 PROMOTED(P) DUMPY ARGUMENT(D) EXTERNAL SUBPROGRAM(X) NAMED CONSTANT(K) DYNAMIC COMMON(Y) SUBPROGRAM NAME(R)
 ASSIGNED(S) INITIAL VALUE(V) EXPLICITLY TYPED(T) INTRINSIC FUNCTION(I) ENTRY(N)

NAME	MODE	TAG	DECLARED REFS (F:REFD S:SET B:REFD/MAY BE SET)
BLKDAT			
CMIENT	CHAR	T	1
CYTIME	R*8	AC	4
DADT	R*8	D	6
DELEPC	R*8	D	1
DELEPH	R*8	D	1
END	CHAR	VT	4
FLAG	I*4	DT	1
I	I*4		1
IDUM	I*4	C	20S 20S 21S 21S 21S 23S 24F 24F 24B
NBLOCK	I*4	D	6
NIN	I*4	C	1
NOUJ	I*4	C	5
NTIME	I*4	C	5
THPINF	R*8	AC	7

LABEL CROSS REFERENCE DICTIONARY

TAG: FORMAT(F) NON-EXECUTABLE(N) USED AS ARGUMENT(A) OBJECT OF BRANCH(B) USED IN ASSIGN STATEMENT(S)

LABEL	TAG	DEFINED	REFERENCES
50		25	23
99	B	26	12
1010	NF	28	9
1015	NF	29	15
1020	NF	30	16
1030	NF	31	17
1035	NF	32	18
1040	NF	33	22
1050	NF	34	24

STORAGE MAP

TAG: SET(S) ENTRY(N) ASSIGNED(G) IN COMMON(C) EQUIVALENCED(E) INITIAL VALUE(V) INTRINSIC FCT(I) REFERENCED(F) SUBPROGRAM(X) NAMED CONSTANT(K) STATEMENT FUNCTION(T) USED AS ARGUMENT(A) SUBPROGRAM NAME(R)

PROGRAM NAME: BLKDAT. SIZE OF PROGRAM: 670 HEX BYTES.

NAME	MODE	TAG	ADDR.	NAME	MODE	TAG	ADDR.	NAME	MODE	TAG	ADDR.
BLKDAT	R		000000	CMMENT	CHAR	SFA	00038C	CYTIME	R*8	SFCA	000008
DELEPC	R*8	SFA	0003A8	DELEPH	R*8	SFA	0003AC	END	CHAR	FV	000384
I	I*4	SFA	0002A4	IDUM	I*4	C	UNREFD	NBLOCK	I*4	FA	0003B0
NOUT	I*4	FCA	000004	NTIME	I*4	SFCA	000000	TRPINF	R*8	SFCA	000000
VFIXF#	FX		0003B8	VFIXL#	FX		0003BC	VFRSF#	FX		0003C0
VFNFSF#	FX		0003C8								

COMMON INFORMATION

NAME: IOUN. SIZE: 8 HEX BYTES. (E) - EQUIVALENCED

NAME	MODE	DISPL.	NAME	MODE	DISPL.	NAME	MODE	DISPL.
NIN	I*4	000000	NOUT	I*4	000004			

NAME: TMIV. SIZE: 198 HEX BYTES. (E) - EQUIVALENCED

NAME	MODE	DISPL.	NAME	MODE	DISPL.	NAME	MODE	DISPL.
NTIME	I*4	000000	IDUM	I*4	000004	CYTIME	R*8	000008

NAME: TEMP. SIZE: 190 HEX BYTES. (E) - EQUIVALENCED

NAME	MODE	DISPL.	NAME	MODE	DISPL.	NAME	MODE	DISPL.
TMPIF	R*8	000000						

LABEL INFORMATION.

LABEL	DEFINED	ADDR.	LABEL	DEFINED	ADDR.	LABEL	DEFINED	ADDR.
50	25	0005E8	99	26	0005FA	1010	28	000217
1020	30	00019E	1030	31	00015E	1035	32	00011D
1050	34	0000A8					33	0000BA

STATISTICS SOURCE STATEMENTS = 34, PROGRAM SIZE = 1648 BYTES, PROGRAM NAME = BLKDAT PAGE: 19.

STATISTICS NO DIAGNOSTICS GENERATED.

BLKDAT END OF COMPILATION 4 *****

OPTIONS IN EFFECT: NOLIST MAP XREF GOSTMT NODUCK SOURCE TERM OBJECT FIXED TRMFLG NOSRCFLG NOSYM NORENT
 NOSDUMP AUTOOBL(NONE) NOSXM NOVECTOR IL NOTEST NODC NODIRECTIVE
 OPT(3) LANGVL(77) NOFIPS FLAG(1) NAME(MAIN) LINECOUNT(60) CHARLEN(500)

```

IF DO  ISN  *.....1.....2.....3.....4.....5.....6.....7.....8
1      C      SUBROUTINE INCR(NCYC,NUM,INCR,REMAIN)
      C      TEM05450
      C      TEM05460
      C      TEM05470
      C      TEM05480
      C      TEM05490
      C      TEM05500
      C      TEM05510
      C      TEM05520
      C      TEM05530
      C      TEM05540
      C      TEM05550
      C      TEM05560
      C      TEM05570
      C      TEM05580
      C      TEM05590
      C      *****TEM05600*****
      C      TEM05610
      C      TEM05620
      C      TEM05630
      C      TEM05640
      C      TEM05650
      C      TEM05660
      C      TEM05670
      C      TEM05680
      C      TEM05690
      C      TEM05700
      C      TEM05710
      C      TEM05720
      C      TEM05730

2      C      INTEGER*4 REMAIN

3      C      INCR = NCYC/NUM
4      C      REMAIN = MOD(NCYC,NUM)

5      C      IF(NCYC.LE.NUM) INCR = 1
7      C      IF(NCYC.LE.NUM) REMAIN = 0

9      C      RETURN
10     C      END

      C      PURPOSE: ESTABLISH INCREMENT AT WHICH INTERMEDIATE RESULTS ARE
      C      PRINTED
      C      VARIABLES:
      C      INCR      -- THE INCREMENT AT WHICH INTERMEDIATE RESULTS ARE
      C      PRINTED
      C      NCYC      -- TOTAL NUMBER OF CYCLES IN THE CURRENT BLOCK
      C      NUM       -- NUMBER OF PRINTOUTS PER THERMAL CYCLE
      C      REMAIN    -- THE INCREMENT AT WHICH THE LAST RESULT FOR A BLOCK
      C      OF CYCLES IS PRINTED

```

ORIGINAL PAGE IS
 OF POOR QUALITY

SYMBOL CROSS REFERENCE DICTIONARY

PROGRAM NAME: INCREM.

TAG: ARRAY(A) EQUIVALENCED(E) STATEMENT FUNCTION(F) GENERIC NAME(G) COMMON(C) PADDED(Q)
 PROMOTED(P) DUMMY ARGUMENT(D) EXTERNAL SUBPROGRAM(X) NAMED CONSTANT(K) DYNAMIC COMMON(Y) SUBPROGRAM NAME(R)
 ASSIGNED(S) INITIAL VALUE(V) EXPLICITLY TYPED(T) INTRINSIC FUNCTION(I) ENTRY(N)

NAME	MODE	TAG	DECLARED	REFS	(F:REFD	S:SET	B:REFD/MAY BE SET)
INCR	I*4	D	1	3S	6S		
INCREM		R	1				
MOD		GI		4			
NCYC	I*4	D	1	3F	4F	5F	7F
NUM	I*4	D	1	3F	4F	5F	7F
REMAIN	I*4	DT	1	2	4S	8S	

**** NO USER LABELS ****

STORAGE MAP

TAG: SET(S) ENTRY(N) ASSIGNED(G) IN COMMON(C) EQUIVALENCED(E) INITIAL VALUE(V) INTRINSIC FCT(I)
 REFERENCED(F) SUBPROGRAM(X) NAMED CONSTANT(K) STATEMENT FUNCTION(T) USED AS ARGUMENT(A) SUBPROGRAM NAME(R)

PROGRAM NAME: INCREM. SIZE OF PROGRAM: 1A2 HEX BYTES.

NAME	MODE	TAG	ADDR.	NAME	MODE	TAG	ADDR.	NAME	MODE	TAG	ADDR.
INCR	I*4	SF	000104	INCREM	R	000000	MOD				
NUM	I*4	F	000100	REMAIN	I*4	SF	00010C	NCYC	I*4	F	000108

***** NO USER LABELS *****

STATISTICS SOURCE STATEMENTS = 8, PROGRAM SIZE = 418 BYTES, PROGRAM NAME = INCREM PAGE: 23.

STATISTICS NO DIAGNOSTICS GENERATED.

INCREM END OF COMPILATION 5 *****

ORIGINAL PAGE IS
 OF POOR QUALITY

SYMBOL CROSS REFERENCE DICTIONARY

PROGRAM NAME: PLSTRN.

TAG: ARRAY(A) PROMOTED(P) ASSIGNED(S)	EQUIVALENCED(E) DUMMY ARGUMENT(D) INITIAL VALUE(V)	STATEMENT FUNCTION(F) EXTERNAL SUBPROGRAM(X) EXPLICITLY TYPED(T)	GENERIC NAME(G) NAMED CONSTANT(K) INTRINSIC FUNCTION(I)	COMMON(C) DYNAMIC COMMON(Y) ENTRY(N)	PADDED(Q) SUBPROGRAM NAME(R)
---	--	--	---	--	---------------------------------

NAME	MODE	TAG	DECLARED	REFS	(F:REFD S:SET B:REFD/MAY BE SET)
DADT	R*8	D		1	3F
DELEPC	R*8	D		1	3F
DELEPH	R*8	D		1	3F
DELEPP	R*8	D		1	3S
PLSTRN		R		1	

**** NO USER LABELS ****

ORIGINAL FILE IS
OF POOR QUALITY

STORAGE MAP

TAG: SET(S) ENTRY(N) ASSIGNED(G) IN COMMON(C) EQUIVALENCED(E) INITIAL VALUE(V) INTRINSIC FCT(I)
 REFERENCED(F) SUBPROGRAM(X) NAMED CONSTANT(K) STATEMENT FUNCTION(T) USED AS ARGUMENT(A) SUBPROGRAM NAME(R)

PROGRAM NAME: PLSTRN. SIZE OF PROGRAM: 162 HEX BYTES.

NAME	MODE	TAG	ADDR.	NAME	MODE	TAG	ADDR.	NAME	MODE	TAG	ADDR.
DADT	R*8	F	0000F8	DELEPC	R*8	F	0000FC	DELEPH	R*8	F	000100
PLSTRN	R		000000					DELEPP	R*8	SF	000104

***** NO USER LABELS *****

STATISTICS SOURCE STATEMENTS = 5, PROGRAM SIZE = 354 BYTES, PROGRAM NAME = PLSTRN PAGE: 26.

STATISTICS NO DIAGNOSTICS GENERATED.

PLSTRN END OF COMPILATION 6 *****

CHARLEN(500)

SUBROUTINE GROWTH(ICYCLE,THKNES)

VARIABLES:

*****TEM06310*****
*****TEM06320*****
*****TEM06330*****

C *** SEARCH FOR TMAX IN VECTOR CYTIME

```

      8    THAX = CYTIME(I)
      9    DO 10 I=2,NTIME
     10    IF(THAX.LT.CYTIME(I)) THAX = CYTIME(I)
     12    10 CONTINUE

```

301

ORIGINAL PAGE IS
OF POOR QUALITY

DATE: JUL 30, 1987 TIME: 15:24:14

VS FORTRAN

LEVEL 2.1.1 (SEPT 1986)

```

IF DO ISN *.....1.....2.....3.....4.....5.....6.....7.....8

```

```

C
13 C C1 = -DELH/R
C
14 C NT = NTIME - 1
15 C DO 20 I=1,NT
C *** CONVERT TEMPERATURE FROM RANKINE TO KELVIN
C
16 C TEMP = 5*THPINF(I)/9
17 C KP = A * DEXP(C1/TEMP)
C *** CONVERT CYCLE TIME TO MISSION TIME
C
18 C XPON1 = 1./ XPON
19 C TIMPRE = ( ( 2.54*THKNES/C2 )**XPON1 ) / KP
C
20 C TTIME1 = TIMPRE
21 C TTIME2 = CYTIME(I+1) - CYTIME(I) + TIMPRE
C
22 C THK1 = C2 * (KP*TTIME1)**XPON
23 C THK2 = C2 * (KP*TTIME2)**XPON
24 C DELGRW = THK2 - THK1
C *** CONVERT THICKNESS FROM CENTIMETER TO INCH
C
25 C DELGRW = DELGRW/2.54
C
26 C THKNES = THKNES + DELGRW
C
27 C 20 CONTINUE
C
28 C ICYCLE = ICYCLE + 1
29 C RETURN
30 C END

```

```

TEM06490
TEM06500
TEM06510
TEM06520
TEM06530
TEM06540
TEM06550
TEM06560
TEM06570
TEM06580
TEM06590
TEM06600
TEM06610
TEM06620
TEM06630
TEM06640
TEM06650
TEM06660
TEM06670
TEM06680
TEM06690
TEM06700
TEM06710
TEM06720
TEM06730
TEM06740
TEM06750
TEM06760
TEM06770
TEM06780
TEM06790
TEM06800
TEM06810
TEM06820
TEM06830
TEM06840
TEM06850
TEM06860
TEM06870
TEM06880
TEM06890
TEM06900

```

SYMBOL CROSS REFERENCE DICTIONARY

PROGRAM NAME: GROWTH.

TAG: ARRAY(A) EQUIVALENCED(E) STATEMENT FUNCTION(F) GENERIC NAME(G) COMMON(C) PADDED(Q)
 PROMOTED(P) DUMMY ARGUMENT(D) EXTERNAL SUBPROGRAM(X) NAMED CONSTANT(K) DYNAMIC COMMON(Y) SUBPROGRAM NAME(R)
 ASSIGNED(S) INITIAL VALUE(V) EXPLICITLY TYPED(T) INTRINSIC FUNCTION(I) ENTRY(N)

NAME MODE TAG DECLARED REFS (F:REFD S:SET B:REFD/MAY BE SET)

A	R*8	C	4	17F						
CYTIME	R*8	AC	5	8F	10F	11F	21F	21F		
C1	R*8			13S	17F					
C2	R*8	C	4	19F	22F	23F				
DELGRM	R*8			24S	25F	25S	26F			
DELH	R*8	C	4	13F						
DEXP	R*8	I	17							
GROWTH	R									
I	I*4			9S	10F	11B	15S	16F	21F	21B
ICYCLE	I*4	D	1	28F	28S					
IDUM	I*4	C	5	UNREFERENCED						
KP	R*8	T	3	17S	19F	22F	23F			
NT	I*4			14S	15F					
NTIME	I*4	C	5	9F	14F					
R	R*8	C	4	13F						
TEMP	R*8			16S	17F					
THKNES	R*8	D	1	19F	26F	26S				
THK1	R*8			22S	24F					
THK2	R*8			23S	24F					
TIMFLUR	R*8	C	7	UNREFERENCED						
TIMPRE	R*8			19S	20F	21F				
TMAX	R*8			8S	10F	11S				
TMNEW1	R*8			20S	22F					
TMNEW2	R*8			21S	23F					
TMPFLUR	R*8	C	7	UNREFERENCED						
TMPINF	R*8	AC	6	16F						
XPON	R*8	C	4	18F	22F	23F				
XPON1	R*8			18S	19F					

LABEL CROSS REFERENCE DICTIONARY

TAG: FORMAT(F) NON-EXECUTABLE(N) USED AS ARGUMENT(A) OBJECT OF BRANCH(B) USED IN ASSIGN STATEMENT(S)

LABEL TAG DEFINED REFERENCES

10	12	9
20	27	15

ORIGINAL PART 10
OF POOR QUALITY

STORAGE MAP

TAG: SET(S) ENTRY(N) ASSIGNED(G) IN COMMON(C) EQUIVALENCED(E) INITIAL VALUE(V) INTRINSIC FCT(I)
 REFERENCED(F) SUBPROGRAM(X) NAMED CONSTANT(K) STATEMENT FUNCTION(T) USED AS ARGUMENT(A) SUBPROGRAM NAME(R)

PROGRAM NAME: GROWTH. SIZE OF PROGRAM: 368 HEX BYTES.

NAME	MODE	TAG	ADDR.	NAME	MODE	TAG	ADDR.	NAME	MODE	TAG	ADDR.
A	R*8	FC	000000	CYTIME	R*8	FC	000008	C1	R*8	SF	000148
DELGRW	R*8	SF	000180	DELH	R*8	FC	000008	DEXP	R*8	FI	0001DC
GROWTH	R		000000	I	I*4	SF	0001A0	ICYCLE	I*4	SF	0001E4
KP	R*8	SF	000150	NT	I*4	SF	0001A4	NTIME	I*4	FC	000000
TEMP	R*8	SF	000158	THKNES	R*8	SF	0001E8	THK1	R*8	SF	000160
TINFUR	R*8	C	UNREFD	TIMPRE	R*8	SF	000188	THAX	R*8	SF	000170
TNEW2	R*8	SF	000198	THPFUR	R*8	C	UNREFD	THPINF	R*8	FC	000000
XPON1	R*8	SF	000178								

COMMON INFORMATION

NAME: CNST. SIZE: 28 HEX BYTES. (E) - EQUIVALENCED

NAME	MODE	DISPL.	NAME	MODE	DISPL.	NAME	MODE	DISPL.
A	R*8	000000	DELH	R*8	000008	R	R*8	000010
XPON	R*8	000020						

NAME: THIV. SIZE: 198 HEX BYTES. (E) - EQUIVALENCED

NAME	MODE	DISPL.	NAME	MODE	DISPL.	NAME	MODE	DISPL.
NTIME	I*4	000000	IDUM	I*4	000004	CYTIME	R*8	000008

NAME: TEMP. SIZE: 190 HEX BYTES. (E) - EQUIVALENCED

NAME	MODE	DISPL.	NAME	MODE	DISPL.	NAME	MODE	DISPL.
THPINF	R*8	000000						

NAME: FURN. SIZE: 10 HEX BYTES. (E) - EQUIVALENCED

NAME	MODE	DISPL.	NAME	MODE	DISPL.	NAME	MODE	DISPL.
TINFUR	R*8	000000	THPFUR	R*8	000008			

LABEL INFORMATION.

LABEL	DEFINED	ADDR.	LABEL	DEFINED	ADDR.	LABEL	DEFINED	ADDR.

STATISTICS SOURCE STATEMENTS = 29, PROGRAM SIZE = 872 BYTES, PROGRAM NAME = GROWTH PAGE: 29.
STATISTICS NO DIAGNOSTICS GENERATED.
GROWTH END OF COMPILATION 7 *****

OF PAGES 33

SYMBOL CROSS REFERENCE DICTIONARY

PROGRAM NAME: DAMAGE.

NAME	MODE	TAG	DECLARED	REFS	(F:REFD	S:SET	B:REFD/MAY BE SET)	COMMON(C)	DYNAMIC COMMON(Y)	ENTRY(N)	PADED(Q)	SUBPROGRAM NAME(R)
B	R*8	C	4	9F								
C	R*8	C	4	9F								
D	R*8	C	4	9F								
DAMAGE	R		1									
DAMCYC	R*8	D	1	10S								
DELEPF	R*8	C	4	5F								
DELEPP	R*8	D	1	5F								
E	R*8	C	4	9F								
N	R*8	T	3	9S								
RATIO	R*8			10F								
THK	R*8			5S								
THKCR7	R*8	D	1	6S								
THKNES	R*8	D	1	6F								

**** NO USER LABELS ****

STORAGE MAP

TAG: SET(S) ENTRY(N) ASSIGNED(G) IN COMMON(C) EQUIVALENCED(E) INITIAL VALUE(V) INTRINSIC FCT(I)
 REFERENCED(F) SUBPROGRAM(X) NAMED CONSTANT(K) STATEMENT FUNCTION(T) USED AS ARGUMENT(A) SUBPROGRAM NAME(R)

PROGRAM NAME: DAMAGE. SIZE OF PROGRAM: 234 HEX BYTES.

NAME	MODE	TAG	ADDR.	NAME	MODE	TAG	ADDR.	NAME	MODE	TAG	ADDR.
B	R*8	FC	000008	C	R*8	FC	000010	D	R*8	FC	000018
DAMCYC	R*8	SF	000154	DELEPF	R*8	FC	000000	DELEPP	R*8	F	000158
FDXPD#	R*8	FX	00015C	N	R*8	SF	000120	RATIO	R*8	SF	000130
THKCR	R*8	F	000160	THKNES	R*8	F	000164				
								DAMAGE	R*8	FC	000000
								E	R*8	FC	000020
								THK	R*8	SF	000128

COMMON INFORMATION

NAME: INPT. SIZE: 28 HEX BYTES. (E) - EQUIVALENCED

NAME	MODE	DISPL.	NAME	MODE	DISPL.	NAME	MODE	DISPL.
DELEPF	R*8	000000	B	R*8	000008	C	R*8	000010
E	R*8	000020						D
								R*8
								000018

***** NO USER LABELS *****

STATISTICS SOURCE STATEMENTS = 11, PROGRAM SIZE = 564 BYTES, PROGRAM NAME = DAMAGE PAGE: 34.

STATISTICS NO DIAGNOSTICS GENERATED.

DAMAGE END OF COMPILATION 8 *****

1 800 215 5511

SUBROUTINE CHECK(DAMCYC,DAMISN,STOP)

PURPOSE: SUMMING CURRENT CYCLE'S DAMAGE TO MISSION DAMAGE AND CHECKING IF THE DAMAGE HAS REACHED 1.0

VARIABLES:

DAMAGE FOR ONE CYCLE
MISSION DAMAGE
INPUT UNIT NUMBER
OUTPUT UNIT NUMBER
A LOGICAL FLAG, INDICATING
REACHED 1.0

TEM07420

```

IMPLICIT REAL*8 (A-H,O-Z)
LOGICAL*1 STOP
COMMON /IOUN/ NIN,NOUT

```

STOP = .FALSE.

DAMISN = DAMISN + DAMCYC

```
IF(DAMISN .LT. 1. ) GO TO 99
```

STOP = .TRUE.

99 CONTINUE

RETURN

21

SYMBOL CROSS REFERENCE DICTIONARY

PROGRAM NAME: CHECK.

TAG: ARRAY(A) EQUIVALENCED(E) STATEMENT FUNCTION(F) GENERIC NAME(G) COMMON(C) PADDED(Q)
 PROMOTED(P) DUMMY ARGUMENT(D) EXTERNAL SUBPROGRAM(X) NAMED CONSTANT(K) DYNAMIC COMMON(Y) SUBPROGRAM NAME(R)
 ASSIGNED(S) INITIAL VALUE(V) EXPLICITLY TYPED(T) INTRINSIC FUNCTION(I) ENTRY(N)

NAME MODE TAG DECLARED REFS (F:REFD S:SET B:REFD/MAY BE SET)

CHECK	R	1				
DAMCYC	R*8 D	1	6F			
DAHISN	R*8 D	1	6F	6S	7F	
NIN	I*4 C	4	UNREFERENCED			
NOUT	I*4 C	4	UNREFERENCED			
STOP	L*1 DT	1	3	5S	8S	

LABEL CROSS REFERENCE DICTIONARY

TAG: FORMAT(F) NON-EXECUTABLE(N) USED AS ARGUMENT(A) OBJECT OF BRANCH(B) USED IN ASSIGN STATEMENT(S)

LABEL TAG DEFINED REFERENCES

99 B 9 7

STORAGE MAP

TAG: SET(S) ENTRY(N) ASSIGNED(G) IN COMMON(C) EQUIVALENCED(E) INITIAL VALUE(V) INTRINSIC FCT(I)
REFERENCED(F) SUBPROGRAM(X) NAMED CONSTANT(K) STATEMENT FUNCTION(T) USED AS ARGUMENT(A) SUBPROGRAM NAME(R)
PROGRAM NAME: CHECK. SIZE OF PROGRAM: 176 HEX BYTES.

NAME	MODE	TAG	ADDR.	NAME	MODE	TAG	ADDR.	NAME	MODE	TAG	ADDR.
CHECK	R		000000	DAMCYC	R*8	F	000110	DAMTSN	R*8	SF	000114
NOUT	I*4	C	UNREFD	STOP	L*1	SF	00010C		I*4	C	UNREFD

COMMON INFORMATION

NAME: IOUN. SIZE: 8 HEX BYTES. (E) - EQUIVALENCED

NAME	MODE	DISPL.	NAME	MODE	DISPL.	NAME	MODE	DISPL.
NIN	I*4	000000	NOUT	I*4	000004			

LABEL INFORMATION.

LABEL	DEFINED	ADDR.	LABEL	DEFINED	ADDR.	LABEL	DEFINED	ADDR.
99	9	000140						

STATISTICS SOURCE STATEMENTS = 11, PROGRAM SIZE = 374 BYTES, PROGRAM NAME = CHECK PAGE: 37.

STATISTICS NO DIAGNOSTICS GENERATED.

CHECK END OF COMPILATION 9 *****

ORIGINAL PAGE IS
OF POOR QUALITY

```

LEVEL 2.1.1 (SEPT 1986)      VS FORTRAN      DATE: JUL 30, 1987      TIME: 15:24:15
OPTIONS IN EFFECT: NOLIST MAP XREF GOSTMT NODCK SOURCE TERM OBJECT FIXED TRMFLG NOSRCFLG NOSYM NORENT
NOSDUMP AUTOOBL(NONE) NOSXM NOVECTOR IL NOTEST NODC NODIRECTIVE
OPT(3) LANGVL(77) NOFIPS FLAG(I) NAME(MAIN) LINECOUNT(60) CHARLEN(500)

IF DO ISN *.....1.....2.....3.....4.....5.....6.....7.....8
1 SUBROUTINE PRINT(NBLK,CYCBLK,ICYCLE,THKNES,THKCR,T,DELEPP,DAMISN) TEM07600
C TEM07610
C TEM07620
C TEM07630
C TEM07640
C TEM07650
C TEM07660
C TEM07670
C TEM07680
C TEM07690
C TEM07700
C TEM07710
C TEM07720
C TEM07730
C TEM07740
C TEM07750
C TEM07760
C TEM07770
C TEM07780
C *****
C TEM07790
C TEM07800
C TEM07810
C TEM07820
C TEM07830
C TEM07840
C TEM07850
C TEM07860
C TEM07870
C TEM07880
C TEM07890
C TEM07900
C TEM07910
C TEM07920
C TEM07930
C TEM07940
C TEM07950
C TEM07960
C TEM07970
C TEM07980
C TEM07990
C TEM08000
C TEM08010
C TEM08020
C TEM08030
C TEM08040
C TEM08050
C TEM08060
C TEM08070

PURPOSE: PRINTING THE INTERMEDIATE RESULTS

VARIABLES:
CURCYC -- NUMBER OF CYCLES IN THE CURRENT BLOCK
CYCBLK(I) -- NUMBER OF CYCLES IN EACH BLOCK
DAMISN -- MISSION DAMAGE
DELEPP -- THE PLASTIC STRAIN PER CYCLE GIVEN BY THE TOTAL OF
ICYCLE -- ALL CYCLIC PLASTIC STRAIN EFFECTS
NBLK -- CYCLE COUNTER FOR THE MISSION
NIN -- THE CURRENT BLOCK NUMBER
NOUT -- INPUT UNIT NUMBER
THKCR -- OUTPUT UNIT NUMBER
THKNES -- CRITICAL OXIDE THICKNESS (IN)
THKNES -- THE OXIDE THICKNESS GAIN (IN)

*****
IMPLICIT REAL*8 (A-H,O-Z)
INTEGER*4 CURCYC,CYCBLK(7000)
COMMON /IOUN/ NIN,NOUT

CURCYC = ICYCLE
IF(NBLK.EQ.1) GO TO 20

NB = NBLK-1
DO 10 I=1,NB
CURCYC = CURCYC - CYCBLK(I)
10 CONTINUE

20 CONTINUE
RATIO = THKNES/THKCR

WRITE(NOUT,1010) ICYCLE,CURCYC,THKNES,RATIO,DELEPP,DAMISN
1010 FORMAT(I10,7X,I9,8X,E12.6,4X,E10.4,5X,E10.4,5X,F8.5)
1011 FORMAT(I9,1X,I9,7X,E12.6,4X,E10.4,5X,E10.4,5X,F8.5)

RETURN

FORMAT STATEMENT
1010 FORMAT(I10,7X,I9,8X,E12.6,4X,E10.4,5X,E10.4,5X,F8.5)
1011 FORMAT(I9,1X,I9,7X,E12.6,4X,E10.4,5X,E10.4,5X,F8.5)

END

```


ORIGINAL PAGE IS
OF POOR QUALITY

LEVEL 2.1.1.1 (SEPT 1986) VS FORTRAN DATE: JUL 30, 1987 TIME: 15:24:15 NAME: PRINT PAGE: 41

SYMBOL CROSS REFERENCE DICTIONARY

PROGRAM NAME: PRINT.

TAG: ARRAY(A) EQUIVALENCED(E) STATEMENT FUNCTION(F) GENERIC NAME(G) COMMON(C) PADDED(Q)
PROMOTED(P) DUMMY ARGUMENT(D) EXTERNAL SUBPROGRAM(X) NAMED CONSTANT(K) DYNAMIC COMMON(Y) SUBPROGRAM NAME(R)
ASSIGNED(S) INITIAL VALUE(V) EXPLICITLY TYPED(T) INTRINSIC FUNCTION(I) ENTRY(N)

NAME	MODE	TAG	DECLARED	REFS	(F:REFD	S:SET	B:REFD/MAY BE SET)
CURCYC	I*4	T	3	5S	9F	9S	13F
CYCBLK	I*4	ADT	1	3	9F		
DAMISN	R*8	D	1	13F			
DELEPP	R*8	D	1	13F			
I	I*4			8S	9B		
ICYCLE	I*4	D	1	5F	13F		
NB	I*4			7S	8F		
NBLK	I*4	D	1	6F	7F		
NIN	I*4	C	4	UNREFERENCED			
NOUT	I*4	C	4	13F			
PRINT		R	1				
RATIO	R*8			12S	13F		
THKCR	R*8	D	1	12F			
THKNES	R*8	D	1	12F	13F		

LABEL CROSS REFERENCE DICTIONARY

TAG: FORMAT(F) NON-EXECUTABLE(N) USED AS ARGUMENT(A) OBJECT OF BRANCH(B) USED IN ASSIGN STATEMENT(S)

LABEL	TAG	DEFINED	REFERENCES
10		10	8
20	B	11	6
1010	NF	15	13
1011	NF	16	UNREFERENCED

STORAGE MAP

TAG: SET(S) ENTRY(N) ASSIGNED(G) IN COMMON(C) EQUIVALENCED(E) INITIAL VALUE(V) INTRINSIC FCT(I)
 REFERENCED(F) SUBPROGRAM(X) NAMED CONSTANT(K) STATEMENT FUNCTION(T) USED AS ARGUMENT(A) SUBPROGRAM NAME(R)

PROGRAM NAME: PRINT. SIZE OF PROGRAM: 2A8 HEX BYTES.

NAME	MODE	TAG	ADDR.	NAME	MODE	TAG	ADDR.	NAME	MODE	TAG	ADDR.	NAME	MODE	TAG	ADDR.
CURCYC	I*4	SFA	000148	CYCBULK	I*4	F	000190	DAMTSN	R*8	FA	000198	DELEPP	R*8	FA	00019C
I	I*4	SF	000138	ICYCLE	I*4	FA	0001A0	NB	I*4	SF	00013C	NBLK	I*4	F	00018C
NIN	I*4	C	UNREFD	NOUT	I*4	FCA	000004	PRINT	R	R	000000	RATIO	R*8	SFA	000130
THKCR	R*8	F	0001A4	THKNES	R*8	FA	0001A8	VFIXF#	FX	FX	0001AC	VFMSF#	FX	FX	0001B0

COMMON INFORMATION

NAME: IOJN. SIZE: 8 HEX BYTES. (E) - EQUIVALENCED

NAME	MODE	DISPL.	NAME	MODE	DISPL.	NAME	MODE	DISPL.
NIN	I*4	000000	NOUT	I*4	000004			

LABEL INFORMATION.

LABEL	DEFINED	ADDR.	LABEL	DEFINED	ADDR.	LABEL	DEFINED	ADDR.
10	10	0001FC	20	11	000204	1010	15	0000A8
						1011	16	000000

STATISTICS SOURCE STATEMENTS = 17, PROGRAM SIZE = 680 BYTES, PROGRAM NAME = PRINT PAGE: 40.

STATISTICS NO DIAGNOSTICS GENERATED.

PRINT END OF COMPILATION 10 *****

IF DO	ISN	*	1.....	2.....	3.....	4.....	5.....	6.....	7*.....	8.....
-------	-----	---	-------	--------	--------	--------	--------	--------	--------	---------	--------

TEM08080

VARIABLE:

```
NUM          -- AN INTEGER NUMBER TO BE OUTPUT TO THE STATUS FILE
```

TEM08200

TEM08220

COMMON /IOUN/ NIN, NOUT

```
IF (ICODE .NE. 5) WRITE(NOUT,1005)
```

FORMAT(///)

```
IF (ICODE .EQ. 1) WRITE(NOUT,1010)
```

```
FORMAT(2X,'>> ERROR << MAXIMUM NUMBER OF BLOCKS ALLOWED IN THE',  
' PROGRAM IS 7000. --- PROGRAM TERMINATED.')
```

```
IF ( ICODE .EQ. 2) WRITE(NOUT,1020)
```

```

FORMAT(2X,'>> ERROR << GAS CONSTANT R SHOULD NOT BE ZERO.',
      '
      '
      ' --- PROGRAM TERMINATED.')

```

IF (ICODE .EQ. 3) WRITE(NOUT,1030) NAM

```

FORMAT(2X,'>> ERROR << NO INPUT DATA FOR BLOCK NUMBER ',I2,
      ' , ---- PROGRAM TERMINATED.')
```

```
IF (ICODE .EQ. 4) WRITE(NOUT,1040)
```

```

FORMAT(2X,'>> ERROR << TOTAL NUMBER OF TIME STEPS IN ONE THERMAL
      ' CYCLE IS GREATER THAN 50.',

```

' -- PROGRAM TERMINATED.')

```
IF (ICODE .EQ. 5) WRITE(NOUT,1050)
```

```
FORMAT(//,2X,'>>> CURRENT DAMAGE IS GREATER THAN OR EQUAL TO ',  
      '1.0.')
```

RETURN

2

SYMBOL CROSS REFERENCE DICTIONARY

PROGRAM NAME: MESSAGE.

TAG: ARRAY(A) EQUIVALENCED(E) STATEMENT FUNCTION(F) GENERIC NAME(G) COMMON(C) PADDED(Q)
 PROMOTED(P) DUMMY ARGUMENT(D) EXTERNAL SUBPROGRAM(X) NAMED CONSTANT(K) DYNAMIC COMMON(Y) SUBPROGRAM NAME(R)
 ASSIGNED(S) INITIAL VALUE(V) EXPLICITLY TYPED(T) INTRINSIC FUNCTION(I) ENTRY(N)

NAME	MODE	TAG	DECLARED	REFS	(F:REFD	S:SET	B:REFD/MAY BE SET)
ICODE	I*4	D	1	3F	6F	9F	12F 15F 18F
MESSAGE	R		1				
NIN	I*4	C	2	UNREFERENCED			
NOUT	I*4	C	2	4F 7F	10F	13F	16F 19F
NUM	I*4	D	1	13F			

LABEL CROSS REFERENCE DICTIONARY

TAG: FORMAT(F) NON-EXECUTABLE(N) USED AS ARGUMENT(A) OBJECT OF BRANCH(B) USED IN ASSIGN STATEMENT(S)

LABEL	TAG	DEFINED	REFERENCES
1005	NF	5	4
1010	NF	8	7
1020	NF	11	10
1030	NF	14	13
1040	NF	17	16
1050	NF	20	19

STORAGE MAP

TAG: SET(S) ENTRY(IN) ASSIGNED(S) IN COMMON(C) EQUIVALENCED(E) INITIAL VALUE(V) INTRINSIC FCT(I)
 REFERENCED(F) SUBPROGRAM(X) NAMED CONSTANT(K) STATEMENT FUNCTION(T) USED AS ARGUMENT(A) SUBPROGRAM NAME(R)

PROGRAM NAME: MESSAGE. SIZE OF PROGRAM: 438 HEX BYTES.

NAME	MODE	TAG	ADDR.	NAME	MODE	TAG	ADDR.	NAME	MODE	TAG	ADDR.
ICODE	I*4	F	000340	MESSAGE	R		000000	NIN	I*4	C	UNREFD
NUM	I*4	FA	00033C	VFIXF#	FX		000344	VFWF#	FX		000348
								NOUT	I*4	FCA	000004

COMMON INFORMATION

NAME: IOUN. SIZE: 8 HEX BYTES. (E) - EQUIVALENCED

NAME	MODE	DISPL.	NAME	MODE	DISPL.	NAME	MODE	DISPL.
NIN	I*4	000000	NOUT	I*4	000004			

LABEL INFORMATION.

LABEL	DEFINED	ADDR.	LABEL	DEFINED	ADDR.	LABEL	DEFINED	ADDR.
1005	5	00026C	1010	8	000203	1020	11	0001B0
1040	17	0000E7	1050	20	0000A8	1030	14	00015D

STATISTICS SOURCE STATEMENTS = 16, PROGRAM SIZE = 1080 BYTES, PROGRAM NAME = MESSAGE PAGE: 43.

STATISTICS NO DIAGNOSTICS GENERATED.

MESSAGE END OF COMPILATION 11 *****

ORIGINAL FILED
 OF POOR QUALITY

LEVEL 2.1.1 (SEPT 1986) VS FORTRAN DATE: JUL 30, 1987 TIME: 15:24:15

SUMMARY OF MESSAGES AND STATISTICS FOR ALL COMPILATIONS

STATISTICS	SOURCE STATEMENTS = 73, PROGRAM SIZE = 30776 BYTES, PROGRAM NAME = MAIN	PAGE: 1.
STATISTICS	NO DIAGNOSTICS GENERATED.	
MAIN	END OF COMPILATION 1 *****	
STATISTICS	SOURCE STATEMENTS = 47, PROGRAM SIZE = 2482 BYTES, PROGRAM NAME = INPUT	PAGE: 11.
STATISTICS	NO DIAGNOSTICS GENERATED.	
INPUT	END OF COMPILATION 2 *****	
STATISTICS	SOURCE STATEMENTS = 12, PROGRAM SIZE = 506 BYTES, PROGRAM NAME = PREXPO	PAGE: 16.
STATISTICS	NO DIAGNOSTICS GENERATED.	
PREXPO	END OF COMPILATION 3 *****	
STATISTICS	SOURCE STATEMENTS = 34, PROGRAM SIZE = 1648 BYTES, PROGRAM NAME = BLKDAT	PAGE: 19.
STATISTICS	NO DIAGNOSTICS GENERATED.	
BLKDAT	END OF COMPILATION 4 *****	
STATISTICS	SOURCE STATEMENTS = 8, PROGRAM SIZE = 418 BYTES, PROGRAM NAME = INCREM	PAGE: 23.
STATISTICS	NO DIAGNOSTICS GENERATED.	
INCREM	END OF COMPILATION 5 *****	
STATISTICS	SOURCE STATEMENTS = 5, PROGRAM SIZE = 354 BYTES, PROGRAM NAME = PLSTRN	PAGE: 26.
STATISTICS	NO DIAGNOSTICS GENERATED.	
PLSTRN	END OF COMPILATION 6 *****	
STATISTICS	SOURCE STATEMENTS = 29, PROGRAM SIZE = 872 BYTES, PROGRAM NAME = GROWTH	PAGE: 29.
STATISTICS	NO DIAGNOSTICS GENERATED.	
GROWTH	END OF COMPILATION 7 *****	
STATISTICS	SOURCE STATEMENTS = 11, PROGRAM SIZE = 564 BYTES, PROGRAM NAME = DAMAGE	PAGE: 34.
STATISTICS	NO DIAGNOSTICS GENERATED.	
DAMAGE	END OF COMPILATION 8 *****	
STATISTICS	SOURCE STATEMENTS = 11, PROGRAM SIZE = 374 BYTES, PROGRAM NAME = CHECK	PAGE: 37.
STATISTICS	NO DIAGNOSTICS GENERATED.	
CHECK	END OF COMPILATION 9 *****	
STATISTICS	SOURCE STATEMENTS = 17, PROGRAM SIZE = 680 BYTES, PROGRAM NAME = PRINT	PAGE: 40.

LEVEL 2.1.1 (SEPT 1986) VS FORTRAN DATE: JUL 30, 1987 TIME: 15:24:15 NAME: MAIN PAGE: 47

STATISTICS NO DIAGNOSTICS GENERATED.

PRINT END OF COMPILATION 10 *****

STATISTICS SOURCE STATEMENTS = 16, PROGRAM SIZE = 1080 BYTES, PROGRAM NAME = MESSAGE PAGE: 43.

STATISTICS NO DIAGNOSTICS GENERATED.

MESSAGE END OF COMPILATION 11 *****

***** SUMMARY STATISTICS ***** 0 DIAGNOSTICS GENERATED. HIGHEST SEVERITY CODE IS 0.

DISTRIBUTION LIST

L. F. Aprigliano
D. W. Taylor Naval Ship R&D Ctr
Annapolis, MD 21402

M. M. Bailey
NASA Lewis Research Center
21000 Brookpark Road (77-6)
Cleveland, OH 44135

Michael Bak
Williams International
P.O. Box 200 (5-16)
Walled Lake, MI 48088

Dr. Richard Barkalow
Government Engine Business
Pratt & Whitney
West Palm Beach, FL 33042

H. Beale
Applied Coatings, Inc.
775 Kaderly Drive
Columbus, OH 43228

Robert Beck
Teledyne - CAE
1330 Laskey Road
Toledo, OH 43612

E. J. Beltran
Materials & Process Tech. Lab.
General Electric Company
1000 Western Avenue
Lynn, MA 01905

Biliyar N. Bhat
NASA Marshall Space Flight Center
Huntsville, AL 35812

David Bott
Muscle Shoals Mineral Company
1202 East 2nd Street
Muscle Shoals, AL 35661

R. J. Bratton
Westinghouse Electric R&D
1310 Beulah Road
Pittsburgh, PA 15235

Walter Bryzik
U.S. Army Tank-Auto Command
Diesel Engine Research RMSTA
Warren, MI 48397

R. F. Bunshah
University of California
6532 Boelter Hall
Los Angeles, CA 90024

Jerry Clifford
U.S. Army Applied Tech. Lab.
SAVDL-ATL-ATP
Fort Eustis, VA 23604

David L. Clingman
Allison Gas Turbine Div.
P.O. Box 420, Speed Code W-5
Indianapolis, IN 46206-0420

Arthur Cohn
E P R I
3412 Hillview Avenue
Palo Alto, CA 94303

Thomas A. Cruse
Southwest Research Inst.
6220 Culebra Rd.
P.O. Drawer 28510
San Antonio, TX 78284

Prof. Sherman D. Brown
University of Illinois
105 South Goodwin Avenue
Urbana, IL 61801

Mr. William Drawl
270 Materials Research Lab.
Penn State University
University Park, PA 16802

DISTRIBUTION LIST (Continued)

Keith Duframe Battelle Laboratories 505 King Avenue Columbus, OH 43216	Mr. Ralph Hecht Pratt & Whitney P.O. Box 2691 West Palm Beach, FL 33402
Mrityunjy Dutta U.S. Army AMSAV-EAS 4300 Goodfellow Boulevard St. Louis, MO 63120	Harold Herman Argonne National Laboratory 9700 South Cass Avenue Argonne, IL 60439
John Fairbanks Department of Energy Office of Fossil Energy Washington, DC 20545	H. Herman Detroit Diesel Allison - GMC P.O. Box 894 (W-8) Indianapolis, IN 46206
N. Geyer AFWAL/MLLM Wright Patterson, A.F.B. Dayton, OH 45433	Prof. H. M. Herman Dept. of Materials Science State Univ. of New York Stonybrook, NY 11794
J. W. Glatz NAPTC R&D Division Naval Air Prop. Test Center Trenton, NJ 08628	Frank Hermanek Alloy Metals, Inc. 1972 Meijer Drive Troy, MI 48084
Turbine Components Corp. 2 Commercial Street Branford, CT 06405	R. Hillary General Electric Company 1 Neuman Way Cincinnati, OH 45215
Dr. H. C. Graham Aerospace Research Laboratory Building 450 (ARZ) Wright Patterson A.F.B. Dayton, OH 45433	J. Stan Hilton University of Dayton 300 College Park Dayton, OH 45469
D. K. Gupta Pratt & Whitney 400 Main Street East Hartford, Ct 06108 MS 114-41	Richard R. Holmes NASA Marshall Space Flight Center Huntsville, AL 35812
William K. Halman Temescal 2850 Seventh Street Berkeley, CA 94710	Lulu Hsu Solar Turbines, Inc. 2200 Pacific Highway San Diego, CA 92138
Doug Harris APS - Materials, Inc. 153 Walbrook Dayton, OH 45405	Information Center Metals & Ceramics Battelle Columbus Laboratories 505 King Avenue Columbus, OH 43201

DISTRIBUTION LIST (Continued)

Dr. R. L. Jones
Chemistry Division
Naval Research Laboratory
Code 6170
Washington, DC 20375

Propulsion Laboratory
U.S. Army Research & Technology
Laboratory
21000 Brookpark Road (302-2)
Cleveland, OH 44135

H. C. Larson
Caterpillar, Inc.
Technical Center
Peoria, IL 61629

Sylvester Lee
AFWAL-MLTM
Wright Patterson A.F.B.
Dayton, OH 45433

A. V. Levy
Lawrence Berkeley Laboratory
University of California
Berkeley, CA 94720

E. L. Long, Jr.
Oak Ridge National Laboratory
P.O. Box X, Bldg. 4508
Oak Ridge, TN 37831

Frank N. Longo
Metco, Inc.
1101 Prospect Avenue
Westbury, L.I., NY 11590

Dr. Krishan L. Luthra
Research & Development Center
General Electric Company
P.O. Box 8
Schenectady, NY 12301

Richard Martin
Boeing Commercial Airplane Co.
P.O. Box 3707 (9W-61)
Seattle, WA 98124

T. E. Mitchell
Los Alamos Research Laboratory
P.O. Box 1663
Los Alamos, NM 87545

Michael L. Moore
Aircraft Propulsion Eng.
Trans World Airlines, Inc.
P.O. Box 20126
Kansas City, MO 64195

S. Naik
AVCO-Lycoming Division
550 South Main Street
Stratford, CT 06497

R. Novak
United Technologies Research Center
Silver Lane MS 22A
East Hartford, CT 06108

Dr. F. S. Pettit
Department of Met. & Materials
University of Pittsburgh
848 Benedum Hall
Pittsburgh, PA 15261

Dr. B. Pletka
Michigan Technical University
Dept. of Metallurgical Eng.
Houghton, MI 49931

R. J. Quentmeyer
NASA Lewis Research Center
21000 Brookpark Road (500-200)
Cleveland, OH 44135

Prof. Robert A. Rapp
Department of Metals Eng.
Ohio State University
116 W. 19th Avenue
Columbus, OH 43210

Gopal Revanton
Deer & Company
3300 River Drive
Moline, IN 61265

DISTRIBUTION LIST (Continued)

David Rigney
General Electric Company
Cincinnati, OH 45215

Joseph Scricca
AVCO-Lycoming Division
550 South Main Street
Stratford, CT 06497

Ravi Shankar
Chromalloy R&T
Chromalloy Amer. Corp.
Orangeburg, NY 10982

Keith Sheffler
Pratt & Whitney
400 Main Street
East Hartford, CT 06108
MS 114-41 (8 copies)

R. W. Soderquist
Pratt & Whitney
400 Main Street
East Hartford, CT 06108
MS 165-03

T. E. Strangman
Garrett Auxiliary Power Div.
2739 E. Washington Street P.O. Box 5227
Phoenix, AZ 85010

Dr. John Stringer
Electric Power Research Inst.
P.O. Box 10412
3412 Hillview Avenue
Palo Alto, CA 94304

T. A. Taylor
Linde Division
Union Carbide Corporation
Indianapolis, IN 46224

Robert P. Tolokan
Brunswick Corporation
2000 Brunswick Lane
DeLand, FL 32724

F. C. Toriz
Rolls Royce, Inc.
1985 Phoenix Boulevard
Atlanta, GA 30349

Donald Whicker
GM Research Laboratory
GM Technical Center
Warren, MI 48090

Dr. I. G. Wright
Battelle Memorial Institute
505 King Avenue
Columbus, OH 43201

Dr. T. Yonushonis
Cummins Engine Company, Inc.
Box 3005
Columbus, IN 47202

NASA Scientific and Tech. Info. Fac.
Attn: Acquisition Branch
Baltimore Washington Int'l
Airport
P.O. Box 8757
Baltimore, MD 21240 (25 copies)

Dr. Mark Van Roode
Solar Turbines, Inc.
2200 Pacific Highway
P.O. Box 85376
San Diego, CA 92138-5376

1. REPORT NO. CR 182230	2. GOVERNMENT AGENCY	3. RECIPIENT'S CATALOG	
4. TITLE AND SUBTITLE Thermal Barrier Coating Life Prediction Model Development		5. REPORT DATE December 1989	6. PERFORMING ORG. CODE
7. AUTHORS Jeanine T. DeMasi, Milton Ortiz	APPROVED BY: Keith D. Sheffler	8. PERFORMING ORG. REPT. NO. PWA-5970-40	
9. PERFORMING ORG. NAME AND ADDRESS UNITED TECHNOLOGIES CORPORATION Pratt & Whitney Commercial Engine Business		10. WORK UNIT NO.	11. CONTRACT OR GRANT NO. NAS3-23944
12. SPONSORING AGENCY NAME AND ADDRESS National Aeronautics and Space Administration Lewis Research Center 21000 Brookpark Road, Cleveland, Ohio 44135		13. TYPE REPT./PERIOD COVERED Final Report	14. SPONSORING AGENCY CODE
15. SUPPLEMENTARY NOTES Project Manager: Dr. Robert A. Miller NASA Lewis Research Center, Cleveland, Ohio			
16. ABSTRACT The objective of this program was to establish a methodology to predict thermal barrier coating (TBC) life on gas turbine engine components. The approach involved experimental life measurement coupled with analytical modeling of relevant degradation modes. Evaluation of experimental and flight service components indicate the predominant failure mode to be thermomechanical spallation of the ceramic coating layer resulting from propagation of a dominant near interface crack. Examination of fractionally exposed specimens indicated that dominant crack formation results from progressive structural damage in the form of subcritical microcrack link-up. Tests conducted to isolate important life drivers have shown MCrAlY oxidation to significantly affect the rate of damage accumulation. Mechanical property testing has shown the plasma deposited ceramic to exhibit a non-linear stress-strain response, creep and fatigue. The fatigue based life prediction model developed accounts for the unusual ceramic behavior and also incorporates an experimentally determined oxide rate model. The model predicts the growth of this oxide scale to influence the intensity of the mechanical driving force, resulting from cyclic strains and stresses caused by thermally induced and externally imposed mechanical loads.			
17. KEY WORDS (SUGGESTED BY AUTHOR(S)) Thermal Barrier Coating Failure Mechanisms Life Prediction		18. DISTRIBUTION STATEMENT	
19. SECURITY CLASS THIS (REPT) Unclassified	20. SECURITY CLASS THIS (PAGE) Unclassified	21. NO. PGS 341	22. PRICE

